

Dissertation  
submitted to the  
Combined Faculty of Mathematics, Engineering and Natural Sciences  
of Heidelberg University, Germany  
for the degree of  
Doctor of Natural Sciences

Put forward by  
Kevin Nico André Jahnke

born in: Hamburg, Germany  
Oral examination: 11.05.2022



# Rational engineering of cytoskeletons for synthetic cells

Referees: Dr. Kerstin Göpfrich  
apl. Prof. Dr. Michael Hausmann



## Abstract

The bottom-up engineering of synthetic cells has emerged as a powerful field to understand the complex environment and processes of natural living cells. In particular, the development and reconstitution of synthetic cells with a cytoskeleton sets a major milestone and challenge for this aim because it is an essential, versatile and multifunctional part of all eukaryotic cells. However, current progress is limited because natural cytoskeletal components are difficult to purify, deliberately engineer and reconstitute within synthetic cells which therefore limits the otherwise multifaceted role of modern cytoskeletons. In this work, I explore means by which natural cytoskeletons can be engineered to assist the shape governing function and motility of synthetic cells. Moreover, I design synthetic cytoskeletons made from deoxyribonucleic acid (DNA) as a building block to overcome current limitations of natural cytoskeletons with DNA as a programmable and versatile tool. I show that DNA-based cytoskeletons can be reversibly assembled inside compartments with multiple stimuli, bundled into more rigid filaments, used for compartment deformation and as tracks for intracellular vesicle transport. This showcases the power of DNA cytoskeletons for bottom-up synthetic cell assembly as fully engineerable entities. All in all, I have shown how to rationally construct multifunctional natural and synthetic cytoskeletons that pave the way for engineering a synthetic cell that truly deserves its name.

## Zusammenfassung

Das Bottom-up-Engineering synthetischer Zellen hat sich zu einem wichtigen Feld entwickelt, um die komplexe Umgebung und die Prozesse natürlicher, lebender Zellen zu verstehen. Insbesondere die Entwicklung und Rekonstitution synthetischer Zellen mit einem Zytoskelett stellt einen wichtigen Meilenstein und eine Herausforderung für dieses Ziel dar, da es ein wesentlicher, vielseitiger und multifunktionaler Bestandteil aller eukaryotischen Zellen ist. Der derzeitige Fortschritt ist jedoch begrenzt, da natürliche Zytoskelettkomponenten nur schwer aufzureinigen, gezielt zu verändern und in synthetischen Zellen zu rekonstituieren sind, wodurch die sonst vielseitige Rolle moderner Zytoskelette eingeschränkt wird. In dieser Arbeit untersuche ich, wie natürliche Zytoskelette so gestaltet werden können, dass sie die formgebende Funktion und Beweglichkeit synthetischer Zellen unterstützen. Darüber hinaus entwerfe ich synthetische Zytoskelette aus Desoxyribonukleinsäure (DNS) als Baustein, um die derzeitigen Einschränkungen natürlicher Zytoskelette mit DNS als programmierbarem und vielseitigem Werkzeug zu überwinden. Ich zeige, dass DNS-basierte Zytoskelette innerhalb von Kompartimenten mit verschiedenen Stimuli reversibel zusammengesetzt, zu steiferen Filamenten gebündelt, zur Deformation von Kompartimenten und als Bahnen für den intrazellulären Vesikeltransport verwendet werden können. Dies zeigt, wie leistungsfähig DNS-Zytoskelette für den synthetischen bottom-up Zellaufbau sind, da sie vollständig konstruierbar sind. Alles in allem habe ich präsentiert, wie man auf rationale Weise multifunktionale natürliche und synthetische Zytoskelette konstruieren kann, die den Weg für die Entwicklung einer synthetischen Zelle ebnen, die ihren Namen wirklich verdient.

# Contents

<b>List of Figures</b>	<b>7</b>
<b>List of Tables</b>	<b>9</b>
<b>List of Abbreviations</b>	<b>13</b>
<b>1 Motivation</b>	<b>15</b>
<b>2 Introduction</b>	<b>17</b>
2.1 Synthetic biology . . . . .	17
2.1.1 What is life? . . . . .	17
2.1.2 Building blocks of natural cells . . . . .	18
2.1.3 Engineering synthetic cells from the bottom-up . . . . .	19
2.2 Compartment types . . . . .	20
2.2.1 Microfluidic water-in-oil droplets and fluid mechanics . . . . .	21
2.2.2 Lipid vesicles and membrane biophysics . . . . .	25
2.3 Cytoskeletons for synthetic cells . . . . .	29
2.3.1 Natural protein-based cytoskeletons . . . . .	29
2.3.2 Synthetic DNA-based cytoskeletons . . . . .	31
<b>3 Publications</b>	<b>34</b>
3.1 Publications within the framework of this thesis . . . . .	34
3.2 General information on publications . . . . .	36
3.3 Author contributions . . . . .	37
3.4 Publication 1: Acto-myosin-assisted pulling of lipid nanotubes from lipid vesicles and cells . . . . .	40
3.5 Publication 2: Autonomous directional motion of actin-containing cell-sized droplets . . . . .	48
3.6 Publication 3: Engineering light-responsive contractile actomyosin networks with DNA nanotechnology . . . . .	57
3.7 Publication 4: Choice of fluorophore affects dynamic DNA nanostructures . . . . .	67
3.8 Publication 5: Proton gradients from light-harvesting <i>E. coli</i> control DNA assemblies for synthetic cells . . . . .	78
3.9 Publication 6: Functional DNA-based cytoskeletons for synthetic cells	88
3.10 Publication 7: Bottom-up assembly of synthetic cells with a DNA cytoskeleton . . . . .	117

3.11	Publication 8: Division and regrowth of phase-separated giant unilamellar vesicles . . . . .	142
<b>4</b>	<b>Discussion</b>	<b>152</b>
4.1	Natural cytoskeletons for synthetic cells . . . . .	152
4.1.1	Control over synthetic cell morphology . . . . .	152
4.1.2	Control over synthetic cell motility . . . . .	153
4.1.3	Control over synthetic cell contractility . . . . .	154
4.2	Synthetic cytoskeletons with programmable functionality . . . . .	155
4.2.1	Dynamic DNA origami structures to deform GUVs . . . . .	155
4.2.2	DNA filaments as multifunctional cytoskeletons . . . . .	156
4.2.3	DNA as a tool to study biophysics . . . . .	158
4.3	Natural versus synthetic cytoskeletons . . . . .	159
<b>5</b>	<b>Summary</b>	<b>160</b>
<b>A</b>	<b>Supporting Information</b>	<b>162</b>
A.1	Supporting Information for Publication 1: Acto-myosin-assisted pulling of lipid nanotubes from lipid vesicles and cells . . . . .	162
A.2	Supporting Information for Publication 2: Autonomous directional motion of actin-containing cell-sized droplets . . . . .	194
A.3	Supporting Information for Publication 3: Engineering light-responsive contractile actomyosin networks with DNA nanotechnology . . . . .	202
A.4	Supporting Information for Publication 4: Choice of fluorophore affects dynamic DNA nanostructures . . . . .	230
A.5	Supporting Information for Publication 5: Proton gradients from light-harvesting <i>E. coli</i> control DNA assemblies for synthetic cells . . . . .	250
A.6	Supporting Information for Publication 6: Functional DNA-based cytoskeletons for synthetic cells . . . . .	285
A.7	Supporting Information for Publication 7: Bottom-up assembly of synthetic cells with a DNA cytoskeleton . . . . .	320
A.8	Supporting Information for Publication 8: Division and regrowth of phase-separated giant unilamellar vesicles . . . . .	355
<b>B</b>	<b>List of Publications</b>	<b>395</b>
<b>C</b>	<b>Permissions</b>	<b>397</b>
	<b>Bibliography</b>	<b>417</b>
	<b>Acknowledgements</b>	<b>426</b>





# List of Figures

2.1	Fundamental building blocks of life . . . . .	20
2.2	Versatile functions reconstituted in bottom-up assembled synthetic cells	21
2.3	Microfluidic generation of monodisperse water-in-oil droplets . . . . .	25
2.4	DNA-based cytoskeletons for synthetic cells . . . . .	32



# List of Tables

2.1	Basic properties of DNA. . . . .	31
2.2	Cytoskeletal DNA structures for synthetic cells . . . . .	32



# List of Abbreviations

**ATP** adenosine triphosphate.

**CMNB** bis-(5-carboxymethoxy-2-nitrobenzyl) ether.

**DNA** deoxyribonucleic acid.

**DOPC** 1,2-dioleoyl-sn-glycero-3-phosphocholine.

**FRAP** fluorescence recovery after photobleaching.

**GUV** giant unilamellar vesicle.

**HFE** hydrofluoroethers.

**HMM** heavy mero-myosin.

**MD** Molecular Dynamics.

**NPE** P3-(1-(2-nitrophenyl)ethyl) ester.

**NSE** Navier-Stokes equation.

**PDMS** polydimethylsiloxane.

**PEG** polyethylene glycol.

**PFPE** perfluorinated polyether.

**ssDNA** single-stranded deoxyribonucleic acid.

**SUV** small unilamellar vesicle.



# Chapter 1

## Motivation

Bottom-up synthetic biology aims to engineer a living cell from scratch. With this highly appealing, yet ambitious long-term goal in mind, it emerged as a highly interdisciplinary field with experimental and theoretical contributions from physics, chemistry, biology and mathematics. It is evident that bold questions like ‘What is life?’ and ‘Can we recreate it?’ appeal to scientists of various disciplines in their quest to understand the complex phenomenon of life. Interdisciplinarity is also a necessity in order to answer these discipline-spanning questions. After all, life is a biological phenomenon made up from chemical entities that are governed by the laws of physics and can be modeled with mathematical descriptions. Synthetic biology therefore is and requires a multidisciplinary effort to enhance our understanding of what defines life, how it emerged, where it could go and if it could possibly be any different. In more detail, synthetic biology strives to answer and shed light on the process called life with the following aims in mind:

**Aim 1: Biomedical applications** The engineering of synthetic cell-like particles has an enormous benefit for drug delivery applications. Especially in times of the COVID19-pandemic it became remarkably clear that the ability to deliberately encapsulate cargo (i.e. messenger ribonucleic acid) into liposomes and selectively deliver them to cells of choice has a huge advantage over other techniques. This was only made possible by an enhanced understanding of membrane vesicles, their manipulation and functionalization.

Moreover, looking a bit further into the future, the prospect of creating synthetic cells with desired functions i.e. to kill specific other cells, to enhance proliferation or to generate energy may provide a shortcut for current state-of-the-art medical treatments.

**Aim 2: Biophysical understanding of natural cells** Even though natural living cells are the most fundamental building blocks of life, the complexity within a single cell still remains far from understood. The simplified environment of *in vitro* reconstituted systems which only contain certain synthesized or purified genes, proteins or lipids provide a fruitful environment for testing, characterizing and probing our current knowledge on cells. The reconstituted systems thereby also showcase flaws or gaps of the current description, which would not be possible within the

complex conditions inside natural living cells.

**Aim 3: Materials engineering** One specific branch of synthetic biology takes on the exciting challenge to create a synthetic cell by fully synthetic means without any purified proteins, lipids, nucleic acids or genes. The shape and function of natural cells are not treated as a template for engineering synthetic cells but merely as one (and not ‘the’) possible solution to the development of life. While this may seem unreasonable from a purely biological background, life is most commonly defined by its functions and not the chemical nature of its molecular constituents. This justifies the use of synthetic materials to engineer life-like functionality in which any means that achieve life-like functions on an abstract level are permitted. With this freedom in component choice, the field serves as a great benefactor to materials engineering. Synthetic biologists are interested not only in the making of novel materials (i.e. metamaterials) but also in the repurposing of existing materials (i.e. deoxyribonucleic acid (DNA) nanotechnology). Therefore, the field of creating synthetic cells by purely synthetic means contributes greatly to technological advancements in the field of material sciences.

**Aim 4: Philosophy** The relatively simple question ‘What is life?’ is remarkably hard to answer. There exist many different theoretical legitimate definitions of life, however, they are either too broad or one can find exceptions. Synthetic biology tries to find an answer to this question from an experimental perspective by creating life-like entities either from the top-down by eliminating unessential genes or from the bottom-up by enhancing complexity step-by-step. Both approaches therefore contribute significantly to an enhancement of understanding life.

In addition to the question of ‘What is life’, there are also many efforts towards understanding how life on earth emerged. Similar to synthetic cells, the first cell was likely to be a very primitive one, stripped off of modern cells complexity. Therefore, the question about the origin of life poses another key motivation for bottom-up synthetic biology. Thus, the far-distant goal of creating a living cell by synthetic constituents would shed light on the question ‘What is life’ and the existence of the world as we know it.

In this PhD thesis, I will engineer dynamic and stimuli-responsive synthetic cells with a cytoskeleton towards these aims. In particular, I will demonstrate the engineering of compartment mobility and membrane modifications (Aim 1). I will develop systems made from natural proteins and DNA to control the shape of cells and giant unilamellar vesicles (GUVs) in order to understand their biophysical properties (Aim 2). Finally, I will present the development of synthetic DNA-based cytoskeletons (Aim 3) in order to engineer life-like functionality from purely synthetic building blocks (Aim 4).



# Chapter 2

## Introduction

### 2.1 Synthetic biology

In this chapter, I want to give an overview on the current definitions of life and its fundamental constituents. The latter will be especially important for engineering synthetic cells with components from natural cytoskeletons like actin filaments. Moreover, it opens up the question if life could also be different or independent from these building blocks. I will explore this question by employing DNA nanotechnology to build up synthetic cytoskeletons that can possess very similar characteristics as natural filaments even though they are rationally engineered from the bottom-up.

#### 2.1.1 What is life?

The question of ‘What is life?’ is, given its obvious relevance and simplicity, extremely difficult to answer. In the following, I will briefly give an overview on current definitions of life and where they might or do fail. This discussion will then pave the way for our focus on the engineering of synthetic cells with certain key characteristics like the possession of a multifunctional cytoskeleton or the ability to divide. Additionally, I will conclude from this that the lack of an overarching definition of life and its typical definition via its functions and not its chemistry allows us to also explore alternative - purely synthetic - possibilities of life-like architectures.

The easiest possible definition of life is descriptive by collecting physiological functions of living systems. Most commonly, these include a program, improvisation, compartmentalization, energy, regeneration, adaptability and seclusion [1]. However, given these features of a living system, a single animal of one species could not be called alive because it cannot reproduce itself [2]. Moreover, given that this definition is descriptive, it arguably does not capture the essence of life that we do not know yet. An alternative definition is based on the underlying physics of living systems and approaches the question from a physical point of view. It states that living systems are systems that are capable of decreasing or maintaining their entropy by consuming energy i.e.  $\Delta S_{\text{living}} \leq 0$  in contrast to the second law of thermodynamics which states  $\Delta S > 0$  for any closed system [3]. As appealing as this

definition might seem from a physicist's point of view, it is too general. Fire, for example, could also be seen as alive since it fuels on the dissipation of energy [2]. A third and most commonly used definition is that life is a self-sustaining chemical system capable of Darwinian evolution. This definition is more general as it relates to a 'system' and not an organism and acknowledges life as a process and not as a set of certain features. Moreover, there is evidence that any living system (the ones we know and might not know) has to undergo Darwinian evolution [4]. A major problem that does arise is for example that humans are on the verge of manipulating Darwinian evolution via directed manipulation of their genes. Even though they are theoretically still capable of undergoing evolution, they are or might not be subjected to it anymore [2]. Given these overall problems for defining life and when to call something alive, many scientists nowadays view life as a continuum process, which does not rely on defining something to be alive or not alive but rather includes a degree of liveliness [5].

All in all, this discussion shows the ambiguity of a universal definition of life while also giving an idea on what criteria a minimal synthetic cell has to fulfill. In this thesis, I will especially focus on the signalling capabilities, the division and cytoskeletal features of synthetic cells which are closely related to the key features that make up living systems.

### 2.1.2 Building blocks of natural cells

In contrast to the definition of living systems, we have a very detailed knowledge on the constituents of natural living cells. The four main macromolecules that make up a natural cell are carbohydrates, lipids, proteins and nucleic acids (Figure 2.1) [6].

Carbohydrates are the main constituents for energy production and storage within cells. The most prominent example for energy generation is glycolysis, in which glucose is degraded to produce adenosine triphosphate (ATP) and reduced nicotinamide adenine dinucleotide (NADH). Alternatively, sugar can also be formed by means of photosynthesis. This has been of particular interest for engineering synthetic chloroplast mimics that were able to harvest light energy for CO<sub>2</sub> fixation [7]. Carbohydrates also enable sensory function of cell membranes, where they are essential for cell recognition [8].

More important for this PhD thesis, however, are lipids since they are the main constituent of the compartment barrier: the membrane. Lipids are amphiphilic molecules that self-assemble into lipid bilayer membranes due to the hydrophobic effect. The lipid bilayer then acts as a semi-permeable compartment barrier enclosing an aqueous phase. Lipid vesicles i.e. membrane-enclosed aqueous containers are the main compartment choice for engineering synthetic cells due to their close resemblance of physiological conditions that we know from natural cells. They are especially interesting for this work because cell membranes are generally shaped by the cellular cytoskeleton, which can stabilize or remodel it and determine its overarching function [9].

The cytoskeleton itself, however, is made up of a different set of macromolecules, namely proteins. Proteins are catalytic units made up of amino acids that typically

serve one particular function. Actin for example, as part of the cytoskeleton, is able to polymerize into micrometer-long filaments that enhance the cellular rigidity and, whose polymerization leads to cell motility [10]. The purification and reconstitution of natural proteins is therefore a major branch in synthetic biology, because of their inherent functionality and direct relatedness to biological systems.

The structure and function of proteins is encoded within nucleic acids, as the last essential cellular macromolecule, which can be transcribed and translated into polypeptide chains that make up a protein. Nucleic acids are thus used as information storage and hence play an important role for Darwinian evolution. The profound knowledge of deoxyribonucleic acid (DNA) in biological systems and the possibility to synthesize it *in vitro* also led to the emergence of the at first sight unrelated field of DNA nanotechnology. DNA nanotechnology is a field in the material sciences which uses DNA as a building material for nano- and micrometer-sized architectures disregarding the natural function of DNA as a genetic storage unit [11, 12]. This led to the emergence of a broad spectrum of DNA structures with multiple different functions for versatile fields [13] including synthetic biology [14].

In the following sections, we will explore two types of compartments, which are water-in-oil droplets and giant unilamellar lipid vesicles. Moreover, I will discuss how to fill the compartments with functions, in particular cytoskeletons, and explain the respective advantages of protein reconstitution and DNA nanotechnology towards this aim.

### 2.1.3 Engineering synthetic cells from the bottom-up

Now that we know the key constituents of natural cells, we can take a deeper look into the engineering of synthetic cells. In order to engineer synthetic cells, there are typically two key questions: First, which compartment type do I choose? Second, what function do I want to establish? On the one hand, this is the case because there are different compartment types available i.e. water-in-oil droplets, polymerosomes and lipid vesicles [16]. On the other hand, it is still very difficult to engineer multiple functions within one giant unilamellar vesicle (GUV), which is why one typically focuses on a particular function to establish. The type of functions can vary from translating certain genes [17, 18], engineering coacervates [19, 20], mimicking signalling cascades [21, 22], encapsulating natural cytoskeletons [23, 24] to using them for energy generation [7, 25, 26] (Figure 2.2). Notably, there have also been diverse efforts to engineer a synthetic cell that does not rely on proteins. The most prominent examples to include functionality employ DNA nanotechnology to create functional higher order structures by design. In this regard, a scramblase [27], cytoskeletal proteins [28], synthetic membrane channels [29, 30] or cell-cell contacts [31] have been built and employed for synthetic cell assembly.

A major drawback of current approaches, however, is their limited potential for multifunctionality: It is challenging to combine the diverse functional modules in one synthetic cellular compartment. In this work, I aim to overcome this issue and establish multiple different functions within one droplet or GUV using actin-based natural and DNA-based synthetic cytoskeletons. I therefore envision to narrow the

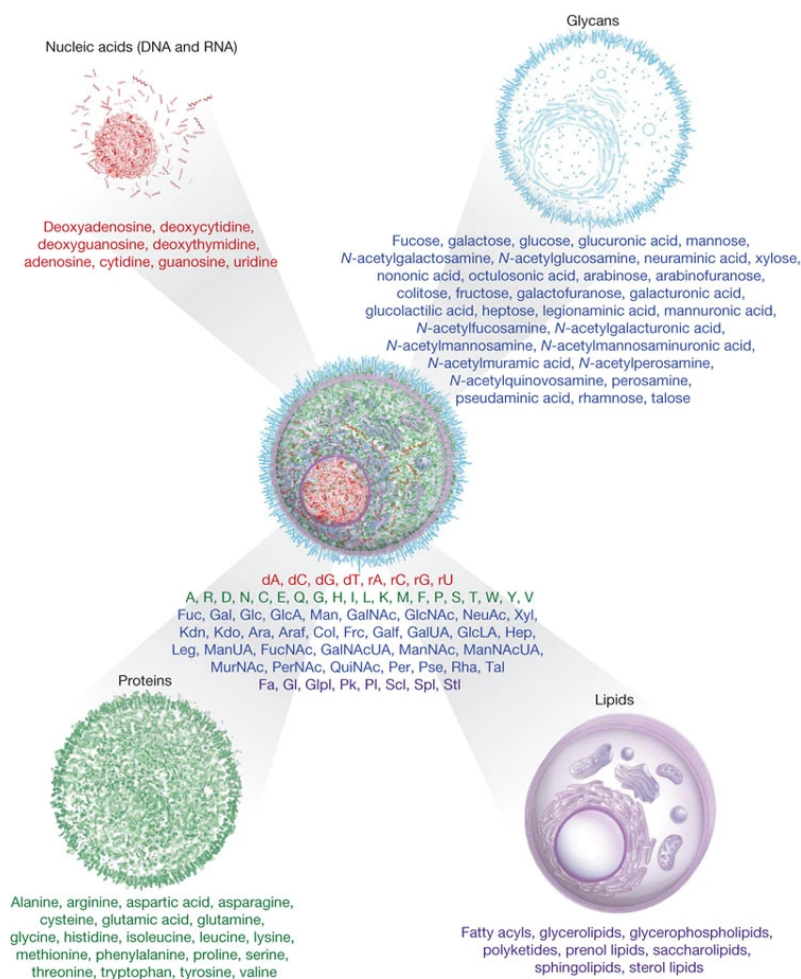


Figure 2.1: Fundamental building blocks of life. The four main macromolecules that make up a natural cell are nucleic acids, carbohydrates (glycans), proteins and lipids. Reprinted with permission from [15].

complexity gap between natural cells and current synthetic cell models and pave the way for truly synthetic cells.

## 2.2 Compartment types

One of the most striking observations of natural living cells is that they are compartmentalized [32]. Compartmentalization allows a cell to have its own chemical environment within a confined reaction space. The distinct chemical environment enables different cells to perform different functions and therefore to differentiate. The confined reaction space, on the other hand, leads to a faster reaction kinetics by decreasing diffusion times. The compartment size typically ranges from 1-100  $\mu\text{m}$ . Why are cells not smaller or bigger? Cells are not smaller because they need a certain volume to accommodate the necessary amount of proteins and nucleic acid to perform its most basic functions e.g. reproduction and transfer of genetic material. A bacterium with a diameter of 1  $\mu\text{m}$  ‘only’ contains  $4.2 \times 10^7$  proteins molecules

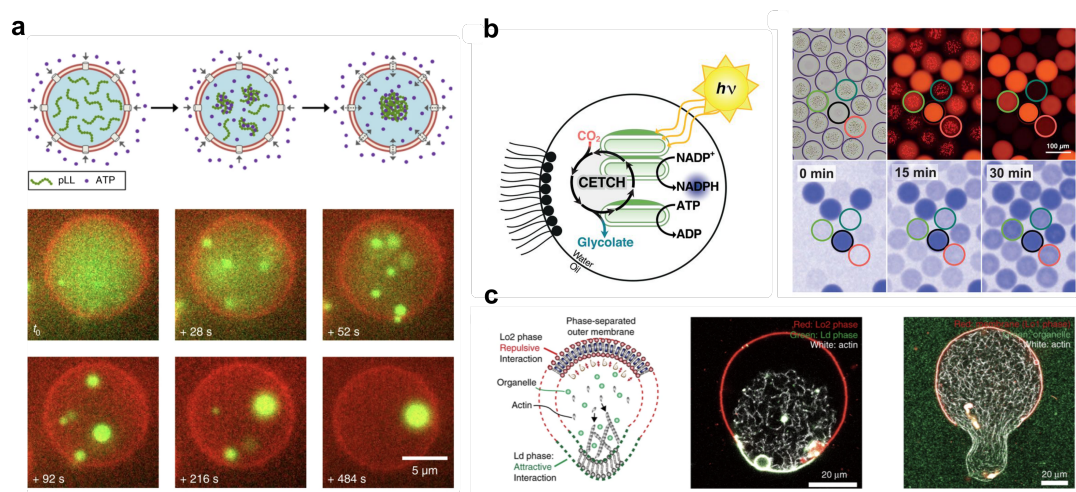


Figure 2.2: Versatile functions reconstituted in bottom-up assembled synthetic cells. **a** Coacervation within GUVs upon ATP influx. Reprinted with permission from [19]. **b** Light-harvesting chloroplast mimics for  $\text{CO}_2$  fixation. Encapsulated photosynthetic membranes lead to energy generation that can be used for the synthetic crotonyl-coenzyme A (CoA)/ethylmalonyl-CoA/hydroxybutyryl-CoA (CETCH) cycle. Reprinted with permission from [7]. **c** Deformation of actin-containing phase-separated GUVs due to actin polymerization. Reprinted with permission from [23].

[33]. A single protein therefore already represents a concentration of 1.67 nM. On the contrary, cells typically do not grow bigger than  $100 \mu\text{m}$  in length because of the decrease in their surface to volume ratio and their need to uptake nutrients via their surface i.e. their membrane [34, 35]. A simple approximation reveals that a spherical cell with a radius of  $r_i = 1 \text{ mm}$  would have to find ways to enhance the uptake via the membrane by a factor of 100 compared to a cell with a radius of  $r_j = 10 \mu\text{m}$ :

$$\frac{A_j/V_j}{A_i/V_i} = \frac{r_i}{r_j} = 100. \quad (2.1)$$

As both of these size boundaries also apply for synthetic cells that are supposed to have the same functionality as natural cells, we need to establish and employ mechanisms that allow us to encapsulate cargo within compartment sizes from  $1\text{-}100 \mu\text{m}$ . In the following, I will introduce two different compartment types, namely surfactant-stabilized water-in-oil droplets and lipid bilayer-enclosed vesicles that yield compartments in these size ranges and are widely employed for bottom-up synthetic biology.

### 2.2.1 Microfluidic water-in-oil droplets and fluid mechanics

One of the most popular compartment types in bottom-up synthetic biology are emulsion droplets. Commonly, water and oil are used as the two immiscible fluids to generate spherical emulsions droplets encapsulating an aqueous phase. The spherical shape of water-in-oil droplets can be understood as a minimization of their interfacial tension  $\gamma$ . The surface energy is minimal, when the surface-to-volume ratio

of droplets in emulsions is minimal. The geometrical shape with minimal surface-to-volume ratio is a sphere, which explains why almost all cell-sized compartments used within bottom-up synthetic biology have a spherical shape.

However, at high densities of droplets, the emulsion droplets are unstable over time because they coalesce with one another to minimize the surface free energy. Therefore, droplets are often stabilized via surfactants to prevent droplet fusion and to keep the compartment integrity. A surfactant (surface active agent) is an amphiphilic molecule that adsorbs at the water-oil interface. This decreases the interfacial tension  $\gamma$  and thereby stabilizes the water-in-oil emulsion as it prevents coalescence of droplets. The decrease in interfacial tension and therefore the amount of stabilization directly correlates with the number of adsorbed surfactant molecules:

$$\Gamma = -\frac{c}{RT} \frac{d\gamma}{dc}, \quad (2.2)$$

with  $\Gamma$  being the surfactant concentration at the interface,  $c$  the surfactant concentration in bulk,  $R$  the gas constant and  $T$  the temperature [36]. In equilibrium conditions, the surfactant concentration at the interface  $\Gamma$  and the interfacial tension  $\gamma$  are constant. However, if there is a gradient in surface tension e.g. due to a gradient in temperature across the droplet this generates a stress at the droplet interface  $\sigma$  as we can directly infer from equation 2.2 [37]:

$$\nabla\gamma \propto \frac{d\gamma}{dx} \left[ \frac{N/m}{m} \right] \propto \sigma \left[ \frac{N}{m^2} \right]. \quad (2.3)$$

The mass transfer via a gradient in surface tension is called Marangoni flow. This Marangoni flow is balanced by viscous stresses of the surrounding solutions, which in turn can lead to the propulsion of the droplet itself [38]. The order of magnitude of propulsion is:

$$v \propto \frac{r\nabla\gamma}{\eta}, \quad (2.4)$$

with  $v$  being the droplet velocity,  $r$  the droplet radius and  $\eta$  the dynamic viscosity [39, 40]. Notably, any effect that creates a gradient in surface tension will cause a tangential stress at the interface. Apart from temperature, this can also be mediated by the localized adsorption or desorption of surfactants. If we insert typical numbers  $r = 10 \mu\text{m}$ ,  $\nabla\gamma = 1 \text{ mN/m}$  and  $\eta = 1 \text{ mPa s}$  this yields propulsion velocities on the order of:  $10 \mu\text{m s}^{-1}$ .

Now that we know the constituents of droplets and their physico-chemical effects, I will discuss the formation and manipulation of surfactant-stabilized water-in-oil droplets via microfluidics. Microfluidics is an established technology for the control and manipulation of fluids on the micrometer scale. Its wide applicability ranges from disease diagnostics [41], basic molecular biology [42, 43] to inkjet printing [44]. The specific branch employed for engineering synthetic cells is droplet-based microfluidics. Droplet-based microfluidics relies on the generation of thousands of monodisperse water-in-oil emulsions on a microfluidic device, which consists of 5-300  $\mu\text{m}$ -wide channels that can be supplied with water and oil or any other immiscible fluids. The main determinant for the droplet generation is the pressure that is applied on the liquids within the microfluidic channels. I now want to discuss the

physics behind the droplet generation and subsequently highlight a few microfluidic devices that are especially relevant for this thesis.

Fluid flow on the micrometer scale, as any fluid flow, is generally described by the Navier-Stokes equation (NSE):

$$\frac{\partial \vec{u}}{\partial t} + (\vec{u} \cdot \nabla) \vec{u} = -\nabla \Phi - \frac{1}{\rho} \nabla p + \nu \Delta \vec{u}, \quad (2.5)$$

where  $\vec{u}$  is the velocity vector field,  $\Phi$  an external potential,  $\rho$  the fluid density,  $p$  the pressure field,  $\nu$  the kinematic viscosity of the fluid and we assumed that the fluid is incompressible ( $\nabla \cdot \vec{u} = 0$ ). The Navier-Stokes equation is therefore a force balance of inertia ( $\frac{\partial \vec{u}}{\partial t} + (\vec{u} \cdot \nabla) \vec{u}$ ) with external potentials ( $-\nabla \Phi$ ) pressure gradients ( $-\frac{1}{\rho} \nabla p$ ) and viscous forces ( $\nu \Delta \vec{u}$ ). Notably, it is still an open question if smooth solutions for this equation always exist [45]. However, in the case of microfluidic channels, we can propose a few reasonable assumptions and boundary conditions. The first one is that we can neglect the external potential, as we e.g. do not apply an electric field to the droplet and assume that gravitational forces are small compared to the pressure gradient and viscous flow. If we further assume a steady and fully developed flow i.e.  $\frac{\partial \vec{u}}{\partial t} = 0$  and  $\nabla \cdot \vec{u} = 0$  and transfer from cartesian to cylindrical coordinates  $u_r, u_\phi, u_x$  where we assume that  $u_r = 0$  and  $u_\phi = 0$  i.e. that no swirls occur, the left hand side of equation 2.5 vanishes. Finally, if we assume axisymmetry, we are left with:

$$0 = -\frac{1}{\rho} \nabla p + \nu \Delta \vec{u} \iff \frac{1}{r} \frac{\partial u_x}{\partial r} r \frac{\partial}{\partial r} = \frac{1}{\rho \nu} \frac{\partial p}{\partial x}. \quad (2.6)$$

Upon integration and applying the boundary conditions  $u_x(r=0) = 0$  as well as  $u_x(r=R) = 0$  this yields a velocity profile of the form:

$$u_x = \frac{1}{4\nu\rho} \frac{\partial p}{\partial x} (r^2 - R^2), \quad (2.7)$$

which is also called the Hagen-Poiseuille equation. Since  $\frac{\partial p}{\partial x}$  is typically constant across the channel length, the flow profile is parabolic with a maximum velocity in the center of the channel. A flow that can be described with the Hagen-Poiseuille equation is called laminar. Now we can deduce a useful characteristic of microfluidics: the volumetric flow rate, which is strongly determined by the channel geometries. We can calculate it by integrating the flow profile over the channel radius:

$$Q = \int_0^R u_x 2\pi r dr = \frac{\pi R^4}{8\rho\nu} \frac{\partial p}{\partial x}. \quad (2.8)$$

From this we learn that the channel geometries of microfluidic devices are of great importance for controlling fluid flow as e.g. a decrease in radius by a factor of two leads to an decrease of the flow rate by a factor of 16 when keeping the applied pressure constant. With typical flow rates for microfluidics of 10  $\mu\text{L}/\text{min}$  for the aqueous phase, and a given droplet diameter of 25  $\mu\text{m}$  (hence a volume of  $\approx 65 \text{ pL}$ ) therefore allows the generation of up to 2500 monodisperse droplets per second.

As we said earlier, these equations only hold for steady, fully developed and axisymmetrical flows. To determine if a flow actually fulfills these criteria, we can introduce

the so-called Reynolds number as a general parameter to distinguish between flow profiles. To obtain this parameter, we transform the Navier-Stokes equation for incompressible fluids in absence of any potential to its dimensionless form. By introducing a characteristic length scale  $L$  and velocity  $U$ , we get the following scaling parameters:

$$\vec{u}_* = \frac{\vec{u}}{U}, \quad (2.9)$$

$$t_* = \frac{t}{L/U}, \quad (2.10)$$

$$\nabla_* = L\nabla, \quad (2.11)$$

$$p_* = \frac{pL}{\rho U \nu}, \quad (2.12)$$

from which we obtain the dimensionless Navier-Stokes equation:

$$\frac{\partial \vec{u}_*}{\partial t_*} + (\vec{u}_* \cdot \nabla_*) \vec{u}_* = -\nabla_* p_* + \frac{\nu}{UL} \Delta_* \vec{u}_*. \quad (2.13)$$

As a measure for the flow profile, we have to determine the ratio of inertial and viscous forces. To do so, we define the Reynolds number as

$$Re = \frac{\text{inertial forces}}{\text{viscous forces}} = \frac{(\vec{u} \cdot \nabla) \vec{u}}{\nu \Delta \vec{u}} = \frac{U^2/L}{\nu U/L^2} = \frac{UL}{\nu}, \quad (2.14)$$

i.e. as the prefactor for the amount of the viscosity-related acceleration  $\Delta_* \vec{u}_*$ . At high Reynolds numbers, viscous forces are negligible and the flow profile is therefore only determined via inertia and pressure gradients. The flow is then called turbulent. On the contrary, at low Reynolds numbers viscous forces dominate and we can assume that equation 2.6 holds, which will lead to a laminar flow profile. Notably, the transition in between both flow profiles is still poorly understood, which is why typically the following definition applies:

$$Re = \frac{UL}{\nu} = \begin{cases} < 2300 & \text{laminar flow} \\ 2300 < x < 2900 & \text{intermediate} \\ > 2900 & \text{turbulent flow} \end{cases} \quad (2.15)$$

By inserting typical numbers for a microfluidic device with a channel diameter of  $100 \mu\text{m}$ , a fluid velocity of  $Q/A_{\text{cross}} = 10 \mu\text{L min}^{-1}/\pi(10 \times 10^{-6} \mu\text{m}^2)^2 = 21 \text{ mm s}^{-1}$  and a kinematic viscosity of  $1 \text{ mm}^2/\text{s}$  for water, we obtain a Reynolds number of 2.1, which means that the flow within a microfluidic device is laminar and follows the Hagen-Poiseuille equation 2.7.

All in all, we have found that the flow profile in microfluidics is laminar, that it can be used to generate monodisperse water-in-oil droplets at rates of several kHz and that the physicochemical environment of the droplet is influenced by the surfactant molecule.



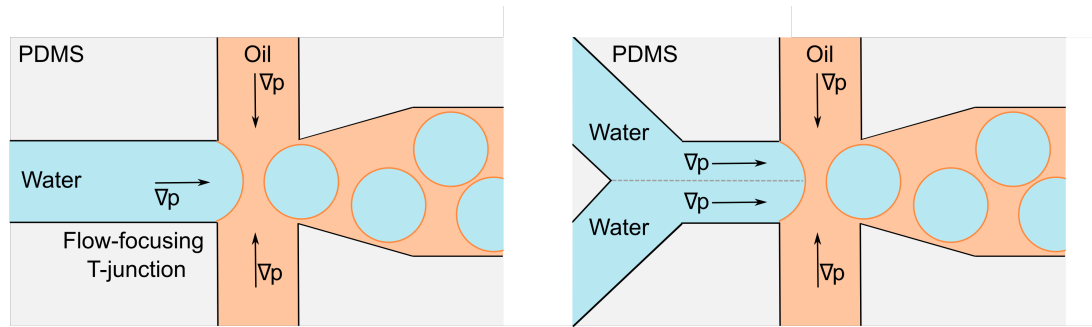


Figure 2.3: Microfluidic generation of monodisperse water-in-oil droplets with a single (left) and a double-inlet device (right) at a flow-focusing T-junction. Liquid solutions are propelled through microfluidic channels via pressure gradients that can be supplied with pressure pumps. At a flow-focusing T-junction, the oil phase cuts off the aqueous solution and generates monodisperse water-in-oil compartments. Typically, the oil phase contains a surfactant that self-assembles at the water-oil interface and stabilizes the droplet. An alternative design is the use of a two-inlet device (right image), which can supply two aqueous phases and prevents mixing of the solutions before encapsulation.

Finally, we want to take a look at two different microfluidic devices in more detail. Figure 2.3 depicts a schematic representation of the droplet generating junction of two microfluidic polydimethylsiloxane (PDMS)-devices. The simplest device to generate droplets contains only a single inlet for the aqueous phase and another one for the oil inlet. The flows are generated with pressure gradients that can be supplied via pressure pumps. At a flow-focusing T-junction the aqueous phase is cut off by the oil phase, which leads to the generation of monodisperse water-in-oil droplets at up to kHz-frequencies. In order to stabilize the compartment, the oil phase (consisting of fluorinated oils like hydrofluoroethers (HFE)) contains perfluorinated polyether (PFPE)-polyethylene glycol (PEG) surfactants that accumulate at the water-in-oil droplet interface and stabilize the compartment. A second microfluidic device that was used for the study is the so-called two-inlet device, which has two different channels for the supply of the aqueous phase. These merge just before arriving at the flow focusing T-junction and only mix after the encapsulation due to the laminar flow profile at their interface. This device therefore allows to encapsulate components that should not mix before the encapsulation. In this work, the advantages of the reliable generation of monodisperse surfactant-stabilized water-in-oil droplets was used for the encapsulation of an actin cytoskeleton (Publications 2 and 3) as well as for DNA-based nanostructures (Publications 4, 5 and 6).

## 2.2.2 Lipid vesicles and membrane biophysics

We have seen that droplet-based microfluidics has great advantages when it comes to the reliable encapsulation of cargo into monodisperse water-in-oil droplets at kHz-frequencies. However, the physicochemical environment of water-in-oil droplets also has its limitations. Two key differences are the absence of a lipid bilayer as compartment boundary and the presence of the oil phase in the outer solution. Whereas this

ensures compartment stability, it limits the possibilities for multicellular assemblies, morphology changes or transfer of material between synthetic cells. Moreover, it restricts the use of proteins for bottom-up synthetic cell assembly on the inside of the compartment, neglecting transmembrane or extracellular proteins. This is why lipid vesicles are a more physiologically relevant and versatile - albeit more difficult to handle - compartment choice.

Lipid vesicles are compartments enclosed by a lipid bilayer. They form through self-assembly of amphiphilic lipids via hydrophobic interactions. Each lipid has a hydrophilic headgroup and a hydrophobic tail consisting of fatty acids. The chemical properties of vesicles are therefore mainly dependent on the types of lipids present within the lipid bilayer. The most important factors are the charge of the lipid headgroup, the length of the fatty acid chain, the number of fatty acid chains per headgroup and the saturation of the fatty acid. A standard lipid that was used for this work is for example 1,2-dioleoyl-sn-glycero-3-phosphocholine (DOPC), which has an uncharged but polar headgroup, two fatty acids that are each 18 carbon atoms long and an unsaturated C-C double bond at position 9. The head group has a cross-sectional area of  $0.7 \text{ nm}^2$  and the fatty acid chains are  $2.7 \text{ nm}$  long, yielding an approximate bilayer thickness of  $6 \text{ nm}$  [46, 47]. Additionally, it has a phase transition temperature of  $-16.5 \text{ }^\circ\text{C}$ , which leads to its fluid like liquid crystalline state at room temperature [48]. Given that these properties are different for each lipid, the versatile choice of lipids is crucial for engineering synthetic cells. In accordance with this, for each vesicle-based engineered system different lipids were chosen i.e. biotinyl-modified ones (Publication 1), fluorescent ones (Publication 4), negatively charged ones (Publication 6) or phase-separating lipid mixes (Publication 7). However, the properties of lipid vesicles are not only governed by the choice of lipids but also by the physics underlying fluid membranes. In addition to the chemical toolbox for lipid modifications, we therefore now also want to gain a physical understanding of lipid vesicles.

For this purpose, I will focus on the physics of lipid membranes from a classical mechanic rather than thermodynamic point of view and expand the concept to not chemically inert elastic membranes [49]. Three basic deformations a lipid membrane can undergo are stretching, bending and compression. To describe the membrane, we will use the height function  $h(x_i, x_j)$  that defines the shape of the curved membrane. Assuming a harmonic potential between lipid molecules, we can describe the free energy cost  $G$  of stretching the membrane via:

$$G_{\text{stretch}} = \kappa_a/2 \int \left( \frac{\Delta a}{a_0} \right)^2 da, \quad (2.16)$$

with  $\kappa_a$  being the area-stretch modulus and  $\Delta a$  the change in area compared to a reference area  $a_0$ . Similarly, we can attribute a free energy cost to the thickness change of a membrane:

$$G_{\text{compression}} = \kappa_c/2 \int \left( \frac{\Delta w}{w_0} \right)^2 da, \quad (2.17)$$

with  $\kappa_c$  being the compression modulus and  $\Delta w$  the change in area compared to a reference area  $w_0$ . As basic parameters for the bending of the membrane, we will use

the so-called principal curvatures of the membrane, which are defined as eigenvalues of the Hesse-matrix of the height function:

$$\kappa_{ij} = \frac{\partial h(x_i, x_j)}{\partial x_i \partial x_j} . \quad (2.18)$$

We refer to the eigenvalues as principal curvatures  $\kappa_1$  and  $\kappa_2$  of the membrane with  $\kappa_1$  being the minimal and  $\kappa_2$  the maximal curvature. This allows us to compute the bending free energy as:

$$G_{\text{bending}} = \kappa_b/2 \int (\kappa_1 + \kappa_2)^2 da . \quad (2.19)$$

We can see that in general there can also be an attribution of the product of the two principal curvatures  $\kappa_1\kappa_2$  contributing to the bending. Therefore, instead of talking about principal curvatures, one typically defines the sum  $H = \frac{1}{2}(\kappa_1 + \kappa_2)$  as mean curvature and  $K = \kappa_1\kappa_2$  as Gaussian curvature. At this point I also want to note that a more rigorous description of the bending energy with differential geometry including the chemical properties of lipids requires the use of the so-called Helfrich-Canham Hamiltonian to describe the membrane bending [50]. This Hamiltonian is given as:

$$\hat{H} = \int (\sigma + 2\kappa_b(H - c_0) + \bar{\kappa}K) da , \quad (2.20)$$

with  $\sigma$  being the surface tension,  $c_0$  being the spontaneous curvature describing membrane asymmetry and  $\bar{\kappa}$  the saddle-splay modulus describing the membrane topology [51, 52]. However, for the case of a spherical vesicle as typically used in this study we can neglect the contribution of surface tension, we assume no membrane asymmetry and integrate of a closed surface, hence  $\sigma = 0$ ,  $c_0 = 0$  and  $\bar{\kappa} = 0$ , leaving [53]:

$$\hat{H} = \int 2\kappa_b H da = 2\kappa_b \int \left( \frac{(\kappa_1 + \kappa_2)}{2} \right)^2 da = \kappa_b/2 \int (\kappa_1 + \kappa_2)^2 da . \quad (2.21)$$

In this case, equations 2.20 and 2.19 are therefore identical. Since for a vesicle the two principal curvatures are identical,  $\kappa_1 = \kappa_2 = 1/R$  [52], and we can treat the membranes as incompressible and instretchable due to their description as a fluid, integration for a spherical vesicle yields:

$$\hat{H} = 2\kappa_b \frac{1}{R^2} \int da = 2\kappa_b \frac{1}{R^2} 4\pi R^2 = 8\kappa_b . \quad (2.22)$$

First of all, this shows that we need energy to form vesicles. Moreover, we can see the energy cost corresponding to vesicle formation is independent of the radius and therefore the same for all vesicles sizes. This is a particularly favorable result since we are mostly interested in the generation of giant unilamellar vesicles with compartment radii of 1-50  $\mu\text{m}$ . To form vesicles in these size ranges, various methods emerged over the past decades such as electroformation [54], octanol-assisted liposome assembly [55], hydration [56], continuous droplet interface crossing encapsulation [57] or the droplet-stabilized method [25, 58]. In this work, we achieve

the formation of vesicles via electroformation and the droplet-stabilized technique. For electroformation, a lipid film is covered with water and energy for the vesicle generation is supplied via an electromagnetic field and temperature. In the case of the droplet-stabilized method, small unilamellar vesicles are fused with the droplet periphery due to electrostatic interactions that provide the necessary energy to overcome the cost of vesicle formation.

Finally, we want to look at actively deformed vesicles. This can be achieved via acto-myosin-assisted pulling of lipid nanotubes from GUVs as we will see in Publication 1. There, a lipid nanotube is pulled from a spherical GUV via external forces. To quantify this pulling of lipid tethers, we start again with a simplified Helfrich-Canham Hamiltonian:

$$\hat{H} = \int (\sigma + 2\kappa_b H) da - FL, \quad (2.23)$$

for which we assumed a symmetrical membrane, closed surfaces, a cylindrical lipid nanotube with length  $L$  and an applied force  $F$ . For a cylinder, the principal curvatures are  $\kappa_1 = 1/R$  and  $\kappa_2 = 0$ , the equation therefore becomes:

$$\hat{H} = \left(\sigma + \left(\frac{1}{2R^2}\right)\right) \int da - FL = \left(\sigma + \left(\frac{1}{2R^2}\right)\right) 2\pi RL - FL, \quad (2.24)$$

with the nanotube length  $L$ . In an equilibrium, the external force applied and the membrane energy balance out, which yields:

$$FL = \left(\sigma + \left(\frac{1}{2R^2}\right)\right) 2\pi RL \iff F = 2\pi\sqrt{2\kappa_b\sigma}. \quad (2.25)$$

Additionally, we can compute the tether radius by minimizing the Hamiltonian with respect to  $R$ :

$$\frac{\partial H}{\partial R} = 0 \iff R = \sqrt{\frac{\kappa_b}{2\sigma}}. \quad (2.26)$$

By inserting typical values for the bending modulus of  $\kappa_b = 20 \text{ k}_B\text{T}$  and measured forces of  $10 \text{ pN}$  in equilibrium conditions [59], we can calculate the typical surface tension of a membrane to be on the order of  $0.015 \text{ mN/m}$  and the tether radius to be roughly  $50 \text{ nm}$ . We want to recall that the interfacial tension of water-in-oil droplets is on the order of several  $\text{mN/m}$ , which directly shows that GUVs can undergo morphological changes at much lower forces. This will be of special interest for deforming GUVs using DNA-based systems (Publications 4 and 7). Additionally, we will see in Publication 1 that the tether radius approximation is in very good agreement with our experimental findings.

To summarize, in this section I have presented two types of compartment systems that are relevant for synthetic biology, namely water-in-oil droplets and GUVs. I have shown that compartments with diameters from  $1\text{-}100 \mu\text{m}$  can be generated at a given energy cost. Moreover, we have seen that each compartment type has its own chemical environment that can be used for their manipulation (e.g. surfactants for Marangoni flow or lipids for vesicle deformation). However, our compartments are still empty. In the next chapter we want to fill the compartments with rationally engineered dynamic structures to go one step further towards synthetic cells with life-like functionality.

## 2.3 Cytoskeletons for synthetic cells

The aim of this PhD thesis is the rational engineering of cytoskeletons for synthetic cells. We already have established different ways of generating cell-sized compartments i.e. water-in-oil droplets and GUVs. As a next step, we will look in more detail at cytoskeletons in order to establish versatile functions inside these compartments. First of all, we explore how we can benefit from the use of natural cytoskeletons for this purpose and subsequently investigate means to programmably mimic and go beyond what nature provides by engineering DNA-based cytoskeletons.

Cytoskeletons are multifunctional dynamic entangled networks of filaments present within all eukaryotic cells. Among the most important functions of cytoskeletons are the intracellular transport, cell division, cell stability, cell migration and endocytosis [6]. Even though cellular cytoskeletons as a whole consist out of hundreds of proteins to perform these versatile functions, it is in general only made up of three different kinds of filaments: intermediate filaments, microtubules and actin filaments. Each filament is a polymer consisting of hundreds and thousands of subunits that govern the filament properties and functions. In natural cytoskeletons, these filament subunits are proteins that can undergo polymerization to form the filament. The polymerization of individual subunits is restricted to quasi one dimension, which is why all filaments are much longer than they are thick. Typically filaments have a mean length of several micrometers, whereas they are only about 10 nm in diameter [60]. In these size-ranges, DNA nanotechnology developed as a useful tool to programmably design structures on the nanoscale that can assemble up to the micrometer-scale via Watson-Crick-Franklin base pairing. Therefore, we will investigate means to engineer synthetic cytoskeletons that can potentially even succeed its natural counterparts.

### 2.3.1 Natural protein-based cytoskeletons

A straight-forward approach to engineer cytoskeletons inside synthetic cells is to reconstitute natural filaments. This can be done via purification of the desired protein from cells, their in vitro polymerisation and subsequent encapsulation. Given that intermediate filaments are not strictly essential for cells to survive and many of their functions remain unknown [61], we will focus on microtubules and actin filaments. Microtubules consist of two protein subunits termed  $\alpha$ -tubulin and  $\beta$ -tubulin, which polymerize into hollow filamentous structures with an outer diameter of 25 nm consisting of 13 protofilaments [62]. On the other hand, actin filaments are only made up from one protein subunit termed G-actin [63]. Actin filaments are much thinner and more flexible than microtubules with a diameter of 4-7 nm. A particularly interesting difference is their different behavior during bending. For this, we describe the filaments as beams with bending energy  $E_b$ . Similar to the treatment of membranes, we can describe the bending energy via the curvature of the beam:

$$E_b = \frac{EI}{2} \int_0^L \frac{1}{R(s)^2} ds, \text{ with } I = \int_A z^2 dA, \quad (2.27)$$

being the area moment of inertia,  $E$  being the Young's modulus of the material,  $\kappa = 1/R(s)$  the curvature of the beam,  $z$  the perpendicular distance from the neutral axis and  $A$  the cross sectional area of the beam. Note that in this case there is only one principal curvature since we treat the problem in two dimensions. This is equivalent to

$$E_b = \frac{EI}{2} \int_0^L \left| \frac{d\vec{t}}{ds} \right|^2 ds, \quad (2.28)$$

with  $\vec{t}$  being the tangent vector along the filament at point  $s$ . In case the curvature is constant along the filament, we can therefore express the bending energy as:

$$E_b = \frac{EIL}{2R^2}, \quad (2.29)$$

where  $L$  is the filament length. Moreover, we can use the tangent vector to define an important property of filaments, which is the persistence length  $l_p$ . Experimentally, the persistence length can be calculated by fitting the tangent correlation function with an exponential decay:

$$g(\Delta s) = \langle \vec{t}(s) \cdot \vec{t}(s + \Delta s) \rangle = e^{-\Delta s/l_p}. \quad (2.30)$$

Thus, the persistence length can be determined by knowing only the coordinates of the filament. Additionally, it is connected to the bending of the polymer via:

$$l_p = \frac{EI}{k_B T}, \quad (2.31)$$

with  $k_B$  being the Boltzmann constant and  $T$  the temperature. From this equation, it becomes already obvious that the different filament architecture of actin filaments and microtubules also leads to different persistence lengths. Actin filaments that are composed of two helical strands of closely packed G-actin and having a diameter of only 7 nm will have a much lower area moment of inertia compared to microtubules consisting of 13 protofilaments arranged in a hollow cylinder with a diameter of 25 nm. This has also been shown with experiments where the microtubule persistence length has been found to be on the order of several millimeter (i.e.  $l_p \gg L$ ) [64] compared to 18  $\mu\text{m}$  for actin filaments (i.e.  $l_p \simeq L$ ) [65].

Apart from the filament stiffness and persistence which is crucial for cellular morphology and shape in equilibrium, another important set of functions of cytoskeletons is based on their dynamics and remodeling in order to actively generate forces. This is especially important for bottom-up synthetic biology because it is a major challenge to engineer dynamic, motile and rearranging synthetic cells. The most prominent example of force-generating proteins are myosins. Myosins can bind to actin and lead to its ATP-dependent translocation by one subunit via a so-called power stroke. This allows a single myosin to generate forces up to a few nN [66].

In the context of synthetic biology, cytoskeletons have been successfully encapsulated in water-in-oil droplets and GUVs [67]. Actin polymerization within GUVs has been used to deform GUVs upon a light stimulus [23]. Additionally, by incorporating other actin binding proteins and motors, actin filaments have been used to deform

GUVs upon acto-myosin contraction [24, 68]. Microtubules have also been encapsulated within GUVs and kinesin-mediated aster formation has been reproducibly engineered inside water-in-oil droplets [69] and GUVs [70]. However, it remained elusive how to generate synthetic cell motility, induce symmetry breaking inside synthetic cells or if acto-myosin systems can be used from the outside to establish GUV and cell morphology. In this work, I will employ the myosin-mediated force generation to actively pull lipid nanotubes from spherical GUVs and cells (Publication 1) and to induce the contraction of reconstituted actin filaments inside water-in-oil droplets (Publication 3). Moreover, I will use reconstituted actin filaments to drive the autonomous motion of water-in-oil droplets (Publication 2) and even investigate the polymerization of actin filaments inside cell-sized compartments (Publication 6).

### 2.3.2 Synthetic DNA-based cytoskeletons

As we have seen, the reconstitution of natural cytoskeletons has proven to be very powerful for engineering synthetic cells. However, there are also many limitations and drawbacks when working with natural filaments. First and foremost, the proteins need to be purified, which is time-consuming and often highly challenging. Additionally, their handling is tedious and they are very sensitive to changes in the chemical environment. This is also why the different proteins are often incompatible with certain encapsulation techniques or require complex buffer compositions that are incompatible for different proteins. Lastly, the degree to which proteins can be engineered is comparably low since their chemical modification can interfere with their functionality and require protein design [71] or directed evolution [72]. However, since cytoskeletons consist of nanometer subunits that polymerize into micron-sized structures, we can make use of DNA nanotechnology to rationally engineer subunits made from DNA molecules that can polymerize into cytoskeletal structures.

DNA nanotechnology has emerged as a powerful tool to programmably design nucleic acids that can form higher order structures via Watson-Crick-Franklin base pairing [13]. DNA consists of a sugar and phosphate backbone and four nucleobases adenosine, cytosine, guanine and thymidine [6].

DNA property	Value
Radius	1 nm
Basepairs per helical turn	10.5
Rise per basepair	3.4 Å
Rotation per base pair	34.3°
Volume per base pair	0.1 nm <sup>3</sup>
Weight per base pair	600 Da
Energy of a hydrogen bond	2-12 k <sub>B</sub> T
Charge per nucleotide	-e (1.61 × 10 <sup>-19</sup> C)
Persistence length of dsDNA	50 nm

Table 2.1: Basic properties of DNA [73].

DNA strands up to hundred or more nucleobase pairs can be easily synthesized

via the phosphoramidite method [74]. Furthermore, many versatile functionalization strategies exist creating a large toolbox of possible DNA strands. Since nucleobases can bind via hydrogen bonding and additional base-stacking interactions, they can form a double-stranded DNA helix or a duplex. Their basic properties are listed in table 2.1. With this knowledge at hand, a tremendous library of DNA structures has emerged over the past decades. Of particular interest for synthetic biology are structures that mimic the behavior of natural proteins [14]. These include DNA-origami based scramblases [27], ion channels [29], assembly platforms [75] or adhesion sites [31]. However, in the following I want to focus on specific structures that are especially interesting for the design of cytoskeletons for synthetic cells. For this, three different DNA shapes are relevant: Y-motifs, DNA tiles and DNA origami. The table 2.2 below summarizes their use as cytoskeletons for synthetic cells.

DNA structure	On GUVs?	In GUVs?	Refs
Y-motif lattice	Yes	Yes	[28, 76]
DNA origami rod	Yes	No	[77, 78]
DNA origami square	Yes	No	[79, 80]
DNA nanotube	No	No	-

Table 2.2: Cytoskeletal DNA structures for synthetic cells

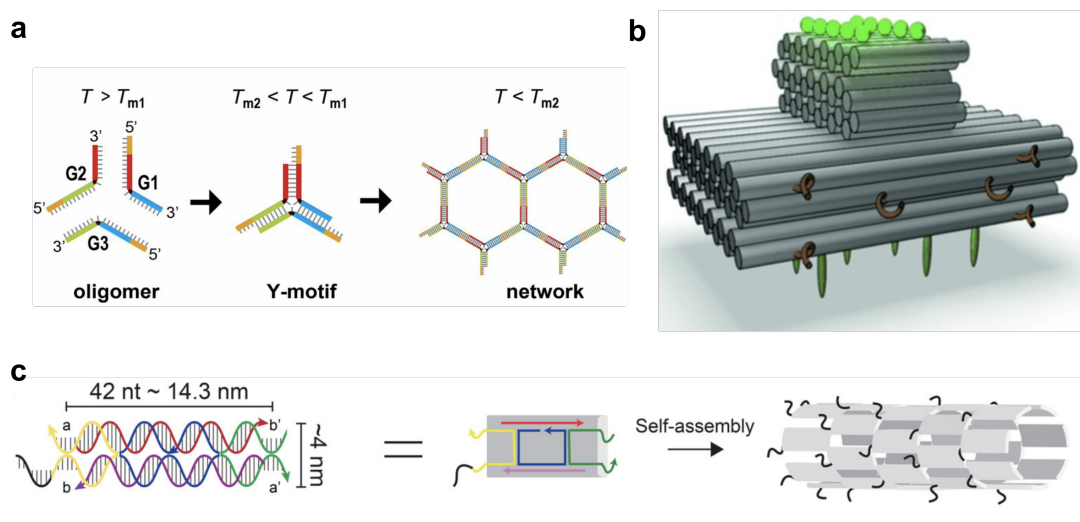


Figure 2.4: DNA-based cytoskeletons for synthetic cells. **a** Y-motifs consisting out of three individual DNA strands can polymerize into entangled networks that can be used to stabilize giant vesicles. Reprinted with permission from [28]. **b** DNA origami structure with cholesterol-anchors consisting of more than hundred staple strands. DNA origami structures can be polymerized to deform GUVs. Reprinted with permission from [79]. **c** DNA tiles consisting of five single-strands that can polymerize into micrometer long hollow tubular structures. Reprinted with permission from [81].



Y-motifs consist of three individual single-stranded DNA strands (ssDNA) with complementary overhangs that can polymerize into a lattice (Figure 2.4a). So far, it has been used inside droplets and on the inner and outer GUV membrane to stabilize giant vesicles [28, 76]. The linkage of DNA structures to the membrane can either be achieved via electrostatic interactions with polar or charged lipid head-groups or directly by modifying them covalently with lipids like cholesterol, which self-assemble into lipid bilayers. In comparison to the GUV stabilization in the case of the Y-motifs, DNA origami rods and squares have been used to deform GUVs from their spherical shape (Figure 2.4b). DNA origami are different from Y-motifs because they consist out of one long ( $> 7000$  nucleobases) scaffold strand that is brought into the desired shape via smaller DNA staple strands (typically  $< 50$  nucleobases) [11]. DNA origami rods and squares are therefore much bigger than individual Y-motifs and do have a higher rigidity, especially if the DNA origami consists of multiple layers. This is why they generate a stress on the membrane that is able to ultimately deform it. It becomes evident that most cytoskeletal DNA-based structures are only supplied from the outside to GUVs and only have the purpose to stabilize or deform vesicles. As we have discussed before, the cytoskeleton has many more functions next to the control over the cell morphology. One way to address these could potentially be by using closer filament mimics since Y-motifs and DNA origami are neither filamentous and comparably small or large, respectively. An approach to overcome this issue is the use of DNA nanotubes as filament mimics. DNA nanotubes are supramolecular DNA-based structures that contain a so-called DNA tile as a subunit, which can polymerize into hollow tubular structures (Figure 2.4c) [60]. Each DNA tile is made out of five single-strands forming a double crossover structure with four single-stranded overhangs that allow their polymerization into nanotubes [82]. This special design choice already makes them twice as rigid as a linear DNA duplex [83]. Despite the fact that DNA nanotubes have not been encapsulated inside GUVs, they have only recently been encapsulated into water-in-oil droplets [84]. Moreover, there has been much work focusing on the reversible [81] or directed assembly [85, 86], branching [87] or capping [88] of DNA nanotubes, which offers great potential for their use in synthetic cell assembly. However, their encapsulation into GUVs as well as their potential to form a cortex-like structure remains unachieved. Additionally, the development of dynamic processes like cargo transport along DNA nanotubes has not been demonstrated. In this work, I show the successful encapsulation of DNA nanotubes into water-in-oil droplets and GUVs, their stimuli-responsive reversible assembly, form cortex-like structures from within GUVs, engineer the vesicle transport along DNA nanotubes and induce the bundling of DNA nanotubes with controlled persistence lengths (Publications 6 and 7).

# Chapter 3

## Publications

### 3.1 Publications within the framework of this thesis

The present PhD thesis is based on an ‘understanding-by-engineering approach’ (i.e. ‘What I cannot create I do not understand’, Richard Feynman). Here, I seek to engineer a cell, or components of it, from the bottom up. I will focus on natural and synthetic filaments to build up a functional cytoskeleton for synthetic cells.

Each publication is therefore focused on the mimicry of one or more essential determinants that make up the complexity of the cytoskeletons of natural living cells. In this way, I will engineer GUV and cell shape (Publication 1), droplet motility (Publication 2), acto-myosin contractility (Publication 3), signalling cascades (Publication 4), pH-sensitive dynamics (Publication 5), reversible filament assembly and intracellular transport (Publication 6), shape control and filament bundling (Publication 7) and vesicle division (Publication 8). I first put to use natural cytoskeletal elements in the context of bottom-up synthetic biology (Publications 1-3) and then move on to de novo assembled filaments with engineerable characteristics made from DNA nanotechnology (Publications 4-7).

First, we will explore how the reconstitution of actin filaments as one of the main components of natural cytoskeletons can be used within the framework of bottom-up synthetic biology. Towards this aim, we develop a mechanism that allows the pulling of lipid nanotubes from giant unilamellar vesicles and cells. This mechanism therefore allows to control the GUV and cell shape (Publication 1).

Subsequently, we will perform an essential transfer step from bulk applications into cell-sized confinement. We therefore encapsulate actin filaments into cell-sized water-in-oil droplets as a reaction compartment and characterize the droplets’ autonomous rotational motion. This motion is caused by actin-induced Marangoni flows due to presence of negatively charged surfactants. By tuning the friction at the droplet interface, we transfer the rotational motion of the droplets into a translational motion (Publication 2).

Next, we will add reconstituted heavy mero-myosin as motor proteins to our actin-containing droplets. We show that the light-induced release of adenosine triphos-

phate (ATP) leads to the contraction of these acto-myosin networks. We next employ DNA nanotechnology to link actin filaments to the droplet periphery. Upon inducing the ATP release we now realize the symmetry-breaking contraction of acto-myosin networks within cell-sized confinement (Publication 3).

However, the use of purified proteins and their *in vitro* reconstitution is limited. This is for multiple reasons: i) not all proteins can be purified in their functional state, ii) their purification and reconstitution is difficult and time-consuming and iii) each protein requires a specific chemical environment, which limits the possibility to arbitrarily combine different proteins of choice. Thus, the rest of this work focuses on the use of DNA nanotechnology as synthetic mimic of cytoskeletal elements with engineerable characteristics.

In order to engineer DNA cytoskeletons, we first have to understand the dynamics of DNA nanostructures. For this reason, we investigated the pH-sensitive DNA triplex and found that the pH-sensitive dynamics of the employed triplex motif critically depends on the choice of fluorophore the DNA strand is modified with. We investigated this further with experiments and molecular dynamics simulations which revealed that the triplex is stabilized by the presence of specific fluorophores (e.g. cyanine dyes). Moreover, we found that single-stranded DNA is compactified in presence of a fluorophore. This led to an overall understanding of the free energy landscape of triplex-motif binding to complementary single-stranded DNA (Publication 4).

Following the investigation of single-stranded DNA binding, we engineer a DNA origami cytoskeleton mimic that contains a pH-sensitive triplex strand and that can deform GUVs after attaching to their membrane. To engineer complex signalling pathway within synthetic cells, we employ top-down engineered genetically modified *E. coli* that overexpress the proton pump xenorhodopsin. The genetically-modified *E. coli* induce a pH-gradient across their membrane and therefore, change the pH of the external solution. Upon the light-induced change of the pH via the *E. coli*, the DNA origami thus attaches to the GUV membrane and deforms them from their initially spherical shape (Publication 5).

To increase the functional versatility of DNA-based cytoskeletons, we employed DNA nanotubes i.e. DNA filaments that form hollow cylinder with nanometer diameters and micrometer lengths from individual DNA tile structures. The DNA tile structures can be modified with additional sequences such that they can undergo toehold-mediated strand displacement reactions that lead to filament disassembly and reassembly. We also show that we can achieve the reversible assembly using ATP and nucleolin DNA aptamers. Lastly, we engineer a mechanism to induce intracellular transport of small unilamellar vesicles (SUVs) along DNA filaments (Publication 6).

As the previous work was still mainly in water-in-oil droplets, we now successfully encapsulate DNA filaments into GUVs as more biomimetic compartments. We modify the DNA tiles with azobenzene that allows their reversible assembly using light. Additionally, we show that membrane-bound DNA filaments can deform the GUV and suppress membrane fluctuations upon deflation. Finally, we develop and characterize a mechanism for the bundling of DNA filaments using molecular crowders. Due to the filaments longer persistence length in presence of crowders, we observe

the occurrence of ring-like bundles across the GUV equator (Publication 7). GUV division could potentially be achieved if these DNA bundles form closed and contractile rings. While this remains a long-term goal, we next set out to provide a shortcut of GUV division. With this aim, we set out to develop a mechanism for the controlled division of phase-separated GUVs via osmosis. By deflating GUVs, we find that the line tension along the phase boundary of phase-separated GUVs is sufficient to lead to the formation of dumbbell-shaped GUVs and their neck fission. As the GUVs are now single-phased we also develop the regrowth of phase-separated GUVs via fusion of SUVs to single-phased GUVs reinstating phase-separation (Publication 8).

Thus, this presents different ways of engineering individual functional units that mimic specific key natural cell features using natural and synthetic filaments and provides means by which these features can be engineered inside cell-sized compartments which may ultimately be able to divide. This thesis therefore presents the rational design of multifunctional natural and synthetic cytoskeletons and thereby paves the way for the bottom-up construction of fully-functional complex synthetic cells.

## 3.2 General information on publications

The main body of this PhD thesis is written in the cumulative form i.e. consists of copies of the publication texts. To the current date, all publications are either published (Publications 2, 3, 4, 5, 8) or accepted (Publications 1, 6, 7) at internationally peer-reviewed and acclaimed journals. I am first (Publications 1, 3, 4, 5, 7) or co-first (Publications 2, 6, 8) author of all publications and none of the publications has been reprinted in other PhD theses. The respective Supporting Information for the publications can be found in Appendix A, a full list of publications is stated in Appendix B. The following provides an overview with general information on the publications:

### Publication 1:

‘Acto-myosin-assisted pulling of lipid nanotubes from lipid vesicles and cells’

Authors: **Jahnke K**, Maurer S.J., Weber C, Hernandez-Bücher J.E., Schönit A, D’Este E, Cavalcanti-Adam E.A., Göpfrich K

Published in *Nano Letters* 2022

<https://doi.org/10.1021/acs.nanolett.1c04254>

Reference: [89]

### Publication 2:

‘Autonomous Directional Motion of Cell-Sized Droplets’

Authors: Haller B\*, **Jahnke K\***, Weiss M, Göpfrich K, Platzman I, Spatz J.P.

Published in *Advanced Intelligent Systems* **3**, 2000190 (2020)

<https://doi.org/10.1002/aisy.202000190>

Reference: [90]

### Publication 3:

‘Engineering Light-Responsive Contractile Actomyosin Networks with DNA Nanotechnology’

Authors: **Jahnke K**, Weiss M, Weber C, Platzman I, Göpfrich K, Spatz J.P.

*Advanced Biosystems* **4**, 2000102 (2020)

<https://doi.org/10.1002/adbi.202000102>

Reference: [91]

#### **Publication 4:**

‘Choice of fluorophore affects dynamic DNA nanostructures’

Authors: **Jahnke K**, Grubmüller H, Igaev M, Göpfrich K

Published in *Nucleic Acids Research* **49**, 4186-4195 (2021)

<https://doi.org/10.1093/nar/gkab201>

Reference: [92]

#### **Publication 5:**

‘Proton-gradients from light-harvesting *E. coli* control DNA assemblies for synthetic cells’

Authors: **Jahnke K**, Ritzmann N, Fichtler J, Nitschke A, Dreher Y, Abele T, Hoffhausen G, Platzman I, Schröder R, Spatz J.P., Müller D, Göpfrich K

Published in *Nature Communications* **12**, 3967 (2021)

<https://doi.org/10.1038/s41467-021-24103-x>

Reference: [80]

#### **Publication 6:**

‘DNA-based functional cytoskeletons for synthetic cells’

Authors: Zhan P\*, **Jahnke K\***, Liu N, Göpfrich K

accepted in *Nature Chemistry*

#### **Publication 7:**

‘Bottom-up assembly of synthetic cells with a DNA cytoskeletons’

Authors: **Jahnke K**, Huth V, Mersdorf U, Liu N, Göpfrich K

under review in *ACS Nano*

#### **Publication 8:**

‘Division and regrowth of phase-separated giant unilamellar vesicles’

Authors: Dreher Y\*, **Jahnke K\***, Bobkova E, Spatz J.P., Göpfrich K

Published in *Angewandte Chemie International Edition* **133**, 10756-10764 (2020)

<https://doi.org/10.1002/anie.202014174>

Reference: [93]

### **3.3 Author contributions**

**Publication 1: ‘Acto-myosin-assisted pulling of lipid nanotubes from lipid vesicles and cells’**

In this work, I performed most experiments. In more detail, I established, performed and characterized random and aligned actin filament motility experiments. Moreover, I demonstrated the pulling of lipid nanotubes from GUVs and cells using an acto-myosin-assisted approach. Lastly, I verified the cytoskeletal remodeling of cells during pulling of lipid nanotubes and supervised Master student Stefan Maurer. Together with Stefan Maurer and Cornelia Weber, I performed and analyzed GUV and cell pulling experiments. Cornelia Weber purified heavy mero-myosin and actin. Jochen Hernandez Bücher prepared the cells. Andreas Schönit analyzed the actin filament velocity vector fields. Elisa D’Este and me performed stimulated emission depletion (STED) experiments and I analyzed the acquired STED images. Elisabetta Ada Cavalcanti-Adam provided additional input for cell experiments regarding the actin filament remodeling inside Jurkat cells. Kerstin Göpfrich supervised the study. Kerstin Göpfrich and I wrote the manuscript with input from all authors.

### **Publication 2: ‘Autonomous Directional Motion of Cell-Sized Droplets’**

Barbara Haller and I contributed equally to this work. Barbara Haller discovered actin-induced Marangoni flow in droplets and conducted all initial experiments as presented in her PhD thesis. Barbara Haller and I characterized the actin-droplet interface interaction depending on the Krytox concentration. Both of us conducted droplet rotation experiments and analyzed their rotational motility in presence and absence of methylcellulose as molecular crowder. I established, performed and analyzed droplet-rolling experiments on perfluorinated surfaces. I revised the manuscript and prepared the figures with Barbara Haller. Barbara Haller, Marian Weiss, Kerstin Göpfrich, Ilia Platzman and I discussed and analyzed the results. Kerstin Göpfrich, Ilia Platzman and Joachim P. Spatz supervised the study. Barbara Haller, Kerstin Göpfrich, Ilia Platzman, Joachim P. Spatz and I wrote the manuscript.

### **Publication 3: ‘Engineering Light-Responsive Contractile Actomyosin Networks with DNA Nanotechnology’**

I performed most experiments and analysis. More specifically, I conducted and analyzed bead displacement experiments, developed actin filament linking to the droplet periphery using single-stranded DNA linkers and exploited their potential to induce symmetry breaking contraction. Lastly, I analyzed three-dimensional center-of-mass displacement of actin/heavy mero-myosin bead networks inside cell-sized confinement. Marian Weiss performed initial proof-of-concept experiments regarding heavy mero-myosin bead-induced actin contractility. Cornelia Weber performed gel electrophoresis, actin, and heavy mero-myosin purification. Marian Weiss, Kerstin Göpfrich, Ilia Platzman, Joachim P. Spatz and I designed the experiments. I prepared the figures and wrote the manuscript with help from all authors.

### **Publication 4: ‘Choice of fluorophore affects dynamic DNA nanostructures’**

In this study, I performed all experiments. In more detail, these are the fluorophore sensitive attachment of DNA nanostructures to the water-in-oil droplet

periphery, their analysis and fluorophore screening as well as light-induced dynamic acidification experiments in water-in-oil droplets and their analysis. I discovered fluorophore specific differences on the triplex-conformation and binding of DNA nanostructures. Maxim Igaev conducted molecular dynamics simulations. Kerstin Göpfrich and Helmut Grubmüller supervised the study. All authors discussed the results. Maxim Igaev, Kerstin Göpfrich and I wrote the manuscript.

#### **Publication 5: ‘Proton-gradients from light-harvesting *E. coli* control DNA assemblies for synthetic cells’**

I performed most experiments and analysis. This includes the pH-switching experiment inside cell-sized droplets as well as GUVs and their analysis, absorbance measurements of pH-sensitive dye pyranine, the encapsulation of genetically engineered *E. coli* into water-in-oil droplets with microfluidics, the pH-sensitive switching of triplex-DNA with genetically engineered *E. coli* or propylamine/trifluoroacetic acid and GUV deformation experiments with DNA origami. Noah Ritzmann designed and prepared genetically engineered *E. coli* and performed pH electrode measurements supervised by Daniel J. Müller. Julius Fichtler and Kerstin Göpfrich designed the DNA origami. Julius Fichtler and I carried out pH-sensitive deformation experiments. During this work I supervised the bachelor student Anna Nitschke. Anna Nitschke and I established the use of pyranine as pH-sensor within droplets or GUVs. Yannik Dreher and I performed and analyzed pH-sensitive DNA attachment to GUVs. Tobias Abele helped in analyzing the fluorescence intensity ratios. Götz Hofhaus and Rasmus R. Schröder designed and carried out cryo-EM experiments. Ilya Platzman and Joachim P. Spatz contributed expertise in encapsulation and microfluidics. Kerstin Göpfrich and I designed the study. Kerstin Göpfrich and I wrote the manuscript with help from all authors.

#### **Publication 6: ‘DNA-based functional cytoskeletons for synthetic cells’**

Pengfei Zhan and I contributed equally to this work. Pengfei Zhan designed the DNA-based filaments and performed their validation with transmission electron microscopy and atomic force microscopy. I performed the encapsulation of DNA-based and actin filaments into water-in-oil droplets, conducted all fluorescence imaging experiments, prepared small unilamellar vesicles, analyzed the data and compiled the figures. Kerstin Göpfrich and I developed the RNase H-mediated movement of small unilamellar vesicles along DNA-based filaments. Na Liu and Kerstin Göpfrich conceived and supervised the project. Na Liu, Kerstin Göpfrich and I wrote the manuscript with contributions from all authors.

#### **Publication 7: ‘Bottom-up assembly of synthetic cells with a DNA cytoskeletons’**

I performed most experiments. I realized the encapsulation of DNA filaments into giant unilamellar vesicles. Kerstin Göpfrich and I developed the concept of light-induced filament disassembly using azobenzene. I designed and adapted the DNA sequences. I performed DNA filament polymerization experiments and analysis, developed, verified and characterized the bundling mechanism for DNA fila-

ments using molecular crowders as well as their encapsulation into giant unilamellar vesicles. I developed the linking of DNA filaments to the giant unilamellar vesicle interior using cholesterol-modified single-stranded DNA, performed fluorescence recovery after photobleaching experiments (FRAP) and giant unilamellar deformation experiments as well as their analysis. During this study I supervised the Master student Vanessa Huth. Vanessa Huth and I analyzed the filament length and persistence length and characterized the cholesterol-mediated filament linking to the vesicle membrane. Ulrike Mersdorf performed transmission electron microscopy and cryo electron microscopy. Kerstin Göpfrich and I designed the study and wrote the manuscript with input from Na Liu.

### **Publication 8: ‘Division and regrowth of phase-separated giant unilamellar vesicles’**

Yannik Dreher and I contributed equally to this manuscript. Yannik Dreher performed most experiments and conceptualized the model. I performed the light-triggered division experiments as well as the DNA-mediated and some  $\text{Ca}^{2+}$ -mediated fusion experiments. I developed the concept of light-triggered division of phase-separated vesicles using caged compounds. Yannik Dreher and I supervised Elizaveta Bobkova. Elizaveta Bobkova studied the phase separation behavior of different lipid mixtures. Kerstin Göpfrich supervised the research. Yannik Dreher and Kerstin Göpfrich wrote the manuscript with contributions from all authors.

## **3.4 Publication 1: Acto-myosin-assisted pulling of lipid nanotubes from lipid vesicles and cells**

The morphology of natural living cells is crucial for their function. It is known that the cell shape governs cell growth [94], stem cell fate [95] or control over focal adhesion assembly [96]. It is evident that shape control is equally important for the engineering of synthetic cells. In the following work, we present an approach to manipulate the shape of natural cells and GUVs using an acto-myosin-assisted approach to pull lipid nanotubes from their membranes. The approach is based on standard actin motility assays in which actin is translationally moved across a heavy mero-myosin-coated surface [97]. The myosin heads bind the actin filaments to the surface and their consecutive ATP-dependent power strokes move the actin filaments. We make use of this by simultaneously linking the actin filaments to the GUV membrane using a biotin-streptavidin-biotin linkage. Upon addition of GUVs to the motility assay, we now observe the shape deformation of GUVs by pulling of lipid nanotubes via translocated actin filaments. We quantify the actin velocities and lipid nanotube patterns and ultimately transfer this approach to the morphology control of natural cells. We find that the degree of lipid nanotube formation crucially depends on the chosen cell type. This can possibly be explained due to the different membrane-to-cortex attachment of the chosen cell types. Lastly, we also verify that the morphology control from the outside changes the interior cytoskeletal actin arrangement by forcing the cells to form protrusions.

All in all, this first work shows how the use of natural proteins namely actin filaments



and heavy mero-myosin allows to pull lipid nanotubes from GUVs and cells and thereby control their morphology.

# Actomyosin-Assisted Pulling of Lipid Nanotubes from Lipid Vesicles and Cells

Kevin Jahnke, Stefan J. Maurer, Cornelia Weber, Jochen Estebano Hernandez Bücher, Andreas Schoenit, Elisa D'Este, Elisabetta Ada Cavalcanti-Adam, and Kerstin Göpfrich\*



Cite This: <https://doi.org/10.1021/acs.nanolett.1c04254>



Read Online

ACCESS |



Metrics & More



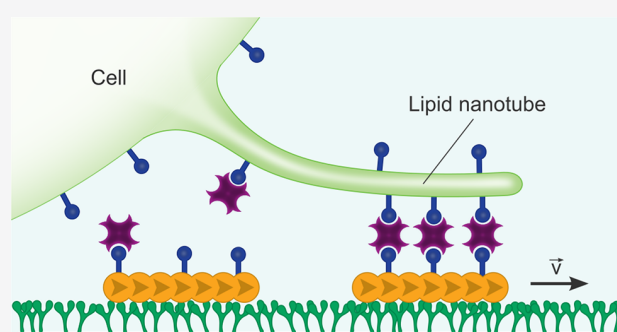
Article Recommendations



Supporting Information

**ABSTRACT:** Molecular motors are pivotal for intracellular transport as well as cell motility and have great potential to be put to use outside cells. Here, we exploit engineered motor proteins in combination with self-assembly of actin filaments to actively pull lipid nanotubes from giant unilamellar vesicles (GUVs). In particular, actin filaments are bound to the outer GUV membrane and the GUVs are seeded on a heavy meromyosin-coated substrate. Upon addition of ATP, hollow lipid nanotubes with a length of tens of micrometer are pulled from single GUVs due to the motor activity. We employ the same mechanism to pull lipid nanotubes from different types of cells. We find that the length and number of nanotubes critically depends on the cell type, whereby suspension cells form bigger networks than adherent cells. This suggests that molecular machines can be used to exert forces on living cells to probe membrane-to-cortex attachment.

**KEYWORDS:** Lipid nanotubes, lipid tether pulling, motility assay, giant unilamellar vesicle, membrane-to-cortex attachment, actin, heavy mero-myosin



Molecular motors govern various cellular processes from intracellular transport to contraction and cell division. While the development of artificial macroscale motors flourishes, many biophysical goals benefit from the engineering of motors on the nanoscale.<sup>1,2</sup> In particular, man-made machines like optical tweezers or atomic force microscopes have long been employed to probe cellular properties like membrane-to-cortex adhesion,<sup>5</sup> yet the use of molecular machines for this purpose remains largely unexplored. To date, natural motor proteins have been used to deform giant vesicles,<sup>4–7</sup> assemble contractile systems,<sup>8–10</sup> or transport cargo.<sup>11–15</sup> Moreover, noteworthy efforts have been made to build synthetic nanoscale motors with DNA nanotechnology as transporters,<sup>16,17</sup> rotors<sup>18</sup> or sliders.<sup>19</sup> However, due to their comparably low processivity and force generation compared to natural motors, the amount of suitable applications for synthetic motors is still limited. On the other hand, recent progress has been made using a minimal system of vesicles and natural motor proteins to elucidate the complex interplay of membrane tubulation of synthetic vesicles<sup>20,21</sup> and membrane dynamics.<sup>22</sup> Still, it remains elusive and uncertain how these minimal systems perform in more complex environments of natural cells and if they can possibly provide direct evidence of a cell's biophysical properties or even guide cell functions.

Here, we develop a minimal system to actively pull lipid nanotubes from giant unilamellar vesicles (GUVs) and natural

cells. Lipid nanotubes are membrane-enclosed tubes with nanoscale diameters that can guide the transfer of vesicles and organelles between cells.<sup>23</sup> We analyze the network length per cell and find that it critically depends on the cell type. This indicates that our minimal motor-based system could be used as a straightforward method to probe membrane-to-cortex attachment as a crucial biophysical indicator for the cell state.<sup>3</sup>

First, we set out to establish a motor-based force-generating system that can be used to actively pull lipid nanotubes. This requires a mechanism for directional force generation. For this purpose, we engineer two variants of an *in vitro* actin motility assay as illustrated in Figure 1a. First, the substrate is functionalized with a truncated version of myosin consisting of only the functional headgroup of myosin II. This so-called heavy meromyosin (HMM) is capable of performing a power stroke like myosin II but is still easily soluble in water at physiological conditions. We purify the HMM and actin from rabbit skeletal muscle and verify the successful purification with denaturing polyacrylamide gel electrophoresis (SDS-

Received: November 4, 2021

Revised: January 23, 2022

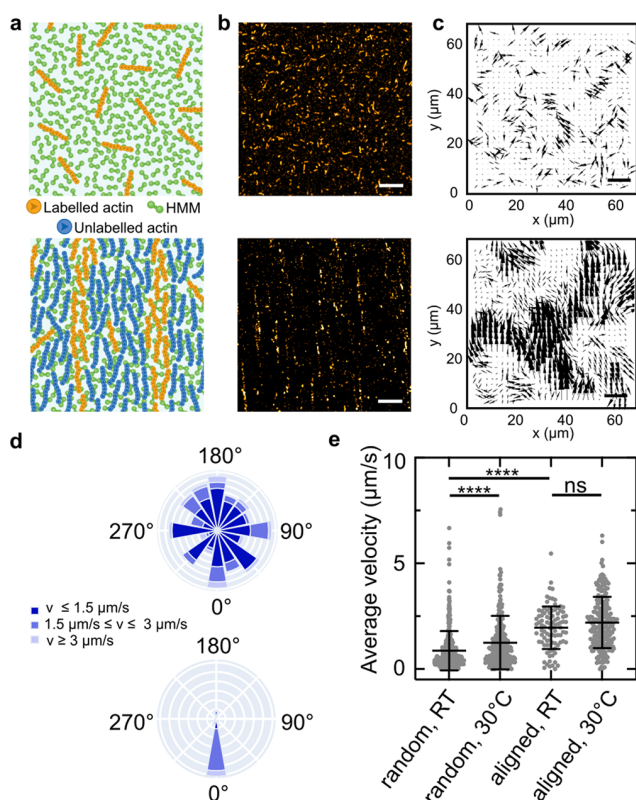


**Figure 1.** Engineered directional motility of actin filaments. (a) Schematic representations of actin filaments in a standard *in vitro* motility assay moving with random orientations (termed random filaments) or aligned orientations due to nematic ordering at high concentrations (termed aligned filaments). (b) Confocal images of rhodamine-labeled random and aligned actin filaments ( $\lambda_{\text{ex}} = 561 \text{ nm}$ ) in an *in vitro* motility assay. (c) Particle image velocimetry of random and aligned actin filaments. (d) Rose diagram depicting the orientation and velocity of random and aligned filaments. In contrast to random filaments, aligned filaments move along one axis with a strong bias (>77%) toward one direction. (e) Actin filament velocity for random and aligned filaments at room temperature and 30 °C. Values depict mean  $\pm$  SD of  $n \geq 94$  tracked filaments.

PAGE, Supporting Information (SI) Figure S1). The HMM is immobilized on the substrate where it binds prepolymerized actin filaments to the substrate and translocates them in the presence of adenosine triphosphate (ATP) like in a conventional motility assay.<sup>24</sup> At low actin concentrations from 0.5 to 20 nM, we observe the attachment and random movement of individual actin filaments, termed random filaments, with confocal microscopy (Figure 1b, SI Video S1). In order to make the movement of actin filaments directional, we induce the nematic ordering of actin filaments by adding a high concentration (24  $\mu\text{M}$ ) of unlabeled F-actin to the motility assay. We thereby surpass the critical filament density  $\rho_c$  of 5 filaments/ $\mu\text{m}^2$  above which filament ordering takes place.<sup>25</sup> This causes the alignment and movement of actin filaments on parallel tracks (Figure 1b, SI Video S2). With particle image velocimetry (PIV), we obtain the velocity vector field which yields a correlation length of  $6.7 \pm 3.9 \mu\text{m}$  for random filaments and  $29.1 \pm 12.5 \mu\text{m}$  for aligned filaments (Figure 1c).<sup>26</sup> From the confocal images (Figure 1b) and the corresponding velocity vector field (Figure 1c), we verify the alignment of actin filaments within equidistant filament streams with a spacing of  $3.6 \pm 1.4 \mu\text{m}$ . We analyze the

orientation, that is, the direction of the velocity vector, of individual actin filaments over time and find that in the standard *in vitro* actin motility assay the filaments move in random directions (Figure 1d), whereas they move along one axis with a strong bias to one direction when the actin was nematicially aligned. For the aligned condition, some filaments move in the 180° opposing direction and swirls and vortices can occur inducing a global change in the direction of the bias (SI Figure S2 and Video S3).<sup>27</sup> To probe the effect that the alignment has on the actin filament velocity, we quantified the average filament velocity for both, random and aligned actin at room temperature (RT) and 30 °C (Figure 1e), which is closer to the optimum temperature for HMM activity.<sup>28</sup> The velocity for random filaments at RT is significantly smaller than at 30 °C. Additionally, the alignment significantly enhances the average velocity of actin filaments from  $0.9 \pm 0.9$  to  $2.0 \pm 1.0 \mu\text{m s}^{-1}$  ( $p \leq 0.0001$ ). This might be due to the existence of defined tracks for aligned actin that allow for a higher motor processivity compared to when actin filaments are randomly distributed. Additionally, dysfunctional HMM may be blocked by unlabeled actin filaments increasing the overall actin filament velocity.<sup>29</sup>

Next, we test if we can pull lipid nanotubes from GUVs using the directional force of gliding actin filaments. In order to bind actin filaments to the lipid membrane of GUVs as illustrated in Figure 2a, we prepare filaments with 10% biotinylated actin monomers and verify the successful functionalization with SDS-PAGE (SI Figure S1). Additionally, we form GUVs containing 20 mol % biotinylated lipids. We observe that actin filaments bind to the GUVs in the presence of streptavidin forming an actin exoskeleton on the GUV membrane which links the GUVs to the HMM substrate. A few minutes after addition of the actin-coated GUVs to the *in vitro* motility assay, we observe the formation of lipid nanotubes on the HMM substrate at the bottom of the GUVs (Figure 2b). Note that the GUVs remain intact as proven by the images taken at the equatorial plane (Figure 2b, top). Some GUV clustering is expected due to the use of biotinylated lipids in the presence of streptavidin. We verify the tubular structure of the lipid nanotubes pulled from GUVs using 3D stimulated emission depletion (3D-STED) microscopy (Figure 2c).<sup>30</sup> The 3D-STED reveals a typical lipid nanotube diameter of around 200 nm (Figure 2d, SI Figure S3). Importantly, the lipid nanotubes are continuously pulled out of the GUVs due to the motor activity, and we can observe the lipid nanotube networks grow over time. Within 37.5 s, more than 30  $\mu\text{m}$  of nanotubes are pulled from a single GUV (Figure 2e). Remarkably, the lipid nanotube networks undergo further remodeling after being pulled from the GUV leading to the emergence of nanotube networks composed of multiple GUVs (SI Video S4). Next, we quantify the network length per GUV for random and aligned actin filaments and GUVs containing 0 or 20 mol % biotinylated lipids (Figure 2f,g). In absence of biotinylated lipids and for random actin filaments, the actin filaments do not bind to the GUVs. Hence, no lipid nanotubes are formed, whereas the network length per GUV and the number of lipid nanotube branches (SI Figure S4) significantly increases in the presence of 20 mol % biotinylated lipids. In accordance with the increased actin filament velocity and directionality, the network length per GUV increases further for aligned actin filaments. Interestingly, even though the trend is the same for random and aligned filaments, we observe pulling of lipid nanotubes even in the absence of

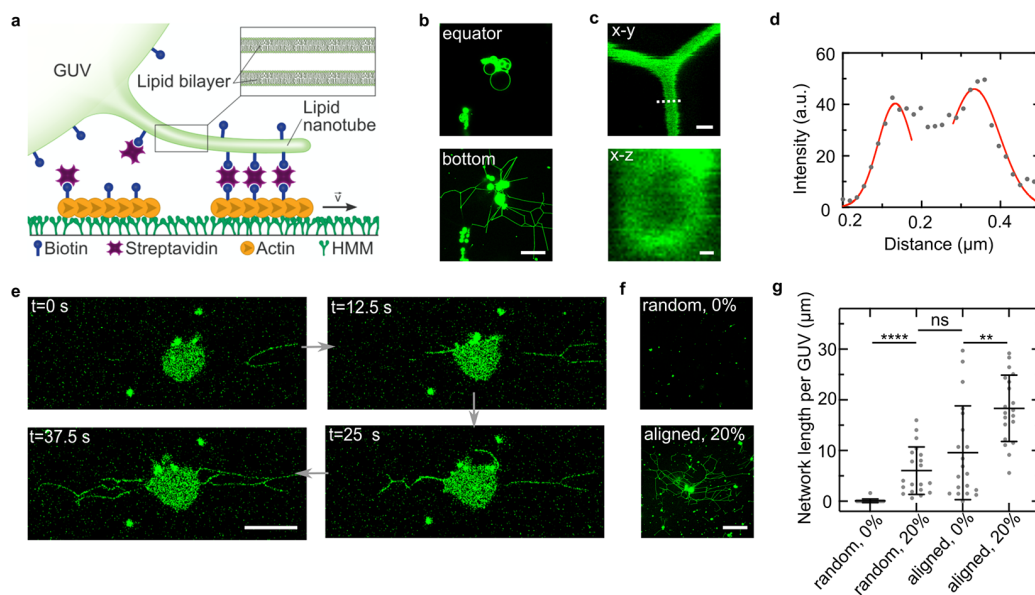


**Figure 2.** Actin filaments actively pull lipid nanotubes from GUVs. (a) Schematic representation of actin filaments bound to biotinylated lipids in a GUV membrane on an *in vitro* actin motility assay. Motile actin filaments pull lipid nanotubes over the HMM surface. (b) Confocal images of a GUV (membrane labeled with DOPE-488,  $\lambda_{\text{ex}} = 488$  nm) containing biotinylated lipids after pulling of lipid nanotubes in the equatorial (top) and the bottom plane (bottom). Scale bar: 20  $\mu\text{m}$ . (c) 3D-STED images of lipid nanotubes pulled from GUVs. Scale bars: 500 nm (*x-y*), 100 nm (*x-z*). (d) Intensity line profile (pixel width: 18 nm) across a lipid nanotube imaged with 3D-STED (indicated as white dashed line in panel c). (e) Confocal time series of a GUV during the lipid nanotube pulling process imaged on the bottom plane at the substrate interface. Scale bar: 20  $\mu\text{m}$ . (f) Confocal images of GUVs in the presence of randomly oriented or aligned actin filaments with 0% or 20% biotinylated lipids, respectively, 60 min after the start of the motility assay. Scale bar: 50  $\mu\text{m}$ . (g) Network length per GUV for randomly oriented or aligned actin filaments with 0% or 20% biotinylated lipids. Values depict mean  $\pm$  SD for  $n = 20$  acquired frames per condition.

biotinylated lipids. We hypothesize that this is due to the high amount of unlabeled F-actin present in the assay to induce the alignment which promotes electrostatic interactions of actin filaments with the GUV membrane (SI Figure S5). This might even be enhanced by the presence of divalent ions in the final buffer.<sup>31</sup> However, we still observe the longest networks in the presence of 20 mol % biotinylated lipids and for aligned actin filaments. We also find that different lipid compositions can be used to form lipid nanotubes (SI Figure S6). Notably, when we encapsulated a membrane impermeable dye inside the GUV compartment, we find that it can permeate from the GUV lumen into the lipid nanotubes confirming the formation of defect-free hollow nanotubes (SI Figure S7). In summary, it is possible to exploit natural motors to engineer distinct vesicle morphologies which visually resemble neurons.<sup>32</sup>

As a next step, we translate the nanotube pulling assay from GUVs to living cells, where the membrane is attached to the underlying cytoskeletal cortex. We first probe whether our motor system can pull lipid nanotubes from T-lymphocyte (Jurkat) cells. We verify that cholesterol self-assembles into the cell plasma membrane (SI Figure S8). This allows us to functionalize the Jurkat cells with biotinylated cholesterol. Like for the GUVs, this enables biotinylated actin filaments to bind to the cell in the presence of streptavidin. We observe that the Jurkat cells, despite being nonadherent suspension cells, adhere to the HMM-functionalized substrate due to the artificial linkage established via the actin filaments. Notably, they exhibit many lipid nanotubes at the cell–substrate interface (SI Video S5). By tracking individual cells over time, we find that the pulling of lipid nanotubes mediated by motile actin filaments sets in after about 5 min after the attachment of cells to the HMM (Figure 3a). Note that the cells remain near-stationary

during the nanotube pulling process (SI Figure S9 and Videos S6 and S7). Tens of micrometer-long lipid nanotubes are pulled out of each cell over the course of minutes (SI Videos S5, S8, and S9). In the absence of biotinylated cholesterol (0  $\mu\text{M}$ ), Jurkat cells do not bind to the substrate and maintain their spherical morphology without the formation of any lipid nanotubes for random as well as aligned filaments (Figure 3b, SI Videos S10 and S11). The absence of unspecific interactions for cells compared to GUVs may be due to their dense glycocalyx, a more complex lipid composition or increased membrane-to-cortex adhesion. By quantifying the network length per cell, we find that whereas the network length for random filaments with 25  $\mu\text{M}$  biotinylated cholesterol is similar to the network length previously determined for GUVs ( $23 \pm 33$   $\mu\text{m}$ ), the length for aligned filaments exceeds it by an order of magnitude ( $131 \pm 116$   $\mu\text{m}$ , Figure 3c). This can partially be explained by the smaller size of the GUVs compared to the Jurkat cells. Since actin-mediated structures provide support of the cell shape and are linked to the cell membrane forming the actin cortex, we focused on the intracellular actin filament organization and dynamics in proximity of lipid nanotubes. Therefore, we stained the intracellular actin with SiR-actin (Figure 3d) and performed live cell imaging. Interestingly, the cellular actin is indeed remodeled and actin filaments are found to extend into the lipid nanotubes, although not along their full length (SI Figure S10). More specifically, we find that no actin filament reaches further than 6  $\mu\text{m}$  into the lipid nanotubes and that they are on average only present within less than half of the nanotube length (SI Figure S11 and Videos S12 and S13). We hypothesize that this is due to the membrane-to-cortex attachment of cellular actin to the cell membrane which

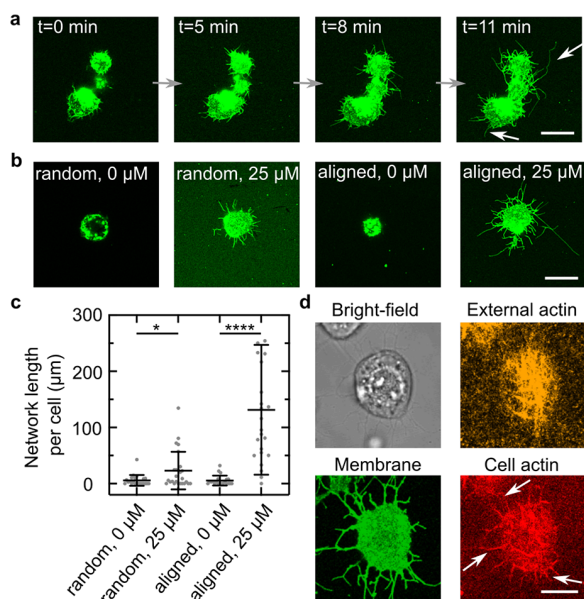


**Figure 3.** Actin filaments actively pull lipid nanotubes from Jurkat cells. (a) Confocal time series of Jurkat cells (membrane labeled with WGA-Alexa488,  $\lambda_{ex} = 488$  nm) functionalized with biotinylated cholesterol depicting the pulling of lipid nanotubes over time from the bottom plane at the substrate interface. Scale bar: 20  $\mu\text{m}$ . (b) Confocal images of Jurkat cells in the presence of randomly oriented or aligned actin filaments with 0 or 25  $\mu\text{M}$  biotinylated cholesterol, respectively. Scale bar: 20  $\mu\text{m}$ . (c) Lipid nanotube network length per cell for randomly oriented or aligned actin filaments with 0 or 25  $\mu\text{M}$  biotinylated cholesterol. Values depict mean  $\pm$  SD of  $n \geq 21$  observed cells for each condition. (d) Confocal live cell images of a Jurkat cell membrane (green, labeled with WGA-Alexa 488,  $\lambda_{ex} = 488$  nm), extracellular (orange, labeled with rhodamine,  $\lambda_{ex} = 561$  nm), and intracellular actin (red, labeled with SiR-actin  $\lambda_{ex} = 640$  nm). Actin filaments are dragged into lipid nanotubes. Scale bar: 10  $\mu\text{m}$ .

causes the actin filaments to be dragged along the membrane during the pulling process. However, the fact that cellular actin filaments only occur at the beginning of nanotubes suggests that the membrane-to-cortex attachment is disrupted at elevated distances and forces of the outer filaments pulling on the cell membrane. Beyond actin, we also stained the mitochondria and the lysosomes of Jurkat cells, as it has been shown that these organelles can be present within tunneling nanotubes of living cells.<sup>23</sup> However, we do not find any evidence for their presence in the lipid nanotubes pulled from Jurkat cells (SI Figure S12).

Having shown that molecular motors can pull lipid nanotubes from Jurkat cells, we test if we can expand our assay to a range of different cell types to probe membrane-to-cortex attachment depending on the cells' adhesive interaction with the surface. We choose keratinocytes (HaCaTs) and fibroblasts (NIH 3T3) as adherent cells and compare them to semiadherent macrophages (J774A.1) and nonadherent Jurkat cells. In order to obtain the best nanotube pulling efficiency, we use aligned actin at 30  $^{\circ}\text{C}$ . As shown in the confocal images in Figure 4a, we observe the pulling of lipid nanotubes for Jurkat cells and macrophages, whereas we do not observe nanotubes for HaCaTs and fibroblasts. We quantify the network length per cell (Figure 4b) and find that Jurkat cells form significantly bigger networks than macrophages ( $136 \pm 116$   $\mu\text{m}$  vs  $60 \pm 58$   $\mu\text{m}$ ). Noteworthy, the cell size is not the dominant factor that determines the network size per cell as

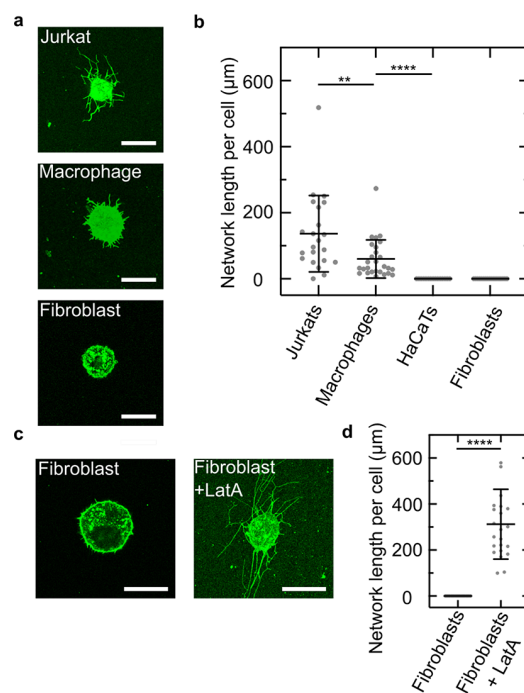


**Figure 4.** Pulling of lipid nanotubes from different cell types to probe membrane-to-cortex attachment. (a) Confocal images of Jurkat cells, macrophages, and fibroblasts in the presence of 25  $\mu\text{M}$  biotinylated cholesterol and aligned actin filaments on an HMM-coated substrate. Scale bar: 20  $\mu\text{m}$ . (b) Network length per cell for different cell types (mean  $\pm$  SD of  $n \geq 15$  observed cells for each condition). (c) Confocal images of untreated fibroblasts and fibroblasts treated with the actin-polymerization inhibitor Latrunculin A. Scale bar: 20  $\mu\text{m}$ . (d) Corresponding network length per cell. Inhibiting the actin polymerization allows pulling of lipid nanotubes indicating that this process depends on the cell-to-cortex adhesion. Values depict mean  $\pm$  SD of  $n \geq 18$  observed cells for each condition.

Jurkat cells are smaller than macrophages, keratinocytes, and fibroblasts.<sup>33</sup> This indicates that the nanotube length is cell type dependent. We hypothesize that no lipid nanotubes form for HaCaTs (SI Figure S13) and fibroblasts due to their high membrane-to-cortex attachment and stiffness compared to nonadherent cells.<sup>3</sup> The pulling force is therefore likely not sufficient to transiently disrupt the membrane-to-cortex attachment, so that a nanotube can form and actin remodeling can take place. To test this hypothesis, we treat fibroblasts with the actin polymerization inhibitor Latrunculin A (LatA) and perform our lipid nanotube pulling assay. Strikingly, under these conditions we observe the formation of lipid nanotubes (Figure 4c) confirming that the network length per cell is influenced by the membrane-to-cortex attachment of the respective cell type. Importantly, the network length per cell for fibroblasts treated with LatA increased to  $312 \pm 152$   $\mu\text{m}$  and thus exceeds the one for Jurkat cells ( $136 \pm 116$   $\mu\text{m}$ , Figure 4d). Possibly, this can be explained by the bigger cell size of fibroblasts or due to the complete absence of any attachment sites for fibroblasts treated with LatA compared to untreated Jurkat cells which still possess membrane-cortex attachment sites.<sup>34</sup> To summarize, we have shown that our minimal motor-based system can successfully be transferred to natural cells and be used to probe cell type dependent membrane properties.

The question of how mechanical properties of cell membranes and their underlying cortex regulate cell function and behavior is pivotal for a quantitative understanding of force transduction, cell motility, and cell morphology. Here, we developed a minimal system consisting of natural motor proteins that induce membrane deformation and lipid nanotube extraction from GUVs. In the context of bottom-up synthetic biology, this allows one to establish and explore different vesicle morphologies, in particular morphologies that resemble neurons. Moving toward more immediate biological questions, we translate our findings from GUVs to cells, demonstrating how simplified model membrane systems can allow the development of biological assays. By pulling lipid nanotubes from different cell types, we find cell type specific differences in the lipid nanotube length, whereby nonadherent cells exhibit longer nanotubes compared to adherent cells. This pinpoints toward their different membrane mechanics and the level of membrane-to-cortex attachment. Unlike studies using atomic force microscopy or optical tweezers, we are able to screen the mechanical properties on a single-cell level at very high throughput since nanotubes are extracted from multiple cells simultaneously. Moreover, the use of fluorescence microscopy as a readout of cell morphology also allows for the investigation of other cellular processes in real time in parallel. It will be especially exciting to combine this assay with novel fluorescent membrane-tension probes to enhance our understanding of membrane-to-cortex attachment. In general, it will be exciting to witness a conceptual shift from man-made macroscale machines to molecular machines as biophysical tools in the biosciences.

## ■ ASSOCIATED CONTENT

### SI Supporting Information

The Supporting Information is available free of charge at <https://pubs.acs.org/doi/10.1021/acs.nanolett.1c04254>.

Additional experimental details and control experiments including further quantification, confocal images and (Experimental Methods 1.1 to 1.18); Supporting Figures S1–S13 with an SDS-PAGE of the purified proteins, a confocal image of actin swirls, 3D-STED images of lipid nanotubes, quantification of the number of lipid nanotube branches pulled from GUVs, images showing unspecific interactions of actin and the GUV membrane, the number of lipid nanotubes pulled from GUVs with different lipid compositions, confocal images of dye permeation into lipid nanotubes of GUVs, the verification of the self-assembly of cholesterol-PEG into cell membranes, confocal images of the GUV and cell displacement over time, confocal images and quantification of cellular actin inside lipid nanotubes, confocal images of stained mitochondria and lysosomes after pulling of lipid nanotubes, and a confocal image of HaCaT cells after the pulling assay (PDF)

Video of time series of random actin filaments (MP4)

Video of time series of aligned actin filaments (MP4)

Video of time series of aligned actin filament patterns (MP4)

Video of time series of lipid nanotube dynamics after pulling from GUVs (MP4)

Video of time series of lipid nanotube pulling from Jurkat cells (MP4)

Video of displacement over time of a Jurkat cell during lipid nanotube pulling (MP4)

Video of displacement over time of a GUV during lipid nanotube pulling (MP4)

Video of 3D projection of Jurkat cells with random actin and biotinylated cholesterol (MP4)

Video of 3D projection of Jurkat cells with aligned actin and biotinylated cholesterol (MP4)

Video of 3D projection of Jurkat cells with random actin and no biotinylated cholesterol (MP4)

Video of 3D projection of Jurkat cells with aligned actin and no biotinylated cholesterol (MP4)

Video of actin filament dynamics during lipid nanotube pulling of a Jurkat cell (DOPE-Atto488) (MP4)

Video of actin filament dynamics during lipid nanotube pulling of a Jurkat cell (SiR-actin) (MP4)

## ■ AUTHOR INFORMATION

### Corresponding Author

**Kerstin Göpfrich** – Biophysical Engineering Group, Max Planck Institute for Medical Research, D-69120 Heidelberg, Germany; Department of Physics and Astronomy, Heidelberg University, D-69120 Heidelberg, Germany; [orcid.org/0000-0003-2115-3551](https://orcid.org/0000-0003-2115-3551); Email: [kerstin.goepfrich@mr.mpg.de](mailto:kerstin.goepfrich@mr.mpg.de)

### Authors

**Kevin Jahnke** – Biophysical Engineering Group, Max Planck Institute for Medical Research, D-69120 Heidelberg, Germany; Department of Physics and Astronomy, Heidelberg University, D-69120 Heidelberg, Germany

**Stefan J. Maurer** – Biophysical Engineering Group, Max Planck Institute for Medical Research, D-69120 Heidelberg, Germany; Department of Physics and Astronomy, Heidelberg University, D-69120 Heidelberg, Germany

**Cornelia Weber** – Department of Cellular Biophysics, Max Planck Institute for Medical Research, D-69120 Heidelberg, Germany

**Jochen Estebano Hernandez Bücher** – Department of Cellular Biophysics, Max Planck Institute for Medical Research, D-69120 Heidelberg, Germany

**Andreas Schoenit** – Biophysical Engineering Group, Max Planck Institute for Medical Research, D-69120 Heidelberg, Germany

**Elisa D'Este** – Optical Microscopy Facility, Max Planck Institute for Medical Research, D-69120 Heidelberg, Germany

**Elisabetta Ada Cavalcanti-Adam** – Department of Cellular Biophysics, Max Planck Institute for Medical Research, D-69120 Heidelberg, Germany; [orcid.org/0000-0003-0243-1552](https://orcid.org/0000-0003-0243-1552)

Complete contact information is available at: <https://pubs.acs.org/doi/10.1021/acs.nanolett.1c04254>

### Author Contributions

K.J. performed most experiments. K.J., S.M., and C.W. performed and analyzed GUV and cell pulling experiments. C.W. purified HMM and actin. J.H. prepared cells. A.S. analyzed the actin filament velocity vector fields. E.A.C.-A. provided additional input for cell experiments. K.G. supervised the study. K.J. and K.G. wrote the manuscript with input from all authors.

## Funding

Open access funded by Max Planck Society.

## Notes

The authors declare no competing financial interest.

## ACKNOWLEDGMENTS

The authors thank V. Levario Diaz for providing fibroblasts and D. Missirlis for providing Latrunculin A. Furthermore, they thank I. Platzman, J. P. Spatz, and S. W. Hell for their support. K.G. received funding from the Deutsche Forschungsgemeinschaft (DFG, German Research Foundation) under Germany's Excellence Strategy via the Excellence Cluster 3D Matter Made to Order (EXC-2082/1-390761711) and the Max Planck Society as well as the optical microscopy facility. K.J. thanks the Carl Zeiss Foundation and the Joachim Herz Foundation for financial support. E.A.C.-A. acknowledges support from the DFG (SFB1129 P15) and the Baden-Württemberg Stiftung (3D MOSAIC). The Max Planck Society is appreciated for its general support.

## REFERENCES

- (1) van den Heuvel, M. G. L.; Dekker, C. Motor Proteins at Work for Nanotechnology. *Science* **2007**, *317*, 333–336.
- (2) Saper, G.; Hess, H. Synthetic Systems Powered by Biological Molecular Motors. *Chem. Rev.* **2020**, *120*, 288–309.
- (3) Sitarska, E.; Diz-Muñoz, A. Pay attention to membrane tension: Mechanobiology of the cell surface. *Curr. Opin. Cell Biol.* **2020**, *66*, 11–18.
- (4) Leduc, C.; Campás, O.; Joanny, J.-F.; Prost, J.; Bassereau, P. Mechanism of membrane nanotube formation by molecular motors. *Biochimica et Biophysica Acta (BBA) - Biomembranes* **2010**, *1798*, 1418–1426.
- (5) Vutukuri, H. R.; Hoore, M.; Abaurrea-Velasco, C.; van Buren, L.; Dutto, A.; Auth, T.; Fedosov, D. A.; Gompper, G.; Vermant, J. Active particles induce large shape deformations in giant lipid vesicles. *Nature* **2020**, *586*, 52–56.
- (6) Shaklee, P. M.; Idema, T.; Koster, G.; Storm, C.; Schmidt, T.; Dogterom, M. Bidirectional membrane tube dynamics driven by nonprocessive motors. *Proc. Natl. Acad. Sci. U. S. A.* **2008**, *105*, 7993–7997.
- (7) Oriola, D.; Roth, S.; Dogterom, M.; Casademunt, J. Formation of helical membrane tubes around microtubules by single-headed kinesin KIF1A. *Nat. Commun.* **2015**, *6*, 8025.
- (8) Jahnke, K.; Weiss, M.; Weber, C.; Platzman, I.; Göpflich, K.; Spatz, J. P. Engineering Light-Responsive Contractile Actomyosin Networks with DNA Nanotechnology. *Advanced Biosystems* **2020**, *4*, 2000102.
- (9) Juniper, M. P. N.; Weiss, M.; Platzman, I.; Spatz, J. P.; Surrey, T. Spherical network contraction forms microtubule asters in confinement. *Soft Matter* **2018**, *14*, 901–909.
- (10) Litschel, T.; Kelley, C. F.; Holz, D.; Koudehi, M. A.; Vogel, S. K.; Burbaum, L.; Mizuno, N.; Vavylonis, D.; Schwille, P. Reconstitution of contractile actomyosin rings in vesicles. *Nat. Commun.* **2021**, *12*, 2254.
- (11) Persson, M.; Gullberg, M.; Tolf, C.; Lindberg, A. M.; Månsson, A.; Kocer, A. Transportation of Nanoscale Cargoes by Myosin Propelled Actin Filaments. *PLoS One* **2013**, *8*, e55931.
- (12) Hess, H.; Clemmens, J.; Qin, D.; Howard, J.; Vogel, V. Light-Controlled Molecular Shuttles Made from Motor Proteins Carrying Cargo on Engineered Surfaces. *Nano Lett.* **2001**, *1*, 235–239.
- (13) Suzuki, H.; Yamada, A.; Oiwa, K.; Nakayama, H.; Mashiko, S. Control of actin moving trajectory by patterned poly-(methylmethacrylate) tracks. *Biophys. J.* **1997**, *72*, 1997–2001.
- (14) Herold, C.; Leduc, C.; Stock, R.; Diez, S.; Schwille, P. Long-Range Transport of Giant Vesicles along Microtubule Networks. *ChemPhysChem* **2012**, *13*, 1001–1006.
- (15) Diez, S.; Reuther, C.; Dinu, C.; Seidel, R.; Mertig, M.; Pompe, W.; Howard, J. Stretching and Transporting DNA Molecules Using Motor Proteins. *Nano Lett.* **2003**, *3*, 1251–1254.
- (16) Cha, T.-G.; Pan, J.; Chen, H.; Salgado, J.; Li, X.; Mao, C.; Choi, J. H. A synthetic DNA motor that transports nanoparticles along carbon nanotubes. *Nat. Nanotechnol.* **2014**, *9*, 39–43.
- (17) Wickham, S. F. J.; Bath, J.; Katsuda, Y.; Endo, M.; Hidaka, K.; Sugiyama, H.; Turberfield, A. J. A DNA-based molecular motor that can navigate a network of tracks. *Nat. Nanotechnol.* **2012**, *7*, 169–173.
- (18) Ketterer, P.; Willner, E. M.; Dietz, H. Nanoscale rotary apparatus formed from tight-fitting 3D DNA components. *Science Advances* **2016**, *2*, e1501209.
- (19) Urban, M. J.; Both, S.; Zhou, C.; Kuzyk, A.; Lindfors, K.; Weiss, T.; Liu, N. Gold nanocrystal-mediated sliding of doublet DNA origami filaments. *Nat. Commun.* **2018**, *9*, 1454.
- (20) Roux, A.; Cappello, G.; Cartaud, J.; Prost, J.; Goud, B.; Bassereau, P. A minimal system allowing tubulation with molecular motors pulling on giant liposomes. *Proc. Natl. Acad. Sci. U. S. A.* **2002**, *99*, 5394–5399.
- (21) Leduc, C.; Campas, O.; Zeldovich, K. B.; Roux, A.; Jolimaître, P.; Bourel-Bonnet, L.; Goud, B.; Joanny, J.-F.; Bassereau, P.; Prost, J. Cooperative extraction of membrane nanotubes by molecular motors. *Proc. Natl. Acad. Sci. U. S. A.* **2004**, *101*, 17096–17101.
- (22) Campillo, C.; Sens, P.; Köster, D.; Pontani, L.-L.; Lévy, D.; Bassereau, P.; Nassoy, P.; Sykes, C. Unexpected Membrane Dynamics Unveiled by Membrane Nanotube Extrusion. *Biophys. J.* **2013**, *104*, 1248–1256.
- (23) Rustom, A.; Saffrich, R.; Markovic, I.; Walther, P.; Gerdes, H.-H. Nanotubular Highways for Intercellular Organelle Transport. *Science* **2004**, *303*, 1007–1010.
- (24) Kron, S. J.; Spudich, J. A. Fluorescent actin filaments move on myosin fixed to a glass surface. *Proc. Natl. Acad. Sci. U. S. A.* **1986**, *83*, 6272–6276.
- (25) Iwase, T.; Sasaki, Y.; Hatori, K. Alignment of actin filament streams driven by myosin motors in crowded environments. *Biochimica et Biophysica Acta (BBA) - General Subjects* **2017**, *1861*, 2717–2725.
- (26) Das, T.; Safferling, K.; Rausch, S.; Grabe, N.; Boehm, H.; Spatz, J. P. A molecular mechanotransduction pathway regulates collective migration of epithelial cells. *Nat. Cell Biol.* **2015**, *17*, 276–287.
- (27) Schaller, V.; Weber, C.; Semmrich, C.; Frey, E.; Bausch, A. R. Polar patterns of driven filaments. *Nature* **2010**, *467*, 73–77.
- (28) Homsher, E.; Wang, F.; Sellers, J. R. Factors affecting movement of F-actin filaments propelled by skeletal muscle heavy meromyosin. *American Journal of Physiology-Cell Physiology* **1992**, *262*, C714–C723.
- (29) Salhotra, A.; Zhu, J.; Surendiran, P.; Meinecke, C. R.; Lyttleton, R.; Ušaj, M.; Lindberg, F. W.; Norrby, M.; Linke, H.; Månsson, A. Prolonged function and optimization of actomyosin motility for upscaled network-based biocomputation. *New J. Phys.* **2021**, *23*, 085005.
- (30) Roy, D.; Steinkühler, J.; Zhao, Z.; Lipowsky, R.; Dimova, R. Mechanical Tension of Biomembranes Can Be Measured by Super Resolution (STED) Microscopy of Force-Induced Nanotubes. *Nano Lett.* **2020**, *20*, 3185–3191.
- (31) Schroer, C. F. E.; Baldauf, L.; van Buren, L.; Wassenaar, T. A.; Melo, M. N.; Koenderink, G. H.; Marrink, S. J. Charge-dependent interactions of monomeric and filamentous actin with lipid bilayers. *Proc. Natl. Acad. Sci. U. S. A.* **2020**, *117*, 5861–5872.
- (32) Schubert, P. J.; Dorkenwald, S.; Januszewski, M.; Jain, V.; Kornfeld, J. Learning cellular morphology with neural networks. *Nat. Commun.* **2019**, *10*, 2736.
- (33) Milo, R.; Jorgensen, P.; Moran, U.; Weber, G.; Springer, M. BioNumbers—the database of key numbers in molecular and cell biology. *Nucleic Acids Res.* **2010**, *38*, D750–D753.
- (34) Clausen, M. P.; Colin-York, H.; Schneider, F.; Eggeling, C.; Fritzsche, M. Dissecting the actin cortex density and membrane-cortex distance in living cells by super-resolution microscopy. *J. Phys. D: Appl. Phys.* **2017**, *50*, 064002.

### 3.5 Publication 2: Autonomous directional motion of actin-containing cell-sized droplets

Having shown how we can use cytoskeletal actin filaments from the outside of compartments to modulate their shape, we now want to study how we can engineer functionality from within cell-sized confinements. For this purpose, we again rely on natural actin filaments as a driving force for the motility of surfactant-stabilized water-in-oil droplets. Motility itself is a key characteristics of living cells. It allows cells to migrate along a substrate or within a solution and is important for wound healing [98] or cancer metastasis [99]. Whereas the dominating form of actin-based motility in eukaryotic cells (crawling) is based on the interplay of actin polymerization on the leading edge and acto-myosin-induced retraction on the trailing edge [10], here we develop a mechanism that is only based on actin filaments and makes use of surface tension gradients rather than contractility. In order to achieve this, we make use of Marangoni flows within the surfactant-stabilized layer of water-in-oil droplets. The Marangoni flows are generally induced by a gradient of the surface tension and lead to a propulsive motion. In our case the gradient in surface tension is achieved by micellar exclusion and binding of actin filaments to the negatively charged surfactant Krytox. The amount of actin and Krytox thus allows us to control the magnitude of the gradient in surface tension and therefore the velocity of the droplets' motion. This motion is inherently rotational due to the absence of friction forces actin on the water-in-oil droplet. By deliberately inducing friction forces of the droplet with the coverslide we can transfer the rotation into a rolling motion of the droplet.

We have therefore exemplified how a simple physical mechanism can be used to engineer the motility of cell-sized compartments using reconstituted actin filaments.



# Autonomous Directional Motion of Actin-Containing Cell-Sized Droplets

Barbara Haller, Kevin Jahnke, Marian Weiss, Kerstin Göpfrich,\* Ilija Platzman,\* and Joachim Pius Spatz\*

Cell motility is potentially the most apparent distinction of living matter, serving an essential purpose in single cells and multicellular organisms alike. Thus, the bottom-up reconstitution of autonomous motion of cell-sized compartments remains an exciting but challenging goal. Herein, actin-driven Marangoni flows are engineered to generate rotational and translational motility of surfactant-stabilized emulsion droplets. The interaction between actin filaments and the negatively charged block-copolymer Krytox is identified as the driving force for Marangoni flows at the droplet interface. Tuning the actin–Krytox interplay, sustained autonomous unidirectional droplet rotation with  $1.7 \text{ rot h}^{-1}$  is achieved. Ultimately, this rotational motion is transformed into a translational rolling motion by introducing interactions between the droplets and the surface of the observation chamber. Accordingly, translational motility of actin-containing droplets at velocities of  $0.061 \pm 0.014 \mu\text{m s}^{-1}$  is reported herein and an overall displacement of several hundreds of micrometers within 30 min is observed. These self-propelled systems with biologically active molecules demonstrate how motility could be implemented for synthetic cells.

mechanisms has hindered a full understanding.<sup>[1]</sup> In addition to intracellular contractile and pushing cytoskeletal forces cell movement is governed by cell–cell<sup>[2]</sup> and cell–extracellular matrix interactions.<sup>[3]</sup> Moreover, cell membrane flows have an additional effect on cellular locomotion.<sup>[4]</sup> Despite being less discussed in the literature, membrane flows allow for membrane surface enlargement in the front of the cell due to locomotion-mediated protrusions.<sup>[4]</sup> The additional membrane surface can be provided for example by exocytosis of internal vesicles at the front of the cell body and the according endocytosis at the cell rear.<sup>[5]</sup> These processes generate a lateral flow of lipids in the membrane from the front to the rear.<sup>[4]</sup> Thus, it is conceivable that membrane accesion and release together with the accompanied flows are directly involved in the propulsion mechanism.<sup>[6]</sup> Supporting this hypothesis, a theoretical model showed that tangential traveling surface waves


could cause a translational movement in spherical micro-sized objects.<sup>[7]</sup> In any case, the exact contribution of these membrane flows is not well understood and requires further investigations.<sup>[5]</sup> Bottom-up synthetic biology offers a possible route toward a systematic understanding of membrane flows in the context of cellular locomotion. By generating an autonomous motion in a synthetic system consisting of minimal biological building blocks, one could draw conclusions on how propulsion

## 1. Introduction

Many processes in living cells, including chemotaxis in unicellular organisms or embryonic development, immune response, tissue formation, and wound healing, are governed by motility. Mechanisms of motion, such as flagella propulsion in bacteria and spermatozoa or cytoskeletal forces in migrating cells, are widely studied, but the extensive complexity of these

Dr. B. Haller, Dr. M. Weiss, Dr. I. Platzman, Prof. J. P. Spatz  
Department of Cellular Biophysics  
Max Planck Institute for Medical Research  
Jahnstraße 29, D 69120 Heidelberg, Germany  
E-mail: ilia.platzman@mr.mpg.de; spatz@mr.mpg.de

Dr. B. Haller, Dr. M. Weiss  
Department of Biophysical Chemistry  
Heidelberg University  
Im Neuenheimer Feld 253, D 69120 Heidelberg, Germany

 The ORCID identification number(s) for the author(s) of this article can be found under <https://doi.org/10.1002/aisy.202000190>.

© 2020 The Authors. Advanced Intelligent Systems published by Wiley-VCH GmbH. This is an open access article under the terms of the Creative Commons Attribution License, which permits use, distribution and reproduction in any medium, provided the original work is properly cited.

DOI: 10.1002/aisy.202000190

K. Jahnke, Dr. K. Göpfrich  
Biophysical Engineering Group  
Max Planck Institute for Medical Research  
Jahnstraße 29, D 69120 Heidelberg, Germany  
E-mail: kerstin.goepfrich@mr.mpg.de

K. Jahnke, Dr. K. Göpfrich  
Department of Physics and Astronomy  
Heidelberg University  
D 69120 Heidelberg, Germany

Dr. I. Platzman, Prof. J. P. Spatz  
Institute for Molecular Systems Engineering (IMSE)  
Heidelberg University  
Im Neuenheimer Feld 225, D 69120 Heidelberg, Germany

Prof. J. P. Spatz  
Max Planck School Matter to Life  
Jahnstraße 29, D 69120 Heidelberg, Germany

evolved in similarly primitive cells at the onset of life and elucidate what role it may play in today's living systems. Using the toolbox of synthetic biology, several studies have shown the internal dynamics of the cytoskeleton leading to a contraction or deformation of the cell rim.<sup>[8–11]</sup> The autonomous motion of the entire minimal cell, however, is more difficult to achieve. For example, autonomous motion was obtained via reconstitution of fluid flows initiated by kinesin activity and collective dynamics of microtubule bundles.<sup>[12–15]</sup> In contrast to that, autonomous propulsion of inorganic particles has been achieved by several groups, often exploiting osmotic or phoretic forces, for example, in enzyme-powered Janus particles<sup>[16,17]</sup> or surface tension gradients as the Marangoni effect.<sup>[18,19]</sup>

The Marangoni effect is governed by local inhomogeneities of the interfacial tension (IFT) at interfaces of emulsions such as water-in-oil droplets. The IFT gradient in turn creates a stress and thus a tangential liquid flow at the interface.<sup>[20]</sup> Various factors could be responsible for a nonuniform IFT in water-in-oil droplets, for example, heterogeneous surfactant mixtures, local chemical reactions, and gradients in temperature or surfactant concentrations.<sup>[21]</sup>

In this study, by applying bottom-up synthetic biology strategies we provide a systematic investigation of autonomous Marangoni-driven directed motion of a minimal cell system. To achieve that, a minimal actin cytoskeleton was reconstituted within water-in-oil droplets by means of a droplet-based microfluidic technology. Following the formation of actin filaments, we specifically created the interactions of the actin with the surfactants on the droplet's inner interface, thereby creating a nonuniform IFT leading to fluid flows and rotational motion of the droplet at a velocity of up to  $1.7 \pm 0.5 \text{ rot h}^{-1}$ . Moreover, by modifying the interaction of surfactants with a glass interface we show that translational motion of actin-containing

droplets can be achieved. Notably, unlike the motion of enzyme-accelerated Janus particles, the motion demonstrated here is mainly a spontaneous directional motion.<sup>[22]</sup> Importantly, this study shows how biologically relevant elements of the cellular motility system, namely, actin filaments, can generate autonomous directional motion based on the Marangoni effect.

## 2. Results and Discussion

Migration of natural cells is mainly induced by the forces applied on the cell rim due to cytoskeletal dynamics. In the process of locomotion, actin-mediated protrusions on the cellular membrane induce lipid membrane flow to compensate for the growth of the membrane surface area. Inspired to reconstitute a minimal locomotion system, we set out to establish an actin-containing synthetic cell model system that will be able to generate autonomous membrane flow-mediated directed motion. Due to mechanical and chemical instabilities of the cell-sized lipid-based vesicles,<sup>[23]</sup> we decided to use surfactant-stabilized water-in-oil droplets as a stable compartment system. Moreover, instead of a cytoskeletal dynamics mediated membrane flow we aimed to apply actin filaments to generate autonomous directional surfactant membrane motion based on the physicochemical Marangoni effect. To generate mass transfer along the surfactant layer at the oil–water interface, a gradient of the surface tension must be maintained over time. Therefore, a continuous interaction between the actin filaments and the droplet interface is required to preserve the IFT gradient. **Figure 1** shows a schematic representation of the envisioned concept for the Marangoni-driven motion of the actin-containing synthetic cell. To create charge-mediated interactions between actin filaments and the droplets' inner interface, the water-in-oil droplets are stabilized by a mixture of two types of surfactants exhibiting distinct interfacial properties: an uncharged triblock

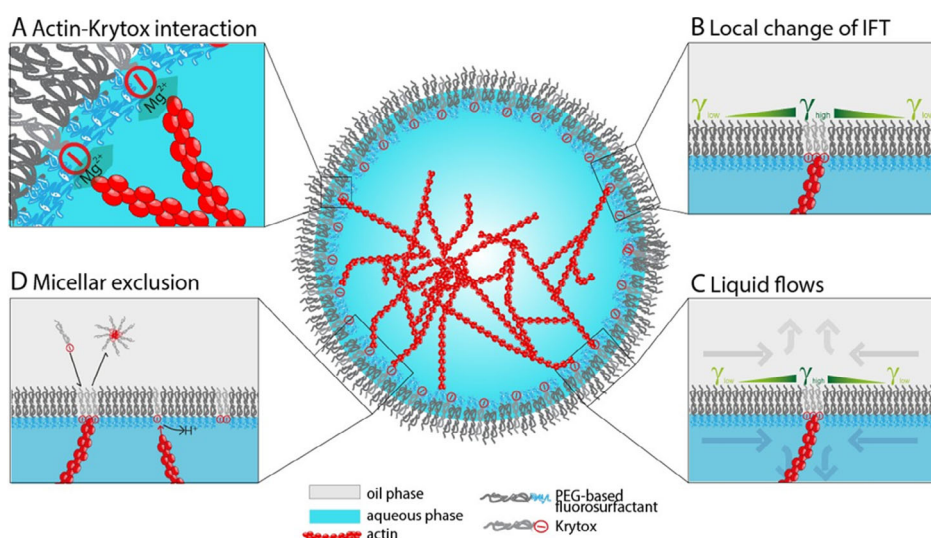


**Figure 1.** Schematic illustration of the physicochemical processes driving the actin-induced Marangoni flow within water-in-oil droplets. A surfactant-stabilized water-in-oil droplet containing actin filaments is shown in the center of the figure. The insets illustrate actin–surfactant interactions, including A)  $\text{Mg}^{2+}$  ions-mediated interactions of the negatively charged actin filaments and Krytox at the droplet periphery; B) the local formation of Krytox clusters and a corresponding change in IFT; C) the rearrangement of the diffusive surfactant layer due to IFT gradients; D) micellar exclusion of actin monomers due to surfactant desorption from the surfactant layer.

copolymer perfluoropolyether-poly(ethylene glycol)-perfluoropolyether (PEG-based) fluorosurfactant and a negatively charged perfluoropolyether (PFPE) carboxylic acid fluorosurfactant (Krytox). The distribution of negatively charged surfactants at the droplet interface attract  $Mg^{2+}$  ions<sup>[24]</sup> that, in turn, induce electrostatic interactions with the negatively charged actin filaments. In a natural cell, the linkage of actin to the cellular membrane is mediated by numerous components, including transmembrane proteins such as integrin and a variety of anchor proteins.<sup>[2]</sup> Therefore, by using the electrostatic interaction between the encapsulated actin and Krytox as shown in Figure 1A we bypass the complexity of actin–membrane interactions in natural cells. The local interaction of actin filaments with the Krytox surfactant leads to Krytox clusters at the interaction points, creating IFT gradients across the interface (Figure 1B). As a response to the interfacial stresses, the diffusive surfactant layer<sup>[25]</sup> rearranges laterally (Figure 1C). In addition to lateral mobility, surfactants also absorb to and desorb from the droplet periphery, leading to micellar exclusion of actin monomers (Figure 1D). Note that depolymerization and denaturation of actin filaments at the droplet interface can be attributed to a local Krytox-mediated acidic environment. These processes are crucial for the creation of a continuous liquid flow due to the formation of new actin–Krytox interactions that in turn maintain a distinct IFT gradient at these interaction points.

### 2.1. Interaction of Actin with Krytox

To test our concept, we initially set out to establish a connection between actin and the droplet interface. For that purpose, we first

used droplet-based microfluidics to encapsulate 10  $\mu\text{m}$  actin filaments (containing 1% Alexa568- or Alexa633-labelled actin) in actin polymerization buffer (see Experimental Section) into water-in-oil droplets (see Figure S1, Supporting Information, for the layout of the microfluidic device). The droplets were stabilized by a mixture of 1.4 wt% uncharged PEG-based fluorosurfactant and different concentrations of negatively charged Krytox (0.04, 0.54, 1.04, and 5.04 mM). Note, pure PEG-based surfactants with no traces of Krytox cannot be achieved due to the synthesis and purification procedures. Therefore, the commercially available surfactants also contain Krytox traces.<sup>[24]</sup> The fluorescence signal of actin filaments within the droplets was observed by confocal fluorescence microscopy. As visible in Figure 2A, nearly no actin filaments are colocalized with the droplet interface in the presence of only 0.04 mM Krytox (note that the 0.04 mM Krytox is the minimal achievable concentration,<sup>[24]</sup> no Krytox was added here). However, at the higher Krytox concentrations a clear actin fluorescence ring at the droplet interface was observed. Moreover, as visible in the confocal images, the fluorescence signal of actin in the droplet interior (excluding the periphery) is decreasing with increasing Krytox concentrations. Eventually, actin loses its fibrous structure at elevated Krytox concentrations (see Video S1, Supporting Information). The loss of fibrous structures at high Krytox concentrations can be attributed to depolymerization and denaturation of actin at low pH values.<sup>[26]</sup> Note that the pH is dropping inside the droplet, because Krytox acts as a proton donor at the droplet interface.<sup>[24]</sup> The inert PEG-based fluorosurfactant inhibits the interaction between encapsulated actin and the droplet interface while Krytox introduces negative charges at

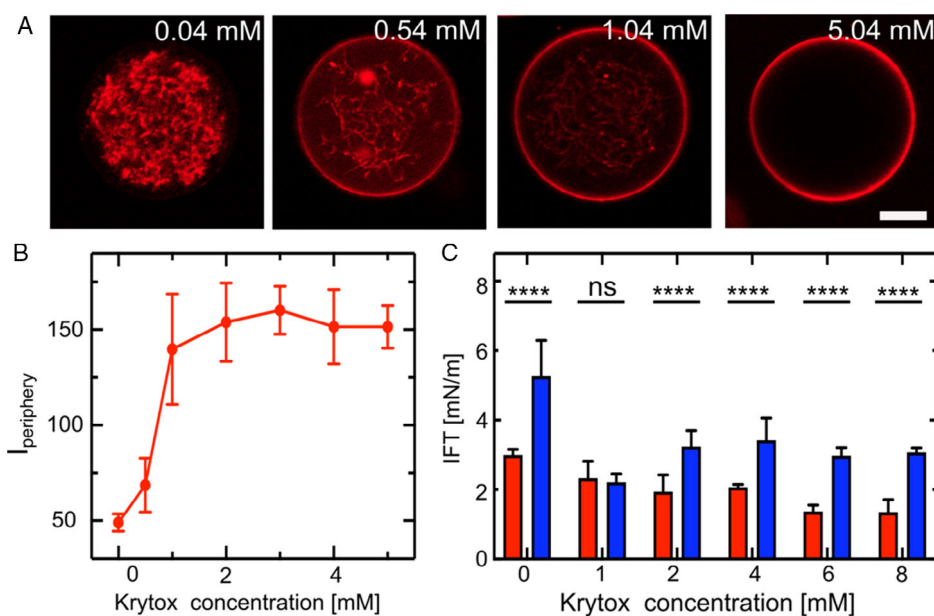


**Figure 2.** Interaction between actin and Krytox at the droplet periphery is concentration-dependent. A) Confocal fluorescence images of actin filaments (labeled with 1% Alexa633,  $\lambda_{\text{ex}} = 633$  nm) encapsulated into water-in-oil droplets at different Krytox concentrations in the oil phase. Scale bar: 10  $\mu\text{m}$ . B) Fluorescence intensity of actin at the droplet periphery dependent on the Krytox concentration. With increasing Krytox concentration, the fraction of actin at the droplet periphery increases and reaches a plateau at 3 mM. Error bars correspond to the standard deviation of  $n = 8$ –19 evaluated droplets. C) IFT of actin buffer with (red) and without actin monomers (blue) at different Krytox concentrations as determined with pendant drop measurements ( $n \geq 70$  evaluated droplet shapes). The IFT values are elevated in the presence of actin monomers in the buffer due to the formation of actin–Krytox clusters for all tested Krytox concentrations. The significance was tested using an unpaired Welch's *t*-test.

the interface which attract  $Mg^{2+}$  ions from the actin polymerization buffer and, in turn, attract negatively charged actin filaments. Quantitative analysis of the fluorescence intensity at the droplet periphery ( $I_{periphery}$ ) revealed clear attraction of actin toward the droplet interface at Krytox concentrations above 0.04 mM (Figure 2B).

As an independent confirmation of the Krytox-dependent interaction of actin with the droplet interface, we performed pendant drop measurements (Figure 2C). By the addition of actin monomers to the buffer, the IFT values increased significantly. This confirms the interaction of actin with the Krytox molecules. Note that a higher IFT corresponds to a lower coverage of interfacially active molecules. Thus, the actin–Krytox clusters at the interface form a less dense interface coverage than surfactants in a protein-free surfactant layer. It is important to mention here that the high IFT change as observed for 0.04 mM Krytox can be attributed to the fact that actin monomers were used for this experiment and not polymerized actin fibers, which are less diffusive. Therefore, in the case of experimental conditions, where the actin is polymerized, we do not detect as high IFT as in the case of unpolymerized actin monomers. Note that actin monomers were chosen for this experiment because any traces of magnesium ions in the actin polymerization buffer prevented a stable hanging droplet formation due to electrostatic interactions between Krytox and magnesium at the droplet interface.<sup>[27]</sup>

## 2.2. Turnover of Actin–Krytox Interactions

To maintain the motility, which is generated due to local changes in the IFT values on the droplet interface, the system has to be kept out of equilibrium for an extended period of time. To achieve that, local actin–Krytox interactions have to be reformed continuously, meaning that new actin and Krytox molecules have to be constantly recruited to the droplet interface. This condition can be achieved when there is a constant renewal of the actin–Krytox interactions as a result of denaturation and depolymerization and therefore loss of contact and subsequent micellar exclusion of the actin. To test this assumption, we monitored actin-containing droplets (10  $\mu$ M actin, 1% fluorescently

labelled in 10 mM Tris pH7.4, 20 mM  $MgCl_2$ ) stabilized by an inert fluorosurfactant and different concentrations of Krytox (0.04, 0.54, and 1.04 mM) over time for 100 min using confocal fluorescence microscopy. The same imaging settings were used for all conditions shown in Figure 3A. In all conditions, the fluorescence intensity inside the droplets dropped over time. Furthermore, the mean fluorescence intensity ratio at the droplet periphery over the droplet interior increased with increasing Krytox concentrations (Figure 3B). Within 100 min, the fluorescence intensity ratio  $I_{periphery}/I_{inner}$  for 1 mM Krytox increased even by a factor of 2.7. Notably, the choice of the photostable Alexa633 dye and the presence of actin agglomerates in the oil phase indicate that photobleaching only has a minor contribution to the intensity loss. Thus, the plot shown in Figure 3A clearly indicates a correlation of actin loss and the amount of Krytox used to stabilize the droplets, which can be explained by the fact that actin is pulled out of the aqueous droplet interior due to interactions with Krytox. Krytox is assembling at the interface, attracting actin, and desorbing it from the interface by micellar exclusion. Note that the oil reservoir around the droplets is much bigger than the aqueous phase within the droplet, and thus the leakage of actin into the oil phase cannot be monitored by the increase of fluorescence intensity of the oil phase. However, agglomerates of fluorescent actin particles can be detected in the oil phase (see Video S1, Supporting Information), unambiguously confirming that there is a leakage of actin from the droplets. This, in turn, allows for the continuous turnover of actin–Krytox interactions at the interface, maintaining nonequilibrium interfacial stresses which result in Marangoni flows over a prolonged time period until the actin inside the droplet is largely depleted.

## 2.3. Rotational Motility of Droplets

Time-lapse fluorescence imaging experiments were performed to analyze the conditions required for actin-containing droplet motility. As shown in Figure 4A and in Video S2, Supporting Information, we observed a directed rotational motion of the

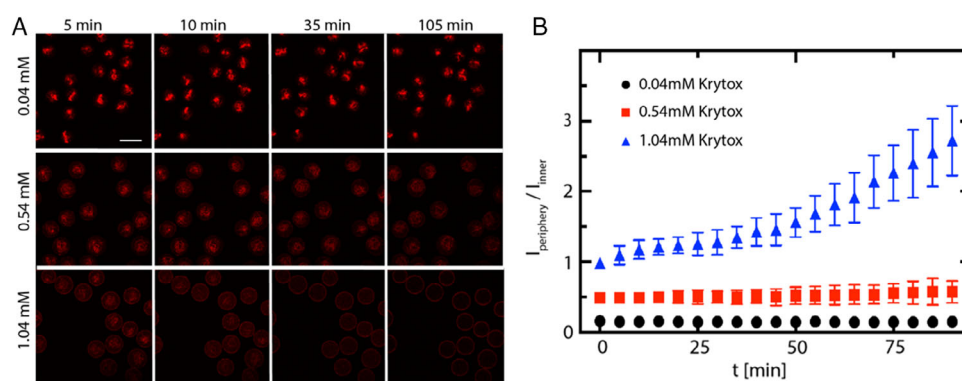


**Figure 3.** Turnover of actin–Krytox interactions at the droplet interphase. A) Confocal fluorescence images of microfluidic droplets containing actin filaments (labeled with 1% Alexa633,  $\lambda_{ex} = 633$  nm) over time at different Krytox concentrations. Scale bar: 50  $\mu$ m. B) Fluorescence intensity ratio  $I_{periphery}/I_{inner}$  of actin filaments inside the droplets over time at different Krytox concentrations ( $n \geq 28$  evaluated droplets). The fluorescence intensity ratio of actin at the droplet periphery over actin in the droplet lumen increases with increasing Krytox concentrations. This indicates a correlation of actin loss and the amount of Krytox because actin is depleted from the aqueous droplet interior due to interactions with Krytox. Error bars correspond to the standard deviation.

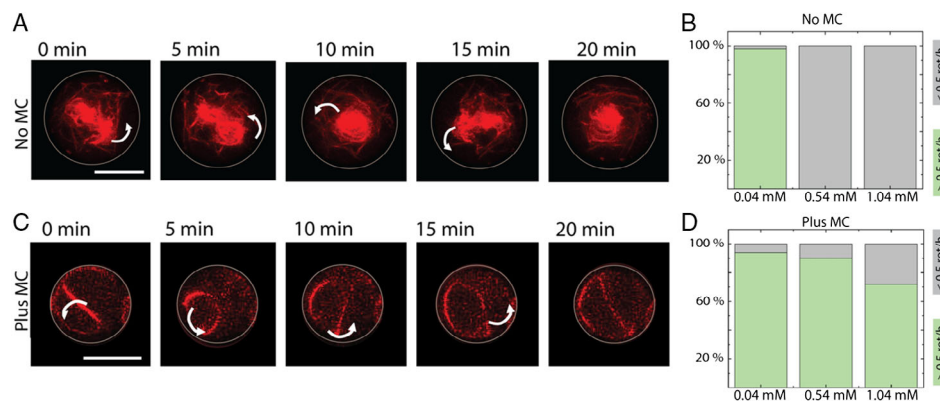


**Figure 4.** Actin-containing droplets exhibit an autonomous rotational motion at low Krytox concentrations or in presence of MC. A,C) Confocal fluorescence images of rotating microfluidic droplets containing actin filaments (labeled with 1% Alexa568,  $\lambda_{\text{ex}} = 561 \text{ nm}$ ) in absence (A) and presence (C) of MC. Scale bar: 20  $\mu\text{m}$ . B,D) Relative abundance of droplets displaying more (green) or less (gray) than  $0.5 \text{ rot h}^{-1}$  in presence or absence of MC at different Krytox concentrations ( $n = 30$  evaluated droplets). Without MC, 96% of the droplets rotate with an angular velocity of  $1.7 \pm 0.5 \text{ rot h}^{-1}$  at 0.04 mM Krytox. At higher Krytox concentrations, the rotation is significantly lower due to fast depolymerization of actin filaments. In presence of MC, even at elevated Krytox concentrations,  $>0.5 \text{ rot h}^{-1}$  can be observed due to the bundling of actin filaments by MC and therefore lower depolymerization rates.

droplets at the lowest Krytox concentration (0.04 mM). Rotation, instead of translational movement, is caused because the droplets experience insufficient friction at the upper cover slide of the observation chamber. Remarkably, around 96% ( $n = 82$ ) of the examined droplets exhibit a rotational motion over several hours with rotational velocity of  $1.7 \pm 0.5 \text{ rot h}^{-1}$ . In particular, the actin-containing droplets have a constant and a very similar angular velocity, but the axis of rotation of the droplets is random in  $x$ -,  $y$ -, and  $z$ -direction. The high rotational velocity we obtain is remarkable given that the rotational motion is around 28 times faster than the rotational diffusion coefficient (see Supporting Note 1, Supporting Information). In comparison, the enhanced diffusion observed for Janus particles exceeds their diffusion coefficient only by a factor of around 1.5.<sup>[22]</sup> Surprisingly, when the Krytox concentration in the oil phase was higher than 0.04 mM no droplet rotation or only minor movements ( $<0.5 \text{ rot h}^{-1}$ ) were observed ( $n = 57$ ) (Figure 4B and Video S3 and S4, Supporting Information). The absence of motility at high Krytox-concentrations can be attributed to fast actin filaments depolymerization and denaturation. Due to depolymerization, actin monomers create interactions with the droplet interface in a homogeneous manner with no localized change in IFT. Therefore, the Marangoni flows are inhibited. To prevent depolymerization of actin filaments at elevated Krytox concentrations, the filaments must be stabilized. Toward this end, we bundled the filaments by adding 0.4 wt% methylcellulose (MC) to the actin polymerization buffer.<sup>[28,29]</sup> Availability of MC in the actin polymerization buffer leads to a strong bundling of actin fibers due to the depletion effect, as can be observed in Figure 4C.<sup>[30]</sup> As expected, under these conditions, we observed a rotational motility of the droplets also in the presence of 0.54 mM Krytox (for 90% of the droplets) and even in the presence of 1.04 mM Krytox (for 72% of the droplets) (Figure 4D).

For a final confirmation that Krytox–actin interactions are the driving force for the autonomous movement of the droplets, we completely inhibited the interaction between the droplet interface and the encapsulated actin. This was achieved by using

an outer fluorinated oil phase in which Krytox could not be dissolved (see Experimental Section). Not surprisingly, no rotation of the actin-containing droplets and no decrease in actin fluorescence intensity could be observed in this case (Video S5, Supporting Information). Taking the presented evidence together, we have proven that the model shown in Figure 1 is indeed explaining the observed motion. We can conclude that Marangoni flows can cause motion in minimal cells, fueled by autonomous transport of biologically relevant molecules.

#### 2.4. Translational Motility of Droplets

Ultimately, we set out to engineer translational motility of actin-containing droplets induced by Marangoni flow. From the previous experiments, we know that actin-containing droplets exhibit a rotational motion in an observation chamber assembled from untreated glass cover slides, as shown in Figure 5A. Due to the higher density of the fluorinated oil compared to the aqueous phase, buoyancy forces act on the droplets and bring them in contact with the upper cover slide. We hypothesize that the fact that we observe a rotational motion can be attributed to the absence of friction forces between the droplets and the hydrophilic glass surface. To test this hypothesis, and to induce translational motility, we used the fluorinated glass cover slide to generate friction between a actin-containing droplets and the cover slide, as shown in Figure 5B. As expected, we observed a translational rolling motion of actin-containing droplets in contact with the fluorinated cover slide. The actin-containing droplets, which experience Marangoni flows, cover a distance of several hundreds of micrometers, whereas droplets filled only with ultrapure (Milli-Q) water in the same observation chamber only show insignificant random movement (see Figure S2, Supporting Information). Note that we used actin mixed with 0.4% MC to enhance actin filament stability and therefore increase the observation period. Importantly, we proved that the rolling motion is solely induced through actin-mediated

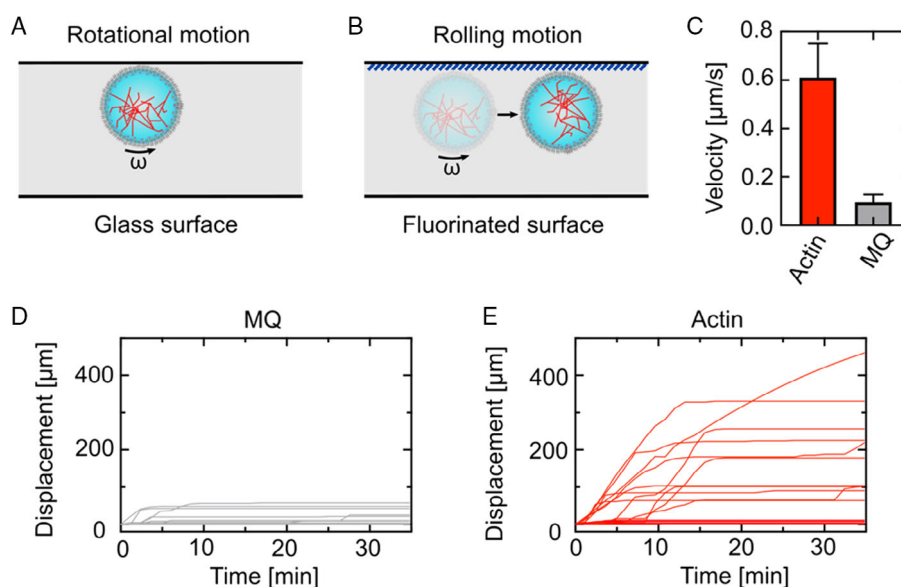


**Figure 5.** Fluorination of a cover slide surface leads to a translational rolling motion of actin-containing droplets due to enhanced friction. A,B) Schematic illustrations of an actin-containing water-in-oil droplet in contact with (A) a hydrophilic glass surface undergoing rotational motion or (B) a fluorinated surface undergoing a rolling motion with a frequency  $\omega$ . C) Translational velocity of actin-containing ( $0.061 \pm 0.014 \mu\text{m s}^{-1}$ ) and MQ-containing droplets ( $0.010 \pm 0.003 \mu\text{m s}^{-1}$ ) in an observation chamber with a fluorinated glass surface ( $n = 18$ ). D,E) Displacement from the initial location of individual MQ-containing (D) and actin-containing (E) droplets over time. Actin-containing droplets alternate in between a rolling and rotational motion, whereas MQ-containing droplets do not show significant displacement within 35 min of acquisition.

Marangoni flow by mixing MQ- and actin-containing droplets within the same observation chamber. We analyzed their respective velocities for  $n = 18$  droplets and found that actin-containing droplets move with an average velocity of  $0.061 \pm 0.014 \mu\text{m s}^{-1}$ , whereas MQ-containing droplets are almost stationary with  $0.010 \pm 0.003 \mu\text{m s}^{-1}$  (see Figure 5C). Thus, the velocity of actin-containing droplets exceeds that of MQ-containing droplets by a factor of six. Moreover, from the observations it is evident that the movement of MQ droplets is often caused simply by interactions with passing actin-containing droplets. Figure 5D,E shows the displacement of individual droplets over time. Even the fastest moving MQ droplets cover a maximum distance of 58  $\mu\text{m}$ , whereas the fastest actin-containing droplets move more than 400  $\mu\text{m}$ . In addition, it shows that some actin droplets stick to a rotational motion in presence of a fluorinated surface, whereas others alternate between a rolling and a rotational motion. This could be potentially attributed to imperfections of the fluorination of the surface. Note that large droplets with diameters of 60  $\mu\text{m}$  or bigger do not exhibit any rotational or rolling motion because they experience too much friction with the coverslip. To exclude the effect of droplet size on the motility, we set the diameter to  $\approx 40 \mu\text{m}$ .

To compare rolling and rotation, we calculated the corresponding rotational frequency from the average translational displacement of actin-containing droplets. This yields a frequency of  $\omega = v_{\text{trans}}/2\pi r = 1.75 \pm 0.40 \text{ rot h}^{-1}$  for a droplet radius of 20  $\mu\text{m}$ . This is in excellent agreement with the presented values for rotating droplets in contact with an untreated cover slide, which we found to be  $1.7 \pm 0.5 \text{ rot h}^{-1}$ .

### 3. Conclusion

In this study, we demonstrated a method to generate directed autonomous motion of cell-sized actin-containing droplets mediated by Marangoni flows. Key elements are 1) a locally restricted  $\text{Mg}^{2+}$ -mediated interaction of the negatively charged actin filaments with the negatively charged fluorosurfactant (Krytox) at the droplet interface, 2) the resulting local change in IFT, and 3) the maintenance of this out-of-equilibrium state by constant assembly and disassembly of Krytox-actin interactions along with the transport of actin across the interface. These conditions lead to Marangoni flows at the oil-water boundaries that result in an autonomous rotational motion of the droplets. As water-in-oil droplets are commonly used compartment systems in bottom-up synthetic biology, our study also highlights the physicochemical effects that come into play due to the chemical nature of the surfactants. We show how important it is to be aware of the presence of Krytox in the surfactant mix and how it can even be exploited to achieve desirable functions such as motility. Whereas in other systems enzyme-propelled Janus particles' motion is in the magnitude of 1.5 times higher than their diffusion coefficient, the here presented rotational speed is significant as it exceeds its rotational diffusion coefficient by the magnitude of  $\approx 28$  (rotational diffusion coefficient  $D = 0.059$  versus  $\approx 1.7 \text{ rot h}^{-1}$ ). Moreover, we engineered translational motion of actin-containing droplets by fluorinating the glass interface. This caused a rolling motion of actin-containing droplets over hundreds of micrometers with an average velocity of  $0.061 \pm 0.014 \mu\text{m s}^{-1}$  due to the friction between the droplet and the fluorinated surface. Transforming this into a rotational

frequency, we obtain  $1.75 \pm 0.40 \text{ rot h}^{-1}$  for a droplet radius of  $20 \mu\text{m}$ , which is in very good agreement with the rotational motion of the droplet and therefore proves that the observed motion is based on actin-induced Marangoni flow.

The presented directed autonomous motion of the water-in-oil droplets could serve as an adequate model system because it mimics membrane flows as described in some primitive living cells. Furthermore, the fatty acid membranes of protocells were more permeable than the phospholipid membranes of today's cells.<sup>[31]</sup> Therefore, a mechanism of substrate exchange was certainly present. These facts allow for the assumption that the Marangoni flows may have also generated cellular motion in early evolutionary life. Further, it is feasible that the here presented system could be transferred into a physiological more relevant water-in-water system by using an adequate surfactant mixture that allows for a double-layer structure. Self-propelled systems with biologically active molecules are not only a milestone toward the bottom-up assembly of synthetic cells, but also exciting for the development of active drug delivery systems.

#### 4. Experimental Section

**Confocal Fluorescence Microscopy:** A confocal laser scanning microscope LSM 880, LSM900 (Carl Zeiss AG), or Leica SP5 (Leica Microsystems GmbH) was used for confocal imaging. The pinhole aperture was set to one Airy unit and experiments were performed at room temperature. The images were acquired using a  $20\times$  (Objective Plan-Apochromat  $20\times/0.8 \text{ M27}$ , Carl Zeiss AG) or an  $63\times$  oil-immersion objective (HCX PL APO  $63\times/1.40\text{--}0.60$ ; Leica Microsystems GmbH, Germany). For confocal fluorescence imaging, the preformed droplets were sealed in a custom-made observation chamber consisting of two glass cover slides spaced with a double-sided tape. The cover slides were either untreated (Figure 1–4, purchased from Carl Roth) or fluorinated (Figure 5, purchased from Ran Biotechnologies). Images were analyzed and processed with ImageJ (NIH, brightness and contrast adjusted). To analyze the relative intensity of the droplet periphery over the droplet center,  $I_p/I_i$  (see Figure 3), a custom-written Python script was used. It first detects the droplet periphery from brightfield images and then defines a 10 pixel wide rim along it to define  $I_p$ .

**Actin Preparation:** Actin (purified from acetone powder from New Zealand white rabbit skeletal muscle, based on the method of Pardee and Spudich,<sup>[32]</sup> modified after Kron et al.<sup>[33]</sup>) was stored in so-called general actin buffer (GAB) containing 2 mM Tris/HCl, pH 8, 0.2 mM  $\text{CaCl}_2$ , 0.2 mM adenosine triphosphate (ATP), 0.005%  $\text{NaN}_3$ , and 0.2 mM dithiothreitol (DTT), at  $-80^\circ\text{C}$ . The actin monomers were either labeled with methanol-dissolved rhodamine-phalloidin (Biotium), Alexa568, or Alexa633 (Sigma-Aldrich) by mixing  $20 \mu\text{L}$  actin with  $20 \mu\text{L}$  double-density actin buffer (50 mM 4-(2-hydroxyethyl)-1-piperazineethanesulfonic acid (HEPES), pH 7.4, 50 mM KCl, 8 mM  $\text{MgCl}_2$ , 20 mM ethylene glycol-bis( $\beta$ -aminoethyl ether)- $N,N,N',N'$ -tetraacetic acid (EGTA), 20 mM DTT) and  $4 \mu\text{L}$   $10\times$  actin polymerization buffer (20 mM Tris-HCl, pH 8, 500 mM KCl, 20 mM  $\text{MgCl}_2$ , 10 mM NaATP). The actin monomers were left on ice to polymerize for 30 min. Subsequently,  $10 \mu\text{L}$  of rhodamine-phalloidin (10 units) was added to the solution. As an alternative to the rhodamine labeling, 1% custom-made Alexa568 or Alexa633-labeled actin monomers was used. In the indicated cases, 0.4% MC was added to the actin filaments directly before the experiment.

**Formation of Surfactant-Stabilized Water-in-Oil Droplets:** PDMS-based (Sylgard 184, Dow Corning) microfluidic devices for the formation of water-in-oil droplets were produced and assembled according to previously described protocols.<sup>[34]</sup> The device layout is shown in Figure S1, Supporting Information. The aqueous phase for droplet production is made of Milli-Q water containing 10 mM  $\text{MgCl}_2$ , 10 mM

actin,  $1\times$  double-density actin buffer (50 mM HEPES, pH 7.4, 50 mM KCl, 8 mM  $\text{MgCl}_2$ , 20 mM EGTA, 20 mM DTT). The oil phase contained 1.4 wt% of perfluoro-polyether-polyethylene glycol (PFPE-PEG) block-copolymer fluorosurfactants (PEG-based fluorosurfactant, Ran Biotechnologies, Inc.) dissolved in HFE-7500 oil (DuPont) and in the indicated cases mixed with Krytox 157 FS(H) (carboxylic acid-terminated PFPE, DuPont). The fluid pressures were controlled by an Elveflow microfluidic flow control system or syringe pumps (Harvard Apparatus). The fluids were injected into the channels with 1 mL syringes (OmniFix, B. Braun, Germany) connected by a cannula (Sterican  $0.4 \text{ mm} \times 20 \text{ mm}$ , BL/LB, B. Braun) as well as PTFE tubing ( $0.4 \times 0.9 \text{ mm}$ , BOLA). To observe the production process, an Axio Vert.A1 (Carl Zeiss AG) inverse microscope was used. As an alternative to the microfluidic formation of droplets, the aqueous phase was layered on top of the oil phase within a microtube (Eppendorf) and droplet formation was induced by manual shaking as described by Göpfrich et al.<sup>[35]</sup> The microfluidic approach was used for Figure 2C, 3, and 4, whereas droplets in Figure 2A,B and 5 were produced via the shaking method.

**IFT Measurements:** A contact angle system OCA (DataPhysics, USA), equipped with a CCD high-speed camera for pendant drop measurement, was used to determine the IFT between MQ or the actin-containing solution and HFE-7500 oil droplets containing PEG-based fluorosurfactants and Krytox. The Young–Laplace equation was chosen to fit the droplet shape to determine the IFT values. To investigate the effect of Krytox on the actin or MQ solution, 0–8 mM Krytox was added to the oil solution. A stable oil droplet was generated manually into the aqueous solution using a syringe. IFT values were recorded until a stable value was reached. When IFT values fell below  $1 \text{ mN m}^{-1}$  and stable droplet creation was not possible, values were set to  $0 \text{ mN m}^{-1}$ .

#### Supporting Information

Supporting Information is available from the Wiley Online Library or from the author.

#### Acknowledgements

B.H. and K.J. contributed equally to this work. The authors acknowledge Ms. Cornelia Weber for the preparation of actin filaments and Prof. Michael Grunze for helpful feedback and discussions. The authors acknowledge funding from the European Research Council, Grant Agreement no. 294852, SynAd, and the MaxSynBio Consortium, which is jointly funded by the Federal Ministry of Education and Research of Germany and the Max Planck Society. The authors also acknowledge the support from Klaus Tschira Stiftung, the German Science Foundation SFB 1129 and the Volkswagen Stiftung (priority call "Life?"). J.P.S. is the Weston Visiting Professor at the Weizmann Institute of Science and part of the excellence cluster CellNetworks at the University of Heidelberg. K.G. received funding from the European Union Horizon 2020 research and innovation program under the Marie Skłodowska-Curie grant agreement No. 792270, from the Deutsche Forschungsgemeinschaft (DFG, German Research Foundation) under Germany's Excellence Strategy via the Excellence Cluster 3D Matter Made to Order (EXC-2082/1 - 390761711), and the Max Planck Society. K.J. thanks the Carl Zeiss Foundation for the financial support. The Max Planck Society is appreciated for its general support. Open access funding enabled and organized by Projekt DEAL.

#### Conflict of Interest

The authors declare no conflict of interest.

## Keywords

actin, droplet-based microfluidics, Marangoni effect, motility, surfactants, synthetic biology

Received: August 12, 2020

Revised: September 22, 2020

Published online: November 16, 2020

- 
- [1] D. A. Fletcher, R. D. Mullins, *Nature* **2010**, 463, 485.
- [2] R. Zaidel-Bar, S. Itzkovitz, A. Maayan, R. Iyengar, B. Geiger, *Nat. Cell Biol.* **2007**, 9, 858.
- [3] B. Geiger, A. Bershadsky, R. Pankov, K. M. Yamada, *Nat. Rev. Mol. Cell Biol.* **2001**, 2, 793.
- [4] M. Tanaka, T. Kikuchi, H. Uno, K. Okita, T. Kitanishi-Yumura, S. Yumura, *Sci. Rep.* **2017**, 7, 1.
- [5] M. S. Bretscher, *Nat. Rev. Mol. Cell Biol.* **2008**, 9, 916.
- [6] C. Bailey, M. Chen, F. Keller, E. Kandel, *Science* **1992**, 256, 645.
- [7] H. A. Stone, A. D. T. Samuel, *Phys. Rev. Lett.* **1996**, 77, 4102.
- [8] E. A. Shah, K. Keren, *eLife* **2014**, 3, 1.
- [9] M. Miyazaki, M. Chiba, H. Eguchi, T. Ohki, S. Ishiwata, *Nat. Cell Biol.* **2015**, 17, 480.
- [10] F.-C. Tsai, G. H. Koenderink, *Soft Matter* **2015**, 11, 8834.
- [11] Y. Nishigami, H. Ito, S. Sonobe, M. Ichikawa, *Sci. Rep.* **2016**, 6, 1.
- [12] T. Sanchez, D. T. N. Chen, S. J. DeCamp, M. Heymann, Z. Dogic, *Nature* **2012**, 491, 431.
- [13] B. V. V. S. Pavan Kumar, A. J. Patil, S. Mann, *Nat. Chem.* **2018**, 10, 1154.
- [14] S. M. Bartelt, E. Chervyachkova, J. Ricken, S. V. Wegner, *Adv. Biosyst.* **2019**, 3, 1800333.
- [15] A. Kodama, Y. Sakuma, M. Imai, T. Kawakatsu, N. Puff, M. I. Angelova, *Langmuir* **2017**, 33, 10698.
- [16] U. Choudhury, L. Soler, J. G. Gibbs, S. Sanchez, P. Fischer, *Chem. Commun.* **2015**, 51, 8660.
- [17] M. N. Popescu, W. E. Uspal, C. Bechinger, P. Fischer, *Nano Lett.* **2018**, 18, 5345.
- [18] T. Ban, T. Yamagami, H. Nakata, Y. Okano, *Langmuir* **2013**, 29, 2554.
- [19] S. Thutupalli, R. Seemann, S. Herminghaus, *New J. Phys.* **2011**, 13, 073021.
- [20] M. Schmitt, H. Stark, *Phys. Fluids* **2016**, 28, 012106.
- [21] J.-C. Baret, *Lab Chip* **2012**, 12, 422.
- [22] X. Ma, A. Jannasch, U.-R. Albrecht, K. Hahn, A. Miguel-López, E. Schäffer, S. Sánchez, *Nano Lett.* **2015**, 15, 7043.
- [23] I. L. Jørgensen, G. C. Kemmer, T. G. Pomorski, *Eur. Biophys. J.* **2016**, 46, 103.
- [24] B. Haller, K. Göpfrich, M. Schröter, J.-W. Janiesch, I. Platzman, J. P. Spatz, *Lab Chip* **2018**, 18, 2665.
- [25] M. Weiss, J. P. Frohnmayer, L. T. Benk, B. Haller, J.-W. Janiesch, T. Heitkamp, M. Börsch, R. B. Lira, R. Dimova, R. Lipowsky, E. Bodenschatz, J.-C. Baret, T. Vidakovic-Koch, K. Sundmacher, I. Platzman, J. P. Spatz, *Nat. Mater.* **2017**, 17, 89.
- [26] A. H. Crevenna, N. Naredi-Rainer, A. Schönichen, J. Dzubiella, D. L. Barber, D. C. Lamb, R. Wedlich-Söldner, *J. Biol. Chem.* **2013**, 288, 12102.
- [27] Q. Brosseau, Ph.D. thesis, Georg-August-Universität Göttingen **2014**.
- [28] K. Takiguchi, *J. Biochem.* **1991**, 109, 520.
- [29] S. Köhler, O. Lieleg, A. R. Bausch, *PLoS ONE* **2008**, 3, e2736.
- [30] K. Jahnke, M. Weiss, C. Weber, I. Platzman, K. Göpfrich, J. P. Spatz, *Adv. Biosyst.* **2020**, 4, 2000102.
- [31] S. S. Mansy, J. W. Szostak, *Proc. Natl. Acad. Sci.* **2008**, 105, 13351.
- [32] J. D. Pardee, J. Aspudich, *Methods in Enzymology*, Elsevier, Amsterdam, Netherlands **1982**, pp. 164–181.
- [33] S. J. Kron, Y. Y. Toyoshima, T. Q. Uyeda, J. A. Spudich, *Methods In Enzymology*, Elsevier, Amsterdam, Netherlands **1991**, pp. 399–416.
- [34] K. Jahnke, M. Weiss, C. Frey, S. Antona, J.-W. Janiesch, I. Platzman, K. Göpfrich, J. P. Spatz, *Adv. Funct. Mater.* **2019**, 29, 1808647.
- [35] K. Göpfrich, B. Haller, O. Staufer, Y. Dreher, U. Mersdorf, I. Platzman, J. P. Spatz, *ACS Synth. Biol.* **2019**, 8, 937.



### 3.6 Publication 3: Engineering light-responsive contractile actomyosin networks with DNA nanotechnology

As mentioned in the previous section, the dominating form of actin-based motility in eukaryotic cells (crawling) is based on the interplay of actin polymerization on the leading edge and acto-myosin-induced retraction on the trailing edge [10]. In the following work, we will aim to engineer a system towards this goal by including myosin motor proteins to actively generate forces on the actin filaments. For this reason, we produced heavy mero-myosin-coated beads, where the active head domain remains accessible for actin filament binding and power strokes. We verify this in bulk by using caged adenosine triphosphate (ATP) that can be released upon UV illumination. We characterize the bead displacement over time after the release of ATP and establish the formation of an acto-myosin contracting network in bulk. Next, we transfer the system into surfactant-stabilized water-in-oil droplets, where we show that we can induce the symmetric contraction of acto-myosin-networks to the droplet center after ATP release. As prominently shown in the case of motility, where retraction only occurs on the trailing edge, acto-myosin contractions are generally direction i.e. asymmetrical within natural cells. To mimic this, we employ DNA nanotechnology as a highly versatile and programmable tool to engineer linkers based on complementary base-pairing between the water-in-oil droplet periphery and the actin filaments. This strategy is based on a previous work from our group, in which we found that cholesterol-tagged DNA strands localize at the droplet periphery. This allows us to selectively induce interactions of actin filaments with the surfactant layer and therefore a directionality. We show that the previously symmetrically contractin acto-myosin networks now contract asymmetrically towards the droplet periphery upon UV illumination.

This work therefore shows that we can engineer complex systems by using purified reconstituted natural proteins within synthetic environments like water-in-oil droplets. However, it still remains an open challenge how to link the contraction to the motility of primitive synthetic cells.

# Engineering Light-Responsive Contractile Actomyosin Networks with DNA Nanotechnology

Kevin Jahnke, Marian Weiss, Cornelia Weber, Iliia Platzman,\* Kerstin Göpfrich,\* and Joachim P. Spatz\*

External control and precise manipulation is key for the bottom-up engineering of complex synthetic cells. Minimal actomyosin networks have been reconstituted into synthetic cells; however, their light-triggered symmetry breaking contraction has not yet been demonstrated. Here, light-activated directional contractility of a minimal synthetic actomyosin network inside microfluidic cell-sized compartments is engineered. Actin filaments, heavy-meromyosin-coated beads, and caged ATP are co-encapsulated into water-in-oil droplets. ATP is released upon illumination, leading to a myosin-generated force which results in a motion of the beads along the filaments and hence a contraction of the network. Symmetry breaking is achieved using DNA nanotechnology to establish a link between the network and the compartment periphery. It is demonstrated that the DNA-linked actin filaments contract to one side of the compartment forming actin asters and quantify the dynamics of this process. This work exemplifies that an engineering approach to bottom-up synthetic biology, combining biological and artificial elements, can circumvent challenges related to active multi-component systems and thereby greatly enrich the complexity of synthetic cellular systems.

## 1. Introduction

Bottom-up synthetic biology aims to construct synthetic cellular systems from molecular constituents—enhancing our understanding of life itself while potentially providing new directions for biomedical applications.<sup>[1,2]</sup> Conventionally, biomolecules, often proteins, have been isolated from cells and reconstituted in cell-sized confinement to reconstruct versatile cellular functions and sophisticated processes like adhesion,<sup>[3–5]</sup> energy generation,<sup>[6,7]</sup> or motility.<sup>[8–10]</sup> For efficient encapsulation of biocontent, droplet-based microfluidics proved to be a very useful technique due to its high degree of controllability and high-throughput formation of monodisperse compartments.<sup>[3,11–14]</sup>

In particular, actin networks have been reconstituted into water-in-oil droplets<sup>[15–17]</sup> and giant unilamellar vesicles<sup>[18–20]</sup> to observe the role of specific proteins regulating cellular morphology.

Besides increased stability,<sup>[6]</sup> actin-containing synthetic cells further mimic versatile cellular functions like adhesion<sup>[21]</sup> and the formation of protrusions.<sup>[6]</sup>

However, actomyosin-containing minimal systems are often still lacking stimuli-induced symmetry breaking contractility. This is a key feature that governs cytoskeleton-related functions in living cells, like cell motility and division.<sup>[22,23]</sup> Notably, 2D bottom-up engineered actomyosin networks have been contracted upon external stimulation,<sup>[24]</sup> for example, on supported lipid bilayers.<sup>[25,26]</sup> Reconstitution of actomyosin networks further helped to elucidate the molecular mechanisms that govern actomyosin contraction and aster formation like filament sliding,<sup>[27,28]</sup> buckling,<sup>[29]</sup> and polarity sorting.<sup>[28,30]</sup> However, in 3D confinement stimuli-responsive contraction and symmetry breaking has only been achieved with a cell lysate and not relying on purified proteins.<sup>[16,17,31]</sup> The challenge lies in the multitude of required components, which are often difficult to purify from living cells or incompatible with one another in cell-like compartments.<sup>[32]</sup> Hence, we believe that the combination of natural and synthetic parts is the most promising route toward more complex functionality. In particular, engineering of controlled symmetry breaking benefits from a tuneable link between the actin and the compartment periphery. DNA nanotechnology has previously been employed in bottom-up synthetic biology to create linkers between biocomponents,<sup>[33]</sup>


K. Jahnke, Dr. K. Göpfrich  
Biophysical Engineering Group  
Max Planck Institute for Medical Research  
Jahnstraße 29, Heidelberg D 69120, Germany  
E-mail: kerstin.goepfrich@mr.mpg.de

K. Jahnke, Dr. K. Göpfrich  
Department of Physics and Astronomy  
Heidelberg University  
Heidelberg D 69120, Germany

Dr. M. Weiss, C. Weber, Dr. I. Platzman, Prof. J. P. Spatz  
Department of Cellular Biophysics  
Max Planck Institute for Medical Research  
Jahnstraße 29, Heidelberg D 69120, Germany  
E-mail: ilia.platzman@mr.mpg.de; spatz@mr.mpg.de

Dr. M. Weiss, C. Weber, Dr. I. Platzman, Prof. J. P. Spatz  
Institute for Molecular Systems Engineering (IMSE)  
Heidelberg University  
Im Neuenheimer Feld, Heidelberg D 69120, Germany

Prof. J. P. Spatz  
Max Planck School Matter to Life  
Jahnstraße 29, Heidelberg D 69120, Germany

 The ORCID identification number(s) for the author(s) of this article can be found under <https://doi.org/10.1002/adbi.202000102>.

© 2020 The Authors. Published by WILEY-VCH Verlag GmbH & Co. KGaA, Weinheim. This is an open access article under the terms of the Creative Commons Attribution License, which permits use, distribution and reproduction in any medium, provided the original work is properly cited.

DOI: 10.1002/adbi.202000102

to regulate transport and self-organization of microtubules<sup>[34]</sup> as well as to establish a link to the compartment periphery.<sup>[35]</sup>

Here, we merge bottom-up synthetic biology with DNA nanotechnology to achieve light-triggered symmetry breaking of minimal actomyosin cortices. Toward this end, we employ droplet-based microfluidics to engineer a minimal actomyosin cortex consisting of purified actin, synthetic DNA linkers, heavy meromyosin-coated (HMM-coated) beads as force-generators and caged ATP as a light-induced trigger in cell-sized confinement. The minimal actomyosin cortex is linked to the periphery of the water-in-oil droplets via DNA linkers. Furthermore, we show that we can selectively and locally trigger the contraction of this network by light and thereby induce a symmetry breaking contraction with high spatiotemporal control. We quantify symmetry breaking by analyzing the 3D displacement of the actin filaments over time during the aster formation process. All in all, we showcase how an engineering approach to synthetic biology, combining natural and synthetic components, can provide a shortcut toward complex function.

## 2. Results

### 2.1. Contraction of Minimal Actomyosin Networks

We first set out to engineer light-activated contractility of a minimal actomyosin network in bulk. **Figure 1a–d** shows illustrations (top) and confocal fluorescence images (bottom) of how we assemble the contractile system step-by-step: Starting with actin filaments (**Figure 1a**), we add methylcellulose to the actin solution to create bundles of actin filaments as visible in **Figure 1b** (see also **Figure S1** and **Video S1**, Supporting Information). By doing so, we mimic the effect of a cytosol that contains large amounts of macromolecules, which introduce depletion forces in a very simplified manner.<sup>[15,27,36–38]</sup> Due to entropic depletion, the mixing of actin and methylcellulose leads to the formation of thick and several tens of micrometer long filaments.<sup>[38–40]</sup> Interestingly, the formation of actin bundles in presence of methylcellulose is largely independent of the ATP concentration, bundles form also in the absence of ATP (see **Figure S2**, Supporting Information). The ATP-independent filament assembly allows us to decouple actin polymerization from the spatiotemporally controlled contraction of the actin network. In order to induce active contraction, we prepare heavy meromyosin-coated polystyrene beads (HMM-beads) with a diameter of 2  $\mu\text{m}$  (see **Section 4**).<sup>[41]</sup> The use of HMM-coated beads offers several advantages over the reconstitution of myosin filaments or high concentrations of free myosin since they are highly and easily tuneable. First of all, the beads have a defined size and can be coated with a defined amount of HMM. Second, they can be visualized and tracked with simple brightfield microscopy or in case of fluorescent beads even with fluorescence microscopy. Finally, the bead diameter and hence the bead velocity is tuneable.<sup>[41]</sup> Note that we chose the diameter to maximize the bead velocity. Since one bead contains a large number of HMM ( $\approx 10^5$ ), it can bind to several actin filaments and link the filaments to form an actomyosin network. In combination with the use of methylcellulose, three effects

contribute to the generation of large forces on the actin network: 1) Methylcellulose increases the filament length, meaning that HMM-coated beads can travel long distances. The larger displacement directly corresponds to larger force exertion. 2) Methylcellulose further increases the filament thickness, hence multiple heavy meromyosin proteins from one bead can bind. 3) Methylcellulose stiffens the filaments. In its absence, the filaments can wrap around the beads, preventing force generation on the network (see **Figure S3**, Supporting Information). In this regard, HMM-beads can mimic bipolar myosin bundles such as thick filaments in the sarcomere during muscle contraction. **Figure 1c** shows a representative confocal fluorescence image of the attachment of the fluorescently labeled HMM-beads to the bundled actin filaments. To achieve spatiotemporal control over contractile dynamics, we add biologically inactive NPE-caged ATP to the actin solution. Illumination with UV or blue light cleaves the NPE and hence releases ATP.<sup>[42]</sup> After illumination of the entire confocal frame with blue light (405 nm) for 5 s, we observe a contraction of the actin network toward actin-dense regions as visible in **Figure 1d**. The dynamics can be appreciated from the **Video S2**, Supporting Information. Importantly, in absence of methylcellulose we could not observe actomyosin contraction with the HMM coated beads (see **Figure S3**, Supporting Information) showcasing the need of a bundling agent to provide sufficient filament crowding and thus HMM-coated bead-mediated force generation.<sup>[28]</sup> Furthermore, we showed that the same concentration of soluble HMM, which is not bound to the bead, does not induce actomyosin contraction (see **Figure S4**, Supporting Information). To verify that the contraction is caused by the unidirectional movement of the beads along the filaments, we tracked their motion and quantified the bead-velocity before (**Figure 1e**) and after (**Figure 1f**) light-triggered release of ATP (see also **Video S3**, Supporting Information). As shown in **Figure 1g**, we obtain velocities of  $0.017 \pm 0.005 \mu\text{m s}^{-1}$  before and  $0.106 \pm 0.024 \mu\text{m s}^{-1}$  after illumination, which is comparable to previous results.<sup>[41]</sup>

For the sake of completeness, **Figure 1h** verifies the successful formation of the HMM beads using denaturing polyacrylamide gel electrophoresis (PAGE). The bands indicate the presence of HMM (heavy and light chains<sup>[43]</sup>) and bovine serum albumin<sup>[44]</sup> on the polystyrene bead surface functionalized via polylysine-mediated interactions (see **Figure S5**, Supporting Information). To prove that the contraction is only based on HMM activity after ATP release, we performed a control experiment with blebbistatin, which inhibited the contraction of actomyosin networks (see **Figure S6**, Supporting Information).

### 2.2. Actomyosin Contraction in Microfluidic Droplets

As a next step, we set out to transfer the light-activated contractile actomyosin networks from bulk into cell-sized confinement using droplet-based microfluidics. This yields a high number of similar, individual and 3D reaction compartments mimicking the cellular confinement and thereby represents a more relevant approach for reconstituting actomyosin-dynamics compared to 2D studies.<sup>[24,25]</sup> Toward this end, we premixed the solution containing all components introduced in **Figure 1** and encapsulated them into block-copolymer surfactant-stabilized

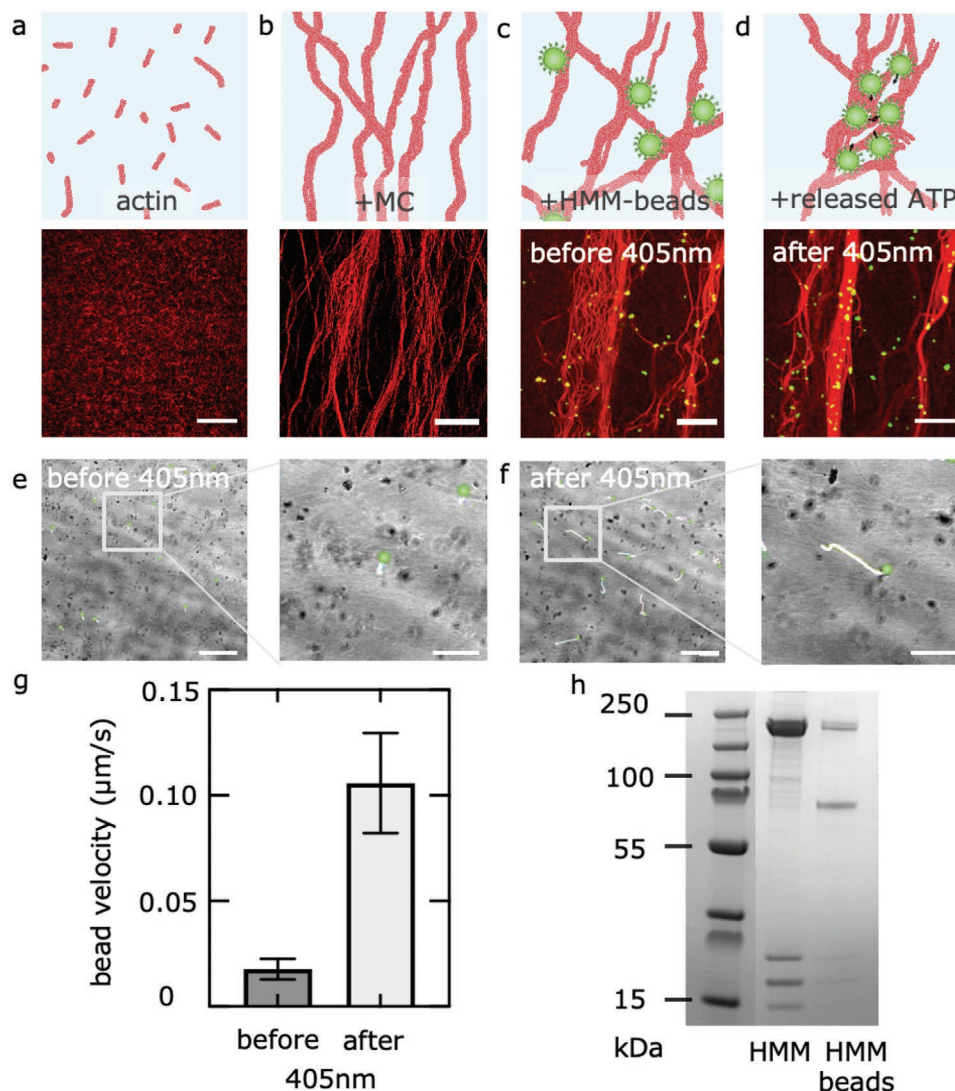


**Figure 1.** Light-triggered contraction of an actomyosin network in bulk. Schematic illustrations (top) and confocal fluorescence images (bottom) of a) actin filaments only (red,  $\lambda_{\text{ex}} = 488 \text{ nm}$  for a, b and  $\lambda_{\text{ex}} = 647 \text{ nm}$  for c, d), in actin buffer); b) actin filaments after addition of methylcellulose, acting as a bundling agent; c) further addition of NPE-caged ATP (unlabeled) and heavy meromyosin-coated beads (green,  $\lambda_{\text{ex}} = 488 \text{ nm}$ ) attached to actin filaments; d) 100 s after illumination ( $\lambda_{\text{ex}} = 405 \text{ nm}$ ), leading to release of ATP. The HMM-beads start to move unidirectionally along the filament leading to a contraction of the actin network toward actin-dense regions. Brightfield images of HMM-coated beads e) before and f) 500 s after illumination ( $\lambda_{\text{ex}} = 405 \text{ nm}$ ) for 5 s. HMM-coated beads start to move unidirectionally along the filaments after ATP-release. g) Velocity of HMM-coated beads before and after illumination ( $n = 20$ ). Error bars correspond to the standard deviation. h) Denaturing polyacrylamide gel electrophoresis (running conditions: 4–12 % polyacrylamide, 200 V, 35 min) of pure HMM in actin buffer (Lane 2) and HMM-coated beads (Lane 3). Polystyrene beads are functionalized with HMM as well as bovine serum albumin (BSA, MW: 67 kDa). Scale bars: a) 20  $\mu\text{m}$ ; b–f) 50  $\mu\text{m}$ ; insets e, f) 10  $\mu\text{m}$ .

droplets as illustrated in **Figure 2a** (see Section 4 and Figure S8, Supporting Information, for a sketch of the microfluidic device). Confocal fluorescence imaging confirmed the successful encapsulation of the biocontent (Figure 2b), showing that all components are stably confined and evenly distributed inside the aqueous droplet lumen. Importantly, prior to illumination with blue light, no movement of the HMM-coated beads or the actin filaments can be observed as shown in Figure 2a,b (for a z-projection see Figure S9, Supporting Information). In order to activate actomyosin contraction by light-triggered ATP release, the confocal field of view is illuminated with blue light for 5 s.

Only after illumination, we observe an immediate contraction of the network inside the confinement of the droplet as we previously observed in bulk and hence have a high degree of spatiotemporal control over the contraction process compared to other studies.<sup>[31]</sup> The contraction stalls after about 6 min, leading to the accumulation of the actin bundles in the droplet center (Figure 2c,d; see also Figure S10, Supporting Information, for more examples). Interestingly, a doubling of the actin concentration leads to a slower contraction and lower degree of compactification (see Figure S11, Supporting Information) whereby a twofold increase of HMM-beads leads to faster but similar response (see Figure S12, Supporting

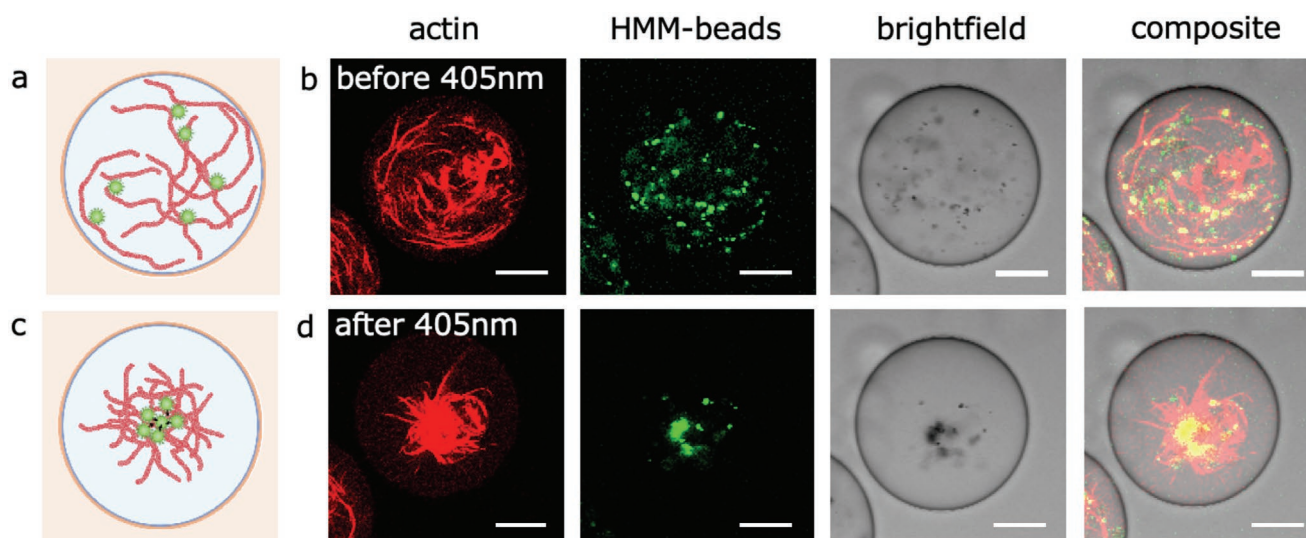


**Figure 2.** Light-triggered contraction of actomyosin networks in cell-sized confinement. a) Schematic illustration of actin filaments (red), HMM-beads (green) and NPE-caged ATP inside water-in-oil droplets before illumination with blue light. b) Confocal fluorescence images of actin filaments (red,  $\lambda_{\text{ex}} = 647 \text{ nm}$ ) and HMM-coated beads (green,  $\lambda_{\text{ex}} = 488 \text{ nm}$ ) encapsulated into water-in-oil droplets as well as brightfield and composite images before illumination with blue light. The minimal actomyosin network is homogeneously distributed in the droplet. c) Schematic illustration of actin filaments and HMM-beads inside water-in-oil droplets after illumination. d) Confocal fluorescence images of actin filaments (red,  $\lambda_{\text{ex}} = 647 \text{ nm}$ ) and HMM-coated beads (green,  $\lambda_{\text{ex}} = 488 \text{ nm}$ ) encapsulated into water-in-oil droplets as well as brightfield and composite images 6 min after illumination with blue light. After ATP-release the minimal actomyosin network contracts toward the droplet center. Scale bars:  $20 \mu\text{m}$ .

Information). This is in excellent agreement with previous studies, in which a global contraction was observed for a myosin motor to actin ratio of  $R_M = 0.01$ .<sup>[30,45,46]</sup> This is comparable to our experiments with  $R_M = 0.013$ , for which we observe global contraction and aster formation. Doubling the actin content (i.e., reducing the HMM to actin ratio by half) leads to a stalled contraction as also observed with reconstituted myosin filaments, consistent with a previous study.<sup>[30]</sup> However, the composition of our asters greatly differs from the biological system as we deliberately chose an engineering approach to achieve light-triggered contractility. Thus, it is even more remarkable that we observe a similar qualitative and quantitative behavior of the actomyosin contraction. The timescale of the contraction agrees well with the bead velocity we determined in Figure 1g and previous works on actomyosin contraction:<sup>[27,29,30–37,46]</sup> Within 6 min, we expect a displacement of approximately  $36 \mu\text{m}$ , which is comparable to the droplet radius. The filaments condense to a small fraction of the droplet's volume (see Figures S10 and S11, and Video S4, Supporting Information). It is thus not surprising, that the contraction happens on that timescale. We suspect that most likely the actin asters formed in our system are initially non-polar and are transformed into at least partially polar actin asters—predominantly governed by actin sliding, polarity sorting, and buckling<sup>[27–30]</sup> as thoroughly discussed in Text S1, Supporting Information. However, the extent to which all of these mechanisms contribute remains to be investigated in detail in further studies. Similar aster-like actin structures have been observed in bulk experiments involving different crosslinking proteins.<sup>[47]</sup> Here, this has been achieved in compartments and successfully been triggered externally with light.

### 2.3. DNA-Based Linkers for Minimal Actomyosin Cortices

Having shown that our minimal actomyosin networks can be encapsulated into cell-sized confinement and contract upon external stimulation, our system is still missing a physical link between the actin network and the compartment periphery. In natural cells, the actin cytoskeleton is constantly recruited to the cellular membranes to produce pushing, pulling and resistance forces during adhesion and motility.<sup>[48]</sup> We previously showed that we can use DNA nanotechnology to functionalize surfactant-stabilized droplets and to link arbitrary components to their periphery.<sup>[35]</sup> In this research, we demonstrated that cholesterol-tagged DNA can be anchored in the surfactant layer via hydrophobic interactions. The cholesterol-tagged DNA serves as an attachment handle for a complementary strand of DNA, which can carry an arbitrary functional group. Here, we exploit this method for the attachment of the actomyosin networks to the compartment periphery as illustrated in Figure 3a,b. Note that we chose an excess concentration ( $1 \mu\text{M}$ ) of the DNA linkers in order to ensure that binding sites are available for the stiff actin bundles. Biotin-modified single-stranded DNA attaches to the cholesterol-tagged DNA at the compartment periphery (yellow). The elongated DNA linker ensures that the biotin-molecule is not hidden in the hydrophilic section of the surfactant layer. It additionally allows for localization due to the possibility to attach a fluorophore. We successfully functionalize actin monomers with biotin and streptavidin as demonstrated by denaturing PAGE (see Figure S13, Supporting Information). Thereby we establish a link to biotinylated actin filaments (5 mol% percent biotinylated over unfunctionalized actin monomers). With confocal fluorescence microscopy, we observe that the actin filaments now span straight across the

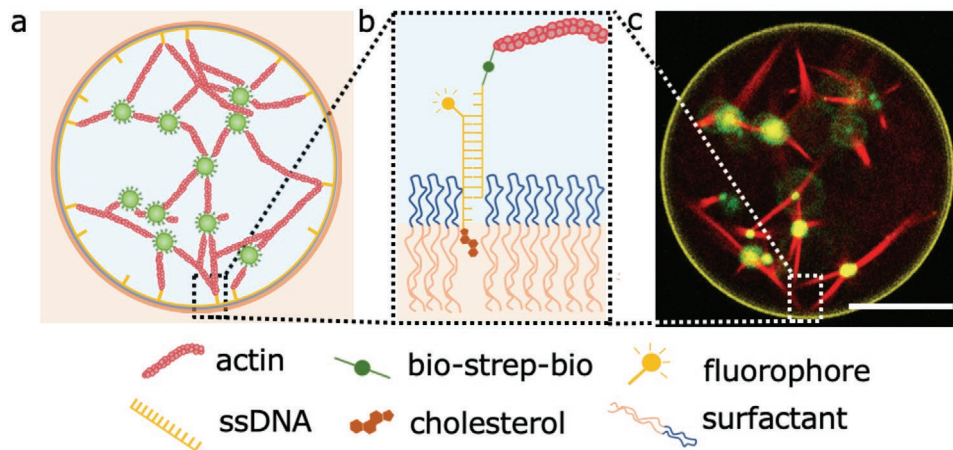


**Figure 3.** DNA nanotechnology-mediated link between the actomyosin network and the compartment periphery. a) Schematic illustration of the linkage of the actomyosin network to the droplet periphery via DNA linkers. Cholesterol-tagged DNA (yellow) self-assembles at the droplet periphery and hybridizes with a complementary DNA strand functionalized with biotin, thereby establishing a strong non-covalent link to the biotin-streptavidin-modified actin filaments. c) Confocal fluorescence composite images of actin filaments (red,  $\lambda_{\text{ex}} = 561 \text{ nm}$ ) linked to the droplet periphery via DNA (yellow,  $\lambda_{\text{ex}} = 647 \text{ nm}$ ) and HMM-coated beads (green,  $\lambda_{\text{ex}} = 488 \text{ nm}$ ). Scale bar:  $30 \mu\text{m}$ .

droplet lumen, with their ends located at the droplet periphery as visible in Figure 3c (for the verification of the binding of the cholesterol-tagged DNA to the periphery, see Figure S14, Supporting Information; DNA sequences are shown in Table S1, Supporting Information). The altered contractile dynamics, described in the next section, will serve as an additional confirmation of the successful attachment of the actin filaments to the compartment periphery.

#### 2.4. Symmetry Breaking Contraction Mediated by DNA Linkers

Finally, we used the DNA linker system to trigger a symmetry break inside the compartment. To demonstrate the spatiotemporal control of the ATP release, this time we illuminated only one half of the field of view with blue light. Only in the illuminated area, we observe a contraction of the actomyosin network toward one hemisphere of the droplet as shown in Figure 4a,b (color-coded z-projection, for images before and after contraction see Figure S15, Supporting Information). The dynamics of the process can be observed in the Video S5, Supporting Information. The diffusive DNA linkers at the droplet periphery induce a symmetry break inside the compartment (Figure 4b,ii,iv). We hence observe altered contractile dynamics compared to the case without DNA linkers (see Figure 2). This again confirms the successful and highly stable linkage of actin to the compartment periphery (see Figure S16, Supporting Information, for individual z-slices). Note that the passive diffusion coefficient of the DNA in the surfactant layer is around  $0.4 \mu\text{m}^2 \text{s}^{-1}$ <sup>[35]</sup> which is too low to allow for the large displacement (for the calculation see Text S2, Supporting Information). This means that the rolling motion of the HMM-beads on the filaments actively pulls the linkers to a pinpoint. Notably, the targeted contraction toward one side of the droplet is not favoring any lateral or axial orientation. The actin network within the droplets that were not illuminated did not contract at all, highlighting that symmetry

breaking can be locally activated inside droplets on a scale of a few micrometer (Figure 4b,i,iii).

In order to quantitatively compare the contraction of the actomyosin networks in the presence and the absence of the DNA linkers, we analyzed the efficiency of the symmetry breaking by determining the position of actin networks within the droplets. For this purpose, we define a spherical 3D region of interest and determine the center of mass of actin filaments in 3D over time for each spherical ROI. Figure 4c depicts the analysis procedure and exemplary 3D projections of the actin filament distribution within a droplet and its corresponding center of mass. Figure 4d shows the normalized mean displacement of  $n = 10$  (+405 nm/+DNA) and  $n = 6$  (+405 nm/-DNA, -405 nm/+DNA) encapsulated actin networks over time. To obtain a quantitative measure for the symmetry breaking over time, we evaluated the displacement of the center of mass of the actin filaments  $R_d$  from the center of mass of the droplet, normalized by the droplet radius  $R_0$ . We find no significant change of the actin filaments center of mass over time in absence of DNA-linker or if ATP was not released via 405 nm illumination. On the contrary, droplets with DNA-linkers and released ATP show an increase in normalized 3D-displacement for 300 s until the contraction stalls and reaches a plateau at  $d = R_d/R_0 = 0.62 \pm 0.12$ . Importantly, the timescale of the contraction agrees well with the bead velocity we determined in Figure 1g: Within 5 min, we expect a displacement of approximately  $30 \mu\text{m}$ , which is comparable to the droplet radius.

Therefore, we conclude that DNA nanotechnology can establish a stable link of the actomyosin networks to the compartment periphery, while subsequent ATP release causes all observed droplets to undergo a symmetry break based on contractility.

### 3. Discussion

In this work, we engineered light-activated minimal contractile actomyosin networks for synthetic cells, capable of symmetry-breaking contraction. This was achieved by combining

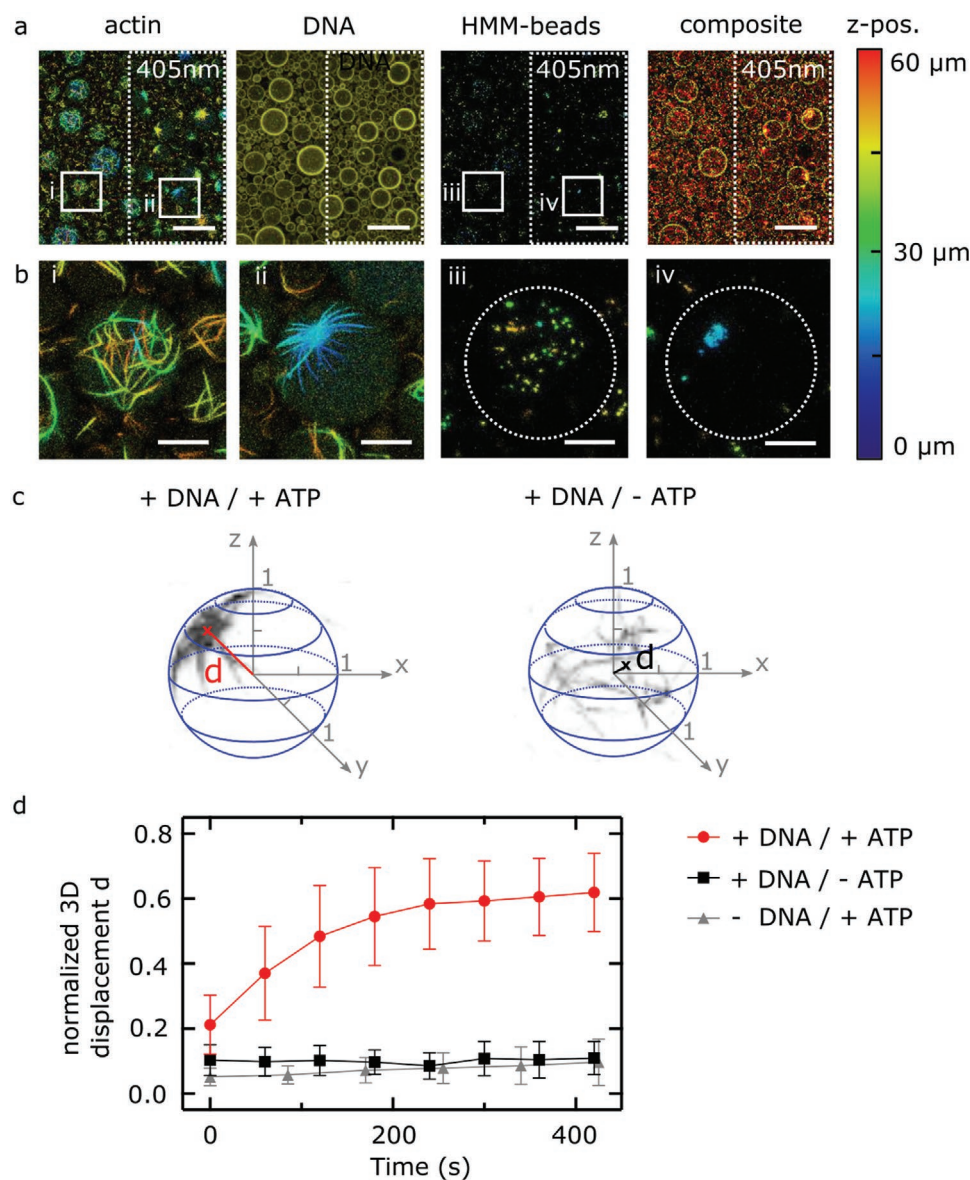


**Figure 4.** DNA nanotechnology-mediated symmetry break of minimal actomyosin cortices in cell-sized compartments. a) Confocal fluorescence images of actin filaments (color-coded z-projection,  $\lambda_{\text{ex}} = 561$  nm), biotinylated DNA (yellow,  $\lambda_{\text{ex}} = 647$  nm) HMM-coated beads (color-coded z-projection,  $\lambda_{\text{ex}} = 488$  nm) and a composite image (actin: red, beads: green, DNA: yellow). The right half of the field of view (indicated by the white dotted line) was illuminated with blue light for 5 s ( $\lambda_{\text{ex}} = 405$  nm). The minimal actomyosin cortices in the illuminated area contract toward the periphery of the droplet whereas there is no contraction in the rest of the confocal frame. b) Exemplary confocal fluorescence color-coded z-projection images of actin filaments ( $\lambda_{\text{ex}} = 561$  nm) and HMM-coated beads ( $\lambda_{\text{ex}} = 488$  nm) for a droplet illuminated with blue light (ii, iv) and a droplet not illuminated with blue light (i, iii). Scale bars: a) 100  $\mu\text{m}$ ; b) 20  $\mu\text{m}$ . The images were taken 7 min after illumination. c) Illustration of the analysis procedure used to quantify symmetry breaking. The center of mass of the actin filaments was evaluated for individual droplets in 3D over time and normalized to the droplet radius. d) Normalized 3D-displacement  $d$  over time for droplets with DNA linkers and after illumination with 405 nm to release ATP (+DNA/+ATP, red), droplets with DNA linker and without released ATP (+DNA/-ATP, black) and droplets without DNA linker but with released ATP (-DNA/+ATP, gray). Only droplets with DNA-linker and released ATP show an increase in normalized 3D-displacement for 300 s until the contraction stalls and reaches a plateau at  $R_d/R_0 = 0.62 \pm 0.12$ .

natural and synthetic components from the bottom-up. We exploited that actin can be bundled into thick and tens of micrometer-long filaments by addition of methylcellulose, mimicking crowding agents in the cytosol of cells. Further, we coated polystyrene beads with heavy meromyosin as active component to induce actomyosin dynamics. To initiate myosin motor activity with high spatiotemporal control, we

used NPE-caged ATP to induce a contraction of the actomyosin network in bulk within minutes after illumination with blue light.

Next, we transferred the bulk approach into cell-sized confinement and found that we can induce a contraction of actomyosin networks toward the droplet center upon illumination. This is the first time the contraction of actomyosin networks

within compartments successfully has been triggered externally by light, offering uniquely high spatiotemporal control.

Increasing the complexity, we used DNA nanotechnology to link the actomyosin network to the droplet periphery to engineer minimal actomyosin cortices. This linkage method offers all benefits associated with DNA nanotechnology, such as sequence programmability and reversibility. Therefore, it is in principle possible to exploit a second trigger, such as pH or temperature, to control cortex formation independently of contraction. Additionally, the use of DNA as a linker provides many possibilities for further advances, including the introduction of stimuli-responsive motifs, DNA aptamers or strand displacement reactions. It will be exciting to transfer the described system into lipid vesicles in the future.

Finally, we observed local symmetry breaking contractility of actomyosin cortices toward the periphery of droplets in presence of the DNA linkers. This yields complex synthetic cells that can undergo a dynamic process—namely a spatiotemporally controlled symmetry break—which can be triggered externally by light. This would not have been possible relying merely on purified components without addition of synthetic custom-made parts. We envision that approaches merging artificial and natural tools to further increase the complexity of synthetic cells will lead to contractile cortical systems for synthetic cell division and motility.

#### 4. Experimental Section

**Confocal Fluorescence Microscopy:** A confocal laser scanning microscope LSM 880 or LSM 800 (Carl Zeiss AG) was used for confocal imaging. The pinhole aperture was set to one Airy Unit and experiments were performed at room temperature. The images were acquired using a 20× (Objective Plan-Apochromat 20×/0.8 M27, Carl Zeiss AG). Images were analyzed and processed with ImageJ (NIH, brightness and contrast adjusted, color-coded representation of confocal z-stacks). Color-coded z-projections were generated from z-stacks and depict the axial dimension of droplets in different colors.

**Actin Preparation:** Actin (purified from acetone powder from New Zealand white rabbit skeletal muscle, based on the method of Pardee and Aspudich,<sup>[49]</sup> modified after Kron et al.<sup>[50]</sup>) was stored in so-called GAB buffer containing 2 mM TRIS/HCl, pH 8, 0.2 mM CaCl<sub>2</sub>, 0.2 mM ATP, 0.005 % NaN<sub>3</sub> and 0.2 mM DTT, at -80 °C. The actin monomers were either labeled with Rhodamine-Phalloidin (Biotium, dissolved in MeOH) or Alexa647 (Sigma-Aldrich) by mixing 20 μL actin with 20 μL AB DTT DD (double-density) buffer (50 mM HEPES, pH 7.4, 50 mM KCl, 8 mM MgCl<sub>2</sub>, 20 mM EGTA, 20 mM DTT) and in some cases 4 μL 10× Actin Polymerization Buffer (20 mM Tris-HCl, pH8, 500 mM KCl, 20 mM MgCl<sub>2</sub>, 10 mM NaATP). The actin monomers were left on ice to polymerize for 30 min. Subsequently, 10 μL of Rhodamine-Phalloidin (10 units) were added to the solution. As an alternative to the Rhodamine labeling, 1 % custom-made Alexa647-labeled actin monomers were used. Directly before the experiment, 2 mM caged ATP and 0.4 % methylcellulose were added to the actin filaments.

**Heavy Meromyosin Beads Preparation:** 10–20 μL (YG-fluorescent) polystyrene microspheres with a diameter of 2 μm (Fluoresbrite) were washed three times with 200 μL 25 mM HEPES pH 7.4 and afterward centrifuged for 5 min at 4 °C and 12000 rpm. As a next step, the beads were diluted in 200 μL poly-L-lysine solution (PLL, 0.1 %) and incubated for 30 min at 4 °C on a rolling mixer. Next, the PLL-coated beads were centrifuged again and diluted in 100 μL AB buffer. To coat the beads with HMM (myosin isolated from New Zealand white rabbit skeletal muscle was used to prepare HMM based on the method of Margossian and Lowey<sup>[51]</sup>), 20 μL sonicated PLL-beads were mixed with 20 μL HMM

(250 μg mL<sup>-1</sup>) and 100 μL AB DTT buffer. The beads were left to incubate on ice for 60 min. Subsequently, 0.5 mg mL<sup>-1</sup> BSA was added to prevent unspecific binding and the beads were left to incubate again for 10 min on ice. As a last step, the HMM-beads were centrifuged and diluted in 50 μL AB DTT buffer. The final bead concentration is on the order of 10<sup>6</sup> particles/μL (see Figure S7, Supporting Information).

**Denaturing Polyacrylamide Gel Electrophoresis:** Precast NuPAGE Bis-Tris Gels (Thermo Fisher) were loaded with 1× NuPAGE lithium dodecyl sulfate (LDS) sample buffer, 1× NuPAGE reducing agent and either 10.4 μg actin conjugated with biotin-streptavidin, 2.7 μg unbound streptavidin after ultracentrifugation of the actin conjugated with biotin-streptavidin, 6 μg pure actin, 6 μg heavy meromyosin or 10 μL of HMM-coated beads. Before mixing, the sample was heated for 10 min at 70 °C. The gel was run in a Xcell SureLock Mini Cell (Thermo Fisher) for 35 min at 200 V in a 1× NuPAGE SDS MES running buffer and afterward stained with InstantBlue (Expedeon). The gel was imaged with either an Amersham Imager 600 (GE Healthcare Life Sciences) or Azure 600 (Azure Biosystems).

**Design and Assembly of the DNA Linkers:** The design and assembly of the DNA linkers was adapted from Jahnke et al.<sup>[35]</sup> In brief, a set of random fixed-length DNA sequences was generated in MATLAB (MathWorks, Inc.) using the *randseq* command. The sequences were analyzed in NUPACK,<sup>[52]</sup> selecting for sequences with minimal secondary structure formation, and purchased from Integrated DNA Technologies, Inc. or biomers.net GmbH. HPLC purification was performed for DNA oligos carrying modifications (Cy3, Cy5, Atto488, cholesterol-TEG, biotin), all other oligos were purified by standard desalting. For a complete list of DNA sequences, see Table S1, Supporting Information. The DNA oligos were diluted in Milli-Q water at a stock concentration of 100 μM, aliquoted and stored at -20 °C until use. Before the experiment, cholesterol-tagged DNA oligos were heated to 60 °C for 5 min to reduce aggregation. A concentration of 2 μM of each oligonucleotide was used in the aqueous solution containing 10 mM MgCl<sub>2</sub>, if not stated otherwise.

**Formation of DNA-Functionalized Surfactant-Stabilized Water-in-Oil Droplets:** As previously described by Jahnke et al.<sup>[35]</sup> microfluidic PDMS-based (Sylgard 184, Dow Corning) devices for the formation of water-in-oil droplets were produced and assembled. The device layout is shown in Figure S8, Supporting Information. The aqueous phase is made up of Milli-Q water containing 10 mM MgCl<sub>2</sub>, 10 μM actin, 1× AB DTT DD (double-density) buffer (50 mM HEPES, pH 7.4, 50 mM KCl, 8 mM MgCl<sub>2</sub>, 20 mM EGTA, 20 mM DTT) and 2–4 μM DNA unless otherwise specified. The oil-phase contains 1.4 wt% of Perfluoro-polyether-polyethylene glycol (PFPE-PEG) block-copolymer fluorosurfactants (PEG-based fluorosurfactant, Ran Biotechnologies, Inc.) dissolved in HFE-7500 oil (DuPont). The fluid pressures were controlled by an Elveflow microfluidic flow control system or syringe pumps (Harvard Apparatus). The fluids were injected into the channels with 1 mL syringes (Omnifix, B.Braun, Germany) connected by a cannula (Sterican 0.4 × 20 mm, BL/LB, B.Braun) as well as PTFE-tubing (0.4 × 0.9 mm, Bola). To observe the production process, an Axio Vert.A1 (Carl Zeiss AG) inverse microscope was used. As an alternative to the microfluidic formation of droplets, the aqueous phase was layered on top of the oil phase within a microtube (Eppendorf) and droplet formation was induced by manual shaking as described by Göpflich et al.<sup>[14]</sup> The microfluidic approach was used for Figures 2 and 3, whereas droplets in Figure 4 were produced via the shaking method.

**Attachment of Actin Filaments to the DNA Linkers:** In order to link actin filaments to the DNA, 2 μM biotinylated actin monomers (Cytoskeleton) were mixed with 38 μM unmodified actin monomers in 25 mM HEPES at pH 7.4 and incubated on ice for 30 min. Afterward, 4 μM streptavidin (Sigma Aldrich), 1× actin polymerization buffer and 0.4% methylcellulose (Sigma-Aldrich) were added with intermediate incubation steps of 30 min on ice. Finally, the solution was centrifuged at 10 000 × g for 45 min, the supernatant removed and the pellet resuspended in the final GAB buffer. To obtain a high yield of biotin-streptavidin functionalized monomers, the solution was furthermore dialyzed overnight against GAB buffer. Before each experiment, the concentration of actin monomers was determined by a NanoPhotometer (Implen) measurement at 280 nm.



**Release of NPE-Caged ATP:** NPE-caged (P3-(1-(2-nitrophenyl)ethyl) ester) ATP disodium salt (Thermo Fisher Scientific) was dissolved to a 100 mM stock concentration in 100 mM Tris (pH8) and stored at  $-20^{\circ}\text{C}$  until use. For the experiments with caged ATP, a final concentration of 2–3 mM was mixed with other components. The release of the NPE group was induced by excitation with a diode laser at a wavelength of 405 nm and (70% laser intensity for 1–5 s).

**Analysis of the Symmetry Breaking Process:** To quantify the degree of symmetry breaking, a spherical 3D region of interest was defined by using the z-stacks of brightfield images of individual droplets. Since the droplets moved slightly over time, the 3D ROI was determined for each time-step and the center of the sphere was determined using the ImageJ plugin 3DRoiManager. The corresponding fluorescence images from the actin channel were filtered with a Gaussian filter and pixel intensities below 25% of the maximum intensity were discarded. With these settings, the signal could be filtered out from free actin monomers and just the filaments could be evaluated. The 3D-center of mass of actin filaments over time was determined for each spherical ROI. The process was repeated for confocal xyz-stacks under three different conditions: +405 nm / +DNA ( $n = 10$ ), +405 nm / -DNA ( $n = 6$ ) and -405 nm / +DNA ( $n = 6$ ). To obtain a quantitative measure for the symmetry breaking over time, the displacement of the center of mass of the actin filaments from the center of mass of the droplet was evaluated, normalized by the droplet radius.

**Statistical Analysis:** The presented data depict mean and standard deviations. To determine the HMM-bead velocity, beads were manually selected and tracked using the ManualTracking plug-in in ImageJ.  $n = 20$  beads were tracked before and after illumination with 405 nm. For the symmetry breaking analysis  $n = 10$  or  $n = 6$  droplets were analyzed for three different conditions as also stated in the main text. Prism (Graphpad) was used to plot the acquired data.

## Supporting Information

Supporting Information is available from the Wiley Online Library or from the author.

## Acknowledgements

The authors acknowledge funding from the European Research Council, Grant Agreement no. 294852, SynAd and the MaxSynBio Consortium, which is jointly funded by the Federal Ministry of Education and Research of Germany and the Max Planck Society. They also acknowledge the support from the SFB 1129 of the German Science Foundation and the VolkswagenStiftung (priority call ‘Life?’). J.P.S. is the Weston Visiting Professor at the Weizmann Institute of Science and part of the excellence cluster CellNetworks at the University of Heidelberg. K.G. received funding from the European Union Horizon 2020 research and innovation program under the Marie Skłodowska-Curie grant agreement No. 792270, from the Deutsche Forschungsgemeinschaft (DFG, German Research Foundation) under Germany’s Excellence Strategy via the Excellence Cluster 3D Matter Made to Order (EXC-2082/1 – 390761711) and the Max Planck Society. The Max Planck Society is appreciated for its general support.

Open access funding enabled and organized by Projekt DEAL.

## Conflict of Interest

The authors declare no conflict of interest.

## Author Contributions

K.J. performed most experiments and analysis, M.W. performed initial experiments. C.W. performed gel electrophoresis, actin, and HMM

purification. K.J., M.W., K.G., I.P., and J.P.S. designed the experiments. K.J. wrote the manuscript with help from all authors.

## Keywords

actomyosin networks, bottom-up synthetic biology, DNA nanotechnology, symmetry break, water-in-oil droplets

Received: April 2, 2020

Revised: June 26, 2020

Published online: July 21, 2020

- [1] P. Schwille, J. Spatz, K. Landfester, E. Bodenschatz, S. Herminghaus, V. Sourjik, T. J. Erb, P. Bastiaens, R. Lipowsky, A. Hyman, P. Dabrock, J. C. Baret, T. Vidakovic-Koch, P. Bieling, R. Dimova, H. Mutschler, T. Robinson, T. Y. D. Tang, S. Wegner, K. Sundmacher, *Angew. Chem., Int. Ed.* **2018**, *57*, 13382.
- [2] P. Schwille, *Science* **2011**, *333*, 1252.
- [3] M. Weiss, J. P. Frohnmayer, L. T. Benk, B. Haller, J. W. Janiesch, T. Heitkamp, M. Börsch, R. B. Lira, R. Dimova, R. Lipowsky, E. Bodenschatz, J. C. Baret, T. Vidakovic-Koch, K. Sundmacher, I. Platzman, J. P. Spatz, *Nat. Mater.* **2017**, *17*, 89.
- [4] J. P. Frohnmayer, D. Brüggemann, C. Eberhard, S. Neubauer, C. Mollenhauer, H. Boehm, H. Kessler, B. Geiger, J. P. Spatz, *Angew. Chem., Int. Ed.* **2015**, *54*, 12472.
- [5] R. Maan, E. Loiseau, A. R. Bausch, *Biophys. J.* **2018**, *115*, 2395.
- [6] K. Y. Lee, S. J. Park, K. A. Lee, S. H. Kim, H. Kim, Y. Meroz, L. Mahadevan, K. H. Jung, T. K. Ahn, K. K. Parker, K. Shin, *Nat. Biotechnol.* **2018**, *36*, 530.
- [7] T. Pols, H. R. Sikkema, B. F. Gaastra, J. Frallicciardi, W. M. Śmigiel, S. Singh, B. Poolman, *Nat. Commun.* **2019**, *10*, 4239.
- [8] F. C. Keber, E. Loiseau, T. Sanchez, S. J. DeCamp, L. Giomi, M. J. Bowick, M. C. Marchetti, Z. Dogic, A. R. Bausch, *Science* **2014**, *345*, 1135.
- [9] S. M. Bartelt, J. Steinkühler, R. Dimova, S. V. Wegner, *Nano Lett.* **2018**, *18*, 7268.
- [10] O. Siton-Mendelson, A. Bernheim-Groswasser, *Cell Adhes. Migr.* **2016**, *10*, 461.
- [11] S. Deshpande, Y. Caspi, A. E. C. Meijering, C. Dekker, *Nat. Commun.* **2016**, *7*, 10447.
- [12] M. P. N. Juniper, M. Weiss, I. Platzman, J. P. Spatz, T. Surrey, *Soft Matter* **2018**, *14*, 901.
- [13] N. N. Deng, M. Yelleswarapu, L. Zheng, W. T. S. Huck, *J. Am. Chem. Soc.* **2016**, *139*, 587.
- [14] K. Göpfrich, B. Haller, O. Staufer, Y. Dreher, U. Mersdorf, I. Platzman, J. P. Spatz, *ACS Synth. Biol.* **2019**, *8*, 937.
- [15] M. Miyazaki, M. Chiba, H. Eguchi, T. Ohki, S. Ishiwata, *Nat. Cell Biol.* **2015**, *17*, 480.
- [16] E. A. Shah, K. Keren, *eLife* **2014**, *3*, e01433.
- [17] M. Malik-Garbi, N. Ierushalmi, S. Jansen, E. Abu-Shah, B. L. Goode, A. Mogilner, K. Keren, *Nat. Phys.* **2019**, *15*, 509.
- [18] K. Dürre, F. C. Keber, P. Bleicher, F. Brauns, C. J. Cyron, J. Faix, A. R. Bausch, *Nat. Commun.* **2018**, *9*, 1630.
- [19] S. Tanaka, K. Takiguchi, M. Hayashi, *Commun. Phys.* **2018**, *1*, 18.
- [20] L. L. Pontani, J. van der Gucht, G. Salbreux, J. Heuvingh, J. F. Joanny, C. Sykes, *Biophys. J.* **2009**, *96*, 192.
- [21] D. Merkle, N. Kahya, P. Schwille, *ChemBioChem* **2008**, *9*, 2673.
- [22] R. Li, B. Bowerman, *Cold Spring Harbor Perspect. Biol.* **2009**, *2*, a003475.
- [23] L. Blanchoin, R. Boujemaa-Paterski, C. Sykes, J. Plastino, *Physiol. Rev.* **2014**, *94*, 235.

- [24] M. Schuppler, F. C. Keber, M. Kröger, A. R. Bausch, *Nat. Commun.* **2016**, 7, 13120.
- [25] I. Linsmeier, S. Banerjee, P. W. Oakes, W. Jung, T. Kim, M. P. Murrell, *Nat. Commun.* **2016**, 7, 12615.
- [26] Sonal, K. A. Ganzinger, S. K. Vogel, J. Mücksch, P. Blumhardt, P. Schwille, *J. Cell Sci.* **2018**, 132, jcs219899.
- [27] K. Takiguchi, *J. Biochem.* **1991**, 109, 520.
- [28] F. Backouche, L. Haviv, D. Groswasser, A. Bernheim-Groswasser, *Phys. Biol.* **2006**, 3, 264.
- [29] M. P. Murrell, M. L. Gardel, *Proc. Natl. Acad. Sci.* **2012**, 109, 20820.
- [30] V. Wollrab, J. M. Belmonte, L. Baldauf, M. Leptin, F. Nédélec, G. H. Koenderink, *J. Cell Sci.* **2018**, 132, jcs219717.
- [31] N. Ierushalmi, M. Malik-Garbi, A. Manhart, E. A. Shah, B. L. Goode, A. Mogilner, K. Keren, *eLife* **2020**, 9, e55368.
- [32] K. Göpfrich, I. Platzman, J. P. Spatz, *Trends Biotechnol.* **2018**, 36, 938.
- [33] S. M. Douglas, I. Bachelet, G. M. Church, *Science* **2012**, 335, 831.
- [34] A. J. M. Wollman, C. Sanchez-Cano, H. M. J. Carstairs, R. A. Cross, A. J. Turberfield, *Nat. Nanotechnol.* **2013**, 9, 44.
- [35] K. Jahnke, M. Weiss, C. Frey, S. Antona, J. W. Janiesch, I. Platzman, K. Göpfrich, J. P. Spatz, *Adv. Funct. Mater.* **2019**, 29, 1808647.
- [36] M. M. A. E. Claessens, M. Bathe, E. Frey, A. R. Bausch, *Nat. Mater.* **2006**, 5, 748.
- [37] Y. Tanaka-Takiguchi, T. Kakei, A. Tanimura, A. Takagi, M. Honda, H. Hotani, K. Takiguchi, *J. Mol. Biol.* **2004**, 341, 467.
- [38] S. Köhler, O. Lieleg, A. R. Bausch, *PLoS One* **2008**, 3, e2736.
- [39] A. R. Bausch, K. Kroy, *Nat. Phys.* **2006**, 2, 231.
- [40] S. Asakura, F. Oosawa, *J. Chem. Phys.* **1954**, 22, 1255.
- [41] Y. Lee, P. Famouri, *Nano Lett.* **2013**, 13, 3775.
- [42] J. A. McCray, L. Herbette, T. Kihara, D. R. Trentham, *Proc. Natl. Acad. Sci.* **1980**, 77, 7237.
- [43] J. Klinth, A. Arner, A. Månsson, *J. Muscle Res. Cell Motil.* **2003**, 24, 15.
- [44] A. Dunker, R. R. Rueckert, *J. Biol. Chem.* **1969**, 244, 5074.
- [45] Y. Ideses, A. Sonn-Segev, Y. Roichman, A. Bernheim-Groswasser, *Soft Matter* **2013**, 9, 7127.
- [46] Y. Ideses, V. Erukhimovitch, R. Brand, D. Jourdain, J. S. Hernandez, U. R. Gabinet, S. A. Safran, K. Kruse, A. Bernheim-Groswasser, *Nat. Commun.* **2018**, 9, 2461.
- [47] M. Fritzsche, D. Li, H. Colin-York, V. T. Chang, E. Moeendarbary, J. H. Felce, E. Sezgin, G. Charras, E. Betzig, C. Eggeling, *Nat. Commun.* **2017**, 8, 14347.
- [48] B. Geiger, J. P. Spatz, A. D. Bershadsky, *Nat. Rev. Mol. Cell Biol.* **2009**, 10, 21.
- [49] J. D. Pardee, J. Aspudich, in *Methods in Enzymology*, Elsevier, New York **1982**, pp. 164–181.
- [50] S. J. Kron, Y. Y. Toyoshima, T. Q. Uyeda, J. A. Spudich, in *Methods in Enzymology*, Elsevier, New York **1991**, pp. 399–416.
- [51] S. S. Margossian, S. Lowey, in *Methods in Enzymology*, Elsevier, New York **1982**, pp. 55–71.
- [52] J. N. Zadeh, C. D. Steenberg, J. S. Bois, B. R. Wolfe, M. B. Pierce, A. R. Khan, R. M. Dirks, N. A. Pierce, *J. Comput. Chem.* **2010**, 32, 170.

### 3.7 Publication 4: Choice of fluorophore affects dynamic DNA nanostructures

The sole use of reconstituted proteins for the bottom-up assembly of synthetic cells quickly reaches its limits when one thinks about combining two, three or even more proteins within cell-sized confinement. The reason is simple: some proteins are hard to purify if this is at all possible [100] and they require specific chemical environments i.e. buffer composition, reconstitution protocols or handling which often makes them incompatible with one another [101]. Therefore, we now investigate means to engineer a synthetic cytoskeleton made from DNA.

We have seen in the previous publications that an essential and advantageous component of bottom-up engineered systems is the control over their dynamics. Therefore, we first need to understand the dynamics of simple DNA nanostructures in order to build more complex cytoskeleton mimics. A powerful example for a dynamic DNA nanostructure is triplex DNA, which can reversibly change its conformation between an open and a closed state depending on the pH. While investigating this mechanism, we made the interesting discovery that the choice of fluorophore on the triplex DNA and the corresponding cholesterol-tagged linker strand had an impact on the pH-mediated dynamics that we observed. This is interesting since fluorophore modifications of DNA nanostructures are often required for imaging purposes but most of the times deliberately chosen depending on the optical setup or other fluorophores present in the experimental system. Therefore, we decided to investigate the change of the triplex DNA's dynamic behavior based on the choice of fluorophore further. To do so, we combined a set of experiments and molecular dynamics (MD) simulations.

At first, we quantified the amount of unbound triplex DNA in presence of the linker strand within water-in-oil droplets depending on the pH and their fluorophore. We found that there is more unbound triplex DNA in presence of a dye compared to an unmodified triplex. Moreover, MD simulations showed the trend that fluorophore presence on single-stranded DNA (ssDNA) causes lower gyration radii and stabilizes more compact conformations of ssDNA. As a third experiment, we performed dynamic detachment of triplex DNA from the droplet periphery by decreasing the pH inside the water-in-oil droplet over time. This revealed that unmodified triplex DNA detaches faster from the droplet periphery than fluorophore-modified one. All in all, this suggests that both the single-stranded state as well as the bound complex of ssDNA and triplex DNA have a lower free energy profile with fluorophore modifications than without. Ultimately, we screen the effect of 12 different fluorophore pairs on ssDNA and triplex DNA, which also reveal crucial differences even in between individual fluorophores themselves.

This work not only shows the tremendous impact of fluorophore modifications on the conformation of DNA nanostructures but also the importance of cautiously controlling dynamics systems.

# Choice of fluorophore affects dynamic DNA nanostructures

Kevin Jahnke<sup>1,2</sup>, Helmut Grubmüller<sup>3</sup>, Maxim Igaev<sup>3,\*</sup> and Kerstin Göpfrich<sup>1,2,\*</sup>

<sup>1</sup>Max Planck Institute for Medical Research, Biophysical Engineering Group, Jahnstraße 29, 69120 Heidelberg, Germany, <sup>2</sup>Department of Physics and Astronomy, Heidelberg University, 69120 Heidelberg, Germany and <sup>3</sup>Max Planck Institute for Biophysical Chemistry, Department of Theoretical and Computational Biophysics, Am Fassberg 11, 37077 Göttingen, Germany

Received December 15, 2020; Revised February 15, 2021; Editorial Decision March 09, 2021; Accepted March 10, 2021

## ABSTRACT

The ability to dynamically remodel DNA origami structures or functional nanodevices is highly desired in the field of DNA nanotechnology. Concomitantly, the use of fluorophores to track and validate the dynamics of such DNA-based architectures is commonplace and often unavoidable. It is therefore crucial to be aware of the side effects of popular fluorophores, which are often exchanged without considering the potential impact on the system. Here, we show that the choice of fluorophore can strongly affect the reconfiguration of DNA nanostructures. To this end, we encapsulate a triple-stranded DNA (tsDNA) into water-in-oil compartments and functionalize their periphery with a single-stranded DNA handle (ssDNA). Thus, the tsDNA can bind and unbind from the periphery by reversible opening of the triplex and subsequent strand displacement. Using a combination of experiments, molecular dynamics (MD) simulations, and reaction-diffusion modelling, we demonstrate for 12 different fluorophore combinations that it is possible to alter or even inhibit the DNA nanostructure formation—without changing the DNA sequence. Besides its immediate importance for the design of pH-responsive switches and fluorophore labelling, our work presents a strategy to precisely tune the energy landscape of dynamic DNA nanodevices.

## INTRODUCTION

DNA nanotechnology has been highly successful in repurposing the iconic DNA double helix to create programmable molecular architectures. Once focused on static shapes, dynamic and stimuli-responsive DNA nanoscale devices are gaining a large surge of interest for various applica-

tions (1)—from sensors (2–4), biocomputing algorithms (5), and drug delivery systems (6,7) to programmable robotic modules (8,9) and functional components for synthetic cells (10–12). In a vast majority of such reconfigurable systems, dynamics are achieved using strand displacement reactions (13,14), flexible single-stranded hinges (15), stimuli-responsive DNA modifications (16,17) or sequence motifs (4,18). The ability to reversibly actuate artificial structures at the nanoscale is therefore at the core of dynamic DNA nanotechnology. Direct measurements of conformational changes in aqueous solutions are often conducted with Förster resonance energy transfer (FRET) or fluorescence microscopy (19–21). These methods can provide a readout of the overall conformational state of the structure, for example, open versus closed, or bound versus unbound. Hence, the use of fluorescent dyes is commonplace to validate and quantify the functionality of the DNA-based devices. Fluorophore-tagged DNA nanostructures have also been used as nanoscopic rulers for fluorescence microscopy (22) and to enable the acquisition of super-resolution images with DNA-PAINT (23). Factors like solubility, photostability and excitation/emission spectra usually play the decisive role in choosing a suitable dye, while potential side effects on the DNA conformation such as overstabilization of DNA duplexes (24) or specific fluorophore-DNA interactions (25) are not the main concern.

Here, we show that the choice of the fluorophore itself can alter the equilibrium conformation and even inhibit a desired dynamic response. We use a pH-responsive triple-stranded DNA motif (tsDNA) combined with a strand-displacement reaction to exemplify that the dynamics can be strongly influenced by the choice of the fluorophore. With all-atom molecular dynamics (MD) simulations, we show that fluorophore-dependent conformational dynamics of the single-stranded DNA (ssDNA) contribute to this observation. By releasing caged protons inside droplet-based confinement, we find that also the duplex dissociation is affected by the fluorophore. Using a reaction-diffusion

\*To whom correspondence should be addressed. Tel: +49 6221 486 443; Email: kerstin.goepfrich@mr.mpg.de  
Correspondence may also be addressed to Maxim Igaev. Tel: +49 5512 012 334; Email: migaev@mpibpc.mpg.de

model, we derive the apparent dissociation constant for 12 different experimentally tested fluorophore combinations. A profound knowledge about the effect that fluorophores and other chemical modifications have on the dynamics of a DNA-based system can be leveraged to realize the desired functionality.

## MATERIALS AND METHODS

### DNA sequence design

The DNA sequences were adapted from Green *et al.* (4). To enable self-assembly at the droplet-periphery, the ssDNA (termed ‘Regulator’ in Green *et al.*) was modified with a cholesterol-tag (sequence: 5′ Cy3/Alexa488/Cy5/-ACCAGACAATACCACACAATTTT-CholTEG 3′, HPLC purified). The tsDNA (termed ‘Sensor’ in Green *et al.*) contained the triple-stranded DNA motif as well as a stem loop complementary to the ssDNA. A fluorophore modification was added to its 5′ end (sequence: 5′ Cy5/Cy3/Atto488/Atto647-TTCTCTTCTCGTTTGC TCTTCTTGTGTGGTATTGTCTAAGAGAAGAG 3′, HPLC purified). Both DNA sequences were purchased from Biomers or Integrated DNA Technologies and dissolved in ultrapure water (Milli-Q) to exclude the impact of DNA storage buffer on the pH.

### Formation of DNA-containing water-in-oil droplets

For the formation of water-in-oil droplets, the DNA-containing aqueous phase was layered on top of the oil phase in a volumetric ratio of 1:3 within a microtube (Eppendorf). Droplet formation was induced by manual shaking for about 4 s as described earlier (26). For the oil-phase, 1.4 vol% of perfluoro-polyether-polyethylene glycol (PFPE-PEG) block-copolymer fluorosurfactants (008-PEG-based fluorosurfactant, Ran Biotechnologies, Inc.) dissolved in HFE-7500 oil (DuPont) was used. The interfacially active surfactants stabilize the droplets. The aqueous phase was composed of 10 mM MgCl<sub>2</sub> and 250 mM potassium phosphate buffer adjusted to pH values from 4.3 to 8.0. Cholesterol-tagged ssDNA and the tsDNA were added to the aqueous phase at concentrations of 1.66 and 1.25 μM, respectively, if not stated otherwise. ssDNA was added in excess to ensure that there are sufficient binding sites for the tsDNA. Other contents were encapsulated by adding them to the aqueous phase as described in text.

### Confocal fluorescence microscopy

For confocal microscopy, the DNA-containing droplets were sealed in a custom-built observation chamber and imaged 10 min after encapsulation using a confocal laser scanning microscope LSM 880 or LSM 800 (Carl Zeiss AG). The pinhole aperture was set to one Airy Unit and experiments were performed at room temperature. The images were acquired using a 20× objective (Plan-Apochromat 20×/0.8 M27, Carl Zeiss AG). Images were analysed and processed with ImageJ (NIH, brightness and contrast adjusted).

### Light-triggered proton release

To dynamically decrease the pH inside individual compartments, we co-encapsulated 40 mM NPE-caged sulfate (Santa Cruz Biotechnology), which undergoes photolysis upon illumination with light of the wavelength 405 nm and releases a proton. For the investigation of the detachment kinetics, 2 μM ssDNA and 1.5 μM tsDNA were mixed with 20 mM potassium phosphate buffer at pH 8 and 5 mM MgCl<sub>2</sub>. The use of the buffer ensures the same starting conditions and delays the acidification, which facilitates the imaging and analysis of the tsDNA fluorescence. After encapsulation, a subset of droplets was illuminated with 20% of the power of a 5 mW 405 nm laser diode while simultaneously recording the detachment of the Cy5-labelled tsDNA. The field of view, the laser intensity and all additional imaging conditions were kept the same.

### Image analysis

The tsDNA fluorescence inside the droplet and at the droplet periphery was analysed with a custom-written ImageJ macro (27). Droplets were identified and assigned a circular region of interest from which the droplet radius  $r_0$  was calculated. We first selected droplets of similar size in the range of 40–50 μm. Afterwards, we manually removed droplets which were in contact with each other and only analysed droplets without direct neighbours to avoid crosstalk of their fluorescent signals. Analysis of almost identical droplets reduces the variance in the measured quantities and allows for statistical robustness. Second, it unifies the acquired data such that mathematical modelling is possible. The intensity within the droplet center,  $I_{in}$ , was defined as the mean intensity within a circle of radius  $r_{in} = 0.5r_0$ . The intensity at the droplet periphery  $I_{peri}$  was quantified by measuring the maximum intensity along a line orthogonal to the droplet circumference. This analysis was repeated 20 times every 18° along the droplet circumference, and the mean value taken as  $I_{peri}$ . Following the determination of the droplet intensities  $I_{in}$ , they were plotted with Prism 8 (GraphPad) and fitted using a sigmoidal function of the form:  $I_{in} = I_{min} + (I_{max} - I_{min}) / (1 + 10^{-\alpha(pH_{turn} - pH)})$ , with  $\alpha$  being the decay constant and  $pH_{turn}$  the  $pK_a$  and the turning point of the fit.

### Atomistic simulations of unlabelled ssDNA

To provide a realistic description of ssDNA dynamics both in the presence and in the absence of fluorescent dyes, we first performed a series of simulations for the dye-free ssDNA using the Parmbsc1 flavour (28) of the standard Amber 99SB force field (29) with CUFIX non-bonded corrections (30) and ion parameter corrections by Joung and Cheatham (31). We also used TIP3P as the water model in our simulations (32). The simulations were initiated from single-stranded helical structures built with Chimera (v. 1.14) (33). The starting structures were solvated in TIP3P water in a dodecahedron box with an edge length of 9.0 nm, yielding a system with ~50 000 atoms. Ion concentrations were set to 250 mM NaCl and 10 mM MgCl<sub>2</sub> to mimic the experimental conditions.

Subsequent MD simulations were performed with GRO-MACS 2019.6 (34). Lennard-Jones and short-range electrostatic interactions were calculated with a 1.0-nm cutoff, while long-range electrostatics was treated using particle-mesh Ewald summation (35) with a 0.12-nm grid spacing. Hydrogen bond lengths were constrained using the LINCS algorithm (36). Velocity rescaling (37) with a heat bath coupling constant of 1.0 ps was used to control the temperature for solute and solvent separately. Center-of-mass correction was applied to solute and solvent separately every 100 steps. Energy minimization was followed by a short equilibration for 1 ns in the NVT ensemble ( $T = 100$  K) and with position restraints applied to the solute's heavy atoms and a 1-fs integration time step. Next, the temperature was increased to  $T = 300$  K, and the system was equilibrated for 5 ns (2-fs time step), while keeping the pressure at 1 atm using the Berendsen barostat (38) with a 1-ps coupling constant. The position restraints were then slowly released during 20 ns of equilibration in the NPT ensemble ( $T = 300$  K,  $p = 1$  atm, 2-fs time step) using the Parrinello-Rahman barostat (39). This initial equilibration step was followed by a total of 17 independent production runs, each being 5  $\mu$ s long. The first  $\sim 1$   $\mu$ s of the trajectories were discarded to exclude the initial relaxation towards the equilibrium state. Unless specified differently, all trajectory analyses were performed with Python (v. 2.7 available at <https://www.python.org/>), VMD (v. 1.9.2) (40) and Chimera (v. 1.14) (33).

### ssDNA simulations with fluorescent dyes covalently attached

Parameters and energy-minimized structures for common Alexa and Cy fluorescent dye families were derived from the AMBER-DYES library (41) that is compatible with most Amber force fields. Alexa488, Cy3 (water-soluble) and Cy5 (water-soluble) dyes were attached to the 5' end of the ssDNA via a neutral lysine linker. To this end, the capping H5T atom of the 5' nucleotide was removed, and the C atom of the linker backbone was bonded with the O5' atom of the 5' nucleotide. Since in the Amber formalism, the 5' and 3' nucleotides possess non-integer charges ( $-0.3e$  and  $-0.7e$ , respectively; unlike the regular nucleotides that have a charge of  $-1.0e$ ), the resulting dye-ssDNA construct had a slightly non-integer charge. To account for this, the residual small charge was redistributed over the O5', C5', C4', C3', O4', C1' and C2' atoms of the 5' nucleotide (sugar backbone).

To accommodate the larger dye-ssDNA, the size of the simulation box was increased to 12 nm, yielding a system with about 120 000 atoms. All subsequent simulations were done under the same conditions as for the unlabelled ssDNA. For the dye-free simulations, multiple 6  $\mu$ s production runs were performed and the first  $\sim 1$   $\mu$ s were discarded as equilibration time. A summary of the simulated systems is given in Table 1.

### Determination of the apparent dissociation constant

The equilibrium distribution of ssDNA and tsDNA molecules in a droplet can be described mathematically using a reaction-diffusion system of equations in which the binding sites (ssDNA attached to the droplet periphery),

**Table 1.** Summary of dye-free and dye-labelled ssDNA simulations

Force field	System	Duration
Parmbsc1 + TIP3P	No dye	$17 \times 5 \mu$ s
Parmbsc1 + TIP3P	Cy3	$6 \times 6 \mu$ s
Parmbsc1 + TIP3P	Cy5	$6 \times 6 \mu$ s
Parmbsc1 + TIP3P	Alexa 488	$6 \times 6 \mu$ s

and hence also the binding and dissociation reactions, are localized in a narrow volumetric layer near the spherical droplet surface (42,43). Briefly, if  $S_{\text{tot}}$  and  $T_{\text{tot}}$  are the total concentrations of ssDNA and tsDNA in the droplet, respectively,  $T_{\text{eq}}$  is the steady-state concentration of tsDNA in equilibrium, and  $K_{\text{D}}$  is the dissociation constant defining the ssDNA/tsDNA binding equilibrium, the ratio between the peripheral and inner intensity of tsDNA fluorescence can be expressed as:

$$\frac{I_{\text{peri}}}{I_{\text{in}}} = 1 + \frac{S_{\text{tot}}}{T_{\text{eq}} + K_{\text{D}}}. \quad (1)$$

Here, both  $I_{\text{in}}$  and  $I_{\text{peri}}$  are per-area intensities averaged over  $\pi r_{\text{in}}^2$  and  $2\pi r_0 \epsilon$ , respectively, where  $\epsilon$  is the apparent thickness of the reaction layer (determined from confocal images as described in the Supplementary Text S1). The steady-state concentration  $T_{\text{eq}}$ ,

$$T_{\text{eq}} = \frac{1}{2} \left[ - (3\epsilon/r_0 S_{\text{tot}} + K_{\text{D}} - T_{\text{tot}}) + \sqrt{(3\epsilon/r_0 S_{\text{tot}} + K_{\text{D}} - T_{\text{tot}})^2 + 4T_{\text{tot}} K_{\text{D}}} \right], \quad (2)$$

is obtained by simultaneously requiring that the ssDNA/tsDNA binding has attained equilibrium and that the number of tsDNA molecules in the droplet is conserved. The apparent  $K_{\text{D}}$  values presented in Figure 4 were determined using Equations (1) and (2), and the corresponding errors were calculated using basic error propagation rules and measured uncertainties of  $I_{\text{peri}}$ ,  $I_{\text{in}}$ ,  $r_0$  and  $\epsilon$ . A detailed mathematical description of the model, estimation of  $\epsilon$ , and error analysis are given in the Supplementary Texts S1 and S2.

### Radius of gyration distributions and estimations of confidence intervals

The gyration radii ( $R_{\text{g}}$ ) of ssDNA were calculated using the `gmx gyrate` tool included in the GROMACS package. The probability distributions  $p(R_{\text{g}})$  shown in Figure 2 were then computed by binning the corresponding data sets and normalizing the histograms. Confidence intervals for  $p(R_{\text{g}})$  were estimated using bootstrap analysis (44). To this end, we used the obtained distributions to bootstrap  $10^6$  new random  $R_{\text{g}}$  samples (each consisting of  $10^5$  data points) such that the newly generated data is distributed according to  $p(R_{\text{g}})$  and properly correlated with the autocorrelation time estimated from the original  $R_{\text{g}}$  trajectories.

## RESULTS

### Fluorophore modification influences pH response

We set out to test the impact of fluorophores on the dynamics of DNA nanostructures. For this purpose, we employed

a popular triple-stranded DNA motif (tsDNA) (4) as an example. Its reversible pH-responsive actuation works as follows: At basic pH, the Hoogsteen-interactions which stabilize the triple-stranded configuration are weaker than at acidic pH. Therefore, an increase in pH leads to unwrapping of the third strand which previously stabilized the duplex. This, in turn, lowers the energy barrier for a strand displacement reaction with a single-stranded DNA (ssDNA), which was designed to be complementary to the hairpin loop of the tsDNA. Thus, a stable DNA duplex can form between the tsDNA and the ssDNA (Figure 1A) (4). To monitor this process, we modified the ssDNA with a cholesterol-tag and encapsulated it together with the tsDNA into water-in-oil droplets. Upon encapsulation, the ssDNA self-assembled at the droplet periphery due to hydrophobic interactions between the cholesterol-tag and the droplet-stabilizing surfactants (11). Thereby, we obtained an attachment handle, which reversibly recruits the tsDNA to the periphery at basic pH (Figure 1B). In contrast to Förster Resonance Energy Transfer (FRET), which is commonly employed to monitor the pH dynamics (21), our system provides freedom regarding the choice of fluorophores—which is absolutely necessary for us to study the impact of different fluorophore combinations. We directly visualized tsDNA binding and investigated the impact of fluorophore modifications on the pH dynamics. At the same time, this system provides a strategic blueprint for the pH-sensitive recruitment of components to the membrane—an interesting function in itself, in particular concerning the bottom-up construction of synthetic cells (45).

Confocal imaging revealed that attachment of the tsDNA to the compartment periphery is shifted to higher pH values if the ssDNA carries a Cy3 compared to the unlabelled ssDNA (Figure 1C, D). The images show the equilibrated state (Supplementary Figure S1) and we confirmed that the shift is neither due to interactions of the Cy3 with the surfactant layer (Supplementary Figure S2) nor an artefact of the droplet size (Supplementary Figure S3). We quantified this effect by extracting the normalized intensity inside the droplets ( $I_{in}$ , periphery excluded) from the confocal images (Figure 1E). Importantly, we could reproduce the sigmoidal pH response curve that was reported for FRET-based detection (46). The turning-point of the pH-sensitive ssDNA-tsDNA binding curve for unlabelled ssDNA was around  $5.80 \pm 0.09$ , whereas it shifted significantly to  $6.05 \pm 0.04$  for the Cy3-modified ssDNA ( $2.53\sigma$ ). Even at pH 8 not all tsDNA was bound to the droplet periphery for the Cy3-modified ssDNA. Importantly, we confirmed our results with polyacrylamide gel electrophoresis (PAGE) as an independent bulk measurement. Also with PAGE we find that the binding between ssDNA and tsDNA is enhanced if the ssDNA does not carry a fluorophore (Supplementary Figure S4). This confirms that our observations are not just an artifact of the measurement system itself, for example, due to unspecific interactions at the water-oil interface. Note that the  $pK_a$  of the DNA itself is far below the pH-range considered here and Cy3 is uncharged throughout the pH-range relevant for ssDNA-tsDNA binding with a  $pK_a$  of 7.8 (Supplementary Table S1).

While it is well known that the pH turning point can be shifted by changing the DNA sequence (46), it was not

known that the same can be achieved by changing the fluorophore modification alone. This striking observation can be explained by either of the two following hypotheses as illustrated in Figure 1F: (i) a fluorophore modification on the ssDNA causes overstabilization of the free ssDNA state by making its equilibrium ensemble more compact and, therefore, less accessible for base pairing. (ii) The fluorophore modification destabilizes the ssDNA-tsDNA complex, thereby raising the bound state in free energy (relative to the unbound one). First, we tested Hypothesis 1 with all-atom molecular dynamics (MD) simulations. Subsequently we examined Hypothesis 2 with experiments.

### MD simulations reveal reduction of ssDNA accessibility by fluorophore modification

To test Hypothesis 1, we used all-atom MD simulations to probe the secondary structure of the Cy3-labelled ssDNA (Figure 2A) and compared it to the unlabelled ssDNA. First of all, the unlabelled ssDNA yielded a very broad probability density distributions for the radius of gyration (Figure 2B), which is a direct measure of the DNA's compactness. The distributions for the unlabelled ssDNA show a significant fraction of extended structures, in which the DNA bases are accessible for complementary base pairing (see also representative snapshots in Figure 2C and Video S1). On the contrary, the Cy3-labelled ssDNA (Figure 2A) yielded a distinctively different probability density distribution for the radius of gyration (Figure 2D), which reflects a much lower propensity for extended conformations. The bases of the Cy3-labelled ssDNA were found to be wrapped around the fluorophore, most likely due to pi-pi stacking interactions between the ssDNA bases and the aromatic groups of Cy3 (Video S2). This entangled conformation renders the ssDNA less accessible for complementary base pairing. An overstabilization of the unbound ssDNA means a lower free energy of the ssDNA compared to the ssDNA-tsDNA complex. This would explain our experimental observations in line with Hypothesis 1. Note that Cy5-labelled ssDNA favored similarly compact conformations wrapped around the dye, which further indicates that the aromatic groups of Cy dyes tend to interact with ssDNA base pairs (Supplementary Figure S5, Video S3).

To test if weaker dye-ssDNA interactions would restore expanded conformations of the ssDNA in our simulations, we used an Alexa488 dye. We selected an Alexa dye (Figure 2F), because its chemical structure is considerably different compared to Cy3, which may render it less prone to base stacking interactions. Moreover, in contrast to the hydrophobic and highly planar Cy dyes, Alexa dyes are more hydrophilic due to their negative charge (Supplementary Table S1) (47) and smaller in size. We thus believe that a combination of electrostatic, steric and hydrophobicity-related effects could render Alexa dyes less prone to unspecific interactions with ssDNA, hence reducing the influence on the conformational ensemble of the ssDNA. We found that the mean radius of gyration for an Alexa488-modified ssDNA laid between that of the unmodified and the Cy3-modified ssDNA (Figure 2G). The MD snapshots show that the fully extended conformation, where the bases are accessible, was partially recovered (Figure 2H, Video S4),

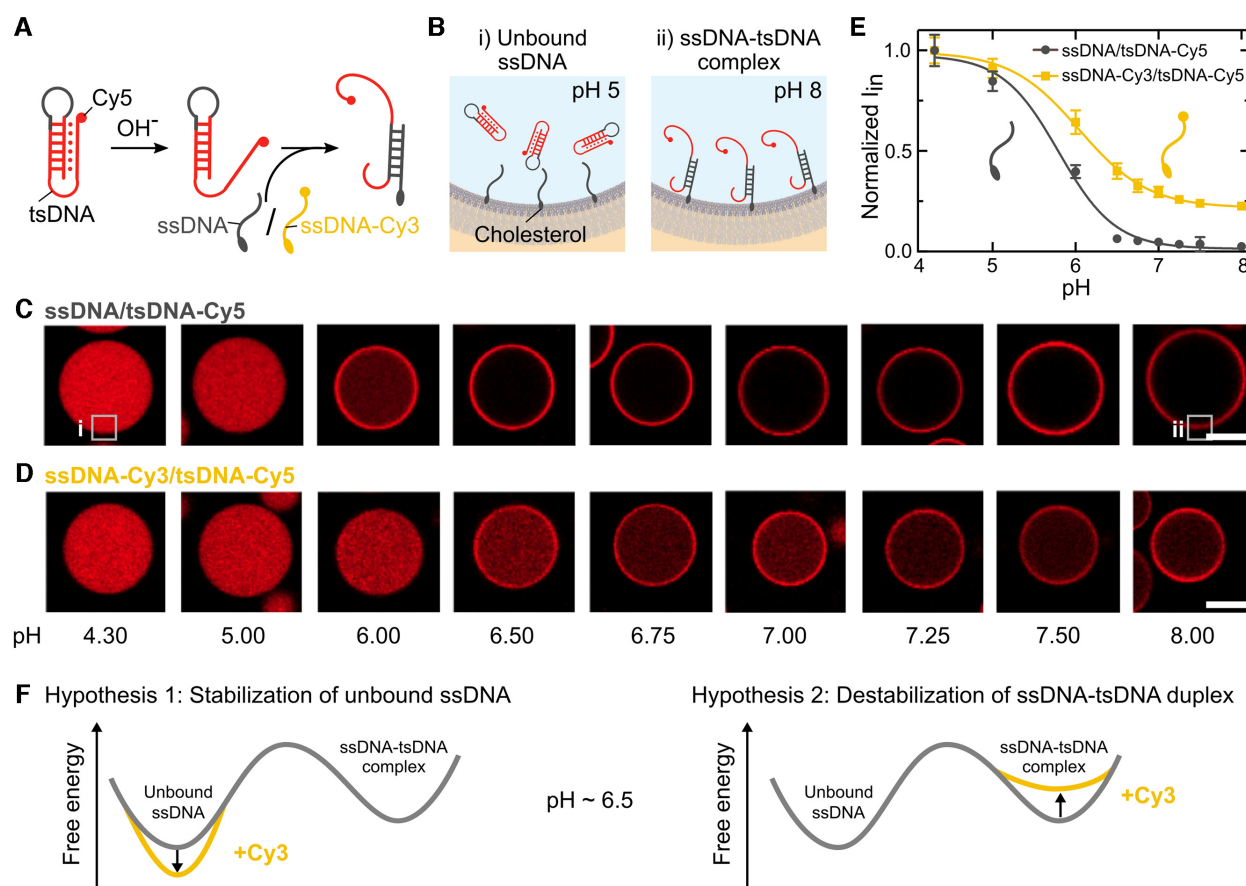


**Figure 1.** Fluorophore modification influences pH response. (A) Sketch of the pH responsive DNA motif. A Cy5-labelled triple-stranded DNA (tsDNA) opens up at basic pH, lowering the energy barrier for strand displacement and hence for complementary base pairing with a cholesterol-tagged single-stranded DNA (ssDNA). (B) This process can be monitored in water-in-oil droplets. The cholesterol-tagged ssDNA self-assembles at the droplet periphery, whereas cholesterol-free tsDNA remains homogeneously distributed within the droplet at acidic pH and attaches to the droplet periphery at higher pH values. (C, D) Representative confocal images of water-in-oil droplets containing Cy5-labelled tsDNA (red,  $\lambda_{\text{ex}} = 647 \text{ nm}$ ) and unlabelled ssDNA (C) or Cy3-labelled ssDNA (D) at different pH values. Attachment of the tsDNA is shifted to higher pH values if the ssDNA is labelled with Cy3. Scale bars: 20  $\mu\text{m}$ . (E) Normalized steady-state fluorescence intensity of the Cy5-labelled tsDNA inside the droplet (periphery excluded) at different pH values for unlabelled (gray) and Cy3-labelled ssDNA (yellow). Error bars correspond to the standard deviation of the intensities of  $n = 20$  droplets per condition. Solid lines represent sigmoidal fits revealing a turning point at  $\text{pH } 5.80 \pm 0.09$  and  $6.05 \pm 0.04$ , respectively. (F) Free energy profile illustrating potential hypotheses for the altered behaviour of the Cy3-tagged ssDNA compared to the unlabelled ssDNA.

improving the accessibility of the strand for complementary base pairing.

Taken together, our simulations suggest that a single fluorophore modification on ssDNA can significantly change the DNA's conformation. The more compact conformation of dye-labelled ssDNA effectively increases the free energy cost for expansion required for duplex formation with tsDNA. Thus, our simulations support Hypothesis 1. Importantly, the ssDNA sequence is random such that the observations can likely be generalized for a broad spectrum of DNA sequences.

#### Dissociation kinetics show fluorophore dependence

As a next step, we investigated the duplex dissociation process to see if the fluorophore modification affects the dissociation constant after duplex formation (Hypothesis 2). Since all-atom MD simulations cannot describe this re-

action due to the limited timescales, we studied the detachment of the tsDNA from the compartment periphery experimentally. We implemented an approach where we achieved light-triggered release of protons in individual compartments—providing full spatio-temporal control over the acidification process. For this purpose, we used NPE-caged-sulfate, which breaks up into a sulfate and a proton upon photolysis (48). To prove that NPE-caged sulfate can be used to decrease the pH inside the droplets, we first encapsulated it together with the pH-sensitive dye pyranine at pH 8 and locally illuminated individual droplets with a 405 nm laser (Figure 3A). The pyranine emission upon 488 nm excitation decreased, confirming the successful pH decrease inside the droplets from initially pH 8 to under pH 5. The buffer kept the pH constant until its capacity is exceeded after  $\sim 20 \text{ s}$ . Then, the pH decreased until most of the NPE-caged sulfate underwent photolysis and hence the pH approached a constant value after  $\sim 50 \text{ s}$ . We used this



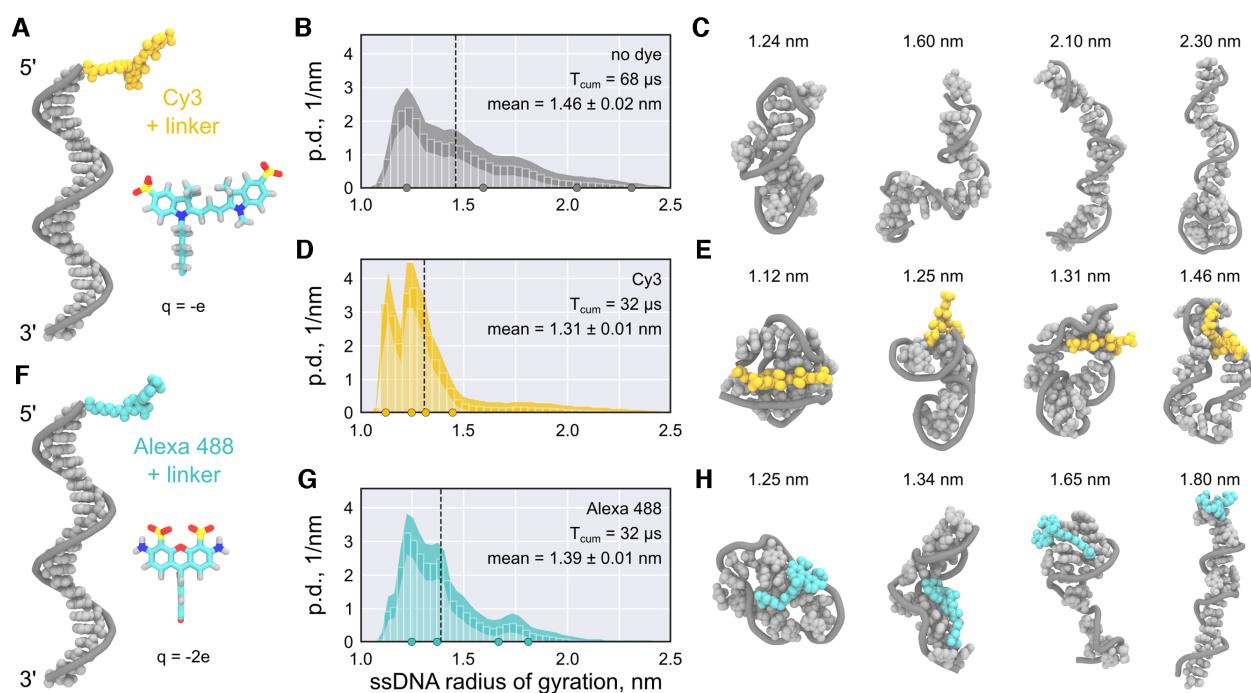


**Figure 2.** MD simulations suggest that fluorophore labelling can stabilize more compact ssDNA conformations. (A, F) Starting conformation of Cy3- (A, yellow) and Alexa488-labelled (F, turquoise) ssDNA (gray). The chemical structure of the fluorophore and its net charge are shown as an inset. (B, D, G) Probability density (p.d.) distributions of the gyration radius of ssDNA without dye (B), labelled with Cy3 (D), and labelled with Alexa488 (G). The shaded areas indicate the 95% confidence intervals estimated using bootstrapping (see Materials and Methods). The black dashed lines indicate the means of the distributions,  $T_{cum}$  the cumulative simulation time. (C, E, H) Representative structure snapshots of the unlabelled ssDNA (C), the Cy3-ssDNA (E) and the Alexa488-ssDNA (H). Positions of the selected snapshots within the corresponding distributions are marked with dots in the probability density distributions.

dynamic light-mediated acidification mechanism to detach the tsDNA from the droplet periphery and to probe dissociation kinetics rather than the steady-state. At  $t = 0$  s, the tsDNA was bound to the ssDNA at the droplet periphery (Figure 3B) and completely detached within 50 s of illumination. Upon detachment, the triplex conformation of the tsDNA was restored. In order to assess the detachment kinetics, we monitored the normalized tsDNA–Cy5 intensity for unmodified, Cy3-modified and Alexa488-modified ssDNA inside the droplet over time (Figure 3C). Following proton-release, the tsDNA detached from the ssDNA for all tested fluorophore modifications (Video S5). The decay times  $t_d = 1/\alpha$  of the sigmoidal fits were comparable for all three fluorophore modifications, indicating similar detachment kinetics. However, detachment (i.e. duplex dissociation) occurred at different time points, hence at different pH values – again pointing towards an altered binding equilibrium. Detachment from the unlabelled ssDNA happened earlier (i.e. at higher pH) indicating that a fluorophore label is stabilizing the ssDNA–tsDNA complex. Taken together, the results obtained so far suggest that fluorophore modifications, in particular Cy-dyes, stabilize not only the unbound ssDNA (Hypothesis 1) but also the ssDNA–tsDNA duplex as illustrated in the free energy profile in Figure 3D. However, the stabilization of compact ssDNA conformations is likely stronger, which explains the observed shift of the pH switching point. This is effectively increasing the energy barrier for the dynamic switching of fluorophore-labelled DNA.

### Reaction-diffusion modelling reveals impact of fluorophores on apparent dissociation constant

Finally, having shown that a fluorophore modification on the ssDNA has a significant influence on the pH switching point, we now additionally tested the impact of fluorophore modifications on tsDNA. For this purpose, we investigated twelve different fluorophore combinations on ssDNA and tsDNA. To quantitatively compare the impact of different fluorophores, we developed an analytical model to derive the apparent dissociation equilibrium constant  $K_D = k_{off}/k_{on}$  at a fixed pH for each individual fluorophore combination. For this purpose, we derived a reaction-diffusion model for spherical compartments (Text S2). It allowed us to determine the apparent dissociation constant  $K_D$  by extracting the droplet radius, the peripheral and the inner intensity of the tsDNA from confocal images with known total concentrations of DNA. We tested combinations of five different fluorophores, namely Cy3, Cy5, Alexa488, Atto488 and Atto647 as well as unlabelled ssDNA on the apparent  $K_D$  (Figure 4). Note that the use of an unlabelled tsDNA was not possible because it would inhibit the monitoring with confocal microscopy.

Remarkably,  $K_D$  varied dramatically for the different combinations. Most striking was the fact that binding is almost fully inhibited for certain fluorophore combinations, like ssDNA/tsDNA–Atto647, ssDNA–Cy5/tsDNA–Atto488 and ssDNA–Alexa488/tsDNA–Atto647 with  $K_D \gg 1$ . On the other hand combinations like ssDNA–Cy3/ts–

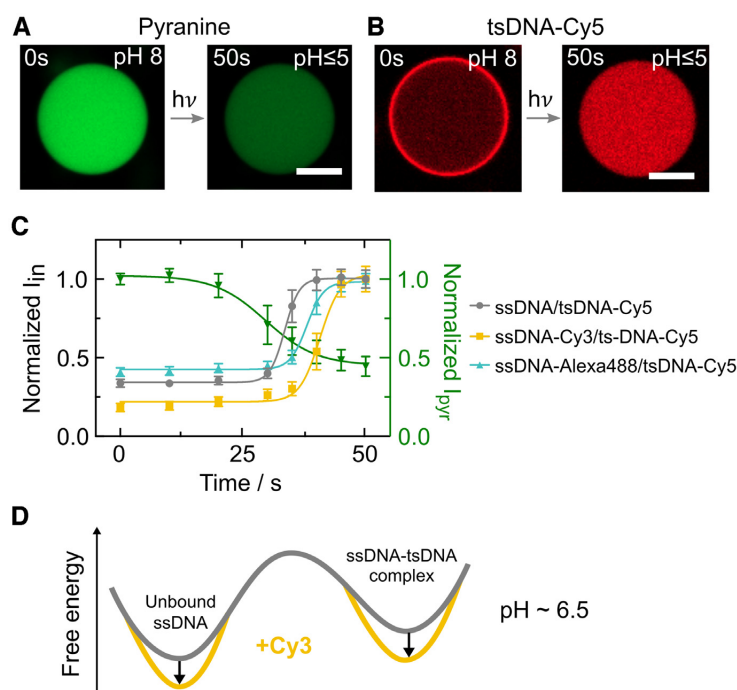


**Figure 3.** Light-mediated acidification of water-in-oil droplets reveals fluorophore-dependent duplex dissociation kinetics. (A) Confocal images of the pH-sensitive dye pyranine ( $50 \mu\text{M}$ ,  $\lambda_{\text{ex}} = 488 \text{ nm}$ , not coupled to DNA) encapsulated into water-in-oil droplets at pH 8. Light-triggered uncaging of NPE-caged sulfate ( $\lambda_{\text{ex}} = 405 \text{ nm}$ ) leads to proton release causing a rapid pH drop from 8 to under 5 within 50 s. The pH drop can be monitored as a decrease in pyranine fluorescence. (B) Representative confocal images of Cy5-labelled tsDNA ( $\lambda_{\text{ex}} = 647 \text{ nm}$ ) encapsulated together with cholesterol-tagged ssDNA into water-in-oil droplets at pH 8. During acidification, the tsDNA detaches from the droplet periphery as the triplex state is energetically favoured. Scale bars:  $20 \mu\text{m}$ . (C) Normalized fluorescence intensity of the tsDNA inside the droplet (periphery excluded) over time for unlabelled, Cy3-labelled and Alexa488-labelled ssDNA as well as pyranine (right axis). Error bars correspond to the standard deviation of the intensities of  $n = 26$  droplets for the ssDNA/tsDNA-Cy5 condition,  $n = 23$  droplets for the ssDNA-Cy3/tsDNA-Cy5 condition,  $n = 24$  droplets for the ssDNA-Alexa488/tsDNA-Cy5 condition and  $n = 5$  droplets containing pyranine. Solid lines represent sigmoidal fits with turning points at  $33.5 \text{ s} \pm 0.1 \text{ s}$  (unmodified ssDNA),  $40.7 \text{ s} \pm 0.5 \text{ s}$  (ssDNA-Cy3) and  $38.0 \text{ s} \pm 0.3 \text{ s}$  (ssDNA-Alexa488). Note that the decay times  $t_{\text{d}} = 1/\alpha$  are similar for all fluorophores  $3.45 \text{ s} \pm 0.24 \text{ s}$  (unmodified ssDNA),  $4.76 \text{ s} \pm 1.13 \text{ s}$  (ssDNA-Cy3) and  $4.00 \text{ s} \pm 0.48 \text{ s}$  (ssDNA-Alexa488). (D) Free energy profile illustrating our conclusion that both equilibrium states are stabilized by the presence of a dye on the ssDNA.

DNACy5, ssDNA/tsDNA-Cy3 and ssDNA/tsDNA-Cy5 bound very efficiently as expected at pH 8. As a general trend, we deduce that Cy-dyes on the tsDNA seemed to lead to a lower apparent  $K_{\text{D}}$  compared to Atto-dyes. Furthermore, it is surprising that the permutation of two Cy-dyes on ssDNA and tsDNA lead to a different apparent  $K_{\text{D}}$ . While ssDNA-Cy3/tsDNA-Cy5 attached very efficiently, we obtained intermediate  $K_{\text{D}}$ 's for ssDNA-Cy5/tsDNA-Cy3. This could be due to the fact that the larger Cy5 dye can interact with multiple bases and therefore stabilize the unbound ssDNA conformation more efficiently. Confirming our observations, the permutation of the tsDNA fluorophore influenced the pH hysteresis (Supplementary Figure S6) and the dynamic detachment in experiments using NPE-caged sulfate (Supplementary Figure S7). Moreover, if we move the fluorophore modification of the tsDNA from the 5' end to the 3' end, binding to the unlabelled ssDNA was enhanced (Supplementary Figure S8). This is likely due to the fact that the dye is placed further away from the stem loop, making the stem loop better accessible for complementary base-pairing with the ssDNA. In addition, a fluorophore modification on the 3' end of the tsDNA may destabilize the triple-stranded state, hence increasing the binding affinity for ssDNA. Indeed, due to the much smaller loop

on that side, steric effects may come into play, which would equally contribute to the lower intensity inside the droplet for tsDNA-Cy5-3'.

Taking all these observations into account, we propose that not only a fluorophore modification on the ssDNA but also on the tsDNA affects the dynamics of pH-responsive DNA nanostructures up to a point that binding is inhibited. The choice of fluorescent dyes can thus be exploited to shape the energy landscape for dynamic DNA nanostructures and to shift the equilibrium towards the bound or the unbound state.

## DISCUSSION

One of the most exciting tasks in the field of DNA nanotechnology is the construction of dynamic molecular devices that can perform mechanical motion upon stimulation. The foundation for this work is an experimental read-out, which is suitable to track dynamic reconfiguration in space and time. Fluorescence microscopy techniques, such as superresolution imaging or FRET, are ideally suited for *in situ* measurements on active DNA origami structures. The fluorophore is normally selected to match the optical setup rather than the DNA nanostructure itself and

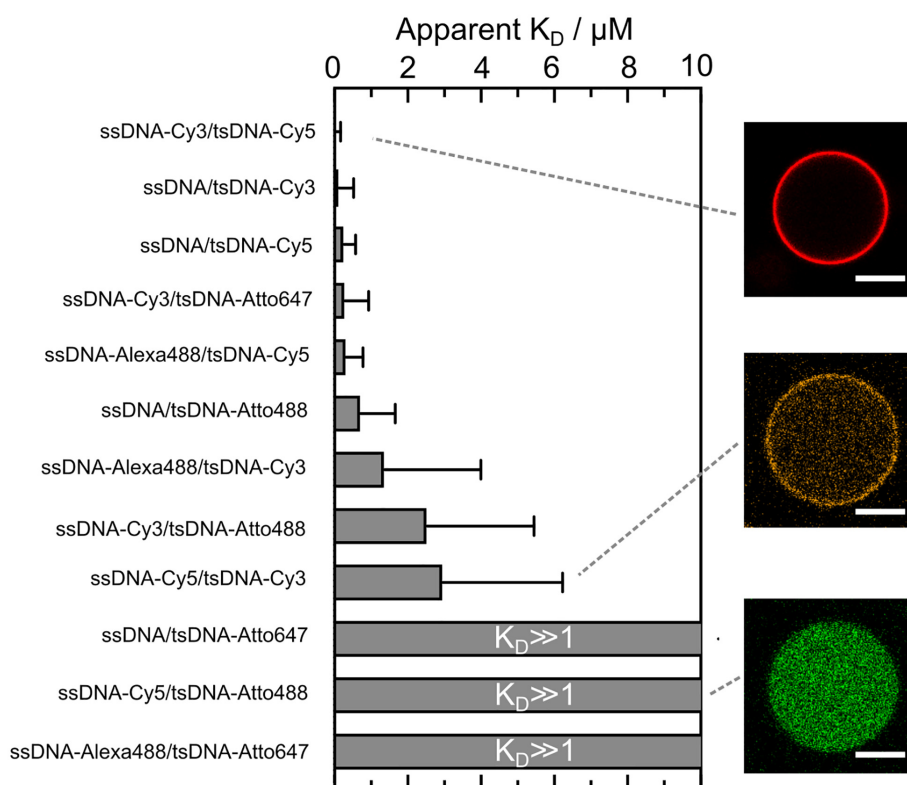


**Figure 4.** Histogram depicting the apparent dissociation constants  $K_D$  for 12 different ssDNA/tsDNA combinations at pH 8 with variable fluorophore modifications including Alexa488 ( $\lambda_{ex} = 488$  nm), Atto488 ( $\lambda_{ex} = 488$  nm), Cy3 ( $\lambda_{ex} = 561$  nm), Cy5 ( $\lambda_{ex} = 647$  nm) and Atto647 ( $\lambda_{ex} = 647$  nm). Confocal images of three fluorophore combinations depicting strong (ssDNA-Cy3/tsDNA-Cy5), intermediate (ssDNA-Cy5/tsDNA-Cy3) and almost no binding to the droplet periphery (ssDNA-Cy5/tsDNA-Atto488). The apparent  $K_D$  is strongly influenced by fluorophore modifications on ssDNA and tsDNA up to the point of almost full inhibition of binding, which results in  $K_D \gg 1$ . Error bars correspond to the standard deviation of  $n = 41$  droplets for ssDNA/tsDNA-Cy5,  $n = 32$  for ssDNA/tsDNA-Cy3,  $n = 11$  for ssDNA/tsDNA-Atto488,  $n = 49$  for ssDNA/tsDNA-Atto647,  $n = 73$  for ssDNA-Cy3/tsDNA-Cy5,  $n = 29$  for ssDNA-Cy3/tsDNA-Atto488,  $n = 67$  for ssDNA-Cy3/tsDNA-Atto647,  $n = 27$  for ssDNA-Cy5/tsDNA-Cy3,  $n = 31$  for ssDNA-Cy5/tsDNA-Atto488,  $n = 72$  for ssDNA-Alexa488/tsDNA-Cy5,  $n = 29$  for ssDNA-Alexa488/tsDNA-Cy3 and  $n = 68$  for ssDNA-Alexa488/tsDNA-Atto647.

exchanged as required by the experiment. Here, we determined why the exchange of fluorophores on dynamic DNA nanostructures can lead to a considerably different experimental outcome. We used a popular pH-sensitive DNA motif combined with a strand displacement reaction as an example to show that the fluorophore alone can alter the steady-state and even completely inhibit the dynamics. Strand-displacement is one of the best understood and highly specific methods of actuating large DNA devices, but still has a large potential for improvement with respect to kinetics (49). Addressing this challenge, we find that fluorophores tend to stabilize the equilibrium states of the system with different effects on its dynamics, whereby Cy-dyes are more prone to inhibit dynamics compared to Atto-dyes. Beyond fluorophore labelling, DNA nanotechnology uses a myriad of other chemical modifications on the DNA, from reactive amine or thiol groups, hydrophobic tags, spacers, photocleavable groups or modifications for click chemistry (50). We anticipate that our observations are not limited to dye molecules – these other chemical modification would very likely have similar effects. It is thus generally possible to shape the energy landscape for dynamic reconfiguration as well as the equilibrium configuration without changing the DNA sequence.

Our results are directly relevant for various applications that capitalize on dynamic DNA systems, from bottom-up synthetic biology to biosensing and the increasingly popular superresolution technique DNA-PAINT (23). Without doubt, the possibility to precisely shape energy landscapes for dynamic DNA nanostructures will lead to metastable DNA nanostructures and fully reversible DNA devices with unprecedented complexity – mimicking the intricate workings of natural nanomachines.

#### DATA AVAILABILITY

The experimental data sets were appended to this submission. The MD trajectories, encompassing several TB of data, are available from the authors upon request.

#### SUPPLEMENTARY DATA

Supplementary Data are available at NAR Online.

#### ACKNOWLEDGEMENTS

The authors acknowledge Tobias Abele for help with the analysis of the droplet's peripheral intensity.

## FUNDING

K.G. acknowledges funding from the Deutsche Forschungsgemeinschaft (DFG, German Research Foundation) under Germany's Excellence Strategy via the Excellence Cluster 3D Matter Made to Order [EXC-2082/1 – 390761711]; DFG via the principal investigator grant [IG 109/1-1 to M.I.]; Computational resources were provided by the Max Planck Computing and Data Facility and the Leibniz Supercomputing Centre (Garching, Germany); K.J. thanks the Carl Zeiss Foundation for financial support; all authors acknowledge the Max Planck Society for its general support. Funding for open access charge: Max Planck Vorhaben [M.TN.A.MEFO0001].  
*Conflict of interest statement.* None declared.

## REFERENCES

- Ramezani, H. and Dietz, H. (2020) Building machines with DNA molecules. *Nat. Rev. Genet.*, **21**, 5–26.
- Nickels, P.C., Wünsch, B., Holzmeister, P., Bae, W., Kneer, L.M., Grohmann, D., Tinnefeld, P. and Liedl, T. (2016) Molecular force spectroscopy with a DNA origami-based nanoscopic force clamp. *Science*, **354**, 305–307.
- Dutta, P.K., Zhang, Y., Blanchard, A.T., Ge, C., Rushdi, M., Weiss, K., Zhu, C., Ke, Y. and Salaita, K. (2018) Programmable multivalent DNA-origami tension probes for reporting cellular traction forces. *Nano Lett.*, **18**, 4803–4811.
- Green, L.N., Amodio, A., Subramanian, H. K.K., Ricci, F. and Franco, E. (2017) pH-driven reversible self-assembly of micron-scale DNA scaffolds. *Nano Lett.*, **17**, 7283–7288.
- Ausländer, S., Ausländer, D. and Fussenegger, M. (2017) Synthetic biology—the synthesis of biology. *Angew. Chem. Int. Ed.*, **56**, 6396–6419.
- Jiang, Q., Song, C., Nangreave, J., Liu, X., Lin, L., Qiu, D., Wang, Z.-G., Zou, G., Liang, X., Yan, H. and Ding, B. (2012) DNA origami as a carrier for circumvention of drug resistance. *J. Am. Chem. Soc.*, **134**, 13396–13403.
- Wang, C., Vázquez-González, M., Fadeev, M., Sohn, Y.S., Nechushtai, R. and Willner, I. (2020) Thermoplasmonic-triggered release of loads from DNA-modified hydrogel microcapsules functionalized with Au nanoparticles or Au nanorods. *Small*, **16**, 2000880.
- Marras, A.E., Zhou, L., Su, H.-J. and Castro, C.E. (2015) Programmable motion of DNA origami mechanisms. *Proc. Natl. Acad. Sci. U.S.A.*, **112**, 713–718.
- Simmel, F.C. and Schulman, R. (2017) Self-organizing materials built with DNA. *MRS Bull.*, **42**, 913–919.
- Franquelim, H.G., Dietz, H. and Schwille, P. (2021) Reversible membrane deformations by straight DNA origami filaments. *Soft Matter*, **17**, 276–287.
- Jahnke, K., Weiss, M., Frey, C., Antona, S., Janiesch, J.-W., Platzman, I., Göpfrich, K. and Spatz, J.P. (2019) Programmable functionalization of surfactant-stabilized microfluidic droplets via DNA-tags. *Adv. Funct. Mater.*, **29**, 1808647.
- Jahnke, K., Weiss, M., Weber, C., Platzman, I., Göpfrich, K. and Spatz, J.P. (2020) Engineering light-responsive contractile actomyosin networks with DNA nanotechnology. *Adv. Biosyst.*, **4**, 2000102.
- Zhang, D.Y. and Winfree, E. (2009) Control of DNA strand displacement kinetics using toehold exchange. *J. Am. Chem. Soc.*, **131**, 17303–17314.
- Irmisch, P., Ouldrige, T.E. and Seidel, R. (2020) Modeling DNA-strand displacement reactions in the presence of base-pair mismatches. *J. Am. Chem. Soc.*, **142**, 11451–11463.
- Kopperger, E., List, J., Madhira, S., Rothfischer, F., Lamb, D.C. and Simmel, F.C. (2018) A self-assembled nanoscale robotic arm controlled by electric fields. *Science*, **359**, 296–301.
- Hernández-Ainsa, S., Ricci, M., Hilton, L., Aviñó, A., Eritja, R. and Keyser, U.F. (2016) Controlling the reversible assembly of liposomes through a multistimuli responsive anchored DNA. *Nano Lett.*, **16**, 4462–4466.
- Turek, V.A., Chikkaraddy, R., Cormier, S., Stockham, B., Ding, T., Keyser, U.F. and Baumberg, J.J. (2018) Thermo-responsive actuation of a DNA origami flexor. *Adv. Funct. Mater.*, **28**, 1706410.
- Wang, J., Yue, L., Wang, S. and Willner, I. (2018) Triggered reversible reconfiguration of G-quadruplex-bridged 'Domino'-type origami dimers: application of the systems for programmed catalysis. *ACS Nano*, **12**, 12324–12336.
- Chen, Y., Lee, S.-H. and Mao, C. (2004) A DNA nanomachine based on a duplex-triplex transition. *Angewandte Chemie*, **116**, 5449–5452.
- Yang, M., Zhang, X., Liu, H., Kang, H., Zhu, Z., Yang, W. and Tan, W. (2015) Stable DNA nanomachine based on duplex-triplex transition for ratiometric imaging instantaneous pH changes in living cells. *Anal. Chem.*, **87**, 5854–5859.
- Patino, T., Porchetta, A., Jannasch, A., Lladó, A., Stumpp, T., Schäffer, E., Ricci, F. and Sánchez, S. (2019) Self-sensing enzyme-powered micromotors equipped with pH-responsive DNA nanoswitches. *Nano Lett.*, **19**, 3440–3447.
- Weiss, L.E., Ezra, Y.S., Goldberg, S., Ferdman, B., Adir, O., Schroeder, A., Alalouf, O. and Shechtman, Y. (2020) Three-dimensional localization microscopy in live flowing cells. *Nat. Nanotechnol.*, **15**, 500–506.
- Cnossen, J., Hinsdale, T., Thorsen, R.Ø., Siemons, M., Schueder, F., Jungmann, R., Smith, C.S., Rieger, B. and Stallinga, S. (2020) Localization microscopy at doubled precision with patterned illumination. *Nat. Methods*, **17**, 59–63.
- Moreira, B.G., You, Y. and Owczarzy, R. (2015) Cy3 and Cy5 dyes attached to oligonucleotide terminus stabilize DNA duplexes: predictive thermodynamic model. *Biophys. Chem.*, **198**, 36–44.
- Kaji, T., Ito, S., Iwai, S. and Miyasaka, H. (2009) Nanosecond to submillisecond dynamics in dye-labeled single-stranded DNA, as revealed by ensemble measurements and photon statistics at single-molecule level. *J. Phys. Chem. B*, **113**, 13917–13925.
- Göpfrich, K., Haller, B., Staufer, O., Dreher, Y., Mersdorf, U., Platzman, I. and Spatz, J.P. (2019) One-pot assembly of complex giant unilamellar vesicle-based synthetic cells. *ACS Synth. Biol.*, **8**, 937–947.
- Jahnke, K., Ritzmann, N., Fichtler, J., Nitschke, A., Dreher, Y., Abele, T., Hofhaus, G., Platzman, I., Schröder, R., Müller, D. et al. (2020) Actuation of synthetic cells with proton gradients generated by light-harvesting *E. coli*. doi:10.21203/rs.3.rs-82114/v1.
- Ivani, I., Dans, P.D., Noy, A., Pérez, A., Faustino, I., Hospital, A., Walther, J., Andrio, P., Goñi, R., Balaceanu, A. et al. (2015) Parmbsc1: a refined force field for DNA simulations. *Nat. Methods*, **13**, 55–58.
- Hornak, V., Abel, R., Okur, A., Strockbine, B., Roitberg, A. and Simmerling, C. (2006) Comparison of multiple Amber force fields and development of improved protein backbone parameters. *Proteins: Struct. Funct. Bioinformatics*, **65**, 712–725.
- Yoo, J. and Aksimentiev, A. (2018) New tricks for old dogs: Improving the accuracy of biomolecular force fields by pair-specific corrections to non-bonded interactions. *Phys. Chem. Chem. Phys.*, **20**, 8432–8449.
- Joung, I.S. and Cheatham, T.E. (2008) Determination of alkali and halide monovalent ion parameters for use in explicitly solvated biomolecular simulations. *J. Phys. Chem. B*, **112**, 9020–9041.
- Chatterjee, S., Debenedetti, P.G., Stillinger, F.H. and Lynden-Bell, R.M. (2008) A computational investigation of thermodynamics, structure, dynamics and solvation behavior in modified water models. *J. Chem. Phys.*, **128**, 124511.
- Pettersen, E.F., Goddard, T.D., Huang, C.C., Couch, G.S., Greenblatt, D.M., Meng, E.C. and Ferrin, T.E. (2004) UCSF chimera - a visualization system for exploratory research and analysis. *J. Comput. Chem.*, **25**, 1605–1612.
- Abraham, M., van der Spoel, D., Lindahl, E. and Hess, B. (2019) GROMACS user manual version 2019. <http://doi.org/10.5281/zenodo.2424486>.
- Essmann, U., Perera, L., Berkowitz, M.L., Darden, T., Lee, H. and Pedersen, L.G. (1995) A smooth particle mesh Ewald method. *J. Chem. Phys.*, **103**, 8577–8593.
- Hess, B., Kutzner, C., van der Spoel, D. and Lindahl, E. (2008) GROMACS 4: algorithms for highly efficient, load-balanced, and scalable molecular simulation. *J. Chem. Theory. Comput.*, **4**, 435–47.
- Bussi, G., Donadio, D. and Parrinello, M. (2007) Canonical sampling through velocity rescaling. *J. Chem. Phys.*, **126**, 014101.

38. Berendsen, H. J.C., Postma, J. P.M., van Gunsteren, W.F., DiNola, A. and Haak, J.R. (1984) Molecular dynamics with coupling to an external bath. *J. Chem. Phys.*, **81**, 3684–3690.
39. Parrinello, M. and Rahman, A. (1981) Polymorphic transitions in single crystals: a new molecular dynamics method. *J. Appl. Phys.*, **52**, 7182–7190.
40. Humphrey, W., Dalke, A. and Schulten, K. (1996) VMD: visual molecular dynamics. *J. Mol. Graphics*, **14**, 33–38.
41. Graen, T., Hoefling, M. and Grubmüller, H. (2014) AMBER-DYES: characterization of charge fluctuations and force field parameterization of fluorescent dyes for molecular dynamics simulations. *J. Chem. Theory: Comput.*, **10**, 5505–5512.
42. Hale, J. and Raugel, G. (1992) Partial differential equations on thin domains. In: *Mathematics in Science and Engineering*. pp. 63–97.
43. Fibich, G., Gannot, I., Hammer, A. and Schochet, S. (2007) Chemical kinetics on surfaces: a singular limit of a reaction-diffusion system. *SIAM J. Math. Anal.*, **38**, 1371–1388.
44. Hub, J.S., De Groot, B.L. and van der Spoel, D. (2010) g-wham - a free weighted histogram analysis implementation including robust error and autocorrelation estimates. *J. Chem. Theory: Comput.*, **6**, 3713–3720.
45. Czogalla, A., Franquelim, H.G. and Schwille, P. (2016) DNA nanostructures on membranes as tools for synthetic biology. *Biophys. J.*, **110**, 1698–707.
46. Idili, A., Vallée-Bélisle, A. and Ricci, F. (2014) Programmable pH-triggered DNA nanoswitches. *J. Am. Chem. Soc.*, **136**, 5836–5839.
47. Zanetti-Domingues, L.C., Tynan, C.J., Rolfe, D.J., Clarke, D.T. and Martin-Fernandez, M. (2013) Hydrophobic fluorescent probes introduce artifacts into single molecule tracking experiments due to non-specific binding. *PLoS ONE*, **8**, e74200.
48. Abbruzzetti, S., Sottini, S., Viappiani, C. and Corrie, J. E.T. (2005) Kinetics of proton release after flash photolysis of 1-(2-nitrophenyl)ethyl sulfate (caged sulfate) in aqueous solution. *J. Am. Chem. Soc.*, **127**, 9865–9874.
49. DeLuca, M., Shi, Z., Castro, C.E. and Arya, G. (2020) Dynamic DNA nanotechnology: toward functional nanoscale devices. *Nanoscale Horiz.*, **5**, 182–201.
50. Madsen, M. and Gothelf, K.V. (2019) Chemistries for DNA nanotechnology. *Chem. Rev.*, **119**, 6384–6458.




### 3.8 Publication 5: Proton gradients from light-harvesting *E. coli* control DNA assemblies for synthetic cells

After understanding the dynamics of pH-sensitive triplex DNA, we next employ it for designing a DNA-based cytoskeleton mimic that can deform and scaffold the membrane of GUVs. We achieve this by engineering a complex signaling pathway by using top-down engineered genetically-modified *E. coli*.

The field of top-down synthetic biology attempts to engineer synthetic cells starting off with a living organism and then remove unessential compartments one by one. Whereas this approach avoids the tedious purification and reconstitution of proteins it has its own limitations since natural cells are still extremely complex entities which makes it difficult to distinguish between essential and unessential genes. In the following work, we merge the strategies of bottom-up and top-down approaches. For this purpose, we overexpress the proton pump xenorhodopsin in *E. coli*. Xenorhodopsin is a light-sensitive transmembrane and inward-directed proton pump that allows us to generate a pH-gradient between the *E. coli* periplasm and the outer aqueous solution via light illumination. We quantify that the *E. coli* lead to reversible pH changes within the outer aqueous solution and encapsulate them as synthetic organelles within water-in-oil droplets. To make use of the proton gradients, as in the previous case, we employ DNA nanotechnology by using the pH-sensitive triplex strand that changes its conformation depending on the pH and therefore bind to the droplet periphery due to presence of a cholesterol-modified linker strand. We show that we can induce the triplex DNA attachment to the droplet periphery using light by coencapsulating *E. coli* and DNA strands. In order to achieve a more meaningful function we design a much more rigid DNA origami that is functionalized with triplex DNA and can undergo blunt-end stacking interactions that lead to clustering of DNA origami structures. Binding the DNA origami to a GUV membrane and inducing their clustering leads to deformation of the GUVs from their initially spherical shape. Finally, we set out to combine the features of membrane-based compartments, DNA origami and *E. coli* within one system. In a first step the light illumination of the *E. coli* leads to an increase of the outer pH, which causes the triplex DNA to open up. This, in turn, leads to attachment of DNA origami monomers to the GUV membrane, which causes their deformation after inducing the blunt-end stacking interactions of DNA origami.

We have thus shown how the merging of two coexisting strategies to engineer synthetic cells - namely bottom-up and top-down synthetic biology - can be combined to achieve a complex system with sophisticated signalling cascades that lead to a morphology change of GUVs.

# Proton gradients from light-harvesting *E. coli* control DNA assemblies for synthetic cells

Kevin Jahnke<sup>1,2</sup>, Noah Ritzmann<sup>3</sup>, Julius Fichtler<sup>1,2</sup>, Anna Nitschke<sup>1,2</sup>, Yannik Dreher<sup>1,2</sup>, Tobias Abele<sup>1,2</sup>, Götz Hofhaus<sup>4</sup>, Ilia Platzman<sup>5,6</sup>, Rasmus R. Schröder<sup>4</sup>, Daniel J. Müller <sup>3</sup>, Joachim P. Spatz<sup>5,6,7</sup> & Kerstin Göpfrich <sup>1,2</sup> 

Bottom-up and top-down approaches to synthetic biology each employ distinct methodologies with the common aim to harness living systems. Here, we realize a strategic merger of both approaches to convert light into proton gradients for the actuation of synthetic cellular systems. We genetically engineer *E. coli* to overexpress the light-driven inward-directed proton pump xenorhodopsin and encapsulate them in artificial cell-sized compartments. Exposing the compartments to light-dark cycles, we reversibly switch the pH by almost one pH unit and employ these pH gradients to trigger the attachment of DNA structures to the compartment periphery. For this purpose, a DNA triplex motif serves as a nanomechanical switch responding to the pH-trigger of the *E. coli*. When DNA origami plates are modified with the pH-sensitive triplex motif, the proton-pumping *E. coli* can trigger their attachment to giant unilamellar lipid vesicles (GUVs) upon illumination. A DNA cortex is formed upon DNA origami polymerization, which sculpts and deforms the GUVs. We foresee that the combination of bottom-up and top down approaches is an efficient way to engineer synthetic cells.

<sup>1</sup>Biophysical Engineering Group, Max Planck Institute for Medical Research, Heidelberg, Germany. <sup>2</sup>Department of Physics and Astronomy, Heidelberg University, Heidelberg, Germany. <sup>3</sup>Department of Biosystems Science and Engineering, Eidgenössische Technische Hochschule (ETH) Zurich, Basel, Switzerland. <sup>4</sup>Centre for Advanced Materials, Heidelberg, Germany. <sup>5</sup>Max Planck Institute for Medical Research, Department of Cellular Biophysics, Heidelberg, Germany. <sup>6</sup>Institute for Molecular Systems Engineering (IMSE), Heidelberg University, Heidelberg, Germany. <sup>7</sup>Max Planck School Matter to Life, Heidelberg, Germany. ✉email: [kerstin.goeprich@mr.mpg.de](mailto:kerstin.goeprich@mr.mpg.de)

Synthetic biology cultivates an engineering approach to biology with the aim to create or to re-purpose biological parts for specific tasks. The field is commonly divided into two branches with distinct tools and methodologies, but also distinct challenges—top-down and bottom-up synthetic biology<sup>1,2</sup>. The top-down approach uses genetic engineering techniques to manipulate natural cells, reprogramming their behavior and equipping them with unique and exciting functions<sup>3</sup>. *Escherichia coli* (*E. coli*) bacteria, for instance, have been engineered for a variety of tasks, including biofuel production<sup>4</sup>, cancer cell targeting<sup>5</sup> or light harvesting<sup>6,7</sup>. Yet living cells remain too complex to achieve full control and not all added functions are compatible with the host<sup>8</sup>.

The bottom-up approach, on the other hand, has been successful at reconstituting natural biomolecules, or artificial components in cell-sized confinement like microfluidic droplets or lipid vesicles<sup>9–11</sup>. Noteworthy modules have been implemented so far, each mimicking a specific function of a living cell, including energy generation<sup>12,13</sup>, metabolism<sup>14</sup>, motility<sup>15,16</sup>, cytoskeletal contraction<sup>17</sup> or division<sup>18</sup>. Yet the combination of these modules towards complex signaling pathways for dynamic systems remains challenging. Merging the capacities of top-down and bottom-up approaches to synthetic biology can be a leap forward towards complex bottom-up assemblies but also more versatile and well-defined top-down systems. Leading to this direction, communication between natural and synthetic cells has been implemented<sup>19–21</sup> and bottom-up assembled vesicles were used as organelle mimics in living cells<sup>22</sup>. Furthermore, engineered prokaryotes have recently been used as artificial organelles in living cells<sup>23,24</sup>, yet this has never been translated into synthetic cells.

Here, we use top-down genetic engineering to equip *E. coli* with light-harvesting capabilities. We employ them as synthetic organelle mimics inside bottom-up assembled synthetic cellular compartments. Thereby, we can reversibly switch the pH upon illumination to trigger an optical or a mechanical response. The latter is based on the pH-sensitive membrane attachment of a triplex-forming DNA motif triggered by proton gradients from light-harvesting *E. coli*. Furthermore, we employ the pH-gradients to sculpt synthetic cellular compartments by attaching a DNA origami plate to the pH-sensitive DNA strand.

## Results

**Top-down engineering of *E. coli* for light-harvesting.** To equip synthetic cells with the capability to generate proton gradients, we set out to assemble an energy module. We genetically engineered *E. coli* to overexpress the light-driven proton pump xenorhodopsin, a transmembrane protein from nanohalosarchaeon *Nanosalina*<sup>25</sup>. It contains a retinal which, upon illumination, undergoes a trans-cis conformational change and shuttles a proton across the lipid membrane. We chose xenorhodopsin because it shows unique features compared to other proton pumps, such as bacteriorhodopsin or proteorhodopsin: First of all, xenorhodopsin exhibits a substantially faster photocycle, which can result in larger proton gradients<sup>25</sup>. Second, as an inward-directed pump<sup>26</sup>, xenorhodopsin increases the pH (instead of decreasing it) in the extracellular space upon illumination (Fig. 1a). As an additional feature, we introduced a C-terminal fluorescent GFP or mCherry tag to xenorhodopsin for visualization of the *E. coli*. The choice of two dyes allows us to work with different combinations of fluorophores as required.

To assess and quantify the proton pumping capabilities of the genetically engineered *E. coli*, we performed a photoactivity assay, where we inserted a micro pH electrode into the *E. coli* suspension and exposed it to multiple light-dark cycles. Since the absorption spectrum of xenorhodopsin covers a broad range,

the use of a white light lamp is more effective than excitation with a specific wavelength (Supplementary Fig. 1). Illumination increased the pH in the extracellular space by almost one pH unit within five minutes (Fig. 1b), because protons are translocated from the extracellular solution to the cytosol. Longer illumination times resulted in saturation of the pH change (Supplementary Fig. 2). In the range from OD<sub>600</sub> = 8 to OD<sub>600</sub> = 40, the *E. coli* concentration did not significantly change the obtained pH gradients and we observed only a very minor increase in the kinetics at higher concentrations (Supplementary Fig. 3). The pH quickly returned to its initial value after the light was turned off due to the dissipation of protons. Even after three complete light-dark cycles, we observed only little decrease in the pH gradient. Compared to previous reports where proton pumps were reconstituted in lipid vesicles<sup>7,27</sup>, we could achieve faster and higher pH gradients using genetically engineered *E. coli*. Moreover, the use of *E. coli* circumvented the need for cumbersome protein purification and reconstitution to prepare proteoliposomes<sup>28</sup>, which highlights a key advantage of merging top-down and bottom-up synthetic biology.

As a next step, we aimed to encapsulate the *E. coli* as a pH switch in synthetic cells, which makes pH monitoring with an electrode impractical. We thus supplement the *E. coli* suspension with the ratiometric pH-sensitive fluorescent dye pyranine. The fluorescence properties of pyranine depend on its protonation state (Fig. 1c, Supplementary Fig. 4). After suitable calibration measurements (Supplementary Fig. 5), we could hence monitor the pH optically<sup>29</sup>. Figure 1d plots the fluorescence intensity ratio over time while the system was exposed to light-dark cycles (Supplementary Movie 1, Supplementary Fig. 6). Notably, we obtained the same results as previously with the pH electrode.

**Light-harvesting *E. coli* as internal pH actuators.** Having demonstrated light-activated pH switching in bulk, we wanted to integrate the engineered *E. coli* as artificial mitochondria mimics in synthetic cell-sized confinements. Using a microfluidic droplet formation device (Fig. 2a), *E. coli* and pyranine were encapsulated in surfactant-stabilized water-in-oil droplets (Fig. 2b; Supplementary Fig. 7). We obtained *E. coli*-containing compartments with a radius of  $27 \pm 5 \mu\text{m}$  (mean  $\pm$  s.d.,  $n = 53$ , Fig. 2c). Pyranine served as a fluorescent pH indicator inside the compartments (Fig. 2d; Supplementary Fig. 8). We exposed the system to three consecutive light-dark cycles. Illumination with white light triggered a pH increase inside the cell-sized compartments due to the light-driven proton transport by the *E. coli*, resulting in an optical response of the compartments themselves (Fig. 2e; Supplementary Movie 2). Taken together, we demonstrated that the genetically engineered *E. coli* can provide light-activated proton gradients in cell-sized compartments.

**pH-sensitive attachment of DNA to the compartment periphery.** Proton gradients in synthetic systems are especially exciting if they can be utilized to control and energize downstream processes. Instead of relying on purified proteins, an increasingly popular approach is to construct such pH-dependent machineries *de novo* from molecular building blocks. DNA nanotechnology, in particular, has been employed to build a variety of functional components for synthetic cells<sup>17,30,31</sup>, including membrane-sculpting<sup>32–35</sup> and pH-responsive components such as filaments<sup>36</sup> or rotors<sup>37,38</sup>. However, pH-responsive actuation is challenging after encapsulation into a compartment. With the *E. coli*, we can circumvent this by converting light into a proton gradient.

Towards this goal, we want to implement pH-induced membrane modification and remodeling. For this purpose, we employ a single-stranded DNA sequence, which consists of



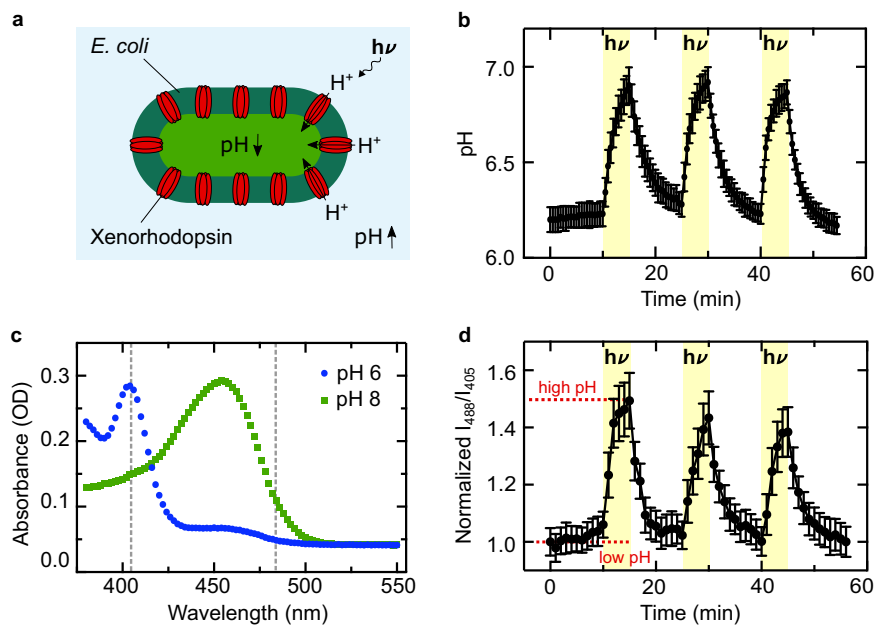


**Fig. 1** Genetically engineered xenorhodopsin-expressing *E. coli* generate a pH gradient upon illumination with white light. **a** Schematic illustration of an *E. coli* expressing xenorhodopsin, a light-driven proton pump (red), allowing for the reversible generation of a directional pH gradient during illumination with white light. The inward pump increases the pH of the external solution. **b** Photoactivity generated by the *E. coli* ( $OD_{600} = 20$ , in 150 mM NaCl) measured with an external pH electrode. The pH is plotted over time during three light-dark cycles (periods of illumination are indicated in yellow). The pH increases by almost one pH unit within 5 min of illumination and nearly returns to its original value after 10 min in the dark (mean  $\pm$  s.d.,  $n = 3$ ). **c** Absorbance measurements of the pH-sensitive ratiometric fluorophore pyranine at pH 6 (blue) and pH 8 (green). The pH can be quantified as the fluorescence intensity ratio at the excitation wavelengths 488 nm and 405 nm (gray dashed lines). **d** Normalized fluorescence intensity ratio  $I_{488}/I_{405}$  of pyranine (50  $\mu$ M) over time in a solution containing *E. coli* and lipid vesicles as determined with confocal fluorescence microscopy (mean  $\pm$  s.d.,  $n = 4$ ). Periods of illumination are indicated in yellow. Source data is available for Fig. 1b–d.

specifically designed sections<sup>36,39</sup>. First, it contains a self-complementary section, which forms a DNA duplex following the Watson-Crick basepairing rules. A single-stranded hairpin loop connects the duplex-forming sections. Another critical single-stranded region is located at the 3' end. At acidic pH it wraps around the DNA duplex to form a triplex, held together by Hoogsteen interactions. At basic pH, the triplex becomes unstable. The remaining duplex can now also open up, if a second DNA strand with higher affinity binds to the hairpin loop<sup>36</sup>. By functionalizing this second DNA strand with a terminal cholesterol tag, it self-assembles at the compartment periphery due to hydrophobic interactions<sup>40</sup>. Thereby, we can recruit the triplex-motif strand to the compartment-periphery in a pH-reversible manner (Fig. 3a). At basic pH, the triplex-motif strand is bound to the periphery (Fig. 3b, inset top right and Supplementary Fig. 9). At acidic pH, on the other hand, it remains homogeneously distributed inside the compartment (Fig. 3b, inset bottom left). Note that the periphery attachment is due to specific interactions between the opened DNA triplex and the complementary cholesterol-tagged DNA. Unspecific absorption in the absence of the cholesterol-tagged DNA was not observed (Supplementary Fig. 10)<sup>41</sup>. To characterize the pH-sensitive membrane attachment, we assessed the fluorescence intensity inside the compartment as a function of pH. The fluorescence intensity decrease with increasing pH follows a sigmoidal fit with a  $pK_a$  of 6.05, which is compatible with the pH range of the *E. coli* and previous works<sup>39</sup>. It is important to note that the choice of fluorophore can affect the pH switching point<sup>41</sup>.

As a next step, we need to verify that membrane attachment of the DNA can also be triggered by the engineered *E. coli*. We hence co-encapsulated them with the cholesterol-tagged as well as

the triplex-forming DNA strand using a microfluidic two-inlet device (Supplementary Figs. 7 and 11). A second inlet proved to be advantageous, because the cholesterol-tagged DNA could bind to the droplet periphery before encountering the *E. coli*, hence preventing unwanted attachment to the *E. coli* due to hydrophobic interactions<sup>42</sup>.

After microfluidic droplet formation in the dark, the triplex-forming DNA was homogeneously distributed inside the compartment with some attachment to the periphery (Fig. 3c). From the calibration curve, we could deduce a starting pH value of around 6.2 inside the droplets, consistent with previous experiments in Fig. 1. Upon illumination, the DNA attached to the compartment periphery over the course of 30 min (Fig. 3d, Supplementary Movie 3). We can deduce a pH increase of approximately one pH unit to about pH 7.25, consistent with the bulk experiments in Fig. 1 (Supplementary Note 1). The dynamic opening of the triplex and subsequent attachment to the periphery was considerably slower than the pyranine response<sup>36</sup>. We observed that the DNA remained attached to the compartment periphery after the light was turned off. We found that this is due to an interesting hysteresis effect: Once the DNA duplex at the droplet periphery was formed, the detachment of the triplex-forming DNA was shifted to substantially lower pH values (Supplementary Fig. 12). Therefore, the DNA did not detach when the pH returned to its original value after turning the light off. This effect can likely be attributed to an effective stabilization of the duplex conformation<sup>41</sup>. Detachment could, however, be achieved with larger pH gradients (Supplementary Movie 4); Fig. 3e shows the reversible attachment of the DNA triplex to the compartment periphery, triggered by the addition of a proton acceptor (1 vol% propylamine in HFE) and subsequent addition of a proton donor (1 vol% trifluoroacetic acid (TFA) in HFE). The

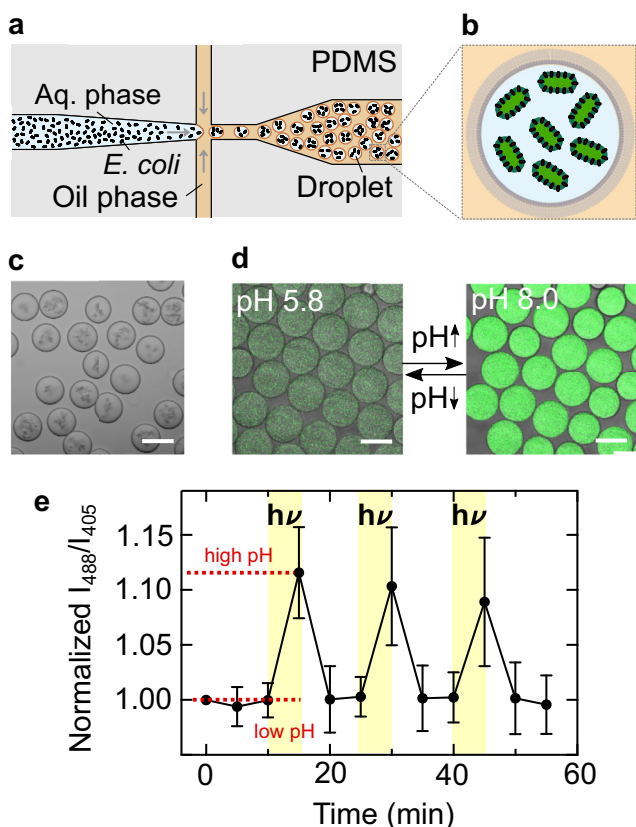


**Fig. 2** *E. coli* as light-activated synthetic organelles that change the pH inside cell-sized confinement. **a** Schematic illustration of the microfluidic device used to encapsulate engineered *E. coli* and pyranine into cell-sized compartments. Water-in-oil droplets were generated at a flow-focusing T-junction of a PDMS-based device. **b** Schematic illustration of a surfactant-stabilized water-in-oil droplet containing engineered *E. coli*. **c** Brightfield image of monodisperse water-in-oil droplets with a radius of  $27 \pm 5 \mu\text{m}$  (mean  $\pm$  s.d.,  $n = 53$ ) containing engineered *E. coli* ( $\text{OD}_{600} = 20$ ). Scale bar:  $50 \mu\text{m}$ . **d** Overlay of confocal fluorescence and brightfield images of pyranine ( $c = 50 \mu\text{M}$ ,  $\lambda_{\text{ex}} = 488 \text{ nm}$ ) inside droplet-based compartments at pH 5.8 and pH 8.0. Scale bar:  $50 \mu\text{m}$ . **e** Normalized fluorescence intensity ratio  $I_{488}/I_{405}$  of *E. coli* and pyranine-containing droplets over time. The fluorescence intensity ratio (mean  $\pm$  s.d.,  $n = 11$  droplets) of pyranine (and hence the pH) increases reversibly during periods of illumination with white light (30 W halogen bulb, highlighted in yellow). Note that the number of recorded frames was reduced because the illumination light had to be turned off each time an image was acquired, which will bias the proton pumping activity. Source data is available for Fig. 2e.

increase in fluorescence after addition of TFA can be attributed to the pH-sensitive nature of the Cy5 dye<sup>43</sup>.

We have thus realized a complex reaction pathway, where illumination activates the internal organelle mimics, causing a proton gradient which, in turn, leads to the stable modification of the compartment periphery. Moreover, the pH-sensitive membrane attachment and the discovered hysteresis effect extend the scope of the DNA triplex motif in DNA nanotechnology.

**pH-induced morphology change.** Next, we can exploit the pH-responsive modification of the compartment periphery to provide a meaningful function. Assuming that the DNA triplex motif could serve as a shuttle to bring components to the periphery, we set out to develop a cytoskeleton mimic, which could sculpt synthetic cellular compartments in a pH-responsive manner. For this purpose, we designed a DNA origami plate made of two

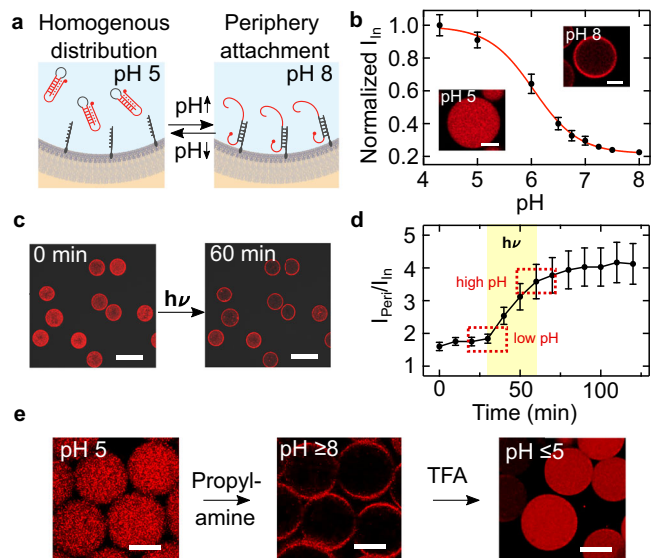


**Fig. 3** pH-sensitive DNA attachment to the droplet periphery stimulated with engineered *E. coli*. **a** Schematic illustration of pH-sensitive duplex formation at the droplet periphery. In response to higher pH, the DNA triplex motif opens up and reversibly attaches to the cholesterol-tagged DNA handles at the compartment periphery. **b** Normalized fluorescence intensity of triplex-forming DNA inside the droplet (excluding the periphery) dependent on the pH (mean  $\pm$  s.d.,  $n = 20$ ). The sigmoidal fit (red curve) has a turning point at pH 6.05. The insets depict confocal fluorescence images of Cy5-labeled triplex-forming DNA ( $\lambda_{\text{ex}} = 633 \text{ nm}$ ,  $1 \mu\text{M}$ ) inside a water-in-oil droplet (containing  $1.5 \mu\text{M}$  cholesterol-tagged DNA) at pH 5 (bottom left) and pH 8 (top right). At pH 8, the triplex-forming DNA is located at the droplet periphery, whereas it is homogeneously distributed at pH 5. Scale bars:  $20 \mu\text{m}$ . **c** Confocal images of microfluidic water-in-oil droplets containing the triplex-forming DNA ( $\lambda_{\text{ex}} = 633 \text{ nm}$ ), cholesterol-tagged DNA and engineered *E. coli* before (0 min) and after (60 min) illumination with white light. Scale bars:  $100 \mu\text{m}$ . **d** Fluorescence intensity ratio  $I_{\text{peri}}/I_{\text{in}}$  (mean  $\pm$  s.d.,  $n = 20$ ) of the triplex-forming DNA over time. The ratio increases during light illumination due to binding of the triplex-forming DNA to the droplet periphery. The time period of illumination is indicated in yellow. **e** Confocal images of microfluidic water-in-oil droplets containing the triplex-forming DNA ( $\lambda_{\text{ex}} = 633 \text{ nm}$ ) and cholesterol-tagged DNA produced at pH 5 (left image). Flushing of the proton acceptor propylamine (1 vol% in HFE) led to a pH increase of the aqueous solution inside the droplets and hence attachment of the triplex-forming DNA (middle). Subsequent flushing of the proton donor trifluoroacetic acid (1 vol% in HFE) decreased the pH and hence causes DNA detachment (right). The attachment of triplex-forming DNA to the droplet periphery is reversible. Scale bars:  $30 \mu\text{m}$ . Source data is available for Fig. 3b, d.

layers of DNA helices (Fig. 4a, Supplementary Fig. 13). The two layers were twisted at a  $90^\circ$  angle as visible in the cryo electron micrographs (Fig. 4b), providing interaction sites for blunt-end stacking<sup>44</sup> on all four sides of the DNA origami. This, in turn, leads to efficient polymerization of the DNA origami monomers into large flat sheets when the edge staples at the scaffold seam are included as verified via cryo-electron microscopy (Supplementary Fig. 14), atomic force microscopy (Supplementary Fig. 15) and agarose gel electrophoresis (Supplementary Fig. 16). The bottom-side of the DNA origami was functionalized with the DNA triplex motif at four positions. At basic pH, the DNA origami thus attached to the periphery of cell-sized droplets functionalized with the complementary cholesterol-tagged strand. However, the droplets remained spherical (Supplementary Fig. 17). This is not surprising given that droplets could also not be deformed with

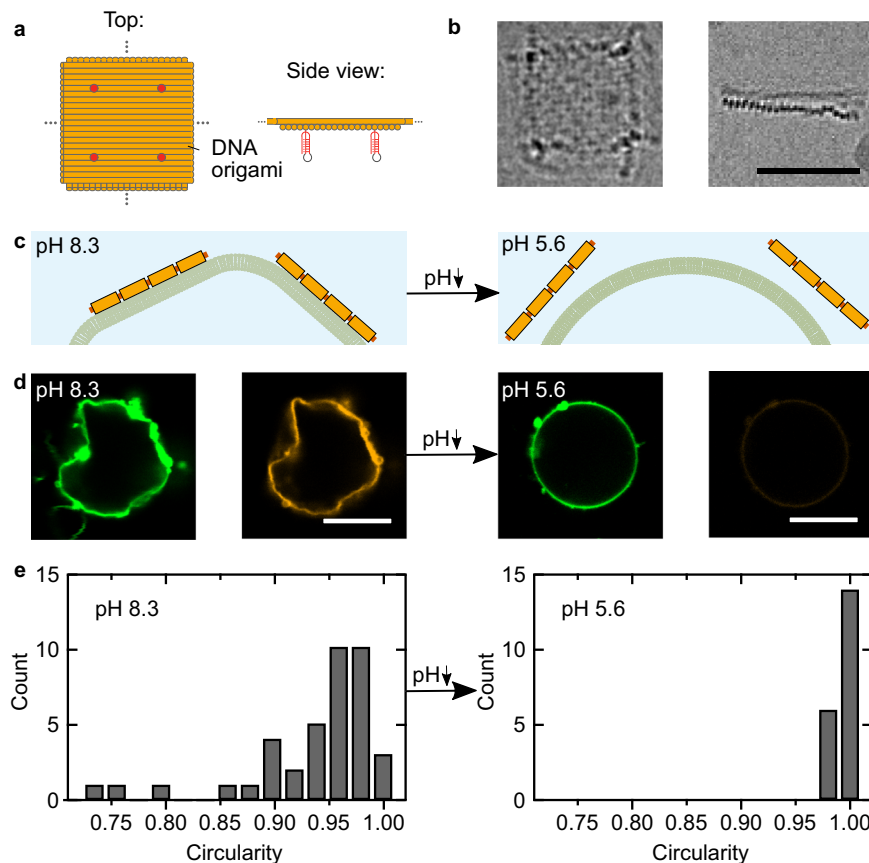


**Fig. 4 Deformation of GUVs with pH-sensitive DNA origami.** **a** Schematic illustration of the DNA origami, which can polymerize into flat DNA origami sheets due to blunt end stacking. The DNA origami was functionalized with four DNA triplex motifs (red, two are shown), such that its assembly on the GUV membrane is pH-dependent. **b** Cryo-EM micrographs of the DNA origami plates. The top view (left) and the side view (right) showing the two DNA layers connected at a 90° angle. Scale bar: 50 nm. **c** Schematic illustration of a section of a GUV membrane functionalized with cholesterol-tagged pH-sensitive polymerized DNA origami. At high pH the DNA origami sculpts the GUV membrane. At low pH, it detaches and the GUV relaxes into its spherical shape. (Continued on the following page) **d** Confocal images of GUVs before (left) and after (right) decreasing the pH from pH 8.3 to pH 5.6 by addition of iso-osmotic potassium dihydrogenphosphate buffer. The GUV (lipids labeled with Atto488,  $\lambda_{ex} = 488$  nm) is initially deformed due to the membrane-bound polymerized DNA origami (labeled with Cy3,  $\lambda_{ex} = 561$  nm). The DNA origami detaches upon lowering the pH (the fluorescence from the detached DNA origami in the background is too weak to be visible). Scale bars: 10  $\mu$ m. **e** Histograms of GUV circularity before (left) and after (right) lowering the pH. At pH 8.3, the mean circularity is  $0.94 \pm 0.06$  ( $n = 39$ ) compared to  $0.991 \pm 0.004$  ( $n=20$ ) at pH 5.6, respectively. Source data is available for Fig. 4e.

cytoskeletal proteins due to their interfacial properties<sup>17,45</sup>. We thus moved to a compartment system which better mimics the mechanical properties of cellular membranes. We produced giant unilamellar lipid vesicles (GUVs) and functionalized them externally with the cholesterol-tagged DNA. We then added the pH-sensitive DNA origami to the GUVs at pH 8.3. At this pH, the DNA origami binds to the GUV membrane. Upon addition of the staples at the scaffold seam, which enable blunt-end stacking, we observed considerable deviations from the initially spherical shape of the GUV (Fig. 4c, d). Large flat sections appeared on the GUV with kinks at the phase boundaries between the polymerized flat DNA sheets. In fluorescence recovery after photobleaching (FRAP) experiments, we find that the polymerized DNA origami layer is not diffusive, as expected for large interconnected sheets, in particular in the presence of  $Mg^{2+}$ <sup>46</sup>. For the underlying deformed lipid membrane, we obtain a diffusion coefficient of  $1.23 \pm 0.14 \mu m^2 s^{-1}$  which is comparable to the lipid diffusion in bare GUVs<sup>47</sup> (Supplementary Fig. 18). In addition to the morphological change, we observe a suppression of membrane fluctuations (Supplementary Fig. 19, Supplementary Movie 5), indicating a mechanical stabilization of the compartment<sup>35,48</sup> by the DNA-based exoskeleton mimic

(Supplementary Note 2). The stabilization effect could potentially be exploited for drug delivery applications. Both the morphological and the mechanical alterations are reversible (Supplementary Fig. 20): Addition of an acid led to pH decrease and hence to the detachment of the DNA origami from the GUV membrane. Notably, the GUVs relax back into their initial spherical shape (Fig. 4d, more images in Supplementary Figs. 21 and 22). Note that a pH decrease to pH 5.6 is required to fully detach the DNA origami from the GUV membrane, which is below the pH decrease that can be provided by the *E. coli* (see Fig. 1). The larger pH gradients required for attachment and detachment of the DNA origami compared to the triplex strand alone can be explained with a cooperativity effect. Each DNA origami is modified with four triplexes. Therefore, complete detachment took several hours and hence the addition of an acid was necessary. The histograms in Fig. 4e quantify the pH-reversible morphology change of the GUVs, revealing lower and more broadly distributed circularities when the DNA origami was attached at high pH. Taken together, the self-assembly of nanoscopic pH-responsive building blocks could trigger the microscopic morphological remodeling of the shape of lipid-membrane-based synthetic cellular compartments.

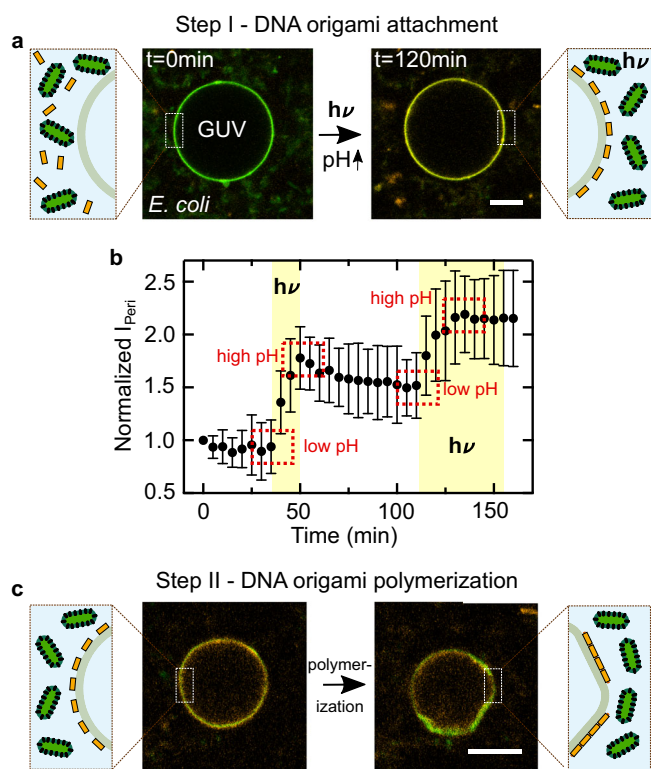


**Fig. 5 Light-harvesting *E. coli* trigger DNA origami attachment and GUV deformation.** **a** Confocal images of a GUV ( $\lambda_{ex} = 488$  nm, green) functionalized with cholesterol-tagged DNA immersed in an *E. coli* and DNA origami ( $\lambda_{ex} = 561$  nm, orange) containing solution before (left) and after (right) light illumination. Scale bar: 10  $\mu$ m. After light illumination, the DNA origami (orange) attaches to the GUV due to the pH increase triggered by the *E. coli*. **b** Normalized fluorescence intensity  $I_{peri}$  (mean  $\pm$  s.d.,  $n = 11$ ) of the triplex-forming DNA at the GUV periphery monitored over time. The time period of illumination is indicated in yellow, illumination leads to a pH increase and hence DNA origami attachment. **c** Confocal images of a GUV ( $\lambda_{ex} = 488$  nm, green) after light-mediated DNA origami ( $\lambda_{ex} = 561$  nm, orange) attachment to the membrane and addition of the DNA staple strands at the scaffold seam which enable blunt-end stacking. DNA origami polymerization leads to the deformation of the GUV membrane within 2 h. Scale bar: 10  $\mu$ m. Source data is available for Fig. 5b.

Finally, we set out to combine the DNA origami-mediated pH-sensitive deformation of GUVs with the light-responsive proton-pumping capabilities of the *E. coli*. First, we showed that the GUVs remained stable in the *E. coli* culture and that we can attach the plain triplex-forming DNA to the GUV membrane upon illumination (Supplementary Figs. 23 and 24; Supplementary Movie 6). Thus, the pH-signal-transduction between the top-down engineered *E. coli* and bottom-up assembled synthetic cells is also successful when the *E. coli* are used as external actuators. Next, we immersed the GUVs in a solution of *E. coli* and pH-sensitive DNA origami. We observed the attachment of the pH-sensitive DNA origami to the GUV membrane upon illumination (Fig. 5a, Supplementary Movie 7). Fig. 5b quantifies the amount of DNA origami attachment, i.e., normalized fluorescence intensity at the GUV periphery  $I_{peri}$ , over time during periods of illumination and darkness. DNA origami attachment happens repeatedly and only during periods of illumination, until saturation is reached. The attachment occurs due to the pH increase triggered by the light-harvesting *E. coli*. After illumination, in periods of darkness, the pH gradient dissipates. Nevertheless, the amount of DNA origami attachment remains roughly

constant (Fig. 5b,  $t = 50$  min until  $t = 110$  min). This can be attributed to the observed pH hysteresis effect (Supplementary Fig. 12): The pH would have to drop below the starting value for detachment, which cannot be achieved with the *E. coli* alone. Nevertheless, a second illumination cycle (from  $t = 110$  min) showed that the *E. coli* remain active and that the DNA origami attachment continued until saturation was reached.

After attachment, we enabled the polymerization of individual DNA origami monomers by adding the staple strands at the scaffold seam, which induce blunt-end stacking. This leads to the deformation of GUVs within two hours (Fig. 5c, Supplementary Movie 8), when the solution was illuminated with light, whereas GUVs remained spherical when they were left in the dark (Supplementary Figs. 25 and 26). Note that the deformation is weaker compared to the deformation achieved with conventional pH switching due to the smaller pH gradient. We can thus exploit the light-harvesting *E. coli* to actuate a morphology change of the GUVs.

## Discussion

In summary, we have shown that the use of top-down engineered bacteria can enhance bottom-up assembled synthetic cells. The light-induced proton gradients we achieve with xenorhodopsin-overexpressing *E. coli* are not only larger than what was previously achieved with purified and reconstituted proteins – we also circumvent the laborious processes involved in their preparation. Especially membrane proteins, which can provide transient or chemically storable forms of energy as well as signal transduction and molecular transport in living cells, can be challenging to purify and reconstitute. Therefore, we can exploit the engineered *E. coli* to drive sophisticated downstream dynamics in synthetic cells. In particular, we demonstrate the pH-sensitive attachment of a triplex-motif-carrying DNA origami to the compartment periphery upon illumination. The polymerized DNA origami, in turn, leads to a shape change of the GUVs triggered by the proton-pumping activity of the *E. coli*. The possibility to manipulate lipid membranes and not just the DNA nanostructures themselves broadens the scope of the popular DNA triplex-motif. For biotechnological applications, compartments that modify themselves as a response to environmental factors are highly desirable. More general, the integration of top-down engineered cells into bottom-up synthetic biology, contributing to bridge a long-standing divide, will provide the potential to realize diverse functions beyond light-harvesting<sup>49</sup>. We envision that the integration of top-down engineered components in synthetic cells will be a leap forward in their complexity and functionality.

## Methods

**Cloning.** The plasmid pNR31 harboring the xenorhodopsin gene from *Nanosalina* (NsXeR) fused to the gene coding for superfolder-GFP (sf-GFP) was assembled by replacing the gene coding for proteorhodopsin in plasmid pNR03<sup>7</sup> with the NsXeR gene (Supplementary Table 1). Therefore, a codon-optimized NsXeR gene based on the amino-acid sequence<sup>25</sup> with a 5' NdeI and a 3' BamHI restriction site was synthesized by GenScript (<https://www.genscript.com>) and cloned into the pUC57 plasmid. Using these two restriction enzymes (New England Biolabs, Ipswich, MA), the NsXeR gene was then subcloned into the pNR03 plasmid. The plasmid pNR33 harboring the NsXeR gene fused to mCherry (Supplementary Table 1) was assembled in multiple steps. First the sf-GFP gene in pNR03 was replaced by the gene coding for mCherry. To that end, the mCherry gene was amplified from the pNR09 plasmid using primers 5'-GGC GGA TCC ATG CAT AGC AAG GGC GAG-3' and 5'-GCC AAG CTT CTT GTA CAG C-3' (Microsynth AG) to introduce 5' BamHI and 3' HindIII restriction sites<sup>7</sup>. The resulting PCR-product was then cloned into plasmid pNR03 where it replaced the sf-GFP gene. Subsequently the same subcloning as for plasmid pNR31 was performed to replace the gene coding for proteorhodopsin with the NsXeR gene.

**Overexpression of fusion-proteins in *E. coli*.** *E. coli* C41 (DE3) cells (Sigma-Aldrich) were transformed with the plasmids pNR31 and pNR33. 100 mL Luria-

Bertani (Fisher Scientific) liquid cultures (100 µg/mL ampicillin, Sigma-Aldrich) were inoculated 1:100 from overnight cultures. The *E. coli* cells were grown at 37°C while shaking at 220 rpm until an OD<sub>600</sub> of 0.4 was reached. Then, all-trans-retinal (Sigma-Aldrich) was added to a concentration of 10 µM and the expression of the fusion-protein was induced with the addition of 1 mM isopropyl-D-thiogalactopyranoside (IPTG, Sigma-Aldrich). The cells were incubated for another 4 h at 37°C while shaking at 220 rpm. Subsequently they were harvested by centrifugation (3200 × g for 10 min at 4°C) and resuspended in 150 mM NaCl. The cells were stored at 4°C and protected from light until further use.

**Photoactivity measurements with a micro pH-electrode.** *E. coli* cells over-expressing either XeR-GFP or XeR-mCherry were washed twice with 150 mM NaCl (3200 × g for 10 min at 4°C) prior to photoactivity measurements. Immediately before the measurement, another washing step was performed. The bacteria were concentrated to an OD<sub>600</sub> of 20. Photoactivity measurements were conducted using a micro pH-electrode (InLab Micro Pro, Mettler Toledo, Columbus, OH) and a sample volume of 800 µL. The pH was recorded every 10 s. During the measurements the bacteria were protected from ambient light and continuously stirred to prevent sedimentation. The sample was illuminated with a KL 1500 LCD halogen lamp (Schott) for 5 min during each light-dark cycle. After each illumination-period the sample was kept in the dark for 10 min. All measurements were performed at room temperature.

**Confocal fluorescence microscopy.** A confocal laser scanning microscope LSM 880, LSM 800 or LSM 700 (Carl Zeiss AG) was used for confocal imaging. The pinhole aperture was set to one Airy Unit and experiments were performed at room temperature. The images were acquired using a 20x objective (Plan-Apochromat 20x/0.8 M27, Carl Zeiss AG). Images were analyzed and processed with ImageJ (NIH, brightness and contrast adjusted) and Zen imaging software (Version 2.3). Confocal images were analyzed using a custom-written ImageJ macro (available here: <https://doi.org/10.5281/zenodo.4738934>). Cell-sized compartments were identified, their radius calculated and the intensity within the compartment center defined as mean inner intensity  $I_{in}$ . The peripheral intensity was determined by quantifying the maximum intensity along a line orthogonal to the compartment periphery. This was repeated every 18° and the mean value taken as  $I_{peri}$ . The resulting data was plotted with Prism 8 (Version 8.4.3) and figures were compiled with Inkscape (Version 1.0rc1).

**Formation of surfactant-stabilized water-in-oil droplets.** Microfluidic PDMS-based (Sylgard 184, Dow Corning) devices for the formation of water-in-oil droplets were produced and assembled<sup>40</sup>. The device layouts of the single and two-inlet devices are shown in the Supplementary Fig. 7. The oil-phase contained 1.4 wt% of Perflouro-polyether-polyethylene glycol (PFPE-PEG) block-copolymer fluorosurfactants (PEG-based fluorosurfactant, Ran Biotechnologies, Inc.) dissolved in HFE-7500 oil (DuPont). The aqueous phase contained the encapsulated content and was varied as described in the corresponding sections. The fluid pressures to induce droplet formation were controlled by an Elveflow microfluidic flow control system or syringe pumps (Harvard Apparatus). The fluids for the syringe pumps were injected into the channels with 1 ml syringes (Omnifix, B. Braun, Germany) connected by a cannula (Sterican® 0.4 × 20 mm, BL/LB, B. Braun) as well as PTFE-tubing (0.4 × 0.9 mm, Bola). To observe the droplet production process, an Axio Vert.A1 (Carl Zeiss AG) inverse microscope was used. As an alternative to the microfluidic formation of droplets, the aqueous phase was layered on top of the oil phase within a microtube (Eppendorf) and droplet formation was induced by manual shaking<sup>50</sup>.

**Photoactivity measurements in droplets.** Photoactivity measurements in droplets were performed by encapsulating *E. coli* (OD<sub>600</sub> ≈ 20) with pyranine (50 µM) into surfactant-stabilized droplets using the microfluidic device described above. The droplets were stored at 4°C after formation to allow for equilibration of the pH inside the droplet. Subsequently, droplets were sealed in an observation chamber and observed with confocal fluorescence microscopy. After 10 min of imaging in the dark, the sample was illuminated for 5 min using a Photonic PL 1000 lamp (light intensity 8 Mlx using a 30 W halogen bulb). The lightguide was placed 5–10 cm above the sample. These cycles were repeated for 1 h.

**pH-sensitive attachment of DNA to the droplet periphery.** Cholesterol-tagged DNA (sequence: 5' (Cy3)-ACCAGACAATACCACACAATTTT-CholTEG 3', HPLC purified) and the Cy-5 labeled triplex-forming DNA (sequence: 5' Cy5-TTCTCTTCGTTTGTCTCTCTCTGTGTGGTATTGTCTAAGAGAAGAG 3', adapted from Green et al.<sup>36</sup>, HPLC purified) were purchased from Biomers or Integrated DNA Technologies. Both DNA sequences were encapsulated in microfluidic droplets at a concentration of 1.5 µM and 1 µM, respectively. For the calibration measurement (Fig. 3b), the aqueous solution inside the droplets additionally contained 50 mM potassium phosphate buffer at the respective pH. Propylamine (from Sigma Aldrich) and Trifluoroacetic Acid (TFA, from Sigma Aldrich) were flushed to dynamically change the pH of the droplets' aqueous phase. For the co-encapsulation of the DNA together with the *E. coli* (OD<sub>600</sub> ≈ 20), a two-inlet

droplet formation device was used (see Supplementary Fig. 7). Droplets were sealed in an observation chamber for confocal fluorescence imaging experiments.

**GUVs electroformation and DNA attachment.** GUVs consisting of 99% DOPC (1,2-dioleoyl-sn-glycero-3-phosphocholine, from Avanti Polar Lipids) and 1% Atto488-DOPE (1,2-dioleoyl-sn-glycero-3-phosphoethanolamine-Atto488, from AttoTEC) in 120 mM sucrose were produced via electroformation using a Vesicle Prep Pro (Nanion)<sup>34</sup>. An AC-current with an amplitude of 3 V and a frequency of 5 Hz was applied for 2 h at 37°C. The cholesterol-tagged DNA and the triplex-forming DNA were added to the GUVs at a concentration of 0.6 µM and 0.4 µM, respectively, before the addition of the *E. coli* (OD<sub>600</sub> ≈ 20), in an unbuffered solution containing 150 mM NaCl and 5 mM MgCl<sub>2</sub>.

**DNA origami design and assembly.** DNA origami structures were adapted from an earlier design by Kopperger et al.<sup>51</sup> using the open-access software *cadnano*<sup>52</sup>. Several changes were introduced, in particular: (1) Addition of nine DNA staple strand overhangs on the top layer, complementary to single stranded fluorescent Cy3-tagged DNA; (2) Addition of four single stranded overhangs on the bottom layer, complementary to the triplex-forming DNA; (3) Complete redesign of the edge staples resulting in a cross-shaped plate. The sticky cross DNA origami contained edge staples that finish the scaffold seam, enabling blunt-end stacking with neighboring origami. (4) Use of the longer single-stranded scaffold DNA, type p8064. A complete list of the DNA sequences is shown in Supplementary Data 1, the details of the design are shown in Supplementary Fig. 13. DNA origami was assembled by adding all unmodified staple strands (Integrated DNA Technologies, Inc., purification: standard desalting) in fivefold excess compared to the p8064 scaffold strand (tilbit nanosystems GmbH). The solution contained 1 × TAE (Tris-Acetate-EDTA, Sigma-Aldrich) and 20 mM MgCl<sub>2</sub> (Sigma-Aldrich) at pH 7.4. The DNA origami was annealed in a thermocycler (Bio-Rad T100) that controls a temperature ramp from 70°C to 20°C over 12 h and successively holds the temperature at 40°C for at least 3 h<sup>51</sup>. The unpurified samples were stored at 4°C until further use.

**Purification of the DNA origami.** Prior to purification from excess staples, the DNA origami was mixed with 1 µM Cy3-tagged single-stranded DNA (Integrated DNA Technologies, Inc., DNA sequence: 5' Cy3- AAAAAAAAAAAAAAAAAAAA AA 3', purification: HPLC) as well as a pH-sensitive triplex-forming DNA motif (Integrated DNA Technologies, Inc., DNA sequence: 5' TTCTCTCTCCTGTTTGGTCTCTCTCTGTGTGGTATTGTCTAAGAGAAGAGTTTGTATGCATAGAA GG 3'). The DNA origami was then suspended in 500 µL of 1 × TAE, 5 mM MgCl<sub>2</sub> and purification was performed by spin filtration in a Biofuge Fresco microtitre centrifuge (Heraeus 75005521) using 100 kDa cutoff filters from Amicon (Amicon Ultra-15, PLHK Ultracel-PL Membran, UFC910008)<sup>31</sup>. After filtration, the MgCl<sub>2</sub> concentration was raised to 20 mM again. Before the experiment, microvolume spectrophotometry (PEQLAB Biotechnologie GmbH) yielded a DNA origami concentration of 6.54 ± 0.42 nM.

**Cryo electron microscopy.** In total, 3 µL of the assembled DNA origami in 10 mM sodium phosphate pH 8.3 containing 20 mM MgCl<sub>2</sub> were blotted for 5–10 s in a (Vitrobot Mark IV, Thermo Fischer) on Quantifoil 2/1 grids with zero blot force at 100% humidity. Plunge frozen samples were imaged in a Krios equipped with a K3 camera behind an energy filter at a pixel size of 0.137 nm. Images were taken by single particle program (EPU, Thermo Fischer) with a total dose of 20 e<sup>-</sup>/Å<sup>2</sup>. Movies of 20 frames were corrected<sup>53</sup> then cropped, normalized, low-pass filtered (0.0625) and 4x binned<sup>54</sup>.

**GUV deformation with pH-sensitive DNA origami.** The DNA origami (in 1 × TAE, 20 mM MgCl<sub>2</sub>) was incubated with cholesterol-tagged DNA at 50 nM for 25 minutes and immediately mixed with Atto488-labeled iso-osmotic (120 mOsmol) GUVs in a ratio of one to three. DNA origami-coated GUVs were imaged after 24 hours of incubation in the fridge. Subsequently, the GUVs were incubated for another 24 hours with 48 mM KH<sub>2</sub>PO<sub>4</sub> buffer in order to detach the DNA origami from the GUV membrane.

**GUV deformation with pH-sensitive DNA origami and light-responsive *E. coli*.** For these experiments, the DNA origami was suspended in a solution of 75 mM NaCl and 10 mM MgCl<sub>2</sub> without addition of a pH-buffering agent. In order to prevent DNA origami polymerization prior to GUV-attachment, the staple strands at the scaffold seam were excluded. The single-stranded scaffold loops prevent base stacking. Subsequently, Atto488-labeled GUVs in sucrose (195 mOsmol) were diluted in 75 mM NaCl and 10 mM MgCl<sub>2</sub> and mixed with 2 µM cholesterol-tagged DNA. After 5 min incubation, *E. coli* resuspended at an OD<sub>600</sub> = 60 in 75 mM NaCl and 10 mM MgCl<sub>2</sub> and DNA origami were mixed in a 1:1:1 ratio with GUVs. For the DNA origami attachment the solution was put into an observation chamber and illuminated with white light during confocal imaging. For subsequent GUV deformation, the staples at the scaffold seam were added to induce base stacking interactions between the membrane-bound DNA origami. The solution

was illuminated for 30 min in bulk before the addition of 50 nM staple strands and imaged 14 h later.

**Statistics and reproducibility.** The experiments were performed independently at least two times. In particular, values in Fig. 1b correspond to three independent experiments and in Fig. 1d to four independent experiments. Experiments for Figs. 2e, 3b, d and 4e were performed two times or more. Fig. 5 was only replicated once, however due to the sequential attachment via light and appropriate controls, we believe that this is adequate. All representative confocal, atomic force and electron microscopy images are only a subset of at least 10 or more images showing similar results.

### Data availability

The data that support the findings of this study are available from the corresponding author upon reasonable request. Source data for main figures 1b, c, d, 2e, 3b, d, 4e, 5b and supplementary figures 1a, c, d, 2, 3a, b, 5, 8, 12, 16, 18b, 19a, b and 24c are provided with this paper.

### Code availability

Image J macro for the analysis of the intensity inside the compartment and at the compartment periphery is provided under the following link: <https://doi.org/10.5281/zenodo.4738934>.

Received: 28 January 2021; Accepted: 27 May 2021;

Published online: 25 June 2021

### References

- Benner, S. A. & Sismour, A. M. Synthetic biology. *Nat. Rev. Genet.* **6**, 533–543 (2005).
- Schwille, P. Jump-starting life? Fundamental aspects of synthetic biology. *J. Cell Biol.* **210**, 687–690 (2015).
- Cameron, D. E., Bashor, C. J. & Collins, J. J. A brief history of synthetic biology. *Nat. Rev. Microbiol.* **12**, 381–390 (2014).
- Zhang, F., Carothers, J. M. & Keasling, J. D. Design of a dynamic sensor-regulator system for production of chemicals and fuels derived from fatty acids. *Nat. Biotechnol.* **30**, 354–359 (2012).
- Anderson, J., Clarke, E., Arkin, A. & Voigt, C. Environmentally Controlled Invasion of Cancer Cells by Engineered Bacteria. *J. Mol. Biol.* **355**, 619–27 (2006).
- Schuerger, N., Werlang, C. & Boghossian, A. A. A synthetic biology approach to engineering living photovoltaics. *Energy Environ. Sci.* **10**, 1102–1115 (2017).
- Ritzmann, N. et al. Fusion domains guide the oriented insertion of light-driven proton pumps into liposomes. *Biophys. J.* **113**, 1181–1186 (2017).
- Ausländer, S., Ausländer, D. & Fussenegger, M. Synthetic biology—the synthesis of biology. *Angewandte Chemie International Edition* **56**, 6396–6419 (2017).
- Göpfrich, K., Platzman, I. & Spatz, J. P. Mastering complexity: towards bottom-up construction of multifunctional eukaryotic synthetic cells. *Trends Biotechnol.* **36**, 938–951 (2018).
- Schwille, P. et al. MaxSynBio: avenues towards creating cells from the bottom up. *Angewandte Chemie Int. Ed.* **57**, 13382–13392 (2018).
- Supramaniam, P., Ces, O. & Salehi-Reyhani, A. Microfluidics for artificial life: techniques for bottom-up synthetic biology. *Micromachines* **10**, 299 (2019).
- Otrin, L. et al. Toward artificial mitochondrion: mimicking oxidative phosphorylation in polymer and hybrid membranes. *Nano Lett.* **17**, 6816–6821 (2017).
- Berhanu, S., Ueda, T. & Kuruma, Y. Artificial photosynthetic cell producing energy for protein synthesis. *Nat. Commun.* **10**, 1325 (2019).
- Miller, T. E. et al. Light-powered CO<sub>2</sub> fixation in a chloroplast mimic with natural and synthetic parts. *Science* **368**, 649–654 (2020).
- Keber, F. C. et al. Topology and dynamics of active nematic vesicles. *Science* **345**, 1135–1139 (2014).
- Bartelt, S. M., Steinkühler, J., Dimova, R. & Wegner, S. V. Light-Guided Motility of a Minimal Synthetic Cell. *Nano Lett.* **18**, 7268–7274 (2018).
- Jahnke, K. et al. Engineering light-responsive contractile actomyosin networks with DNA nanotechnology. *Adv. Biosyst.* **2020**, 2000102.
- Steinkühler, J. et al. Controlled division of cell-sized vesicles by low densities of membrane-bound proteins. *Nat. Commun.* **11**, 1–11 (2020).
- Schwarz-Schilling, M., Aufinger, L., Mückl, A. & Simmel, F. C. Chemical communication between bacteria and cell-free gene expression systems within linear chains of emulsion droplets. *Integrative Biol.* **8**, 564–570 (2016).
- Lentini, R. et al. Two-way chemical communication between artificial and natural cells. *ACS Central Sci.* **3**, 117–123 (2017).
- Lentini, R. et al. Integrating artificial with natural cells to translate chemical messages that direct E. coli behaviour. *Nat. Commun.* **5**, 1–6 (2014).
- Stauer, O., Schröter, M., Platzman, I. & Spatz, J. P. Bottom-up assembly of functional intracellular synthetic organelles by droplet-based microfluidics. *Small* **2020**, 1906424.
- Mehta, A. P. et al. Engineering yeast endosymbionts as a step toward the evolution of mitochondria. *Proc. Natl. Acad. Sci. USA* **115**, 11796–11801 (2018).
- Lau, Y. H., Giessen, T. W., Altenburg, W. J. & Silver, P. A. Prokaryotic nanocompartments form synthetic organelles in a eukaryote. *Nat. Commun.* **2018**, 9.
- Shevchenko, V. et al. Inward H<sup>+</sup> pump xenorhodopsin: mechanism and alternative optogenetic approach. *Sci. Adv.* **3**, e1603187 (2017).
- Inoue, K. et al. A natural light-driven inward proton pump. *Nat. Commun.* **7**, 13415 (2016).
- Marušič, N. et al. Constructing artificial respiratory chain in polymer compartments: Insights into the interplay between bo3oxidase and the membrane. *Proc. Natl. Acad. Sci.* **117**, 15006–15017 (2020).
- Goers, R. et al. Optimized reconstitution of membrane proteins into synthetic membranes. *Commun. Chem.* **2018**, 1.
- Kano, K. & Fendler, J. H. Pyranine as a sensitive pH probe for liposome interiors and surfaces. pH gradients across phospholipid vesicles. *Biochimica et Biophysica Acta (BBA) - Biomembranes* **509**, 289–299 (1978).
- Langecker, M. et al. Synthetic lipid membrane channels formed by designed DNA nanostructures. *Science* **338**, 932–6 (2012).
- Göpfrich, K. et al. Large-conductance transmembrane porin made from DNA origami. *ACS Nano* **2016**, 10.
- Czogalla, A. et al. Amphipathic DNA origami nanoparticles to scaffold and deform lipid membrane vesicles. *Angewandte Chemie International Edition* **54**, 6501–5 (2015).
- Franquelim, H. G., Khmelinskaia, A., Sobczak, J.-P., Dietz, H. & Schwille, P. Membrane sculpting by curved DNA origami scaffolds. *Nat. Commun.* **9**, 811 (2018).
- Göpfrich, K. et al. DNA-tile structures lead to ionic currents through lipid membranes. *Nano Lett.* **15**, 3134–3138 (2015).
- Franquelim, H. G., Dietz, H. & Schwille, P. Reversible membrane deformations by straight DNA origami filaments. *Soft Matter* **17**, 276 (2020).
- Green, L., Amodio, A., Subramanian, H. K. K., Ricci, F. & Franco, E. pH-driven reversible self-assembly of micron-scale DNA scaffolds. *Nano Lett.* **17**, 7283–7288 (2017).
- Göpfrich, K., Urban, M. J., Frey, C., Platzman, I. & Spatz, J. P. Dynamic actuation of DNA-assembled plasmonic nanostructures in microfluidic cell-sized compartments. *Nano Lett.* **20**, 1571–1577 (2020).
- Kuzyk, A., Urban, M. J., Idili, A., Ricci, F. & Liu, N. Selective control of reconfigurable chiral plasmonic metamolecules. *Sci. Adv.* **3**, e1602803 (2017).
- Porchetta, A., Idili, A., Vallée-Bélisle, A. & Ricci, F. General strategy to introduce pH-induced allostery in DNA-based receptors to achieve controlled release of ligands. *Nano Lett.* **15**, 4467–4471 (2015).
- Jahnke, K. et al. Programmable functionalization of surfactant-stabilized microfluidic droplets via DNA-tags. *Adv. Funct. Mater.* **29**, 1808647 (2019).
- Jahnke, K., Grubmüller, H., Igaev, M. & Göpfrich, K. Choice of fluorophore affects dynamic DNA nanostructures. *Nucleic Acids Res.* **2021**, gkab201.
- Jia, H.-R., Zhu, Y.-X., Chen, Z. & Wu, F.-G. Cholesterol-assisted bacterial cell surface engineering for photodynamic inactivation of gram-positive and gram-negative bacteria. *ACS Appl. Mater. Interfaces* **9**, 15943–15951 (2017).
- Cooper, M. E., Gregory, S., Adie, E. & Kalinka, S. pH-Sensitive Cyanine Dyes for Biological Applications. *J. Fluorescence* **12**, 425–429 (2002).
- Kilchherr, F. et al. Single-molecule dissection of stacking forces in DNA. *Science* **353**, aaf5508 (2016).
- Vogel, S. K. et al. Symmetry breaking and emergence of directional flows in minimal actomyosin cortices. *Cells* **9**, 1432 (2020).
- Kocabay, S. et al. Membrane-assisted growth of DNA origami nanostructure arrays. *ACS Nano* **9**, 3530–3539 (2015).
- Schaich, M., Sobota, D., Sleath, H., Cama, J. & Keyser, U. F. Characterization of lipid composition and diffusivity in OLA generated vesicles. *Biochimica et Biophysica Acta (BBA) - Biomembranes* **1862**, 183359 (2020).
- Baumann, K. N. et al. Coating and stabilization of liposomes by clathrin-inspired DNA self-assembly. *ACS Nano* **14**, 2316–2323 (2020).
- Elani, Y. Interfacing living and synthetic cells as an emerging frontier in synthetic biology. *Angewandte Chemie Int. Ed.* **59**, 2–12 (2020).
- Göpfrich, K. et al. One-pot assembly of complex giant unilamellar vesicle-based synthetic cells. *ACS Synthetic Biology* **8**, 937–947 (2019).
- Kopperger, E. et al. A self-assembled nanoscale robotic arm controlled by electric fields. *Science* **359**, 296–301 (2018).
- Douglas, S. M. et al. Rapid prototyping of 3D DNA-origami shapes with caDNAno. *Nucleic Acids Res.* **37**, 5001–5006 (2009).

53. Zheng, S. Q. et al. MotionCor2: anisotropic correction of beam-induced motion for improved cryo-electron microscopy. *Nat. Methods* **14**, 331–332 (2017).
54. Schindelin, J. et al. Fiji: an open-source platform for biological-image analysis. *Nat. Methods* **9**, 676–682 (2012).

### Acknowledgements

K.J., R.R.S., J.P.S. and K.G. acknowledge funding from the Deutsche Forschungsgemeinschaft (DFG, German Research Foundation) under Germany's Excellence Strategy via the Excellence Cluster 3D Matter Made to Order (EXC-2082/1 – 390761711). K.J. thanks the Carl Zeiss Foundation. J.P.S. and I.P. acknowledge funding from the European Research Council, Grant Agreement no. 294852, SynAd, the MaxSynBio Consortium (jointly funded by the Federal Ministry of Education and Research of Germany and the Max Planck Society), from the SFB 1129 of the German Science Foundation and from the VolkswagenStiftung (priority call 'Life?'). J.P.S. is the Weston Visiting Professor at the Weizmann Institute of Science. G.H. and R.R.S. acknowledge the services SDShd and bwHPC supported by the Ministry of Science, Research and the Arts Baden-Württemberg. The Krios microscope is part of the Cluster of Excellence "Cell-Networks" (Exc 81) at the Universität Heidelberg. K.G. received funding from the European Union Horizon 2020 research and innovation program under the Marie Skłodowska-Curie grant agreement No. 792270. The authors acknowledge the Max Planck Society for its general support. N.R. and D.J.M. thank the Swiss Nanoscience Institute (SNI, Basel, Switzerland), the Swiss National Science Foundation and NCCR Molecular Systems Engineering for their support.

### Author contributions

K.J. performed most experiments and analysis. N.R. designed and prepared genetically engineered *E. coli* and performed pH electrode measurements. J.F. and K.G. designed the DNA origami. J.F. and K.J. carried out pH-sensitive deformation experiments. A.N. and K.J. established the use of pyranine as pH-sensor within droplets or GUVs. Y.D. and K.J. performed and analyzed pH-sensitive DNA attachment to GUVs. T.A. helped in analyzing the fluorescence intensity ratios. G.H. and R.R.S. designed and carried out cryo-EM experiments. K.J., K.G., I.P., D.J.M. and J.P.S. designed the study. K.J. and K.G. wrote the manuscript with help from all authors.

### Funding

Open Access funding enabled and organized by Projekt DEAL.

### Competing interests

The authors declare no competing interests.

### Additional information

**Supplementary information** The online version contains supplementary material available at <https://doi.org/10.1038/s41467-021-24103-x>.

**Correspondence** and requests for materials should be addressed to K.G.

**Peer review information** *Nature Communications* thanks the anonymous reviewers for their contribution to the peer review of this work.

**Reprints and permission information** is available at <http://www.nature.com/reprints>

**Publisher's note** Springer Nature remains neutral with regard to jurisdictional claims in published maps and institutional affiliations.



**Open Access** This article is licensed under a Creative Commons Attribution 4.0 International License, which permits use, sharing, adaptation, distribution and reproduction in any medium or format, as long as you give appropriate credit to the original author(s) and the source, provide a link to the Creative Commons license, and indicate if changes were made. The images or other third party material in this article are included in the article's Creative Commons license, unless indicated otherwise in a credit line to the material. If material is not included in the article's Creative Commons license and your intended use is not permitted by statutory regulation or exceeds the permitted use, you will need to obtain permission directly from the copyright holder. To view a copy of this license, visit <http://creativecommons.org/licenses/by/4.0/>.

© The Author(s) 2021

### 3.9 Publication 6: Functional DNA-based cytoskeletons for synthetic cells

To summarize, so far we have seen how the reconstitution of natural proteins, in particular actin filaments and heavy mero-myosin, or even whole cells like genetically-modified *E. coli* in combination DNA origami cytoskeletons can be beneficial for the bottom-up engineering of synthetic cells. A truly synthetic cell, however, does not necessarily rely on protein engineering and purification but would consist out of purely synthetic and ideally programmable building blocks. In the next two publications we will therefore explore how synthetic cytoskeletons can be rationally designed employing synthetic DNA nanotubes (termed DNA filaments). The first publication focuses on the design and characterization of DNA filaments within water-in-oil droplets, whereas the second one reconstitutes functional DNA cytoskeletons inside GUVs.

At first, we chose a DNA tile structure consisting out of five individual strands that can hybridize via addressable overhangs into DNA nanotubes with a diameter of 12 nm and an average length of 7.7  $\mu\text{m}$ . These DNA filaments can be reconstituted within microfluidic water-in-oil droplets creating a meshwork of filaments. As a next step, we make use of the programmability of DNA and design two ways to reversibly assemble DNA filaments via: i) DNA aptamers and ii) toehold-mediated strand displacement. Both approaches can be engineered to assemble DNA filaments in a reversible manner. The aptamer-based approach allows us to engineer ATP-sensitive DNA filaments that only assemble in presence of ATP. We also combine this assembly approach with actin polymerization within confinements and find that they can work equally fast. Lastly, a cytoskeleton mimic should be capable of promoting intracellular transport. We achieve the transport of SUVs along the DNA filament tracks by adapting an RNase H-mediated burnt-bridge mechanism [102, 103] that can be fine tuned via the amount of RNase H present within the water-in-oil droplet. Notably, the SUV transport along DNA filaments could, in principle, also be achieved without proteins via toehold-mediated strand displacement at the expense of a decrease in velocity to about 1 nm/min [104, 105].

We have thus achieved the reversible assembly of purely synthetic DNA cytoskeleton mimics and intracellular transport of vesicles on defined tracks.





## Abstract

The cytoskeleton is an essential component of a cell. It controls the cell shape, establishes the internal organization, and performs vital biological functions. Building synthetic cytoskeletons that mimic key features of their natural counterparts delineates a crucial step towards synthetic cells assembled from the bottom-up. To this end, DNA nanotechnology represents one of the most promising routes, given the inherent sequence specificity, addressability, and programmability of DNA. Here, we demonstrate functional DNA-based cytoskeletons operating in microfluidic cell-sized compartments. The synthetic cytoskeletons consist of DNA tiles self-assembled into filament networks. These filaments can be rationally designed and controlled to imitate features of natural cytoskeletons, including dynamic instability, ATP-triggered polymerization, and guided vesicle transport in cell-sized confinement. Also, they possess engineerable characteristics, including assembly and disassembly powered by DNA hybridization or aptamer-target interactions and autonomous transport of gold nanoparticles. This work underpins DNA nanotechnology as a key player in building synthetic cells.

The cytoskeleton in a living cell functions far more powerful than what the etymon “skeleton” conveys. Apart from serving as the mechanical support, it is involved in diverse cellular processes, ranging from cell division and motility to signal transduction and intracellular transport [1, 2]. Nevertheless, the multifunctional nature of the cytoskeleton provokes great challenges to build their biomimetic analogs in pursuit of bottom-up cell-free synthetic cells. Meanwhile, in the field of DNA nanotechnology, a variety of DNA-based multifunctional devices have been accomplished beyond nanoscopic art and sophisticated nanoarchitectures [3, 4, 2]. Remarkable examples include a plethora of biomimetic systems, such as DNA-based ion-channels [5, 6], walkers [7, 8], rotors [9, 10] and assembly lines [11], among others, which closely resemble the molecular machines in living cells. Recently, preliminary attempts have been made to achieve the stimuli-responsive assembly of DNA-based filaments [12, 13, 14]. However, there is still lack of cytoskeleton mimics with controlled multi-functionality in cell-sized compartments to master complexity and advance a crucial step towards synthetic cells. Here, we demonstrate DNA-based cytoskeleton mimics, which possess the most representative characteristics of natural cytoskeletons, including compartmentalization, ATP-triggered polymerization, dynamic instability, and intracellular cargo transport. Also, we show that these DNA-based cytoskeleton

35 mimics can be programmably designed to achieve assembly and disassembly powered by DNA  
36 hybridization or aptamer-target interactions with unprecedented degrees of freedom.

## 37 **Results**

### 38 **Design of the DNA cytoskeletons**

39 Figure 1 presents a conceptualized illustration of our synthetic system, including compart-  
40 mentalization of different functional components in cell-sized confinement using microfluidic  
41 technologies, assembly and disassembly of DNA-based filaments triggered by DNA hybridization  
42 or aptamer and target interactions, as well as autonomous transport of lipid membrane vesicles  
43 or gold nanoparticles along the filaments powered by ribonuclease H (RNase H)-mediated  
44 hydrolysis. To implement DNA-based filaments as cytoskeleton mimics, a DNA tile design  
45 containing five individual DNA strands [12, 15] is employed to yield micrometer-long hollow  
46 DNA tubes through self-assembly. As shown in Fig. 1, the DNA tile is functionalized with four  
47 short sticky ends (light purple and blue) that serve as binding domains (see Supplementary Fig.  
48 S1 and Supplementary Dataset 1 for a complete list of DNA sequences). Such an arrangement of  
49 the sticky ends can guide the interaction of the DNA tiles to form tubular DNA filaments with  
50 a range of circumferences comprising 6–8 tiles [13, 15]. The confocal microscopy image of  
51 the formed structures in Fig. 2a confirms the successful assembly of the filaments. Structural  
52 analysis using atomic force microscopy (AFM) images reveal an average filament diameter  
53 of 12 nm (see Supplementary Fig. S2), corresponding to 6 tiles (12 DNA duplexes) around  
54 the tubular cross-sections. The assembly conditions, including the DNA tile concentration,  
55 buffer conditions and temperature, have been optimized to provide a high yield of correctly  
56 assembled long filaments (see Methods, Supplementary Figs. S2-S4). The confocal microscopy  
57 analysis yields an average length of 7.74  $\mu\text{m}$  (see Fig. 2b and Supplementary Fig. S5). Next,  
58 all the components for the filament assembly are encapsulated into cell-sized droplets using

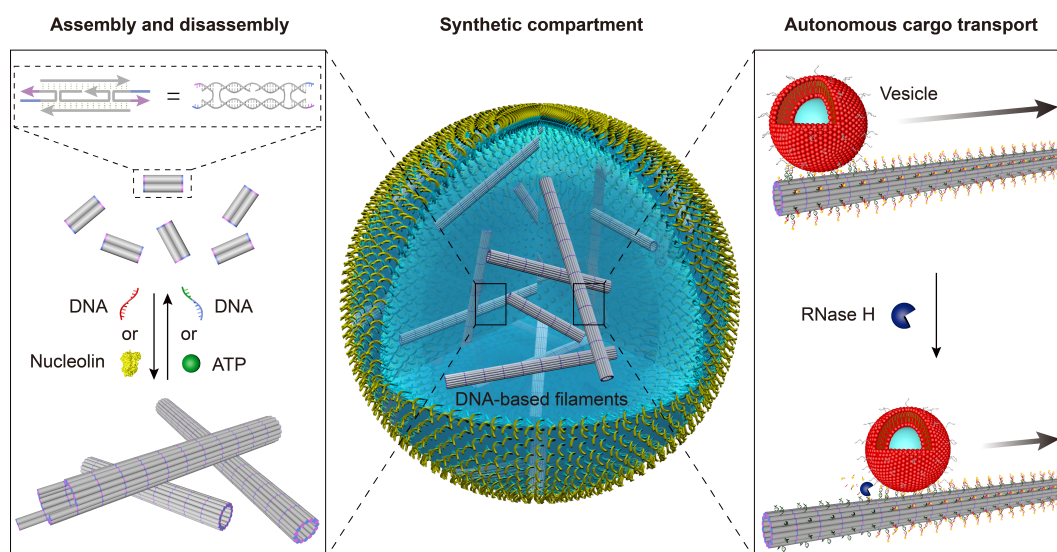


Figure 1: Functional DNA-based cytoskeletons for synthetic cells. Schematic illustration of a cell-sized microfluidic droplet, containing multifunctional DNA-based filaments. The DNA-based filaments undergo dynamic assembly and disassembly triggered by strand displacement reactions or aptamer-target interactions. Moreover, guided directional transport of organic lipid membrane vesicles or inorganic gold nanoparticles along the filament tracks is powered by ribonuclease H (RNase H)-mediated hydrolysis.

59 microfluidics (see Supplementary Fig. S6). The confocal microscopy image in Fig. 2c proves  
 60 the formation of monodisperse droplets, which confine meshworks of the DNA-based filaments  
 61 inside their lumina. The average droplet diameter is engineerable and can be varied according  
 62 to different experimental requirements. As shown in Supplementary Video S1, the filaments  
 63 remain dynamic, displaying constant remodeling and rearrangement of the assemblies in 3D  
 64 confinement.

### 65 **Reversible assembly by strand-displacement**

66 Capitalizing on the unique programmability of DNA, dynamic assembly and disassembly of the  
 67 filaments are enabled by sequential toehold-mediated DNA strand displacement reactions [16].  
 68 More specifically as shown in Fig. 2d, the DNA tiles [17] are modified with toeholds that can be

69 displaced upon addition of the invader strands prior to encapsulation (see Supplementary Fig.  
70 S7). This results in the disassembly of the filaments, giving rise to a homogeneous distribution of  
71 the fluorophore-tagged DNA inside the droplet lumen (see Fig. 2e). Subsequent addition of the  
72 anti-invader strands directly before encapsulation restores the initial filament morphology inside  
73 the droplet (see Figs. 2d, 2e and Supplementary Fig. S8). Using an optimized sequence design  
74 [18], comparably fast kinetics have been achieved. The assembly and disassembly processes  
75 take place within ten minutes. To quantify the reversibility of the dynamic processes, the  
76 porosity  $\Phi$  inside the droplets, which is a direct measure for the degree of filament assembly, is  
77 evaluated after two subsequent strand displacement reactions. As shown in Fig. 2f, the degree of  
78 polymerization  $((1 - \Phi) \cdot 100\%)$  decreases from  $55.1 \pm 14.6 \%$  to  $19.2 \pm 2.8 \%$  and then returns  
79 approximately to its initial value of  $54.4 \pm 4.4 \%$ . This demonstrates the excellent reversibility  
80 of the disassembly and assembly processes powered by DNA hybridization.

### 81 **Reversible assembly by aptamer-target interactions**

82 To integrate biologically relevant components into our synthetic system, next we regulate the  
83 assembly and disassembly of the DNA-based filaments by aptamer-target interactions. As shown  
84 in Fig. 3a, each DNA tile is functionalized with a split ATP aptamer [19] with its two segments  
85 positioned on the opposite ends of the tile. In the presence of ATP, the two aptamer segments  
86 can bind, leading to the assembly of the filaments. The dynamic polymerization process inside  
87 the individual droplets is tracked and quantified by confocal microscopy as shown in Fig. 3b  
88 (see also Supplementary Video S2, Fig. S9). After approximately 40 min, the growth of the  
89 DNA-based filaments inside the compartments reaches a reaction plateau. The ATP aptamer  
90 has a lower affinity to ATP compared to the affinity between the toehold and the invader/anti-  
91 invader [20]. This means that higher concentrations of ATP are needed to achieve similarly fast  
92 reaction kinetics. Filament assembly within 10 minutes requires only  $37.5 \mu\text{M}$  of the anti-invader

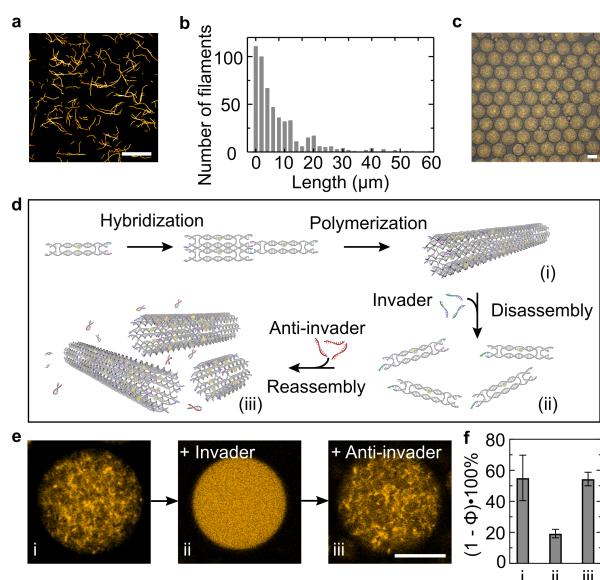


Figure 2: Assembly and disassembly of the DNA-based filaments in cell-sized confinement. **a** Confocal microscopy image of the Cy3-labelled DNA-based filaments (excitation wavelength,  $\lambda_{ex} = 561$  nm). Scale bar:  $20 \mu\text{m}$ . **b** Histogram of the filament lengths determined by confocal microscopy, revealing a mean length of  $7.74 \mu\text{m}$  ( $n = 516$ ). **c** Overlay of the confocal and bright-field overview images of the monodisperse microfluidic water-in-oil droplets containing Cy3-labelled DNA-based filaments (excitation wavelength,  $\lambda_{ex} = 561$  nm). Scale bar:  $50 \mu\text{m}$ . **d** Schematic of the DNA tile design with toeholds. Addition of the invader strands leads to the disassembly of the filaments, whereas addition of the anti-invader strands leads to the reassembly. **e** Representative confocal images of the DNA-based filaments encapsulated into droplets (i) before, (ii) after the addition of the invader strands and (iii) after the addition of the anti-invader strands. Upon addition of the invader strands the filaments are disassembled, leading to a homogeneous distribution of the fluorescence signals inside the droplet. Scale bar:  $20 \mu\text{m}$ . **f** Histogram of the porosity  $((1 - \Phi) \cdot 100\%$ , reflecting the degree of polymerization) of the DNA-based filaments encapsulated into water-in-oil droplets (i) in the absence, (ii) in the presence of the invader strands ( $10 \mu\text{M}$ ) and (iii) after addition of the anti-invader strands ( $37.5 \mu\text{M}$ ). Error bars correspond to the standard deviation of  $n \geq 5$  droplets.

93 (see Supplementary Fig. S8). However, 2 mM ATP are needed to reach the steady-state for  
94 the ATP-triggered polymerization after about 40 minutes as shown in Fig. 3b. To provide  
95 a direct comparison between the synthetic and natural cytoskeletons, we also track the ATP-  
96 triggered polymerization of rhodamine-labeled actin filaments inside individual droplets over  
97 time (see Supplementary Video S3). The DNA-based filaments and the actin filaments bear close  
98 resemblance, in terms of the dynamics of the time-resolved polymerization processes (Fig. 3b).  
99 More specifically, the  $(1 - \Phi) \cdot 100\%$  values start from 43.3 % (orange) and 40.1 % (red) for the  
100 DNA-based and actin systems, respectively. Both systems reach their polymerized states within  
101 75 min and the corresponding  $(1 - \Phi) \cdot 100\%$  values change to 59.2 % and 59 %, respectively. The  
102 actin polymerization inside compartments can be reversed by adding trifluoroacetic acid (TFA,  
103 Fig. 3c) to the oil phase inducing actin depolymerization [21]. In parallel, for the DNA-based  
104 filaments each DNA tile is functionalized with two different aptamers, which can bind to nucleolin  
105 (NCL) and ATP targets, respectively. This enables dual-responsive DNA-based filaments, which  
106 can be assembled and disassembled in the presence of NCL and ATP, respectively, as depicted in  
107 Fig. 3d and verified by atomic force microscopy (see Supplementary Fig. S10). The confocal  
108 microscopy images in Fig. 3e demonstrate the assembled and disassembled state within the  
109 cell-sized confinement upon addition of NCL and ATP directly before encapsulation, respectively.  
110 Supplementary Video S4 shows the dynamics of the polymerized filaments after the addition  
111 of NCL. A comparison between Figs. 3c and 3e reveals similar network morphologies of the  
112 DNA-based and actin filaments despite the fundamentally different building blocks involved.  
113 Another important feature of natural cytoskeletal elements is their directional growth from one  
114 end. We mimic this behaviour by implementing the seeded growth of the DNA-based filaments  
115 using a DNA origami segment as the nucleation seed (see Supplementary Figs. S11, S12, S13,  
116 Supplementary Dataset 1) [22].

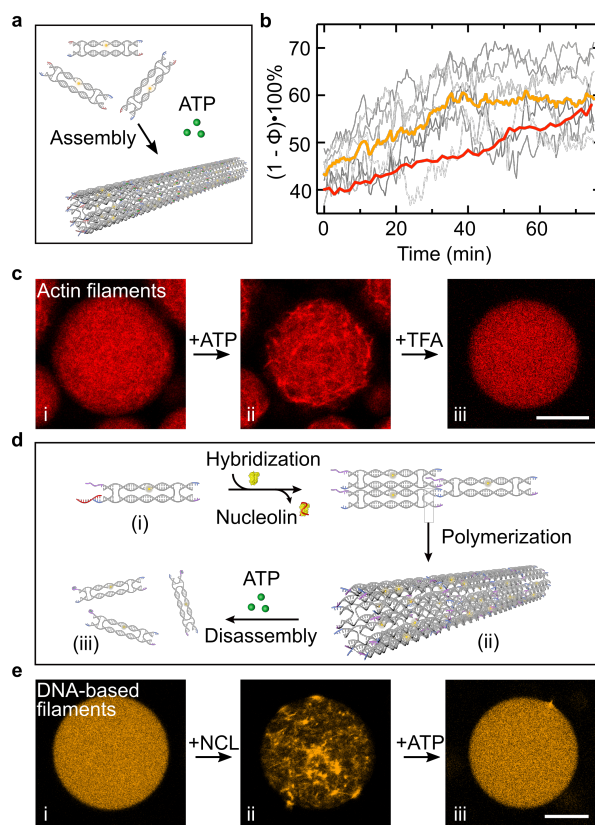


Figure 3: Comparison between DNA-based and actin filaments in cell-sized confinement. **a** Schematic of polymerization of the DNA tiles containing split ATP aptamers upon addition of ATP. **b** Normalized porosity  $((1 - \Phi) \cdot 100\%$ , corresponding to the degree of polymerization) in seven individual droplets (gray) and average polymerization for the DNA-based filaments (orange) and the actin filaments (red) over time during the polymerization processes. The degree of polymerization for the DNA-based filaments inside the droplets increases over time, until it reaches a dynamic steady-state after 40 min. Actin filaments are polymerized with a comparable rate, reaching a similar degree of polymerization. **c** Confocal microscopy images of droplets containing rhodamine-labeled actin filaments ( $\lambda_{ex} = 561$  nm) directly after encapsulation (i), 30 min after addition of ATP (ii) and after subsequent addition of trifluoroacetic acid (TFA, iii). Actin filaments are assembled upon ATP addition and disassembled after adding TFA. **d** Schematic of the dual-responsive DNA tile containing a nucleolin (NCL)-specific aptamer to trigger assembly and an ATP-specific aptamer to trigger disassembly of the filaments. **e** Confocal microscopy images of droplets containing dual-stimuli-responsive Cy3-labeled filaments ( $\lambda_{ex} = 561$  nm) without NCL or ATP (i), after addition of NCL (ii) and after subsequent addition of ATP (iii). The DNA-based filaments are assembled upon NCL addition and subsequently disassembled after addition of ATP. Scale bars: 20  $\mu\text{m}$ .



## 117 **Cargo transport along DNA filaments**

118 Finally, we set out to showcase guided directional cargo transport along the DNA-based fila-  
119 ments, taking direct inspiration from the active vesicle transport by cytoskeletal motor proteins  
120 along microtubules within cells [23]. As depicted in Fig. 4a, the DNA-based filaments are  
121 modified with RNA overhangs to serve as transport tracks. The cargo is fully decorated with  
122 complementary DNA, whereby the choice of the cargo is versatile. It can be organic, such  
123 as small unilamellar vesicles (SUVs) or inorganic, such as gold nanoparticles. SUVs are pre-  
124 pared from phosphatidylcholine (DOPC) lipids with a mean hydrodynamic diameter of  $65$   
125  $\pm 16$  nm as determined by dynamic light scattering (see Supplementary Fig. S14) to mimic  
126 transport vesicles on microtubuli [23]. They are functionalized with cholesterol-tagged DNA  
127 and attached to the filaments via complementary base pairing with multiple RNA-overhangs  
128 on the filaments. The guided directional movement of the vesicle is based on a burnt-bridge  
129 mechanism [24, 25, 26, 27]. Upon addition of RNase H, which selectively cleaves RNA in  
130 DNA-RNA hybrids, the hybridized RNA is hydrolyzed. This promotes the rolling of the vesicle  
131 along the filament through the hybridization of new single-stranded RNA further along the track  
132 with the DNA, which is abundantly coated on the vesicle. Because the DNA on the vesicle  
133 remains intact but the RNA track is depleted at the rear of the vesicle, this imposes a guided  
134 transport of the vesicle towards one end of the filament. The successful binding of SUVs to the  
135 DNA-based filaments is verified by the TEM images in Fig. 4b. In addition, stimulated emission  
136 depletion (STED) images in Fig. 4c corroborates the attachment of Atto633-labeled SUVs to  
137 the filaments (see also Supplementary Fig. S15). Subsequently, the SUV-DNA networks are  
138 encapsulated in 3D confinement in the presence of RNase H. The color-coded z-projection image  
139 in Fig. 4d is processed from a representative droplet and it nicely reveals the SUV-DNA filament  
140 networks with great depth of field in 3D confinement. To optically disseminate the transport,  
141 each RNA overhang is modified with a fluorophore. The fluorophores are successively cleaved

142 from the filament while the SUV rolls directionally along the track. Hence, the dissociation of  
143 the fluorophores from the filaments, which eventually leads to their homogeneous distribution  
144 inside the compartment, provides direct proof of the active SUV transport as demonstrated in  
145 Fig. 4e (see also Supplementary Video S5). The porosity inside the confinement of individual  
146 droplets is monitored over time to evaluate the transport kinetics using confocal microscopy  
147 (see also Supplementary Figs. S16 and S17). It is noteworthy that previously we have used  
148 the porosity to quantify the filament assembly by attaching the fluorophore directly to one of  
149 the constituent strands in a DNA tile. In the current case, the fluorophore is positioned on the  
150 cleavable RNA-DNA chimeric strand. Therefore, a decrease in  $(1 - \Phi) \cdot 100\%$  is correlated  
151 with the active SUV transport rather than filament disassembly. We have released the contents  
152 from the droplets after cargo transport and confirmed using TEM that the DNA-based filaments  
153 remain intact (Supplementary Fig. S18). This proves that the decrease in  $(1 - \Phi) \cdot 100\%$  is due  
154 to cleavage of the fluorophores from intact filaments but not due to filament disassembly. The  
155 average transport velocity is estimated to be in the range of hundreds of nanometer per minute at  
156 an SUV concentration of 25 pM (see Supplementary Note S1). A control experiment without  
157 RNase H proves that bleaching of the fluorophores only contributes 2 % to the apparent decrease  
158 in  $(1 - \Phi) \cdot 100\%$  (Fig. 4f, Supplementary Fig. S19a). Furthermore, we have performed an  
159 additional control experiment to evaluate the contributions of unspecific cutting of RNase H,  
160 which show negligible effects (Supplementary Fig. S19b). Importantly, the versatile transport  
161 mechanism is not limited to biological cargo. A similar strategy is utilized to attach inorganic  
162 gold nanoparticles (20 nm in diameter) as cargo to the DNA-based filaments. The nanoparticles  
163 are functionalized with DNA, which binds to the sequence-complementary RNA overhangs  
164 (see Supplementary Fig. S20) and roll along the droplet-encapsulated DNA filaments in the  
165 presence of RNase H (see Supplementary Fig. S21). To further corroborate the guided rolling  
166 mechanism, the RNA overhangs are modified with biotin-streptavidin in this case, so that the

167 progressive cleavage along the filament can be visualized and confirmed by TEM (Supplementary  
168 Fig. S21). If the free DNA on the cargo is deactivated by hybridization with blocking DNA  
169 strands (Supplementary Fig. S22a), the rolling motion will be inhibited, while hopping or gliding  
170 motion could still take place. Importantly, the porosity measurements inside confinement show  
171 no decrease in the presence of the blocking strands after the addition of RNase H, neither for  
172 the gold nanoparticles, nor for the SUVs (Supplementary Fig. S22b). Therefore, the transport  
173 takes place via cargo rolling along the DNA filaments. The cargo transport halts, if the rolling  
174 motion is inhibited. It is noteworthy that the quenching effects from the gold particles in principle  
175 would facilitate the fluorescence decrease process. However, the transport velocity of the gold  
176 nanoparticles (6 nM) seems to be significantly lower than that of SUVs (25 pM), when comparing  
177 the two systems that exhibit similar porosity change dynamics (see Fig. 4f). In agreement with  
178 previous work [25], we find that a denser DNA coating on the particle generally leads to faster  
179 motion (here  $0.10 \pm 0.01$  strands/nm<sup>2</sup> for gold nanoparticles vs.  $0.18 \pm 0.01$  strands/nm<sup>2</sup>  
180 for SUVs as determined by UV spectrophotometer measurements, Supplementary Figs. S23,  
181 S24). The rolling mechanism relies on the DNA strands on the cargo to processively search  
182 for new RNA overhangs on the track for binding. Moreover, lipid vesicles are fundamentally  
183 different from inorganic particles, because their membranes are diffusive. This likely promotes  
184 the hybridization of the cholesterol-anchored DNA strands on the lipid vesicles with the RNA  
185 overhangs on the filaments. These characteristics highlight the advantage of lipid vesicles as  
186 efficient cargo transport carriers in synthetic cells. Crucially, the overall cargo transport rate  
187 can be tuned by a set of experimental parameters, such as the concentration of RNase H (see  
188 Supplementary Fig. S25) as well as the concentration ratio between cargo and filaments. More  
189 specifically, the decay constant increases from negligible decay for 2.5 pM SUVs to  $0.017 \pm$   
190  $0.001 \text{ min}^{-1}$  for 25 pM SUVs and to  $0.028 \pm 0.001 \text{ min}^{-1}$  for 250 pM SUVs (Supplementary  
191 Fig. S25). This indicates that a higher concentration of SUVs leads to a faster decrease in

192 network fluorescence (Fig. 4g). Different from previous reports, in which DNA origami or  
193 inorganic particles rolled on a surface [24, 25, 26, 27], the cargo transport in our case is guided  
194 along a linear filament track within 3D confinement. A key challenge is that SUVs tend to  
195 fuse with surfaces, especially in the presence of  $Mg^{2+}$ , which is often required to stabilize  
196 DNA nanostructures. Here, droplet encapsulation provides an elegant solution. Because lipid  
197 vesicles are not only hollow containers but also the typical cargo carried by motor proteins  
198 for intracellular transport in living cells, their integration into DNA-based systems outlines an  
199 exciting route with rich opportunities in pursuit of synthetic cells from the bottom-up.

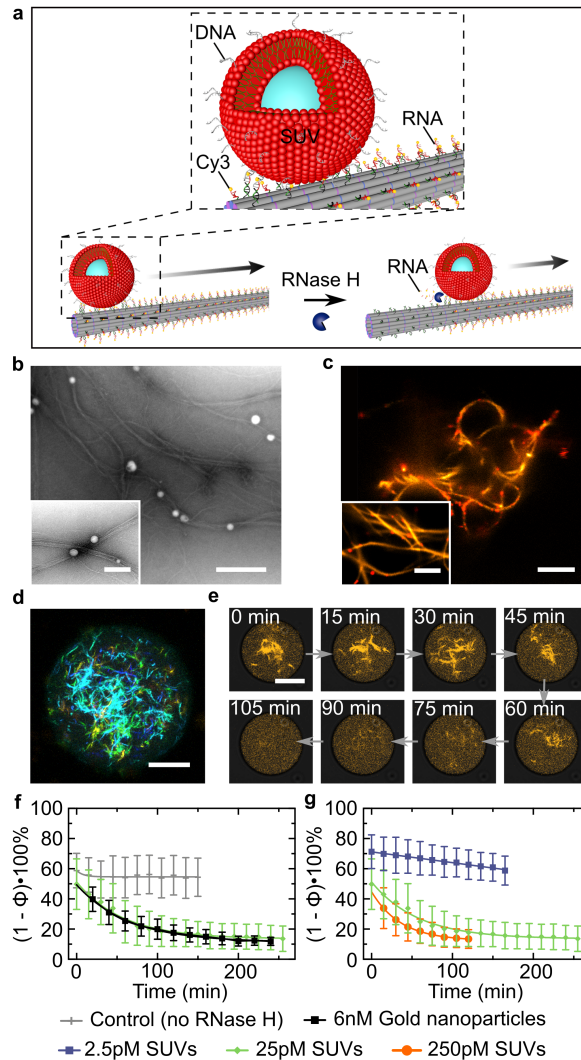


Figure 4: Directional cargo transport guided along DNA-based filament. **a** Schematic of cargo translocation by rolling along the DNA-based filament powered by RNase H-mediated hydrolysis. **b** TEM images of the SUVs attached to the DNA-based filaments via cholesterol-tagged DNA. Scale bars: 500 nm and 200 nm (inset). **c** STED images of the DNA-SUV networks. Scale bars: 5  $\mu\text{m}$  and 2  $\mu\text{m}$  (inset). **d** Color-coded z-projection of a DNA filament network in the presence of SUVs encapsulated into cell-sized confinement. Scale bar: 20  $\mu\text{m}$ . **e** Representative confocal time series of the DNA-based filaments within a water-in-oil droplet from  $t=0$  min to 105 min in time intervals of 15 min. The filaments lose their fluorescence over time due to the RNase H-mediated transport of SUVs (25 pM), while the fluorophores are successively cleaved along the DNA-based filaments. (Continued on the following page)

Figure 4: **f** Porosity ( $(1 - \Phi) \cdot 100\%$ ) corresponding to the SUV transport in droplets over time without RNase H (gray), with gold nanoparticles (6 nM, black) and SUVs (25 pM, green). **g** Porosity ( $(1 - \Phi) \cdot 100\%$ ) corresponding to the SUV transport in droplets over time at different SUV concentrations. The more SUVs are bound to the DNA filaments, the faster they lose their fluorescence, as more SUVs are transported along them. Error bars correspond to the standard deviation of  $n = 5-18$  droplets.

## 200 **Discussion**

201 Living cells possess a remarkable integral organization featuring transport and communication  
202 among distant components within a cell. In recent years, structurally similar replica of some of  
203 these natural architectures have been constructed de novo from DNA. While mere geometry is  
204 relatively straightforward to emulate thanks to the rapid advances in DNA nanotechnology, the  
205 realization of functional, and particularly multi-functional mimics remains an exciting challenge  
206 towards the bottom-up construction of synthetic cells. Our study has outlined DNA-based  
207 cytoskeleton mimics and their operation in cell-sized confinement. Such filaments can undergo  
208 dynamic assembly and disassembly driven by biologically relevant molecules, such as ATP or  
209 engineerable synthetic triggers, including DNA fuel strands or aptamer-target interactions. After  
210 encapsulation, the sequential addition of molecules could be achieved by using microfluidic  
211 picoinjection [28], fusion [29] or light-triggered release of caged compounds [30, 31]. The  
212 filaments further support directional cargo transport along the filamentous tracks. As cargo we  
213 have chosen inorganic gold nanoparticles and lipid vesicles inspired by the vast technological  
214 possibilities on one hand and by the biological counterpart on the other hand. Our DNA-based  
215 cargo transport takes place guided along a track, traveling several tens of micrometers within tens  
216 of minutes. Concomitantly, the transport rate of vesicles on microtubules in living cells is still  
217 much faster [32]. Our work thus stimulates ambition for future research, in which DNA-based  
218 systems could approach or even surpass the capabilities of nature. It will be of particular interest  
219 to engineer dynamic instability and filament polarity towards active force-generating DNA

220 filaments. On the route, we may engineer synthetic cells at the interface between technology and  
221 biology for applications in biomedicine, robotic drug delivery, nanomachinery, artificial cellular  
222 signaling and communication and beyond.

## 223 **Methods**

### 224 **DNA tile design and assembly**

225 The tile design and sequences in this study were adopted from Rothmund et al. with minor  
226 revisions [15]. DNA tiles for all the presented systems were prepared as follows: Each DNA  
227 tile strand was mixed at a final concentration of 5  $\mu\text{M}$  in a Tris-EDTA (TE)/ $\text{Mg}^{2+}$  (10 mM Tris,  
228 1 mM EDTA, 12 mM  $\text{MgCl}_2$ , 5 mM NaCl, pH 8) buffer. A 100  $\mu\text{L}$  solution was annealed using  
229 a thermocycler (Eppendorf AG) by heating the solution to 90  $^\circ\text{C}$ , and cooling it to 25  $^\circ\text{C}$  at  
230 a constant rate of 0.18  $^\circ\text{C}/\text{min}$  for a 6 h period. For the assembly of gold nanoparticles and  
231 filaments, 10 nM gold nanoparticles were mixed with 5  $\mu\text{M}$  DNA filaments at room temperature  
232 and incubated overnight. All DNA strands were purchased from Sigma Aldrich and RNA-DNA  
233 conjugate strands from Integrated DNA Technologies. The DNA sequences for all DNA-based  
234 filament designs can be found in the Supplementary Dataset 1.

### 235 **Transmission electron microscopy**

236 For TEM imaging of the DNA-based filaments, 10  $\mu\text{L}$  of 100 nM DNA tiles were deposited on  
237 freshly glow-discharged carbon/formvar TEM grids. Before depositing the DNA tile solution,  
238 the grids were treated by negative glow discharge for 1 min. After 10 min of deposition, TEM  
239 grids were treated with a uranyl formate solution (2 %) for 15 s.

### 240 **Atomic force microscopy**

241 20  $\mu\text{L}$  of 100 nM DNA-based filaments were deposited onto freshly cleaved mica (Ted Pella,  
242 Inc.) and left to adsorb for 20 min. 100  $\mu\text{L}$  buffer (1 $\times$ TE/ $\text{Mg}^{2+}$ ) was added on top of the sample

243 and the sample was imaged in fluid tapping mode using an AFM (Molecular Imaging, Bruker  
244 Technologies) with ScanAsyst In Fluid+ (Veeco Probes, Inc.).

#### 245 **Confocal fluorescence microscopy**

246 A confocal laser scanning microscope LSM 880 or LSM 900 (Carl Zeiss AG) was used for  
247 confocal microscopy imaging. The pinhole aperture was set to one Airy Unit and the experiments  
248 were performed at room temperature. The images were acquired using a 20× (Plan-Apochromat  
249 20×/0.8 Air M27, Carl Zeiss AG) or 63× objective (Plan-Apochromat 63×/1.4 Oil DIC M27).  
250 Images were analyzed and processed with ImageJ (NIH, brightness and contrast adjusted).

#### 251 **Formation of surfactant-stabilized droplets**

252 As previously described [33], microfluidic PDMS-based (Sylgard 184, Dow Corning) devices  
253 for the formation of water-in-oil droplets were produced and assembled. The device layout of a  
254 single inlet device as used for encapsulation of the DNA filaments is shown in Supplementary  
255 Information Fig. S6. For the oil-phase, 1.4 vol% of Perfluoro-polyether-polyethylene glycol  
256 (PFPE-PEG) block-copolymer fluorosurfactants (PEG-based fluorosurfactant, Ran Biotechnolo-  
257 gies, Inc.) dissolved in HFE-7500 oil (DuPont) was used. The aqueous phase contained the  
258 encapsulated content and was varied as described in the corresponding sections. The fluid  
259 pressures were controlled by an Elveflow microfluidic flow control system. The fluids were  
260 injected into the channels via PTFE-tubing (0.4 × 0.9 mm, BOLA). To observe the production  
261 process, an Axio Vert.A1 (Carl Zeiss AG) inverse microscope was used. As an alternative to the  
262 microfluidic formation of droplets, the aqueous phase was layered on top of the oil phase within  
263 a microtube (Eppendorf) and droplet formation was induced by manual shaking as described  
264 earlier [34].



### 265 **Polymerization of the ATP-sensitive DNA tiles**

266 DNA tiles were stored in Tris-Acetate-EDTA (TAE, 40 mM Tris, 20 mM acetic acid, 1 mM  
267 EDTA) at pH 8 containing 20 mM MgCl<sub>2</sub>. For an instant polymerization into filaments, 500 nM  
268 DNA tiles were mixed with 10 mM adenosine triphosphate (ATP) and encapsulated via microflu-  
269 idics into surfactant-stabilized droplets. In order to visualize the polymerization process, 1 μM  
270 DNA tiles were mixed with 2 mM ATP and immediately encapsulated into droplets via the  
271 shaking approach. The reduced DNA to ATP ratio resulted in slower polymerization kinetics.  
272 The droplets were imaged directly after the encapsulation to monitor the process of filament  
273 formation over time inside individual droplets.

### 274 **Assembly and disassembly of the DNA tiles via aptamer-target interactions or strand dis-** 275 **placement reactions**

276 For the aptamer-specific assembly, 500 nM DNA tiles were mixed with 1.5 μM nucleolin (Sigma-  
277 Aldrich, St. Louis, MO, catalog no. N2662) in 1× TAE buffer containing 20 mM MgCl<sub>2</sub>. For the  
278 subsequent disassembly of the DNA filaments, 10 mM ATP was added to the solution. In the  
279 case of the strand displacement-mediated (de-)polymerization, 500 nM DNA tiles were mixed  
280 with and 10 μM invader strands and encapsulated into droplets immediately afterwards, which  
281 induced the disassembly of the DNA filaments. By addition of 37.5 μM anti-invader strands  
282 directly before encapsulation, the filaments were reassembled.

### 283 **Actin encapsulation**

284 Actin (purified from acetone powder from New Zealand white rabbit skeletal muscle, based on the  
285 method of Pardee and Spudich [35], modified after Kron et al. [36]) was stored in the so-called  
286 GAB buffer containing 2 mM Tris/HCl, pH 8, 0.2 mM CaCl<sub>2</sub>, 0.2 mM ATP, 0.005 % NaN<sub>3</sub> and  
287 0.2 mM DTT, at -80 °C. The actin monomers were labeled with methanol-dissolved rhodamine-  
288 phalloidin (Biotium) by mixing 20 μL actin with 20 μL with 3.3 μL 10× Actin Polymerisation

289 Buffer (20 mM Tris-HCl, pH8, 500 mM KCl, 20 mM MgCl<sub>2</sub>, 10 mM NaATP). Subsequently,  
290 13 μL of rhodamine-phalloidin (13 units) were added to the solution, which was immediately  
291 encapsulated into droplets and imaged during polymerization.

### 292 **Analysis of the degree of polymerization**

293 To analyze the degree of polymerization for DNA-based and actin filaments, images were  
294 thresholded using Otsu's method. For each droplet a circular area in the droplet center of  
295 133 μm<sup>2</sup> was chosen and the relative amount of fluorescent pixels was analyzed using the  
296 image analysis tool in ImageJ. The degree of polymerization was defined via the porosity  $\Phi$  as  
297  $(1 - \Phi) \cdot 100\% = (1 - A_{\text{empty}}/A_{\text{total}}) \cdot 100\% = A_{\text{filament}}/A_{\text{total}} \cdot 100\%$ . Here,  $A_{\text{empty}}$  is the void  
298 area,  $A_{\text{total}}$  is the total area, and  $A_{\text{filament}}$  is the area that is occupied by the DNA filaments. It  
299 corresponded to the degree of polymerization of the DNA tiles inside the droplets.

### 300 **Preparation of the DNA origami seeds**

301 The seed consisted of a layer of 12 helices modified with staples that connect the 1st and 12th  
302 helix to form a hollow cylinder. The designed nanotube seed consisted of a single-stranded  
303 M13mp18 scaffold (tilibit nanosystems), 72 short staple strands, 6 capture strands and 24 adapter  
304 strands (for DNA sequences, see Supplementary Dataset 1, for the strand routing diagram see  
305 Supplementary Fig. S11). The mixture was annealed in a ratio of 1:10:10:10 for scaffold, capture  
306 strands, adapter strands, and staple strands, respectively. All samples were assembled in TAE  
307 buffer (40 mM Tris-Acetate, 1 mM EDTA) with 12.5 mM MgCl<sub>2</sub> by slowly cooling it from  
308 90 °C to 25 °C for a 3 h period. The product was then purified by spin filtration with a 100 kDa  
309 molecular weight cutoff filter (Amicon, Millipore) to remove the extra staple strands, adapter  
310 strands and capture strands.

### 311 **Functionalization of the gold nanoparticles with DNA**

312 TCEP (200 mM, 1 hour) was used to reduce thiol-modified oligonucleotides (5'-GAC ACT AAC  
313 TAA TGA TTT-Thiol-3' from IDT, HPLC purified) in water. Thiol-modified oligonucleotides  
314 and gold nanoparticles (20 nm diameter, Sigma Aldrich) were then incubated at a molar ratio of  
315 DNA to particles of 2000:1 in a 0.5× TBE buffer solution for 20 hours at room temperature. The  
316 concentration of NaCl was slowly increased to 500 mM to increase the thiolated DNA density on  
317 the particles. The particle-DNA conjugates were then washed using a 0.5× TBE buffer solution  
318 in 100-kDa (MWCO) centrifuge filters to remove the free oligonucleotides. The concentration  
319 of the gold nanoparticle was measured at 520 nm (extinction coefficient =  $9.21 \cdot 10^8 \text{ M}^{-1} \text{ cm}^{-1}$ )  
320 using a spectrophotometer (Eppendorf AG).

### 321 **Quantification of the DNA density on gold nanoparticles**

322 The density of the DNA strands on gold nanoparticle (also see Supplementary Fig. S23) was  
323 quantified by releasing the DNA from the gold nanoparticles and measuring the released DNA  
324 concentration using Ultraviolet-visible (UV-Vis) spectroscopy (Eppendorf AG) according to a  
325 protocol adapted from Baldock and Hutchinson [37]. Specifically, 0.5 mL 6 nM DNA-modified  
326 gold nanoparticles with 1× TBE buffer were prepared. Its concentration was measured by UV-Vis  
327 spectroscopy at the absorbance maximum of 520 nm, extinction coefficient  $\epsilon_{\text{AuNP}} = 9.21 \cdot 10^8$   
328  $\text{M}^{-1} \text{ cm}^{-1}$ . The DNA on the particles was released by adding 20  $\mu\text{L}$  of a 1 M DTT solution. The  
329 mixture was incubated with DTT for 2 h to ensure complete dissolution and then centrifuged  
330 at a speed of 8500 rcf for 30 min. The supernatant was carefully collected and then measured  
331 using UV-Vis spectroscopy (at the absorbance maximum of 260 nm, extinction coefficient  
332  $\epsilon_{\text{DNA}} = 180400 \text{ M}^{-1} \text{ cm}^{-1}$ ) to calculate the concentration of DNA released from the particles.  
333 The amount of DNA on the gold nanoparticles was calculated using  $(A_{260}/\epsilon_{\text{DNA}})/(A_{520}/\epsilon_{\text{AuNP}})$ .  
334  $A_{260}$  and  $A_{520}$  were the absorbance values at 260 nm and 520 nm, respectively. The obtained

335 result was divided by the surface area of the 20 nm gold nanoparticle to yield the DNA density  
336 per gold nanoparticle, which gave rise to  $0.10 \pm 0.01$  DNA strands per  $\text{nm}^2$ .

### 337 **Attachment of gold nanoparticles on the DNA origami seeds**

338 Purified DNA origami seeds were mixed with DNA-functionalized gold nanoparticles in a ratio  
339 of 1:5 and then annealed from 35 °C to 25 °C for 12 hours. The annealed product of the seeds  
340 with gold nanoparticles were purified by agarose gel electrophoresis (running buffer: 0.5×TBE  
341 with 11 mM  $\text{MgCl}_2$ ; voltage: 15 V/cm; running time: 1 h). Selected bands were cut out and the  
342 seed with gold nanoparticles were extracted from the gel in Freeze-Squeeze columns (Bio-Rad)  
343 at 4 °C. The gold-nanoparticle-labelled seeds were then imaged with TEM (see Supplementary  
344 Fig. S12).

### 345 **Seeded growth of the DNA-based filaments**

346 Purified DNA origami seeds and gold nanoparticles were mixed with two different tiles (see  
347 Supplementary Dataset 1) in a ratio of 1:1000:1000 and were then incubated at 32 °C for 12 h.  
348 After incubation, the seeded filaments were imaged with TEM or encapsulated into water-in-oil  
349 droplets (see Supplementary Fig. S13).

### 350 **STED imaging**

351 DNA filaments and SUVs were imaged on an Abberior expert line (Abberior Instruments GmbH,  
352 Germany) with a pulsed STED line at 775 nm using excitation lasers at 560 nm and 640 nm  
353 and spectral detection. Detection windows were set to 650–725 nm and 580–630 nm to detect  
354 Atto633-labeled SUVs and Cy3-labeled DNA filaments, respectively. Images were acquired with  
355 a 100×/1.4 NA magnification oil immersion lens (Olympus). The pixel size was set to 30 nm  
356 and the pinhole was set to 1AU. Atto633 and Cy3 were imaged semi-simultaneously during a  
357 first acquisition with STED at 775 nm. Images were analyzed and processed with ImageJ (NIH,

358 brightness and contrast adjusted).

### 359 **SUV extrusion**

360 Small unilamellar vesicles (SUVs) composed of 99 % 18:1 DOPC (1,2-dioleoyl-sn-glycero-3-  
361 phosphocholine) and 1 % Atto633-DOPE (Atto633 1,2-Dioleoyl-sn-glycero-3-phosphoethanolamin)  
362 were formed by mixing the lipids dissolved in  $\text{CHCl}_3$  in a glass vial and subsequent solvent  
363 evaporation under a stream of nitrogen gas. The glass vial was then placed under a vacuum  
364 for 30 min to remove residual traces of solvent. Afterwards, the lipids were resuspended in  
365 phosphate buffered saline pH 7.4 (PBS, Thermo Fisher) at a final concentration of 1 mM lipids.  
366 The solution was vortexed for 10 min to trigger liposome formation. SUVs were then formed by  
367 extruding the liposome solution thirteen times through a polycarbonate filter with a pore size of  
368 50 nm (Avanti Polar Lipids, Inc.). The SUVs were stored at 4 °C until use.

### 369 **Quantification of the DNA density on SUVs**

370 To quantify the DNA density on SUVs (Supplementary Fig. S24), we first measured the  
371 amount of lipids after SUV extrusion. The fluorescence intensity of the lipid mixture (99%  
372 DOPC, 1% Atto633-DOPE) was determined before and after extrusion with a microplate  
373 reader (Spark, Tecan). This revealed that 9.07% of the lipids are lost during the extrusion  
374 process (mean and standard deviation from n=4 independent measurements). Subsequently, the  
375 incorporation efficiency of single-stranded cholesterol-tagged DNA into SUVs was determined.  
376 For this, the concentration of DNA was quantified from UV-Vis absorbance measurements  
377 with a spectrophotometer (Nanophotometer, Implen). A reference measurement was taken  
378 before addition of the DNA to SUVs. Afterwards, the cholesterol-tagged DNA was incubated  
379 in excess with SUVs for 10 min, then the SUVs were centrifuged at 100000 g for 1 h (Optima  
380 Ultracentrifuge, Beckman Coulter). The supernatant was extracted carefully and the DNA  
381 concentration in the supernatant was measured with UV-vis spectroscopy. It corresponds to

382 the unbound fraction of DNA and yielded that  $27.8\pm 2.2\%$  of  $2\ \mu\text{M}$  cholesterol-tagged DNA  
383 binds to SUVs ( $10\ \mu\text{M}$  lipids before extrusion). Taken together, this leads to a DNA density of  
384  $0.18\pm 0.01$  DNA strands per  $\text{nm}^2$ .

### 385 **SUV transport**

386 For the transport experiments SUVs were incubated for 2 min with cholesterol-tagged DNA  
387 ( $5'$ -GAC ACT AAC TAA TGA TTT-Chol- $3'$ ) in a lipid to DNA ratio of 2.5:1. In the meantime,  
388 DNA filaments (final concentration:  $250\ \text{nM}$ ) were mixed with  $1\times$  RNase H reaction buffer  
389 ( $50\ \text{mM}$  Tris-HCl,  $75\ \text{mM}$  KCl,  $3\ \text{mM}$   $\text{MgCl}_2$ ,  $10\ \text{mM}$  DTT, pH 8.3) and incubated for 2 min.  
390 Subsequently, DNA filaments and SUVs were mixed with  $5\ \text{mM}$   $\text{MgCl}_2$ . Finally,  $0.25\ \text{units}/\mu\text{L}$   
391 of RNase H (final concentration,  $50\ \text{mM}$  KCl,  $10\ \text{mM}$  Tris-HCl,  $0.1\ \text{mM}$  EDTA,  $1\ \text{mM}$  DTT,  
392  $200\ \mu\text{g}/\text{ml}$  BSA,  $50\ \%$  glycerol, pH 7.4, NEB) were added. Water-in-oil droplets were formed  
393 using the shaking method, put into an observation chamber and immediately observed using  
394 confocal microscopy for 2-6 h.

### 395 **Analysis of the SUV transport along the DNA filaments**

396 To analyze the vesicle transport along the DNA filaments, images were thresholded using Otsu's  
397 method. For each droplet, a circular area in the droplet center of  $900\ \mu\text{m}^2$  was chosen and the  
398 relative amount of fluorescing pixels was analyzed. By analyzing the porosity, a direct measure  
399 of the amount of SUV transport within the droplets was obtained.

### 400 **Gold nanoparticle transport**

401 DNA tile strands and biotin RNA substrate were mixed and assembled at a final concentration of  
402  $1\ \mu\text{M}$ . Then  $1\ \mu\text{M}$  streptavidin was mixed with the filaments and incubated at  $4\ ^\circ\text{C}$  for 4 hours.  
403 After that,  $10\ \text{nM}$  gold particles with a diameter of  $20\ \text{nm}$  were added to the mixed solution and  
404 incubated overnight at room temperature. For the transport, filaments were mixed with  $1\times$  RNase

405 H reaction buffer first, then 0.1 units of RNase H were added. After 2 hours, 10  $\mu$ L reaction  
406 solution was taken for TEM imaging.

## 407 **Data availability**

408 All the data reported in this paper are available from the corresponding authors upon request.

## 409 **Acknowledgments**

410 K.G. received funding from the Deutsche Forschungsgemeinschaft (DFG, German Research  
411 Foundation) under Germany's Excellence Strategy via the Excellence Cluster 3D Matter Made to  
412 Order (EXC-2082/1 - 390761711) and the Max Planck Society. K.J. thanks the Carl Zeiss Foun-  
413 dation for financial support. P.Z. and N.L. were supported by the European Research Council  
414 (ERC Dynamic Nano). N.L. also acknowledges the support from the Max Planck Society (Max  
415 Planck Fellow). The authors thank Elisa D'Este and the Optical Microscopy facility at the MPI  
416 for Medical Research as well as the kind help of Frank Neubrech for material transportation.

417

## 418 **Author contributions**

419 N.L. and K.G. conceived and supervised the project. P.Z. designed the DNA-based filaments  
420 and performed their validation with TEM and AFM. K.J. performed the encapsulation of DNA-  
421 based and actin filaments, conducted all fluorescence imaging experiments, prepared the SUVs,  
422 analyzed the data and compiled the figures. K.J., N.L. and K.G. wrote the manuscript with  
423 contributions from all authors.

## 424 **Competing interests**

425 The authors declare no competing interests.





## References

- [1] Brouhard, G. J. & Rice, L. M. Microtubule dynamics: an interplay of biochemistry and mechanics. *Nature Reviews Molecular Cell Biology* **19**, 451–463 (2018).
- [2] Murrell, M., Oakes, P. W., Lenz, M. & Gardel, M. L. Forcing cells into shape: the mechanics of actomyosin contractility. *Nature Reviews Molecular Cell Biology* **16**, 486–498 (2015).
- [3] Rothmund, P. W. K. Folding DNA to create nanoscale shapes and patterns. *Nature* **440**, 297–302 (2006).
- [4] Tikhomirov, G., Petersen, P. & Qian, L. Fractal assembly of micrometre-scale DNA origami arrays with arbitrary patterns. *Nature* **552**, 67–71 (2017).
- [5] Langecker, M. *et al.* Synthetic lipid membrane channels formed by designed DNA nanostructures. *Science* **338**, 932–936 (2012).
- [6] Göpfrich, K. *et al.* DNA-tile structures induce ionic currents through lipid membranes. *Nano Letters* **15**, 3134–3138 (2015).
- [7] Shin, J.-S. & Pierce, N. A. A synthetic DNA walker for molecular transport. *Journal of the American Chemical Society* **126**, 10834–10835 (2004).
- [8] Yin, P., Yan, H., Daniell, X. G., Turberfield, A. J. & Reif, J. H. A unidirectional DNA walker that moves autonomously along a track. *Angewandte Chemie International Edition* **43**, 4906–4911 (2004).
- [9] Kopperger, E. *et al.* A self-assembled nanoscale robotic arm controlled by electric fields. *Science* **301**, 296–301 (2018).

- 447 [10] Göpfrich, K., Urban, M. J., Frey, C., Platzman, I. & Spatz, J. P. Dynamic Actuation of  
448 DNA-Assembled Plasmonic Nanostructures in Microfluidic Cell-Sized Compartments.  
449 *Nano Letters* **20**, 1571–1577 (2020).
- 450 [11] Gu, H., Chao, J., Xiao, S.-J. & Seeman, N. C. A proximity-based programmable DNA  
451 nanoscale assembly line. *Nature* **465**, 202–205 (2010).
- 452 [12] Green, L., Amodio, A., Subramanian, H. K. K., Ricci, F. & Franco, E. pH-driven reversible  
453 self-assembly of micron-scale DNA scaffolds. *Nano Letters* **17**, 7283–7288 (2017).
- 454 [13] Green, L. N. *et al.* Autonomous dynamic control of DNA nanostructure self-assembly.  
455 *Nature Chemistry* **11**, 510–520 (2019).
- 456 [14] Del Grosso, E., Prins, L. J. & Ricci, F. Transient dna-based nanostructures controlled by  
457 redox inputs. *Angewandte Chemie International Edition* **59**, 13238–13245 (2020).
- 458 [15] Rothmund, P. W. K. *et al.* Design and characterization of programmable DNA nanotubes.  
459 *Journal of the American Chemical Society* **126**, 16344–16352 (2004).
- 460 [16] Yurke, B., Turberfield, A. J., Mills, A. P., Simmel, F. C. & Neumann, J. L. A DNA-fuelled  
461 molecular machine made of DNA. *Nature* **406**, 605–608 (2000).
- 462 [17] Lin, C., Liu, Y., Rinker, S. & Yan, H. DNA tile based self-assembly: Building complex  
463 nanoarchitectures. *ChemPhysChem* **7**, 1641–1647 (2006).
- 464 [18] Zhang, D. Y. & Winfree, E. Control of dna strand displacement kinetics using toehold  
465 exchange. *Journal of the American Chemical Society* **131**, 17303–17314 (2009). PMID:  
466 19894722.
- 467 [19] Huizenga, D. E. & Szostak, J. W. A DNA aptamer that binds adenosine and ATP. *Biochem-*  
468 *istry* **34**, 656–665 (1995).

- 469 [20] Debiais, M., Lelievre, A., Smietana, M. & Müller, S. Splitting aptamers and nucleic  
470 acid enzymes for the development of advanced biosensors. *Nucleic Acids Research* **48**,  
471 3400–3422 (2020).
- 472 [21] Briehner, W. Mechanisms of actin disassembly. *Molecular Biology of the Cell* **24**, 2299–2302  
473 (2013).
- 474 [22] Schaffter, S. W. *et al.* Reconfiguring dna nanotube architectures via selective regulation of  
475 terminating structures. *ACS Nano* **14**, 13451–13462 (2020). PMID: 33048538.
- 476 [23] Verdeny-Vilanova, I. *et al.* 3d motion of vesicles along microtubules helps them to  
477 circumvent obstacles in cells. *Journal of Cell Science* **130**, 1904–1916 (2017).
- 478 [24] Bazrafshan, A. *et al.* DNA Gold Nanoparticle Motors Demonstrate Processive Motion with  
479 Bursts of Speed Up to 50 nm Per Second. *ACS Nano* (2021).
- 480 [25] Du, Y., Pan, J., Qiu, H., Mao, C. & Choi, J. H. Mechanistic Understanding of Surface  
481 Migration Dynamics with DNA Walkers. *Journal of Physical Chemistry B* **125**, 507–517  
482 (2021).
- 483 [26] Bazrafshan, A. *et al.* Tunable dna origami motors translocate ballistically over  $\mu\text{m}$  distances  
484 at nm/s speeds. *Angewandte Chemie International Edition* **59**, 9514–9521 (2020).
- 485 [27] Yehl, K. *et al.* High-speed DNA-based rolling motors powered by RNase h. *Nature*  
486 *Nanotechnology* **11**, 184–190 (2015).
- 487 [28] Weiss, M. *et al.* Sequential bottom-up assembly of mechanically stabilized synthetic cells  
488 by microfluidics. *Nature Materials* **17**, 89–98 (2018).
- 489 [29] Link, D. R. *et al.* Electric control of droplets in microfluidic devices. *Angewandte Chemie -*  
490 *International Edition* **45**, 2556–2560 (2006).

- 491 [30] Dreher, Y., Jahnke, K., Bobkova, E., Spatz, J. P. & Kerstin, G. Controlled division and  
492 regrowth of phase-separated giant unilamellar vesicles. *Angewandte Chemie International*  
493 *Edition* **133**, 10756–10764 (2020).
- 494 [31] Jahnke, K. *et al.* Engineering Light-Responsive Contractile Actomyosin Networks with  
495 DNA Nanotechnology. *Advanced Biosystems* **4**, 2000102 (2020).
- 496 [32] Lodish, H. *Molecular Cell Biology. 4th edition. Section 19.3, Kinesin, Dynein, and*  
497 *Intracellular Transport.* (New York: W. H. Freeman, 2000).
- 498 [33] Jahnke, K. *et al.* Programmable functionalization of surfactant-stabilized microfluidic  
499 droplets via DNA-tags. *Advanced Functional Materials* **29**, 1808647 (2019).
- 500 [34] Göpflich, K. *et al.* One-pot assembly of complex giant unilamellar vesicle-based synthetic  
501 cells. *ACS Synthetic Biology* **8**, 937–947 (2019).
- 502 [35] Pardee, J. D. & Aspudich, J. Purification of muscle actin. In *Methods in Enzymology*,  
503 164–181 (Elsevier, 1982).
- 504 [36] Kron, S. J., Toyoshima, Y. Y., Uyeda, T. Q. & Spudich, J. A. Assays for actin sliding  
505 movement over myosin-coated surfaces. In *Methods in Enzymology*, 399–416 (Elsevier,  
506 1991).
- 507 [37] Baldock, B. L. & E, H. J. UV–Visible Spectroscopy-Based Quantification of Unlabeled  
508 DNA Bound to Gold Nanoparticles. *Anal. Chem.* **88**, 12072–12080 (2016).

### 3.10 Publication 7: Bottom-up assembly of synthetic cells with a DNA cytoskeleton

In the next work, we transfer our DNA cytoskeletons from surfactant-stabilized water-in-oil droplets to water-in-water system of membrane-enclosed GUVs. This is not only important because water-in-water systems are physiologically more relevant but it for example also allows us to deform the GUVs due to their lower surface tension.

After achieving the encapsulation of DNA filaments into GUVs, we set out to engineer a non-invasive mechanism for the DNA filaments' reversible assembly using light. Therefore, we incorporate the light-sensitive molecule azobenzene into the DNA tile overhangs, which can isomerize between a trans- and a cis-state. The trans-cis isomerization can be triggered using UV light. After UV-illumination, the azobenzene relaxes back into its trans-state due to thermal energy. The important thing is that azobenzene in the trans-state favours duplex formation i.e. DNA filament assembly, whereas cis-azobenzene decreases the binding strength by blocking a base. We verify the reversible assembly of DNA filaments inside GUVs by performing up to 5 assembly-disassembly cycles.

Subsequently, we imitate the filament bundling within natural cells with our DNA filaments by making use of molecular crowders. These big molecules lead to the condensation of DNA filaments into hundreds of filaments-containing bundles according to the entropic depletion effect. These DNA bundles are not only thicker but also longer and have a higher persistence length than single DNA filaments. The increase in the filament persistence length leads to the formation of ring-like DNA bundles that form within the confinement of a GUV. Finally, we engineer DNA cortices by linking the DNA filaments to the GUV membrane using cholesterol-tagged DNA membrane anchors. We find that the amount of cholesterol-tagged DNA present within the GUVs allows us to fine-tune the amount of DNA filaments at the GUV membrane and therefore the degree of cortex formation. By further deflating the GUVs i.e. decreasing the surface-to-volume ratio of the GUVs, we achieve the deformation of GUVs and their suppression of membrane fluctuations.

All in all, in this work we have expanded the use of DNA cytoskeletons to GUV-based systems and engineered their reversible assembly using light, their bundling and the deformation of GUVs.

# Bottom-Up Assembly of Synthetic Cells with a DNA Cytoskeleton

Kevin Jahnke,<sup>†,‡</sup> Vanessa Huth,<sup>†,‡</sup> Ulrike Mersdorf,<sup>¶</sup> Na Liu,<sup>§,||</sup> and Kerstin Göpfrich<sup>\*,†,‡</sup>

<sup>†</sup>*Biophysical Engineering Group, Max Planck Institute for Medical Research,  
Jahnstraße 29, D-69120 Heidelberg, Germany*

<sup>‡</sup>*Department of Physics and Astronomy, Heidelberg University,  
D-69120 Heidelberg, Germany*

<sup>¶</sup>*Department of Biomolecular Mechanisms, Max Planck Institute for Medical Research,  
Jahnstraße 29, D-69120 Heidelberg, Germany*

<sup>§</sup>*2nd Physics Institute, University of Stuttgart,  
Im Pfaffenwaldring 57, D-70569 Stuttgart, Germany*

<sup>||</sup>*Max Planck Institute for Solid State Research,  
Heisenbergstraße 1, D-70569 Stuttgart, Germany*

E-mail: kerstin.goepfrich@mr.mpg.de

## Abstract

Cytoskeletal elements, like actin and myosin, have been reconstituted inside lipid vesicles towards the vision to reconstruct cells from the bottom up. Here, we realize the de novo assembly of entirely artificial DNA-based cytoskeletons with programmed multifunctionality inside synthetic cells. Giant unilamellar lipid vesicles (GUVs) serve as cell-like compartments, in which the DNA cytoskeletons are repeatedly and reversibly assembled and disassembled with light using the cis-trans-isomerization of an azobenzene moiety positioned in the DNA

tiles. Importantly, we induced ordered bundling of hundreds of DNA filaments into more rigid structures with molecular crowders. We quantify and tune the persistence length of the bundled filaments to achieve the formation of ring-like cortical structures inside GUVs, resembling actin rings that form during cell division. Additionally, we show that DNA filaments can be programmably linked to the compartment periphery using cholesterol-tagged DNA as a linker. The linker concentration determines the degree of cortex formation and we demonstrate that the DNA cortex can deform GUVs from within. All in all, this demonstrates the potential of DNA nanotechnology to mimic the diverse functions of a cytoskeleton in synthetic cells.

**Keywords:** DNA nanotechnology, giant unilamellar vesicles, azobenzene, DNA nanotube, synthetic cell, bottom-up synthetic biology

Growth and development, organization, adaptation, stimuli response or reproduction – many of the features that characterize living cells are dependent on their active cytoskeletons. Engineering multifunctional cytoskeletons for synthetic cells thus brings us closer towards the audacious vision of engineering life from the bottom up. The reconstitution of natural cytoskeletal filaments, like actin or microtubules, inside cell-sized lipid vesicles shed light on the minimal set of proteins needed for the formation of biologically relevant structures, such as actin rings<sup>1,2</sup> or membrane protrusions.<sup>3-5</sup> Concomitantly, the combination of these minimal functional units proved to be challenging because the functionality of one element is often compromised by the addition of others. This hints that a true engineering approach to synthetic biology may benefit from customized materials to not only mimic but ultimately exceed the functionality of natural cytoskeletons. Here, DNA nanotechnology allows to precisely and programmably design nanoscale objects that self-assemble into predefined architectures, including transmembrane channels,<sup>6-9</sup> motors,<sup>10-12</sup> scaffolds<sup>13,14</sup> and, in particular, DNA filaments.<sup>15-18</sup> Despite their obvious relevance for bottom-up synthetic biology, most of these components have not yet been reconstituted inside of lipid vesicles. This is in particular desirable in the case of DNA filaments, since features like the formation of ring-like structures or protrusions require confinement. While the encapsulation of DNA scaffolds

into lipid vesicles to provide passive mechanical support has been achieved,<sup>13</sup> it is now crucial to engineer multiple DNA-based dynamic functions inside GUVs. Towards this aim, DNA filaments as more versatile cytoskeleton mimics, have only very recently been encapsulated into water-in-oil droplets.<sup>19</sup> However, the high surface tension compared to lipid vesicles and the lack of a surrounding aqueous environment prevents the implementation of downstream functions.

Here, we realize a programmable and multifunctional DNA cytoskeleton composed of DNA filaments. The DNA filaments can be engineered to self-assemble reversibly upon a light-stimulus inside giant unilamellar lipid vesicles (GUVs). Moreover, DNA filaments can be bundled using molecular crowders and their persistence length tuned *via* the choice of crowder. Finally, they can be engineered to form ring-like architectures and membrane protrusions in confinement.

## Results & Discussion

### Assembly and Encapsulation of DNA Cytoskeletons into GUVs

First, we set out to reconstitute DNA cytoskeletons inside GUVs (Fig. 1a). The DNA cytoskeleton is assembled from individual DNA tiles composed of five single-stranded DNA oligomers that self-assemble into hollow filamentous DNA nanotubes.<sup>15</sup> To realize versatile functions inside GUVs, we use three different sets of DNA tiles for the filament formation: The single-tile DNA filaments (st) consist of only one type of DNA tile with sequence-complementary five nucleotide long sticky overhangs on its ends. The two-tile design uses two orthogonal tiles (tt), which can only polymerize into filaments once they are combined. Here, the sticky overhang of Tile A is designed to bind to Tile B but not to itself. Alternatively, the st DNA tiles are modified with light-sensitive azobenzene moieties at the sticky overhangs of the single tile (st-azo). We verify the assembly of all three types of tiles into DNA filaments with cryo electron microscopy (Fig. 1b, Supporting Fig. 1) revealing a diameter of  $14.5 \pm 1.8$  nm consistent with the formation of a 12-14 helix bundle for all tile designs (Supporting Fig. 2). Furthermore, we analyze the filament length with confocal



microscopy revealing that st and tt DNA filaments do not differ significantly in their mean length of  $6.8 \pm 4.3 \mu\text{m}$  and  $6.4 \pm 3.6 \mu\text{m}$ , respectively (Fig. 1c). On the other hand, st-azo filaments are shorter with a mean length of  $4.7 \pm 2.3 \mu\text{m}$  likely due to the addition of azobenzene into the sticky overhangs. Importantly, micrometer-long filaments are successfully formed from all three types of tiles. It is notable that st DNA filaments assemble inside GUVs at high yield (Fig. 1d). This is achieved by first encapsulating the DNA tiles together with small unilamellar lipid vesicles (SUVs, consisting of 69% DOPC, 30% DOPG, 1% Atto488-DOPE) inside surfactant-stabilized water-in-oil droplets. In presence of negatively charged surfactants and divalent ions, the SUVs fuse at the droplet periphery to form a spherical supported lipid bilayer at the water-oil interface.<sup>20-22</sup> By breaking up the water-in-oil emulsion with a destabilizing surfactant, we are able to release free-standing DNA-tile-containing GUVs into the aqueous phase (Supporting Fig. 3). Importantly, the DNA filaments assemble in confinement. They only form after the release into the aqueous phase due to DNA filament disassembly in presence of negatively charged surfactants in the oil phase (Supporting Fig. 4). After the GUV release and DNA filament assembly, st DNA filaments are homogeneously distributed and dynamic in the lumen of GUVs (Supporting Movie 1). We find that both st and tt tiles form filaments inside GUVs, however, the assembly kinetics are slower for the tt tiles (Fig. 1e, see Supporting Fig. 5 for more examples). By quantifying the assembly processes inside GUVs for st and tt DNA filaments we observe that st DNA filament assembly takes about 30 min and is at least two-fold faster than tt filament assembly (Supporting Fig. 6). After longer periods of time (20 h), the tt filaments cluster likely due to the presence of  $\text{Mg}^{2+}$ . In the st design this was prevented by adding a single-stranded DNA overhang to every tile.

## **Light-Triggered Reversible Assembly of DNA Cytoskeletons**

An important feature of cellular cytoskeletons is the possibility to reversibly assemble inside cells in a stimuli-responsive manner. Here, we exploit the technological advantage of DNA nanotechnology to gain full spatio-temporal control over the assembly and disassembly of the DNA filaments

inside GUVs. For this purpose, we place a photoswitchable azobenzene moiety internally in the sticky overhangs of the st design. In its trans form, azobenzene can intercalate into DNA and induce base stacking interactions that stabilize the DNA duplex (Fig. 1f).<sup>23</sup> However, in its cis form azobenzene blocks the hydrogen bonds of its neighboring base. We position the azobenzene moiety two bases before the end of the five nucleotide long sticky overhang, such that the trans-cis isomerization should render the connection between the tiles unstable and hence induce filament disassembly. Importantly, filament disassembly can be triggered locally with UV-illumination. Over time, azobenzene relaxes back into the energetically favourable trans form, which, in turn, allows the filaments composed of the st-azo tiles to reassemble.

We encapsulate the st-azo tiles into GUVs and follow the assembly and disassembly process inside individual GUVs with confocal microscopy. The trans-to-cis isomerization and thereby filament disassembly was induced with 15 s of illumination with a UV-lamp integrated into the confocal microscope (Fig. 1g, Supporting Fig. 7). We quantify the reversibility by analyzing the normalized porosity of the DNA filament fluorescence, which serves as a measure for the degree of polymerization. Note that the porosity drops within seconds from 100 % to 18.2 % after UV illumination. Over the course of 30 min, the azobenzene relaxes back into its trans-isomer leading to filament re-assembly inside the same GUV at a comparable rate to the tt filaments (Supporting Fig. 6). The initial porosity is nearly restored (96.0 %, Supporting Fig. 8). The full disassembly-assembly cycle can be repeated reproducibly for five times with only little fatigue likely due to azobenzene molecules trapped in the cis form in combination with photobleaching and possibly UV-damage (for additional examples see Supporting Fig. 9). Note that due to the short illumination times of seconds, UV damage is expected to be minimal even after repeated cycles.<sup>24</sup> We verify that standard st DNA filaments without azobenzene do not disassemble after UV illumination (Supporting Fig. 10).

In summary, we have shown that DNA filaments can be reconstituted into GUVs and that DNA nanotechnology allows for the implementation of the highly dynamic assembly and disassembly with full spatiotemporal control inside the confinement of a synthetic cell.

## Bundling of DNA Filaments

Inspired by cytoskeletal cortex formation which modulates cell morphology and stiffness, we engineer DNA filament cortices on the inner GUV membrane to modulate the stiffness and the morphology of the GUVs. Cortex formation can, in principle, be achieved by physical or chemical means, namely by increasing the filament's persistence length above the diameter of the compartment or by introducing chemical interactions with the lipid membrane. For example, actin filaments are bundled during cell division, which increases their persistence length and thus supports the formation of actin rings.<sup>25</sup> We achieve bundling of DNA filaments based on the depletion effect by addition of molecular crowders (20 mg/ml, Fig. 2a). We find that the addition of macromolecular dextran (Supporting Fig. 11), methylcellulose (MC, Supporting Fig. 12) as well as polyethyleneglycol (Supporting Movie 2) completely changes the appearance of the DNA filaments. They bundle into tens of micrometer long filamentous materials, whereby the length depends on the chemical nature of the crowder as well as on its molecular weight (Fig. 2b). Filaments bundled with methylcellulose (MC) are significantly longer than dextran-bundled filaments at the same molecular weight of the crowder (500 kDa), but both bundling agents cause a remarkable increase in filament length compared to the bare st filaments ( $6.8 \pm 4.3 \mu\text{m}$  vs  $34.6 \pm 20.8 \mu\text{m}$  in presence of MC, Fig. 2c). Importantly, we can tune the bundle length by using dextran of different molecular weights (6 kDa, 35 kDa or 500 kDa) yielding filaments with lengths of  $8.1 \pm 4.6 \mu\text{m}$ ,  $20.2 \pm 10.2 \mu\text{m}$  and  $25.4 \pm 12.0 \mu\text{m}$ , respectively. The bundling process influences not only the length but also the persistence of the DNA filaments: A larger molecular weight of the crowder generally lead to increased filament length and increased persistence length with values of up to  $26.8 \pm 0.8 \mu\text{m}$  (Fig. 2d and Supporting Fig. 13). This indicates that the filaments indeed form bundles, which we verify with cryo and transmission electron microscopy. The DNA filament bundles are comprised of hundreds of individual DNA filaments, which are aligned with a high degree of order. The bundles have an average diameter of  $418 \pm 144 \text{ nm}$  in the presence of 35 kDa dextran (Fig. 2e, Supporting Fig. 14

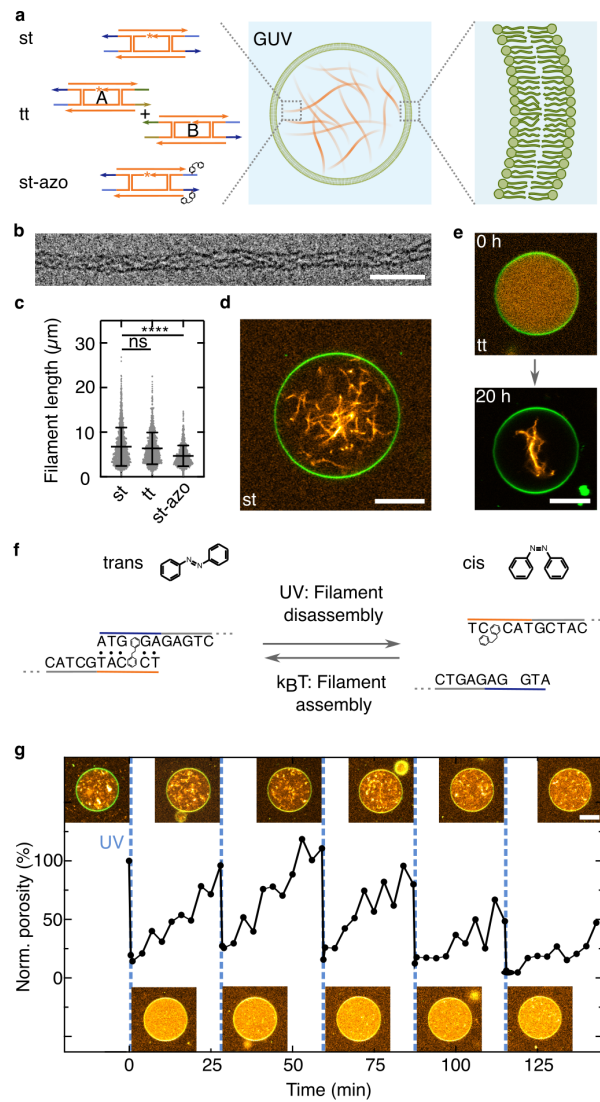


Figure 1: DNA cytoskeletons can be assembled reversibly inside GUVs as lipid-bilayer enclosed synthetic cell models. **a** Schematic representation of a GUV containing a DNA cytoskeleton composed of DNA filaments. DNA cytoskeletons were assembled from a single tile (st) with sticky overhangs, two tiles (tt) with orthogonal complementarity or single tiles modified internally with two azobenzene moieties (st-azo). The asterisk indicates the position of a single-stranded overhang modified with a fluorophore. **b** Cryo-electron micrograph of an st DNA filament. Scale bar: 50 nm. **c** DNA filament length ( $n > 1000$  filaments, mean  $\pm$  SD). st and tt filaments have the same length ( $p = 0.16$ ), st-azo filaments are shorter ( $p \leq 0.001$ ). **d** Confocal image of an st DNA cytoskeleton (orange, labelled with Cy3,  $\lambda_{ex} = 561$  nm) inside a GUV (green, 69% DOPC, 30% DOPG, 1% Atto488-DOPE,  $\lambda_{ex} = 488$  nm). Scale bar: 10  $\mu$ m. **e** Confocal images of tt cytoskeletons prior to (0 h) and after assembly (20 h) inside a GUV. Scale bar: 10  $\mu$ m. (continued on the following page)

Figure 1: (Continued) **f** Schematic representation of the st overhang modified with azobenzene (st-azo) for reversible cytoskeleton assembly with UV light. **g** Light-mediated reversible assembly of 500 nM st-azo cytoskeletons inside a GUV. The porosity measures the degree of filament polymerization over time. Timepoints of UV illumination (15 s) are indicated (blue dashed line). Insets depict confocal images of the same GUV at the respective time points. Scale bar: 10  $\mu\text{m}$ .

and 15).

Next, we reconstitute the bundled DNA filaments inside GUVs. We choose dextran as a crowding agent, since GUVs formation in the presence of MC was not successful. In particular, the fusion process of the SUVs at the droplet periphery was inhibited, likely due to the higher viscosity of MC (Supporting Fig. 16).<sup>26</sup> We choose dextran with a molecular weight of 35 kDa because the resulting persistence length of  $21.7 \pm 0.6 \mu\text{m}$  is maximal and matches the GUV diameter. After encapsulating DNA filaments in the presence of dextran, the large persistence length and the depletion effect cause the DNA filament bundles to localize and condense at the GUV periphery (Supporting Fig. 11, Supporting Movie 3). Moreover, for GUVs with a diameter below 15  $\mu\text{m}$ , i.e. smaller than the persistence length of the DNA bundle ( $20.2 \pm 10.2 \mu\text{m}$ ), we achieve the reproducible formation of ring-like structures inside the GUVs around their circumference (Fig. 2f, Supporting Fig. 17). We have thus realized the formation of DNA filament bundles and reconstituted ring formation based on these entirely synthetic building blocks inside GUVs.

## DNA Cortex Formation within GUVs

In cells, ring formation requires bundling of filaments, while membrane deformation relies on a link between the actin filaments and the cell's periphery to establish cell shape or to form protrusions during cell migration.<sup>27,28</sup>

In analogy, to establish GUV shape with a DNA-based cortex, we link the DNA cytoskeleton to the membrane with cholesterol-tagged DNA (chol-DNA). For this purpose, one of the strands of the st was extended with a single-stranded DNA overhang. A sequence complementary cholesterol-tagged DNA is added to the SUVs that fused at the droplet interface during GUV formation. In this way,

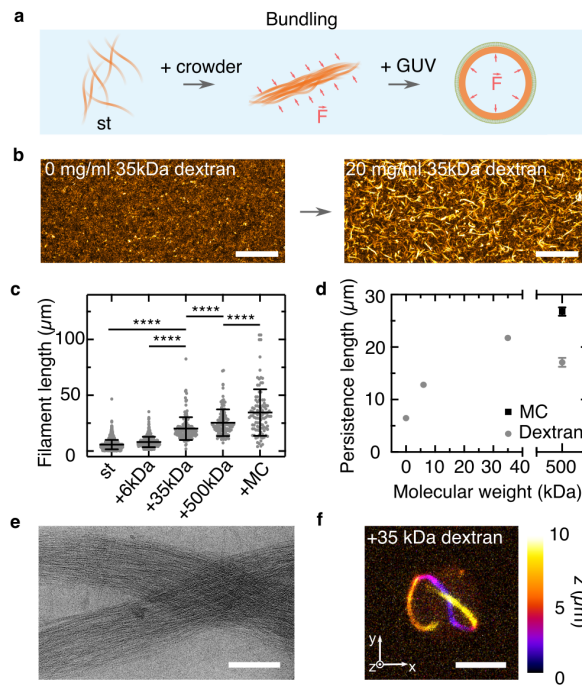


Figure 2: DNA filament bundling leads to the formation of ring-like structures within GUVs. **a** Schematic representation of the bundling of DNA filaments caused by the addition of a molecular crowder and the subsequent DNA cortex formation inside GUVs. **b** Confocal z-projection of st DNA filaments (orange, labelled with Cy3,  $\lambda_{ex} = 561$  nm) in absence and presence of 20 mg/ml 35 kDa dextran. Scale bar: 50  $\mu$ m. **c** Length distribution of DNA filaments in absence of bundling agents (st,  $n = 1896$ ) and st DNA filaments in presence of 20 mg/ml 6 kDa dextran ( $n = 510$ ), 35 kDa dextran ( $n = 180$ ), 500 kDa dextran ( $n = 129$ ) and 500 kDa methylcellulose (MC,  $n = 104$ ). All conditions are significantly different in length ( $p \leq 0.001$ ). **d** Persistence length of DNA filaments over molecular weight of the crowder ( $n = 11-15$ , mean  $\pm$  SD). **e** Cryo-electron micrograph of bundled st filaments in presence of 20 mg/ml dextran (MW = 35 kDa). Scale bar: 200 nm. **f** Color-coded confocal z-projection of 50 nM st filaments in presence of 20 mg/ml 35 kDa dextran inside a GUV. Scale bar: 5  $\mu$ m.

the chol-DNA localizes at the inner bilayer leaflet of the GUV and serves as an attachment point for the filaments (Fig. 3a). To first of all verify that the membrane-bound DNA filaments are intact on the membrane, we form a supported lipid bilayer (SLB) and functionalize it with the chol-DNA. With confocal microscopy, we verify the successful binding of st-chol DNA filaments to the SLB. We find that DNA filaments are diffusive and even undergo membrane-assisted growth and occasionally breakage (Fig. 3b, Supporting Movie 4). On average, st-chol DNA filaments on an SLB are smaller than bare st DNA filaments ( $l = 3.3 \pm 2.7 \mu\text{m}$  vs.  $l = 6.8 \pm 4.3 \mu\text{m}$ ) likely due to the additional electrostatic and diffusive forces acting on the filaments once they are bound to the membrane (Fig. 3c). Similar to the case of DNA bundling, we observe the formation of a DNA filament cortex underneath the inner GUV membrane when the DNA filaments are linked with chol-DNA (Fig. 3d, Supporting Movie 5). Interestingly, we also observe a significantly higher yield of GUVs ( $\approx 8000 \text{ GUVs}/\mu\text{L}$  for st-chol and  $\approx 1500 \text{ GUVs}/\mu\text{L}$  for st) with our droplet-stabilized GUV method<sup>20</sup> indicating a mechanical stabilization of the GUVs (Supporting Fig. 18). As shown in Fig. 3e, fluorescence recovery after photobleaching (FRAP) confirms the presence of intact DNA filaments on the GUV membrane, which yield six-fold lower diffusion coefficients of  $D_{\text{filament}} = 0.38 \pm 0.21 \mu\text{m}^2 \text{ s}^{-1}$  compared to unpolymerized cholesterol-anchored DNA tiles ( $D_{\text{tile}} = 2.3 \pm 0.8 \mu\text{m}^2 \text{ s}^{-1}$ ). Additionally, we confirm that lipid diffusion is only weakly affected by the presence of the DNA cortex ( $D_{\text{lipid, tile}} = 2.9 \pm 0.7 \mu\text{m}^2 \text{ s}^{-1}$  vs.  $D_{\text{lipid, filament}} = 2.4 \pm 0.4 \mu\text{m}^2 \text{ s}^{-1}$ ,  $p = 0.17$ ). By changing the amount of cholesterol-tagged DNA at the GUV periphery, we tune the degree of DNA cortex formation (Fig. 3f, Supporting Fig. 19). The degree of cortex formation can be quantified by the ratio of the DNA filament intensity on the membrane  $I_{\text{peri}}$  over the filament intensity in the GUV lumen  $I_{\text{in}}$ .<sup>29</sup> Cortex formation is enhanced at higher concentrations of chol-DNA and saturates when the chol-DNA is supplied at a ratio of 1:1 compared to the DNA tiles.

Ultimately, a membrane-linked DNA cortex should be capable of establishing GUV shape. For this purpose, we use two-fold higher amounts of DNA filaments ( $1 \mu\text{M}$ ) and deflate the GUVs to an osmolarity ratio of  $c_{\text{out}}/c_{\text{in}} = 2$ . Deflation provides sufficient excess membrane area to allow for GUV deformation. Fig. 3g depicts representative examples of the successful deformation of

GUVs from within. The internal DNA cortex establishes the GUV shape. The GUVs often exhibit straight segments, which likely correspond to straight DNA filaments aligning at their periphery. It is conceivable that initially randomly ordered filaments increase their nematic order when the available membrane area shrinks due to the deflation process. To quantify the degree of deformation, we analyze the GUV circularity and find that deflated GUVs are significantly less spherical than undeflated GUVs with circularities of  $0.955 \pm 0.013$  and  $0.995 \pm 0.001$ , respectively (Fig. 3h). GUVs also remain static in their deformed shape over time (Supporting Movie 6), again confirming their mechanical stabilization. In contrast, deflated GUVs that contain st DNA filaments without the chol-DNA handles exhibit apparent membrane fluctuations (Supporting Movie 7).

Previously, GUVs were deformed externally with multi-layer DNA origami structures only.<sup>29–31</sup> But it remained unclear whether DNA filaments, or DNA tile structures in general, are sufficiently rigid to deform membranes. Furthermore it was unclear whether deformation can be achieved from within the GUV, where the confined volume limits the amount of DNA that is available for membrane attachment. Hence, in addition to ring formation, we have implemented another pivotal characteristic of cytoskeletal filaments inside synthetic cells, namely their linkage to the inner membrane for mechanical support to stabilize non-spherical GUV shapes.

## Conclusion

In summary, we have engineered programmable, versatile and functional cytoskeletons made from DNA inside GUVs as synthetic cell models. Despite recent progress in the assembly of GUVs and the reconstitution of natural cytoskeletal filaments, the multitude of necessary proteins to achieve meaningful functions limits the scope of protein reconstitution for the bottom-up assembly of synthetic cells. Here, we achieved a diverse set of functions based on nucleic acids as engineerable and inherently biocompatible molecular building blocks and reconstitute them inside GUVs. Furthermore, we showed that by adapting the DNA tile design DNA filaments with a variety of customized functions can be obtained. These include the reversible light-mediated filament assembly and



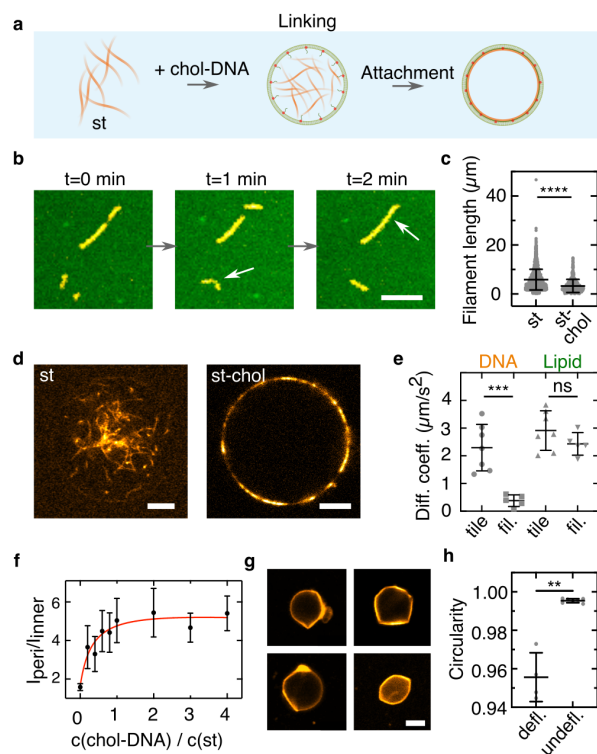


Figure 3: Deformation of GUVs from within by a membrane-linked DNA cortex. **a** Schematic illustration of the linkage of DNA filaments to the GUV membrane which cholesterol-tagged DNA. **b** Confocal images of cholesterol-linked DNA filaments (st-chol, Cy3,  $\lambda_{ex} = 561$  nm) on a supported lipid bilayer (SLB, green, Atto488-DOPE,  $\lambda_{ex} = 488$  nm). st-chol filaments diffuse and grow on the SLB. Scale bar:  $10 \mu\text{m}$ . **c** Length distribution of st DNA filaments on glass ( $n = 1896$ ) and st-chol DNA filaments on SLBs ( $n = 429$ ). st-chol filaments are significantly shorter ( $p \leq 0.001$ , mean  $\pm$  SD). **d** Confocal images of  $500 \text{ nM}$  st (left) and st-chol filaments inside GUVs. Scale bar:  $5 \mu\text{m}$ . **e** Diffusion coefficients of DNA filaments on SLBs determined by FRAP. Disassembled st-chol filaments (tile) exhibit 6-fold increased diffusion speeds compared to polymerized st-chol filaments (fil.,  $p = 0.0007$ ). The diffusion of the lipids of the SLB is not influenced by the polymerization state of the DNA filaments ( $n = 5-7$ , mean  $\pm$  SD).

Figure 3: (Continued) **f** Fluorescence ratio  $I_{\text{peri}}/I_{\text{inner}}$  of 500 nM st-choI filaments inside GUVs at varying chol-DNA to st ratios. **g** Confocal images of deformed GUVs containing 1  $\mu\text{M}$  st-choI filaments at an osmolarity ratio of  $c_{\text{out}}/c_{\text{in}} = 2$ . Scale bar: 5  $\mu\text{m}$ . **h** Circularity of deflated ( $c_{\text{out}}/c_{\text{in}} = 2$ ) and undeflated ( $c_{\text{out}}/c_{\text{in}} = 1$ ) GUVs containing 1  $\mu\text{M}$  st-choI filaments ( $n = 4$  and  $n = 7$ , respectively, mean  $\pm$  SD,  $p = 0.008$ ).

disassembly, DNA bundles with precise persistence lengths to trigger the formation of ring-like structures and the formation of DNA cortices that can deform GUVs from within. Notably, these are only a few examples of conceivable functions of DNA-based cytoskeletons due to the variety of possible DNA structures. In the future, it will be especially exciting to equip DNA filaments with molecular motors for intracellular cargo transport, force generation and contractility. Moreover, the encapsulation of DNA filaments into GUVs sets a milestone for the reconstitution of any of the other DNA-based components that have already been developed for synthetic cells. It should be straight forward to use the same droplet-stabilized GUV for all of these components, which have rarely been implemented in confinement. All in all, DNA nanotechnology proves to be a versatile tool to build various functional modules for synthetic cells. Their inherent compatibility and the here demonstrated possibility to reconstitute them inside GUVs raise the prospects for a synthetic cell that consists of merely de novo synthesized parts. It will be exiting to witness if fully de novo assembled synthetic cells may even be achieved before their counterparts consisting of biological building blocks.

## Experimental Section

### DNA Tile Design and Assembly

DNA filament sequences were adapted from Rothmund et al.<sup>15</sup> The individual DNA oligomers (5 per tile) were mixed to a final concentration of 5  $\mu\text{M}$  in 10 mM Tris (pH 8), 1 mM EDTA, 12 mM  $\text{MgCl}_2$ , 5 mM NaCl. 67 to 200  $\mu\text{L}$  of the solution were annealed using a thermocycler (Bio-Rad) by heating the solution to 90  $^\circ\text{C}$  and cooling it to 25  $^\circ\text{C}$  in steps of 0.5  $^\circ\text{C}$  for 4.5 h. The assembled DNA filaments were stored at 4  $^\circ\text{C}$  and used within a week after annealing. The DNA strands were

either purchased from Integrated DNA Technologies or Biomers (purification: standard desalting for unmodified DNA oligomers, HPLC for DNA oligomers with modifications). All DNA sequences are listed in Supporting Tables S1-S3.

### **Confocal Fluorescence Microscopy**

A confocal laser scanning microscope LSM 880 or LSM 900 (Carl Zeiss AG) was used for confocal microscopy. The pinhole aperture was set to one Airy Unit and the experiments were performed at room temperature. Images of DNA filaments in GUVs in Figure 1 and Video S1 were acquired using the Airyscan mode. The images were acquired using a 20× (Plan-Apochromat 20×/0.8 Air M27, Carl Zeiss AG) or 63× objective (Plan-Apochromat 63×/1.4 Oil DIC M27). Images were analyzed and processed with ImageJ (NIH, brightness and contrast adjusted).

### **Analysis of DNA Filament Length**

Annealed DNA filaments were diluted in 1x phosphate-buffered saline (PBS, Thermo Fisher) and 10 mM MgCl<sub>2</sub> to a final concentration of 5 nM. DNA filaments were imaged in an untreated observation chamber made from two glass coverslides. Filaments attached to the glass slide *via* electrostatic interactions due to the presence of divalent magnesium ions in the buffer. Most of the images were analyzed using the Ridge Detection plugin in ImageJ. The parameters were chosen depending on the contrast of the image in a range from 1.15 to 2 for  $\sigma$ , 0 to 5 for the lower threshold and from 26 to 28 for the upper threshold. Some long filaments were manually analyzed using the ImageJ plugin FilamentJ.

### **Cryo Electron Microscopy**

Samples were prepared for cryo-EM by applying 5  $\mu$ L of sample solution (1x PBS, 10 mM MgCl<sub>2</sub>, 1  $\mu$ M DNA filaments) onto a glow-discharged 300 mesh Quantifoil holey carbon-coated R3.5/1 grid (Quantifoil Micro Tools GmbH, Großlöbichau). The grid was blotted for 3 s and plunge-frozen in liquid ethane using a Vitrobot Mark IV (FEI NanoPort, Eindhoven, The Netherlands)

at 100 % humidity and stored under liquid nitrogen. Cryo-EM specimen grids were imaged on a FEI Tecnai G2 T20 twin transmission electron microscope (FEI NanoPort, Eindhoven, The Netherlands) operated at 200 kV. Electron micrographs were recorded with an FEI Eagle 4k HS, 200 kV CCD camera with a total dose of  $\approx 40$  electrons/ $\text{\AA}^2$ . Images were acquired at 50000x nominal magnification.

### **Transmission Electron Microscopy**

For negative staining, 5  $\mu\text{L}$  of DNA filament-containing solution (1x PBS, 10 mM  $\text{MgCl}_2$ , 1  $\mu\text{M}$  DNA filaments, 20 mg/ml dextran or 0.4 wt% MC) 0.5 % PFA was applied onto a glow-discharged 100 mesh copper grid with carbon-coated Formvar (Plano GmbH, Wetzlar, Germany) and removed after 2 min by gentle blotting from one side with filter paper. The grid was rinsed with 3 drops of water, blotted again, and treated with 10  $\mu\text{L}$  of 0.5 % (w/v) uranyl acetate solution for 20 s. After removing the staining solution thoroughly by blotting with filter paper, the grid was air dried and were imaged on a FEI Tecnai G2 T20 twin transmission electron microscope (FEI NanoPort, Eindhoven, The Netherlands) operated at 200 kV. Electron micrographs were acquired with an FEI Eagle 4k HS, 200 kV CCD camera at 20000x nominal magnification.

### **Preparation of Small Unilamellar Vesicles**

Lipids were stored in chloroform at  $-20$  °C and used without further purification. Small unilamellar vesicles (SUVs) were formed by mixing the chloroform-dissolved lipids (69 % 1,2-dioleoyl-sn-glycero-3-phosphocholine (DOPC, Avanti Polar Lipids), 30 % 1,2-dioleoyl-sn-glycero-3-phospho-(1'-rac-glycerol) (sodium salt, DOPG, Avanti Polar Lipids) and 1 % Atto488-1,2-dioleoyl-sn-glycero-3-phosphoethanolamine (Atto488-DOPE, Atto TEC)) in a glass vial. The lipid solution was dried under a stream of nitrogen gas. To remove traces of solvent, the vial was kept under vacuum in a desiccator for at least 20 min. Lipids were resuspended in 10 mM Tris (pH 8) and 1 mM EDTA at a final lipid concentration of 2.5 mM. The solution was vortexed for 10 min to trigger vesicle formation. Subsequently, vesicles were extruded to form homogeneous SUVs with eleven passages

through a polycarbonate filter with a pore size of 50 nm (Avanti Polar Lipids, Inc.). SUVs were stored at 4 °C for up to a week or used immediately for GUV formation.

### **Preparation of Giant Unilamellar Vesicles**

Giant unilamellar vesicles (GUVs) were formed using the droplet-stabilized GUV formation method.<sup>20</sup> Briefly, 1.25 mM SUVs, 5  $\mu$ M DNA filaments (if not stated otherwise), 10 mM MgCl<sub>2</sub> and phosphate buffered saline (PBS consisting of 137 mM NaCl, 2.7 mM KCl, 10 mM Na<sub>2</sub>HPO<sub>4</sub> and 1.8 mM KH<sub>2</sub>PO<sub>4</sub>) were mixed together. The aqueous mix was layered on top of an oil-surfactant mix containing 1.4 wt% perfluoropolyether–polyethylene glycol (PFPE–PEG) fluorosurfactants (Ran Biotechnologies) and 10.5 mM PFPE–carboxylic acid (Krytox, MW, 7000–7500 g/mol, DuPont) in a microtube (Eppendorf). The ratio in between aqueous and oil phase was 1:3, generally leading to volumes of 100  $\mu$ L:300  $\mu$ L. Droplet-stabilized GUVs were generated by shaking the microtube vigorously by hand. The water-in-oil emulsion droplets were left at room temperature for 1–2h. Within this incubation period, the SUVs fused at the droplet periphery to create a spherical supported lipid bilayer, termed droplet-stabilized GUV. Afterwards, the oil phase was removed and 100  $\mu$ L of 1x PBS was added on top of the emulsion droplets. The droplet-stabilized GUV was destabilized by addition of 100  $\mu$ L of perfluoro-1-octanol (PFO, Sigma-Aldrich) to release freestanding GUVs into the PBS. GUVs were stored for up to two days at 6 °C. GUVs were imaged in a custom-built observation chamber that was coated with 2 mg/ml bovine serum albumin (Sigma Aldrich) for 15 min to prevent fusion of the GUVs with the glass coverslide. Additionally, DNA filaments in the outer aqueous solution due to an imperfect release were disassembled due to the absence of MgCl<sub>2</sub> in the release buffer and the addition of 4  $\mu$ M of an invader strand (Supporting Table 3) that leads to filament disassembly by a toehold-mediated strand displacement reaction.

### **Light-Mediated Disassembly of DNA Filaments**

Light-mediated disassembly was achieved by incorporating two azobenzene modifications at the sticky overhangs of the S4 strand (Supporting Table 3), positioned 2 bases before the 3' and 5' ends,

respectively. This breaks up the sticky end sequence into two segments with 2 or 3 bases each, which renders them able to hybridize in the presence of trans-azobenzene and instable with cis-azobenzene. GUVs with azobenzene-modified DNA filaments were formed as before. Disassembly was achieved by illumination of a GUV with a mercury lamp using a DAPI filter set (excitation: 365 nm/bandwidth: 10) for 15 s. Subsequently, filaments reassembled within 30 min before they were illuminated again with a mercury lamp (HBO 100). The confocal images of the DNA filaments were thresholded in ImageJ using Otsu's method and their overall porosity was analyzed. Note that the porosity indicates the degree of polymerization of the DNA filaments. The porosity values were corrected for bleaching by determining the slope of linear fits  $x_{slope}$  for the porosity of disassembled states. This leads to the corrected values:  $p_{corr} = p \cdot (1 + x_{slope}t)$ .

### **Bundling of DNA Filaments**

Bundling of DNA filaments was induced by addition of molecular crowders like dextran (molecular weight 6, 35 and 500 kDa, Carl Roth), polyethylene glycol (PEG, molecular weight 8 kDa, Carl Roth) or methylcellulose (molecular weight: 500 kDa, Carl Roth). The bundling agent was mixed with DNA filaments directly before GUV formation. For TEM and confocal imaging of DNA bundles in bulk, DNA filaments were incubated for 5 min with the respective bundling agent.

### **Determination of the DNA Filament's Persistence Length**

For the persistence length analysis, DNA filaments with a length around the mean value of the filament length of each condition were considered. DNA filaments were traced and filament coordinates were extracted using an automated tracing algorithm.<sup>32</sup> The coordinates had a unit spacing of  $\Delta s = 4 \text{ pixels} = 0.62 \mu\text{m}$ . Subsequently, we calculated the average tangent correlation  $\langle \hat{t}(x) \cdot \hat{t}(x + \Delta x) \rangle$  for each filament using a custom-written Python script. We then averaged the tangent correlation for each distance between the tangents  $\Delta x$  from all considered filaments. The resulting values were used to fit a function of the form  $\langle \hat{t}(x) \cdot \hat{t}(x + \Delta x) \rangle = e^{-\Delta x/2P}$  from  $\Delta x = 2$  to  $\Delta x = 8$  to obtain the filament's persistence length  $P$ . The principle of this persistence length

analysis is based on previous work with DNA filaments.<sup>33</sup>

### **Linking of DNA Filaments to Supported Lipid Bilayers**

SUVs were diluted in 1x PBS containing 10 mM MgCl<sub>2</sub> to a final lipid concentration of 1 mM and flushed into an untreated observation chamber. The chamber was sealed and the SUVs were left to fuse with the coverslide for 1 h. The chamber was then opened up and flushed twice with deionized water to remove remaining SUVs that did not fuse to form a supported lipid bilayer (SLB). Subsequently, 20 μL of 1x PBS and 2 μM of chol-DNA (chol-link, Supporting Table 3) were flushed in and incubated with the SLB for 10 min. Finally, 5 nM Cy3-labeled DNA filaments were added in 1x PBS and 10 mM MgCl<sub>2</sub>. Note that the single-stranded overhang on the S3 strand is complementary to the chol-link DNA. The chamber was sealed for confocal imaging.

### **DNA-Cortex Formation inside Giant Unilamellar Vesicles**

For DNA cortex formation, we designed a cholesterol-tagged complementary DNA (chol-link) that can hybridize with a single-stranded DNA overhang on the S3 strand (Supporting Table 3). Before GUV formation, SUVs and 2 μM chol-link DNA were incubated for 2 min to bind the DNA filaments to the GUV periphery. The acquired images were analyzed by determining the peripheral intensity of the DNA filaments over the interior DNA filament intensity using a custom written ImageJ macro (available here: <https://doi.org/10.5281/zenodo.4738934>). GUV deformation was achieved by osmotic deflation of the GUVs such that the concentration of ions outside the GUV is increased by a factor of two ( $c/c_0 = 2$ ). After osmotic deflation, the DNA filaments inside the GUVs were reannealed in the thermocycler (BioRad).

### **Fluorescence Recovery after Photobleaching**

For fluorescence recovery after photobleaching (FRAP) experiments a circular region of interest (ROI) with a diameter of 10 μm at the top confocal plane of the GUV was chosen. By choosing the top of the GUV, we reduce the risk of measuring artefacts due to the interaction with the

BSA-coated glass slide at the bottom. Three images were acquired before the ROI was illuminated for 100 iterations at the 100 % laser power with 488 nm (for the Atto488-labeled lipids) or 561 nm (for Cy3-labeled DNA tiles and filaments). Afterwards, the ROI was imaged for up to 60 s to track the recovery of the fluorescence. To quantify the diffusion coefficient, we used a custom-written Matlab (R2019a) script.<sup>22</sup>

### **Statistical Analysis**

All the experimental data were reported as mean  $\pm$  SD from n experiments, filaments or GUVs. The respective value for n is stated in the corresponding figure captions. All experiments were repeated at least twice. To analyze the significance of the data, a Student's t-test with Welch's correction was performed using Prism GraphPad (Version 9.1.2) and p-values correspond to \*\*\*\*\*:  $p \leq 0.0001$ , \*\*\*:  $p \leq 0.001$ , \*\*:  $p \leq 0.01$ , \*:  $p \leq 0.05$  and ns:  $p \geq 0.05$ .

### **Acknowledgement**

The authors thank Christoph Karfusehr and Kristina Ganzinger for helpful discussions. K.G. received funding from the Deutsche Forschungsgemeinschaft (DFG, German Research Foundation) under Germany's Excellence Strategy *via* the Excellence Cluster 3D Matter Made to Order (EXC-2082/1 - 390761711) and the Max Planck Society. K.J. thanks the Carl Zeiss and the Joachim Herz Foundation for financial support. N.L. was supported by the European Research Council (ERC Dynamic Nano). The Max Planck Society is acknowledged for its general support.

### **Supporting Information Available**

Supporting Information is available containing

- 19 Figures with additional experimental results
- 3 Tables containing the used DNA sequences



- and 7 Supporting Movies.

## References

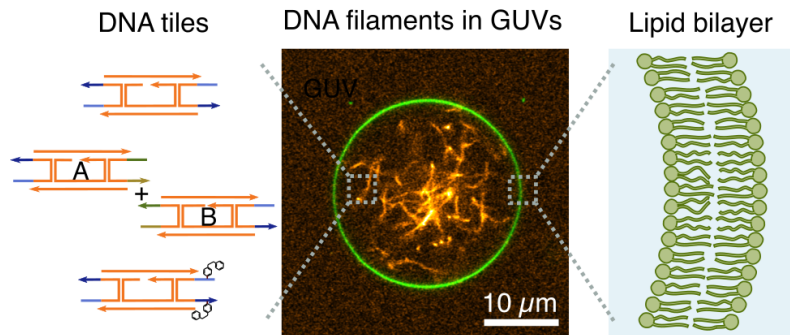
- (1) Litschel, T.; Kelley, C. F.; Holz, D.; Koudehi, M. A.; Vogel, S. K.; Burbaum, L.; Mizuno, N.; Vavylonis, D.; Schwille, P. Reconstitution of contractile actomyosin rings in vesicles. *Nature Communications* **2021**, *12*.
- (2) Maan, R.; Loiseau, E.; Bausch, A. R. Adhesion of Active Cytoskeletal Vesicles. *Biophysical Journal* **2018**, *115*, 2395–2402.
- (3) Lee, K. Y.; Park, S.-J.; Lee, K. A.; Kim, S.-H.; Kim, H.; Meroz, Y.; Mahadevan, L.; Jung, K.-H.; Ahn, T. K.; Parker, K. K.; Shin, K. Photosynthetic artificial organelles sustain and control ATP-dependent reactions in a protocellular system. *Nature Biotechnology* **2018**, *36*, 530–535.
- (4) Vutukuri, H. R.; Hoore, M.; Abaurrea-Velasco, C.; van Buren, L.; Dutto, A.; Auth, T.; Fedosov, D. A.; Gompper, G.; Vermant, J. Active particles induce large shape deformations in giant lipid vesicles. *Nature* **2020**, *586*, 52–56.
- (5) Loiseau, E.; Schneider, J. A. M.; Keber, F. C.; Pelzl, C.; Massiera, G.; Salbreux, G.; Bausch, A. R. Shape remodeling and blebbing of active cytoskeletal vesicles. *Science Advances* **2016**, *2*, e1500465.
- (6) Langecker, M.; Arnaut, V.; Martin, T. G.; List, J.; Renner, S.; Mayer, M.; Dietz, H.; Simmel, F. C. Synthetic Lipid Membrane Channels Formed by Designed DNA Nanostructures. *Science* **2012**, *338*, 932–936.
- (7) Göpfrich, K.; Li, C.-Y.; Mames, I.; Bhamidimarri, S. P.; Ricci, M.; Yoo, J.; Mames, A.; Ohmann, A.; Winterhalter, M.; Stulz, E.; Aksimentiev, A.; Keyser, U. F. Ion Channels Made from a Single Membrane-Spanning DNA Duplex. *Nano Letters* **2016**, *16*, 4665–4669.

- (8) Fragasso, A.; Franceschi, N. D.; Stömmer, P.; van der Sluis, E. O.; Dietz, H.; Dekker, C. Reconstitution of Ultrawide DNA Origami Pores in Liposomes for Transmembrane Transport of Macromolecules. *ACS Nano* **2021**,
- (9) Burns, J. R.; Stulz, E.; Howorka, S. Self-Assembled DNA Nanopores That Span Lipid Bilayers. *Nano Letters* **2013**, *13*, 2351–2356.
- (10) Wickham, S. F. J.; Bath, J.; Katsuda, Y.; Endo, M.; Hidaka, K.; Sugiyama, H.; Turberfield, A. J. A DNA-based molecular motor that can navigate a network of tracks. *Nature Nanotechnology* **2012**, *7*, 169–173.
- (11) Cha, T.-G.; Pan, J.; Chen, H.; Salgado, J.; Li, X.; Mao, C.; Choi, J. H. A synthetic DNA motor that transports nanoparticles along carbon nanotubes. *Nature Nanotechnology* **2013**, *9*, 39–43.
- (12) Urban, M. J.; Both, S.; Zhou, C.; Kuzyk, A.; Lindfors, K.; Weiss, T.; Liu, N. Gold nanocrystal-mediated sliding of doublet DNA origami filaments. *Nature Communications* **2018**, *9*.
- (13) Kurokawa, C.; Fujiwara, K.; Morita, M.; Kawamata, I.; Kawagishi, Y.; Sakai, A.; Murayama, Y.; ichiro M. Nomura, S.; Murata, S.; Takinoue, M.; Yanagisawa, M. DNA cytoskeleton for stabilizing artificial cells. *Proceedings of the National Academy of Sciences* **2017**, *114*, 7228–7233.
- (14) Czogalla, A.; Kauert, D. J.; Franquelim, H. G.; Uzunova, V.; Zhang, Y.; Seidel, R.; Schwille, P. Amphipathic DNA Origami Nanoparticles to Scaffold and Deform Lipid Membrane Vesicles. *Angewandte Chemie International Edition* **2015**, *54*, 6501–6505.
- (15) Rothmund, P. W. K.; Ekani-Nkodo, A.; Papadakis, N.; Kumar, A.; Fygenson, D. K.; Winfree, E. Design and Characterization of Programmable DNA Nanotubes. *Journal of the American Chemical Society* **2004**, *126*, 16344–16352.
- (16) Green, L. N.; Subramanian, H. K. K.; Mardanlou, V.; Kim, J.; Hariadi, R. F.; Franco, E.

- Autonomous dynamic control of DNA nanostructure self-assembly. *Nature Chemistry* **2019**, *11*, 510–520.
- (17) Mohammed, A. M.; Šulc, P.; Zenk, J.; Schulman, R. Self-assembling DNA nanotubes to connect molecular landmarks. *Nature Nanotechnology* **2016**, *12*, 312–316.
- (18) Mohammed, A. M.; Schulman, R. Directing Self-Assembly of DNA Nanotubes Using Programmable Seeds. *Nano Letters* **2013**, *13*, 4006–4013.
- (19) Agarwal, S.; Klocke, M. A.; Pungchai, P. E.; Franco, E. Dynamic self-assembly of compartmentalized DNA nanotubes. *Nature Communications* **2021**, *12*.
- (20) Göpfrich, K.; Haller, B.; Staufer, O.; Dreher, Y.; Mersdorf, U.; Platzman, I.; Spatz, J. P. One-Pot Assembly of Complex Giant Unilamellar Vesicle-Based Synthetic Cells. *ACS Synthetic Biology* **2019**, *8*, 937–947.
- (21) Haller, B.; Göpfrich, K.; Schröter, M.; Janiesch, J.-W.; Platzman, I.; Spatz, J. P. Charge-controlled microfluidic formation of lipid-based single- and multicompartiment systems. *Lab on a Chip* **2018**, *18*, 2665–2674.
- (22) Weiss, M. et al. Sequential bottom-up assembly of mechanically stabilized synthetic cells by microfluidics. *Nature Materials* **2017**, *17*, 89–96.
- (23) Kuzyk, A.; Yang, Y.; Duan, X.; Stoll, S.; Govorov, A. O.; Sugiyama, H.; Endo, M.; Liu, N. A light-driven three-dimensional plasmonic nanosystem that translates molecular motion into reversible chiroptical function. *Nature Communications* **2016**, *7*.
- (24) Dreher, Y.; Jahnke, K.; Schröter, M.; Göpfrich, K. Light-Triggered Cargo Loading and Division of DNA-Containing Giant Unilamellar Lipid Vesicles. *Nano Letters* **2021**,
- (25) Miyazaki, M.; Chiba, M.; Eguchi, H.; Ohki, T.; Ishiwata, S. Cell-sized spherical confinement induces the spontaneous formation of contractile actomyosin rings in vitro. *Nature Cell Biology* **2015**, *17*, 480–489.

- (26) Köhler, S.; Lieleg, O.; Bausch, A. R. Rheological Characterization of the Bundling Transition in F-Actin Solutions Induced by Methylcellulose. *PLoS ONE* **2008**, *3*, e2736.
- (27) Fletcher, D. A.; Mullins, R. D. Cell mechanics and the cytoskeleton. *Nature* **2010**, *463*, 485–492.
- (28) Mangione, M. C.; Gould, K. L. Molecular form and function of the cytokinetic ring. *Journal of Cell Science* **2019**, *132*.
- (29) Jahnke, K.; Ritzmann, N.; Fichtler, J.; Nitschke, A.; Dreher, Y.; Abele, T.; Hofhaus, G.; Platzman, I.; Schröder, R. R.; Müller, D. J.; Spatz, J. P.; Göpfrich, K. Proton gradients from light-harvesting *E. coli* control DNA assemblies for synthetic cells. *Nature Communications* **2021**, *12*.
- (30) Franquelim, H. G.; Khmelinskaia, A.; Sobczak, J.-P.; Dietz, H.; Schwille, P. Membrane sculpting by curved DNA origami scaffolds. *Nature Communications* **2018**, *9*.
- (31) Franquelim, H. G.; Dietz, H.; Schwille, P. Reversible membrane deformations by straight DNA origami filaments. *Soft Matter* **2021**, *17*, 276–287.
- (32) Wiggins, P. A.; van der Heijden, T.; Moreno-Herrero, F.; Spakowitz, A.; Phillips, R.; Widom, J.; Dekker, C.; Nelson, P. C. High flexibility of DNA on short length scales probed by atomic force microscopy. *Nature Nanotechnology* **2006**, *1*, 137–141.
- (33) Schiffels, D.; Liedl, T.; Fygenson, D. K. Nanoscale Structure and Microscale Stiffness of DNA Nanotubes. *ACS Nano* **2013**, *7*, 6700–6710.

## Table of Contents Graphic



### 3.11 Publication 8: Division and regrowth of phase-separated giant unilamellar vesicles

The challenge of dividing synthetic cells in order to produce offspring is one of the most important for synthetic biology [106]. As we have seen in the previous publication, the formation of ring-like DNA bundles might in future work be employed for the division of GUVs e.g. upon bundle contractility. However, the generation of a contractile DNA-based system and the related necessary force generation and processivity still remain an unachieved, yet desirable, goal. Therefore, other ways to achieve GUV division are required. In the following work, we establish a mechanism that does not rely on cytoskeletons for the reliable division of phase-separated GUVs along the phase boundary and their regrowth. However, the incorporation of cytoskeletal structures that are coupled to the division process will be an exciting challenge for future work.

After observing the division process of phase-separated GUVs, we explore the mechanism in more detail and find that it relies on the deflation i.e. reduction of the volume to surface ration of the GUV and the line tension across the phase boundary, which needs to be sufficient to lead to neck fission. Moreover, we expand the division mechanism beyond the simple addition of solutions for deflation but also establish an enzyme-mediated mechanism that relies on the increase of the osmolarity by cutting carbohydrates into its monomers and a second approach that makes use of an osmolarity increase via light-induced release of caged compounds. A major problem that occurs is, however, that the GUVs only contain one membrane phase and are not phase-separated anymore. The division process can therefore only be performed once and not repeatedly. To overcome this drawback, we developed the regrowth of GUVs via fusion of SUVs with the opposite membrane phase to restore phase-separation within GUVs. The fusion of SUVs can thereby be initiated via calcium which induces the electrostatic attraction of SUVs to the GUV membrane or via linking DNA strands that form in a zipper arrangement and therefore bring the SUVs in close proximity to the GUVs ultimately leading to fusion.

As an overall picture, we can present a sustainable division mechanism of GUVs. The GUVs can now be filled with engineerable subunits in order to build complex synthetic cells with programmed multifunctionality.



# Division and Regrowth of Phase-Separated Giant Unilamellar Vesicles\*\*

Yannik Dreher<sup>+</sup>, Kevin Jahnke<sup>+</sup>, Elizaveta Bobkova, Joachim P. Spatz, and Kerstin Göpfrich\*

**Abstract:** Success in the bottom-up assembly of synthetic cells will depend on strategies for the division of protocellular compartments. Here, we describe the controlled division of phase-separated giant unilamellar lipid vesicles (GUVs). We derive an analytical model based on the vesicle geometry, which makes four quantitative predictions that we verify experimentally. We find that the osmolarity ratio required for division is  $\sqrt{2}$ , independent of the GUV size, while asymmetric division happens at lower osmolarity ratios. Remarkably, we show that a suitable osmolarity change can be triggered by water evaporation, enzymatic decomposition of sucrose or light-triggered uncaging of CMNB-fluorescein. The latter provides full spatiotemporal control, such that a target GUV undergoes division whereas the surrounding GUVs remain unaffected. Finally, we grow phase-separated vesicles from single-phased vesicles by targeted fusion of the opposite lipid type with programmable DNA tags to enable subsequent division cycles.

## Introduction

“*Omni cellulae e cellulae.*” From the point of view of modern science, Raspail’s realization from 1825,<sup>[1]</sup> popularized by Virchow,<sup>[2]</sup> may state the obvious: Every living cell found on Earth today originates from a preexisting living cell. Bottom-up synthetic biology, however, is challenging this paradigm with the vision to create a synthetic cell from scratch.<sup>[3,4]</sup> Success unquestionably entails that the synthetic cells must have the capacity to produce offspring, making the implementation of synthetic cell division an exciting goal.<sup>[5–8]</sup> Over the course of evolution, living cells have developed a sophisticated machinery to divide their compartments in a highly regulated manner. The reconstitution of a minimal set of cellular components seems to be a plausible albeit

challenging route towards synthetic cell division.<sup>[9–11]</sup> These challenges leave room for creative approaches, seeking solutions beyond the mimicry of today’s biological cells. One exciting strategy is to assemble a division machinery de novo, by designing active, not necessarily protein-based nanomachines. DNA origami structures have been used to shape and remodel lipid vesicles,<sup>[12–14]</sup> although active force-generating motors remain a distant goal. A shortcut towards synthetic cell division is the non-autonomous mechanical division of liposomes,<sup>[15]</sup> which may jump-start exciting directions. The exploitation of physicochemical mechanisms, on the other hand, could lead to autonomous division. Noteworthy theoretical work describes the shape transformations of single-phase<sup>[16–18]</sup> as well as phase-separated liposomes<sup>[19–21]</sup> depending on the surface-to-volume ratio. Two vesicles connected with a tight neck have been theoretically predicted<sup>[20]</sup> and can readily be observed in experiments. A remarkable recent report triggered shape transformations of lipid vesicles by an internal enzymatic reaction, but neck fission did not occur.<sup>[22]</sup> There are few experimental reports describing the complete dissociation of small buds from a parent vesicle.<sup>[23,24]</sup> Division into more equally sized compartments has once been reported as an occasional observation<sup>[25]</sup> or it relied on multilamellar vesicles<sup>[26]</sup> or liquid–liquid phase separation.<sup>[27]</sup> Moreover, multilamellar fatty acid vesicle systems have been shown to deform and sometimes divide<sup>[28]</sup> and recently, division was shown as a result of spontaneous curvature.<sup>[29]</sup> However, we are still missing a well-controlled division mechanism where designated vesicles divide with a success rate close to 100%, combined with a suitable growth mechanism. This would be an important step for the field of bottom-up synthetic biology since it could provide the basis for the evolution of synthetic cells.

[\*] Y. Dreher,<sup>[†]</sup> K. Jahnke,<sup>[†]</sup> E. Bobkova, Dr. K. Göpfrich  
Biophysical Engineering Group,  
Max Planck Institute for Medical Research  
Jahnstraße 29, 69120 Heidelberg (Germany)  
and  
Department of Physics and Astronomy, Heidelberg University  
69120 Heidelberg (Germany)  
E-mail: kerstin.goepfrich@mr.mpg.de  
Prof. J. P. Spatz  
Department of Cellular Biophysics,  
Max Planck Institute for Medical Research  
Jahnstraße 29, 69120 Heidelberg (Germany)  
and  
Institute for Molecular Systems Engineering (IMSE),  
Heidelberg University  
Im Neuenheimer Feld 225, 69120 Heidelberg (Germany)

and  
Max Planck School Matter to Life  
Jahnstraße 29, 69120 Heidelberg (Germany)

[†] These authors contributed equally to this work.

[\*\*] A previous version of this manuscript has been deposited on a preprint server (<https://doi.org/10.1101/2019.12.30.881557>).

Supporting information and the ORCID identification number(s) for the author(s) of this article can be found under: <https://doi.org/10.1002/anie.202014174>.

© 2020 The Authors. Angewandte Chemie International Edition published by Wiley-VCH GmbH. This is an open access article under the terms of the Creative Commons Attribution License, which permits use, distribution and reproduction in any medium, provided the original work is properly cited.

Here, we experimentally demonstrate full spatiotemporal control over the division of phase-separated GUVs with an unprecedented success rate. To predict the process quantitatively, we show that it is sufficient to look at the vesicle geometry. We describe the shape transformations of phase-separated vesicles without fitting parameters, while previous theoretical work relies on membrane-specific parameters.<sup>[19–21]</sup> From these geometrical considerations, we can extract the precise conditions required for division and thereby provide a reproducible and highly controlled division mechanism. Notably, we demonstrate that the division of GUVs can be regulated by a metabolic reaction or triggered locally by light. We further implement vesicle fusion via programmable DNA tags as a mechanism to regrow phase-separated vesicles from single-phased ones to enable subsequent division cycles. While our synthetic division mechanism distinctively differs from that of nowadays living cells, our results prompt to ask whether similar mechanisms may have sustained cell division at the onset of life<sup>[30,31]</sup> or if remnants thereof may still play a role for the generation of intracellular vesicles or to support certain division processes of today's cells.<sup>[32–34]</sup>

## Results and Discussion

### Division of Phase-Separated GUVs Triggered by Metabolic Decomposition

GUVs—that is, micron-sized vesicles enclosed by a single lipid bilayer—are the most commonly used compartment type for the assembly of synthetic cells.<sup>[4]</sup> To realize a controllable and efficient mechanism for their division, we propose a strategy that is based on three steps: Step 1) Define the plane of division; Step 2) Increase the surface-to-volume ratio, and Step 3) Enable neck fission to allow for the formation of two smaller second-generation compartments from a single large compartment. To realize Step 1, we choose lipid phase separation to define the plane of division as the interface of the liquid-disordered (ld, orange) and the liquid-ordered (lo, green) phase as illustrated in Figure 1 a. Hence, an increase in the surface-to-volume ratio (Step 2) requires a reduction of the GUV's inner volume. To this end, we exploit osmosis. An increase of the osmolarity outside the GUVs, that is, a higher concentration of solutes in the outer aqueous solution, causes water efflux through the GUV membrane<sup>[35]</sup> as illustrated in Figure 1 b. Note that the number of lipids in the membrane, that is, the surface area of the GUV, remains constant during this process (Figure S1). There is no lipid addition. As described in previous theoretical work,<sup>[20]</sup> the GUV deforms to minimize the energy associated with the line tension at the phase boundary until a bud is connected to the first-generation vesicle by a tight neck. A common assumption is that the energy barrier for neck scission (i.e. the final pinching of the second-generation vesicle) is too large to enable vesicle fission without coat proteins. However, while pinching of the lipid constriction comes with an energy cost for opening up the bilayer structure, it also removes the phase boundary.<sup>[21,36]</sup> Therefore,

#### a Define division plane: Phase separation



#### b Increase surface-to-volume-ratio: Osmosis

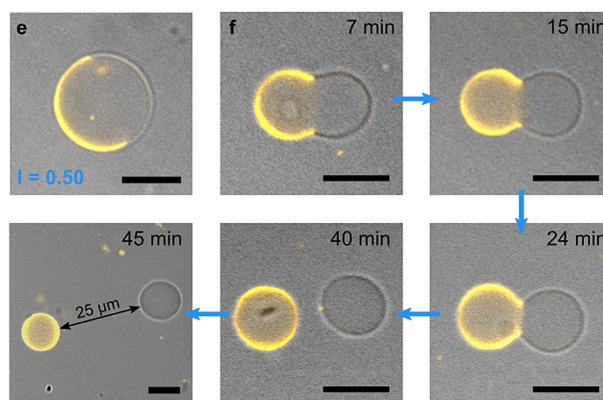
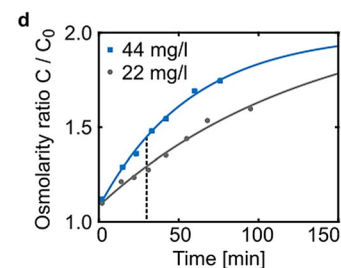
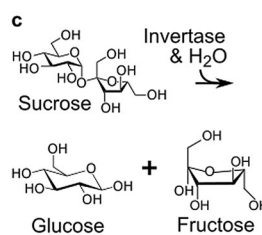
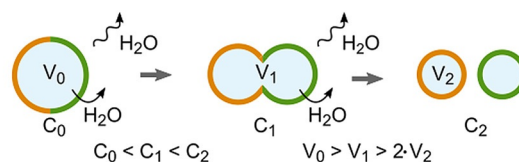


**Figure 1.** Division of phase-separated GUVs. Schematic illustration of the division mechanism relying on a) phase separation of the GUVs and b) osmosis.  $C_0$ ,  $C_1$ , and  $C_2$  denote the osmolarity outside of the GUVs and  $V_1$ ,  $V_2$ , and  $V_3$  describe their volume at different time points. c) Chemical reaction pathway of sucrose degradation catalyzed by the enzyme invertase. d) Osmolarity ratio  $C/C_0$  over time for GUV-containing solutions composed of 300 mM sucrose, 10 mM HEPES (pH 7.4) and 44 mg L<sup>-1</sup> (blue) or 22 mg L<sup>-1</sup> invertase (gray). Error bars are too small to be visible. The data was fitted with limited growth fits (solid lines). The dotted black line indicates the time point at which division occurs (see f). e) Overlay of brightfield and confocal image of a phase-separated GUV with equally large hemispheres (Lipid Mix 1, Table S2, ld phase labeled with LissRhod PE (orange),  $\lambda_{ex}$  = 561 nm). f) Confocal fluorescence time series depicting the division process in the presence of 44 mg L<sup>-1</sup> invertase. The vesicles are fully separated and quickly diffuse apart after division (see 45 min time point). Scale bars: 10  $\mu$ m.

we postulate that complete division could be favorable if the line tension is high enough (Step 3). To implement the proposed division mechanism experimentally, we first need a controlled mechanism to increase the outer osmolarity of the solution. Metabolic processes, that is, the decomposition of molecules through enzymes, inevitably lead to an osmolarity increase. We thus set out to metabolize the sugar



solution in which GUVs are often immersed. For this purpose, we make use of the enzyme invertase. Extracellular invertase is secreted by yeast as a form of cell–cell cooperation to decompose sucrose into fructose and glucose (Figure 1 c).<sup>[37]</sup> We performed osmometer measurements to test if extracellular invertase in a solution of phase-separated GUVs can produce an increase of the osmolarity ratio  $C/C_0$  as required for division. Indeed we find that the osmolarity of the initially 300 mM sucrose solution increases significantly over time (see Figure 1 d). The rate of increase depends on the enzyme concentration. In the presence of 44 mg L<sup>-1</sup> invertase, the initial osmolarity almost doubles over the course of 150 minutes.

Note that we did not optimize the conditions for invertase activity but chose conditions compatible with the proposed mechanism for GUV division. Phase-separated GUVs with two distinct hemispheres (Figure 1 e), were successfully electroformed using a lipid mixture consisting of DOPC, cholesterol, DPPC, CL and LissRhod PE (DOPC (18:1 1,2-dioleoyl-sn-glycero-3-phosphocholine), DPPC (16:0 1,2-dipalmitoyl-sn-glycero-3-phosphocholine), CL (Cardiolipin (Heart, Bovine)), LissRhod PE (18:1 1,2-dipalmitoyl-sn-glycero-3-phosphoethanolamine-N-(lissamine rhodamine B sulfonyl)); Tables S1 and S2, Mix 1).<sup>[38]</sup> LissRhod PE labels the ld phase (orange). To test the proposed mechanism for division, we add 44 mg L<sup>-1</sup> invertase to the GUV-containing sucrose solution. Figure 1 f shows a time series taken over the course of 45 minutes (see Figure S2 for an overview image with multiple dividing vesicles). We observe the formation of a constriction at the interface of the two phases, eventually leading to complete division. As visible in the final timestep, the second-generation vesicles diffuse apart as soon as the division is completed, proving that complete neck scission occurred. Control experiments confirm that neither phase separation, nor osmosis alone are sufficient to promote GUV

division (Figure S3). To appreciate the continuous deformation process leading to division, Video S1 is recommended. To probe the versatility, we tested twelve additional lipid mixtures and obtain GUVs with two distinct hemispheres from mixtures containing positively, neutral, and negatively charged lipids. Interestingly, we find that the choice of fluorophore attached to the lipid affects the phase separation behaviour (Figure S4, Tables S2–S4). Division was also obtained for GUVs composed from a distinctively different lipid mixture (Table S2, Mix 2, Video S2). We have thus achieved the division of phase-separated GUVs by increasing the outer osmolarity with an enzymatic reaction. It is interesting to consider that phase separation may have come into play when phospholipids emerged.<sup>[30,31]</sup> By regulating the transcription of a metabolic enzyme like invertase, primitive cells could, in principle, maintain a high level of control over their division without a sophisticated division machinery.

### Theoretical Prediction of the Division Process

To gain control over the process, we set out to predict the osmolarity ratio required to achieve division of a phase-separated GUV. For this purpose, we develop an analytical model describing the geometrical GUV shape throughout the deformation process as two spherical caps with a base radius  $s_0$  for the initially spherical GUV and  $s < s_0$  for the deformed GUV. One of them represents the ld phase with a surface area  $A_{ld}$  and the other one the lo phase with a surface area  $A_{lo}$ , respectively. The relevant geometrical properties (Figure 2 a) can be extracted from confocal images. This representation provides a good approximation of our experimentally observed GUV shapes including a kink at the phase boundary compared to the dumbbell shape expected for single-phased GUVs. We assume that the total area  $A_{tot}$  remains constant

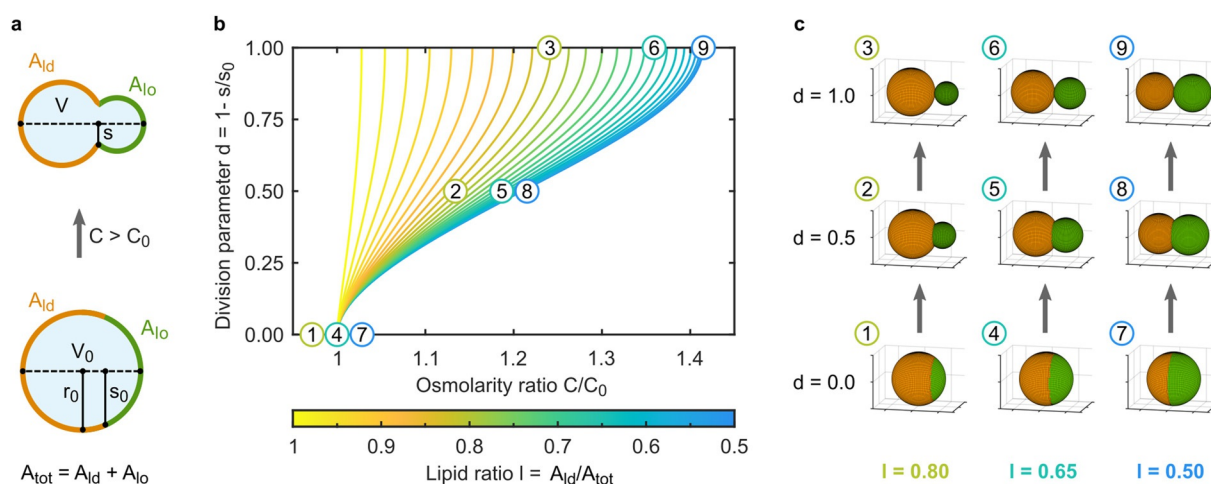


**Figure 2.** Theoretical predictions for the division process of phase-separated GUVs based on an increase in the osmolarity ratio. a) Schematic illustration describing the relevant geometrical properties of a deformed GUV (top) and its initially spherical state (bottom).  $A_{ld}$  and  $A_{lo}$  are the surface areas of the spherical caps representing the two phases.  $s_0$  is the radius of the base of the caps,  $V_0$  the volume and  $r_0$  the radius of the initially spherical GUV.  $s$  is the reduced radius of the base of the caps and  $V$  the reduced volume of the deformed GUV. b) Theoretical prediction of the division parameter  $d$  as a function of the osmolarity ratio  $C/C_0$  for different lipid ratios  $l$ .  $d=0$  corresponds to a spherical GUV,  $d=1$  to a fully divided one. c) Predicted shapes of GUVs with different lipid ratios ( $l=0.80, 0.65, 0.50$ ) at defined points during the division process ( $d=0.0, 0.5, 1.0$ ). The corresponding positions (1–9) are indicated in the plot in (b).

throughout the division process. If the outer osmolarity increases ( $C > C_0$ ), the volume of the GUV will decrease due to water efflux. This process is fast compared to the time scale of the division process<sup>[39]</sup> and therefore assumed to be instantaneous in our model. The equilibrated inner volume is then given by  $V = C/C_0 V_0$ . The resulting excess membrane area allows for deformation of the initially spherical GUV. Deformation minimizes the phase boundary ( $s < s_0$ ) to reduce the energy associated with the line tension.<sup>[20]</sup> To quantify the progression of the division process, we define a division parameter  $d$ :

$$d = 1 - \frac{s}{s_0}. \quad (1)$$

$d$  is 0 for the initial spherical GUV and 1 for a divided GUV. Based on these geometrical considerations, the osmolarity ratio  $C/C_0$  needed to achieve a certain deformation  $d$  for a symmetric GUV ( $A_{id} = A_{io}$ ) can be calculated as

$$C/C_0 = \frac{2}{\sqrt{2 - (1-d)^2((1-d)^2 + 1)}}. \quad (2)$$

The model thus postulates that the osmolarity ratio required for complete division ( $d = 1$ ) is  $C/C_0 = \sqrt{2} \approx 1.41$  (Prediction 1). Since Equation (2) does not depend on the initial radius  $r_0$  of the GUV, the osmolarity ratio required for division is independent of the size of the GUV (Prediction 2). While living cells normally undergo symmetric division, where both second-generation compartments are of similar size, some processes like oocyte maturation rely on asymmetric division.<sup>[40]</sup> To extend our model for asymmetric GUVs with  $A_{id} \neq A_{io}$  we define a lipid ratio parameter  $l = A_{id}/A_{tot} = 1 - A_{io}/A_{tot}$  and hence obtain

$$C/C_0 = \frac{1}{T_1 + T_2}$$

with the terms  $T_1 = \sqrt{1 - (1-d)^2(l-l^2)}(2(1-d)^2(l-l^2) + l)$   
and  $T_2 = \sqrt{(1-l) - (1-d)^2(l-l^2)}(2(1-d)^2(l-l^2) + (1-l))$ .  
(3)

See Note S1 in the Supporting Information for a detailed derivation of the equations.

It follows that GUVs with higher asymmetry should require lower osmolarity ratios for complete division and should hence divide faster (Prediction 3). Figure 2b shows the predicted division parameter  $d$  as a function of the osmolarity ratio  $C/C_0$  for different lipid ratios  $l$ . A GUV with  $l = 0.8$  divides already at an osmolarity ratio of approximately 1.22 (compared to 1.41 for symmetric GUVs with  $l = 0.5$ ). For clarity, Figure 2c displays the predicted shapes of the GUVs corresponding to specific points of the phase space spanned by the division parameter and the osmolarity ratio as indicated in Figure 2b. Finally, any process that provides a sufficient change in the osmolarity ratio should lead to division of phase-separated vesicles, independent of the chemical nature of the process (Prediction 4). Compared to previous models describing the shape transformations of lipid vesicles,<sup>[19-21]</sup> our model merely considers geometric proper-

ties without fitting parameters. Nevertheless, the model yields four predictions, which we will now test experimentally.

### Quantitative Comparison of Experiments and Theoretical Predictions

To test the predictions of our model in a quantitative manner, we first observe symmetric phase-separated GUVs ( $l = 0.5$ ) in solutions with different well-defined osmolarity ratios  $C/C_0$ . It is crucial to immerse the GUVs slowly to avoid lipid tubulation (see Figures S2 and S5). To be able to extract geometrical parameters more precisely from the confocal images, we additionally label the lo phase. For this purpose, we add cholesterol-tagged 6-FAM-labeled DNA to the GUVs, which self-assembles selectively into the lo phase (green) in a  $Mg^{2+}$ -containing buffer (see Figure S6). Note that  $Mg^{2+}$  leads to a significant reduction of the invertase activity in the presence of GUVs (see Figure S7), likely due to electrostatic interactions between the invertase and the GUVs mediated by divalent ions. Therefore, labelling of the lo phase was omitted for experiments involving invertase. Similarly, we find that in the presence of  $Mg^{2+}$  ions, the vesicles remain in close contact after division, again likely due to electrostatic interactions. After soft shaking, they are found in complete isolation (see Figure S8). Figure 3a shows the theoretically predicted shapes for the different osmolarity ratios. The corresponding representative confocal fluorescence images are presented in Figure 3b. Note that the shapes are static since the osmolarity ratio is kept constant, unlike in the case of invertase activity. We extract the geometrical parameters required to calculate the division parameter  $d$  from multiple images. As postulated, we observe division at an osmolarity ratio of approximately  $\sqrt{2}$  (Prediction 1). We find that 90% percent of the GUVs are single-phased ( $n = 200$ ) at this osmolarity ratio, suggesting a remarkably high division rate. To verify the size independence of the division process (Prediction 2), we used the images of the deformed GUVs to calculate the radius  $r_0$  of the initially spherical GUV. The scatter plot of the division parameter  $d$  over  $r_0$  is shown in Figure 3c. As expected, no significant size-dependent deviations from the theoretical value (blue line) can be observed in the size range of GUVs. For vesicles below  $1 \mu m$ , size effects and membrane-specific parameters will likely come into play. As a quantitative comparison of the experimental results with the theoretical prediction [Eq. (2)], we plot the mean division parameter as a function of the osmolarity ratio. Figure 3d shows that the experimental data agrees well with the theoretical prediction. Deviations may occur due to the fact that GUVs are imaged in solution and can hence rotate in the confocal plane. Trapping can lead to lipid tubulation and hinder the division process (see Figure S9). Note that the quantitative understanding of the vesicle shape as a function of the osmolarity ratio allows us to use phase-separated GUVs as precise osmolarity sensors. This could for instance be useful for measuring extracellular osmolarity in cell culture based on conventional microscopy without any additional equipment (conventional osmometer measurements require freezing of the sample).

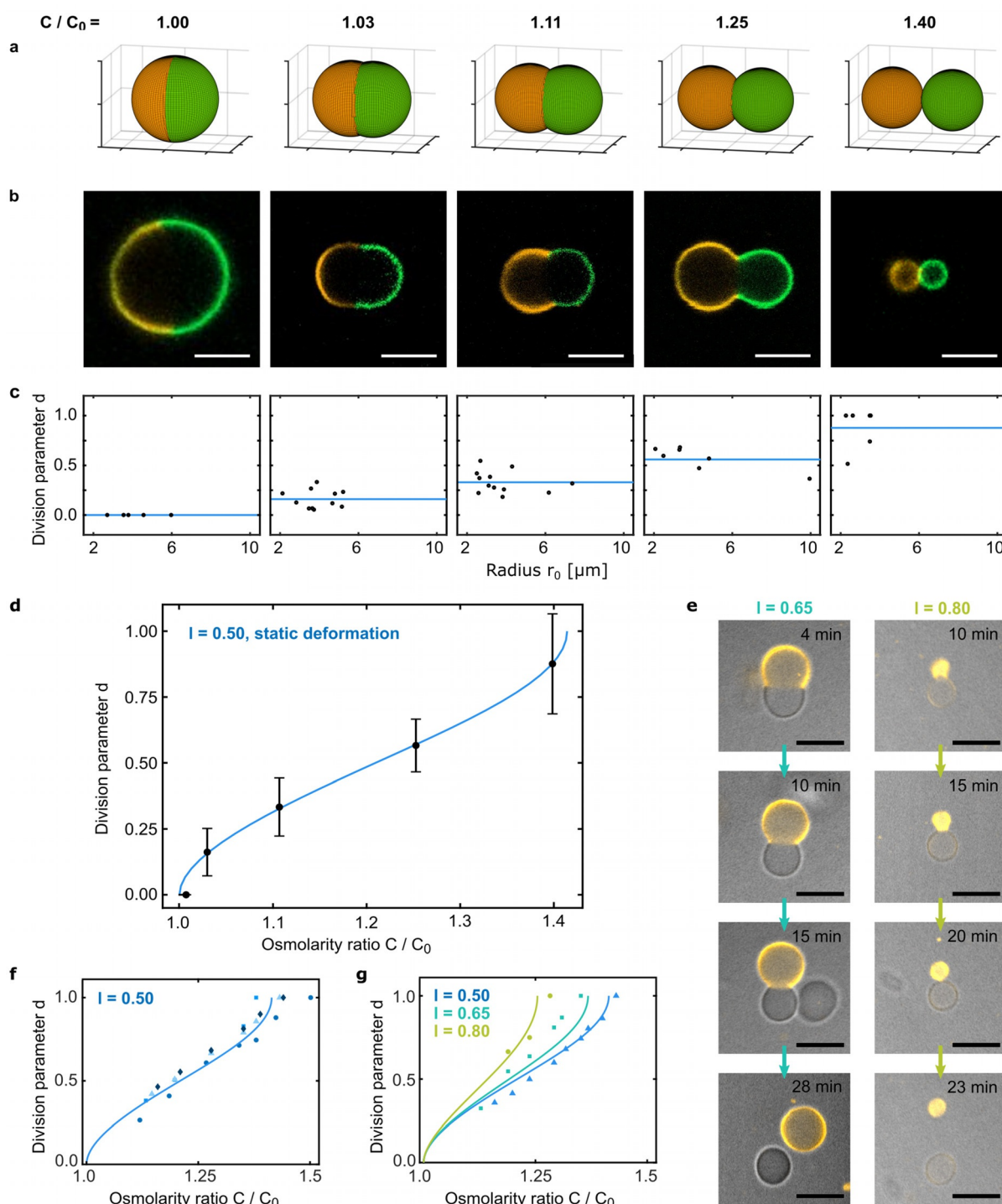


**Figure 3.** Quantitative comparison of experiment and theoretical prediction. a) Theoretically predicted shapes of symmetric GUVs at different osmolarity ratios  $C/C_0$  as indicated. b) Representative confocal fluorescence images of symmetric phase-separated GUVs immersed in solutions of the corresponding osmolarity ratios  $C/C_0$ . The  $l_d$  phase is labeled with LissRhod PE (orange,  $\lambda_{ex}=561$  nm), the  $l_o$  phase with 6-FAM-labeled cholesterol-tagged DNA (green,  $\lambda_{ex}=488$  nm). Scale bars: 10  $\mu\text{m}$ . c) Scatter plots of the experimentally determined division parameters plotted against the radius of the initially spherical GUVs. Solid blue lines represent the theoretical prediction, which postulates size-independence of the division process. d) Division parameter  $d$  as a function of osmolarity ratio  $C/C_0$ . The mean values of the measured division parameters (black) and the theoretical prediction from Equation (2) (solid blue line) are plotted. Error bars correspond to the standard deviation of the values for  $d$  extracted from confocal fluorescence images. e) Confocal fluorescence time series of GUVs with asymmetric lipid ratios ( $l=0.65$  and  $l=0.80$ ) in the presence of  $44 \text{ mg L}^{-1}$  invertase. Scale bars: 10  $\mu\text{m}$ . f) Division parameter  $d$  of four different symmetric GUVs ( $l=0.50$ ) in the presence of  $44 \text{ mg L}^{-1}$  invertase plotted against the osmolarity ratio  $C/C_0$ . The values for  $C/C_0$  were obtained from the osmolarity measurements displayed in Figure 1d. The solid blue line shows the theoretically predicted division curve. g) Division parameter  $d$  of GUVs with different lipid ratios in the presence of invertase plotted against the osmolarity ratio  $C/C_0$ . Solid lines are the theoretically predicted division curves for the corresponding lipid ratios.

To show that our geometrical description does not only predict the static GUV shapes but also the dynamic division process, we analyse confocal time lapses of the division process in the presence of invertase. We can extract the osmolarity ratio at a given time point from the osmometer measurements in Figure 1d. Figure 3f confirms that the division process of symmetric GUVs with two equally large hemispheres ( $l=0.5$ ) agrees well with the prediction. Finally, asymmetric GUVs with  $l>0.5$  should require lower osmolarity ratios for division and hence divide faster (Prediction 3). To test this, we observed GUVs with different lipid ratios. Figure 3e shows that asymmetric GUVs indeed exhibit shorter division times—approximately 27 min for  $l=0.65$  and 20 min for  $l=0.80$  compared to 40 min for  $l=0.50$  (see Figure 1f). Figure 3g confirms that the division parameter plotted as a function of the osmolarity ratio follows the theoretical predictions [solid lines, Eq. (3)]. The fact that asymmetric division happens at lower osmolarity ratios may explain why budding was more frequently reported in the literature<sup>[23,24]</sup> than symmetric division.

### Light-Triggered Local Division

Any process that achieves a sufficient increase of the osmolarity ratio should, in principle, be suitable to trigger division of phase-separated GUVs (Prediction 4). We first demonstrate this by showing that water evaporation can be used instead of invertase activity to increase the osmolarity ratio, see Figure S3a. This confirms that the division process is not dependent on the chemical nature of the enzymatic reaction but relies on the resulting osmolarity increase. Exploiting this versatility, we want to realize a mechanism with full spatiotemporal control over the division process, such that a selected vesicle divides at a chosen time point whereas surrounding vesicles remain unaffected. We successfully achieve this aim based on the light-triggered uncaging of bis-(5-carboxymethoxy-2-nitrobenzyl)-ether (CMNB)-caged fluorescein. Upon 405 nm illumination, this initially non-fluorescent compound splits into three components—two CMNB molecules and the fluorophore fluorescein (Figure 4a). Its contribution to the overall osmolarity should thus triple. The successful uncaging of fluorescein can be monitored with UV/Vis spectrometry (see Figure S10a). Figure 4b illustrates our concept for the localized light-triggered division: Phase-separated vesicles are immersed in a solution containing CMNB-fluorescein. Subsequently, a target GUV is chosen for division. The division process is initiated by illuminating the surrounding area with a 405 nm laser diode leading to uncaging of CMNB-fluorescein. Fluorescein release increases the osmolarity locally, hence leading to division of the selected GUV, while surrounding GUVs remain unaffected. Based on theoretical considerations (Note S2) and osmometer measurements (Figure S10b), we set the initial concentrations to achieve the required increase of  $\sqrt{2}$  in the overall osmolarity. Figure 4c shows snapshots from a confocal fluorescence time series before (i) and during illumination (ii) of the selected area (Video S3). While division previously happened within tens of minutes

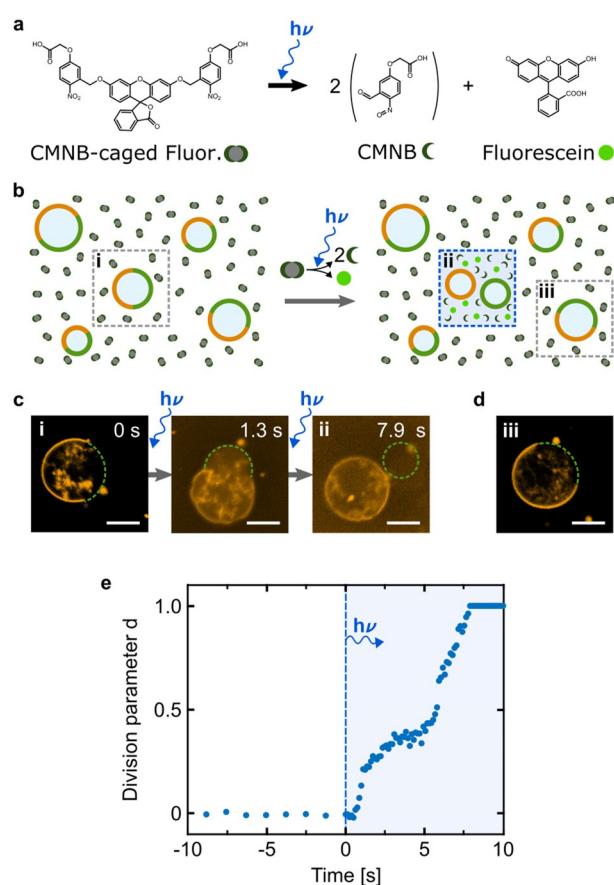


**Figure 4.** Light-triggered local division of phase-separated GUVs via uncaging of CMNB-fluorescein. a) Chemical reaction pathway of fluorescein release induced by UV or 405 nm illumination. CMNB-caged fluorescein decomposes into three products thus tripling its contribution to the osmolarity. b) Schematic illustration of the localized light-triggered division process. Phase-separated GUVs are immersed in a solution containing CMNB-fluorescein. Illumination with a 405 nm laser diode leads to a local increase in osmolarity by uncaging of CMNB-fluorescein and hence to GUV division. c) Representative confocal fluorescence images of a phase-separated GUV (1d phase labeled with LissRhod PE,  $\lambda_{\text{ex}}=561$  nm) undergoing full division within seven seconds of 405 nm illumination (time points i and ii are illustrated in b). d) Confocal fluorescence image of a phase-separated GUV outside the illuminated area maintains its spherical shape (iii as illustrated in b). Scale bars: 10  $\mu\text{m}$ . e) Division parameter  $d$  of the GUV shown in (c) over time. The GUV instantly deforms with start of 405 nm illumination (indicated by the vertical blue dashed line) and fully divides within seconds.

(see Figures 1 and 3), the rapid uncaging dynamics of CMNB-fluorescein promote division after a few seconds. Other representative examples of GUVs undergoing similarly fast division are shown in Figure S11. Note that we could only record one fluorescence track to capture the fast dynamics. The increase in the background fluorescence intensity is due to bleed through from the 405 nm excitation and the release of fluorescein (for confocal images of the fluorescein channel before and after release, see Figure S12). Finally, Figure 4d highlights the locality of the division: As expected, a vesicle outside the illuminated area does not undergo division. Moreover, illumination alone, in the absence of CMNB-

fluorescein, does not lead to division of phase-separated GUVs (Figure S13). Figure 4e plots the division parameter for the vesicle shown in c as a function of time (for more examples see Figure S11). The plot clearly shows that no shape changes occur before illumination (the frame rate was reduced to avoid bleaching and the GUV was observed for in total 100 s before illumination). As soon as the local osmolarity change is induced by uncaging of CMNB-fluorescein at  $t = 0$  s, the vesicle starts to deform and fully divides after 7.9 s. The shape of the curve is likely to be a result of the non-linear increase in osmolarity (Figure S10b): Uncaging increases the osmolarity locally in the illuminated confocal volume, yet components freely diffuse in and out. Caged compounds have previously been used to change the osmolarity to induce compartment rupture.<sup>[41]</sup> Here, we have shown that they offer the additional possibility to trigger the division of phase-separated GUVs locally with light, achieving a rapid time response and division within seconds.

### Regrowth of Phase-Separated Vesicles After Division

Crucially, synthetic cell division should be followed by a growth phase in order to ultimately sustain multiple growth and division cycles. In our system, this process has to restore the initial phase separation of the GUV. Different methods for vesicle fusion have previously been employed to grow GUVs.<sup>[42–45]</sup> However, it is not trivial that these conventional fusion mechanisms can lead to phase-separated GUVs: The emerging line tension adds to the energy barrier for the fusion of a lo-phase vesicle to a ld-phase vesicle. As a proof-of-principle experiment, we produced carboxyfluorescein-la-

beled lo GUVs and rhodamine-labeled ld GUVs separately, mimicking the single-phase GUVs after division. With this strategy we can be absolutely sure that a GUV, which contains both fluorescent dyes, results from a fusion event.

We mixed ld and lo GUVs and added  $\text{Ca}^{2+}$ -ions. This leads to attractive interactions between the GUVs<sup>[46]</sup> and has been shown to mediate fusion between identical lo-phase GUVs.<sup>[47]</sup> We find that this process yields phase-separated GUVs, which unambiguously demonstrates that fusion between the lo and ld GUVs has occurred (Figure S14, Video S4). It should be noted, however, that despite frequently observed hemifusion and attachment of GUVs to one another, full fusion is a rare event and the vast majority of GUVs (over 95%) remains single-phased. Moreover, fusing GUVs again after division cannot lead to growth of the GUV population.

We ultimately need a “feeding mechanism” as illustrated in Figure 5 a, where each growth-division cycle can increase the total number of GUVs.  $\text{CaCl}_2$ -mediated fusion can restore phase-separation upon addition of small unilamellar vesicles (SUVs) to GUVs (Figure S15). However, this approach lacks programmability. In order to achieve targeted fusion of SUVs to GUVs of the, respectively other lipid phase in a mixture, we thus make use of the sequence-programmable base-pairing of DNA. As we already demonstrated, cholesterol-tagged DNA self-assembles selectively into the liquid-ordered phase. We find that in our system tocopherol-tagged DNA, on the other hand, attaches to both phases equally (Figure S16). By designing complementary single-strands of DNA, one with a 3' cholesterol and the other one with a 5' tocopherol, we can thus selectively bring vesicle membranes into close proximity as illustrated in the zoom in Figure 5 a. Such zipper-like DNA-based mimics of SNARE proteins

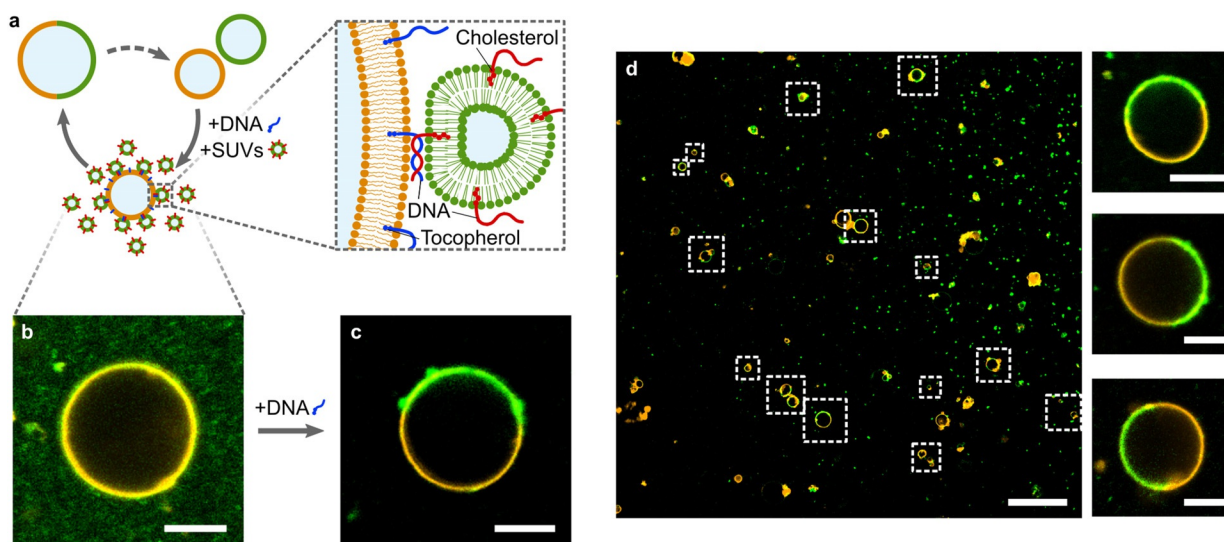


**Figure 5.** Regrowth of phase-separated vesicles. a) Schematic illustration of a programmable vesicle growth and division cycle mediated via fusogenic membrane-bound DNA. The zoom image shows the zipper-like arrangement of the DNA, bringing the membranes into close proximity. b) Representative confocal fluorescence image of a fluorescently labeled ld-phase GUV (orange,  $\lambda_{\text{ex}} = 561$  nm) in a feeding bath of lo SUVs functionalized with cholesterol-tagged 6-FAM-labeled DNA (green,  $\lambda_{\text{ex}} = 488$  nm). c) Addition of complementary tocopherol-tagged DNA leads to SUV fusion and hence the formation of phase-separated vesicles (as identified via partitioning of cholesterol-tagged 6-FAM DNA in presence of unlabeled SUVs). Scale bars: 10  $\mu\text{m}$ . d) Confocal fluorescence overview image (left, scale bar: 50  $\mu\text{m}$ ) after the DNA-mediated fusion process. Fusion took place for the majority of GUVs (highlighted with white boxes). Zoom images (right, scale bars: 10  $\mu\text{m}$ ) show the successful regeneration of phase-separated GUVs with a lipid ratio of  $l \approx 0.5$ .

have been used to trigger fusion of SUVs of the same kind,<sup>[44]</sup> but it is not trivial that phase-separated vesicles can be formed. We hence immersed 1d GUVs in a feeding bath containing DNA-functionalized 1o SUVs (Figure 5b). Note that the SUVs (green) with a diameter of around 100 nm (Figure S17) are too small to be resolved individually. Upon addition of the complementary DNA, we observe phase-separated GUVs with a sufficiently large 1o phase to restore the initial condition. Given the area of the 1d phase in Figure 5c, we estimate that approximately 5600 SUVs have fused to the GUV. We hypothesize that the line tension at phase boundary present after the first fusion event lowers the energy barrier for subsequent fusion. Lipid phase boundaries have been shown to promote other fusion events including HIV entry.<sup>[48]</sup> The time-resolved growth process is depicted in Figure S18. Note that the SUVs have a larger surface-to-volume ratio compared to the GUVs and thus are supplied in a lower osmolarity solution in order to obtain spherical GUVs after fusion. The small osmolarity mismatch is likely to be beneficial for the fusion process itself.<sup>[15]</sup> By preventing duplex formation, that is, in absence of tocopherol-tagged DNA, we do not observe vesicle fusion (Figure S19). Compared to  $\text{Ca}^{2+}$  mediated fusion, we did not only gain programmability, but also increased the efficiency of the process. Figure 5d shows an overview image, which demonstrates that phase-separation was restored in the majority of GUVs after incubation. A lipid ratio of  $l \approx 0.5$  could be restored reproducibly.

## Conclusion

Synthetic cell division is one of the most exciting albeit challenging tasks towards the bottom-up construction of cellular systems. Our study realizes the division of GUVs, fully controllable by two physical parameters—phase separation and osmosis. Phase separation of the lipids in the GUV membrane defines the plane of division such that an increase of the surface-to-volume ratio by osmosis leads to contraction at the phase boundary and thus the formation of two second-generation compartments. We derived a model of the division process based on geometrical considerations. The analytical model makes four predictions, which were all verified experimentally: First of all, the osmolarity ratio required for division of GUVs with equally sized phases is  $\sqrt{2}$ ; secondly, the time-point of division is independent of vesicle size; third, asymmetric division happens faster (i.e. at lower osmolarity ratios) and fourth, any process, which leads to a sufficiently large osmolarity increase, can trigger division. We showcased the latter by demonstrating division as a result of fundamentally distinct processes, including water evaporation, metabolic decomposition of sugars and light-triggered uncaging of CNMB-fluorescein. Using light as a stimulus for division provides full spatiotemporal control, which could, in the future be exploited to perform directed evolution of a vesicle population. The concept to exploit caged compounds for local vesicle division is new and broadly applicable. It does not rely on specific environmental conditions and can directly be extended from CMNB-caged fluorescein to other caged

compounds. Any suitable division mechanism for synthetic cells should have the capacity to sustain multiple growth-and-division cycles. In our case, growth has to restore phase separation in the second-generation compartments. We achieve fusion of SUVs of the other phase to single-phased GUVs with programmable DNA-based SNARE protein mimics—thus restoring the initial conditions for subsequent division cycles, which will undoubtedly be a prerequisite for the evolution of synthetic cellular systems. The future integration of information storage and replication will be yet another important milestone towards the visionary transition from matter to life, or, in other words, towards a synthetic cell which truly deserves its name. In the meantime, our engineering approach to synthetic cell division prompts questions about cellular life as we know it: We may be curious to discover whether phase separation and osmosis may have sustained compartment division at the onset of life, possibly regulated by the expression of metabolic enzymes. And we may further ask how remnants thereof play a role in cell biology today—continuously nurturing the emergence of cells from cells.

## Acknowledgements

The authors thank Martin Schröter, Desiree Sauter and Alexandra Teslenko for helpful discussions. K.J. thanks the Carl Zeiss Foundation for financial support. J.P.S. acknowledges funding from the European Research Council, Grant Agreement no. 294852, SynAd and the MaxSynBio Consortium, funded by the Federal Ministry of Education and Research of Germany and the Max Planck Society, from the SFB 1129 of the German Science Foundation and the VolkswagenStiftung (priority call “Life?”). J.P.S. is the Weston Visiting Professor at the Weizmann Institute of Science and part of the excellence cluster CellNetworks at Heidelberg University. K.G. received funding from the Deutsche Forschungsgemeinschaft (DFG, German Research Foundation) under Germany’s Excellence Strategy via the Excellence Cluster 3D Matter Made to Order (EXC-2082/1-390761711) and the Max Planck Society. The Max Planck Society is appreciated for its general support. Open access funding enabled and organized by Projekt DEAL.

## Conflict of interest

The authors declare no conflict of interest.

**Keywords:** DNA structures · GUV division · osmosis · synthetic biology · vesicles

- [1] F. V. Raspail, *Ann. Sci. Nat.* **1825**, 224, 384–427.
- [2] R. Virchow, *Die Cellularpathologie in ihrer Begründung und in ihrer Auswirkung auf die physiologische und pathologische Gewebelehre*, Verlag A. Hirschwald, Berlin, **1858**.
- [3] P. Schwille, *Science* **2011**, 333, 1252–1254.
- [4] K. Göpfrich, I. Platzman, J. P. Spatz, *Trends Biotechnol.* **2018**, 36, 938–951.

- [5] P. Schwille, *Emerging Top. Life Sci.* **2019**, *3*, 551–558.
- [6] D. A. Ramirez-Diaz, A. Merino-Salomon, M. Heymann, P. Schwille, *bioRxiv* **2019**, <https://doi.org/10.1101/587790>.
- [7] K. Vogeles, T. Pirzer, F. C. Simmel, *ChemSystemsChem* **2019**, *1*, e1900016.
- [8] Y. Caspi, C. Dekker, *Syst. Synth. Biol.* **2014**, *8*, 249–269.
- [9] M. Osawa, D. E. Anderson, H. P. Erickson, *Science* **2008**, *320*, 792–794.
- [10] T. Litschel, B. Ramm, R. Maas, M. Heymann, P. Schwille, *Angew. Chem. Int. Ed.* **2018**, *57*, 16286–16290; *Angew. Chem.* **2018**, *130*, 16522–16527.
- [11] T. Wollert, C. Wunder, J. Lippincott-Schwartz, J. H. Hurley, *Nature* **2009**, *458*, 172EP.
- [12] H. G. Franquelim, A. Khmelinskaia, J.-P. Sobczak, H. Dietz, P. Schwille, *Nat. Commun.* **2018**, *9*, 811.
- [13] Z. Zhang, Y. Yang, F. Pincet, M. C. Llaguno, C. Lin, *Nat. Chem.* **2017**, *9*, 653–659.
- [14] K. Göpfrich, T. Zettl, A. E. C. Meijering, S. Hernandez-Ainsa, S. Kocabay, T. Liedl, U. F. Keyser, *Nano Lett.* **2015**, *15*, 3134–3138.
- [15] S. Deshpande, W. K. Spoelstra, M. van Doorn, J. Kerssemakers, C. Dekker, *ACS Nano* **2018**, *12*, 2560–2568.
- [16] U. Seifert, K. Berndt, R. Lipowsky, *Phys. Rev. A* **1991**, *44*, 1182–1202.
- [17] J. Käs, E. Sackmann, *Biophys. J.* **1991**, *60*, 825–844.
- [18] R. Lipowsky, *Curr. Opin. Struct. Biol.* **1995**, *5*, 531–540.
- [19] R. Lipowsky, *J. Phys. II France* **1992**, *2*, 1825–1840.
- [20] F. Jülicher, R. Lipowsky, *Phys. Rev. E Stat. Phys. Plasmas Fluids Relat. Interdiscip. Top.* **1996**, *53*, 2670–2683.
- [21] T. Baumgart, S. Das, W. W. Webb, J. T. Jenkins, *Biophys. J.* **2005**, *89*, 1067–1080.
- [22] Y. Miele, Z. Medveczky, G. Holló, B. Tegze, I. Derényi, Z. Hörvölgyi, E. Altamura, I. Lagzi, F. Rossi, *Chem. Sci.* **2020**, *11*, 3228–3235.
- [23] M. Yanagisawa, M. Imai, T. Taniguchi, F. Ade, *Phys. Rev. Lett.* **2008**, *100*, 148102.
- [24] H. G. Döbereiner, J. Käs, D. Noppl, I. Sprenger, E. Sackmann, *Biophys. J.* **1993**, *65*, 1396–1403.
- [25] T. Baumgart, S. T. Hess, W. W. Webb, *Nature* **2003**, *425*, 821–824.
- [26] J. M. Castro, H. Sugiyama, T. Toyota, *Sci. Rep.* **2019**, *9*, 165.
- [27] M. Andes-Koback, C. D. Keating, *J. Am. Chem. Soc.* **2011**, *133*, 9545–9555.
- [28] T. F. Zhu, J. W. Szostak, *J. Am. Chem. Soc.* **2009**, *131*, 5705–5713.
- [29] J. Steinkühler, R. L. Knorr, Z. Zhao, T. Bhatia, S. M. Bartelt, S. Wegner, R. Dimova, R. Lipowsky, *Nat. Commun.* **2020**, *11*, 905.
- [30] M. Morasch, J. Liu, C. F. Dirscherl, A. Ianeselli, A. Kühnlein, K. Le Vay, P. Schwintek, S. Islam, M. K. Corpinot, B. Scheu, D. B. Dingwell, P. Schwille, H. Mutschler, M. W. Powner, C. B. Mast, D. Braun, *Nat. Chem.* **2019**, *11*, 779–788.
- [31] J. W. Szostak, *Angew. Chem. Int. Ed.* **2017**, *56*, 11037–11043; *Angew. Chem.* **2017**, *129*, 11182–11189.
- [32] G. van Meer, H. Sprong, *Curr. Opin. Cell Biol.* **2004**, *16*, 373–378.
- [33] K. C. Huang, R. Mukhopadhyay, N. S. Wingreen, *PLoS Comput. Biol.* **2006**, *2*, e151.
- [34] H. T. McMahon, J. L. Gallop, *Nature* **2005**, *438*, 590–596.
- [35] D. W. Deamer, J. Bramhall, *Chem. Phys. Lipids* **1986**, *40*, 167–188.
- [36] A. Callan-Jones, B. Sorre, P. Bassereau, *Cold Spring Harbor Perspect. Biol.* **2011**, *3*, a004648.
- [37] J. H. Koschwanetz, K. R. Foster, A. W. Murray, *PLoS Biol.* **2011**, *9*, e1001122.
- [38] P. A. Beales, J. Nam, T. K. Vanderlick, *Soft Matter* **2011**, *7*, 1747–1755.
- [39] M. Jansen, A. Blume, *Biophys. J.* **1995**, *68*, 997–1008.
- [40] N. Klughammer, J. Bischof, N. D. Schnellbacher, A. Callegari, P. Lenart, U. S. Schwarz, *PLoS Comput. Biol.* **2018**, *14*, e1006588.
- [41] A. Peyret, E. Ibarboure, A. Tron, L. Beauté, R. Rust, O. Sandre, N. D. McClenaghan, S. Lecommandoux, *Angew. Chem. Int. Ed.* **2017**, *56*, 1566; *Angew. Chem.* **2017**, *129*, 1588.
- [42] S. Deshpande, S. Wunna, D. Hueting, C. Dekker, *Small* **2019**, *15*, 1902898.
- [43] J. Dervaux, V. Noireaux, A. J. Libchaber, *Eur. Phys. J. Plus* **2017**, *132*, 284.
- [44] Y.-H. M. Chan, B. van Lengerich, S. G. Boxer, *Proc. Natl. Acad. Sci. USA* **2009**, *106*, 979–984.
- [45] R. B. Lira, T. Robinson, R. Dimova, K. A. Riske, *Biophys. J.* **2019**, *116*, 79–91.
- [46] D. Papahadjopoulos, S. Nir, N. Duzgunes, *J. Bioenerg. Biomembr.* **1990**, *22*, 157–179.
- [47] J. Bentz, N. Duezguenes, *Biochemistry* **1985**, *24*, 5436–5443.
- [48] S.-T. Yang, V. Kiessling, L. K. Tamm, *Nat. Commun.* **2016**, *7*, 11401.

Manuscript received: October 22, 2020

Revised manuscript received: December 13, 2020

Accepted manuscript online: December 23, 2020

Version of record online: March 24, 2021

# Chapter 4

## Discussion

The rational engineering of multifunctional cytoskeletons is a key challenge of bottom-up synthetic biology. In the eight publications, we have seen how natural actin and synthetic DNA-based cytoskeletons can be engineered for versatile functions and processes like morphology control, (intra-)cellular motility and stimuli-responsive reversible assembly. In the following, I discuss the most important results and conclusions and give an outlook on how these can be used to tackle exciting new goals.

### 4.1 Natural cytoskeletons for synthetic cells

Cytoskeletons inside natural eukaryotic cells are highly efficient systems responsible for multiple functions. The main challenge for engineering natural cytoskeletons is to reduce the complexity of a living cell while maintaining the cytoskeletal functions. Given that for actin itself there are more than a hundred actin-binding proteins, the difficulty of this task becomes evident [107]. Therefore, we focused on one application of actin-based natural cytoskeletons for synthetic cells at a time. By doing so, we were able to engineer different functional units that rely on at most two proteins to govern synthetic cell morphology, motility and contractility.

#### 4.1.1 Control over synthetic cell morphology

The easiest way to generate control over the GUV morphology is to deform the membrane by active forces from the outside because it does not require the difficult step of encapsulation and leaves an ‘infinite’ reservoir to recruit necessary components, which can be supplied sequentially at the right time points. In Publication 1, we achieved control over GUV morphology by linking lipids from the GUV membrane to actin filaments that slide along a surface due to force generation by heavy mero-myosin (HMM). This led to the pulling of lipid nanotubes from the GUVs with different lengths depending on the lipid composition and the amount of biotinylated lipids. Whereas a similar behavior has been found using a different set of filament and motor, i.e. microtubules and kinesin [108–110], it was remarkable that we could achieve the formation of lipid nanotubes and even bigger networks than previous work using the non-processive motor heavy mero-myosin. This is because HMM detaches after every power stroke from the actin filament, whereas kinesins



are processive motors that stay in contact with the microtubules, which prevents a retraction of the lipid nanotube after every power stroke [111].

Moreover, after verifying the different lipid nanotube network sizes for GUVs with varying lipid compositions, we successfully subjected the pulling assay to natural cells. Here, the cell type made a difference in the generated nanotube networks also including the absence of nanotubes for adherent cells. We found that this was determined by the intracellular cytoskeleton of the cells since they do form nanotubes in the absence of internal actin filaments. We proposed that this allows our system to infer the membrane-to-cortex attachment of different cell types. Typically, these measurements are performed using optical or magnetic tweezers or atomic force microscopy [112]. These techniques have a low throughput of a couple of cells per hour. Our assay might be useful for a higher-throughput screening of the membrane-to-cortex attachment of natural cells with up to hundreds of cells per hour since it is only limited by the size of the observation chamber and the acquisition speed of a confocal microscope. However, this would require further characterization and verification of the system in respect to the cell type and downstream signalling. Additionally, a major limitation of our assay is that a large fraction of cells does not survive more than 1 h on the HMM-coated slides in presence of actin filaments. The survival time could potentially be increased by using an open observation chamber with constant media and CO<sub>2</sub>-supply.

To summarize, in this work we developed a new assay to control the morphology of GUVs and natural cells - a key feature of cytoskeletons - using only two types of proteins: actin filaments and myosin motors. However, this is done by generating active forces from the outside of synthetic cells, which contradicts the autonomous capabilities we desire a synthetic cell to have. Therefore, we went on to explore how we could achieve a different function by encapsulating actin filaments inside synthetic cells.

### 4.1.2 Control over synthetic cell motility

Since the presented assay for the control over GUV morphology requires a substrate coated with HMM, it cannot be directly translated into cell-sized compartments. For this reason, we started to investigate a different function of natural cytoskeletons that could be triggered from the inside, namely their involvement in cell motility (Publication 2).

To achieve synthetic cell motility, we encapsulated actin filaments inside surfactant-stabilized water-in-oil droplets. The binding of actin filaments to the negatively charged surfactant Krytox at the droplet interface leads to a gradient in surface tension and thus to Marangoni flows that cause the rotation of the droplet. By tuning the interaction with the droplet substrate we can moreover transfer the rotational into a rolling motion. We have thereby used the cytoskeleton to induce droplet motility. This system is especially interesting because the reconstitution of cellular actin-based locomotion within synthetic cells remains unachieved due to its complexity [10]. Moreover, droplet motility due to Marangoni flows could also be generated using cytoskeleton-independent mechanisms [38]. This can be seen as advantageous because it makes this propulsion strategy more versatile. On the other

hand it also clearly shows that we did not exploit the whole spectrum of the possible filament properties. Nonetheless, the velocities achieved with our system very well match the ones of crawling cells with up to  $\mu\text{m min}^{-1}$  [73], whereas swimming cells with velocities on the order of  $10 \mu\text{m s}^{-1}$  still remain a far-distant goal.

Another major drawback of our system is that it still relies on an oil phase containing the negatively charged surfactant. It is therefore unsuitable for biological systems as it is not biocompatible. Whereas recently this issue has been overcome by stabilizing the emulsion droplet with liposomes [113], liposome and GUV motility via Marangoni flow have not been reported yet. Notably, also no other mechanisms for the reliable and directed motility of GUVs has been found so far. Common approaches to overcome this limitation include the use of enzyme-enhanced diffusion, which can already be used for SUV motility [114], the use of light-stimulated GUV rolling [115] or the combination of GUVs with acto-myosin machinery [32]. Alternatively, we later on show that a burnt-bridge mechanism can also be employed to induce vesicle locomotion.

In the following work, we explored the strategy of acto-myosin-mediated motility by engineering a symmetry-breaking contraction, which next to the polymerization of actin filaments on the leading edge, is required for actin-based crawling motion of natural cells.

### 4.1.3 Control over synthetic cell contractility

Having shown the successful encapsulation of actin filaments into the confinement of water-in-oil droplets, we went one step further by adding heavy mero-myosin coated beads as force-generating element (Publication 3). We verify that the HMM-beads are functional by binding them to actin filaments and inducing the contraction in presence of ATP. As a controlling element for the contraction, we made use of ATP with a P3-(1-(2-nitrophenyl)ethyl) ester (NPE-caged ATP), which uncages ATP upon illumination with a 405 nm laser. By transferring the system into water-in-oil droplets and linking the actin filaments to the compartment periphery, we showed that we can use light to trigger the symmetry-breaking contraction of actomyosin-networks.

Our system thereby showcases not only the successful integration of myosin to actin filaments inside cell-sized confinement but also presents NPE-caged ATP as a powerful non-invasive trigger for engineering synthetic cells. However, in contrast to natural cells, the contraction of our actomyosin-networks is still not reversible. If we would want to generate a sustainable motion of a synthetic cell, this mechanism would require continuous network remodeling and ATP production. In our case, the ATP is consumed within minutes after light illumination and the contracted network remains static. The inclusion of an ATP regenerating system could help to overcome this issue [116, 117]. However, this also requires the addition of more proteins to the system, which might not be functional in the droplet-based confinement or interfere and interact with the actomyosin-contraction.

Moreover, in order to generate synthetic cell motility based on actin-based locomotion, we would still require the polymerizing force of actin filaments on the leading edge of compartment and the connection of the droplet to a substrate. The simulta-

neous arrangement of these processes inside confinement, however, is very challenging. Additionally, we have seen in the control over the synthetic cell morphology that the high interfacial tension at the droplet periphery makes GUVs the better compartment choice because the amounts of forces needed to induce a deformation or motion are lower. Given that recent works showed the successful encapsulation of actin and actin-binding proteins into GUVs [24, 68, 118], this might be a possible aim of following work.

All in all, we have seen how we can engineer natural actin filaments to change the GUV morphology based on their lipid composition, how the encapsulation of actin can lead to the motility of droplets and how we can induce the symmetry-breaking contraction of actomyosin networks inside cell-sized confinement, which make up some of the most fundamental features of cytoskeletons. By doing so, we went from a complex functionality on the outside of the compartment to the encapsulation of first one protein and then two proteins inside of compartments - making the essential transfer step for engineering an autonomous synthetic cell. However, we also saw that the droplet-based system has its limitations due to its bioincompatibility and that the reconstitution of natural proteins can be challenging especially when one wants to integrate multiple different functions at the same time. For this reason, we explored the use of synthetic cytoskeletons next.

## 4.2 Synthetic cytoskeletons with programmable functionality

An essential bottleneck for the use of natural cytoskeletons is the need to purify and successfully reconstitute them into cell-sized compartments. This is especially challenging if one wants to increase the complexity and functionality as one needs to add more proteins. DNA nanotechnology offers a solution for this problem by using DNA as a building block for versatile and programmable structures that are relevant for bottom-up synthetic biology [14]. We employed this for rationally engineering multifunctional cytoskeleton mimics from DNA (Publications 4-7).

### 4.2.1 Dynamic DNA origami structures to deform GUVs

As a first application, we set out to deform GUVs using DNA origami structures. The deformation is based on the polymerization of individual DNA origami that are attached to the membrane into sheets that scaffold the GUV membrane. Whereas this approach has been used already to deform GUVs in previous studies [77–79], we expand it by making the deformation reversible. We achieved this with a pH-sensitive triplex motif that opens up at a  $\text{pH} > 7$  and allows the DNA origami to bind the GUV membrane. After attaching the DNA origami to the membrane and inducing the deformation, they can be subsequently removed by lowering the pH and leaving the GUV in its spherical state again. Importantly, we find that the choice of fluorophore on the triplex motif determines its switching behavior. This is of relevance for the field of DNA nanotechnology beyond this study, since fluorophores are typically deliberately exchanged based on experimental modalities.

Our work shows that this should be done with caution as the fluorophore influences the conformation of the DNA.

After verifying the use of our DNA origami cytoskeleton mimic to deform GUVs, we moreover expand the system by integrating genetically-modified *E. coli* that overexpress a light-sensitive proton pump. Therefore, their integration makes the system responsive to an external light stimulus. The genetic modification of *E. coli* has already previously been shown to generate proton gradients [119, 120]. In our work, however, we achieve higher absolute gradients and find a purpose for the generated proton gradients by allowing the attachment of DNA origami to the GUV membrane. We therefore use the *E. coli* to generate a complex signalling pathway following a light stimulus.

However, our DNA origami-mediated deformation is still based on their attachment from the outside. The main reason for this is the fact that we were neither able to encapsulate a sufficient amount of *E. coli* to induce sufficient pH gradients nor to encapsulate a sufficient amount of DNA origami to induce GUV deformation. These could be overcome by generating *E. coli* with higher gradients or by finding ways to concentrate the DNA origami even further. The main difficulty, however, is the interference of the *E. coli* themselves with the encapsulation process during formation of the free-standing GUV. As a consequence, we focused further on easy-to-encapsulate components like DNA that can also be formed at high concentrations.

#### 4.2.2 DNA filaments as multifunctional cytoskeletons

As DNA origami has to be purified and is typically annealed at concentrations  $< 100$  nM due to the necessity of a scaffolding strand, we looked out for a different DNA cytoskeleton mimic that could also be annealed at higher concentrations without the need for purification. DNA nanotubes (termed DNA filaments), which consist of DNA tiles and are 12 nm in diameter as well as up to tens of micrometer in length fulfill these criteria because of their visual resemblance to microtubules and the fact that they are made up of only 5 single strands with  $< 70$  bp.

First, we verified that we could incorporate cytoskeletal functions into the DNA filaments within water-in-oil droplets. By incorporating aptamers into the tile structure, we were able to induce the reversible DNA filament assembly upon addition of ATP or nucleolin. Moreover, we achieved the same by using toehold-mediated strand displacement reactions showcasing the applicability of already two orthogonal triggers for DNA filament assembly. Whereas strand displacement reactions have already been used for filament disassembly [81], the use of aptamers for this purpose has never been demonstrated. It also offers the great advantage of using physiological triggers like ATP for DNA filament polymerization, which is also needed for actin filament polymerization. However, in both cases - aptamer-induced assembly and strand-displacement-induced disassembly - the molecules are still supplied from the outside. Ideally, one would envision to have an external and non-invasive stimulus or an autonomously regulated system that does not require the addition of molecules from the outside. Possible ways to achieve these aims would be the use of pH- or light-sensitive nucleic acids, an ATP-consuming and replenishing unit or the use of transcriptional oscillators [121].

Another key feature of natural cytoskeletons is the ability to transport cargo using molecular motors. Therefore, we set out to engineer a vesicle transport system along our DNA filaments based on a burnt-bridge RNase H-dependent mechanism [102]. Previously this mechanism has been shown to propel silica particles [102] or DNA origami [103] on two-dimensional substrates. However, it was unclear if the same mechanism could be applied to lipid vesicles with their fluid and diffusive membranes as well as to the DNA filament geometry. We were not only able to implement this mechanism but to also integrate it within water-in-oil droplets achieving translocation velocities on the order of  $\mu\text{m min}^{-1}$ . Since this is still far away from the transport velocities of natural motors, a relevant goal is to increase the transport velocity even further and to directly track individual SUVs moving along the filament tracks, which is very difficult in three dimensions due to filament dynamics in the compartments. Moreover, the motility mechanism still relies on the use of the enzyme RNase H. An efficient DNA-based or synthetic protein-independent mechanism would therefore be required to build a truly synthetic transport pathway. Even though there are many efforts in this direction [122–124], it still remains an open goal to build similarly processive DNA-based motors.

Another goal for improvement would be the replenishment of the filament track after cargo transport. This could possibly be achieved by using smaller DNA oligomers that dynamically bind and unbind from the DNA filament. A similar mechanism is already employed for DNA-based superresolution microscopy (DNA-PAINT). Lastly, now that these functions are established, it is desirable to transfer them from water-in-oil droplet into GUVs.

Towards this goal, we used the droplet-stabilized technique to form GUVs that can selectively encapsulate cargo of choice [25]. In contrast to the encapsulation of proteins, the encapsulation of DNA with this method is straightforward and reliable. In order to overcome the addition of molecules from the outside into the compartment as for the aptamer- and strand-displacement-based assembly, we modified the DNA tile with two light-sensitive azobenzene moieties. Azobenzene, as a light-sensitive molecular switch, has recently been used throughout various fields and is known for its efficient photoswitching [125, 126]. We made use of this by reversibly photoswitching azobenzenes and thereby induce filament disassembly upon light illumination of the individual GUV. Similar to the use of caged-ATP or light-sensitive *E. coli* this gives us a handle on the control of the dynamics within the compartments. Next, we showcase the broad and easy applicability of our DNA cytoskeletons by binding them to the GUV membrane from within using DNA linkers. Note that if we would only rely on the use of proteins to, e.g., bind actin to the GUV membrane this would require dozens of proteins [127]. Thereby, we generate a cortex-like DNA cytoskeleton that also determines the GUV shape upon deflation. In this regard, it would be exciting to see if one could also engineer mechanisms for the active deformation of GUVs, like protrusions, that are independent of vesicle deflation.

Finally, we achieved the alignment of DNA filaments into thick and rigid bundles due to the molecular crowding effect. The DNA bundles consist out of hundreds of DNA filaments, are longer than individual filaments and have a higher persistence length. The successful generation of functional DNA structures with this size is remarkable and reminds of other microscale DNA architectures [128]. By tuning

the persistence length, the DNA bundles even align along the membrane in ring-like shapes, which resemble the cytokinetic ring during cell division [129]. However, as before, the current lack of efficient DNA-based motors to generate sufficient forces for the sliding, i.e. contraction of these bundles presents a boundary for their further integration towards diving a synthetic cell with DNA bundles. By improving already existing DNA origami sliders [130, 131], it might be conceivable that these could be used to deform GUVs and ultimately lead to fission of the GUV membrane.

Before we can connect the division to an interior cytoskeleton, we therefore have to find different ways to divide GUVs. That is why we established a mechanism to divide GUVs based on lipid phase separation and osmotic deflation (Publication 8). To integrate stimuli-responsiveness, we also developed the concept of osmotic deflation upon light-triggered uncaging of bis-(5-carboxymethoxy-2-nitrobenzyl) ether (CMNB)-fluorescein, which allows to locally trigger the division of a selected GUV. In this regard, our developed GUV division mechanism also overcomes other concepts based on the division due to changes in the spontaneous curvature of the membrane, which cannot be triggered locally [132]. However, it remains an open but exciting challenge on how to connect the deformation and division of GUVs to the contraction of a DNA-based cytoskeleton.

All in all, we have developed multi-functional DNA cytoskeletons that can not only mimic features of natural cytoskeletons but can, in principle, even go beyond their natural counterparts. They possess programmable and biocompatible characteristics that can be used to engineer versatile functions within synthetic cells. In the future, it will be especially exciting to equip the DNA-based cytoskeletons with molecular motors to achieve the active force generation and contraction inside confinement. With this in my mind, DNA cytoskeletons are a powerful addition to the toolbox for engineering synthetic cells from the bottom-up and provide the potential for assembling a fully-functional synthetic cell only consisting of de novo assembled building blocks.

### 4.2.3 DNA as a tool to study biophysics

So far we have discussed how the engineered natural and synthetic cytoskeletons can be used for bottom-up synthetic biology. However, we have actually also engineered functional tools to study basic biophysics of cells.

In Publication 1 we have seen how shape deformation and control over morphology can be used to study the membrane-to-cortex attachment of natural cells. By designing DNA cytoskeletons - either DNA origami or DNA filaments - that can deform GUVs we have thus also engineered a tool to control membrane rigidity, shape and induce membrane curvature. This makes it a very easy-to-use and versatile device to study biophysical properties of cells. The easy possibility to functionalize DNA nanostructures also allows to decorate them with antibodies or relevant molecules for specific biological processes. This has already been applied to study and control the activity of specific cell receptors using the defined spatial arrangement of antibodies on DNA origami structures [133]. Moreover, the linkage of DNA nanotubes to specific receptor sites on cells proves to be promising to engineer biomolecular devices and also to measure stresses on cells [134]. Additionally, already the designed

DNA linkers to bind the cytoskeletons to the membrane can be used to control cell adhesion and migration [135]. Going one step further, the transfer of DNA origami functionalities onto RNA origami might even lead to the cotranscriptional folding of RNA origami inside the cytosol by themselves [136]. This would lead the cell to autonomously generate a tool that could be used for biophysical studies.

### 4.3 Natural versus synthetic cytoskeletons

In the present PhD thesis we have engineered natural and synthetic cytoskeletons for their use in bottom-up synthetic biology. Even though both types of cytoskeletons resemble each other in terms of their functions, there are fundamental differences in their respective building blocks. The main difference is that natural cytoskeletons, i.e. actin in this case consist of proteins, which themselves are made up of hundreds of amino acids that fold into a quaternary structure. Their design and folding is therefore very complex which makes it difficult to predict and engineer proteins. Recent progress in the prediction of protein folding, however, may benefit the cause of engineering natural cytoskeletons from the bottom-up [137]. Moreover, cytoskeletal proteins cannot be synthesized, which bears the need of purifying them from natural cells. This process itself is time-consuming, not a hundred percent exact and often impossible. On the other hand, the building blocks of DNA cytoskeletons are only made up of single DNA strands that contain four nucleobases. They can be synthesized, functionalized and their folding predicted [138]. This helps the cause of engineering functional structures. In addition, the encapsulation of DNA nanostructures into GUVs is straightforward due to their superior stability over proteins. However, advances in the field of GUV formation methods, may make this negligible as they have shown high encapsulation efficiencies for proteins and especially actin filaments [118].

Another key advantage of the use of proteins over DNA is their efficiency when it comes to catalytic functionalities. The forces generated by a molecular motor like myosin are thus still orders of magnitude higher than the one of any DNA nanostructure. That being said, there are increasing efforts for the development of DNA-based motors to overcome these limitations. However, for these reasons most functions that require force generation are still more efficient with using molecular motors (as we have also seen in Publication 1, 3, 4 and 6). On the contrary, the huge toolbox of DNA nanotechnology offers great potential for the design of static nano- and microstructures that can be functionalized in an easy and versatile way. To summarize, it became clear that it is easier to actively engineer multiple functions in synthetic cytoskeletons compared to natural ones. However, current limitations in terms of force generation still suggest the use of natural motors for specific purposes. With the aim of creating a fully-synthetic cell without any natural components, it will be exciting to see which solutions will arise for synthetic motors in order to benefit the cause of engineering a synthetic cell from the bottom-up.

# Chapter 5

## Summary

In the present PhD thesis, we have engineered multifunctional cytoskeletons for the bottom-up construction of synthetic cells. For this purpose, we reconstituted natural actin filaments and myosin motors to induce GUV deformation, droplet motility and symmetry-breaking contraction. Thereby, it became clear that it is essential, yet difficult, to also find means to successfully encapsulate natural cytoskeletons inside physiologically more relevant GUVs. Surprisingly, we achieved the establishment of sophisticated functions by only relying on two proteins. However, the addition of more functions would require the addition of more proteins. Since protein purification is difficult, we developed a strategy to assemble synthetic DNA-based cytoskeletons. Additionally, it is conceptually interesting to build materials with protein-like functionality from entirely different chemical constituents.

By using DNA origami structures that can bind to the GUV membrane and polymerize into even larger sheets, we achieved the sculpting and suppression of membrane fluctuations of GUVs. Moreover, by including genetically-modified *E. coli*, the DNA origami can attach to the membrane following a light-induced pH change. In this regard, we also investigated the pH-sensitive triplex motif and found that its conformation is significantly influenced by the choice of fluorophore. However, even though we have integrated cytoskeletal function i.e. the control over cell morphology into synthetic DNA-based structures, we could not achieve this function inside GUVs due to low assembly yield of DNA origami and missing ways to encapsulate sufficient amounts. Therefore, we investigated DNA nanotubes (termed DNA filaments) that consist of only five single strands as a more versatile cytoskeleton mimic.

Having verified the successful encapsulation and assembly of DNA filaments inside water-in-oil droplets and GUVs, we implemented versatile functions in them. These include the stimuli-responsive reversible assembly (aptamers, nucleic acids, light), bundling, GUV deformation and intracellular transport. We therefore presented a programmable, easy-to-encapsulate, powerful and fully synthetic alternative to the use of natural cytoskeletons for engineering synthetic cells. Nevertheless, it remains a challenge to induce active force generation using DNA structures. In order to couple cytoskeletal features to the compartment division - as a main function of natural cytoskeletons - we need more powerful DNA motors.

To provide a shortcut towards the aim of compartment division, we implemented a different approach for the division of GUVs based on lipid phase-separation and



osmotic deflation. We show that we can use evaporation, an enzyme- or light-mediated osmotic increase to divide GUVs. Ultimately, we envision to couple the division process, e.g. at the phase boundary, to DNA cytoskeletons via the ring-like DNA bundles presented in this work.

All in all, we have shown versatile ways to rationally engineer multifunctional natural and synthetic cytoskeletons for synthetic cells. It became clear that natural cytoskeletons provide many advantages when it comes to active force generation, however, DNA cytoskeletons are a strong competitor because of their programmable, sophisticated and versatile engineerable characteristics. This work therefore paves the way for the assembly of more complex and potentially fully-synthetic cells with multifunctional cytoskeletons from the bottom-up.

# Appendix A

## Supporting Information

### A.1 Supporting Information for Publication 1: Actomyosin-assisted pulling of lipid nanotubes from lipid vesicles and cells

# **Supporting Information: Acto-myosin-assisted pulling of lipid nanotubes from lipid vesicles and cells**

Kevin Jahnke<sup>1,2</sup>, Stefan J. Maurer<sup>1,2</sup>, Cornelia Weber<sup>3</sup>, Jochen Estebano  
Hernandez Bücher<sup>3</sup>, Andreas Schoenit<sup>1</sup>, Elisa D'Este<sup>4</sup>, Elisabetta Ada  
Cavalcanti-Adam<sup>3</sup>, Kerstin Göpfrich<sup>1,2\*</sup>

<sup>1</sup>Biophysical Engineering Group, Max Planck Institute for Medical Research,  
Jahnstraße 29, D-69120 Heidelberg, Germany

<sup>2</sup>Department of Physics and Astronomy, Heidelberg University,  
D-69120 Heidelberg, Germany

<sup>3</sup>Department of Cellular Biophysics, Max Planck Institute for Medical Research,  
Jahnstraße 29, D-69120 Heidelberg, Germany

<sup>4</sup>Optical Microscopy Facility, Max Planck Institute for Medical Research,  
Jahnstraße 29, D-69120 Heidelberg, Germany

\*

E-mail: kerstin.goepfrich@mr.mpg.de

# Contents

<b>1</b>	<b>Experimental Methods</b>	<b>5</b>
1.1	Confocal fluorescence microscopy . . . . .	5
1.2	Actin polymerization . . . . .	5
1.3	Heavy meromyosin purification . . . . .	6
1.4	Polyacrylamide gel electrophoresis . . . . .	6
1.5	<i>In vitro</i> motility assay . . . . .	6
1.6	Particle image velocimetry analysis . . . . .	7
1.7	Velocity correlation length calculation . . . . .	8
1.8	Analysis of actin filament velocity . . . . .	8
1.9	GUV formation . . . . .	9
1.10	Pulling lipid nanotubes from GUVs . . . . .	9
1.11	STED microscopy . . . . .	10
1.12	Analysis of lipid nanotube networks for GUVs . . . . .	10
1.13	Cell culture . . . . .	10
1.14	Cell staining . . . . .	11
1.15	Pulling lipid nanotubes from cells . . . . .	11
1.16	Analysis of lipid nanotube networks for cells . . . . .	12
1.17	Statistical analysis . . . . .	12
1.18	Data availability . . . . .	13
<b>2</b>	<b>Supporting Figures</b>	<b>14</b>
	Supporting Figure S1: SDS-PAGE of HMM and actin . . . . .	14
	Supporting Figure S2: Aligned actin filaments can form swirls . . . . .	15
	Supporting Figure S3: 2D- and 3D-STED reveals the tubular structures of lipid nanotubes . . . . .	16
	Supporting Figure S4: Total number of lipid nanotube branches pulled from GUVs	17

Supporting Figure S5: Unspecific interaction of actin and DOPC bilayers in presence of divalent ions . . . . .	18
Supporting Figure S6: Nanotube networks for different lipid compositions . . . . .	19
Supporting Figure S7: Encapsulated dye permeates into lipid nanotubes of GUVs	20
Supporting Figure S8: Self-assembly of cholesterol-PEG into membranes of different cell types . . . . .	21
Supporting Figure S9: GUVs and cells show little to no movement during the lipid nanotube pulling assay . . . . .	22
Supporting Figure S10: Actin filaments are present within lipid nanotubes pulled from cells . . . . .	23
Supporting Figure S11: Characterization of actin filaments extending into lipid nanotubes . . . . .	24
Supporting Figure S12: Mitochondria and lysosomes do not enter lipid nanotubes of Jurkat cells . . . . .	25
Supporting Figure S13: HaCaT cells do not form lipid nanotubes . . . . .	26
<b>3 Supporting Videos</b>	<b>27</b>
Supporting Video S1: Time series of random actin filaments . . . . .	27
Supporting Video S2: Time series of aligned actin filaments . . . . .	27
Supporting Video S3: Time series of aligned actin filament patterns . . . . .	27
Supporting Video S4: Time series of lipid nanotube dynamics after pulling from GUVs . . . . .	27
Supporting Video S5: Time series of lipid nanotube pulling from Jurkat cells . . .	28
Supporting Video S6: Displacement over time of a Jurkat cell during lipid nanotube pulling . . . . .	28
Supporting Video S7: Displacement over time of a GUV during lipid nanotube pulling . . . . .	28

Supporting Video S8: 3D projection of Jurkat cells with random actin and biotinylated cholesterol . . . . .	28
Supporting Video S9: 3D projection of Jurkat cells with aligned actin and biotinylated cholesterol . . . . .	29
Supporting Video S10: 3D projection of Jurkat cells with random actin and no biotinylated cholesterol . . . . .	29
Supporting Video S11: 3D projection of Jurkat cells with aligned actin and no biotinylated cholesterol . . . . .	29
Supporting Video S12: Actin filament dynamics during lipid nanotube pulling of a Jurkat cell (DOPE-Atto488) . . . . .	29
Supporting Video S13: Actin filament dynamics during lipid nanotube pulling of a Jurkat cell (SiR-actin) . . . . .	30
<b>References</b>	<b>30</b>

# 1 Experimental Methods

## 1.1 Confocal fluorescence microscopy

A confocal laser scanning microscope LSM 880 or LSM 900 (Carl Zeiss AG) was used for confocal imaging. The pinhole aperture was set to one Airy Unit and the experiments were performed at room temperature. The images were acquired at RT or 30 °C using a 63× oil immersion objective (Plan-Apochromat 63×/1.4 Oil DIC M27). Images were analyzed and processed with ImageJ (NIH, brightness and contrast adjusted).

## 1.2 Actin polymerization

Actin from New Zealand white rabbit skeletal muscle was purified from acetone powder based on the method of Pardee and Spudich,<sup>1</sup> modified after Kron *et al.*<sup>2</sup> To form actin filaments, we mixed the actin monomers 1/10 with the standard working buffer named 10× Actin Buffer (AB, containing 250 mM imidazol-HCl, 250 mM KCl, 10 mM EGTA, 40 mM MgCl<sub>2</sub>, pH 7.4) and 1/10 APB 10× Actin Polymerization Buffer (APB, 20 mM Tris-HCl, pH 8, 500 mM KCl, 20 mM MgCl<sub>2</sub>, 10 mM Na<sub>2</sub>ATP), to make a 20 μM actin stock. The actin/APB mix was left at RT to polymerize for 20-30 min. Subsequently, 8 units of rhodamine-phalloidin (from Invitrogen dissolved in MeOH) were added to stabilize the actin filaments after evaporating half the volume of methanol. Biotinylated actin bFa: G-actin monomers were mixed in a ratio of 10:1 with biotinylated G-actin (Cytoskeleton, Cat #AB07) and left to polymerize as described before after addition of 10 μL vaporized rhodamin-phalloidin (8 units) to the 20 μL actin mix. Biotinylated actin was aliquoted and stored at −80 °C until use. Unlabeled F-actin FA: G-actin monomers (5 mg/ml) were mixed in AB<sub>DTT</sub> buffer (standard working buffer supplemented with 20 mM DTT) and 1/10 of APB. The solution was left to polymerize for 30 min at RT and then kept on ice. Directly before use, the solution was diluted to 1 mg/mL in AB<sub>GOC</sub> (AB supplemented with 3 mg/ml glucose, 0.1 mg/mL glucose oxidase, 0.02 mg/mL catalase and 20 mM DTT).

### 1.3 Heavy meromyosin purification

Myosin isolated from New Zealand white rabbit skeletal muscle was used to prepare HMM based on the method of Margossian and Lowey.<sup>3</sup> To obtain a highly functional motor driven motility, we first remove non-functional myosin heads (rigor heads) *via* an actin affinity purification.<sup>4</sup> In short, the myosin motor fragments (heavy meromyosin, HMM) are mixed with actin filaments and MgATP in solution, followed by ultracentrifugation at  $1 \times 10^5$  g to pellet any MgATP insensitive motors together with the actin filaments. The high functional HMM then is supplemented with 20 % sucrose and will be stored at  $-80^\circ\text{C}$  until use.

### 1.4 Polyacrylamide gel electrophoresis

Samples of protein were electrophoresed on a precast gradient SDS-PAGE of 4-12 % bis-tris gel (1 mm, NuPage, Invitrogen) according to the Invitrogen protocol. For HMM 5  $\mu\text{g}$  protein were loaded per lane and for actin 1-7  $\mu\text{g}$  protein. The gel was run for 50 min at 200 V. After the electrophoresis the gel was stained for 30 min with the colloidal Coomassie stain ReadyBlue (Sigma-Aldrich). Imaging was performed with the Azure 600 (Azure Biosystems).

### 1.5 *In vitro* motility assay

A thin glass slide (24 x 60 mm<sup>2</sup>, Menzel) was washed with isopropanol in an ultrasonic bath and dried afterwards. Subsequently, they were dip-coated with 0.3 % nitrocellulose solved in amylacetate and allowed to dry overnight. A second coverslip (18 x 18 mm<sup>2</sup>, Menzel) was placed on the top of the coated glass slide spaced with two stripes of a double-sided sticky tape (tesa SE, Germany) to form a flow cell chamber FC with 0.1 mm gap and 15  $\mu\text{L}$  volume. The standard working solution (called AB) was prepared as a 10x concentrated stock solution made of (250 mM imidazole-HCl, 250 mM KCl, 10 mM EGTA, 40 mM MgCl<sub>2</sub>, pH 7.4). Aliquots of 1 ml were stored in  $-20^\circ\text{C}$ . On the day of the experiment the 10x AB stock solution was thawed and the respective supplements were added. We used double



concentrated AB solutions to match the osmotic conditions of GUVs. To minimize the contamination with atmospheric oxygen the mixed solutions were degassed in a vacuum exicator for at least 20 min in the cold room. HMM solution ( $200 \mu\text{g L}^{-1}$ ) was infused and immobilized in the flow cell. After two minutes the unbound HMM was washed off with 2x AB containing 20 mM dithiothreitol (DTT,  $\text{AB}_{\text{DTT}}$ ) and then the liquid was exchanged by 2x AB supplemented with bovine serume albumin (BSA) ( $0.5 \text{ mg/mL}$ ,  $\text{AB}_{\text{BSA}}$ ). The BSA is incubated for two minutes to block binding of labeled actin to the nitrocellulose surface of the coverslip. The flow cell was then washed with 2x  $\text{AB}_{\text{DTT}}$ . For aligned actin filaments, F-actin solution ( $1 \text{ mg/mL}$  in  $\text{AB}_{\text{GOC}}$ ) was washed in the flow cell for another two minutes. Unbound F-actin was removed with 2x  $\text{AB}_{\text{DTT}}$  followed by a wash with 2x  $\text{AB}_{\text{GOC}}$  (AB supplemented with  $3 \text{ mg/ml}$  glucose,  $0.1 \text{ mg/ml}$  glucose oxidase,  $0.02 \text{ mg/ml}$  catalase,  $20 \text{ mM}$  DTT). GOC substances prevent oxidative stress and photobleaching. The ATP-containing solution termed  $\text{AB}_{\text{MC}}$  was supplemented with  $5 \text{ mM}$  MgATP, GOC, DTT and  $0.3 \%$  methylcellulose (MC). MC was purchased from Sigma Aldrich ( $4000 \text{ cP}$  viscosity at  $2 \%$  w/v and a molecular weight of about  $500 \text{ kDa}$ ). Finally, the flow cell was flushed with the GUV or the cell mixture in the respective experiments.

## 1.6 Particle image velocimetry analysis

The background of timelapse videos was subtracted. Therefore, the minimal intensity of the stack was projected and then subtracted using the Calculator Plus plugin in Fiji. Furthermore, images were rotated in a way that actin filaments move from left to right. The individual images of the stack were loaded into JPIV (<https://eguvep.github.io/jpiv/index.html>) run in a Python environment. To obtain the vector field, particle image velocimetry was performed on consecutive images using first a  $64 \times 64$  and then a  $16 \times 16$  pixel interrogation window with a final vector spacing of  $8 \times 8$  pixel. The vector fields were batch-filtered by performing a normalized median test and a median filter, where all invalid vectors were excluded. These invalid vectors were replaced by the median to obtain the final vector field.

## 1.7 Velocity correlation length calculation

A custom-written Python script was used to format the JPIV data for further processing. The velocity correlation length of the actin fibers was calculated in MATLAB using a script described elsewhere.<sup>5,6</sup> In brief, the displacement vectors were divided by the time difference between the two images from which they were generated, resulting in the velocity vector  $\mathbf{r}_{i,j}$ , which was assigned to the central coordinate (i,j) of each 8x8 window. Since the axial movement is the dominant direction in the described experimental setup, only the lateral component  $\mathbf{U}_{i,j}$ , perpendicular to the movement direction was used to calculate the velocity fluctuations  $\mathbf{u}_{i,j}$  as:

$$\mathbf{u}_{i,j} = \mathbf{U}_{i,j} - \sum_{i=1,m} \sum_{j=1,n} \frac{\mathbf{U}_{i,j}}{m \times n} = \mathbf{U}_{i,j} - \mathbf{U}_{\text{mean}}$$

$\mathbf{U}_{\text{mean}}$  is the mean velocity. The lateral correlation function  $\mathbf{C}_r$  was calculated as:

$$\mathbf{C}_r = \frac{\langle \mathbf{u}(r') * \mathbf{u}(r' + r) \rangle_{r'}}{\sqrt{\langle \mathbf{u}(r')^2 \rangle * \langle \mathbf{u}(r' + r)^2 \rangle}}$$

$\langle \dots \rangle$  is the average and  $r = \|\mathbf{r}_{i,j}\|$  is the norm of  $\mathbf{r}_{i,j}$ . The first crossing of the threshold 0.01 with the lateral correlation function  $\mathbf{C}_r$  was defined as the velocity correlation length.

## 1.8 Analysis of actin filament velocity

Moving actin filaments were recorded as a time-lapse and tracked using ImageJ plugins: A classifier in the Trainable Weka Segmentation plugin<sup>7</sup> was trained to detect filaments and create a binary map of well defined particles against the background. This improves the ability of the Trackmate plugin<sup>8</sup> to correctly identify, track and return the trajectories of the individual particles. For each trajectory the magnitude of the average velocity vector and the orientation, *i.e.* the argument of the end-to-end vector were calculated. To display the data in a rose plot the trajectories were binned first by their argument and then within

these bins by the magnitude of their average velocity vector. The rose plots were generated using the plotly library (v4.14.3) for python (v3.7.4).

## 1.9 GUV formation

Giant unilamellar vesicles were prepared using the electroformation method<sup>9</sup> using a VesiclePrepPro device (Nanion Technologies GmbH). 40  $\mu\text{L}$  of 5 mM lipid mix (containing 99 % 1,2-dioleoyl-sn-glycero-3-phosphocholine (DOPC) and 1 % 1,2-dioleoyl-sn-glycero-3-phosphoethanolamine-Atto488 (Atto488-PE)) in  $\text{CHCl}_3$  were homogeneously spread on the conductive side of an indium tin oxide (ITO) coated glass slide (Viontek Systems Ltd). After evaporating the chloroform for 20 min under vacuum, a rubber ring was placed on the lipid-coated ITO slide and filled with 275  $\mu\text{L}$  of 300 mM sucrose solution to match the osmolarity of the double-concentrated AB buffer. The second ITO slide was put on top and the chamber connected to the electrodes of the VesiclePrepPro. An AC field (3 V, 5 Hz) was applied *via* the electrodes for 138 min while the solution was heated to 37 °C. GUVs were collected immediately after electroformation and stored at 4 °C for up to 7 days.

## 1.10 Pulling lipid nanotubes from GUVs

In order to pull lipid nanotubes from GUVs, 10  $\mu\text{L}$  biotinylated GUVs were incubated for 1 min with 2  $\mu\text{L}$  streptavidin (final concentration 90 nM, Sigma Aldrich) and 0.4  $\mu\text{L}$  biotinylated F-actin filaments (bFa\*, final concentration 20 nM). Subsequently, they were mixed with 3.1  $\mu\text{L}$  methylcellulose (final concentration 0.31 w/v%), 1  $\mu\text{L}$  MgATP (final concentration 5 mM) and 3.5  $\mu\text{L}$   $\text{AB}_{\text{MC}}$ . Afterwards the solution was flushed immediately into the flow cell, which was sealed with two-component glue.

### 1.11 STED microscopy

Lipid nanotubes were imaged on an Abberior expert line (Abberior Instruments GmbH, Germany) with a pulsed STED line at 775 nm using an excitation laser at 640 nm and spectral detection. The detection window was set between 650–750 nm to detect Atto633-labeled lipid nanotubes. Images were acquired with a 100×/1.4 NA magnification oil immersion lens (Olympus). The pixel size was set to 15-18 nm and the pinhole was set to 0.8 AU for 2D-STED and to 0.6 AU for 3D-STED. Images were analyzed and processed with ImageJ (NIH, brightness and contrast adjusted).

### 1.12 Analysis of lipid nanotube networks for GUVs

GUVs and nanotubes were classified separately using two different classifiers in the trainable Weka Segmentation plugin. In the segmented image the individual GUVs (imaged cross-sectional area larger than  $6\ \mu\text{m}^2$ ) are then counted and the nanotubes skeletonized, *i.e.* reduced to one-dimensional branches, whose individual lengths can be determined using the Analyze Skeleton plugin. For each micrograph, the sum of all branch lengths, *i.e.* the network length is calculated, omitting branches smaller than  $10\ \mu\text{m}$  to exclude artefacts. The network length is divided by the respective number of GUVs to obtain the normalized network length per GUV for one micrograph, from which the average and standard deviation displayed in the text were calculated.

### 1.13 Cell culture

Jurkat cells (clone E6.1) were cultured in suspension in Roswell Park Memorial Institute 1640 Medium supplemented with GlutaMax<sup>TM</sup>, (RPMI 1640, ThermoFisher Scientific) 1 % penicillin/streptomycin (ThermoFisher Scientific) and 10 % fetal bovine serum (Sigma Aldrich) at 37°C and 5 % CO<sub>2</sub> atmosphere. Cells were passaged by transferring 10 ml of cell suspension to 30 ml of fresh cell culture medium every 2-3 days. HaCaT and NIH3T3 cells were cul-

tured in Dulbecco's Modified Eagle Medium supplemented with GlutaMax<sup>TM</sup> (DMEM, ThermoFisher Scientific), 1 % penicillin/streptomycin and 10 % fetal bovine serum or 10 % FBS South American HI (ThermoFisher Scientific) at 37 °C and 5 % CO<sub>2</sub> atmosphere and passaged at approximately 80 % confluency by 0.05 % trypsin/EDTA treatment. J774A.1 macrophages were cultured in Dulbecco's Modified Eagle Medium supplemented with GlutaMax<sup>TM</sup> and 10 % fetal bovine serum at 37 °C and 5 % CO<sub>2</sub> atmosphere. Subcultures were prepared by scraping and transferring 10 ml of cell suspension to 30 ml of fresh cell culture medium every 3-4 days. Approximately 250 000 cells/ml were used for the experiments.

### **1.14 Cell staining**

For the staining of the plasma membrane Wheat Germ Agglutinin conjugates (Thermo Fisher Scientific) were added at a final concentration of 10 µg/ml to the respective cells. In order to stain the actin filament a final concentration of 10 µM verapamil and 1 µM SiR-Actin (SpiroChrome) was added to the cells. Nih3T3 fibroblasts were treated with a final concentration of 0.2 µg mL<sup>-1</sup> Latrunculin A (Enzo Life Sciences) and incubated for 1 h. For the co-culture experiments Jurkat cells were either stained with CellTracker blue CMHC<sup>TM</sup> (ThermoFisher Scientific), at final concentration of 20 µg/ml, or Wheat Germ Agglutinin Alexa Fluor<sup>TM</sup> 647 conjugate as described above. In order to evaluate the cell viability propidium iodide (ThermoFisher Scientific) was added at a final concentration of 1.5 ng/ml to the Jurkat cell suspension. Lysosomes were stained using LysoTracker Green DND-26 (ThermoFisher Scientific) at a final concentration of 75 nM. For the staining of mitochondria MitoTracker FM green (ThermoFisher Scientific) was added at a final concentration of 500 nM to the cells.

### **1.15 Pulling lipid nanotubes from cells**

Lipid nanotubes were pulled from cells at comparable cell densities around  $1 \times 10^6$  cell/ml. 98.5 µL of the cell suspension in medium was incubated for 10 min with 1 µL cholesterol-

PEG-biotin (10 mM, Nanocs) and 0.5  $\mu$ L membrane staining wheat germ agglutinin conjugated with Alexa488 (WGA-Alexa488). After the incubation, 5  $\mu$ L of the suspension was mixed with 2  $\mu$ L bFa\* (final concentration 100 nM), 1  $\mu$ L streptavidin (final concentration 910 nM), 1  $\mu$ L MgATP (final concentration 5 mM), 3.1  $\mu$ L methylcellulose (final concentration 0.31 s/v% and 7.9  $\mu$ L AB<sub>MC</sub>). Afterwards the solution was flushed immediately into the flow cell, which was sealed with two-component glue.

To test the self-assembly of cholesterol-PEG into the cell membrane, we incubated 99  $\mu$ L of the cell suspension for 10 min with 1  $\mu$ L Chol-PEG-FITC (10 mM, Nanocs).

## 1.16 Analysis of lipid nanotube networks for cells

Micrographs containing several cells were cropped, so that one image contains only a single cell. The trainable Weka Segmentation classifier was trained to separate protrusions extending into the periphery of the cell from the cell itself and the background. For each cell type, an individual classifier was trained. Again, the branch lengths of the lipid nanotubes were determined by skeletonization. For the branches a cut-off of 2.5  $\mu$ m was chosen to only consider nanotubes and no natural cell protrusions like lamellipodia. For each cell the network length was determined and the averages and standard deviations were calculated for each cell type.

## 1.17 Statistical analysis

All the experimental data is reported as mean  $\pm$  SD from n experiments. The respective value for n is stated in the corresponding figure captions. All experiments were repeated at least twice. To analyze the significance of the data, a Student's t-test with Welch's correction was performed using Prism GraphPad (Version 9.1.2) and p-values correspond to \*\*\*\*:  $p \leq 0.0001$ , \*\*\*:  $p \leq 0.001$ , \*\*:  $p \leq 0.01$ , \*:  $p \leq 0.05$  and ns:  $p \geq 0.05$ .

## **1.18 Data availability**

The datasets generated during and analyzed during the current study are available from the corresponding author on reasonable request.

## 2 Supporting Figures

### Supporting Figure S1: SDS-PAGE of HMM and actin

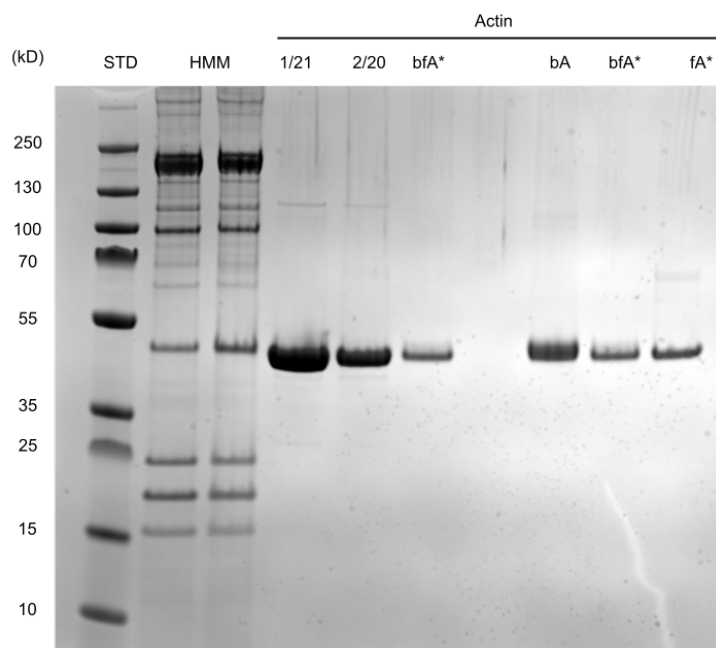


Figure S1: Denaturing polyacrylamide gel electrophoresis (SDS-PAGE) of HMM and actin after purification. HMM: The strong band at 225 kDa indicates the successful HMM purification including the light chains between 15 and 25 kDa. The actin band at 42 kDa results from remnants of the actin affinity purification. Actin: All actin samples show a strong band at 42 kDa. These include two batches of purified actin (1/21 and 2/20) used for this study, polymerized biotinylated actin filaments (bfA<sup>\*</sup>), pure biotinylated actin monomers (bA) and polymerized actin filaments without biotin (fA<sup>\*</sup>).



## Supporting Figure S2: Aligned actin filaments can form swirls

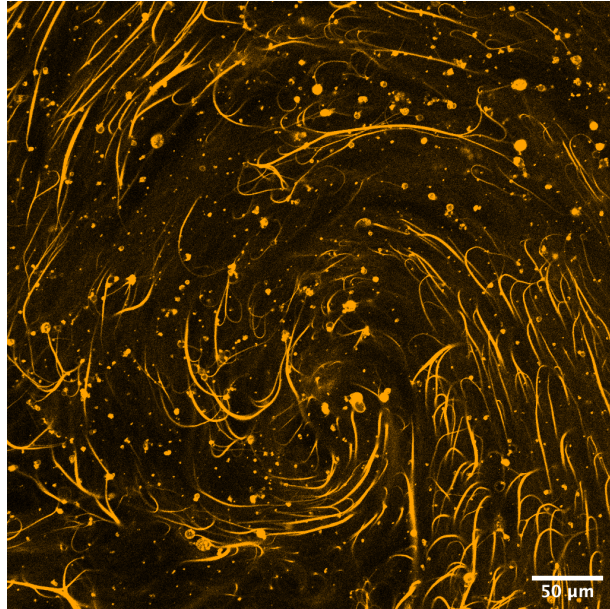


Figure S2: Aligned actin filaments can form swirls. Confocal image of aligned actin filaments (labeled with Rhodamine B,  $\lambda_{ex} = 561$  nm) after 1 h of incubation. Occasionally, aligned actin filaments form swirl-like patterns such that the global direction of the motion is changing.<sup>10</sup> Scale bar: 50  $\mu\text{m}$ .

## Supporting Figure S3: 2D- and 3D-STED reveals the tubular structures of lipid nanotubes

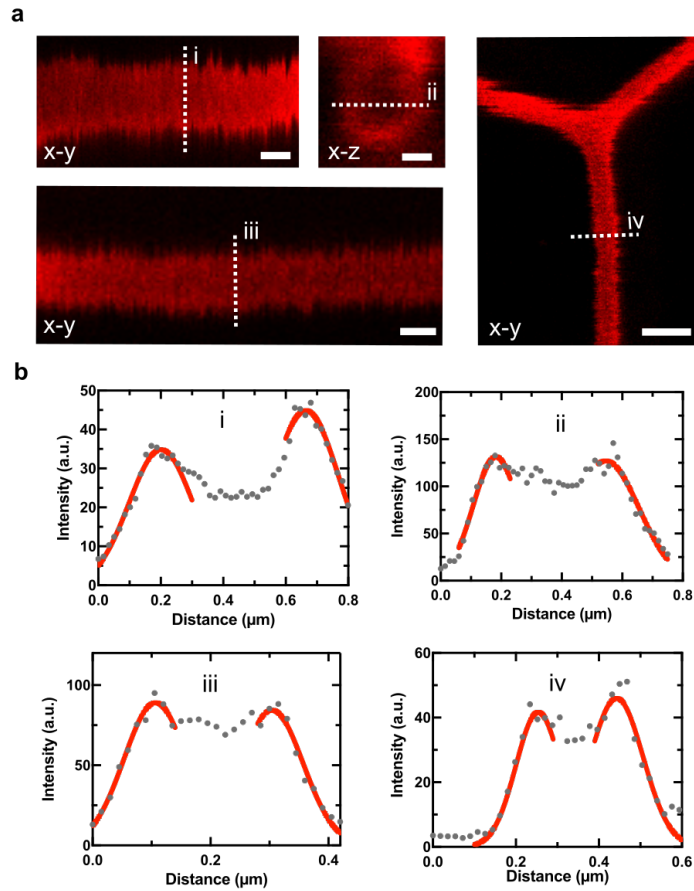


Figure S3: 2D- and 3D-STED reveals the tubular structures of lipid nanotubes. **a** 2D- and 3D-STED images of lipid nanotubes pulled from GUVs (membrane labeled with DOPE-Atto633,  $\lambda_{ex} = 640$  nm) depict the hollow tubular structure of lipid nanotubes. Scale bars: i, ii, iii - 200 nm, iv - 500 nm. **b** Line profiles (pixel width: 18 nm) across lipid nanotubes as indicated in **a**. The intensity profiles were fitted with gaussian fits at the position of the bilayer, which reveal lipid nanotube diameters of 463 nm (i), 362 nm (ii), 197 nm (iii) and 189 nm (iv), which were calculated as the difference of the position of the gaussian fit maxima.

**Supporting Figure S4: Total number of lipid nanotube branches pulled from GUVs**

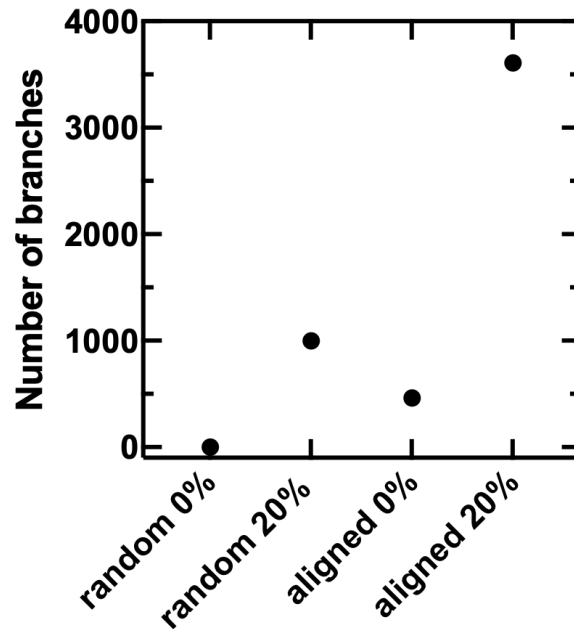


Figure S4: Total number of lipid nanotube branches pulled from GUVs. The number of branches (edge connecting two nodes of a network) increases with the presence of 20% biotinylated lipids and is generally higher for aligned actin filaments. The high amount of branches for 0% biotinylated lipids and aligned filaments can be attributed to the high amount of unlabelled F-actin present in the assay to induce the alignment which promotes unspecific interactions of actin filaments with the GUV membrane. This may be enhanced by the presence of divalent ions in the final buffer.<sup>11</sup>

## Supporting Figure S5: Unspecific interaction of actin and DOPC bilayers in presence of divalent ions

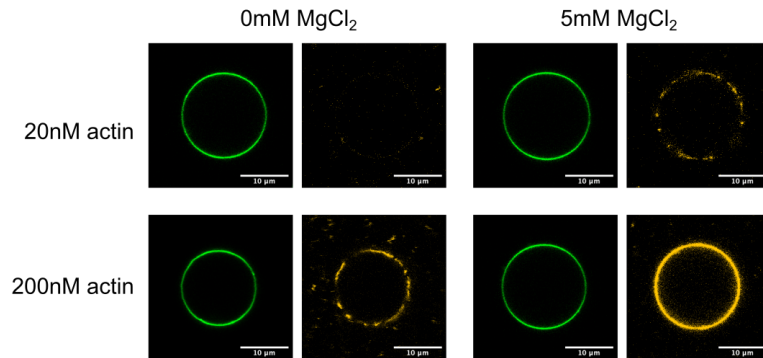


Figure S5: Unspecific interaction of actin and DOPC bilayers in presence of divalent ions. Confocal images of giant unilamellar vesicles (green, membrane labeled with DOPE-488,  $\lambda_{ex} = 488$  nm) in presence of 0 or 5 mM MgCl<sub>2</sub> and 20 or 200 nM filamentous actin (orange, labeled with rhodamine,  $\lambda_{ex} = 561$  nm), respectively. As visible in the confocal images divalent ions increase the amount of unspecific actin filament binding to the GUV membrane. Additionally, high actin concentrations lead to interactions with the membrane. This explains the presence of lipid nanotubes for aligned actin filaments and GUVs containing 0% biotinylated lipids. Scale bar: 10  $\mu$ m.

## Supporting Figure S6: Nanotube networks for different lipid compositions

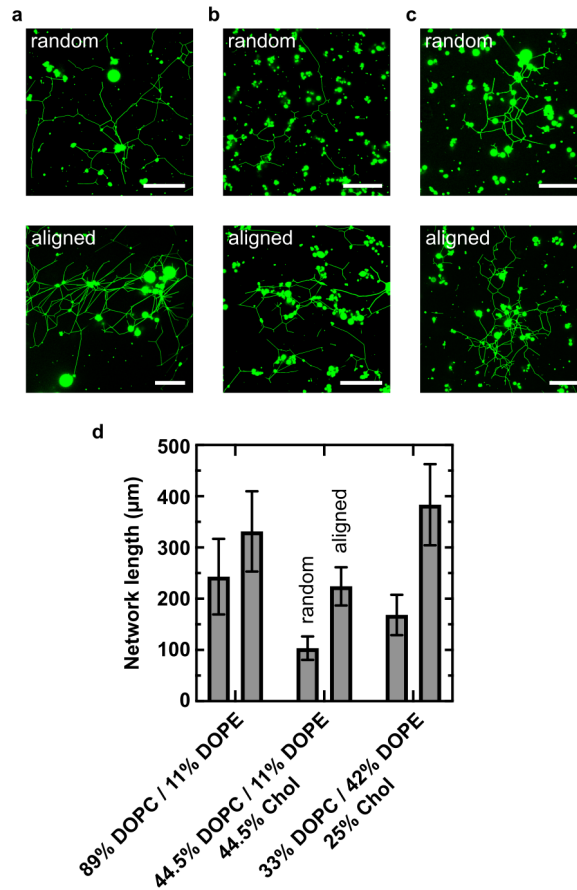


Figure S6: Nanotube networks can be achieved for biotinylated GUVs with different lipid compositions for random and aligned actin filaments. **a** 89% DOPC, 11% DOPE; **b** 44.5% DOPC, 11% DOPE, 44.5% cholesterol; **c** 33% DOPC, 42% DOPE, 25% cholesterol. Scale bar: 40 μm. **d** Mean network length (sum of all branch lengths belonging to one network) with standard error of mean for different lipid compositions. For all conditions, the network length is on average larger when aligned actin filaments (right bar, respectively) are used compared to random filaments (left bar, respectively). Furthermore, the lipid composition seems to influence the network length, whereby increased cholesterol content leads to a decrease in the network length.

## Supporting Figure S7: Encapsulated dye permeates into lipid nanotubes of GUVs

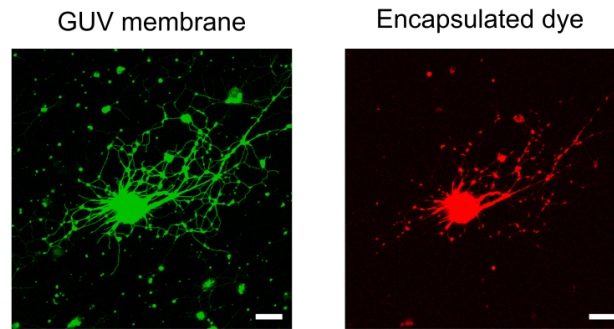


Figure S7: Encapsulated dye permeates into lipid nanotubes of GUVs. Confocal images of a GUV (membrane labeled with Atto488-DOPE,  $\lambda_{ex} = 488$  nm) with an encapsulated dye (Alexa Fluor 647-NHS ester,  $\lambda_{ex} = 640$  nm). After nanotube formation the encapsulated dye is also visible within the lipid nanotubes. Scale bar: 20  $\mu$ m.

Supporting Figure S8: Self-assembly of cholesterol-PEG into membranes of different cell types

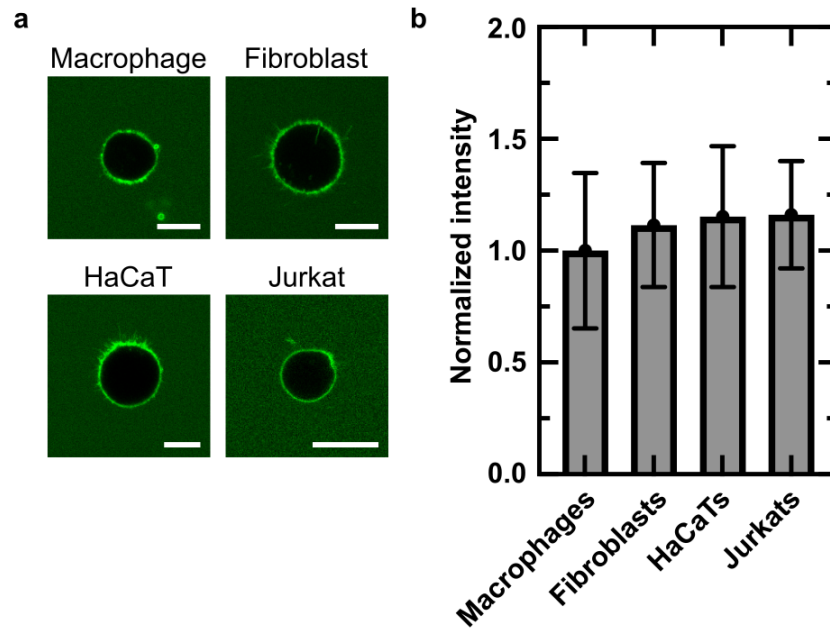


Figure S8: Self-assembly of cholesterol-PEG into membranes of different cell types. Cholesterol-PEG-FITC inserts equally well into the membranes of all cell types used in this study. This verifies the successful functionalization with biotinylated cholesterol. **a** Confocal images of the equatorial plane of the different cell types as indicated. Scale bar: 10  $\mu\text{m}$ . **b** Average intensities of the fluorescence captured from the equatorial plane of each individual cell type ( $n \geq 16$ ), normalized to the minimal fluorescence intensity.

## Supporting Figure S9: GUVs and cells show little to no movement during the lipid nanotube pulling assay

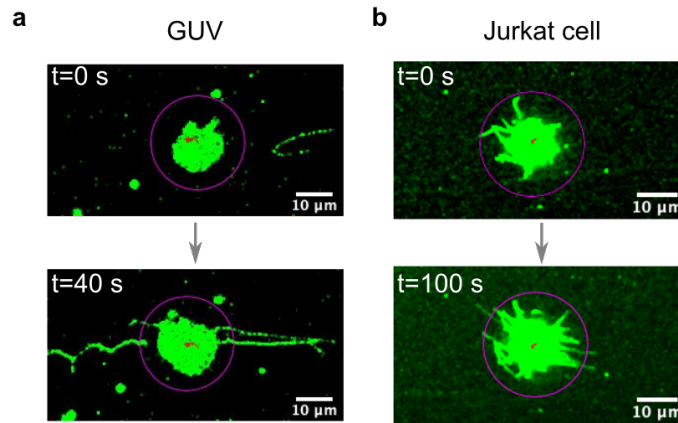


Figure S9: GUVs and cells show little to no movement during the lipid nanotube pulling assay. GUV (**a**, membrane labeled with DOPE-488,  $\lambda_{ex} = 488$  nm)) and Jurkat cell (**b**, membrane labeled with WGA-Alexa488,  $\lambda_{ex} = 488$  nm) during actom-myosin assisted lipid nanotube formation. Over the time course of seconds to minutes there is little to no movement with a mean squared displacement of  $2.9 \mu\text{m}$  or  $1.3 \mu\text{m}$  of the lipid vesicles or cell center, respectively, during nanotube formation (network length  $>100 \mu\text{m}$  and  $>40 \mu\text{m}$ , respectively). The trajectories of the lipid vesicle and the Jurkat cell (violet circle) were tracked with ImageJ (Trackmate<sup>12</sup>) and are shown as red lines in the confocal images. Scale bar:  $10 \mu\text{m}$ .



**Supporting Figure S10: Actin filaments are present within lipid nanotubes pulled from cells**

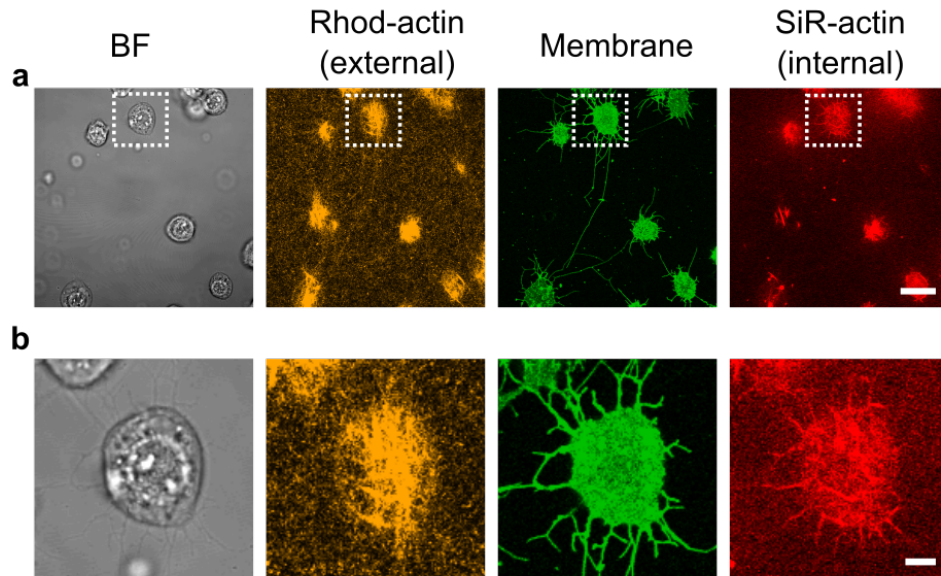


Figure S10: Actin filaments are present within lipid nanotubes pulled from cells. **a,b** Overview (**a**) and zoomed (**b**) confocal fluorescence images of Jurkat cells (membrane labeled with WGA-Alexa488,  $\lambda_{ex} = 488$  nm), extracellular actin filaments (labeled with Rhodamine  $\lambda_{ex} = 561$  nm) and intracellular actin filaments (labeled with Silicon-Rhodamine Actin  $\lambda_{ex} = 640$  nm). Actin filaments are dragged into the lipid nanotubes. Scale bars: 20  $\mu\text{m}$  and 5  $\mu\text{m}$ .

## Supporting Figure S11: Characterization of actin filaments extending into lipid nanotubes

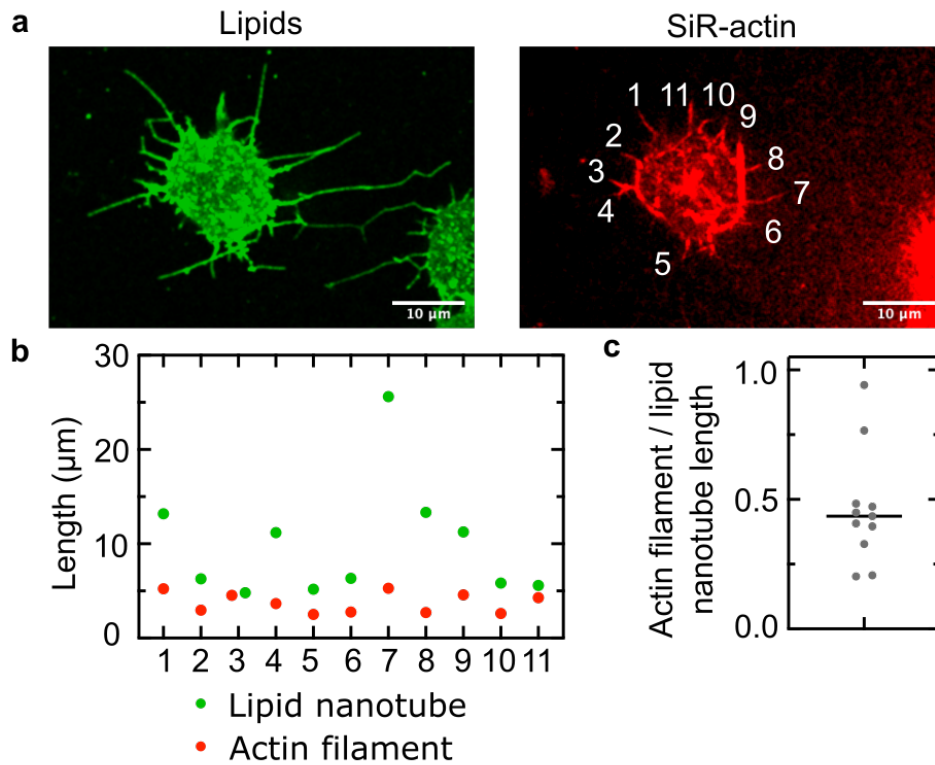


Figure S11: Characterization of actin filaments extending into lipid nanotubes. **a** Confocal image of a Jurkat cell (membrane labeled with WGA-Alexa488,  $\lambda_{ex} = 488$  nm) and cellular actin (red, labeled with SiR-actin  $\lambda_{ex} = 640$  nm) after acto-myosin assisted pulling of lipid nanotubes. Scale bar:  $10 \mu\text{m}$ . **b** Length of eleven lipid nanotubes (green) and actin filaments (red) within the lipid nanotube. The corresponding nanotubes are marked in **a**. **c** Fraction of actin filament over lipid nanotube length (the black line indicates the median,  $n=11$ ).

Supporting Figure S12: Mitochondria and lysosomes do not enter lipid nanotubes of Jurkat cells

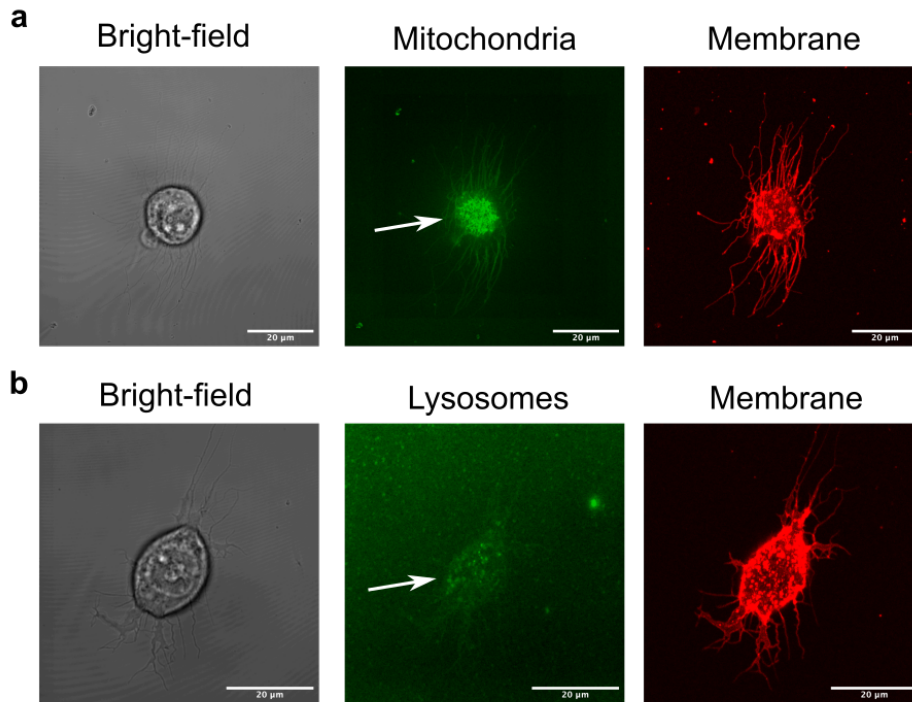


Figure S12: Mitochondria and lysosomes do not enter lipid nanotubes of Jurkat cells. **a**, **b** Confocal images of Jurkat cells (membrane labeled with WGA-Alexa647,  $\lambda_{ex} = 647$  nm) stained for mitochondria (**a**, labeled via LysoTracker green DND-26,  $\lambda_{ex} = 488$  nm) and lysosomes (**b**, labeled via MitoTracker FM green,  $\lambda_{ex} = 488$  nm). Scale bar: 10  $\mu$ m.

### Supporting Figure S13: HaCaT cells do not form lipid nanotubes

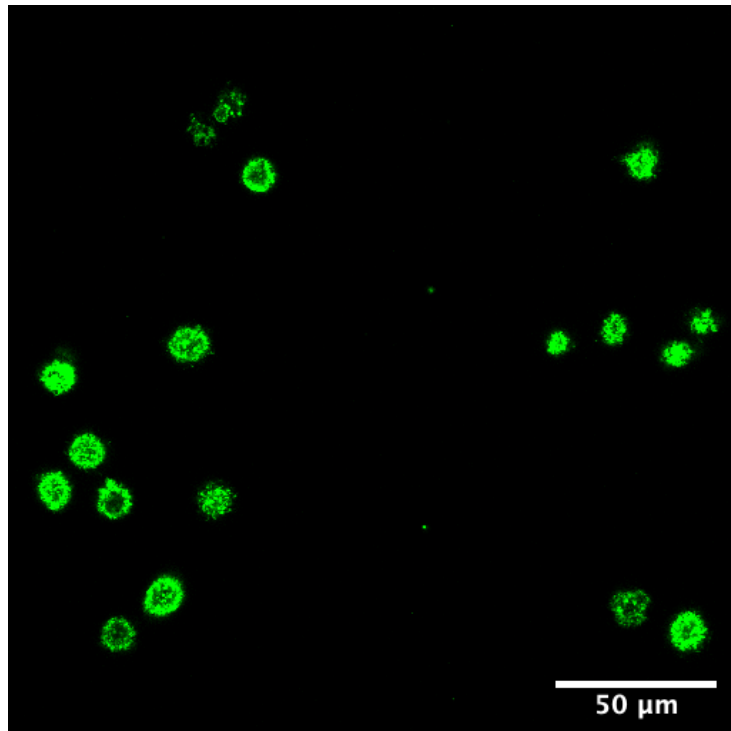


Figure S13: HaCaT cells do not form lipid nanotubes. Confocal image of HaCaTs in presence of 25  $\mu\text{M}$  biotinylated cholesterol and aligned actin filaments on an HMM-coated substrate. Under these conditions we did not observe the formation of lipid nanotubes for Jurkat cells. Scale bar: 50  $\mu\text{m}$ .

### 3 Supporting Videos

#### **Supporting Video S1: Time series of random actin filaments**

Confocal time series of rhodamine-labeled actin filaments ( $\lambda_{ex} = 561$  nm) in an *in vitro* motility assay over the course of 40 s. Actin filaments move randomly without preferred orientation.

#### **Supporting Video S2: Time series of aligned actin filaments**

Confocal time series of rhodamine-labeled aligned actin filaments ( $\lambda_{ex} = 561$  nm) in an *in vitro* motility assay over the course of 40 s. Actin filaments move parallel to each other in one preferred direction.

#### **Supporting Video S3: Time series of aligned actin filament patterns**

Confocal time series of rhodamine-labeled aligned actin filament patterns ( $\lambda_{ex} = 561$  nm) in an *in vitro* motility assay over the course of 10 min. Occasionally, aligned actin filament patterns emerge that form and move around local vortices. Scale bar: 50  $\mu$ m.

#### **Supporting Video S4: Time series of lipid nanotube dynamics after pulling from GUVs**

Confocal time series of GUVs (membrane labeled with Atto488-DOPE,  $\lambda_{ex} = 488$  nm) functionalized with biotinylated lipids depicting the dynamics of lipid nanotubes over time at the substrate interface. Scale bar: 50  $\mu$ m.

### **Supporting Video S5: Time series of lipid nanotube pulling from Jurkat cells**

Confocal time series of Jurkat cells (membrane labeled with WGA-Alexa488,  $\lambda_{ex} = 488$  nm) functionalized with biotinylated cholesterol depicting the pulling of lipid nanotubes over time at the substrate interface. Scale bar: 50  $\mu$ m.

### **Supporting Video S6: Displacement over time of a Jurkat cell during lipid nanotube pulling**

Confocal time series of a Jurkat cell (membrane labeled with WGA-Alexa488,  $\lambda_{ex} = 488$  nm) during lipid nanotube formation. There is almost no displacement of the cell (indicated as red line) over the time course of imaging. Scale bar: 10  $\mu$ m.

### **Supporting Video S7: Displacement over time of a GUV during lipid nanotube pulling**

Confocal time series of a GUV (membrane labeled with DOPE-Atto488,  $\lambda_{ex} = 488$  nm) during lipid nanotube formation. There is almost no displacement of the cell (indicated as red line) over the time course of imaging. Scale bar: 10  $\mu$ m.

### **Supporting Video S8: 3D projection of Jurkat cells with random actin and biotinylated cholesterol**

Confocal 3D projection of a Jurkat cell (membrane labeled with WGA-Alexa488,  $\lambda_{ex} = 488$  nm) functionalized with biotinylated cholesterol depicting the pulling of lipid nanotubes at the substrate interface with random actin filaments.

### **Supporting Video S9: 3D projection of Jurkat cells with aligned actin and biotinylated cholesterol**

Confocal 3D projection of Jurkat cells (membrane labeled with WGA-Alexa488,  $\lambda_{ex} = 488$  nm) functionalized with biotinylated cholesterol depicting the pulling of lipid nanotubes at the substrate interface with aligned actin filaments.

### **Supporting Video S10: 3D projection of Jurkat cells with random actin and no biotinylated cholesterol**

Confocal 3D projection of a Jurkat cell (membrane labeled with WGA-Alexa488,  $\lambda_{ex} = 488$  nm) functionalized without biotinylated cholesterol depicting no pulling of lipid nanotubes at the substrate interface with random actin filaments.

### **Supporting Video S11: 3D projection of Jurkat cells with aligned actin and no biotinylated cholesterol**

Confocal 3D projection of a Jurkat cell (membrane labeled with WGA-Alexa488,  $\lambda_{ex} = 488$  nm) functionalized without biotinylated cholesterol depicting no pulling of lipid nanotubes at the substrate interface with aligned actin filaments.

### **Supporting Video S12: Actin filament dynamics during lipid nanotube pulling of a Jurkat cell (DOPE-Atto488)**

Confocal time series of a Jurkat cell (membrane labeled with WGA-Alexa488,  $\lambda_{ex} = 488$  nm) during lipid nanotube formation. Scale bar: 10  $\mu$ m.

## Supporting Video S13: Actin filament dynamics during lipid nanotube pulling of a Jurkat cell (SiR-actin)

Confocal time series of a Jurkat cell (membrane labeled with WGA-Alexa488,  $\lambda_{ex} = 488$  nm) during lipid nanotube formation with labeled SiR-actin (corresponding to Video S12). There does not seem to be any time delay in between the initial lipid nanotube pulling and actin filament presence within the lipid nanotube. Scale bar: 10  $\mu$ m.

## References

- (1) Pardee, J. D.; Spudich, J. *Methods in Enzymology*; Elsevier, 1982; pp 164–181.
- (2) Kron, S. J.; Spudich, J. A. Fluorescent actin filaments move on myosin fixed to a glass surface. *Proceedings of the National Academy of Sciences* **1986**, *83*, 6272–6276.
- (3) Margossian, S. S.; Lowey, S. *Methods in Enzymology*; Elsevier, 1982; pp 55–71.
- (4) Rahman, M. A.; Salhotra, A.; Månsson, A. Comparative analysis of widely used methods to remove nonfunctional myosin heads for the in vitro motility assay. *Journal of Muscle Research and Cell Motility* **2018**, *39*, 175–187.
- (5) Das, T.; Safferling, K.; Rausch, S.; Grabe, N.; Boehm, H.; Spatz, J. P. A molecular mechanotransduction pathway regulates collective migration of epithelial cells. *Nature Cell Biology* **2015**, *17*, 276–287.
- (6) Ollech, D.; Pflästerer, T.; Shellard, A.; Zambarda, C.; Spatz, J. P.; Marcq, P.; Mayor, R.; Wombacher, R.; Cavalcanti-Adam, E. A. An optochemical tool for light-induced dissociation of adherens junctions to control mechanical coupling between cells. *Nature communications* **2020**, *11*, 472–472.
- (7) Arganda-Carreras, I.; Kaynig, V.; Rueden, C.; Eliceiri, K. W.; Schindelin, J.; Car-



- dona, A.; Sebastian Seung, H. Trainable Weka Segmentation: a machine learning tool for microscopy pixel classification. *Bioinformatics* **2017**, *33*, 2424–2426.
- (8) Jaqaman, K.; Mettlen, M.; Kuwata, H.; Loerke, D.; Danuser, G.; Schmid, S. L.; Grinstead, S. Robust single-particle tracking in live-cell time-lapse sequences. *Nature methods* **2008**, *5*, 695–702.
- (9) Angelova, M. I.; Dimitrov, D. S. Liposome electroformation. *Faraday Discussions of the Chemical Society* **1986**, *81*, 303.
- (10) Schaller, V.; Weber, C.; Semmrich, C.; Frey, E.; Bausch, A. R. Polar patterns of driven filaments. *Nature* **2010**, *467*, 73–77.
- (11) Schroer, C. F. E.; Baldauf, L.; van Buren, L.; Wassenaar, T. A.; Melo, M. N.; Koenderink, G. H.; Marrink, S. J. Charge-dependent interactions of monomeric and filamentous actin with lipid bilayers. *Proceedings of the National Academy of Sciences* **2020**, *117*, 5861–5872.
- (12) Tinevez, J.-Y.; Perry, N.; Schindelin, J.; Hoopes, G. M.; Reynolds, G. D.; Laplantine, E.; Bednarek, S. Y.; Shorte, S. L.; Eliceiri, K. W. TrackMate: An open and extensible platform for single-particle tracking. *Methods* **2017**, *115*, 80–90.

## **A.2 Supporting Information for Publication 2: Autonomous directional motion of actin-containing cell-sized droplets**

# Supporting Information:

## Autonomous Directional Motion of Actin-Containing Cell-Sized Droplets

Barbara Haller,<sup>†,‡,ⓐ</sup> Kevin Jahnke,<sup>¶,§,ⓐ</sup> Marian Weiss,<sup>†,‡</sup> Kerstin Göpfrich,<sup>\*,¶,§</sup> Ilia  
Platzman,<sup>\*,†,||</sup> and Joachim P. Spatz<sup>\*,†,⊥,#</sup>

<sup>†</sup>*Max Planck Institute for Medical Research, Department of Cellular Biophysics,  
Jahnstraße 29, D 69120 Heidelberg, Germany*

<sup>‡</sup>*Department of Biophysical Chemistry, Heidelberg University,  
Im Neuenheimer Feld 253, D 69120 Heidelberg, Germany*

<sup>¶</sup>*Max Planck Institute for Medical Research, Biophysical Engineering Group,  
Jahnstraße 29, D 69120 Heidelberg, Germany*

<sup>§</sup>*Department of Physics and Astronomy, Heidelberg University,  
D 69120 Heidelberg, Germany*

<sup>||</sup>*Institute for Molecular Systems Engineering (IMSE) Heidelberg University,  
Im Neuenheimer Feld 225, Heidelberg D 69120 Germany*

<sup>⊥</sup>*Institute for Molecular Systems Engineering (IMSE) Heidelberg University,  
Im Neuenheimer Feld, Heidelberg D 69120 Germany*

<sup>#</sup>*Max Planck School Matter to Life, Jahnstraße 29, D 69120 Heidelberg, Germany*

<sup>ⓐ</sup>*These authors contributed equally to this work.*

E-mail: kerstin.goepfrich@mr.mpg.de; ilia.platzman@mr.mpg.de; spatzz@mr.mpg.de

# Contents

Supporting Figure 1: Layout of microfluidic device for the encapsulation of actin into surfactant-stabilized water-in-oil droplets. . . . .	3
Supporting Figure 2: Fluorination of the glass slide leads to a rolling motion of actin-containing droplets . . . . .	4
Supporting Note 1: Rotational diffusion coefficient . . . . .	5
Supporting Video 1: Actin adsorbs at the droplet periphery in presence of 5.04 mM Krytox . . . . .	6
Supporting Video 2: Actin-containing droplets exhibit rotational motility in presence of 0.04 mM Krytox . . . . .	6
Supporting Video 3: Actin-containing droplets do not exhibit rotational motility in presence of 0.54 mM Krytox . . . . .	6
Supporting Video 4: Actin-containing droplets do not exhibit rotational motility in presence of 1.04 mM Krytox . . . . .	7
Supporting Video 5: Actin-containing droplets do not exhibit rotational motility in presence of F6H8 oil . . . . .	7
<b>References</b>	<b>7</b>

**Supporting Figure 1: Layout of microfluidic device for the encapsulation of actin into surfactant-stabilized water-in-oil droplets.**

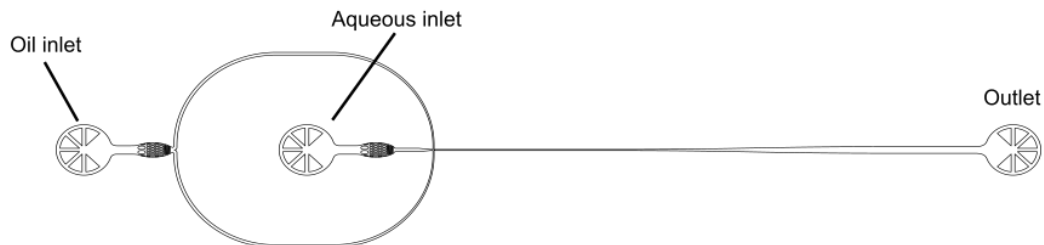


Figure 1: Layout of microfluidic device for the encapsulation of actin into surfactant-stabilized water-in-oil droplets. The microfluidic PDMS devices (Sylgard184, Dow Corning, USA) were fabricated according to a previously published protocol.<sup>[1]</sup> The aqueous phase contained actin at various concentrations and in some cases MC. The oil phase was made up of 1.4 wt% block copolymer surfactants in HFE7500 at various Krytox concentrations. For confocal fluorescence imaging, the droplets were collected from the outlet and sealed in a simple observation chamber as described previously.<sup>[2]</sup>

**Supporting Figure 2: Fluorination of the glass slide leads to a rolling motion of actin-containing droplets**

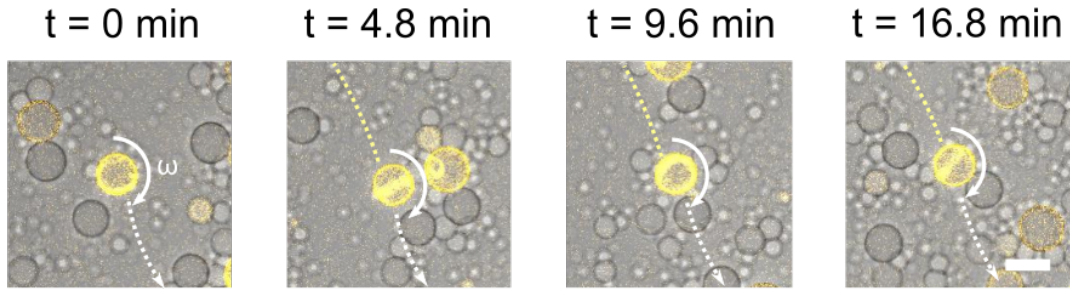


Figure 2: Fluorination of the glass slide leads to a rolling motion of actin-containing droplets. Confocal fluorescence time series of microfluidic actin-containing (labeled with Rhodamine-Phalloidin,  $\lambda_{ex} = 561$  nm) droplets with 0.04 mM Krytox in the oil phase in presence of 0.4% MC. The coverslide was fluorinated to induce friction at the droplet-glass interface. Actin-containing droplets exhibit a translational rolling motion with an average velocity of  $0.061 \pm 0.014$  rot/h. The displacement of a respective droplet is indicated with dashed lines and time points indicated. Scale bar: 20  $\mu$ m.

## Supporting Note 1: Rotational diffusion coefficient

The rotational diffusion coefficient can be calculated using the Einstein-Smoluchowski relation via:

$$D_r = \frac{k_B T}{f_r}, \quad (1)$$

with the Boltzmann constant  $k_B$ , temperature  $T$  and the frictional drag coefficient  $f_r$ . For a spherical object the frictional drag coefficient is given by:

$$f_r = 8\pi\mu\rho r^3, \quad (2)$$

in a solution with density  $\rho$ , kinematic viscosity  $\mu$  and a sphere of radius  $r$ . Assuming a droplet radius of 20  $\mu\text{m}$  and that the kinematic viscosity at the boundary is not significantly higher than in bulk, this yields a rotational diffusion coefficient of

$$D_r = \frac{k_B T}{8\pi\mu\rho r^3} = 1.63 \cdot 10^{-5}/\text{s} = 0.059/\text{h}, \quad (3)$$

for  $T=295\text{ K}$ ,  $\mu=0.77\text{ mm}^2/\text{s}$  and  $\rho=1614\text{ kg}/\text{m}^3$  as physical properties of HFE 7500. Thus, the observed rotational motion of actin-containing droplets, which was found to be  $1.7 \pm 0.5\text{ rot}/\text{h}$ , exceeds the rotational diffusion coefficient by a factor of 28.

### **Supporting Video 1: Actin adsorbs at the droplet periphery in presence of 5.04 mM Krytox**

Confocal fluorescence time series of microfluidic actin-containing (labeled with 1% Alexa568,  $\lambda_{ex} = 561$  nm) droplets with 5.04 mM Krytox in the oil phase. Actin adsorbs at the droplet interface due to interaction with Krytox. Furthermore, the fluorescence signal of actin on the droplet interior is decreasing and losing its fibrous structure. The loss of fibrous structures at high Krytox concentration can be attributed to depolymerization and denaturation of actin at low pH values. Additionally, agglomerates of fluorescent actin particles can be detected in the oil phase, unambiguously confirming that there is a leakage of actin from the droplets. Scale bar: 30  $\mu$ m.

### **Supporting Video 2: Actin-containing droplets exhibit rotational motility in presence of 0.04 mM Krytox**

Confocal fluorescence time series of microfluidic actin-containing (labeled with 1% Alexa568,  $\lambda_{ex} = 561$  nm) droplets with 0.04 mM Krytox in the oil phase. 96 % of the observed droplets (n=57) display more than 0.5 rot/h. Scale bar: 30  $\mu$ m.

### **Supporting Video 3: Actin-containing droplets do not exhibit rotational motility in presence of 0.54 mM Krytox**

Confocal fluorescence time series of microfluidic actin-containing (labeled with 1% Alexa568,  $\lambda_{ex} = 561$  nm) droplets with 0.54 mM Krytox in the oil phase. None of the observed droplets (n=?) displays more than 0.5 rot/h. This can be explained by depolymerization and denaturation of actin at low pH values due to Krytox at the interface and thus homogenous actin spreading at the droplet interface. Scale bar: 30  $\mu$ m.



## **Supporting Video 4: Actin-containing droplets do not exhibit rotational motility in presence of 1.04 mM Krytox**

Confocal fluorescence time series of microfluidic actin-containing (labeled with 1% Alexa568,  $\lambda_{ex} = 561$  nm) droplets with 1.04 mM Krytox in the oil phase. None of the observed droplets ( $n=?$ ) displays more than 0.5 rot/h. This can be explained by depolymerization and denaturation of actin at low pH values due to Krytox at the interface and thus homogenous actin spreading at the droplet interface. Scale bar: 30  $\mu\text{m}$ .

## **Supporting Video 5: Actin-containing droplets do not exhibit rotational motility in presence of F6H8 oil**

Confocal fluorescence color-coded time series of microfluidic actin-containing (labeled with Rhodamine-Phalloidin,  $\lambda_{ex} = 561$  nm) droplets with F6H8 as oil phase. None of the observed droplets ( $n=6$ ) displays rotational motion. This can be explained by the fact that Krytox (as the driving force for Marangoni flows) does not dissolve in F6H8. Scale bar: 50  $\mu\text{m}$ .

## **References**

- (1) Platzman, I.; Janiesch, J.-W.; Spatz, J. P. Synthesis of Nanostructured and Biofunctionalized Water-in-Oil Droplets as Tools for Homing T Cells. *Journal of the American Chemical Society* **2013**, *135*, 3339–3342.
- (2) Weiss, M. et al. Sequential bottom-up assembly of mechanically stabilized synthetic cells by microfluidics. *Nature Materials* **2017**, *17*, 89–96.

### **A.3 Supporting Information for Publication 3: Engineering light-responsive contractile actomyosin networks with DNA nanotechnology**

# Supporting Information:

## Engineering Light-Responsive Contractile Actomyosin Networks with DNA Nanotechnology

Kevin Jahnke,<sup>†,‡</sup> Marian Weiss,<sup>¶,§</sup> Cornelia Weber,<sup>¶,§</sup> Ilia Platzman,<sup>\*,||,§</sup> Kerstin Göpfrich,<sup>\*,†,‡</sup> and Joachim P. Spatz<sup>\*,||,§,⊥</sup>

<sup>†</sup>*Max Planck Institute for Medical Research, Biophysical Engineering Group,  
Jahnstraße 29, D 69120, Heidelberg, Germany*

<sup>‡</sup>*Department of Physics and Astronomy, Heidelberg University,  
D 69120 Heidelberg, Germany*

<sup>¶</sup>*Max Planck Institute for Medical Research, Department of Cellular Biophysics,  
Jahnstraße 29, D 69120 Heidelberg, Germany*

<sup>§</sup>*Department of Biophysical Chemistry, Heidelberg University,  
Im Neuenheimer Feld 253, D 69120 Heidelberg, Germany*

<sup>||</sup>*Max Planck Institute for Medical Research, Department of Cellular Biophysics,  
Jahnstraße 29, D 69120, Heidelberg, Germany*

<sup>⊥</sup>*Max Planck School Matter to Life, Jahnstraße 29, D 69120 Heidelberg, Germany*

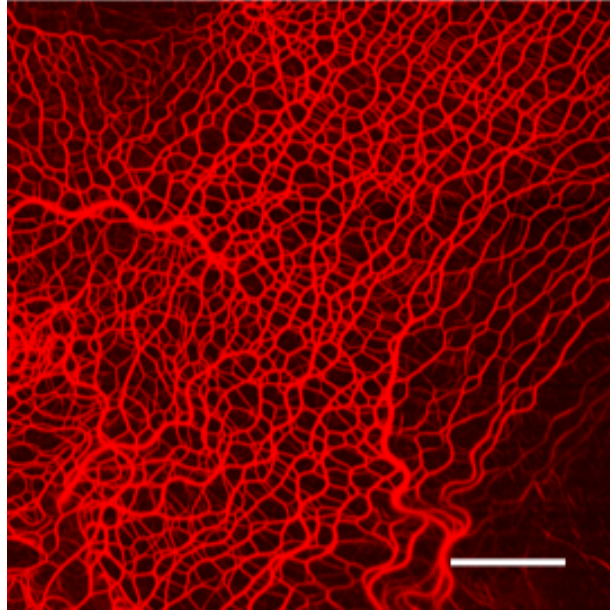
E-mail: ilia.platzman@mr.mpg.de; kerstin.goepfrich@mr.mpg.de; spatz@mr.mpg.de

# Contents

Supporting Figure 1: Methylcellulose bundles and crosslinks actin filaments . . . .	4
Supporting Figure 2: Actin bundle formation is independent of ATP addition . .	5
Supporting Figure 3: Actomyosin contraction requires methylcellulose . . . . .	6
Supporting Figure 4: Soluble HMM does not induce actomyosin contraction . . .	7
Supporting Figure 5: Denaturing polyacrylamide gel electrophoresis to probe HMM-functionalization of polystyrene beads . . . . .	8
Supporting Figure 6: Blebbistatin inhibits actomyosin contraction . . . . .	9
Supporting Figure 7: Estimated number of HMM-beads per droplet . . . . .	10
Supporting Figure 8: Layout of the microfluidic device . . . . .	11
Supporting Figure 9: Encapsulation of actin and HMM-beads into surfactant- stabilized water-in-oil droplets . . . . .	12
Supporting Figure 10: Symmetric contraction of actomyosin networks in cell-sized confinement . . . . .	13
Supporting Figure 11: Contraction of actomyosin networks with high actin concen- tration in cell-sized confinement . . . . .	14
Supporting Figure 12: Symmetric contraction of actomyosin networks in cell-sized confinement with high bead density . . . . .	15
Supporting Table 1: DNA sequences . . . . .	16
Supporting Figure 13: Denaturing polyacrylamide gel electrophoresis to prove actin functionalization with biotin-streptavidin . . . . .	17
Supporting Figure 14: Cholesterol-tagged DNA self-assembles at the droplet pe- riphery . . . . .	18
Supporting Figure 15: DNA-linker-mediated symmetry break of minimal acto- myosin cortices in cell-sized compartments . . . . .	19
Supporting Figure 16: Actomyosin networks contract to the droplet periphery . .	20
Supporting Text 1: Hypothesis for the actin aster formation . . . . .	21

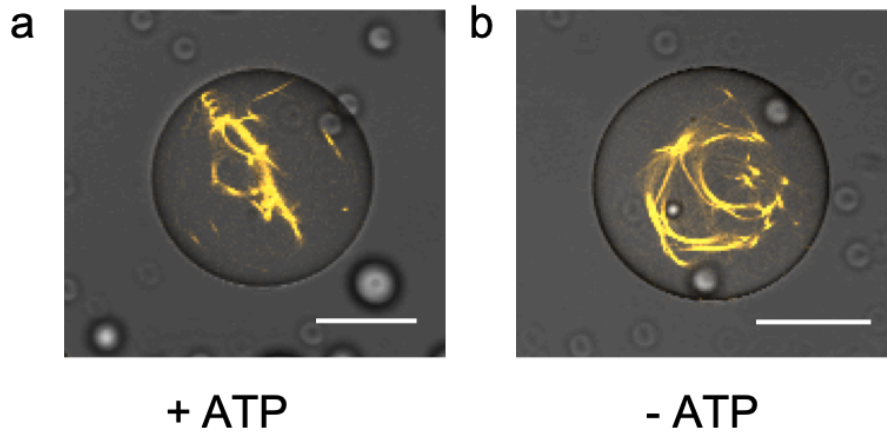
Supporting Text 2: Estimation of the passive diffusion of the DNA linkers . . . .	23
Supporting Video 1: Growth of actin filaments in bulk in the presence of methyl- cellulose . . . . .	24
Supporting Video 2: Actomyosin contraction in bulk . . . . .	24
Supporting Video 3: Velocity of HMM-coated beads in bulk . . . . .	24
Supporting Video 4: Actomyosin contraction in droplets . . . . .	24
Supporting Video 5: Minimal actomyosin networks contract to the periphery of microfluidic droplet . . . . .	25
<b>References</b>	<b>26</b>

**Supporting Figure 1: Methylcellulose bundles and crosslinks actin filaments**



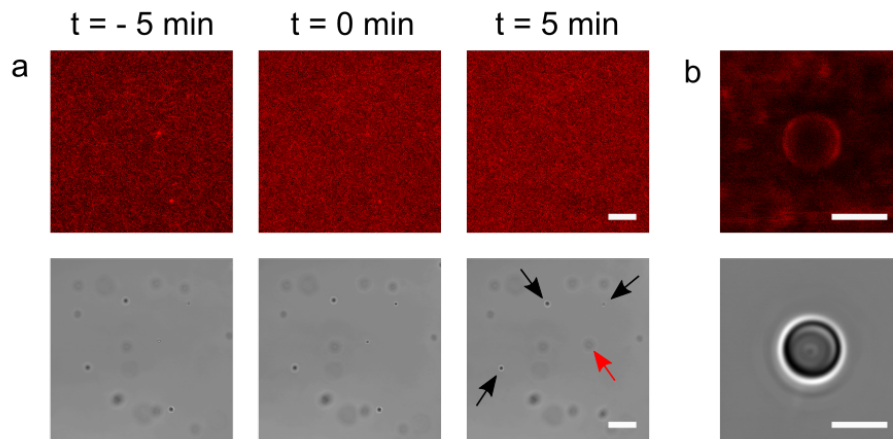
Supporting Figure 1: Methylcellulose bundles and crosslinks actin filaments. Confocal fluorescence image of actin (red,  $\lambda_{ex} = 647 \text{ nm}$ ) after addition of 0.4% methylcellulose. Scale bar: 50  $\mu\text{m}$ . Note that this image was taken close to the coverslide.

**Supporting Figure 2: Actin bundle formation is independent of ATP addition**



Supporting Figure 2: Methylcellulose bundles and crosslinks actin filaments with and without added ATP. Confocal fluorescence image of actin (orange,  $\lambda_{ex} = 561$  nm) after addition of 0.4% methylcellulose with (a)  $\mu$ M traces of ATP (from actin-storage buffer) and (b) 1 mM ATP. Scale bar: 50  $\mu$ m.

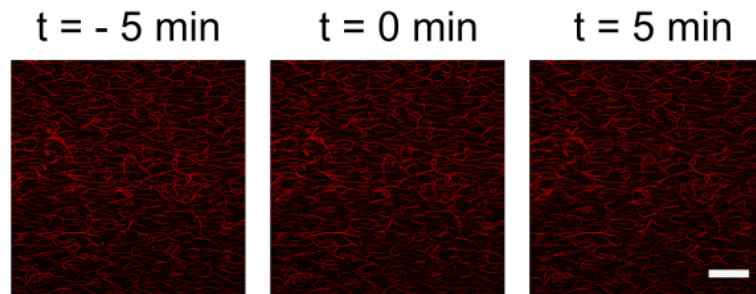
### Supporting Figure 3: Actomyosin contraction requires methylcellulose



Supporting Figure 3: Methylcellulose is required for the contraction of actomyosin networks with HMM-coated beads. Confocal fluorescence images of actin filaments (red,  $\lambda_{ex}$  514 nm, top row) in absence of methylcellulose and corresponding brightfield images depicting HMM-coated beads (bottom row). **a** Actomyosin-network before and after ATP release by 405 nm illumination. HMM-coated beads do not exhibit any movement before ATP release. At  $t = 0$  min ATP was released by illumination with 405 nm for 5 s. Afterwards, most of the HMM-coated beads remain static even after 5 min observation (indicated with black arrows), whereas only very few HMM-beads exhibit motion along the actin network (indicated with red arrow). Scale bar: 20  $\mu$ m. **b** Close up image of a single HMM-coated bead. The bead is covered with an actin filament, inhibiting successful force exertion. Scale bar: 2  $\mu$ m.

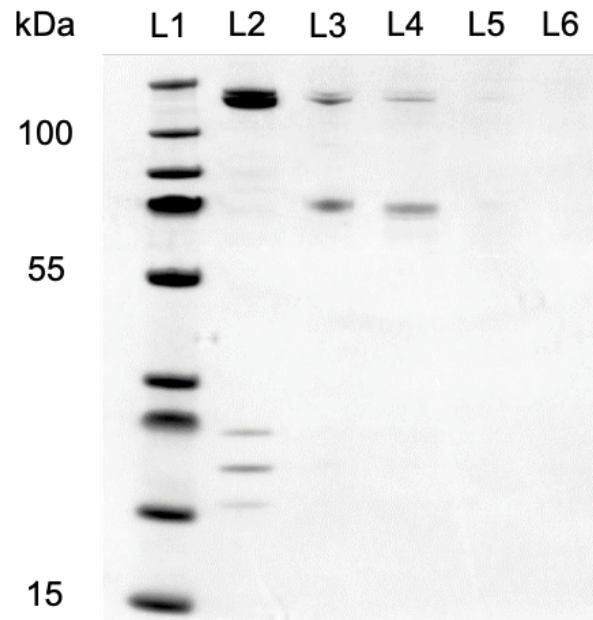


**Supporting Figure 4: Soluble HMM does not induce actomyosin contraction**



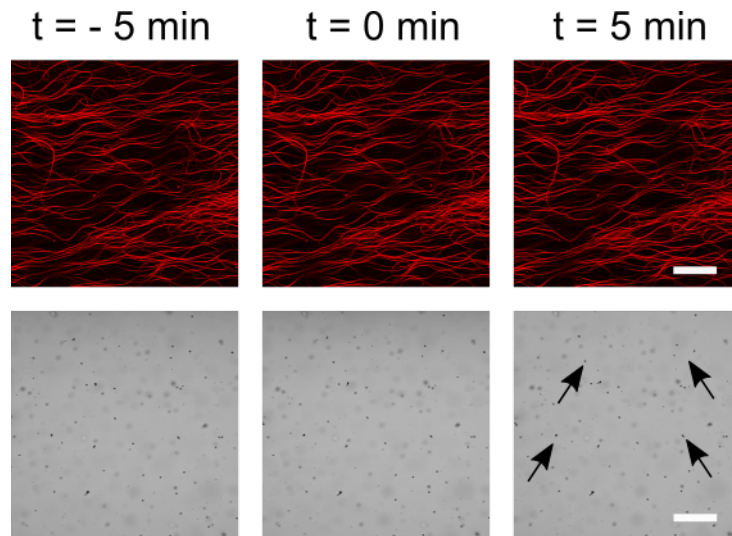
Supporting Figure 4: Soluble HMM does not induce actomyosin contraction. Confocal fluorescence images of actin filaments (red,  $\lambda_{ex}$  514 nm) in presence of 130 nM soluble HMM instead of HMM-coated beads. Actin-network before and after ATP release by 405 nm illumination. At  $t = 0$  min ATP was released by illumination with 405 nm for 5 s. The actin filaments remain static for the whole observation period indicating that soluble HMM does not induce actomyosin-contraction. Scale bar: 100  $\mu$ m

**Supporting Figure 5: Denaturing polyacrylamide gel electrophoresis to probe HMM-functionalization of polystyrene beads**



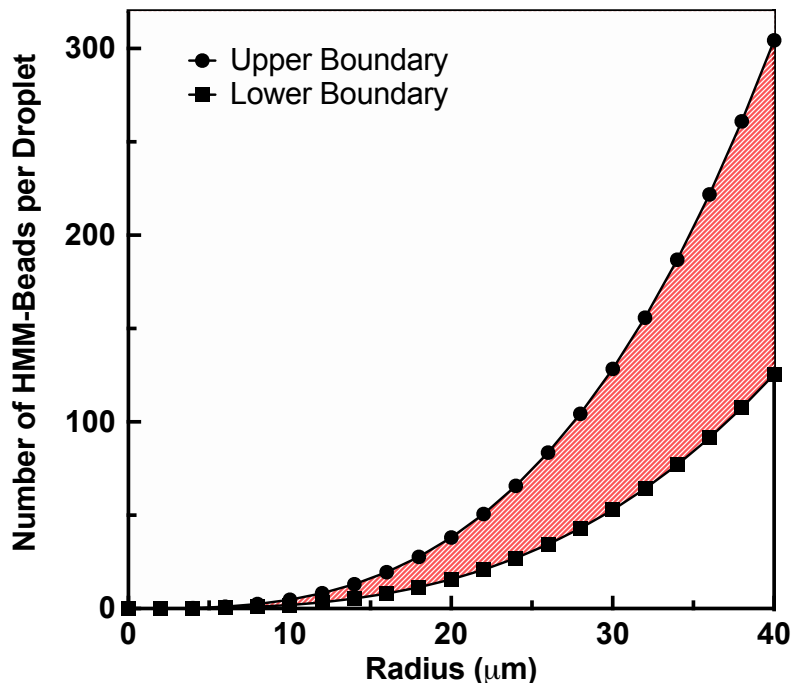
Supporting Figure 5: Denaturing polyacrylamide gel electrophoresis (PAGE) to prove HMM-functionalization of polystyrene beads. Denaturing PAGE (running conditions: 4-12% polyacrylamide (Thermo Fisher), 200 V, 35 min) of pure HMM in actin buffer (L2), HMM-coated beads before washing (L3), HMM-coated beads after washing (L4), supernatant after centrifugation (L5) and washing buffer (L6). HMM and BSA can only be found on the beads and not in the supernatant even after washing, indicating successful functionalization of the polystyrene beads with HMM as well as bovine serum albumin (BSA, MW: 67 kDa).

## Supporting Figure 6: Blebbistatin inhibits actomyosin contraction



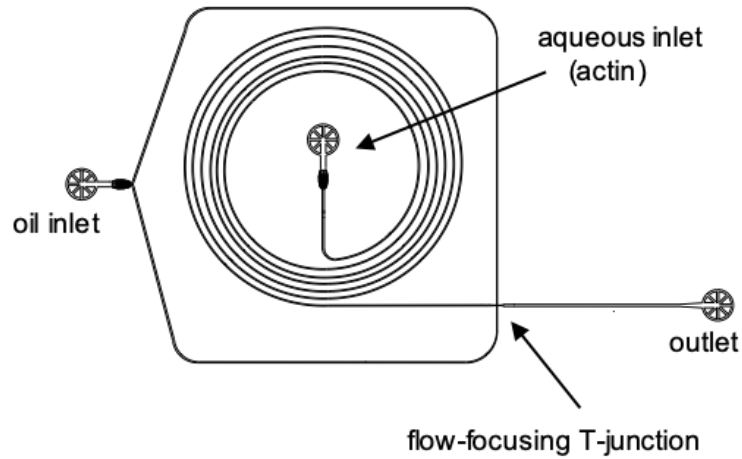
Supporting Figure 6: HMM-inhibition prevents actomyosin network contraction. Confocal fluorescence images of actin filaments (red,  $\lambda_{ex}$  514 nm, top row) and corresponding brightfield images depicting HMM-coated beads (bottom row). HMM-beads were incubated with 50  $\mu$ M blebbistatin for 10 min before acquisition. Actomyosin-networks are shown 5 min before and after ATP release by 405 nm illumination. At  $t = 0$  min ATP was released by illumination with 405 nm for 5 s. All HMM-coated beads remain static (exemplary beads indicated with black arrows) during the whole observation period. This proves that actomyosin contraction is solely based on HMM activity after ATP release and that in our case illumination for 5 s with light below 488 nm does not lead to sufficient photoinactivation of blebbistatin to generate bead motility. Scale bars: 50  $\mu$ m

### Supporting Figure 7: Estimated number of HMM-beads per droplet



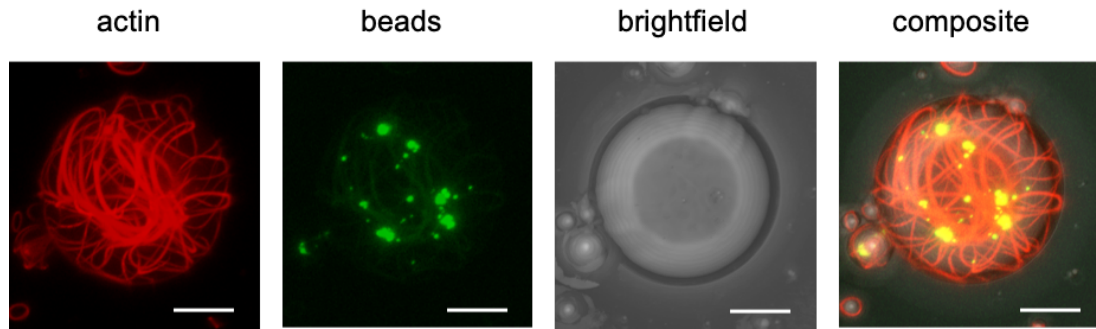
Supporting Figure 7: Estimated number of HMM-coated beads as a function of droplet radius. The upper limit was calculated assuming no loss during the coating procedure. We expect the loss of beads during the production process to be below 20%. Therefore, the lower limit assumes a loss of 20% of beads and depends on the volume of used beads (either 10  $\mu\text{L}$  or 20  $\mu\text{L}$ ). A typical droplet with a radius of 30  $\mu\text{m}$  hence contains roughly around 90 beads, consistent with microscopy observations. We found this to be suitable for efficient contraction, whereas no contraction is observed if significantly less beads are encapsulated.

## Supporting Figure 8: Layout of the microfluidic device



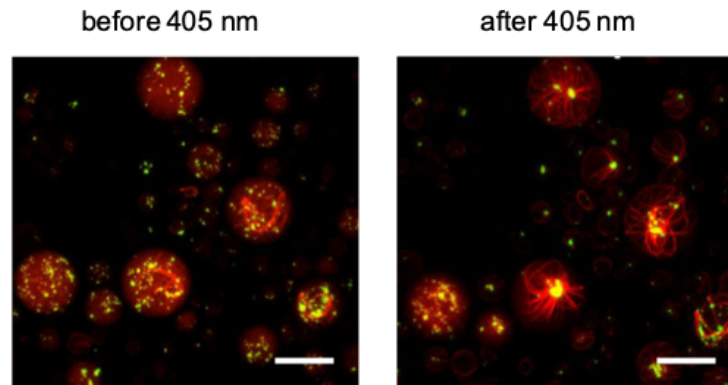
Supporting Figure 8: Layout of the microfluidic device for the production of surfactant-stabilized water-in-oil droplets. Device with one oil inlet and one aqueous inlet for the encapsulation of actin, HMM-beads, caged ATP and DNA linkers. The microfluidic PDMS (Sylgard) devices were produced as described previously.<sup>1</sup> For confocal fluorescence imaging, droplets were collected from the outlet.

**Supporting Figure 9: Encapsulation of actin and HMM-beads into surfactant-stabilized water-in-oil droplets**



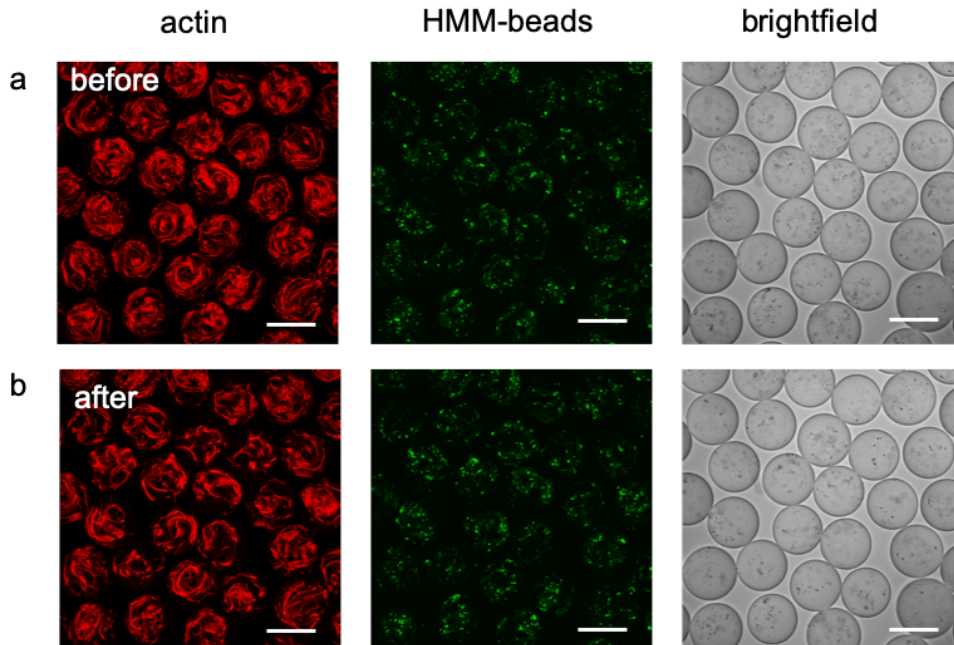
Supporting Figure 9: Encapsulation of actin and HMM-beads into surfactant-stabilized water-in-oil droplets. Confocal fluorescence z-projections of actin (red,  $\lambda_{ex} = 647$  nm) and HMM-coated beads (green,  $\lambda_{ex} = 488$  nm) as well as brightfield and composite images. Actin filaments and HMM-coated beads form minimal actomyosin networks that spread the whole cell-sized confinement. Scale bars: 20  $\mu$ m.

**Supporting Figure 10: Symmetric contraction of actomyosin networks in cell-sized confinement**



Supporting Figure 10: Symmetric contraction of actomyosin networks in cell-sized confinement. Confocal fluorescence images of actin filaments (red,  $\lambda_{ex} = 647$  nm) and HMM-coated beads (green,  $\lambda_{ex} = 488$  nm) encapsulated into water-in-oil droplets before and after illumination with blue light. Before ATP-release the minimal actomyosin network is homogeneously distributed in the droplet. After ATP-release the minimal actomyosin network contracts towards the droplet center. Scale bar: 50  $\mu$ m.

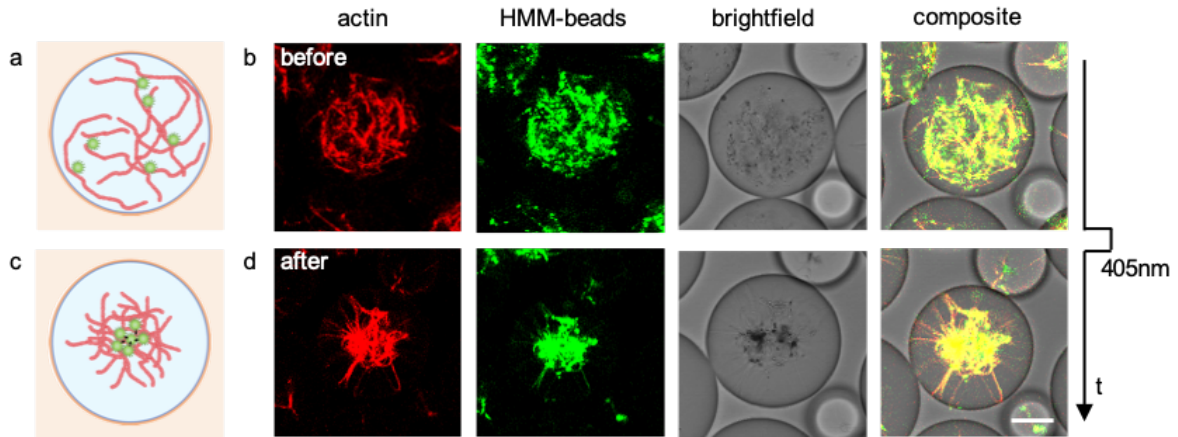
## Supporting Figure 11: Contraction of actomyosin networks with high actin concentration in cell-sized confinement



Supporting Figure 11: Contraction of actomyosin networks with high actin concentration ( $20\ \mu\text{M}$ ) in cell-sized confinement. a) Confocal fluorescence images of actin filaments (red,  $\lambda_{ex} = 647\ \text{nm}$ ) and HMM-coated beads (green,  $\lambda_{ex} = 488\ \text{nm}$ ) encapsulated into water-in-oil droplets as well as brightfield images before illumination with blue light. Before ATP-release, the minimal actomyosin network is homogeneously distributed in the droplet. b) Confocal fluorescence images of actin filaments (red,  $\lambda_{ex} = 647\ \text{nm}$ ) and HMM-coated beads (green,  $\lambda_{ex} = 488\ \text{nm}$ ) encapsulated into water-in-oil droplets as well as brightfield 10 min after illumination with blue light. After ATP-release, the minimal actomyosin network contracts only slightly, likely due to steric hindrance caused by the dense surrounding network of actin filaments. Scale bars:  $100\ \mu\text{m}$ .



**Supporting Figure 12: Symmetric contraction of actomyosin networks in cell-sized confinement with high bead density**



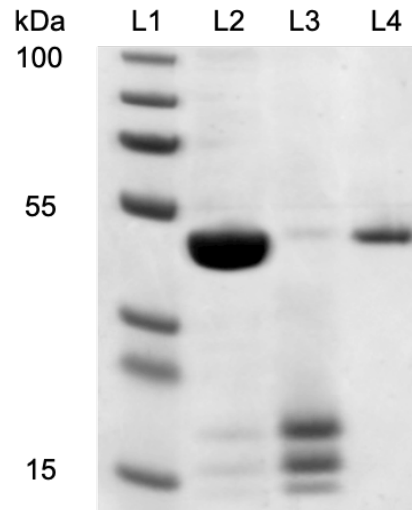
Supporting Figure 12: Symmetric contraction of actomyosin networks in cell-sized confinement. a) Schematic illustration of actin filaments, HMM-beads and NPE-caged ATP inside water-in-oil droplets before illumination with blue light. b) Confocal fluorescence images of actin filaments (red,  $\lambda_{ex} = 647$  nm) and HMM-coated beads (green,  $\lambda_{ex} = 488$  nm) encapsulated into water-in-oil droplets as well as brightfield and composite images before illumination with blue light. Before ATP-release the minimal actomyosin network is homogeneously distributed in the droplet. c) Schematic illustration of actin filaments and HMM-beads inside water-in-oil droplets after illumination with blue light. d) Confocal fluorescence images of actin filaments (red,  $\lambda_{ex} = 647$  nm) and HMM-coated beads (green,  $\lambda_{ex} = 488$  nm) encapsulated into water-in-oil droplets as well as brightfield and composite images 6 min after illumination with blue light. After ATP-release the minimal actomyosin network contracts towards the droplet center. Scale bar: 20  $\mu\text{m}$ . Note that compared to Figure 3 in the main text, we here encapsulated a higher number of beads.

## Supporting Table 1: DNA sequences

Supporting Table 1: DNA sequences for linking actin to the droplet periphery. All sequences were ordered from Integrated DNA Technologies, Inc., and HPLC purified.

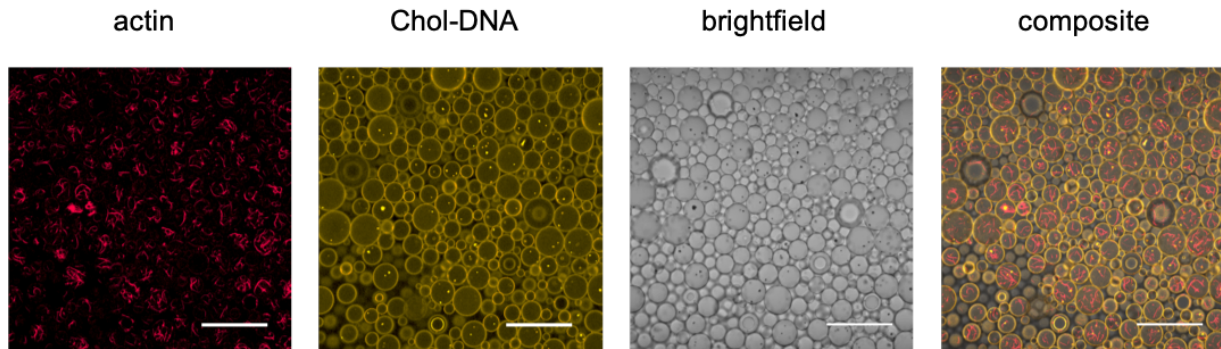
#	DNA sequence
1	5'/ACCAGACAATACCACACAATTTT/3'CholTEG/
2	5' <sup>Cy3</sup> /ACCAGACAATACCACACAATTTT/3'CholTEG/
3	5' <sup>Cy5</sup> /TTCTCTTCTCGTTTGCTCTTCTCTTGTGTGGTATT GTCTAAGAGAAGAGTT/3'BioTEG/

**Supporting Figure 13: Denaturing polyacrylamide gel electrophoresis to prove actin functionalization with biotin-streptavidin**



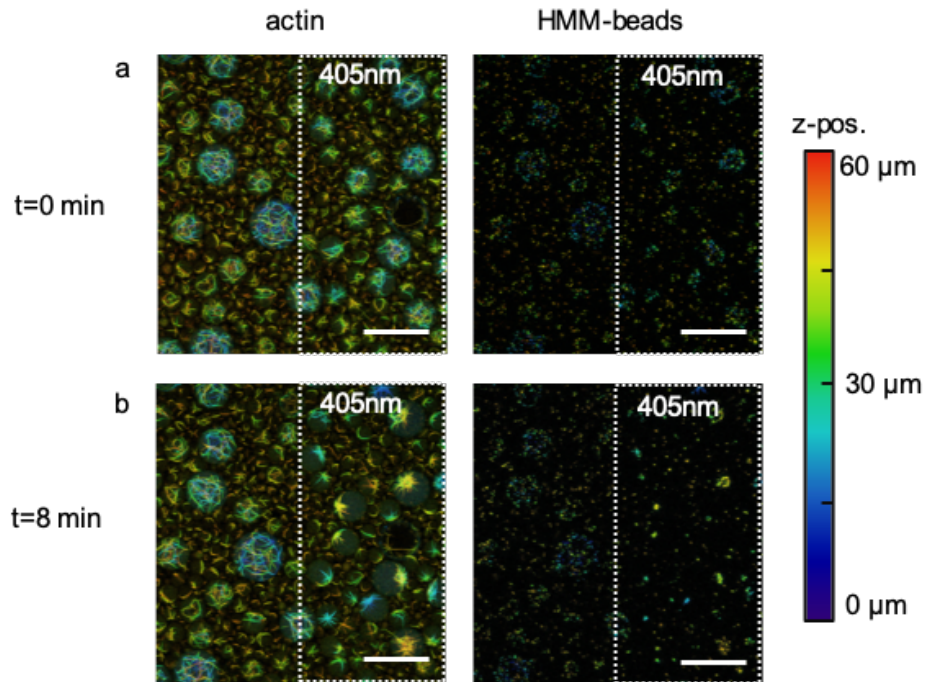
Supporting Figure 13: Denaturing polyacrylamide gel electrophoresis to prove actin functionalization with biotin-streptavidin. Denaturing PAGE (running conditions: 4-12% polyacrylamide, 200 V, 35 min) of actin functionalized with biotin-streptavidin (for details see Material and Methods) (L2), the supernatant containing surplus streptavidin (L3) and pure actin monomers (L4). Biotinylated actin (MW: 42 kDa<sup>2</sup>) could be purified via centrifugation after polymerization from surplus streptavidin (L2) which is found in the supernatant solution (L3).

**Supporting Figure 14: Cholesterol-tagged DNA self-assembles at the droplet periphery**



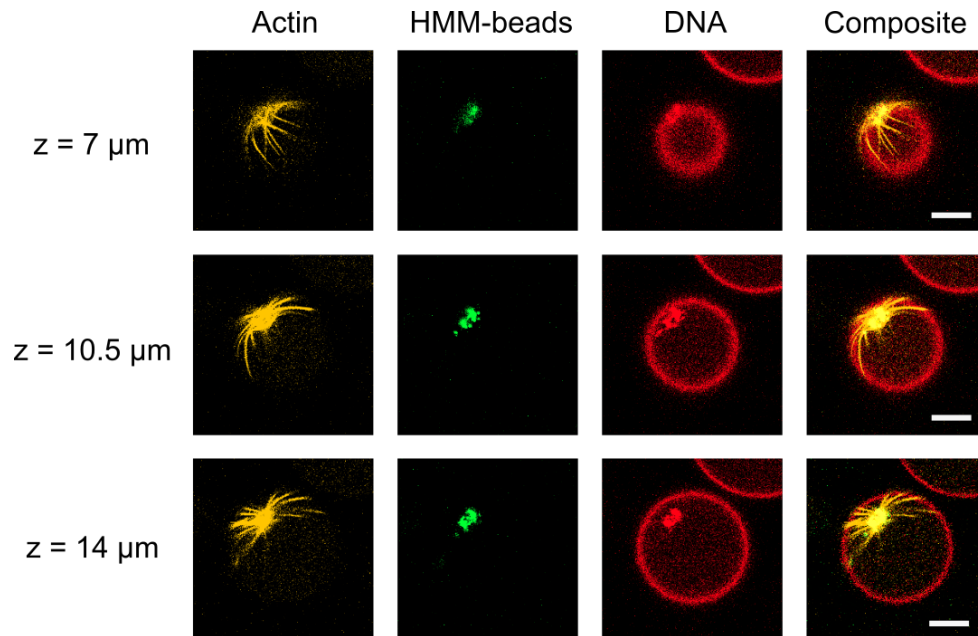
Supporting Figure 14: Cholesterol-tagged DNA self-assembles at the droplet periphery in presence of minimal actomyosin networks. Confocal fluorescence images of actin (red,  $\lambda_{ex} = 647$  nm) and Cy3-labeled cholesterol-tagged DNA (orange,  $\lambda_{ex} = 561$  nm) as well as brightfield and composite images. Cholesterol-tagged DNA can be used as a functional anchor to link actin to the droplet periphery via biotin-streptavidin linkage.<sup>3</sup> Scale bars: 100  $\mu$ m.

Supporting Figure 15: DNA-linker-mediated symmetry break of minimal actomyosin cortices in cell-sized compartments



Supporting Figure 15: DNA-linker-mediated symmetry break of minimal actomyosin cortices in cell-sized compartments. a,b) Confocal fluorescence images of actin filaments (color-coded  $z$ -projection,  $\lambda_{ex} = 561$  nm) and HMM-coated beads (color-coded  $z$ -projection,  $\lambda_{ex} = 488$  nm) immediately after illumination with blue light (a) and 8 min after illumination. Only the right half of the field of view (indicated by the white dotted line) was illuminated for 5 s ( $\lambda_{ex} = 405$  nm). The minimal actomyosin cortices in the illuminated area contract towards the periphery of the droplet whereas there is no contraction in the rest of the confocal frame.

## Supporting Figure 16: Actomyosin networks contract to the droplet periphery



Supporting Figure 16: Confocal fluorescence images of the actomyosin network within a representative symmetry-broken droplet at different axial positions. Actin filaments (orange,  $\lambda_{ex} = 561 \text{ nm}$ ) form aster-like structures with aggregated HMM-beads (green,  $\lambda_{ex} = 488 \text{ nm}$ ) in the contraction center after ATP release. The actomyosin network was linked to the compartment periphery via DNA-linker (red,  $\lambda_{ex} = 647 \text{ nm}$ ). The DNA mainly assembles at the surfactant layer but shows some unspecific interaction with the HMM-beads. The composite image illustrates the contact points of the actin aster with the droplet periphery. Scale bar:  $20 \mu\text{m}$ .

## Supporting Text 1: Hypothesis for the actin aster formation

Actomyosin contraction is mediated by many different processes on the molecular scale. However, many molecular mechanisms leading to contractile force generation remain not fully understood.<sup>4</sup> Especially in our engineered system composed of actin filaments, HMM-coated beads, methylcellulose and caged ATP it is challenging to disentangle the complexity of different mechanisms that can potentially lead to actin aster formation. Nonetheless, we can deduce some of the most important players which, in combination, result in the contractile behaviour of our system upon ATP release.

Actin bundles that are formed by crowding agents like methylcellulose or PEG are presumed to be non-polar.<sup>5,6</sup> Takiguchi found that the double-headed HMM is able to induce a sliding motion of antiparallel actin filaments. He proposed that the interplay of the motor protein concentration and parallel aligned actin filaments determines whether actin networks elongate or contract. He exemplifies the latter via the observation of actin asters in presence of  $2 \text{ mg mL}^{-1}$  HMM ( $\approx 13 \text{ }\mu\text{M}$ ) and  $30 \text{ }\mu\text{g mL}^{-1}$  ( $\approx 0.7 \text{ }\mu\text{M}$ ). Interestingly, the previously non-polar actin bundles were now transformed into polar bundles via the proposed sliding mechanism.<sup>7</sup> In our case, the nominal HMM (128 nM on the beads) and actin concentration (10  $\mu\text{M}$ ) differ dramatically from the concentrations used by Takiguchi (myosin head to actin ratio of 18.5 vs. 0.01). In our revised manuscript, we additionally show that the same concentration of soluble HMM does not lead to aster formation in our system (see Comment 3 and Figure Sxx in the revised version of the manuscript). This was also stated by Takiguchi and shown in Tanaka-Takiguchi (see Figure 4a in their paper).<sup>8</sup> Lastly, we do not see a decrease in actin length or a longitudinal splitting of actin bundles as observed for the system of Takiguchi. Nonetheless, we still think that sliding of antiparallel actin filaments and network rearrangement does occur in our system and may even be promoted by putting HMM on beads. However, the magnitude of the sliding is supposed to be substantially smaller and for the moment we do not have any evidence for a positive effect of the beads on aster formation solely based on a sliding mechanism which leads to a complete

polarization of the actin filaments.

A second mechanism by which actin contractility and formation into asters can be mediated is polarity sorting. Wollrab et al.<sup>4</sup> showed that a disordered actin network can form polar actin asters by myosin filaments dwelling at the filament end. Interestingly, their system also contained 0.3% methylcellulose as a crowding agent. However, in their case it was used to push actin and myosin to the coverslip and not to bundle the filaments. Nonetheless, they (and other studies) showed that crosslinking actin filaments promotes long-range aster formation. They also show that aster formation differs for different motor to actin ratios. Compellingly, this is in excellent agreement with our results, since a global contraction is expected for a motor to actin ratio of 0.01 like it is present in our study, whereas a stalled contraction occurs for a motor to actin ratio of 0.005. This also agrees with our observation as shown in Supplementary Figure x. In light of these similarities between mechanisms mediated by myosin filaments on the one side and beads on the other, it still remains unclear how this can be achieved from non-polar actin bundles since Wollrab et al. use single actin filaments. One explanation could be that bundled filaments do have a nematic ordering or tendency towards one polarisation of actin filaments, which leads to an overall asymmetry in polarity and hence movement of the HMM-beads.

Lastly, actin contractility could also result from buckling of actin filaments.<sup>9</sup> There it was shown that contraction can be induced via the non-linear response of actin to compression e.g. mediated by myosin filaments, which lead to filament buckling. The network connectivity was found to be a main driving factor in determining the scale of contraction. Thus, bundling of filaments with methylcellulose would, in theory, be capable to increase the length scale of actin contraction similar to the observed ones in this manuscript. However, bundling also increases the stiffness of the filaments and therefore hinders bending. This could be overcome by our HMM-beads, which can mediate high forces through  $10 \times 10^5$  HMM – heads and high inertia of the bead. This coincides with a theoretical model in which it was shown that high motor densities can lead to buckling of actin filaments.<sup>10</sup>



All in all, from this we can conclude that most likely the actin asters formed by our system are initially non-polar and transit into a at least partially polar actin aster predominantly governed via actin sliding, polarity sorting and buckling. However, the amount to which all of these mechanisms contribute in detail remains to be investigated in further studies.

## **Supporting Text 2: Estimation of the passive diffusion of the DNA linkers**

Cholesterol-tagged DNA is diffusive after self-assembly at the surfactant layer.<sup>3</sup> To give an estimate of the displacement over time, we assume two-dimensional diffusion on the spherical surface. Therefore, we can estimate:

$$\sigma = \sqrt{4Dt}, \quad (1)$$

where  $\sigma$  is the distance traveled by the DNA-linker,  $D$  the diffusion coefficient of the DNA linker and  $t$  the time. Assuming a droplet with radius  $r = 30 \mu\text{m}$ , the circumference of the equatorial plane yields:

$$C = 2\pi r = 190 \mu\text{m}. \quad (2)$$

The diffusion coefficient of cholesterol-tagged single stranded DNA was previously determined to be  $D = 0.41 \pm 0.01 \mu\text{m}^2 \text{s}^{-1}$ .<sup>3</sup> Inserting this and the time needed for the contraction of the actin filaments from Figure 4a,b (8 min) into (1), this yields a total distance traveled by the DNA linker of  $\sigma = 28 \mu\text{m}$ , which is less than  $\frac{1}{6}$  of the droplet circumference in the equatorial plane. However, if we calculate the time needed for the DNA linker to travel half or a quarter of the droplet circumference, as observed in the experiment, this yields 90 min or 22 min, respectively. Therefore, the DNA-linker have to be pulled by the forces generated by the rolling motion of the HMM-coated beads within the contracting actomyosin network.

### **Supporting Video 1: Growth of actin filaments in bulk in the presence of methylcellulose**

Actin filaments growing in bulk after addition of methylcellulose. Confocal fluorescence time series of growing actin filaments (red,  $\lambda_{ex} = 488$  nm) inside an observation chamber. The addition of methylcellulose mediates the growth and bundling of micrometer-thick and branched actin networks. Scale bar: 20  $\mu\text{m}$ .

### **Supporting Video 2: Actomyosin contraction in bulk**

Minimal actomyosin networks contracting in bulk after release of ATP induced by 2 s illumination with light of  $\lambda_{ex} = 405$  nm. Confocal fluorescence time series of actin filaments (red,  $\lambda_{ex} = 647$  nm) and HMM-coated beads (green,  $\lambda_{ex} = 488$  nm) in bulk. The field of view was illuminated with  $\lambda_{ex} = 405$  nm after 24 s. This leads to a movement of HMM-coated beads and thereby to a contraction of the actin network. Scale bar: 50  $\mu\text{m}$ .

### **Supporting Video 3: Velocity of HMM-coated beads in bulk**

Minimal actomyosin networks contracting in bulk before and after release of ATP induced by 5 s illumination with light of  $\lambda_{ex} = 405$  nm. After 500 s of observation, the field of view was illuminated with blue light. This leads to a movement of HMM-coated beads and thereby to a contraction of the actin network. Scale bar: 100  $\mu\text{m}$ .

### **Supporting Video 4: Actomyosin contraction in droplets**

Minimal actomyosin networks contract to the center of microfluidic droplet after release of ATP induced by 5 s illumination with light of  $\lambda_{ex} = 405$  nm (actin concentration: 10  $\mu\text{M}$ ). Confocal fluorescence time series of actin filaments (red,  $\lambda_{ex} = 647$  nm) and HMM-coated beads (green,  $\lambda_{ex} = 488$  nm) in droplet. This leads to a movement of HMM-coated beads and thereby to a contraction of the actin network to the droplet center. Scale bar: 30  $\mu\text{m}$ .

On the other hand, minimal actomyosin networks with high actin concentration (20  $\mu\text{M}$ ) contract slowly in microfluidic droplets after release of ATP induced by 2 s illumination with  $\lambda_{ex} = 405 \text{ nm}$ . Confocal fluorescence time series of actin filaments (red,  $\lambda_{ex} = 647 \text{ nm}$ ) and HMM-coated beads (green,  $\lambda_{ex} = 488 \text{ nm}$ ) in droplets. The field of view was illuminated after 37 s with  $\lambda_{ex} = 405 \text{ nm}$ . This leads to a movement of HMM-coated beads and thereby to a contraction of the actin network. Scale bar: 50  $\mu\text{m}$ .

### **Supporting Video 5: Minimal actomyosin networks contract to the periphery of microfluidic droplet**

Minimal actomyosin networks contract to the periphery of microfluidic droplet after release of ATP induced by 5 s illumination with light of  $\lambda_{ex} = 405 \text{ nm}$  (actin concentration: 10  $\mu\text{M}$ ) in presence of DNA-linkers. Confocal fluorescence time series of actin filaments (red,  $\lambda_{ex} = 647 \text{ nm}$ ) or HMM-coated beads (green,  $\lambda_{ex} = 488 \text{ nm}$ ) in droplets. This leads to a movement of HMM-coated beads and thereby to a contraction of the actin network to the droplet periphery due to the DNA-mediated link and the diffusivity of the DNA in the droplet periphery. Scale bar: 100  $\mu\text{m}$ .

## References

- (1) Platzman, I.; Janiesch, J.-W.; Spatz, J. P. Synthesis of Nanostructured and Biofunctionalized Water-in-Oil Droplets as Tools for Homing T Cells. *Journal of the American Chemical Society* **2013**, *135*, 3339–3342.
- (2) Holmes, K. C.; Popp, D.; Gebhard, W.; Kabsch, W. Atomic model of the actin filament. *Nature* **1990**, *347*, 44–49.
- (3) Jahnke, K.; Weiss, M.; Frey, C.; Antona, S.; Janiesch, J.-W.; Platzman, I.; Göpfrich, K.; Spatz, J. P. Programmable Functionalization of Surfactant-Stabilized Microfluidic Droplets via DNA-Tags. *Advanced Functional Materials* **2019**, *29*, 1808647.
- (4) Wollrab, V.; Belmonte, J. M.; Baldauf, L.; Leptin, M.; Nédeléc, F.; Koenderink, G. H. Polarity sorting drives remodeling of actin-myosin networks. *Journal of Cell Science* **2018**, *132*, jcs219717.
- (5) Suzuki, A.; Yamazaki, M.; Ito, T. Osmoelastic coupling in biological structures: formation of parallel bundles of actin filaments in a crystalline-like structure caused by osmotic stress. *Biochemistry* **1989**, *28*, 6513–6518.
- (6) Takiguchi, K. Heavy Meromyosin Induces Sliding Movements between Antiparallel Actin Filaments. *The Journal of Biochemistry* **1991**, *109*, 520–527.
- (7) Takiguchi, K.; Negishi, M.; Tanaka-Takiguchi, Y.; Homma, M.; Yoshikawa, K. Transformation of ActoHMM Assembly Confined in Cell-Sized Liposome. *Langmuir* **2011**, *27*, 11528–11535.
- (8) Tanaka-Takiguchi, Y.; Kakei, T.; Tanimura, A.; Takagi, A.; Honda, M.; Hotani, H.; Takiguchi, K. The Elongation and Contraction of Actin Bundles are Induced by Double-headed Myosins in a Motor Concentration-dependent Manner. *Journal of Molecular Biology* **2004**, *341*, 467–476.

- (9) Murrell, M. P.; Gardel, M. L. F-actin buckling coordinates contractility and severing in a biomimetic actomyosin cortex. *Proceedings of the National Academy of Sciences* **2012**, *109*, 20820–20825.
- (10) Lenz, M.; Thoresen, T.; Gardel, M. L.; Dinner, A. R. Contractile Units in Disordered Actomyosin Bundles Arise from F-Actin Buckling. *Physical Review Letters* **2012**, *108*.

## **A.4 Supporting Information for Publication 4: Choice of fluorophore affects dynamic DNA nanostructures**

# Supplementary Information: Choice of fluorophore affects dynamic DNA nanostructures

Kevin Jahnke,<sup>†,‡</sup> Helmut Grubmüller,<sup>¶</sup> Maxim Igaev,<sup>\*,¶</sup> and Kerstin Göpfrich<sup>\*,†,‡</sup>

<sup>†</sup>*Max Planck Institute for Medical Research, Biophysical Engineering Group,  
Jahnstraße 29, 69120 Heidelberg, Germany*

<sup>‡</sup>*Department of Physics and Astronomy, Heidelberg University,  
69120 Heidelberg, Germany*

<sup>¶</sup>*Max Planck Institute for Biophysical Chemistry, Department of Theoretical and  
Computational Biophysics,  
Am Fassberg 11, 37077 Göttingen, Germany*

E-mail: maxim.igaev@mpibpc.mpg.de; kerstin.goepfrich@mr.mpg.de

# Contents

<b>Supplementary Figures</b>	<b>4</b>
Supplementary Figure S1: ssDNA/tsDNA-binding is equilibrated within the first hour . . . . .	4
Supplementary Figure S2: Fluorophore-tagged ssDNA does not interact with droplet-stabilizing surfactants . . . . .	5
Supplementary Figure 3: Droplet size does not significantly influence binding equilibrium . . . . .	6
Supplementary Figure 4: Polyacrylamide gel electrophoresis (PAGE) of ssDNA-tsDNA binding . . . . .	7
Supplementary Figure S5: MD simulations suggest that Cy5-labeling can stabilize more compact ssDNA conformations . . . . .	8
Supplementary Figure S6: pH hysteresis of ssDNA/tsDNA binding . . . . .	9
Supplementary Figure S7: Light-mediated acidification of water-in-oil droplets reveals different detachment kinetics of tsDNA modified with different fluorophores. . . . .	10
Supplementary Figure S8: Influence of 3' modification of tsDNA-Cy5 . . . . .	11
<b>Supplementary Table</b>	<b>12</b>
Supplementary Table S1: Different dyes and their net charge, hydrophobicity and $pK_a$ . . . . .	12
<b>Supplementary Texts</b>	<b>13</b>
Supplementary Text S1: Estimation of the apparent thickness of the reaction layer $\varepsilon$	13
Supplementary Text S2: Reaction-diffusion model of ssDNA-tsDNA interaction in a spherical volume . . . . .	13
<b>Supplementary Videos</b>	<b>17</b>



Supplementary Video S1: MD trajectory of unlabelled ssDNA . . . . .	17
Supplementary Video S2: MD trajectory of Cy3-ssDNA . . . . .	17
Supplementary Video S3: MD trajectory of Cy5-ssDNA . . . . .	17
Supplementary Video S4: MD trajectory of Alexa488-ssDNA . . . . .	17
Supplementary Video S5: Light-mediated detachment kinetics of Cy5-tsDNA . . .	18
<b>References</b>	<b>19</b>

## Supplementary Figures

### Supplementary Figure S1: ssDNA/tsDNA-binding is equilibrated within the first hour

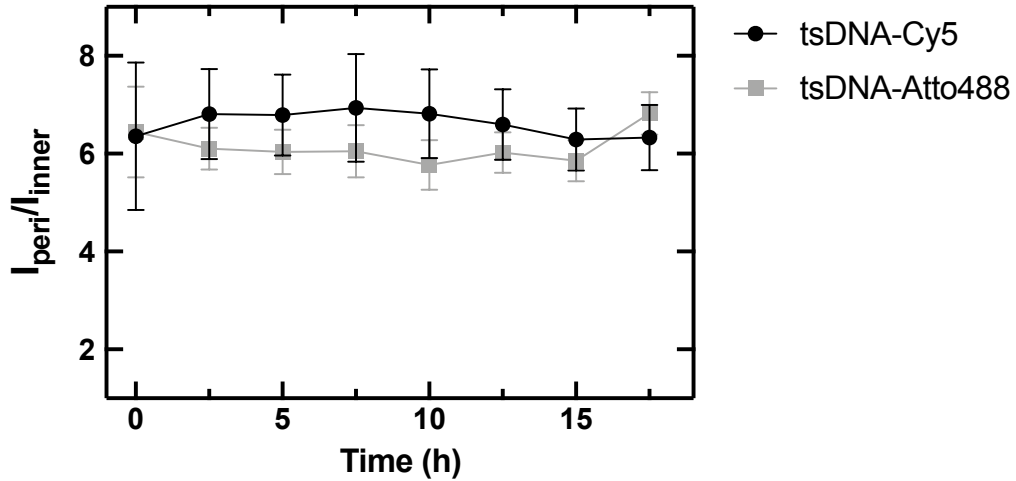


Figure 1: ssDNA/tsDNA-binding efficiency remains constant over time. Fluorescence intensity ratio  $I_{\text{peri}}/I_{\text{in}}$  of tsDNA inside water-in-oil droplets for ssDNA-Cy3/tsDNA-Atto488 (gray) and ssDNA-Alexa488/tsDNA-Cy5 (black) over the course of 17.5 h. The fluorescence intensity ratios remain constant over time. This shows that the ssDNA/tsDNA binding reaches a dynamic steady-state already minutes after the droplet production and importantly before the imaging. Therefore, all experiments in this manuscript show the equilibrated state (with the exception of Figure 3, where we induce a pH change). Error bars correspond to the standard deviation of  $n=9$  droplets.

**Supplementary Figure S2: Fluorophore-tagged ssDNA does not interact with droplet-stabilizing surfactants**

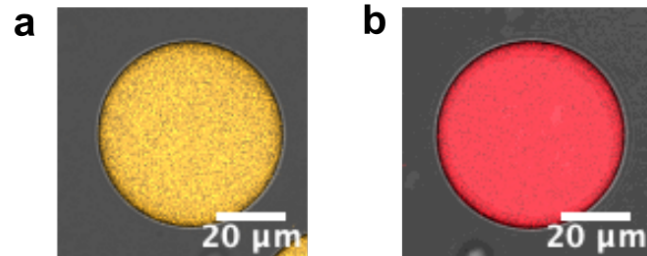


Figure 2: Fluorophore-tagged ssDNA does not interact with droplet-stabilizing surfactants. Representative confocal images of water-in-oil droplets containing Cy3-(**a**,  $\lambda_{ex} = 561$  nm) and Cy5-labeled ssDNA (**b**,  $\lambda_{ex} = 647$  nm) without cholesterol-modification at pH8. The solution contained 20 mM potassium phosphate buffer, 10 mM  $MgCl_2$  and 1.5  $\mu$ M DNA. Scale bars: 20  $\mu$ m.

### Supplementary Figure 3: Droplet size does not significantly influence binding equilibrium

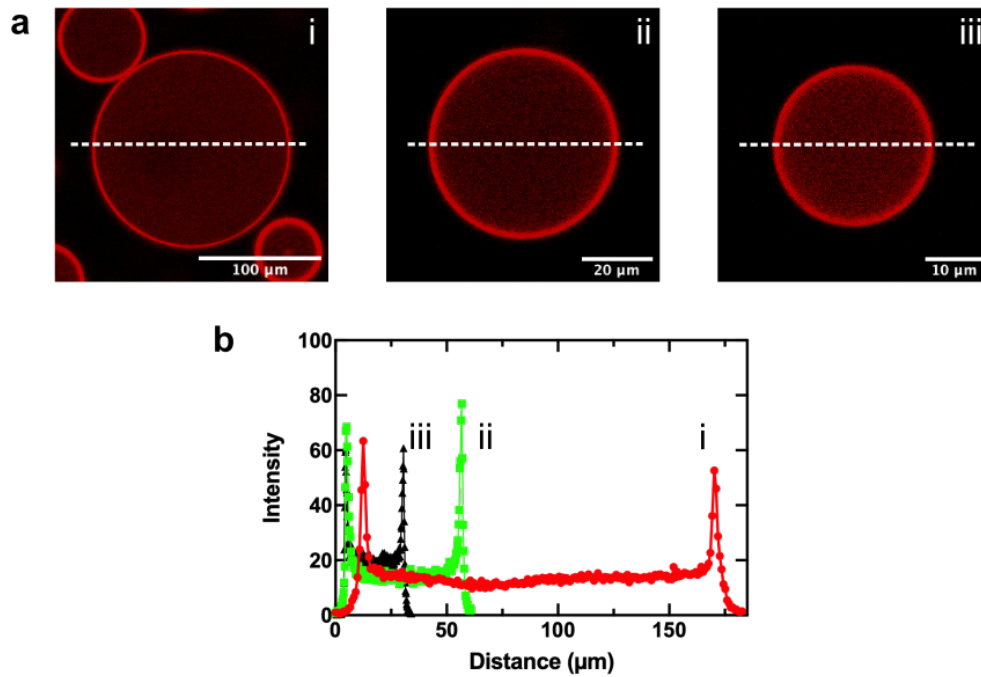


Figure 3: **a** Water-in-oil droplets of different sizes containing ssDNA and tsDNA-Cy5-3' ( $\lambda_{ex} = 633 \text{ nm}$ ) at the intermediate pH 6.5. **b** Corresponding intensity profiles along the equatorial region for the droplets as indicated by the white dashed line in **a**. No significant difference is observed for the intensity distribution of tsDNA-Cy5. Therefore, we can conclude that the droplet size does not influence the binding equilibrium of ssDNA and tsDNA in the size regime of droplet diameters from 25-160  $\mu\text{m}$ .

## Supplementary Figure 4: Polyacrylamide gel electrophoresis (PAGE) of ssDNA-tsDNA binding

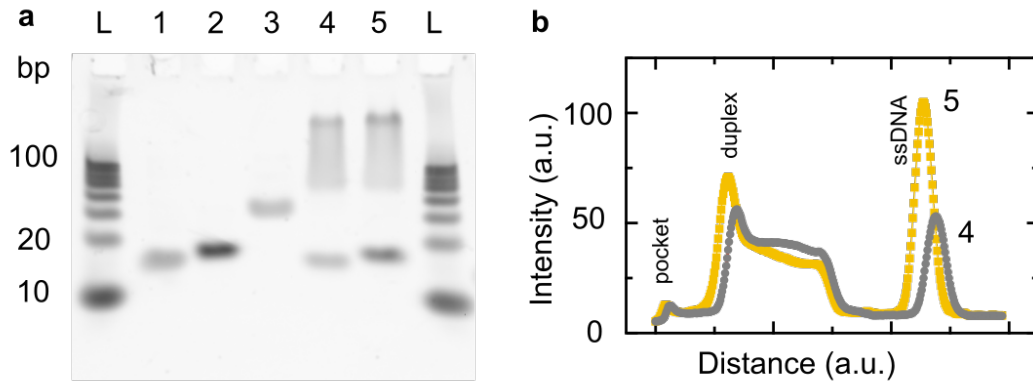


Figure 4: Polyacrylamide gel electrophoresis (PAGE) of ssDNA-tsDNA binding. **a** Non-denaturing PAGE of ss- and tsDNA at pH 6.5. The gel was loaded with a low base pair ladder (L), 4  $\mu$ M ssDNA (1), 4  $\mu$ M ssDNA-Cy3 (2), 3  $\mu$ M tsDNA-Cy5 (3), 4  $\mu$ M ssDNA and 3  $\mu$ M tsDNA-Cy5 (4) and 4  $\mu$ M ssDNA-Cy3 and 3  $\mu$ M tsDNA-Cy5 (5). The loading buffer contained 250 mM potassium phosphate and 10 mM  $\text{MgCl}_2$  as for the results in Figure 1 (main text). The gel was run at 100 V for 90 min and the running buffer contained 0.5x TBE and 11 mM  $\text{MgCl}_2$ . **b** Intensity profile of lanes (4) and (5) analyzed using the ImageJ Gel Analysis tool. The relative amount of unbound ssDNA is higher for the case of Cy3-labeled ssDNA than for unlabeled ssDNA. Quantifying the peak integrals for the ssDNA-tsDNA duplex band relative to the ssDNA band shows that a total of 78.7% of unlabeled ssDNA is bound to the tsDNA-Cy5, whereas only 62.6% of the Cy3-labeled DNA is bound to the tsDNA-Cy5. This serves as an independent confirmation of the observations in the droplet system presented in in Figure 1 (main text).

## Supplementary Figure S5: MD simulations suggest that Cy5-labeling can stabilize more compact ssDNA conformations

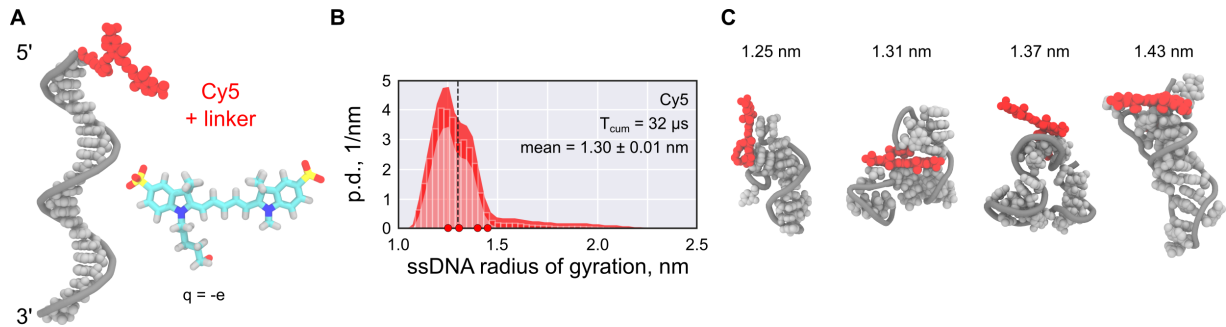


Figure 5: **A** Starting conformation of Cy5-(red) ssDNA (gray). The chemical structure of the fluorophore and its net charge are shown as an inset. **B** Probability density distributions of the gyration radius of ssDNA labeled with Cy5. The shaded area indicates the 95% confidence interval estimated using bootstrapping (see Methods in the main text). The black dashed line indicates the mean of the distribution,  $T_{\text{cum}}$  the cumulative simulation time. **C** Representative structure snapshots of the Cy5-ssDNA. Positions of the selected snapshots within the corresponding distributions are marked with dots in the probability density distribution.

## Supplementary Figure S6: pH hysteresis of ssDNA/tsDNA binding

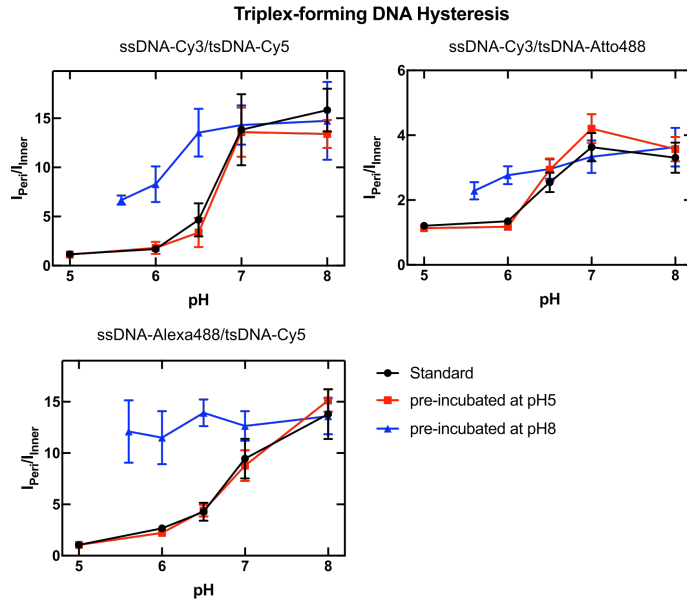


Figure 6: pH hysteresis of ssDNA/tsDNA binding. Fluorescence intensity ratio  $I_{Peri}/I_{Inner}$  of tsDNA within water-in-oil droplets at different pH values for different ssDNA/tsDNA combinations including ssDNA-Cy3/tsDNA-Cy5, ssDNA-Cy3/tsDNA-Atto488 and ssDNA-Alexa488/tsDNA-Cy5. The tsDNA was incubated with ssDNA for 10 min in 10 mM sodium phosphate buffer and 20 mM  $MgCl_2$  at pH 5 (blue curve), pH 8 (red curve) or directly at the indicated pH (black). After incubation the solutions were mixed 1:1 with 200 mM phosphate buffers ranging from pH 5 to 8 and subsequently encapsulated into droplets. The droplets were sealed in an observation chamber and imaged with confocal fluorescence microscopy. From these images, the fluorescence intensity ratio  $I_{Peri}/I_{Inner}$  was extracted. The plots indicate that the duplex dissociation happens at lower pH values compared to the duplex formation. Importantly, this is independent of the type of fluorophore modification as it is visible for all tested ssDNA/tsDNA combinations. In some cases, the attachment to the periphery seems mostly irreversible (see ssDNA-Alexa488/tsDNA-Cy5). Note that it was not possible to revert back to pH 5 because the buffer range of the phosphate buffer used lies between pH 5.8 and pH 8.2. Error bars correspond to the standard deviation of  $n \geq 25$  droplets.

**Supplementary Figure S7: Light-mediated acidification of water-in-oil droplets reveals different detachment kinetics of tsDNA modified with different fluorophores.**

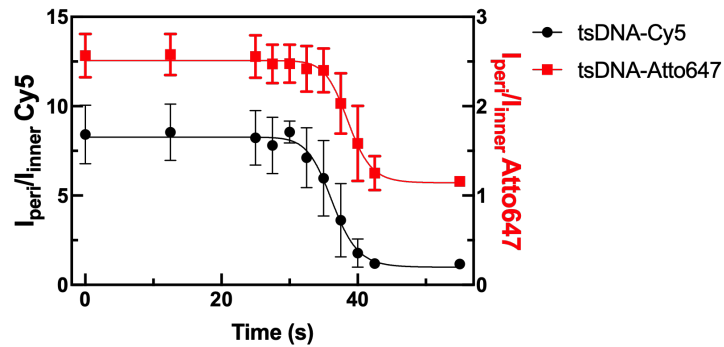


Figure 7: Light-mediated acidification of water-in-oil droplets reveals different detachment kinetics of tsDNA modified with different fluorophores. Fluorescence intensity ratio  $I_{\text{peri}}/I_{\text{inner}}$  of tsDNA-Cy5 (black) and tsDNA-Atto647 (red) within droplets over time with Cy3-labeled ssDNA. Error bars correspond to the standard deviation of  $n \geq 20$  droplets for the DNA experiments. Solid lines represent sigmoidal fits with turning points at  $36.3 \pm 0.3$  s (tsDNA-Cy5) and  $38.6 \pm 0.3$  s (tsDNA-Atto647). tsDNA-Cy5 detaches faster from the droplet periphery during the acidification indicating that the fluorophore modification on tsDNA alone, changes the reaction kinetics.



## Supplementary Figure S8: Influence of 3' modification of tsDNA-Cy5

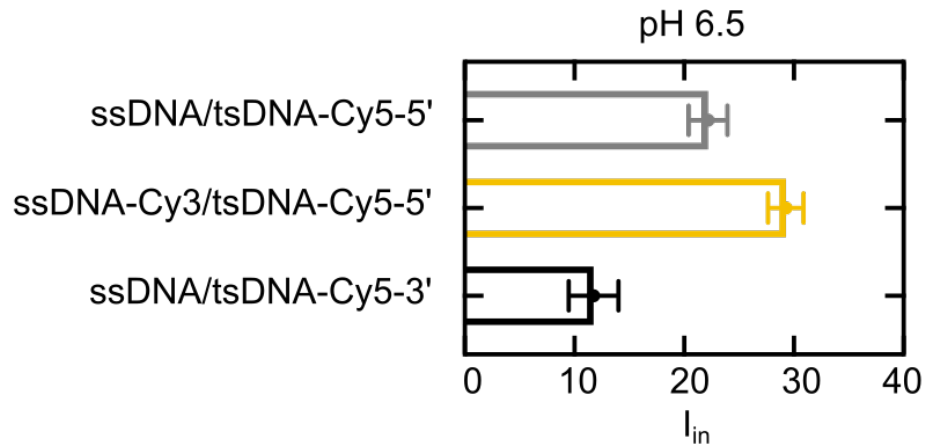


Figure 8: Fluorescence intensity inside of droplets  $I_{in}$  at the intermediate pH 6.5 for ssDNA/tsDNA-Cy5-5', ssDNA-Cy3/tsDNA-Cy5-5' and ssDNA/tsDNA-Cy5-3'. A 3' modification of tsDNA-Cy5 leads to more efficient binding to the unlabeled ssDNA than with a 5' modification. This is likely due to the fact that the fluorophore is placed further away from the stem loop that is complementary to the ssDNA, hence allowing the ssDNA to bind the tsDNA-Cy5-3' more efficiently.

## Supplementary Table

### Supplementary Table S1: Different dyes and their net charge, hydrophobicity and $pK_a$

Table 1: Different dyes and their net charge, hydrophobicity at pH 7.4 and  $pK_a$ . The hydrophobicity of the dyes is expressed by the log of the distribution coefficient,  $\log D$ , which is a measure of the expected ratio of dye concentrations in water and a non-polar solvent. Note that a positive  $\log D$  corresponds to hydrophobic substances, whereas hydrophilic substances have a negative  $\log D$ .  $\log D$  values are taken from <sup>[1]</sup> and  $pK_a$  values from <sup>[2]</sup> Our results show that hydrophilic dyes like Alexa488 are less prone to unspecific interactions with ssDNA.

Dye	Net charge at pH 7.4	$\log D$ at pH 7.4	$pK_a$
Cy3	0	+3.03	7.9 (Cy3B)
Alexa488	-3.94	-10.48	3.0
Atto647N	+0.61	+1.96	6.3 (Atto633)

## Supplementary Texts

### Supplementary Text S1: Estimation of the apparent thickness of the reaction layer $\varepsilon$

The thickness of the reaction layer,  $\varepsilon$ , was determined by analyzing the intensity at the droplet periphery for the ssDNA/tsDNA-Cy5 combination at pH8. The intensity at the droplet periphery  $I_{peri}$  was quantified by fitting a Gaussian distribution along a line orthogonal to the droplet circumference. The fit function was of the form  $y = a + (b - a)e^{-(x-c)/2d^2}$ , where  $a$  is an offset parameter,  $b$  is the maximum intensity,  $c$  is the center point, and  $d$  is the width. This analysis was repeated 20 times every  $18^\circ$  along the droplet circumference for 12 representative droplets.  $\varepsilon$  was defined as the average of the full width at half maximum (FWHM) and calculated via  $\varepsilon = 2\sqrt{2\ln(2)}\bar{d}$  to be  $\varepsilon = 1.82 \pm 0.37 \mu\text{m}$ .

### Supplementary Text S2: Reaction-diffusion model of ssDNA-tsDNA interaction in a spherical volume

To describe the reaction-diffusion of the ssDNA and tsDNA molecules in a spherical droplet with a radius  $r_0$ , we adapted a previously proposed, volumetric model,<sup>[3,4]</sup> in which the binding and dissociation reactions are localized in a layer near the spherical droplet periphery. Outside of this layer, tsDNA is assumed to diffuse freely and isotropically. Let  $\varepsilon$  denote the thickness of the reaction volume  $V_\varepsilon \approx 4\pi r_0^2 \varepsilon$ , in which ssDNA is located,  $T(r, t)$  and  $S(r, t)$  be the volumetric concentrations of *free* tsDNA and ssDNA, respectively, and  $T_{tot}$  and  $S_{tot}$  be the *total* concentrations of tsDNA and ssDNA in the droplet volume. Then, the equations

describing the evolution of  $T(r, t)$  and  $S(r, t)$  take the form:

$$\begin{aligned}\frac{\partial T}{\partial t} &= D\Delta T - k_{on}TS + k_{off}(S_{tot} - S), \\ \frac{\partial S}{\partial t} &= -k_{on}TS + k_{off}(S_{tot} - S), \\ 0 &\leq r \leq r_0, t > 0,\end{aligned}\tag{1}$$

where  $D$  is the diffusion constant of tsDNA,  $k_{on}$  and  $k_{off}$  are the association and dissociation rate constants, respectively. Since all binding sites (ssDNA) are concentrated within  $V_\varepsilon$ , the concentration of ssDNA must vanish outside of this area, *i.e.*  $S(r, t) = 0$  for  $r < r_0 - \varepsilon$ . Furthermore, we assume that the droplet boundary is impermeable, *i.e.*  $\partial T/\partial r|_{r_0} = 0$ . We also note that, strictly speaking, Eq. 1 is solved separately for  $0 \leq r < r_0 - \varepsilon$  and  $r \geq r_0 - \varepsilon$ , but the joint solution must be continuous and differentiable everywhere on  $0 \leq r \leq r_0$ . We therefore require that:

$$\begin{aligned}T^{(0)}|_{r_0-\varepsilon} &= T^{(\varepsilon)}|_{r_0-\varepsilon}, \\ \frac{\partial T^{(0)}}{\partial r}|_{r_0-\varepsilon} &= \frac{\partial T^{(\varepsilon)}}{\partial r}|_{r_0-\varepsilon},\end{aligned}\tag{2}$$

where  $T^{(0)}$  and  $T^{(\varepsilon)}$  are the piecewise solutions of  $T(r, t)$  within and outside of  $V_\varepsilon$ , respectively. Note that for very small droplets (*i.e.* in our system droplets that are smaller than  $1 \mu\text{m}$ ), the approximation  $\varepsilon/r_0 \ll 1$  does not hold anymore. In practice, this affects droplets with the radius of about  $1 \mu\text{m}$  or smaller due to experimental constraints.

We seek for the steady-state solution of Eq. 1 because it reflects experiments in which the ssDNA-tsDNA binding has attained equilibrium (see, *e.g.*, Figure 1 in the main text and Figure S1). The steady-state solution is given by  $T(r, t) = T_{eq}(r)$  and  $S(r, t) = S_{eq}(r)$ . Solving Eq. 1 under Eq. 2 and the boundary conditions yields:

$$\begin{aligned}T_{eq}(r) &= C, \\ S_{eq}(r) &= \frac{K_D S_{tot}}{T_{eq}(r) + K_D},\end{aligned}\tag{3}$$

where we have introduced the apparent dissociation constant  $K_D = k_{off}/k_{on}$ , and where  $C$  is an arbitrary constant. This constant can be found explicitly using the mass conservation of tsDNA within the droplet volume, that is:

$$\int_0^{r_0} T_{eq}(r)4\pi r^2 dr + \int_0^{r_0} (S_{tot} - S_{eq}(r))4\pi r^2 dr = T_{tot} \frac{4}{3}\pi r_0^3. \quad (4)$$

$$\text{free tsDNA} + \text{bound tsDNA} = \text{total tsDNA}$$

By substituting Eq. 3 into Eq. 4 and assuming that  $\varepsilon \ll r_0$ , we finally obtain the explicit expressions for the steady-state concentrations:

$$T_{eq} = -\frac{1}{2} \left[ 3 \frac{\varepsilon}{r_0} S_{tot} + K_D - T_{tot} \right] + \sqrt{\left[ 3 \frac{\varepsilon}{r_0} S_{tot} + K_D - T_{tot} \right]^2 + 4T_{tot}K_D}, \quad (5)$$

$$S_{eq} = \frac{K_D S_{tot}}{T_{eq} + K_D}.$$

In the experiment, the concentrations  $T_{eq}$  and  $S_{eq}$  are not available directly, but only through the respective fluorescent intensities measured in the droplet interior and at the periphery with confocal microscopy. More specifically, the intensity of labelled tsDNA molecules is  $I = E_{ex}E_{em}V_{obs}T_{eq}$ ,<sup>[5,6]</sup> where  $V_{obs}$  is the observation volume, and  $E_{ex}$  and  $E_{em}$  are excitation and emission functions of the light path, respectively. Assuming that imaging settings do not change for the tested fluorophore combinations, the ratio between the peripheral,  $\tilde{I}_{peri}$ , and inner intensity,  $\tilde{I}_{in}$ , of tsDNA fluorescence can be expressed as:

$$\frac{\tilde{I}_{peri}}{\tilde{I}_{in}} = \frac{(S_{tot} - S_{eq}) + T_{eq}}{T_{eq}} = 1 + \frac{S_{tot}}{T_{eq} + K_D} \equiv A(\varepsilon, K_D). \quad (6)$$

Here,  $\tilde{I}_{peri} = I_{peri}/(2\pi r_0 \varepsilon h)$  and  $\tilde{I}_{in} = I_{in}/(\pi r_{in}^2 h)$ , where  $h$  is the characteristic height of the point spread function of the microscope (typically a few microns) and  $r_{in} < r_0$  is the radius of an arbitrary sphere placed within the droplet volume. The expression in Eq. 6 can be now employed to estimate  $K_D$  by experimentally measuring  $A$  and precomputing  $\varepsilon$  (see

Supplementary Text S2). By analogy, the uncertainty of  $K_D$  can be calculated using error propagation on A:

$$\sigma_A^2 \approx \left( \frac{\partial A}{\partial \varepsilon} \right)^2 \sigma_\varepsilon^2 + \left( \frac{\partial A}{\partial K_D} \right)^2 \sigma_{K_D}^2, \quad (7)$$

where the partial derivatives are given by:

$$\begin{aligned} \frac{\partial A}{\partial \varepsilon} &= \frac{3S_{tot}^2}{2r_0(T_{eq} + K_D)^2} \left[ 1 - \frac{3\frac{\varepsilon}{r_0}S_{tot} + K_D - T_{tot}}{\sqrt{(3\frac{\varepsilon}{r_0}S_{tot} + K_D - T_{tot})^2 + 4T_{tot}K_D}} \right], \\ \frac{\partial A}{\partial K_D} &= -\frac{S_{tot}}{2(T_{eq} + K_D)^2} \left[ 1 + \frac{3\frac{\varepsilon}{r_0}S_{tot} + K_D + T_{tot}}{\sqrt{(3\frac{\varepsilon}{r_0}S_{tot} + K_D - T_{tot})^2 + 4T_{tot}K_D}} \right]. \end{aligned} \quad (8)$$

## Supplementary Videos

### Supplementary Video S1: MD trajectory of unlabelled ssDNA

MD trajectory showing the evolution of the starting conformation of the unlabelled ssDNA over the total time of 5  $\mu$ s and sampled every 5 ns. The conformation of the DNA remains, on average, more extended throughout the simulation than the labeled counterparts, thus being more accessible for complementary base pairing. See Fig. 2B for the distribution of the radius of gyration.

### Supplementary Video S2: MD trajectory of Cy3-ssDNA

MD trajectory showing the evolution of the starting conformation of the Cy3-labelled ssDNA over the total time of 6  $\mu$ s and sampled every 5 ns. The Cy3-ssDNA adopts more compact conformations compared to the unlabeled counterpart, in which the hydrophobic bases are wrapped around the Cy3 fluorophore, reducing their accessibility for complementary base pairing. See Fig. 2B for the distribution of the radius of gyration.

### Supplementary Video S3: MD trajectory of Cy5-ssDNA

MD trajectory showing the evolution of the starting conformation of the Cy5-labelled ssDNA over the total time of 6  $\mu$ s. Like in the case of the Cy3 modification, Video S2, the ssDNA adopts more compact conformations, where the bases are wrapped around Cy5 fluorophore, reducing their accessibility for complementary base pairing. See Fig. S3B for the distribution of the radius of gyration.

### Supplementary Video S4: MD trajectory of Alexa488-ssDNA

MD trajectory showing the evolution of the starting conformation of the Alexa488-labelled ssDNA over the total time of 6  $\mu$ s. The accessibility of the bases is, on averaged, higher

compared to the Cy3 and Cy5 modifications (Video S2 and S3), possibly due to weaker dye-ssDNA stacking interactions and the higher negative charge of Alexa 488. See Fig. 2B for the distribution of the radius of gyration.

### **Supplementary Video S5: Light-mediated detachment kinetics of Cy5-tsDNA**

Representative confocal time series of Cy5-labeled tsDNA ( $\lambda_{ex} = 647\text{ nm}$ ) encapsulated together with unlabelled ssDNA and NPE-caged-sulfate into water-in-oil droplets at pH 8. Upon illumination with 405 nm for 50 s, uncaging of NPE-caged-sulfate releases a proton, leading to acidification inside the droplet. During acidification, tsDNA-Cy5 detaches from the droplet periphery as the triplex state is energetically favoured at low pH. The normalized inner intensity  $I_{in}$  over time is shown in Figure 3C (Main). in Scale bars: 20  $\mu\text{m}$ .



## References

- (1) Zanetti-Domingues, L. C.; Tynan, C. J.; Rolfe, D. J.; Clarke, D. T.; Martin-Fernandez, M. Hydrophobic Fluorescent Probes Introduce Artifacts into Single Molecule Tracking Experiments Due to Non-Specific Binding. *PLoS ONE* **2013**, *8*.
- (2) Bak, S. Y.; Hwang, J.; Bae, S.; Lim, S.; Kim, Y.; Alzahrani, K.; Wahab, R.; Alkheldairy, A.; Kim, S. K. General and facile purification of dye-labeled oligonucleotides by pH-controlled extraction. *BioTechniques* **2018**, *64*.
- (3) Hale, J.; Raugel, G. *Mathematics in Science and Engineering*; 1992; pp 63–97.
- (4) Fibich, G.; Gannot, I.; Hammer, A.; Schochet, S. Chemical Kinetics on Surfaces: A Singular Limit of a Reaction-Diffusion System. *SIAM Journal on Mathematical Analysis* **2007**, *38*, 1371–1388.
- (5) Lakowicz, J. R. *Principles of Fluorescence Spectroscopy*; Springer US: Boston, USA, 2006.
- (6) Gell, C.; Brockwell, R.; Smith, A. *Handbook of single molecule fluorescence spectroscopy*; Oxford University Press: Oxford; New York, 2013.

## **A.5 Supporting Information for Publication 5: Proton gradients from light-harvesting *E. coli* control DNA assemblies for synthetic cells**

# Supplementary Information: Proton gradients from light-harvesting *E. coli* control DNA assemblies for synthetic cells

Kevin Jahnke,<sup>†,‡</sup> Noah Ritzmann,<sup>¶</sup> Julius Fichtler,<sup>†</sup> Anna Nitschke,<sup>§</sup> Yannik  
Dreher,<sup>†,‡</sup> Tobias Abele,<sup>†,‡</sup> Götz Hofhaus,<sup>||</sup> Ilia Platzman,<sup>§,⊥</sup> Rasmus Schröder,<sup>||</sup>  
Daniel J. Müller,<sup>¶</sup> Joachim P. Spatz,<sup>§,⊥,#</sup> and Kerstin Göpfrich<sup>\*,†,‡</sup>

<sup>†</sup>*Max Planck Institute for Medical Research, Biophysical Engineering Group,  
Jahnstraße 29, 69120 Heidelberg, Germany*

<sup>‡</sup>*Department of Physics and Astronomy, Heidelberg University,  
69120 Heidelberg, Germany*

<sup>¶</sup>*Department of Biosystems Science and Engineering, Eidgenössische Technische  
Hochschule (ETH) Zurich, Mattenstrasse 26, 4058 Basel, Switzerland*

<sup>§</sup>*Max Planck Institute for Medical Research, Department of Cellular Biophysics,  
Jahnstraße 29, 69120 Heidelberg, Germany*

<sup>||</sup>*Centre for Advanced Materials,  
Im Neuenheimer Feld 267, 69120 Heidelberg, Germany*

<sup>⊥</sup>*Institute for Molecular Systems Engineering (IMSE), Heidelberg University,  
Im Neuenheimer Feld 225, 69120 Heidelberg, Germany*

<sup>#</sup>*Max Planck School Matter to Life, Jahnstraße 29, 69120 Heidelberg, Germany*

E-mail: kerstin.goepfrich@mr.mpg.de

# Contents

<b>Supplementary Figures</b>	<b>4</b>
Supplementary Figure 1: Activation of xenorhodopsin with different light sources.	4
Supplementary Figure 2: Saturation of pH-gradients upon white light illumination	5
Supplementary Figure 3: Photoactivity measurements with different <i>E. coli</i> densities . . . . .	6
Supplementary Figure 4: Chemical structure of pyranine . . . . .	7
Supplementary Figure 5: Calibration curve of pyranine fluorescence in presence of GUVs . . . . .	8
Supplementary Figure 6: Monitoring pH changes with pyranine in the presence of GUVs . . . . .	9
Supplementary Figure 7: Layout of the microfluidic device for the formation of water-in-oil droplets . . . . .	10
Supplementary Figure 8: Calibration curve of pyranine fluorescence in water-in-oil droplets . . . . .	11
Supplementary Figure 9: pH-sensitive attachment of triplex-forming DNA . . . .	12
Supplementary Figure 10: Fluorophore-tagged single-stranded DNA does not interact with droplet-stabilizing surfactants . . . . .	13
Supplementary Figure 11: Brightfield and confocal images of microfluidic droplets containing engineered <i>E. coli</i> . . . . .	14
Supplementary Figure 12: Hysteresis of DNA triplex attachment and detachment	15
Supplementary Figure 13: Cadnano design of the membrane-sculpting DNA origami	16
Supplementary Figure 14: Blunt-end stacking induces polymerization of DNA origami plates . . . . .	17
Supplementary Figure 15: Atomic force microscopy images of the DNA origami .	18
Supplementary Figure 16: Agarose gel electrophoresis of the DNA origami . . . .	19

Supplementary Figure 17: Droplets are not deformed by attaching DNA origami to the droplet periphery . . . . .	20
Supplementary Figure 18: FRAP experiments of GUVs with membrane-bound DNA origami . . . . .	21
Supplementary Figure 19: DNA origami cortex suppresses membrane fluctuations	22
Supplementary Figure 20: Deformation process of GUVs with DNA origami . . .	23
Supplementary Figure 21: Confocal images of deformed GUVs . . . . .	24
Supplementary Figure 22: Confocal images of GUVs after detachment of membrane- bound DNA-origami . . . . .	25
Supplementary Figure 23: Exemplary confocal images of DNA-functionalized GUVs	26
Supplementary Figure 24: Attachment of the single-stranded DNA triplex to GUVs during light illumination . . . . .	27
Supplementary Figure 25: Confocal images of deformed GUVs after light-mediated attachment of DNA origami . . . . .	28
Supplementary Figure 26: Light-mediated deformation of GUVs . . . . .	29
<b>Supplementary Tables</b>	<b>30</b>
Supplementary Table 1: DNA and amino-acid sequences of xenorhodopsin-constructs . . . . .	30
<b>Supplementary Notes</b>	<b>32</b>
Supplementary Note 1: Estimation of the pH change for DNA attachment . . . .	32
Supplementary Note 2: Estimation of DNA origami density per GUV . . . . .	33
<b>References</b>	<b>34</b>

## Supplementary Figures

### Supplementary Figure 1: Activation of xenorhodopsin with different light sources.

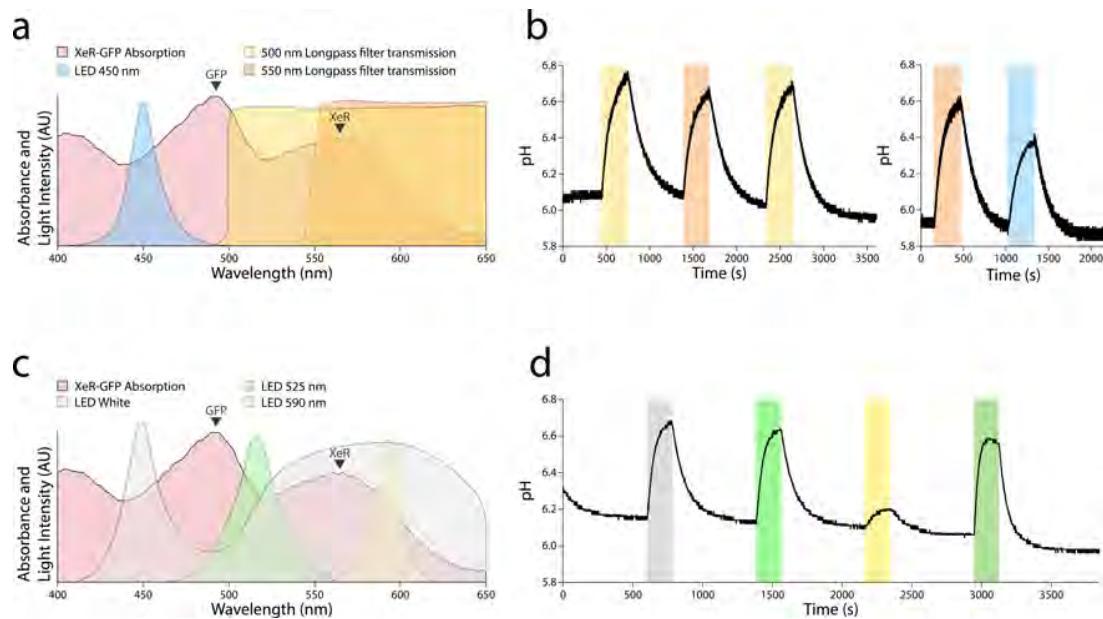


Figure 1: Activation of xenorhodopsin (XeR) with different light sources. **a** Absorption spectrum of the xenorhodopsin-GFP (XeR-GFP) fusion protein shown in light red. Respective absorption peak positions of xenorhodopsin and GFP are indicated. Relative light intensity and transmission profiles of filters and light sources are also shown. **b** Bulk photoactivity traces induced with the light sources presented in **a**. **c** Light intensity profiles of white, green and yellow LEDs plotted together with the XeR-GFP absorption spectrum. **d** Bulk photoactivity traces induced with the light sources shown in **c**. The dark green shaded region represents a combination of all three light sources shown in **c**.

## Supplementary Figure 2: Saturation of pH-gradients upon white light illumination

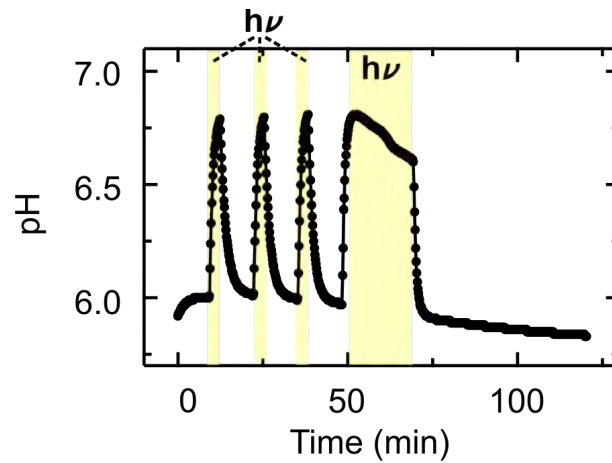


Figure 2: Engineered xenorhodopsin-expressing *E. coli* generate a pH-gradient upon illumination with white light, which saturates after  $\sim 5$  min of illumination. Photoactivity measurements of engineered *E. coli* (at  $OD_{600}=20$ , in 150 mM NaCl) with a pH-electrode. The pH is plotted as a function of time during four light-dark cycles (periods of illumination are indicated in yellow). The pH increases by  $\sim 0.8$  within 5 min of illumination and nearly returns to its original value after 10 min in the dark. A longer illumination time of 20 min (see final illumination period starting at  $t = 50$  min) shows saturation of the pH-gradient and a slow decrease of the pH during continuous illumination.

### Supplementary Figure 3: Photoactivity measurements with different *E. coli* densities

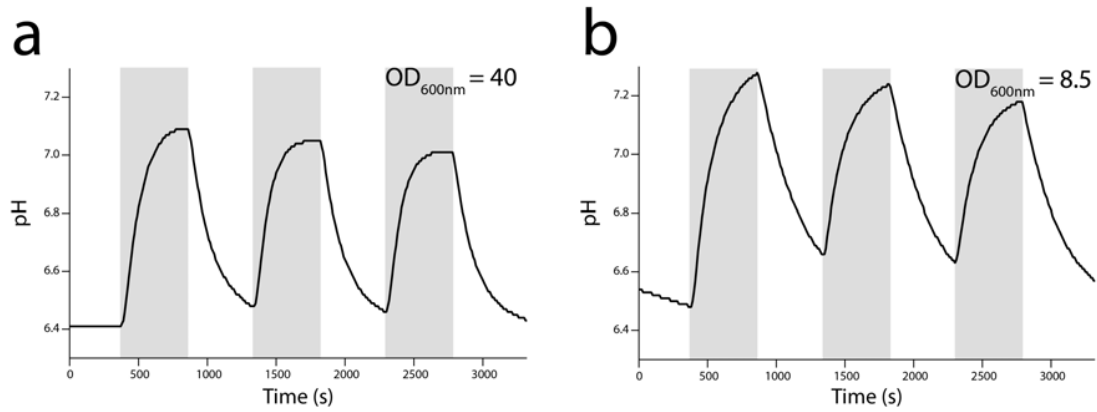


Figure 3: Photoactivity measurements with different *E. coli* densities. **a** Bulk photoactivity measurements with xenorhodopsin-GFP expressing *E. coli* at an  $OD_{600}$  of 40. **b** Bulk photoactivity measurements with the same XeR-GFP expressing *E. coli* as shown in **a**, diluted to an  $OD_{600}$  of 8.5. Illumination in both experiments was performed with a Schott, 1500 LCD lamp. The obtained pH gradients are very similar at both ODs, the kinetics are slightly increased at higher ODs. This could be explained by the hypothesis that the *E. coli* membrane itself cannot maintain pH gradients above one pH unit. Alternatively, it is conceivable that the light is partially absorbed by the denser *E. coli* solution.



## Supplementary Figure 4: Chemical structure of pyranine

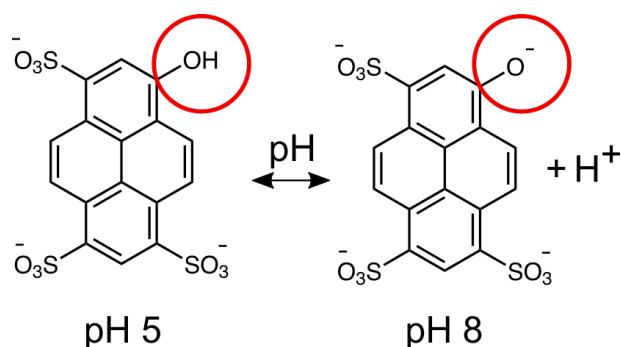


Figure 4: Chemical structure of pyranine at different pH values. The hydroxyl group of pyranine (indicated with a red circle) is deprotonated at high pH values leading to a change of the molecule's fluorescent properties (see Figure 1c). Therefore, pyranine can be used as pH-indicator by measuring the ratio of fluorescence emission upon excitation with the wavelengths 488 nm and 405 nm. A high ratio  $I_{488}/I_{405}$  indicates high pH values and low ratios a low pH value, respectively.

**Supplementary Figure 5: Calibration curve of pyranine fluorescence in presence of GUVs**

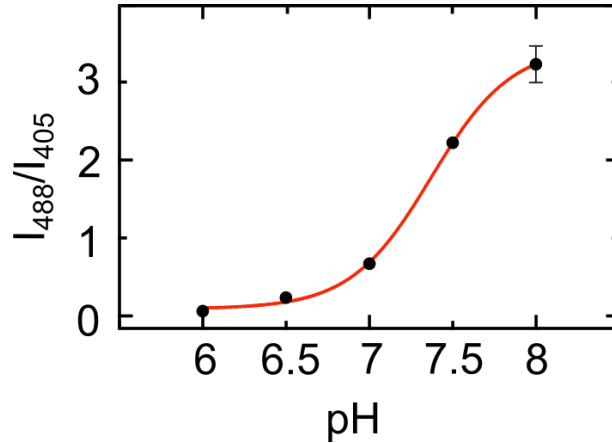


Figure 5: Calibration curve of pyranine fluorescence intensity ( $I_{488}/I_{405}$ ) as a function of pH in a GUV-containing solution (150 mM sucrose, 50  $\mu$ M pyranine, 5 mM  $MgCl_2$ , 100 mM sodium phosphate buffer pre-adjusted to the respective pH value). A sigmoidal fit (red) shows a  $pK_a$  value of pH 7.37. This is in very good agreement with the calibration performed in droplet-based compartments (see Supplementary Figure 8) and literature values.<sup>[1]</sup> Note that the pyranine fluorescence is strongly dependent on the buffer conditions. Therefore, the absolute values cannot be compared to the measurements in an *E. coli*-containing solution.

**Supplementary Figure 6: Monitoring pH changes with pyranine in the presence of GUVs**

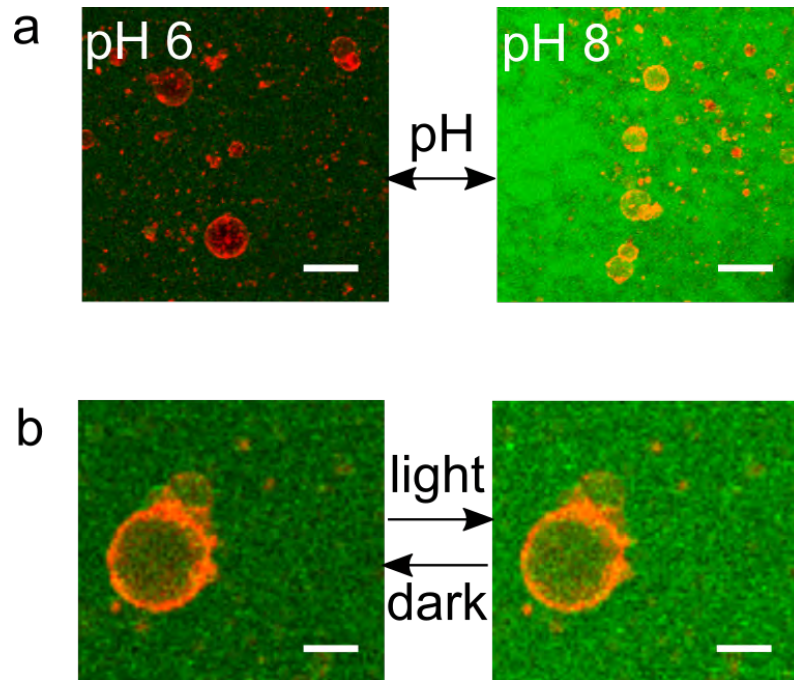


Figure 6: Monitoring pH changes with pyranine in the presence of GUVs. **a** Confocal fluorescence images of GUVs (red,  $\lambda_{ex} = 647$  nm) and pyranine (green,  $\lambda_{ex} = 488$  nm) at pH 6 and pH 8. The pyranine intensity upon 488 nm excitation increases with increasing pH. Scale bar: 50  $\mu\text{m}$ . **b** Confocal fluorescence images of GUVs (red,  $\lambda_{ex} = 647$  nm) and pyranine (green,  $\lambda_{ex} = 488$  nm) in presence of engineered *E. coli* before (left) and after (right) white light illumination. White light illumination leads to an increase of the pH due to the proton-pumping activity of the *E. coli*, which can be visualized by an increase in pyranine fluorescence emission. Scale bar: 20  $\mu\text{m}$ .

**Supplementary Figure 7: Layout of the microfluidic device for the formation of water-in-oil droplets**

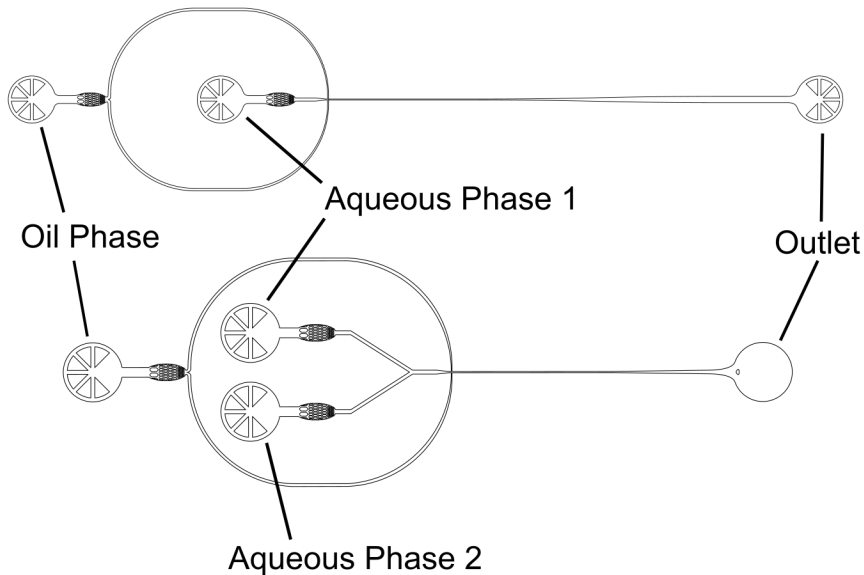


Figure 7: Layouts of single- (top) and two-inlet (bottom) microfluidic devices for the co-encapsulation of DNA and *E. coli* into surfactant-stabilized water-in-oil droplets. The cholesterol-tagged and triplex-forming DNA were supplied via one inlet and the *E. coli* via the second one to avoid attachment of the cholesterol-tagged DNA to the *E. coli* prior to droplet formation. The microfluidic PDMS devices (Sylgard184, Dow Corning, USA) were fabricated according to a previously published protocol<sup>[2]</sup> (see Methods). For confocal fluorescence imaging, the droplets were collected from the outlet and sealed in a simple observation chamber as described previously.<sup>[3]</sup>

## Supplementary Figure 8: Calibration curve of pyranine fluorescence in water-in-oil droplets

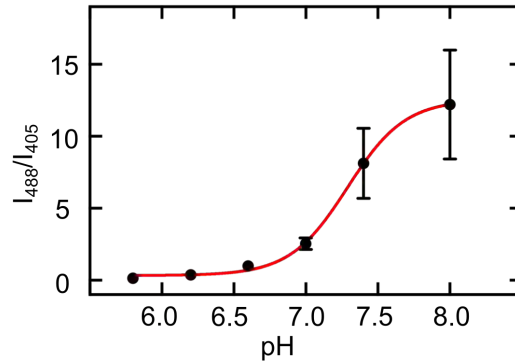


Figure 8: Calibration curve of pyranine fluorescence intensity  $I_{488}/I_{405}$  as a function of pH within water-in-oil droplets (50  $\mu\text{M}$  pyranine, 5 mM  $\text{MgCl}_2$ , 50 mM sodium phosphate buffer pre-adjusted to the respective pH value). A sigmoidal fit (red) has a  $\text{pK}_a$  value of 7.29. This is in very good agreement with the calibration performed in presence of GUVs (see Supplementary Information Figure 5) and literature values.<sup>[1]</sup> Note that the pyranine fluorescence is strongly dependent on the buffer conditions. Therefore, the absolute values cannot be compared quantitatively to the measurements in *E. coli*-containing droplets. The data depicts mean values and error bars correspond to the standard deviation of  $n=22$  droplets for pH 5.8,  $n=31$  for pH 6.2,  $n=25$  for pH 6.6,  $n=28$  for pH 7.0,  $n=23$  for pH 7.4 and  $n=24$  for pH 8.0.

## Supplementary Figure 9: pH-sensitive attachment of triplex-forming DNA

### DNA

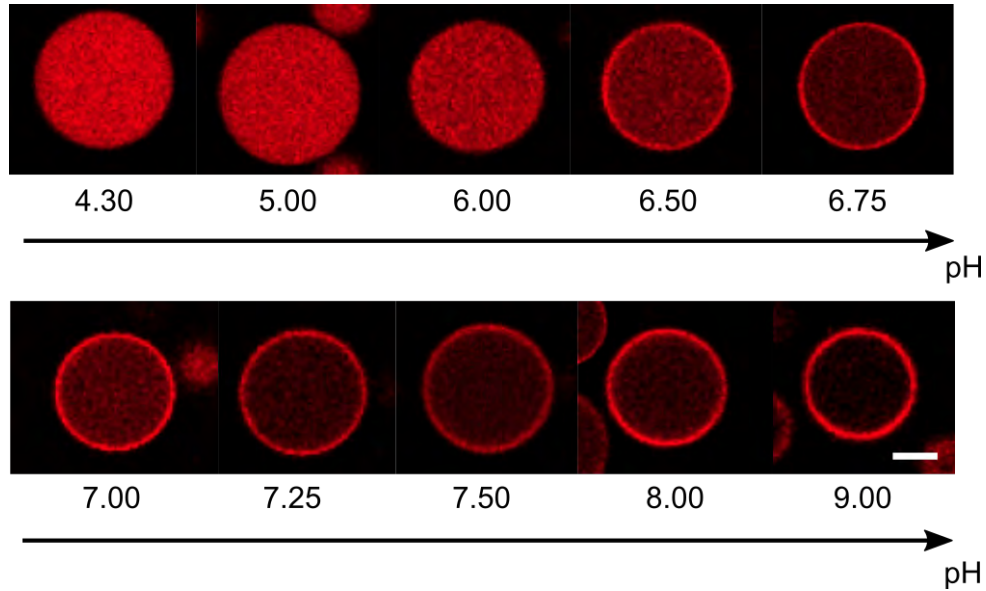


Figure 9: pH-sensitive attachment of triplex-forming DNA. Representative confocal fluorescence images of 1  $\mu\text{M}$  Cy5-labeled triplex-forming DNA (red,  $\lambda_{ex} = 647 \text{ nm}$ ) in droplet-based compartments at different pH values as indicated. The droplet periphery was functionalized with 1.5  $\mu\text{M}$  cholesterol-tagged DNA (complementary to the hairpin region of the triplex, for DNA sequences see Materials and Methods). With increasing pH, Hoogsten interactions become weaker and an increasing amount of the triplex-forming DNA binds to the droplet periphery. For a quantitative plot of the fluorescence intensity inside the droplet at the different pH values, see Figure 3b (main text). Scale bar: 20  $\mu\text{m}$ .

**Supplementary Figure 10: Fluorophore-tagged single-stranded DNA does not interact with droplet-stabilizing surfactants**

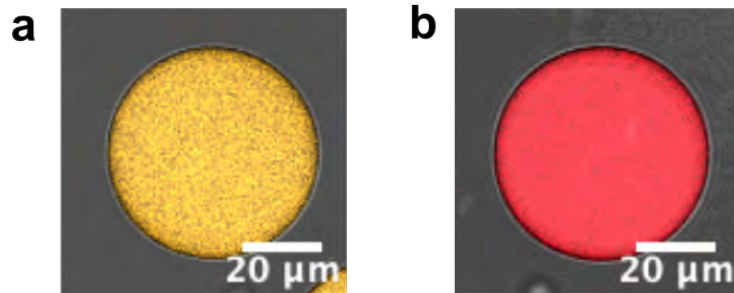


Figure 10: Fluorophore-tagged single-stranded DNA does not interact with droplet-stabilizing surfactants. Representative confocal images of water-in-oil droplets containing Cy3-(**a**,  $\lambda_{ex} = 561$  nm) and Cy5-labeled ssDNA (**b**,  $\lambda_{ex} = 647$  nm) without cholesterol-modification at pH8. The solution contained 20 mM potassium phosphate buffer, 10 mM  $\text{MgCl}_2$  and 1.5  $\mu\text{M}$  DNA. This confirms that there is no unspecific pH-dependent adsorption of the DNA to the droplet periphery at elevated pH. Scale bars: 20  $\mu\text{m}$ .

Supplementary Figure 11: Brightfield and confocal images of microfluidic droplets containing engineered *E. coli*

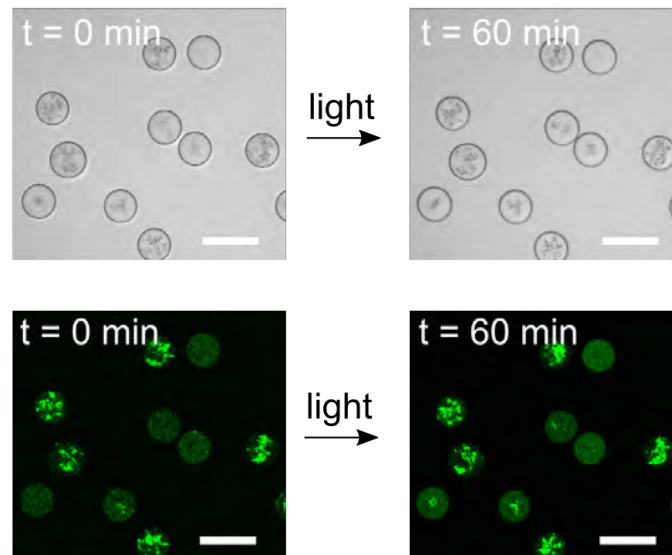


Figure 11: Brightfield (top) and confocal (bottom) images of microfluidic water-in-oil droplets containing the triplex-forming DNA, cholesterol-tagged DNA, pyranine and engineered *E. coli* before (0 min) and after (60 min) illumination with white light. The images confirm the presence of the *E. coli* inside the droplets and their stable confinement. Scale bars: 100  $\mu\text{m}$ .



## Supplementary Figure 12: Hysteresis of DNA triplex attachment and detachment

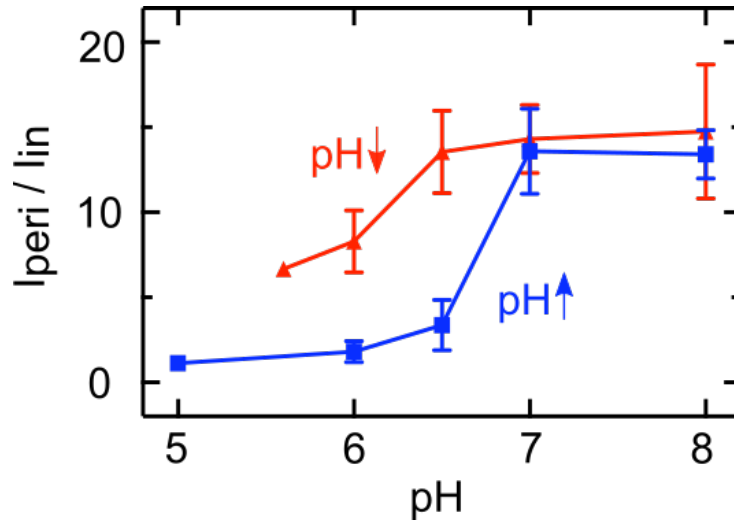


Figure 12: Hysteresis of DNA triplex attachment and detachment. Fluorescence intensity ratio  $I_{\text{peri}}/I_{\text{in}}$  of the Cy5-labeled triplex-forming DNA strand at the droplet periphery over the droplet lumen at different pH values. The triplex-forming DNA was incubated with the complementary cholesterol-tagged strand for 10 min before encapsulation into droplets with 10 mM sodium phosphate buffer and 20 mM  $\text{MgCl}_2$  at pH 5 (blue curve) or pH 8 (red curve). After incubation the solutions were mixed 1:1 with 200 mM phosphate buffers ranging from pH 5 to 8. Droplets were then imaged with confocal fluorescence microscopy. The plot clearly indicates that the duplex dissociation happens at lower pH values compared to the duplex formation. This explains why the *E. coli* can induce attachment but not detachment of the triplex-forming DNA. The data depicts mean values and error bars correspond to the standard deviation of  $n=26$  droplets for pH 5,  $n=57$  for pH 6,  $n=47$  for pH 6.5,  $n=35$  for pH 7,  $n=16$  for pH 8 (blue curve) and  $n=10$  droplets for pH 5.6,  $n=13$  for pH 6,  $n=32$  for pH 6.5,  $n=40$  for pH 7 and  $n=29$  for pH 8 (red curve).

## Supplementary Figure 13: Cadnano design of the membrane-sculpting DNA origami

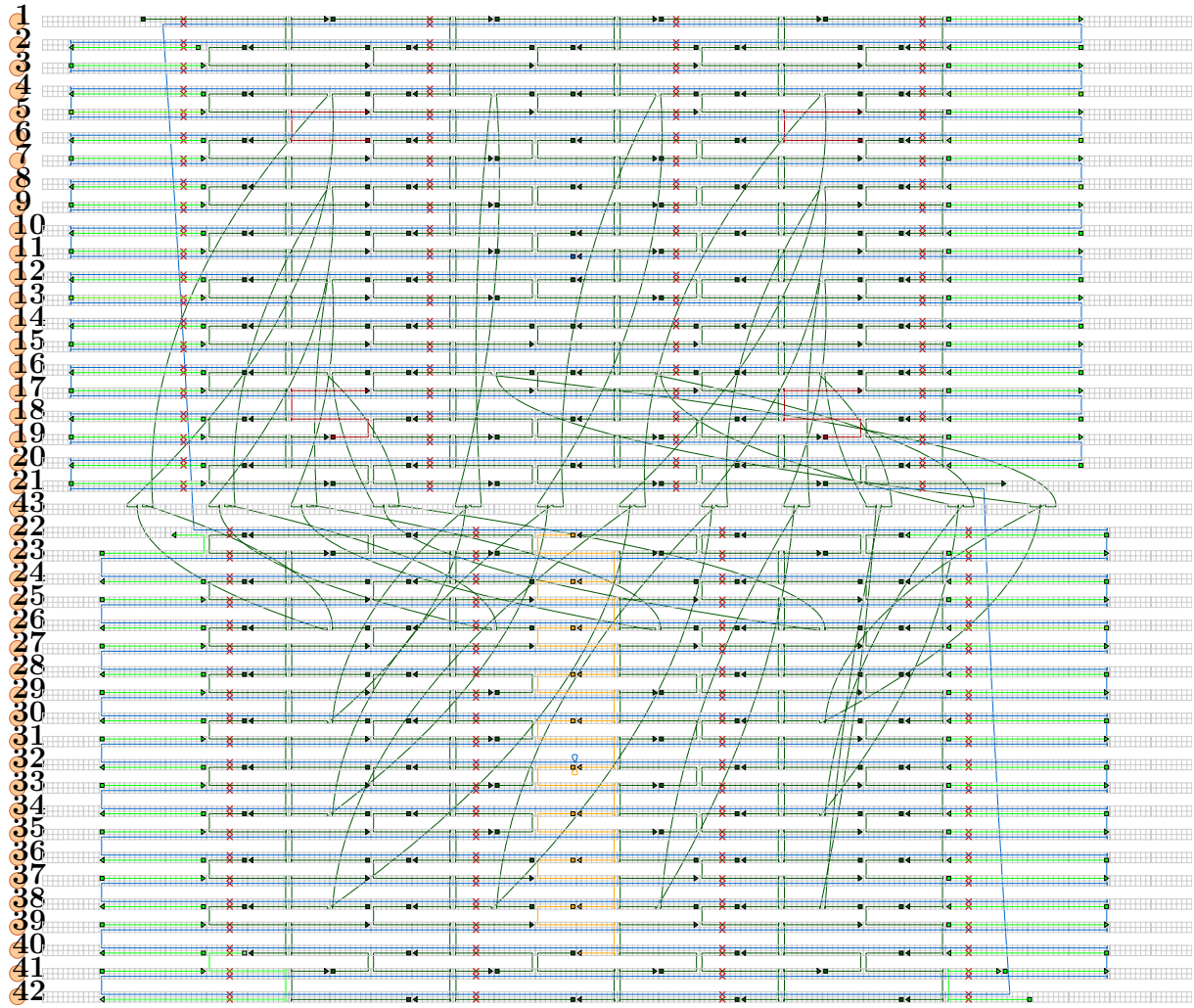


Figure 13: *Cadnano* design of the membrane-sculpting DNA origami. The scaffold (p8064) is shown in blue, bright green staples induce blunt-end stacking, red staples carry overhangs for the triplex-forming DNA on their 3' end, yellow staples carry overhangs for a complementary Cy3-tagged DNA strand on their 3' end.

**Supplementary Figure 14: Blunt-end stacking induces polymerization of DNA origami plates**

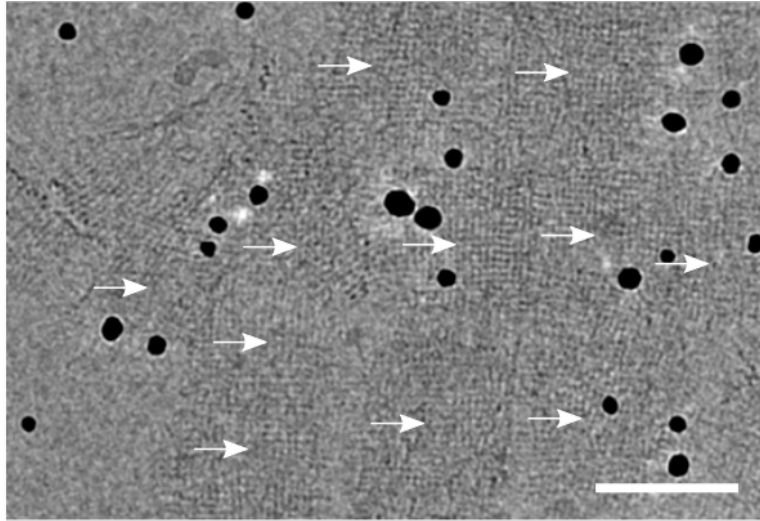


Figure 14: Cryo-EM micrograph of the polymerized DNA origami. The image depicts an arrangement of fused DNA origami squares (indicated by white arrows). Black spots correspond to gold fiducials. This arrangement was used to sculpt the membrane of GUVs. Scale bar: 50 nm.

## Supplementary Figure 15: Atomic force microscopy images of the DNA origami

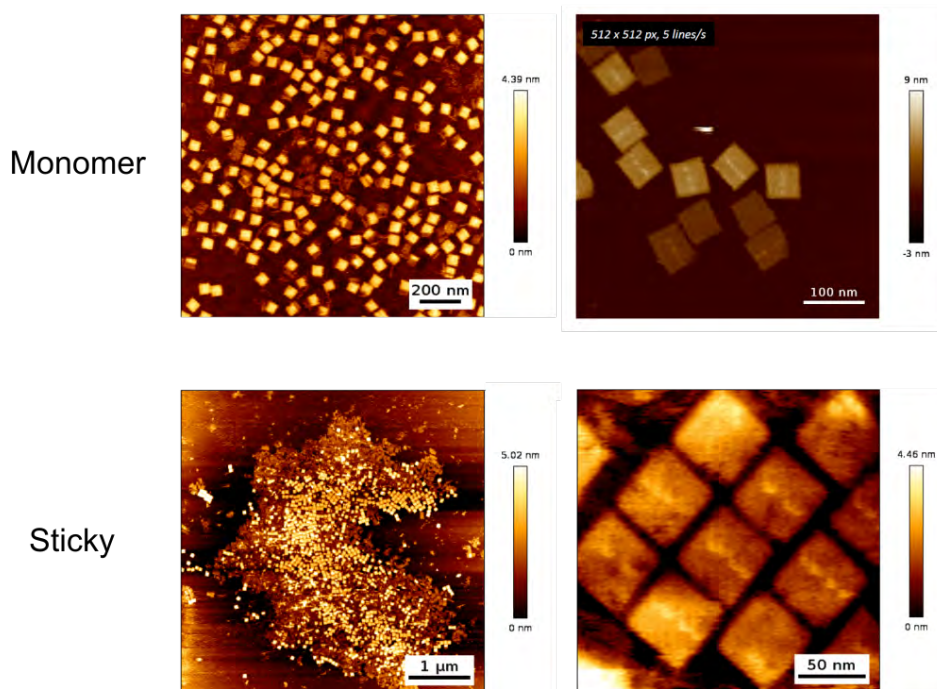


Figure 15: Atomic force microscopy images of the DNA origami without (monomer) and with the overhang strands (sticky). The sticky DNA origami shows a tight packing and cluster formation due to blunt-end stacking, whereas the DNA origami remain loosely distributed when the overhang strands were omitted (monomer). The line that appears across the DNA origami corresponds to the binding sites of the fluorophores. 1 nM of the DNA origami was added to a mica surface, incubated for 90 s and then washed with buffer. Atomic force microscopy was conducted in liquid using a Nanowizzard Ultra Speed 2 (Bruker).

## Supplementary Figure 16: Agarose gel electrophoresis of the DNA origami

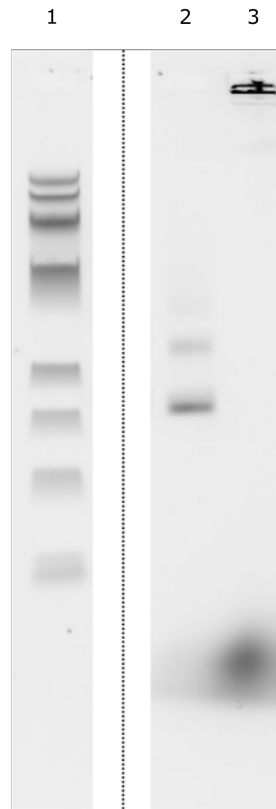


Figure 16: Agarose gel electrophoresis (0.7% agarose) of the DNA origami. Lane 1) 1 kbp DNA ladder; Lane 2) DNA origami without the staples at the scaffold seam (i.e. with single-stranded scaffold loops); Lane 3) DNA origami with the staples at the scaffold seam. Without the the staples at the scaffold seam (Lane 2), there is a clear band for the monomeric DNA origami and weaker bands from oligomers. The single-stranded scaffold loops prevent blunt-end stacking. In presence of the staples at the scaffold seam, blunt-end stacking occurs and the DNA origami does not leave the pocket due to its highly polymerized state. The gel was run at 60 V for 3.5 h at 4°C.

**Supplementary Figure 17: Droplets are not deformed by attaching DNA origami to the droplet periphery**

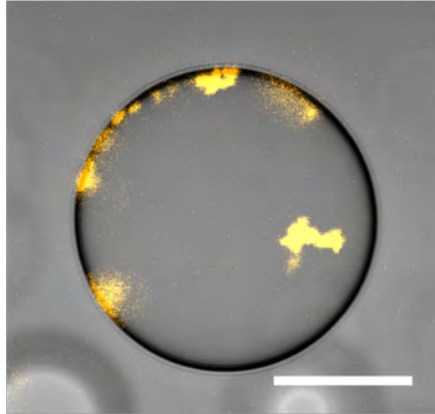


Figure 17: Droplets are not deformed by attaching DNA origami to the droplet periphery. Confocal image of a surfactant-stabilized water-in-oil droplet containing 10 nM cholesterol-tagged Cy3-labeled DNA origami ( $\lambda_{ex}=561$  nm). The droplet remains spherical even though DNA origami clusters were successfully attached to the droplet periphery. Scale bar: 20  $\mu$ m.

## Supplementary Figure 18: FRAP experiments of GUVs with membrane-bound DNA origami

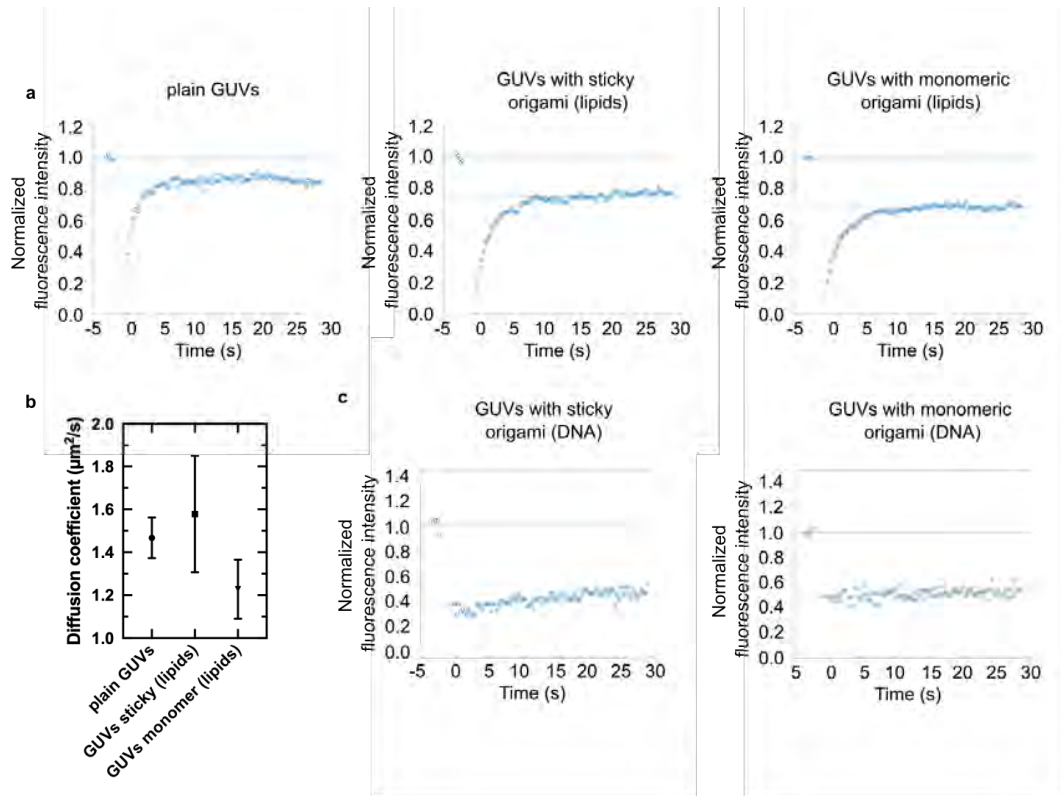


Figure 18: **a** FRAP of lipids ( $\lambda_{ex} = 488 \text{ nm}$ ). Exemplary normalized fluorescence recovery after photobleaching (FRAP) traces for plain GUVs, deformed GUVs with membrane-bound polymerized DNA origami (lipid recovery) and spherical GUVs with membrane-bound monomeric DNA origami (with single-stranded scaffold loops, lipid recovery). **b** Diffusion coefficients of lipids in absence and presence of DNA origami (mean  $\pm$  SD;  $n=3$  for each condition). The lipid diffusivity is not affected significantly by the presence of membrane-bound DNA origami. The diffusion coefficients were calculated according to previous works.<sup>[4]</sup> **c** FRAP of DNA origami ( $\lambda_{ex} = 561 \text{ nm}$ ). Exemplary normalized fluorescence recovery after photobleaching (FRAP) traces for deformed GUVs with membrane-bound polymerized DNA origami (DNA recovery) and spherical GUVs with membrane-bound monomeric DNA origami (with single-stranded scaffold loops, DNA recovery). The DNA origami do not recover after photobleaching as expected in the presence of divalent ions.<sup>[5]</sup>

## Supplementary Figure 19: DNA origami cortex suppresses membrane fluctuations

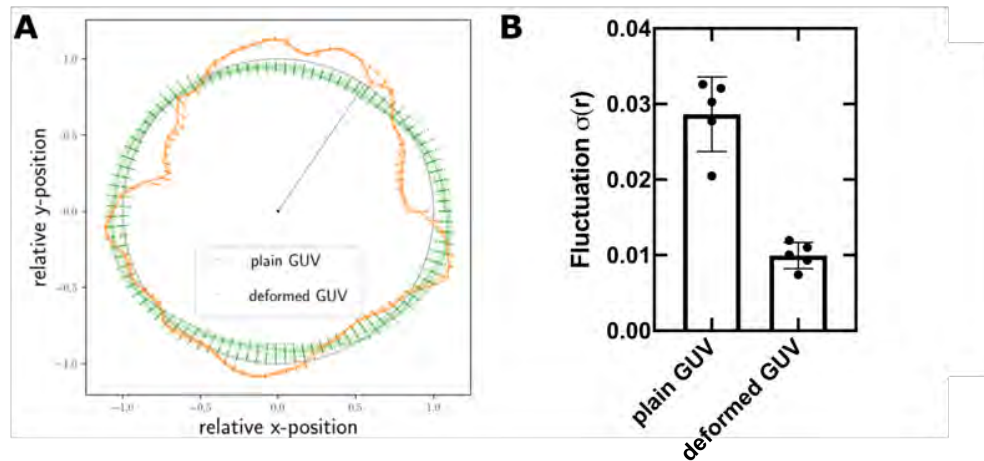


Figure 19: Membrane fluctuations of osmotically deflated GUVs ( $c/c_0 = 1.8$ ) with and without membrane-bound DNA origami. **A** Outline of a plain GUV without membrane-bound DNA origami (green) and a deformed GUV with membrane-bound polymerized DNA origami (orange). The outline was traced from a confocal cross section over time (see also Supplementary Video 5). **B** Standard deviation of the radius  $r$  from the mean radius for plain (green) and deformed GUVs ( $n=5$  individual GUVs tracked over time, mean $\pm$ std.). Higher deviations from the mean radius correspond to larger membrane fluctuations. For the deformed GUV, membrane fluctuations are approximately three times lower than for the plain GUV.



## Supplementary Figure 20: Deformation process of GUVs with DNA origami

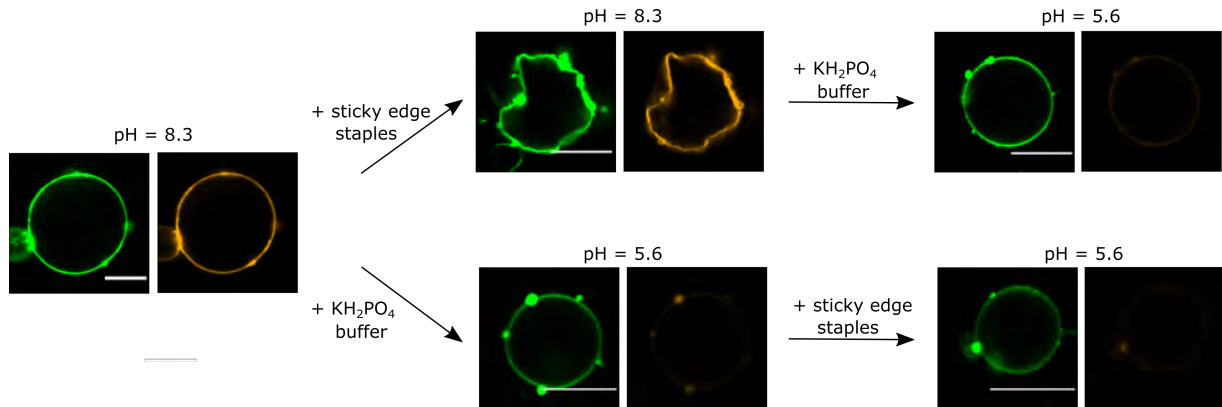


Figure 20: Flow diagram with confocal images of GUVs (lipids labelled with Atto488,  $\lambda_{ex} = 488$  nm) and DNA origami (labelled with Cy3,  $\lambda_{ex} = 561$  nm) depicting the deformation process. First of all, we attached the monomeric pH-sensitive DNA origami to the GUVs at pH 8.3 using cholesterol-tags which bind to the hairpin loop of the triplex motif at elevated pH. Subsequently, we added the sticky edge staples, which allow for blunt-end stacking of the DNA origami and thus induce polymerization of the DNA origami. Polymerization, in turn, deforms the GUVs. Following this step, the DNA origami were detached from the GUVs by lowering the pH to 5.6 (upper panels, the fluorescence from the detached DNA origami in the background is too weak to be visible). As a control, we also first lowered the pH to 5.6 and then added the overhang strands (lower panels). This did not affect the morphology of GUVs. After each mixing step, the GUVs were incubated for 24 h either with overhang strands or at a different pH value. Note that the deformation process takes about two hours. Scale bars: 15  $\mu\text{m}$ .

## Supplementary Figure 21: Confocal images of deformed GUVs

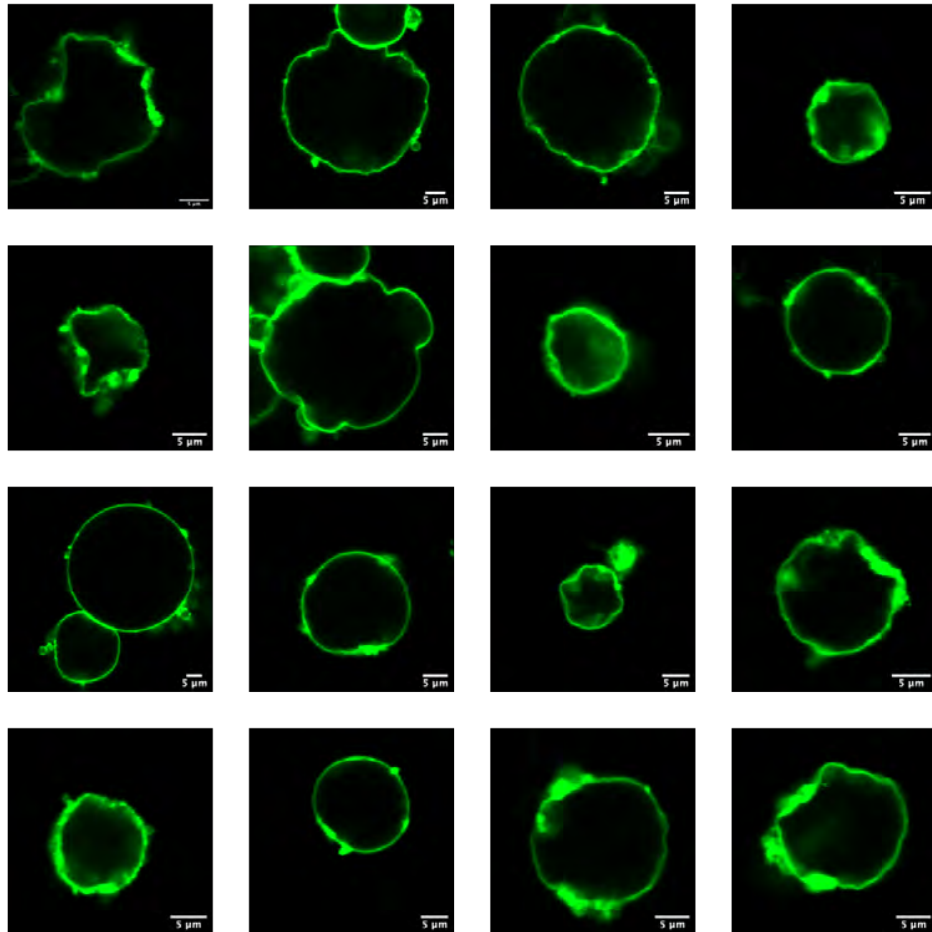


Figure 21: Confocal images of deformed GUVs ( $\lambda_{ex} = 561$  nm) in presence of membrane-bound polymerized DNA origami at pH 8.3. The corresponding quantification of the GUV circularity is shown in Figure 4e (main text). Scale bars: 5  $\mu$ m.

Supplementary Figure 22: Confocal images of GUVs after detachment of membrane-bound DNA-origami

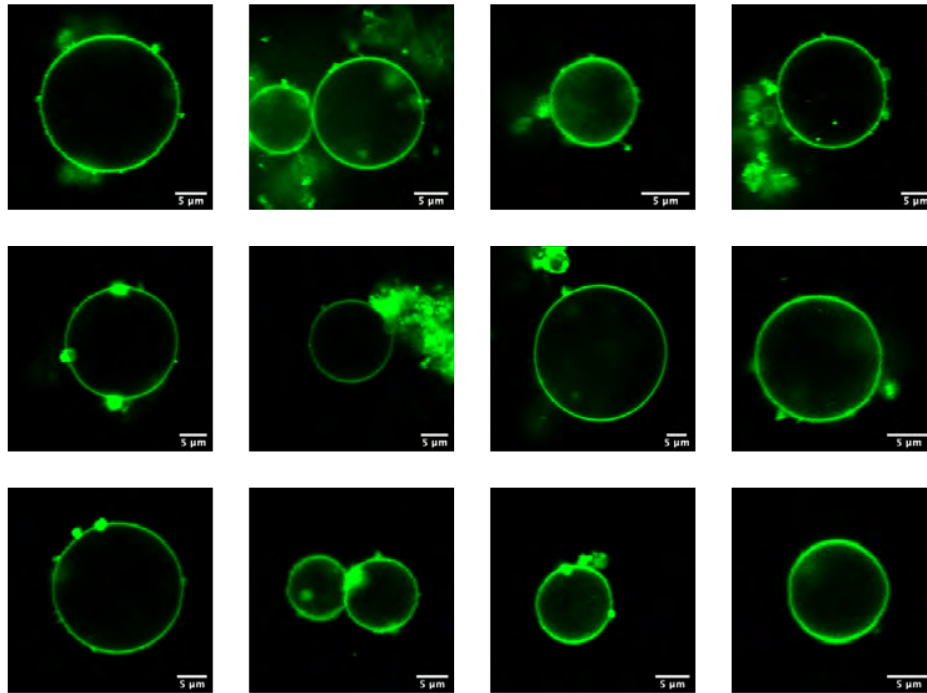


Figure 22: Confocal images of GUVs ( $\lambda_{ex} = 561$  nm) after decreasing the pH from pH 8.3 to pH 5.6 by addition of iso-osmotic potassium dihydrogenphosphate buffer. The DNA origami detaches from the GUV upon lowering the pH and the GUVs return to a spherical shape. The corresponding quantification of the GUV circularity is shown in Figure 4e (main text). Scale bars: 5  $\mu$ m.

## Supplementary Figure 23: Exemplary confocal images of DNA-functionalized GUVs

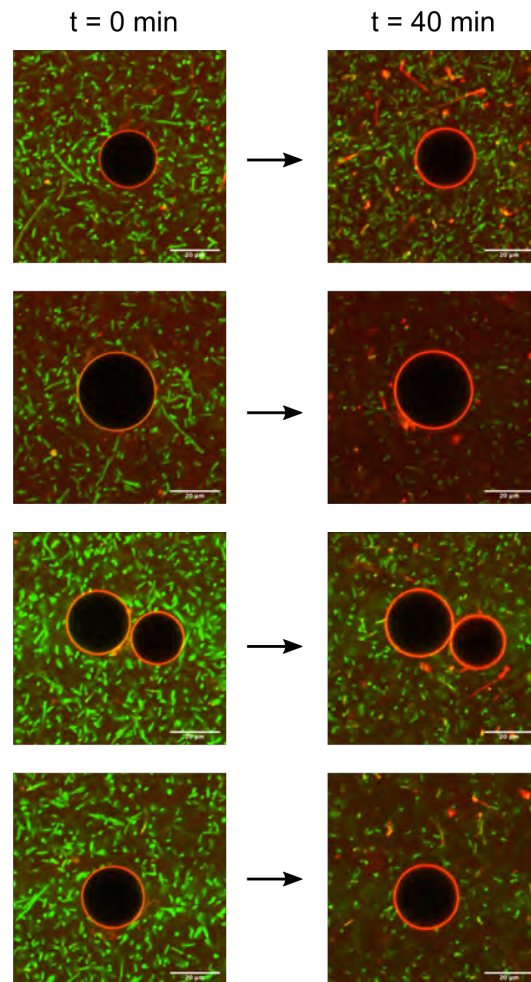


Figure 23: Exemplary confocal images of GUVs coated with cholesterol-tagged DNA ( $0.6 \mu\text{M}$ ) and surrounded by *E. coli* and triplex-forming DNA ( $0.4 \mu\text{M}$ ,  $\lambda_{ex}=561 \text{ nm}$ ). The images show the attachment of the triplex-forming DNA after illumination (40 min time point) as well as the settling of *E. coli*. The droplet was illuminated for 15 min after 25 min in the dark. The corresponding quantification of the peripheral DNA intensity is shown in Figure 24. Scale bars:  $20 \mu\text{m}$ .

**Supplementary Figure 24: Attachment of the single-stranded DNA triplex to GUVs during light illumination**

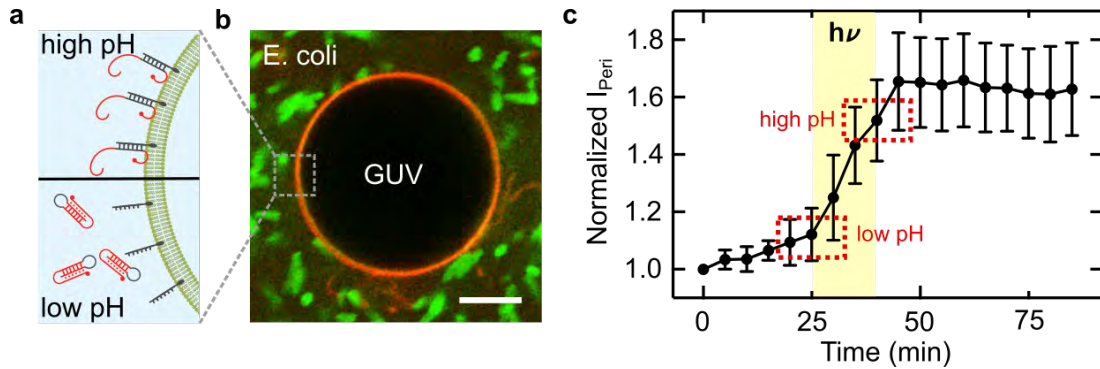


Figure 24: **a** Schematic illustration of a GUV membrane functionalized with cholesterol-tagged DNA in presence of triplex-forming DNA at high and low pH values. **b** Confocal image of a DNA-coated GUV surrounded by *E. coli* as described in **a** ( $0.4 \mu\text{M}$  triplex-forming DNA,  $\lambda_{\text{ex}}=561 \text{ nm}$ ;  $0.6 \mu\text{M}$  cholesterol-tagged DNA). Scale bar:  $10 \mu\text{m}$ . **c** Normalized fluorescence intensity  $I_{\text{peri}}$  (mean $\pm$ s.d.,  $n=15$ ) of the triplex-forming DNA at the GUV periphery monitored over time. The time period of illumination is indicated in yellow, illumination leads to a pH increase and hence DNA attachment. The data is extracted from GUVs as shown in Figure 23.

Supplementary Figure 25: Confocal images of deformed GUVs after light-mediated attachment of DNA origami

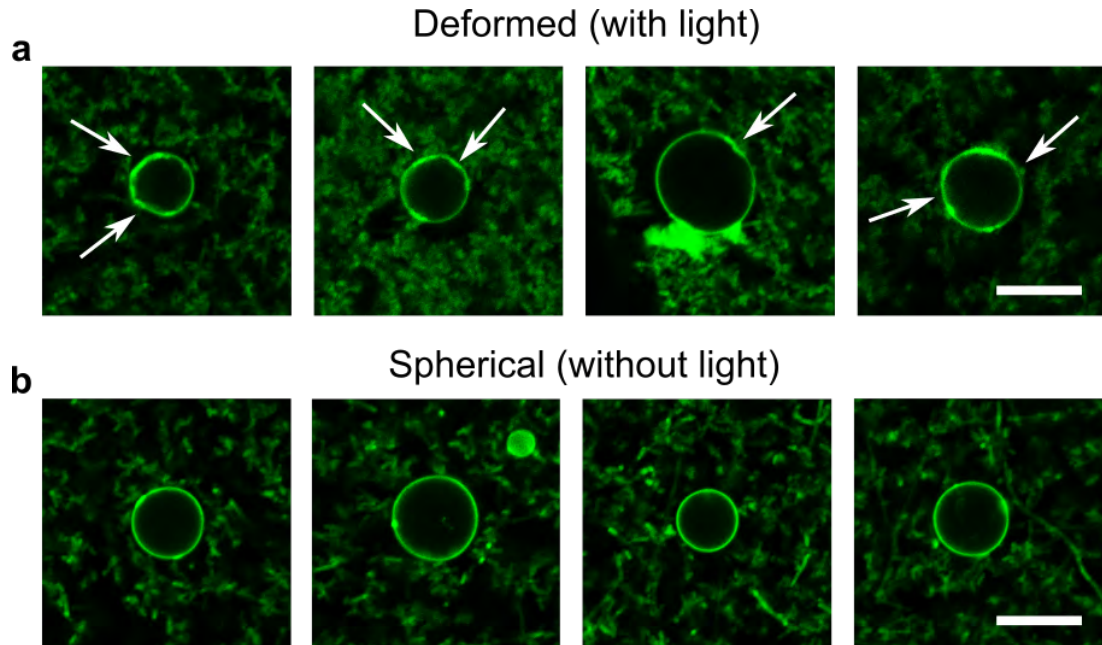


Figure 25: Confocal images of deformed GUVs ( $\lambda_{ex} = 488$  nm) in presence of membrane-bound polymerized DNA origami and *E. coli* after light-mediated attachment of DNA origami and spherical GUVs without light illumination. Note that the deformation is weaker compared to the deformation achieved with conventional pH switching due to the smaller pH gradient. Scale bars: 10  $\mu\text{m}$ .

## Supplementary Figure 26: Light-mediated deformation of GUVs

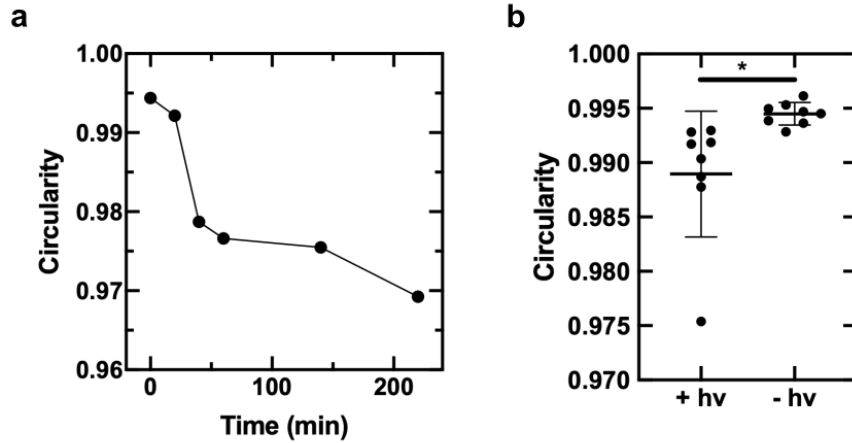


Figure 26: Light-mediated deformation of GUVs. **a** Circularity over time for the representative image of a GUV with attached DNA origami monomers after addition of staple strands at the scaffold seam which enable blunt-end stacking as shown in Figure 5c. The circularity decreases over time corresponding to a deformation of the GUV within 1 h. **b** Circularity of GUVs 14 h after addition of staple strands to the scaffold seam for GUVs that were illuminated with light for 30 min and GUVs that were not illuminated. The circularity for illuminated GUVs is significantly lower than for GUVs that were left in the dark ( $n=8$ , error bars show the standard deviation,  $p = 0.03$ ). Note that the density of *E. coli* was  $OD_{600} = 20$  for both conditions.

# Supplementary Tables

## Supplementary Table 1: DNA and amino-acid sequences of xenorhodopsin-constructs

XeR-GFP DNA sequence:

```
1 ATGGTGTATG AAGCAATTAC CGCAGGCGGT TTTGGTAGCC AGCCGTTTAT TCTGGCATAT
61 ATCATTACCG CAATGATTAG CGGTCTGCTG TTTCTGTATC TGCCTCGTAA ACTGGATGTT
121 CCGCAGAAAT TTGGCATCAT CCATTTTTTC ATTGTGGTTT GGAGCGGTCT GATGTATAAC
181 AATTTTCTGA ATCAGAGCTT CCTGAGCGAT TATGCATGGT ATATGGATTG GATGGTTAGC
241 ACACCGCTGA TTCTGCTGGC ACTGGGTCTG ACCGCATTC ATGGTGCAGA TACCAAACGT
301 TATGATCTGC TGGGTGCACT GCTGGGAGCA GAATTACCC TGGTTATTAC AGGTCTGCTG
361 GCCCAGGCAC AGGGTAGCAT TACCCCGTAT TATGTTGGTG TTCTGCTGCT GCTGGGCGTT
421 GTTATCTGCT TGGCGAAACC GTTTCGTGAA ATTGCCGAAG AAAGCAGTGA TGGTCTGGCA
481 CGTGCGTATA AAATCCTGGC AGGTTATATT GGCATCTTT TTCTGAGCTA TCCGACCGTG
541 TGGTATATTA GCGGTATTGA TGCCTGCCT GGTAGCCTGA ATATTCTGGA CCCGACCCAG
601 ACCAGCATTG CACTGGTTGT TCTGCCGTTT TTTTGCAAAC AGGTTTATGG CTCCTGGAC
661 ATGTATCTGA TTCATAAAGC AGAAGCTCTC GAGGGAGGAA GTCTGGAAGT TCTGTTCCAG
721 GGGCCCGTCG ACGGATCCGA AAACCTGTAT TTCCAGGGCA TGAGTAAAGG AGAAGAACTT
781 TTCACTGGAG TTGTCCCAAT TCTTGTTGAA TTAGATGGTG ATGTTAATGG GCACAAATTT
841 TCTGTCCGTG GAGAGGGTGA AGGTGATGCT ACAAACGGAA AACTCACCTT TAAATTTATT
901 TGCCTACTG GAAAACCTAC TGTTCCTGG CCAACACTTG TCACTACTCT GACCTATGGT
961 GTTCAATGCT TTTCCCGTTA TCCGGATCAC ATGAAACGGC ATGACTTTTT CAAGAGTGCC
1021 ATGCCCGAAG GTTATGTACA GGAACGCACT ATATCTTTCA AAGATGACGG GACCTACAAG
1081 ACGCGTGTCT AAGTCAAGTT TGAAGGTGAT ACCCTTGTTA ATCGTATCGA GTTAAAGGGT
1141 ATTGATTTTA AAGAAGATGG AACATTCTT GGACACAAAC TCGAGTACAA CTTTAACTCA
1201 CACAATGTAT ACATCACGGC AGACAAACAA AAGAATGGAA TCAAAGCTAA CTTCAAATTT
1261 CGCCACAACG TTGAAGATGG TTCCGTTCAA CTAGCAGACC ATTATCAACA AAATACTCCA
1321 ATTGGCGATG GCCCTGTCTT TTTACCAGAC AACCATTACC TGTCGACACA ATCTGTCTTT
1381 TCGAAAGATC CCAACGAAAA GCGTGACCAC ATGGTCCTTC TTGAGTTTGT AACTGCTGCT
1441 GGGATTACAC ATGGCATGGA TGAGCTCTAC AAAGGAGGAT CTGGTGGTTC TGGGAAGCTT
1501 GCGGCCGCAC TCGAGCACCA CCACCACCAC CACTGA
```

XeR-GFP amino-acid sequence:

```
MVYEAITAGGFGSQPFILAYIITAMISGLLFLYLPRKLDVDPKFGIHHFFIVVWSGLMYTNFLNQSFLSD
YAWYMDWMVSTPLILLALGLTAFHGADTKRYDLLGALLGAFTLVITGLLAQAQGSITPYVGVLLLLGV
VYLLAKPFREIAEESDGLARAYKILAGYIGIFLSYPTVWYISGIDALPGSLNILDPTQTSIALVLPF
FCKQVYGFDMYLIHKAEALEGGSEVLFQGPVDGSENLYFQGMKSGEELFTGVVPIVELDGDVNGHKF
SVRGEGERDATNGKLTLLKFICTTGKLPVWPVTLVTTLTLYGVQCFSRYPDHMKRHHDFKSAPEGYVQERT
ISFKDDGTYKTRAEVKFEQDNLVNRIELKIDFKEDGNILGHKLEYNFNHNVYITADKQKNGIKANFKI
RHNVEDGSVQLADHYQQNTPIGDGPVLLPDNHYLSTQSVLSKDPNEKRDMVLEFVTAAGITHGMDELY
KGGSGGSKLAAALEHHHHHH
NsXeR Sf-GFP His6-Tag
```



## XeR-mCherry DNA sequence:

```
1 ATGGTGTATG AAGCAATTAC CGCAGGCGGT TTTGGTAGCC AGCCGTTTAT TCTGGCATAT
61 ATCATTACCG CAATGATTAG CGGTCTGCTG TTTCTGTATC TGCCTCGTAA ACTGGATGTT
121 CCGCAGAAAT TTGGCATCAT CCATTTTTTC ATTGTGGTTF GGAGCGGTCT GATGTATACC
181 AATTTTCTGA ATCAGAGCTT CCTGAGCGAT TATGCATGGT ATATGGATTG GATGGTTAGC
241 ACACCGCTGA TTCTGCTGGC ACTGGGTCTG ACCGCATTTT ATGGTGCAGA TACCAAACGT
301 TATGATCTGC TGGGTGCACT GCTGGGAGCA GAATTTACCC TGGTATTAC AGGTCTGCTG
361 GCCCAGGCAC AGGGTAGCAT TACCCGTAT TATGTTGGTG TTCTGCTGCT GCTGGGCGTT
421 GTTTATCTGC TGGCGAAACC TTTCTGTGAA ATTGCCGAAG AAAGCAGTGA TGGTCTGGCA
481 CGTGCGTATA AAATCCTGGC AGGTATATTT GGCATCTTTT TTCTGAGCTA TCCGACCGTG
541 TGGTATATTA GCGGTATTGA TGCACCTGCC GTAGCCTGA ATATTCTGGA CCCGACCCAG
601 ACCAGCATTG CACTGGTTGT TCTGCCGTTT TTTTGCAAAC AGGTTTATGG CTTCTGGAC
661 ATGTATCTGA TTCATAAAGC AGAAGCTCTC GAGGGAGGAA GTCTGGAAGT TCTGTTCCAG
721 GGGCCCGTCC ACGGATCCAT GCATAGCAAG GGCGAGGAGG ATAACATGGC CATCATCAAG
781 GAGTTCATGC GCTTCAAGGT GCACATGGAG GGCTCCGTGA ACGGCCACGA GTTCGAGATC
841 GAGGGCGAGG GCGAGGGCCG CCCCTACGAG GGCACCCAGA CCGCCAAGCT GAAGGTGACC
901 AAGGGTGGCC CCCTGCCCTT CGCCTGGGAC ATCCTGTCCC CTCAGTTCAT GTACGGCTCC
961 AAGGCCTACG TGAAGCACCC CGCCGACATC CCCGACTACT TGAAGCTGTC CTTCCCCGAG
1021 GGCTTCAAGT GGGAGCGCGT GATGAACTTC GAGGACGGCG GCGTGGTGAC CGTGACCCAG
1081 GACTCCTCCT TGCAGGACCG CGAGTTCATC TACAAGGTGA AGCTGCGCGG CACCAACTTC
1141 CCCTCCGACG GCCCCGTAAT GCAGAAGAAG ACCATGGGCT GGGAGGCCTC CTCGAGCGG
1201 ATGTACCCCG AGGACGGCGC CCTGAAGGGC GAGATCAAGC AGAGGCTGAA GCTGAAGGAC
1261 GCGGGCCACT ACGACGCTGA GGTCAAGACC ACCTACAAGG CCAAGAAGCC CGTGCAGCTG
1321 CCCGGCCGCT ACAACGTCAA CATCAAGTTG GACATCACCT CCCACAACGA GACTACACC
1381 ATCGTGGAAC AGTACGAACG CGCCGAGGGC CGCCACTCCA CCGCGGCAT GGACGAGCTG
1441 TACAAGAAGC TTGCGGCCG ACTCGAGCAC CACCACCACC ACCACTGA
```

## XeR-mCherry amino-acid sequence:

```
MVYEAITAGGFGSQPFILAYIITAMISGLLFLYLPKRLDVPQKFGIIHFFIVVWSGLMYTNFLNQSFLSD
YAWYMDWMVSTPLILLALGLTAFHGADTKRYDLLGALLGAFTLVITGLLAQAQGSITPYVGVLLLLGV
VYLLAKPFREIAEESDGLARAYKILAGYIGIFFLSYPTVWYISGIDALPGSLNILDPTQTSIALVLPF
FCKQVYGFDMYLIHKAEALEGGSLVLFQGPVDGSMHSGEEDNMAIHKFMRFKVHMEGSVNGHEFEI
EGEGEGRPYEGTQTAKLKVTKGGPLPFAWDILSPQFMYGSKAYVKHPADIPDYLLKLSFPEGFKWERVMNF
EDGGVVTVTQDSSLQDGEFIYKVKLRGTNFPDGPVMQKKTMGWEASSERMYPEDGALKGEIKQRLKLD
GGHYDAEVKTTYKAKKPVQLPGAYNVNIKLDITSHNEDYTIVEQYERAEGRHSTGGMDELYKKLAAALE
HHHHHH
NsXeR mCherry His6-Tag
```

## Supplementary Notes

### Supplementary Note 1: Estimation of the pH change for DNA attachment

In principle, we can quantify the pH change from the quantification of the DNA attachment and the corresponding calibration curve (see Figure 3b). However, the problem in comparing the fluorescent ratios from the calibration measurement in Figure 3b and the DNA attachment mediated via *E. coli* is the fact that the *E. coli* containing droplets absorb some of the excitation as well as emission light from the pH-sensitive DNA which makes us cautious regarding fully quantitative statements on the pH. However, we can still approximate the rise in pH. During light illumination of the droplets with *E. coli* the ratio  $I_{\text{peri}}/I_{\text{in}}$  rises from 1.83 to 3.58 and thus by a factor of 1.96. From the confocal images in Supplementary Figure 24 and the pH electrode measurements in Figure 1b, we can deduce the starting point of pH 6.2 before light illumination takes place. This is also in line with the calibration curve in Figure 3b and Supplementary Figure 9, where the DNA starts to attach in between pH 6-6.5. A pH of 6.2 equals a ratio in the calibration measurement of  $I_{\text{peri}}/I_{\text{in}}=1.36$  and is thus smaller than the starting value of the measurement with *E. coli* due to absorption of light by *E. coli* on the inside of the droplet and hence a smaller  $I_{\text{in}}$ . Multiplying the ratio  $I_{\text{peri}}/I_{\text{in}}=1.36$  at pH 6.2 by 1.96 yields 2.72, which corresponds to a pH of 7.25. This means that by this approximation the pH within droplets rises from pH 6.20 to pH 7.25 during light illumination. This is comparable to the pH range obtained from bulk measurements where the pH increases from pH 6.2 to 7.0 and further in line with a comparison of the images from the calibration measurement with the ones of the droplets after light illumination.

## Supplementary Note 2: Estimation of DNA origami density per GUV

To obtain a lower bound estimate for the area coverage of the DNA origami on the GUVs we need to estimate the lipid concentration first. For the electroformation 40  $\mu\text{L}$  of 1 mM lipids in chloroform are spread on the whole ITO slide until all chloroform evaporated. Subsequently, 275  $\mu\text{L}$  of aqueous buffer solution is added into the ring covering  $\frac{1}{5}$  of the area covered with lipids leading to a final lipid concentration of 29  $\mu\text{M}$ . Note that this is an upper bound estimate for the lipid concentration since most likely not all lipids will detach from the ITO slide. After mixing the GUV solution with the DNA origami solution the effective concentrations are  $c_{\text{lipid}} \simeq 20 \mu\text{M}$  and  $c_{\text{DNA}} = 2 \text{ nM}$ . The relative area of the GUV covered with DNA origami is then given by:

$$\alpha = \frac{c_{\text{DNA}} * A_{\text{DNA}}}{2 * c_{\text{lipid}} * A_{\text{lipid}}} = 0.175 \quad (1)$$

with  $A_{\text{DNA}} = 250 \text{ nm}^2$  and  $A_{\text{lipid}} = 0.7 \text{ nm}^2$ . Thus, at least 17% of the membrane area of the GUVs should be covered with DNA origami.

## References

- (1) Paxton, W. F.; Price, D.; Richardson, N. J. Hydroxide ion flux and pH-gradient driven ester hydrolysis in polymer vesicle reactors. *Soft Matter* **2013**, *9*, 11295.
- (2) Platzman, I.; Janiesch, J.-W.; Spatz, J. P. Synthesis of Nanostructured and Biofunctionalized Water-in-Oil Droplets as Tools for Homing T Cells. *Journal of the American Chemical Society* **2013**, *135*, 3339–3342.
- (3) Weiss, M. et al. Sequential bottom-up assembly of mechanically stabilized synthetic cells by microfluidics. *Nature Materials* **2017**, *17*, 89–96.
- (4) Jahnke, K.; Weiss, M.; Weber, C.; Platzman, I.; Göpfrich, K.; Spatz, J. P. Engineering Light-Responsive Contractile Actomyosin Networks with DNA Nanotechnology. *Advanced Biosystems* **2020**, 2000102.
- (5) Kocabey, S.; Kempter, S.; List, J.; Xing, Y.; Bae, W.; Schiffels, D.; Shih, W. M.; Simmel, F. C.; Liedl, T. Membrane-Assisted Growth of DNA Origami Nanostructure Arrays. *ACS Nano* **2015**, *9*, 3530–3539.

## **A.6 Supporting Information for Publication 6: Functional DNA-based cytoskeletons for synthetic cells**

# Supplementary Information: Functional DNA-based cytoskeletons for synthetic cells

Pengfei Zhan<sup>1,2§</sup>, Kevin Jahnke<sup>3,4§\*</sup>, Na Liu<sup>1,2\*</sup>, Kerstin Göpfrich<sup>3,4\*</sup>

<sup>1</sup> 2nd Physics Institute, University of Stuttgart,  
Im Pfaffenwaldring 57, D-70569 Stuttgart, Germany

<sup>2</sup> Max Planck Institute for Solid State Research,  
Heisenbergstraße 1, D-70569 Stuttgart, Germany

<sup>3</sup>Biophysical Engineering Group, Max Planck Institute for Medical Research,  
Jahnstraße 29, D-69120 Heidelberg, Germany,

<sup>4</sup>Department of Physics and Astronomy, Heidelberg University,  
D-69120 Heidelberg, Germany

§These authors contributed equally.

\*

E-mail: kevin.jahnke@mr.mpg.de, na.liu@pi2.uni-stuttgart.de, kerstin.goepfrich@mr.mpg.de

# Contents

<b>Supplementary Notes</b>	<b>4</b>
Supplementary Note S1: Estimation of the SUV velocity along the DNA filaments	4
<b>Supplementary Figures</b>	<b>6</b>
Supplementary Figure S1: Strand routing diagrams for the DNA tiles . . . . .	6
Supplementary Figure S2: Assembly of the DNA filaments at different tile concentrations . . . . .	7
Supplementary Figure S3: Assembly of the DNA filaments at different $Mg^{2+}$ concentrations . . . . .	8
Supplementary Figure S4: Assembly of the DNA filaments at different temperatures	9
Supplementary Figure S5: Confocal images of the DNA-based filaments in bulk .	10
Supplementary Figure S6: Microfluidic device and droplet formation . . . . .	11
Supplementary Figure S7: AFM images of assembly and disassembly of the DNA-based filaments by strand displacement reactions . . . . .	12
Supplementary Figure S8: Determination of the required concentrations of invader and anti-invader strands . . . . .	13
Supplementary Figure S9: Low ATP concentrations do not induce filament assembly	14
Supplementary Figure S10: AFM images of the aptamer-specific assembly and disassembly of the DNA-based filaments . . . . .	15
Supplementary Figure S11: Strand routing diagram for the DNA origami seed . .	16
Supplementary Figure S12: Seeded growth mechanism . . . . .	17
Supplementary Figure S13: TEM and confocal images of seeded growth . . . . .	18
Supplementary Figure S14: Size distribution of the SUVs . . . . .	19
Supplementary Figure S15: STED imaging confirms the binding of the SUVs to the DNA-based filaments . . . . .	20
Supplementary Figure S16: Color-coded z-projections of the DNA-SUV networks .	21

Supplementary Figure S17: Composite images of the DNA-SUV networks . . . . .	22
Supplementary Figure S18: DNA filaments remain intact after transport . . . . .	23
Supplementary Figure S19: Control experiments for SUV transport . . . . .	24
Supplementary Figure S20: TEM images of the gold nanoparticles attached to the DNA filaments . . . . .	25
Supplementary Figure S21: TEM indicates rolling of gold nanoparticles along the DNA-based filaments . . . . .	26
Supplementary Figure S22: Mechanism of motion . . . . .	27
Supplementary Figure S23: DNA density on gold nanoparticles . . . . .	28
Supplementary Figure S24: DNA density on SUVs . . . . .	29
Supplementary Figure S25: Influence of the RNase H concentration on the SUV transport . . . . .	30
Supplementary Figure S26: Decay constants for the DNA network fluorescence decrease . . . . .	31
<b>Supplementary Videos</b>	<b>31</b>
Supplementary Video S1: Dynamics of the toehold-modified DNA filaments inside water-in-oil droplets . . . . .	31
Supplementary Video S2: Time-resolved polymerization of the ATP-aptamer-modified DNA filaments inside water-in-oil droplets . . . . .	32
Supplementary Video S3: Time-resolved polymerization of actin filaments inside water-in-oil droplets . . . . .	32
Supplementary Video S4: Dynamics of the DNA filaments with aptamers for nu- cleolin and ATP targets inside water-in-oil droplets . . . . .	32
Supplementary Video S5: SUV transport on DNA filaments inside water-in-oil droplets . . . . .	33
<b>References</b>	<b>34</b>



## Supplementary Notes

### Supplementary Note S1: Estimation of the SUV velocity along the DNA filaments

From the quantitative measurements of the porosity over time (see Fig. 4f, main text), we can provide a rough estimate for the transport velocity of the individual SUVs. For this purpose we need to first estimate 1) the total length of the DNA filaments inside a droplet and 2) the total number of the SUVs inside a droplet.

1) Each DNA tile has an approximate length of  $l_t = 14$  nm, and the tubular filaments have a circumference of approximately 6 tiles.<sup>[1]</sup> Assuming that all tiles are polymerized into filaments, we can calculate the maximum total length of the DNA filaments per liter to be

$$l_{tot} = \frac{1}{6} \cdot c_t \cdot N_A \cdot l_t \approx 0.35 \cdot 10^9 \text{ m/l}, \quad (1)$$

with  $c_t$  being the DNA tile concentration (250 nM) and  $N_A$  the Avogadro number.

With an average droplet diameter of  $40 \mu\text{m}$  in this experiment and hence a droplet volume of approximately 40 pl, the total filament length per droplet amounts to  $\approx 14$  mm.

2) We can calculate the SUV concentration from the total lipid concentration. We first compute the amount of lipids per SUV and from this the total number of SUVs per volume. The SUV diameter has been measured to be 65 nm. This yields

$$n_{\text{Lipid}} = 2 \cdot \frac{4\pi r^2}{0.7 \text{ nm}^2} \approx 38000 \text{ lipids}, \quad (2)$$

where the area of each lipid is assumed to be  $0.7 \text{ nm}^2$  and the lipid bilayer is composed of two layers of lipids. Given a total lipid concentration of  $10 \mu\text{M}$  as used in the experiment,

this leads to

$$n_{\text{SUV}} = \frac{c_{\text{Lipid}} \cdot N_A}{n_{\text{Lipid}}} \approx 1.6 \cdot 10^{14} / l. \quad (3)$$

This equals an SUV concentration of approximately 250 pM. With a droplet volume of 40 pl, we estimate that a total of 6400 SUVs have been encapsulated per droplet.

From Figure 4, we find that the filament fluorescence decreases with a half life of  $t_{1/2} = 25$  min for 250 pM SUVs. This means that 6400 SUVs roll on average over half of the total filament length in a droplet, hence 7 mm, during this time. A single SUV thus covers a distance of approximately 1  $\mu\text{m}$  in 25 minutes, or  $v_{\text{SUV}} \approx 44$  nm/min. Note that photobleaching only accounts for a 2% decrease of the porosity (see Fig. S19a). This would result in a negligible increase of the calculated transport velocities, but its minor contribution has been disregarded here. This can be transformed into rotations of single SUVs via

$$v_{\text{rot}} = \frac{v_{\text{SUV}}}{2\pi r} \approx 0.22 \text{rot/min}. \quad (4)$$

All in all, this yields transport velocities for the different conditions:

Table 1: Estimation of the vesicle velocity along the DNA filaments.

lipid concentration	# SUVs per droplet	SUV concentration	half-life	velocity
0.1 $\mu\text{M}$	64	2.5 pM	636 min	170 nm/min
1 $\mu\text{M}$	640	25 pM	40 min	280 nm/min
10 $\mu\text{M}$	6400	250 pM	25 min	44 nm/min

Table 2: Estimation of the gold nanoparticle velocity along the DNA filaments.

nanoparticle concentration	# gold nanoparticles per droplet	half-life	velocity
6.4 nM	154200	44 min	1.03 nm/min

## Supplementary Figures

### Supplementary Figure S1: Strand routing diagrams for the DNA tiles

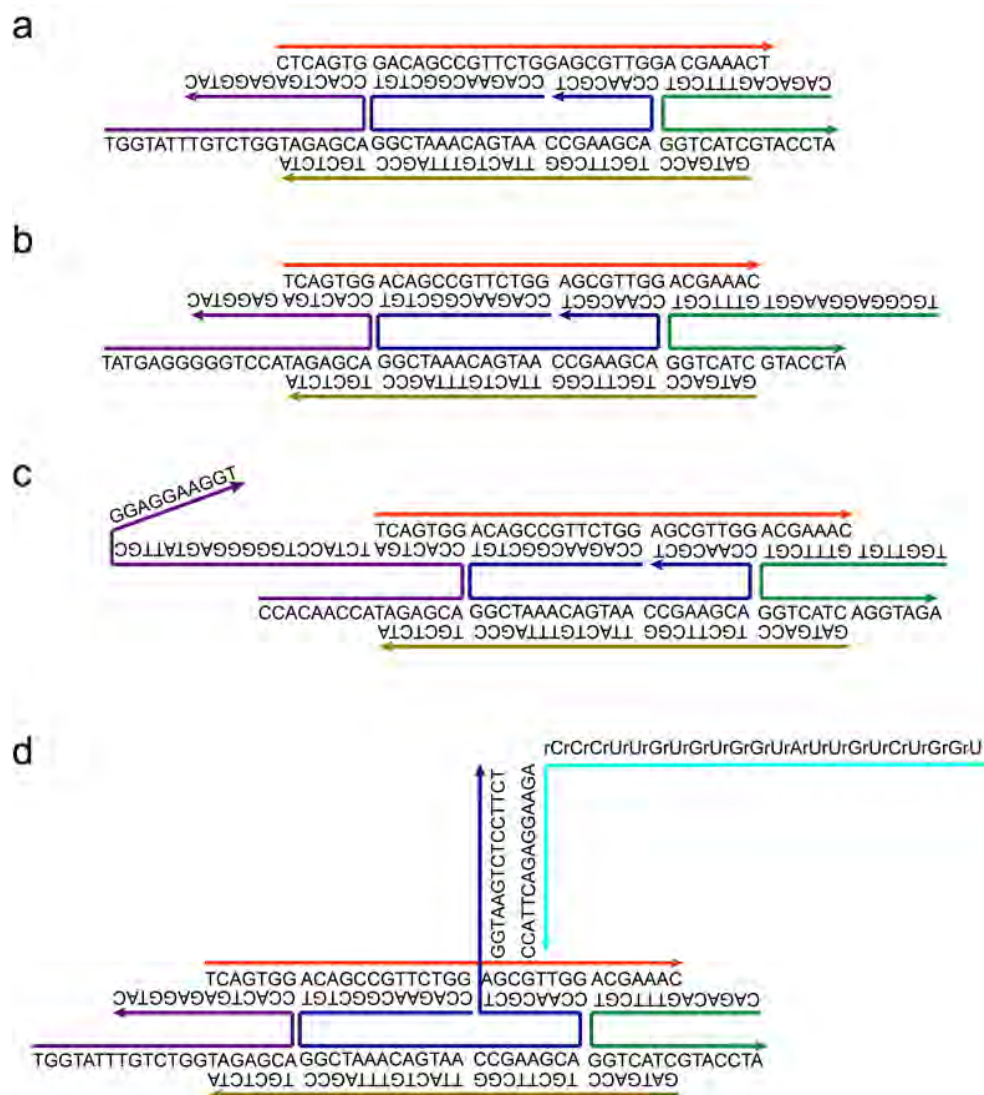


Figure 1: Strand routing diagrams for the DNA tiles. **a** DNA tile for the toehold strand displacement reaction in Fig. 2. **b** DNA tile for the ATP split-aptameric reaction in Figs. 3a and b. **c** DNA tile for the dual-aptamer reaction in Figs. 3d and e. **d** DNA tile for the SUV and gold nanoparticle transport reaction in Fig. 4.

**Supplementary Figure S2: Assembly of the DNA filaments at different tile concentrations**

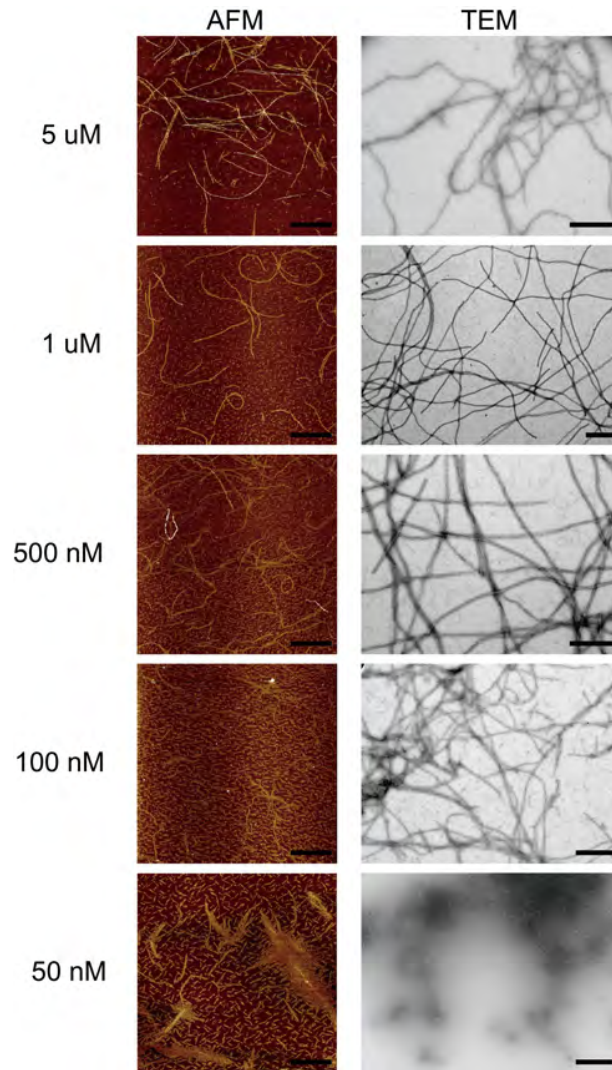


Figure 2: Assembly of the DNA filaments at different tile concentrations. AFM (left column) and TEM (right column) images of the formed DNA filaments annealed at DNA tile concentrations from 5  $\mu$ M (top) to 50 nM (bottom). At a concentration of 5  $\mu$ M used in the most experiments, a high yield of the correctly formed DNA filaments is obtained. Scale bars: 200 nm.

**Supplementary Figure S3: Assembly of the DNA filaments at different  $Mg^{2+}$  concentrations**

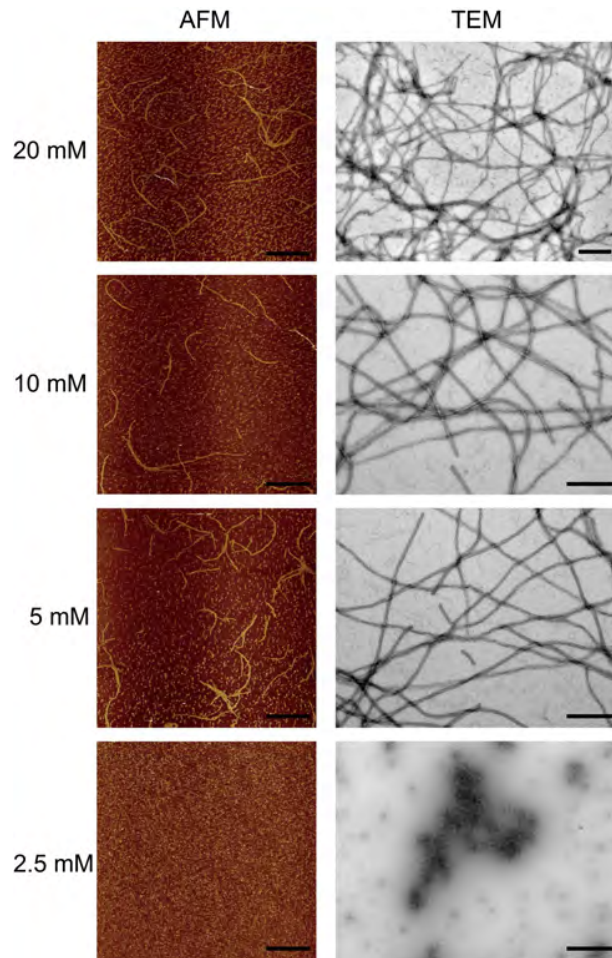


Figure 3: Assembly of the DNA filaments at different  $Mg^{2+}$  concentrations from 2.5 mM to 20 mM. AFM (left column) and TEM (right column) demonstrate successful DNA filament assembly at  $Mg^{2+}$  concentrations from 5 mM. Scale bars: 200 nm.

Supplementary Figure S4: Assembly of the DNA filaments at different temperatures

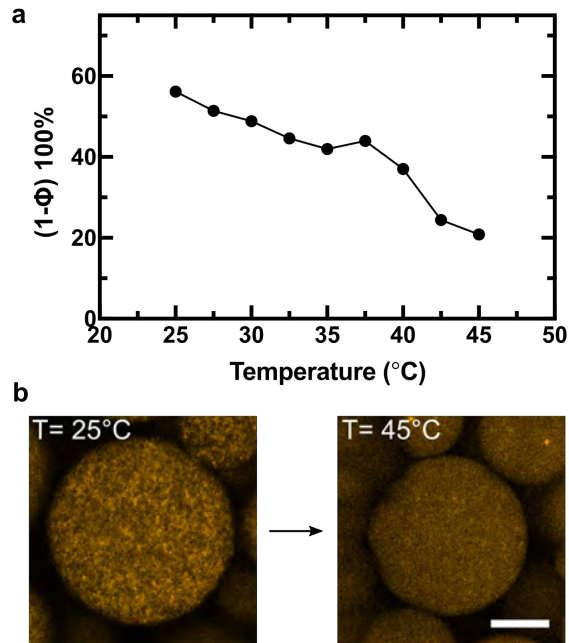


Figure 4: **a** Dependence of the porosity  $(1-\Phi)100\%$  on temperature. **b** Confocal fluorescence microscopy images of DNA filaments at 25 °C and 45 °C, respectively. The filaments are completely disassembled at 45 °C, resulting in a homogeneous distribution of the fluorophores inside the droplet lumen. Scale bar: 20  $\mu\text{m}$ .

**Supplementary Figure S5: Confocal images of the DNA-based filaments in bulk**

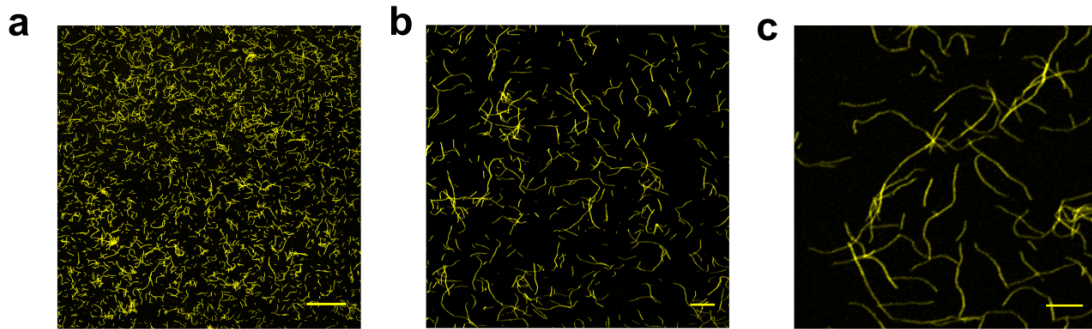


Figure 5: Confocal images of the DNA filaments in bulk. Cy3-labelled DNA filaments ( $\lambda_{ex} = 561$  nm) in  $1\times$  TAE buffer containing 20 mM  $\text{MgCl}_2$  at different magnifications. Due to  $\text{Mg}^{2+}$  mediated interactions, the DNA filaments are prone to attach to the glass coverslide. Scale bars: (a) 50  $\mu\text{m}$ , (b) 10  $\mu\text{m}$  and (c) 5  $\mu\text{m}$ , respectively.

## Supplementary Figure S6: Microfluidic device and droplet formation

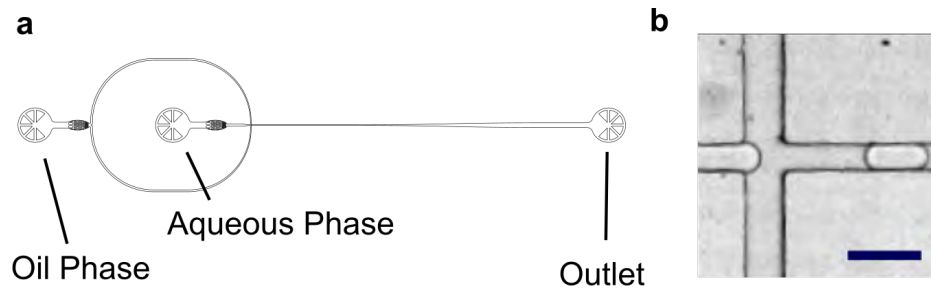


Figure 6: Microfluidic device and droplet formation. **a** Layout of the microfluidic T-junction device for the encapsulation of the DNA filaments (supplied via the aqueous phase) into surfactant-stabilized water-in-oil droplets. The droplets are collected from the outlet for further imaging. The microfluidic PDMS devices (Sylgard184, Dow Corning, USA) have been fabricated according to a previously published protocol<sup>[2]</sup> (see Methods). **b** Bright-field high-speed camera image of a flow-focusing T-junction during the droplet formation. Scale bar: 50  $\mu\text{m}$ .



**Supplementary Figure S7: AFM images of assembly and disassembly of the DNA-based filaments by strand displacement reactions**

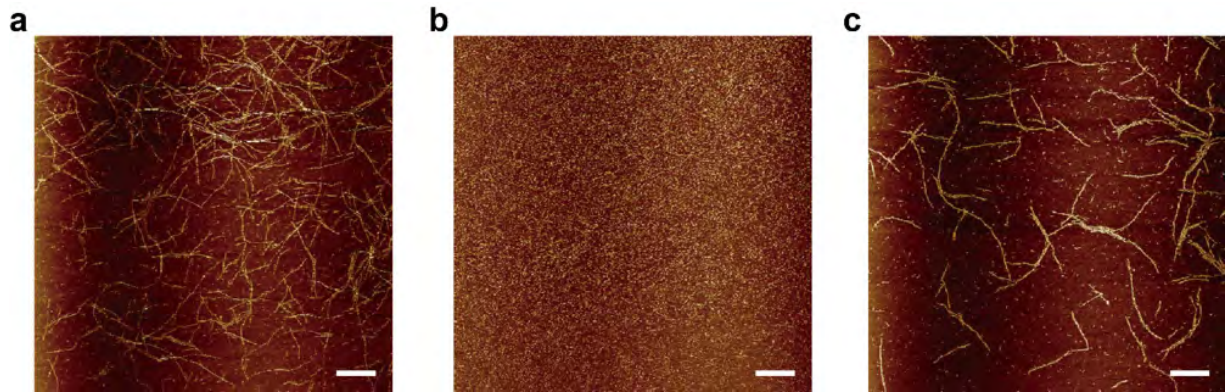


Figure 7: AFM images of reversible assembly and disassembly of the DNA filaments by subsequent strand displacement reactions. **a** AFM image of the assembled DNA filaments before adding the invader strands. **b** AFM image of the disassembled DNA filaments after adding the invader strands. The DNA filaments are disassembled into individual DNA tiles. **c** AFM image of the re-assembled DNA filaments upon adding the anti-invader strands. Scale bars: 100 nm.

Supplementary Figure S8: Determination of the required concentrations of invader and anti-invader strands

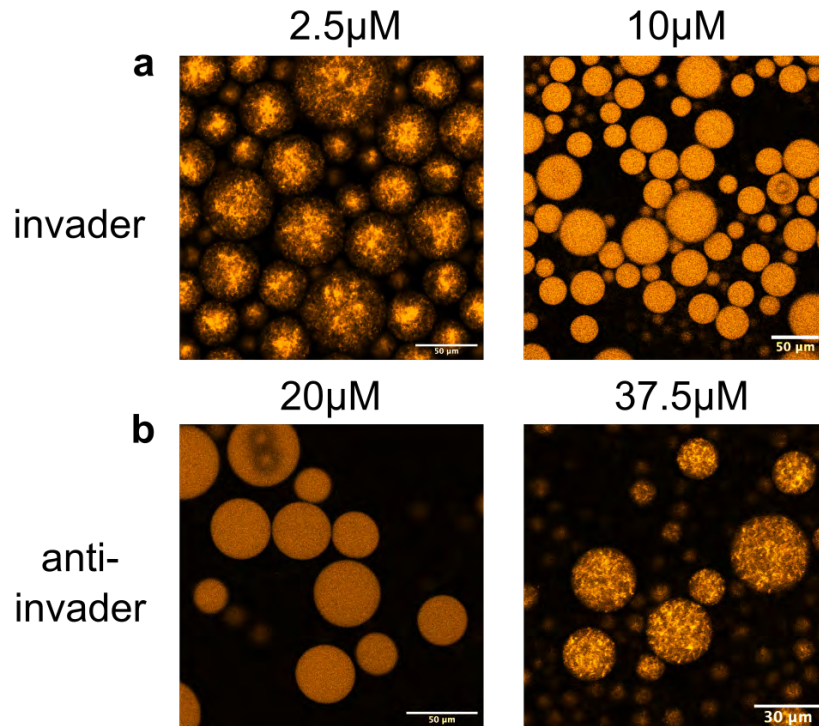


Figure 8: Determination of the required concentrations of invader and anti-invaders. **a** Confocal images of 1  $\mu\text{M}$  Cy3-labelled DNA filaments ( $\lambda_{ex} = 561 \text{ nm}$ ) in 1 $\times$  TAE buffer containing 20 mM  $\text{MgCl}_2$ . Addition of 2.5  $\mu\text{M}$  invader strands is not sufficient to trigger the filament disassembly, whereas 10  $\mu\text{M}$  can trigger the disassembly. **b** Confocal images of 1  $\mu\text{M}$  Cy3-labelled DNA filaments ( $\lambda_{ex} = 561 \text{ nm}$ ) in 1 $\times$  TAE buffer containing 20 mM  $\text{MgCl}_2$ . Addition of 20  $\mu\text{M}$  anti-invader strand is not sufficient to trigger the filament assembly, whereas 37.5  $\mu\text{M}$  can trigger the assembly. Images were taken approximately 10 minutes after droplet production. From these results, the higher concentrations have been chosen for the respective experiments.

**Supplementary Figure S9: Low ATP concentrations do not induce filament assembly**

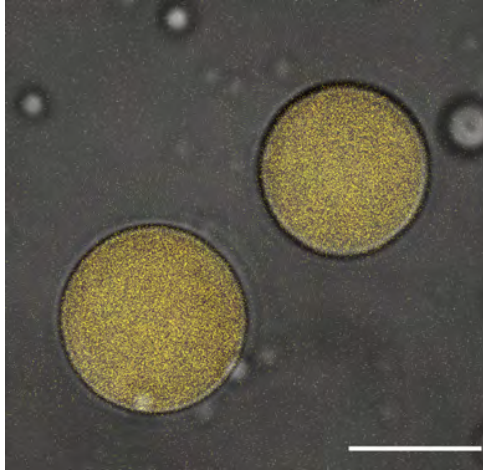


Figure 9: Low ATP concentrations do not induce filament assembly. Confocal microscopy image of 1  $\mu$ M Cy3-labelled DNA tiles ( $\lambda_{ex} = 561$  nm) in 1 $\times$  TAE buffer containing 20 mM  $MgCl_2$  and 1 mM ATP. DNA tiles are still distributed homogeneously within the water-in-oil droplets after about 10 minutes. Scale bar: 20  $\mu$ m.

**Supplementary Figure S10: AFM images of the aptamer-specific assembly and disassembly of the DNA-based filaments**

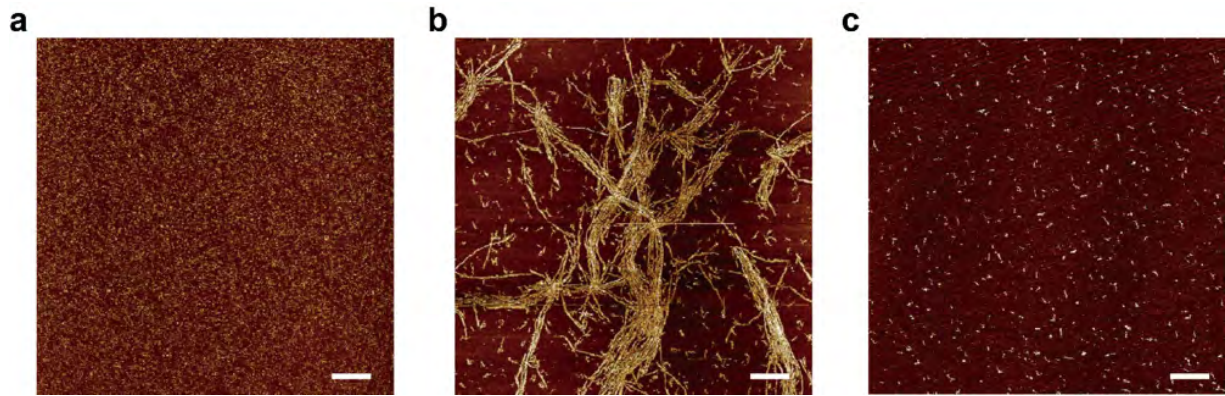


Figure 10: AFM images of the aptamer-specific reversible assembly and disassembly of the DNA filaments. **a** AFM image of the DNA tiles before adding NCL. Scale bar: 50 nm. **b** AFM image of the DNA filaments after adding NCL. DNA tiles are assembled into DNA filaments. Scale bar: 100 nm. **c** AFM image of the DNA tiles upon subsequent addition of ATP. DNA tiles are again disassembled. Scale bar: 50 nm.

Supplementary Figure S11: Strand routing diagram for the DNA origami seed

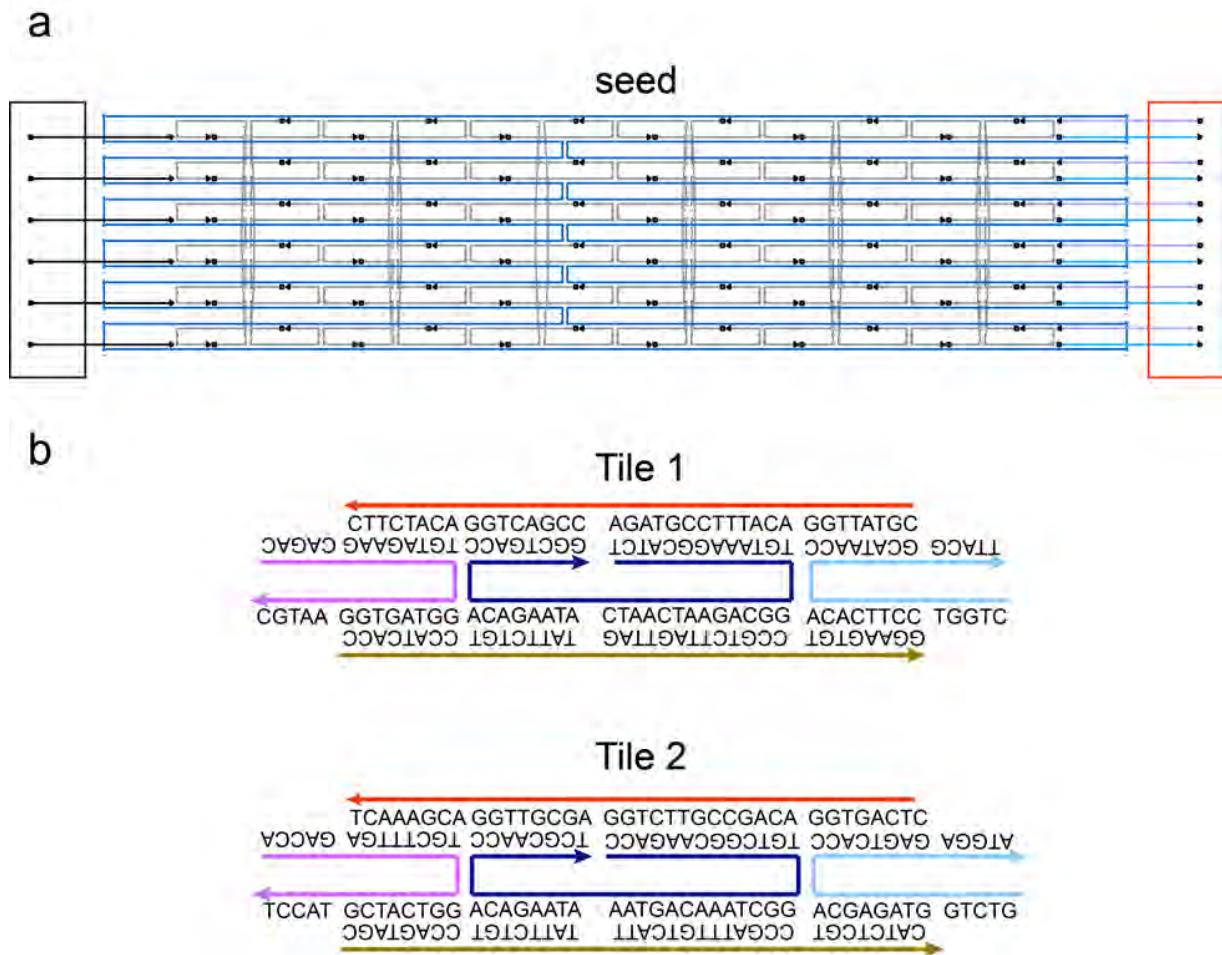


Figure 11: Strand routing diagram for the DNA origami seed to implement a seeded growth mechanism for the DNA filaments. **a** Layout of the DNA origami seed with the DNA overhangs for the attachment of a gold nanoparticle (black box) and the DNA tiles (red box). **b** Design and sequences of the tiles, which are attached to the overhangs on the DNA origami seed for the directional growth of the filament. All DNA sequences are provided in Supplementary Dataset 1.

## Supplementary Figure S12: Seeded growth mechanism

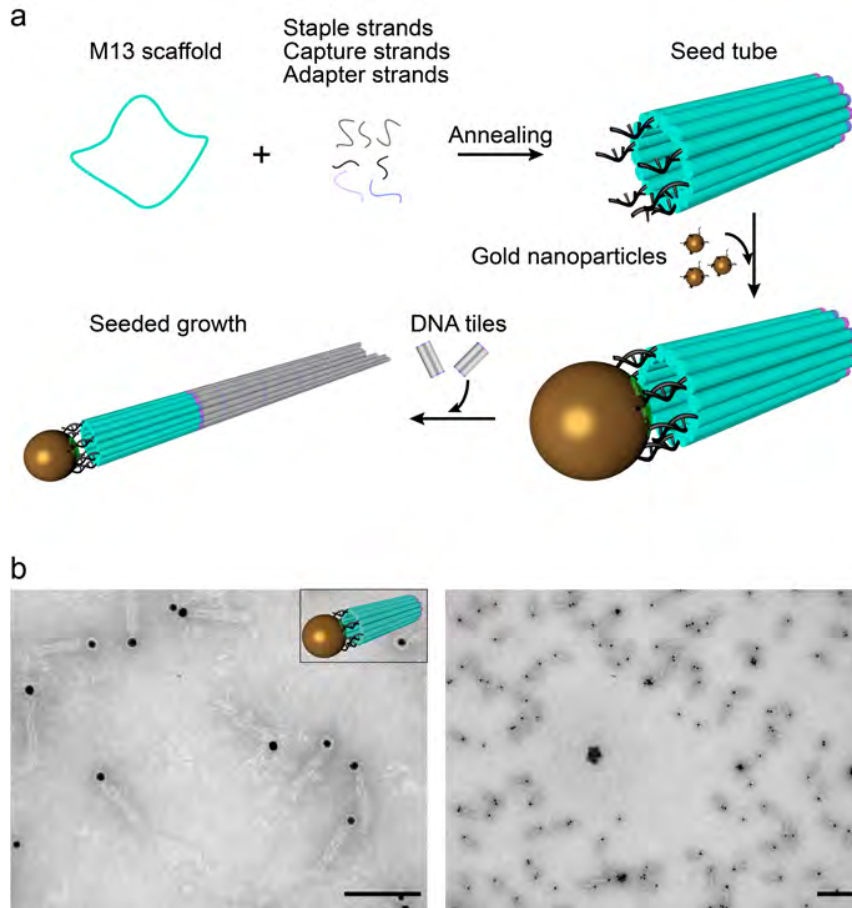


Figure 12: **a** Mechanism for the seeded growth of the DNA filaments. The M13 scaffold is hybridized with specifically designed and custom-synthesized staple strands to form a hollow seed tube. A gold nanoparticle (10 nm diameter) is attached to one end of the tube via complementary base pairing. It serves as a label to distinguish the two ends of the seed for TEM imaging. The DNA tiles are added to the seed to implement seeded and directional growth of the DNA filaments. **b** TEM images of the DNA origami seeds. The gold nanoparticles are clearly visible on one of the ends of the tubes, leaving the other end open for attachment of the DNA tiles. Scale bars: 100 nm (left image) and 200 nm (right image), respectively.

## Supplementary Figure S13: TEM and confocal images of seeded growth

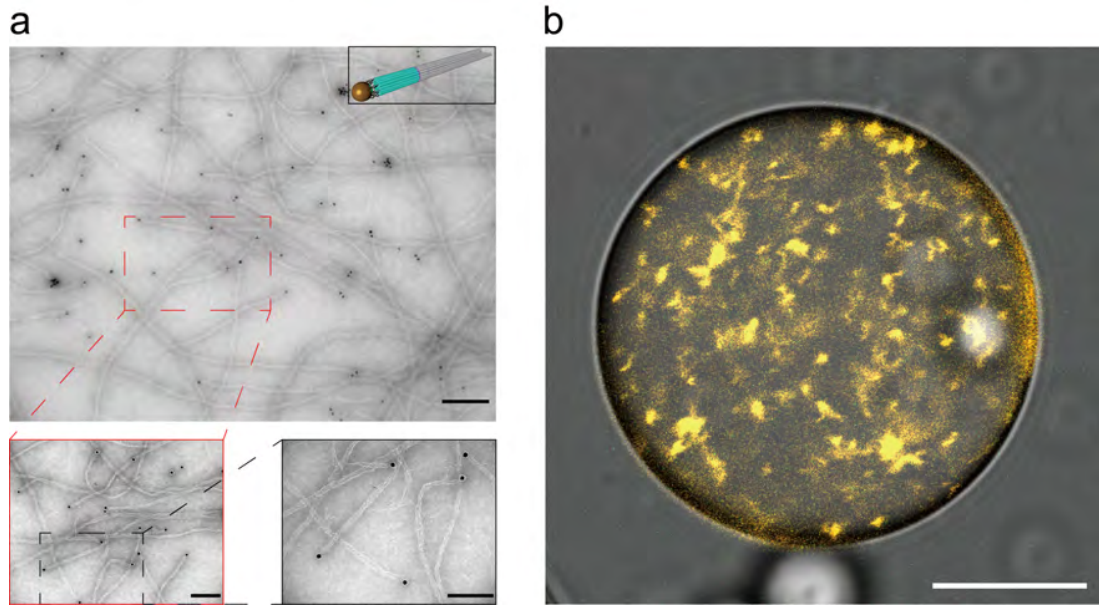


Figure 13: **a** TEM images demonstrating the successful implementation of the seeded growth mechanism as laid out in Fig. S12. The gold nanoparticles are clearly visible at one of the ends of the filaments, which extend from the DNA origami seeds. Scale bars: 200 nm (top image) and 100 nm (bottom images). **b** Confocal fluorescence microscopy image of the seeded DNA filaments encapsulated inside a water-in-oil droplet. Scale bar: 20  $\mu\text{m}$ .

### Supplementary Figure S14: Size distribution of the SUVs

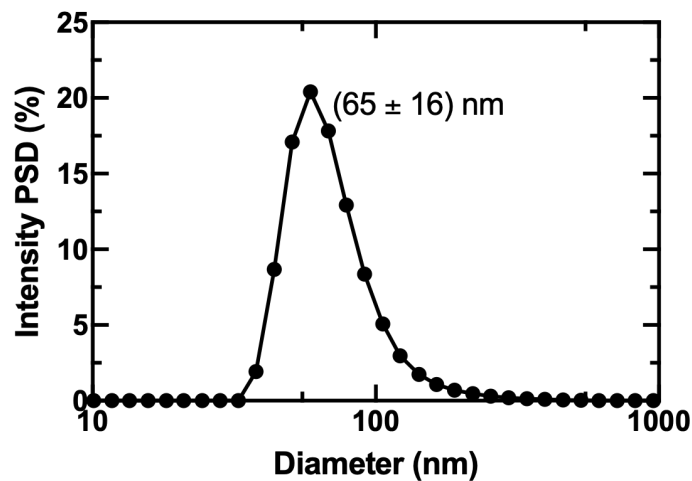


Figure 14: Intensity particle size distribution (PSD) of the SUV diameter determined by dynamic light scattering (DLS). The measurements have been performed using a solution of 1 mL of 200  $\mu\text{M}$  SUVs. The average diameter and the standard deviation have been determined from 3 individual runs each containing 14 measurements. The distribution reveals a mean diameter of  $65 \pm 16 \text{ nm}$ .



**Supplementary Figure S15: STED imaging confirms the binding of the SUVs to the DNA-based filaments**

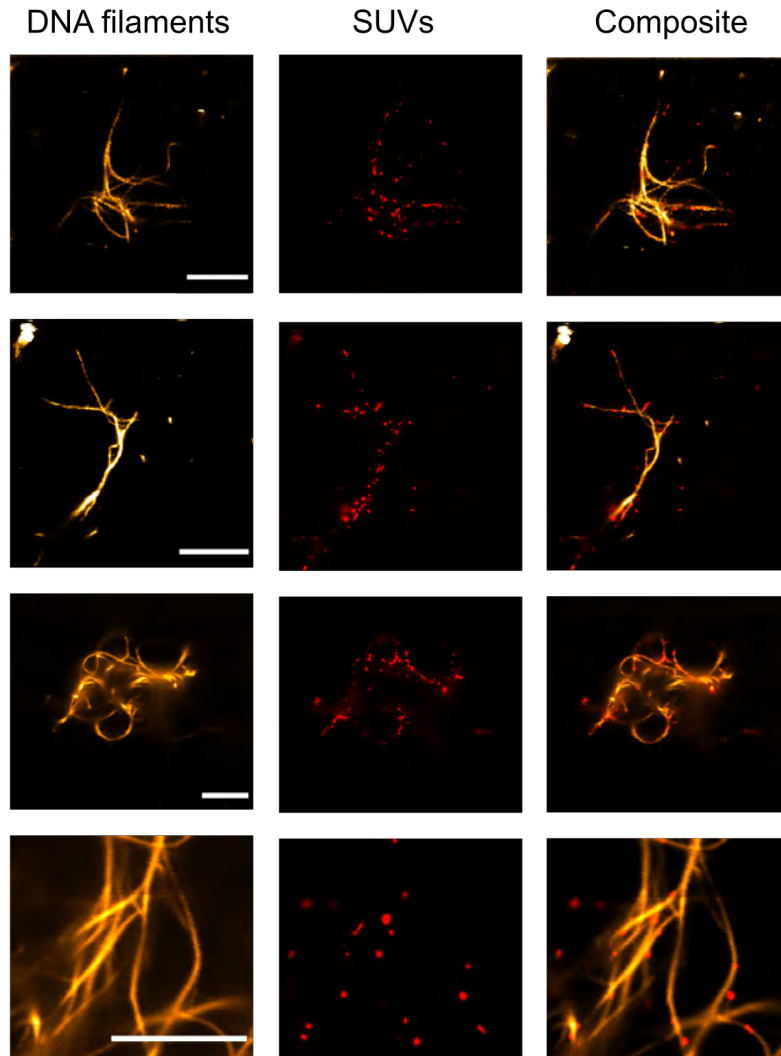


Figure 15: STED imaging confirms binding of the SUVs to the DNA filaments. STED images of the Cy3-labeled DNA filaments ( $\lambda_{ex} = 560$  nm), Atto633-labeled SUVs ( $\lambda_{ex} = 640$  nm) as well as composite images. SUVs colocalize with DNA filaments. Scale bars: 5  $\mu$ m.

## Supplementary Figure S16: Color-coded z-projections of the DNA-SUV networks

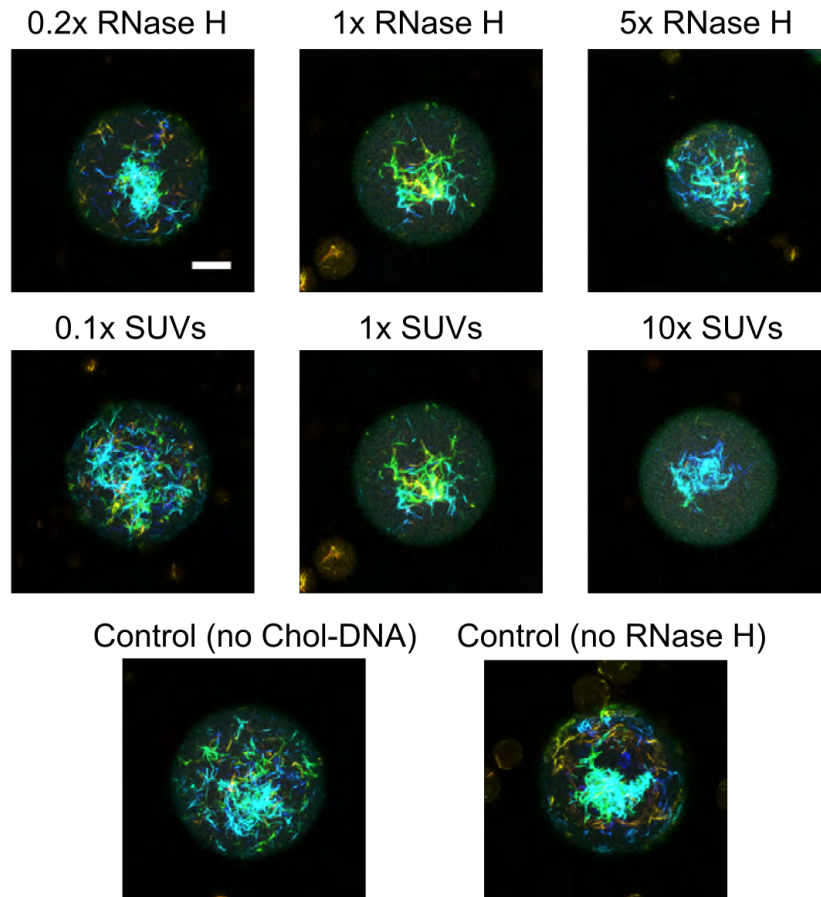


Figure 16: Color-coded confocal z-projections of the DNA networks ( $\lambda_{ex} = 561 \text{ nm}$ ) in the presence of SUVs reconstructed from the confocal microscopy images at  $t = 0 \text{ min}$ . From the images one can deduce the tendency of the DNA filaments to form more compact networks with a higher SUV density, possibly due to crosslinking of multiple DNA filaments by single SUVs.  $1 \times \text{RNase H}$  corresponds to 5 units of RNase H and  $1 \times \text{SUVs}$  corresponds to a concentration of 25 pM. Scale bar: 20  $\mu\text{m}$ .

## Supplementary Figure S17: Composite images of the DNA-SUV networks

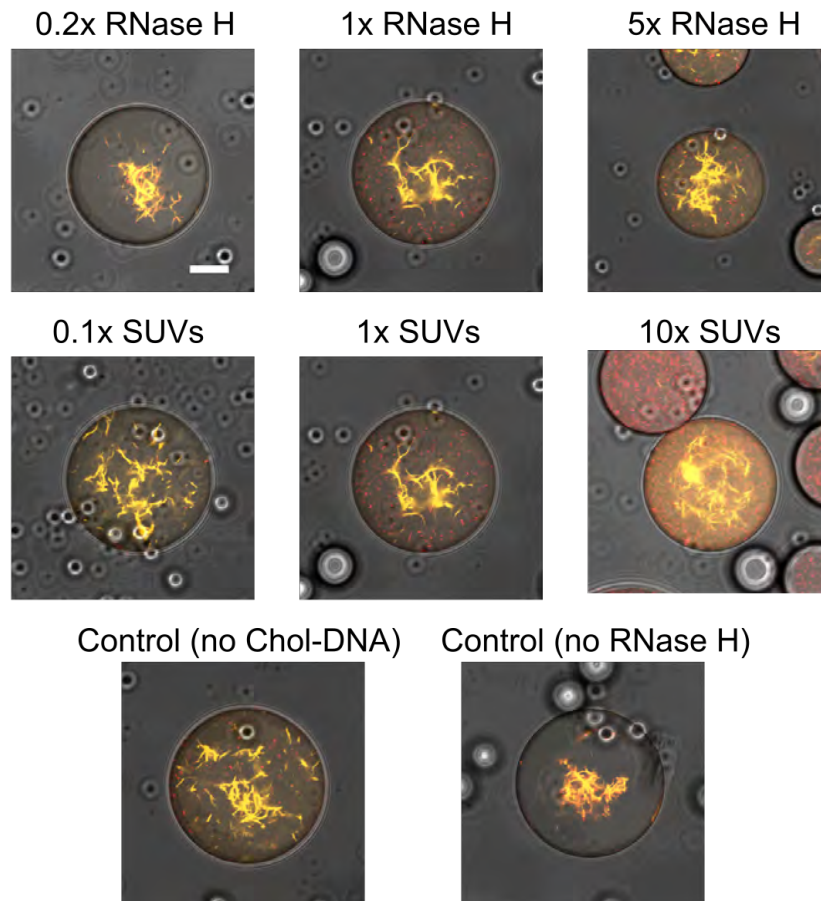


Figure 17: Composite bright-field and confocal microscopy images of the DNA-SUV networks (Cy3-labeled DNA,  $\lambda_{ex} = 561$  nm, orange or Atto633-labeled SUVs  $\lambda_{ex} = 640$  nm, red) encapsulated into water-in-oil droplets at  $t = 0$  min. The images show the loss of fluorescence of the DNA filaments already at  $t = 0$  min as well as complete binding of SUVs to the DNA filaments at low SUV concentrations.  $1 \times$  RNase H corresponds to 5 units of RNase H and  $1 \times$  SUVs corresponds to a concentration of 25 pM. Scale bar: 20  $\mu$ m.

## Supplementary Figure S18: DNA filaments remain intact after transport

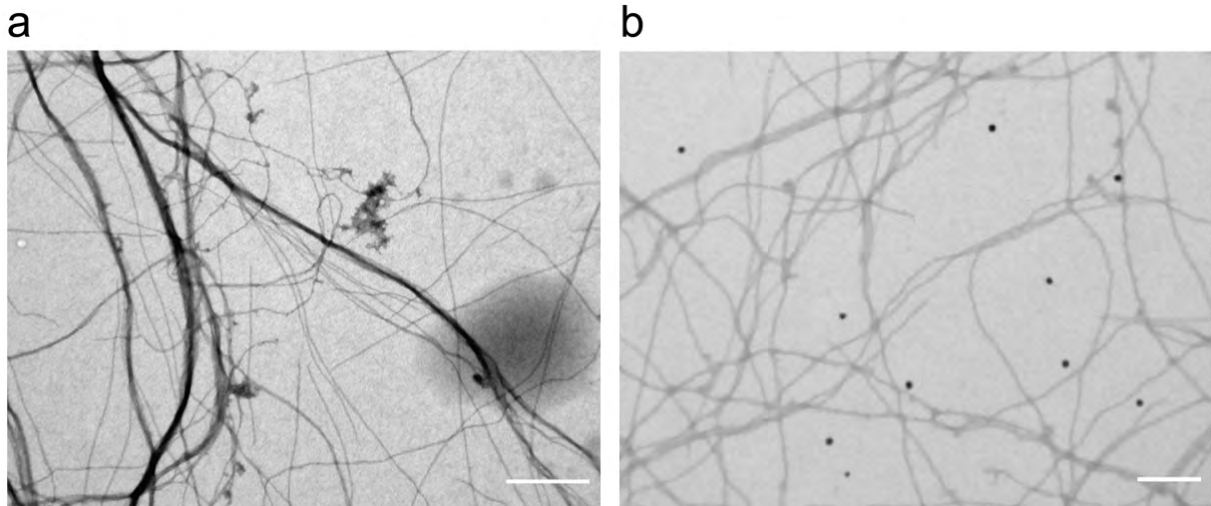


Figure 18: TEM images of the DNA-based filaments after apparent cargo transport of **a** SUVs and **b** gold nanoparticles. The filaments have been released from the droplets after cargo transport by breaking them up with addition of perfluoro-1-octanol (PFO) destabilizing agent.<sup>[3]</sup> The filaments remain intact after transport, confirming that the decrease in porosity ( $(1 - \Phi) \cdot 100\%$ ) is not due to filament disassembly. The fluorophores have been cleaved from the filaments, while leaving the filaments intact. Furthermore, the cargos (SUVs or gold nanoparticles) have detached from the filaments after cargo transport. Scale bar: 200 nm.

## Supplementary Figure S19: Control experiments for SUV transport

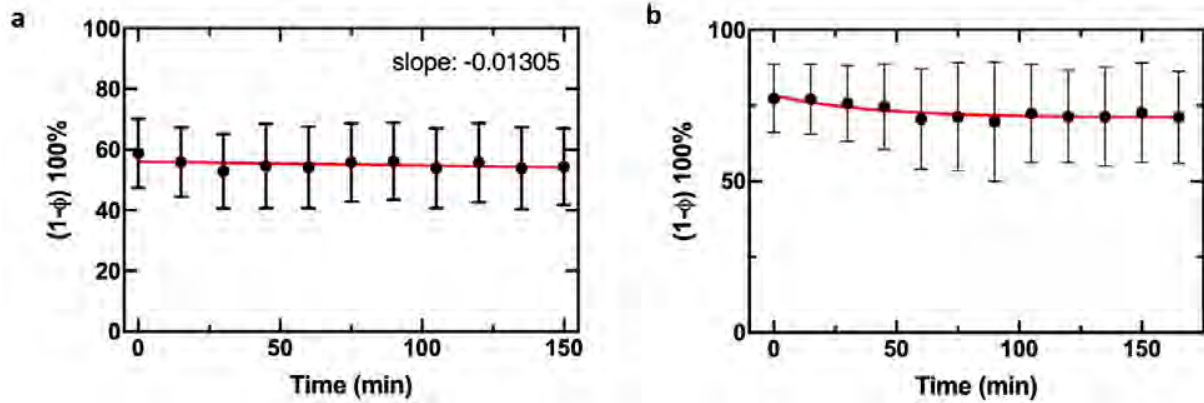


Figure 19: **a** Porosity  $((1 - \Phi) \cdot 100\%)$  in droplets over time without RNase H (mean  $\pm$  standard deviation for  $n = 4$  droplets). The red line represents a linear fit, the decay corresponds to the rate of photobleaching. Photobleaching only causes a decrease of the porosity by 2% over the course of 150 minutes. **b** Porosity  $((1 - \Phi) \cdot 100\%)$  in droplets over time without cholesterol-tagged DNA in the presence of RNase H (mean  $\pm$  standard deviation for  $n = 12$  droplets). In this control experiment, the SUVs do not bind to the DNA filaments. Hence, transport should not occur and any reduction in  $(1 - \Phi) \cdot 100\%$  can be attributed to either photobleaching or unspecific cutting of the RNase H.

**Supplementary Figure S20: TEM images of the gold nanoparticles attached to the DNA filaments**

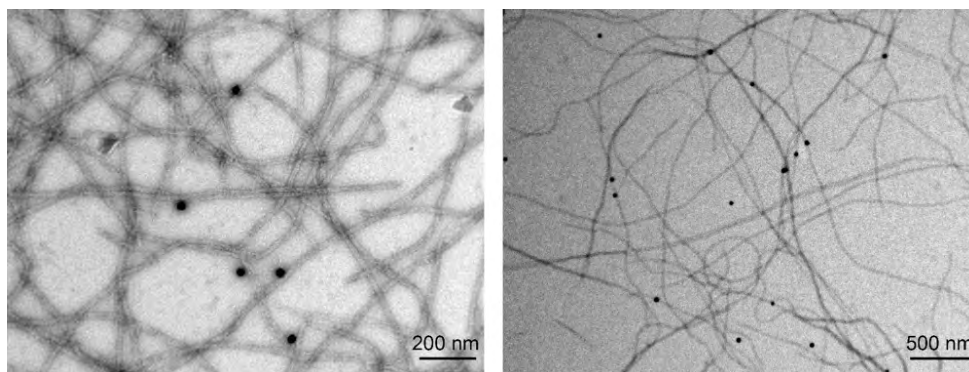


Figure 20: TEM images of the gold nanoparticles attached to the DNA filaments.

## Supplementary Figure S21: TEM indicates rolling of gold nanoparticles along the DNA-based filaments

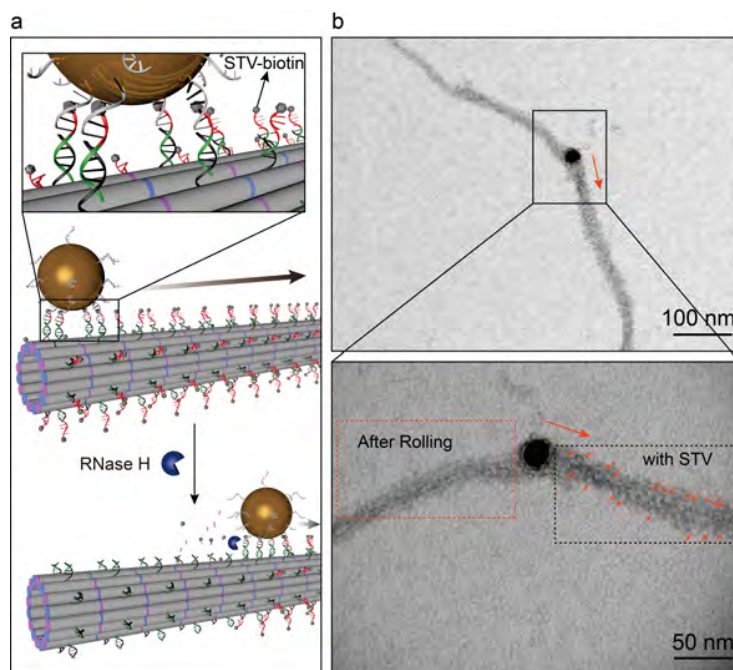


Figure 21: **a** Schematic of gold nanoparticles by rolling motion using RNase H mediated cleaving of the RNA part of an RNA-DNA duplex on a DNA filament. The biotin functionalized single-stranded RNA-DNA (red-green, binds to streptavidin (STV)) is anchored on the filaments through DNA-DNA hybridization (black and green). The DNA strands (gray) on the gold nanoparticle hybridize with the RNA part. Upon addition of RNase H, the DNA-RNA double helix is cut, and STV is released. **b** TEM images of the filaments with STVs after adding RNase H. The dotted red frame demonstrates that RNA strands with STVs are cut since no STVs are attached on the filaments. The dotted black frame shows anchored STVs on the filaments without cutting.

## Supplementary Figure S22: Mechanism of motion

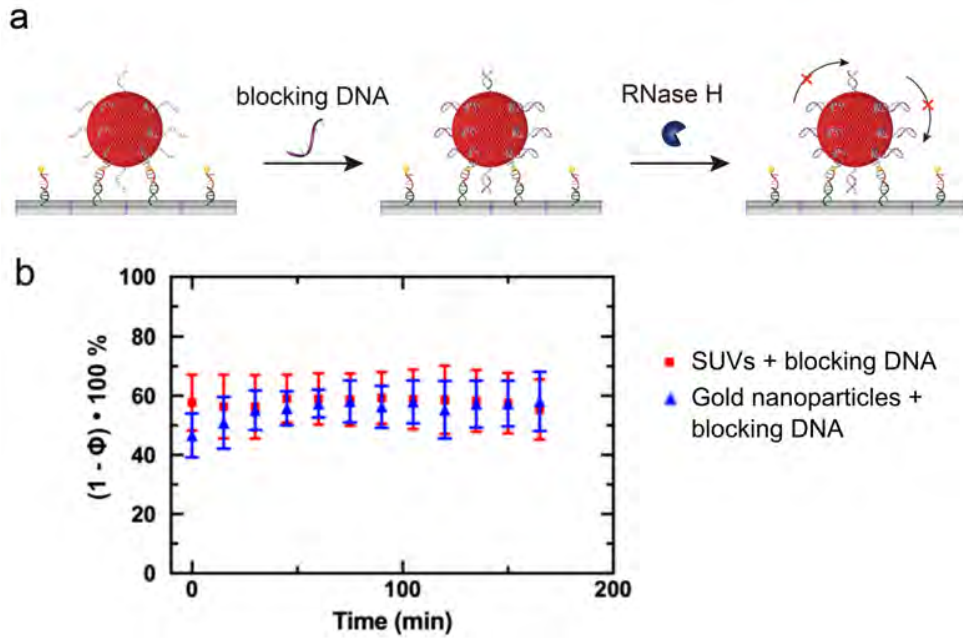


Figure 22: Mechanism of the particle motion. **a** Strategy to verifying how SUVs move along the DNA filaments. To demonstrate whether the SUVs roll, hop or glide along the DNA filaments, the free DNA on the SUVs is blocked by hybridization with blocking DNA strands (purple). The same experiment has been performed for gold nanoparticles. **b** Porosity ( $(1 - \Phi) \cdot 100\%$ ) measurements in the presence of the blocking DNA strands for gold nanoparticles (blue) and SUVs (red), respectively. The measured porosity remains nearly constant in each case. This indicates that the cargo transport along the filaments will halt, when the rolling motion is inhibited.



## Supplementary Figure S23: DNA density on gold nanoparticles

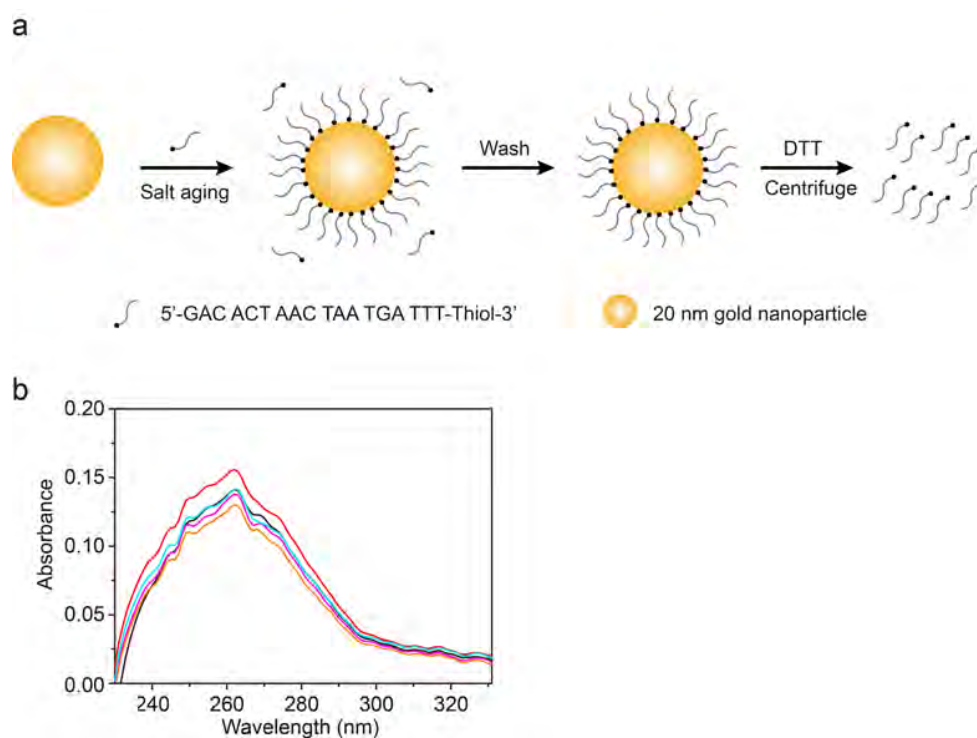


Figure 23: Quantification of the DNA density on gold nanoparticles. **a** Illustration of the experimental procedure used for the quantification of the DNA density on gold nanoparticles. **b** UV-Vis spectra of the released DNA (mean and standard deviation from  $n=5$  independent experiments). DNA coverage of  $126 \pm 10$  strands per gold nanoparticle or a density of  $0.10 \pm 0.01$  strands per  $\text{nm}^2$  is obtained.

## Supplementary Figure S24: DNA density on SUVs

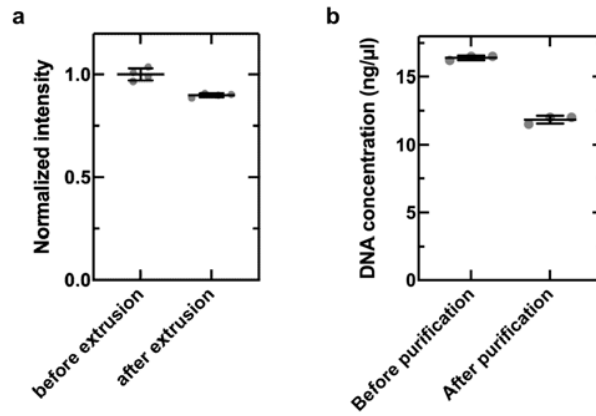


Figure 24: Quantification of the DNA density on SUVs. **a** Quantification of the loss of lipids after SUV extrusion. The fluorescence intensity of the lipid mixture (99% DOPC, 1% Atto633-DOPE) is determined before and after extrusion. 9.07% of the lipids are lost during the extrusion process (mean and standard deviation from  $n=4$  independent measurements). **b** Incorporation efficiency of single-stranded cholesterol-tagged DNA into SUVs. The concentration of DNA is determined from UV absorbance measurements. The reference measurement is taken before addition to SUVs (“before purification”). Afterwards, the cholesterol-tagged DNA is incubated in excess with SUVs. The DNA concentration in the supernatant is measured (“after purification”). It corresponds to the unbound fraction of DNA (mean and standard deviation from  $n=3$  independent experiments).  $27.8 \pm 2.2\%$  of  $2 \mu\text{M}$  cholesterol-tagged DNA binds to SUVs ( $10 \mu\text{M}$  lipids before extrusion). This gives rise to a DNA density on the SUVs of  $0.18 \pm 0.01$  DNA strands per  $\text{nm}^2$ .

## Supplementary Figure S25: Influence of the RNase H concentration on the SUV transport

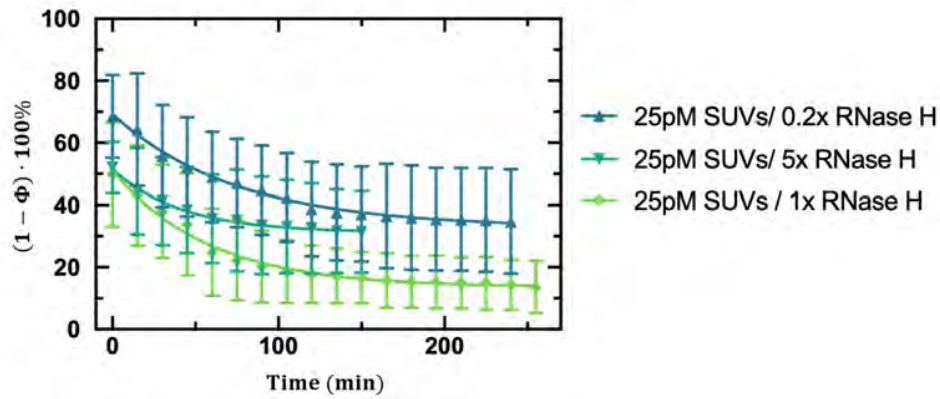


Figure 25: Influence of the RNase H concentration on the apparent SUV transport. Porosity  $((1 - \Phi) \cdot 100\%)$ , as a measure for the SUV transport) of the DNA filaments over time at different RNase H concentrations.  $1 \times$  RNase H corresponds to 5 units of RNase H. Less RNase H ( $0.2 \times$ ) or more RNase H ( $5 \times$ ) lead to a decrease in transport. This could be due to the high viscosity of the RNase H solution, which contains 50 % glycerol and thus reduces diffusion speeds.<sup>[4]</sup>

## Supplementary Figure S26: Decay constants for the DNA network fluorescence decrease

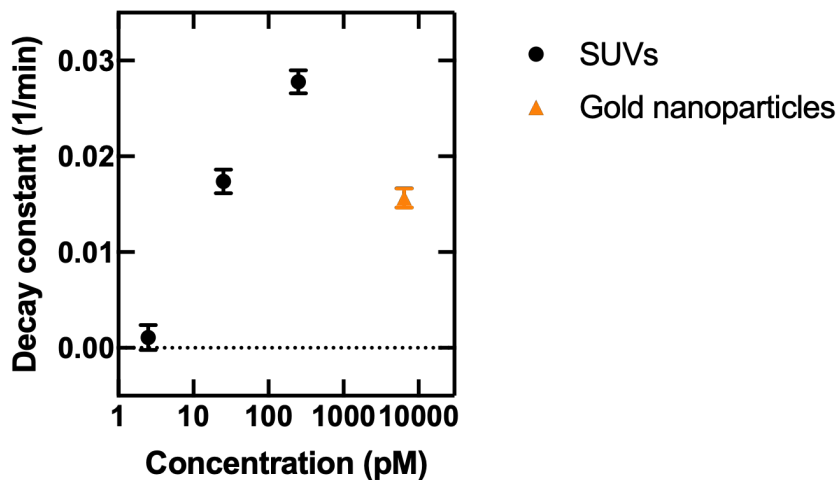


Figure 26: Decay constants for the DNA network fluorescence decrease. The porosity decrease over time is fitted with a one phase exponential decay revealing the apparent decay constant of the network fluorescence. The decay constant increases from negligible decay for 2.5 pM SUVs to  $0.017 \pm 0.001$  1/min for 25 pM SUVs and to  $0.028 \pm 0.001$  1/min for 250 pM SUVs. In the presence of 6 nM gold nanoparticles the decay constant is found to be 0.016 1/min.

## Supplementary Videos

### Supplementary Video S1: Dynamics of the toehold-modified DNA filaments inside water-in-oil droplets

Confocal timelapse of 500 nM Cy3-labelled toehold-modified DNA filaments ( $\lambda_{ex} = 561$  nm) in a  $1 \times$  TAE buffer containing 12 mM  $MgCl_2$ . After polymerization, the DNA filaments remain highly dynamic with constant rearrangement and remodelling. The video corresponds to the filaments shown in Fig. 2c. Scale bar: 50  $\mu$ m.

### **Supplementary Video S2: Time-resolved polymerization of the ATP-aptamer-modified DNA filaments inside water-in-oil droplets**

Confocal time series of 1  $\mu\text{M}$  Cy3-labelled DNA filaments ( $\lambda_{ex} = 561 \text{ nm}$ ) in a  $1\times$  TAE buffer containing 20 mM  $\text{MgCl}_2$  and 2 mM ATP. Over the course of 150 min, DNA filaments assemble inside the surfactant-stabilized water-in-oil droplets. The corresponding quantification of the porosity (i.e. the degree of polymerization) is shown in Fig. 3b (orange curve). Scale bar: 10  $\mu\text{m}$ .

### **Supplementary Video S3: Time-resolved polymerization of actin filaments inside water-in-oil droplets**

Confocal time series of actin-containing water-in-oil droplets (10  $\mu\text{M}$ ) labeled with phalloidin-rhodamine ( $\lambda_{ex} = 561 \text{ nm}$ ). The video depicts a colour-coded z-projection of actin fluorescence over the course of 90 min. In the presence of ATP-containing actin polymerization buffer (see Methods), actin polymerizes over time into micron-sized filaments. The corresponding quantification of the porosity (i.e. the degree of polymerization) is shown in Fig. 3b (red curve). Scale bar: 20  $\mu\text{m}$ .

### **Supplementary Video S4: Dynamics of the DNA filaments with aptamers for nucleolin and ATP targets inside water-in-oil droplets**

Confocal time series of 500 nM Cy3-labelled DNA filaments ( $\lambda_{ex} = 561 \text{ nm}$ ) in a  $1\times$  TAE buffer containing 20 mM  $\text{MgCl}_2$  and 1.5  $\mu\text{M}$  nucleolin. Like the toehold-modified filaments (Video S1), the aptamer-functionalized DNA filaments remain highly dynamic with constant rearrangement and remodelling after polymerization. Scale bar: 20  $\mu\text{m}$ .

## **Supplementary Video S5: SUV transport on DNA filaments inside water-in-oil droplets**

Confocal time series of 250 nM Cy3-labeled DNA filaments ( $\lambda_{ex} = 561$  nm, orange) and 25 pM Atto633-labeled SUVs ( $\lambda_{ex} = 633$  nm, red) inside a water-in-oil droplet containing 0.25 units/ $\mu$ L of RNase H and 1 $\times$  RNase H reaction buffer. The DNA filaments lose their fluorescence over time due to apparent RNase-mediated SUV transport. Scale bar: 20  $\mu$ m.

## References

- (1) Green, L.; Amodio, A.; Subramanian, H. K. K.; Ricci, F.; Franco, E. pH-driven reversible self-assembly of micron-scale DNA scaffolds. *Nano Letters* **2017**, *17*, 7283–7288.
- (2) Platzman, I.; Janiesch, J.-W.; Spatz, J. P. Synthesis of Nanostructured and Biofunctionalized Water-in-Oil Droplets as Tools for Homing T Cells. *Journal of the American Chemical Society* **2013**, *135*, 3339–3342.
- (3) Göpfrich, K.; Haller, B.; Staufer, O.; Dreher, Y.; Mersdorf, U.; Platzman, I.; Spatz, J. P. One-Pot Assembly of Complex Giant Unilamellar Vesicle-Based Synthetic Cells. *ACS Synthetic Biology* **2019**, *8*, 937–947.
- (4) D'Errico, G.; Ortona, O.; Capuano, F.; Vitagliano, V. Diffusion Coefficients for the Binary System Glycerol–Water at 25 °C. A Velocity Correlation Study. *Journal of Chemical & Engineering Data* **2004**, *49*, 1665–1670.

## **A.7 Supporting Information for Publication 7: Bottom-up assembly of synthetic cells with a DNA cytoskeleton**



# Supporting Information: Bottom-up Assembly of Synthetic Cells with a DNA Cytoskeleton

Kevin Jahnke<sup>1,2</sup>, Vanessa Huth<sup>1,2</sup>, Ulrike Mersdorf<sup>3</sup>,

Na Liu<sup>4,5</sup>, Kerstin Göpfrich<sup>1,2\*</sup>

<sup>1</sup>Biophysical Engineering Group, Max Planck Institute for Medical Research,  
Jahnstraße 29, D-69120 Heidelberg, Germany,

<sup>2</sup>Department of Physics and Astronomy, Heidelberg University,  
D-69120 Heidelberg, Germany

<sup>3</sup>Department of Biomolecular Mechanisms, Max Planck Institute for Medical Research,  
Jahnstraße 29, D-69120 Heidelberg, Germany,

<sup>4</sup> 2nd Physics Institute, University of Stuttgart,  
Im Pfaffenwaldring 57, D-70569 Stuttgart, Germany

<sup>5</sup> Max Planck Institute for Solid State Research,  
Heisenbergstraße 1, D-70569 Stuttgart, Germany

\*

E-mail: kerstin.goepfrich@mr.mpg.de

# Contents

<b>Supporting Figures</b>	<b>5</b>
Supporting Figure 1: Cryo electron micrographs of st, tt and st-azo DNA filaments	5
Supporting Figure 2: Single-tile DNA filament diameter from cryo electron micrographs . . . . .	6
Supporting Figure 3: Examples and overview of polymerized single-tile DNA filaments within GUVs . . . . .	7
Supporting Figure 4: Single-tile DNA filaments inside water-in-oil droplets before the release of free-standing GUVs . . . . .	8
Supporting Figure 5: DNA filaments with orthogonal two-tile design polymerize within GUVs . . . . .	9
Supporting Figure 6: DNA filament assembly inside GUVs over time . . . . .	10
Supporting Figure 7: tt DNA filament clustering due to the presence of $Mg^{2+}$ . .	11
Supporting Figure 8: Schematic representation of the st overhang modified with azobenzene (st-azo) . . . . .	12
Supporting Figure 9: Azobenzene-modified DNA filaments disassemble within GUVs after UV illumination . . . . .	13
Supporting Figure 10: UV illumination does not affect unmodified DNA filaments inside GUVs . . . . .	14
Supporting Figure 11: Unmodified st DNA filaments do not disassemble during UV illumination. . . . .	15
Supporting Figure 12: Analysis of the reversible assembly of azobenzene-modified DNA filaments within GUVs . . . . .	16
Supporting Figure 13: Azobenzene-modified DNA filaments assemble reversibly within GUVs . . . . .	17
Supporting Figure 14: Dextran induces bundling of st DNA filaments in bulk and in GUVs . . . . .	18

Supporting Figure 15: Methylcellulose induces bundling of st DNA filaments in bulk	19
Supporting Figure 16: Persistence length analysis	20
Supporting Figure 17: Cryo electron micrographs of st DNA bundles formed by addition of dextran	21
Supporting Figure 18: TEM images of st DNA bundles formed by addition of methylcellulose	22
Supporting Figure 19: st DNA bundles formed by addition of methylcellulose cannot be reconstituted into GUVs	23
Supporting Figure 20: Confocal overlay of bundled st DNA filaments form ring-like structures inside GUVs	24
Supporting Figure 21: Bundled st DNA filaments form ring-like structures inside GUVs	25
Supporting Figure 22: Disassembly of bundled st-azo DNA filaments inside GUVs	26
Supporting Figure 23: GUV formation efficiency increases in presence of cholesterol-tagged DNA filaments	27
Supporting Figure 24: DNA filaments are recruited to the inner membrane of GUVs in the presence of cholesterol-tagged DNA	28
Supporting Figure 25: Membrane-bound DNA filaments suppress membrane fluctuations	29
<b>Supporting Tables</b>	<b>30</b>
Supporting Table 1: DNA sequences for st DNA filaments	30
Supporting Table 2: DNA sequences for two-tile DNA filaments	30
Supporting Table 3: DNA sequences for modified DNA filaments	31
<b>Supporting Movies</b>	<b>32</b>
Supporting Movie 1: Dynamics of st DNA filaments inside GUVs	32

Supporting Movie 2: Bundling of st DNA filaments with polyethylene glycol as molecular crowder . . . . .	32
Supporting Movie 3: DNA cortex formation via bundling agents . . . . .	32
Supporting Movie 4: st-chol DNA filaments diffuse on SLBs . . . . .	32
Supporting Movie 5: DNA cortex formation induced by cholesterol-tagged DNA- mediated linking . . . . .	33
Supporting Movie 6: GUVs are deformed by st-chol DNA filaments . . . . .	33
Supporting Movie 7: Deflated GUV in presence of st DNA filaments . . . . .	33
<b>References</b>	<b>34</b>

## Supporting Figures

### Supporting Figure 1: Cryo electron micrographs of st, tt and st-azo DNA filaments

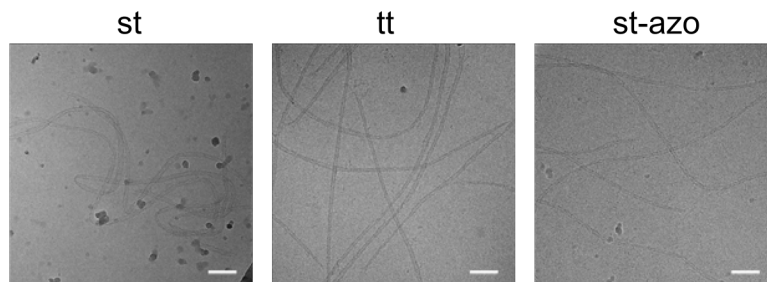


Figure 1: Cryo electron micrographs of st, tt and st-azo DNA filaments verifying the correct assembly of the respective DNA tiles into micrometer long filaments. Scale bars: 100 nm.

## Supporting Figure 2: Single-tile DNA filament diameter from cryo electron micrographs

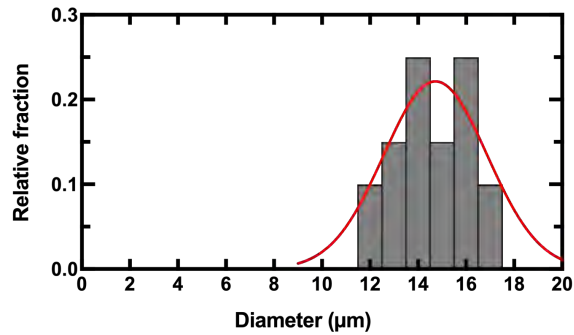


Figure 2: Distribution of single-tile (st) DNA filament diameters as determined from cryo electron micrographs ( $n = 20$ ). Filament diameters were measured with the line profile tool in ImageJ. A Gaussian fit reveals a diameter of  $14.5 \pm 1.8$  nm, consistent with the assembly of filaments consisting of 12-14 DNA duplexes.

**Supporting Figure 3: Examples and overview of polymerized single-tile DNA filaments within GUVs**

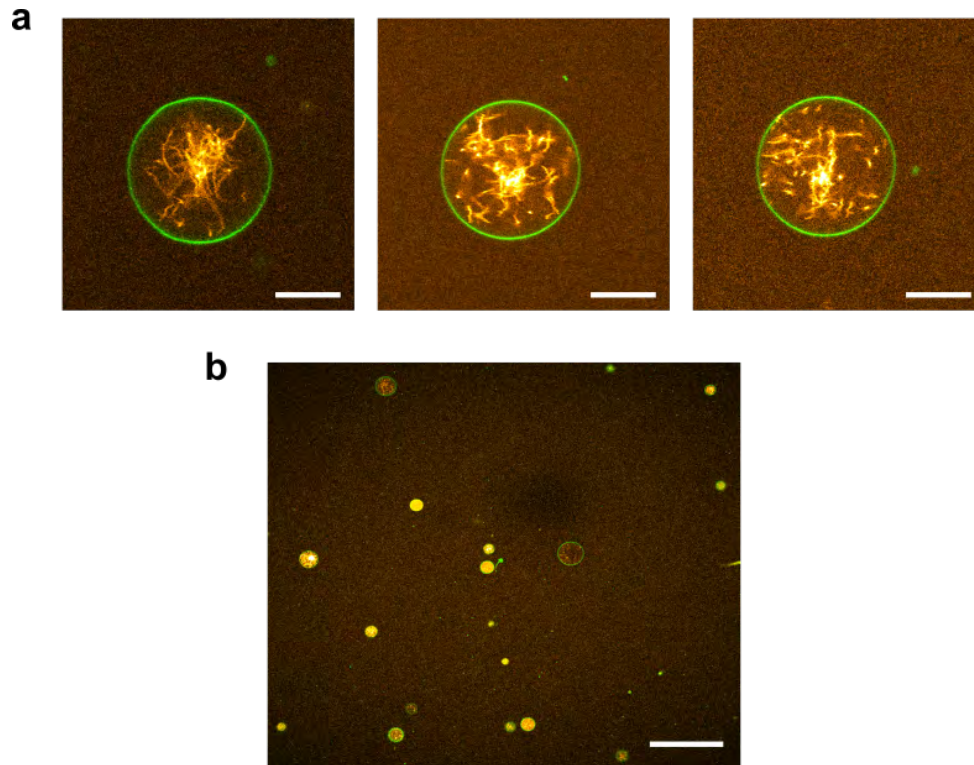


Figure 3: **a** Examples of polymerized single-tile (st) DNA filaments with within GUVs. Confocal fluorescence images of GUVs (green,  $\lambda_{ex} = 488$  nm) containing 500 nM st DNA filaments after GUV formation (orange,  $\lambda_{ex} = 561$  nm, see Supporting Table 1). Scale bars: 10  $\mu\text{m}$ . **b** Overview confocal image of successful encapsulation of st DNA filaments into GUVs at high yield. GUVs (green,  $\lambda_{ex} = 488$  nm) contain 500 nM st DNA filaments (orange,  $\lambda_{ex} = 561$  nm). Scale bar: 100  $\mu\text{m}$ .

## Supporting Figure 4: Single-tile DNA filaments inside water-in-oil droplets before the release of free-standing GUVs

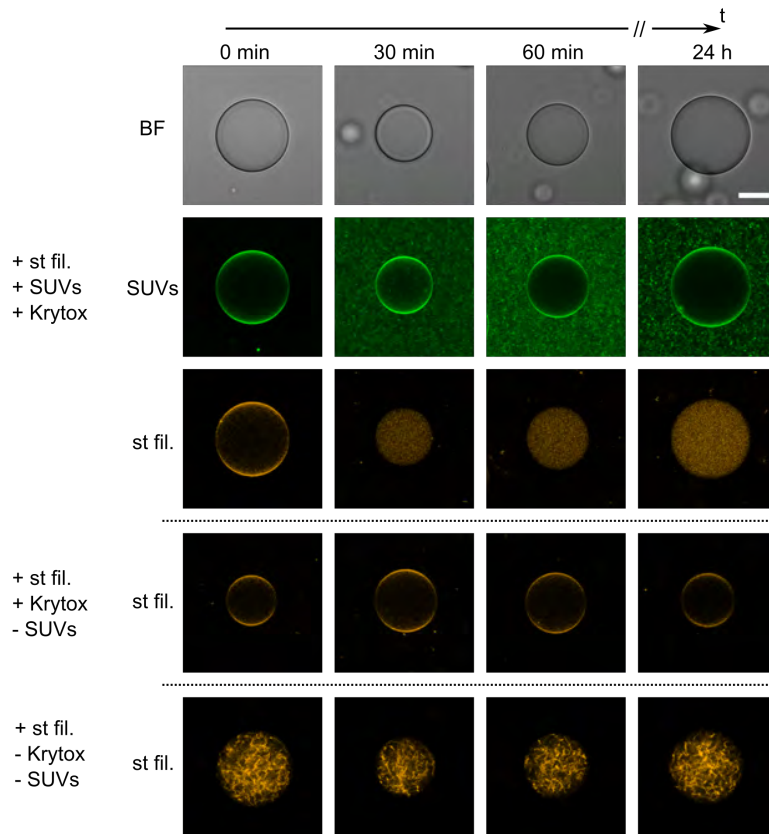


Figure 4: Confocal images of 500 nM st DNA filaments (orange, labelled with Cy3,  $\lambda_{ex} = 561$  nm) within surfactant-stabilized water-in-oil droplets over time in presence of 1.25 mM lipids in the form of SUVs (green, 69% DOPC, 30% DOPG, 1% Atto488-DOPE,  $\lambda_{ex} = 488$  nm) and 10.5 mM Krytox (top three rows), 10.5 mM Krytox (4th row) or in the absence of Krytox (bottom row). After the formation of a supported lipid bilayer at the droplet periphery, access SUVs are dragged out of the aqueous phase inside the droplet into the oil phase.<sup>[1]</sup> st DNA filaments are disassembled and initially localized at the droplet periphery but homogeneously distributed inside the droplet lumen after 30 min i.e. once excess SUVs have been dragged out of the droplet-stabilized GUV. This suggests that st DNA tiles interact with the negatively charged Krytox at the droplet periphery. They are then displaced from the droplet periphery once the SUVs fused and created a droplet-stabilized GUV. This is also confirmed by the fact that the st DNA tiles remain at the droplet periphery in the absence of SUVs (4th row). The fact that the DNA filaments do not reassemble suggests that the presence of Krytox in the oil phase can lead to significant changes of the chemical environment inside water-in-oil droplets by possibly reducing the pH (Krytox has a carboxylic acid head group) or extracting ions by micellar exclusion. Scale bar: 10  $\mu$ m.



**Supporting Figure 5: DNA filaments with orthogonal two-tile design polymerize within GUVs**

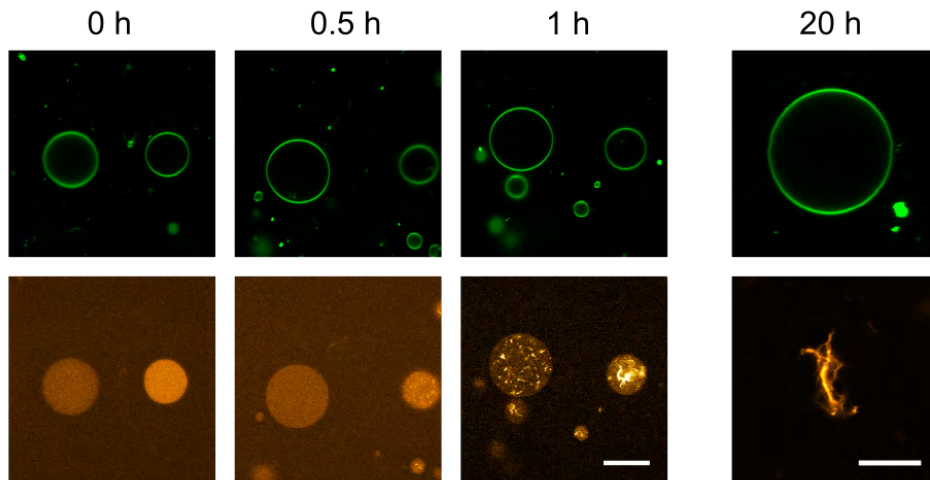


Figure 5: DNA filaments with orthogonal two-tile (tt) design polymerize within GUVs. Confocal fluorescence images of GUVs ( $\lambda_{ex} = 488$  nm, green) containing 250 nM RE and SE tiles ( $\lambda_{ex} = 561$  nm, orange, see Supporting Table 2). DNA filaments assemble within 20 h after GUV formation. Scale bars: 20  $\mu\text{m}$  and 10  $\mu\text{m}$ , respectively.

Supporting Figure 6: DNA filament assembly inside GUVs over time

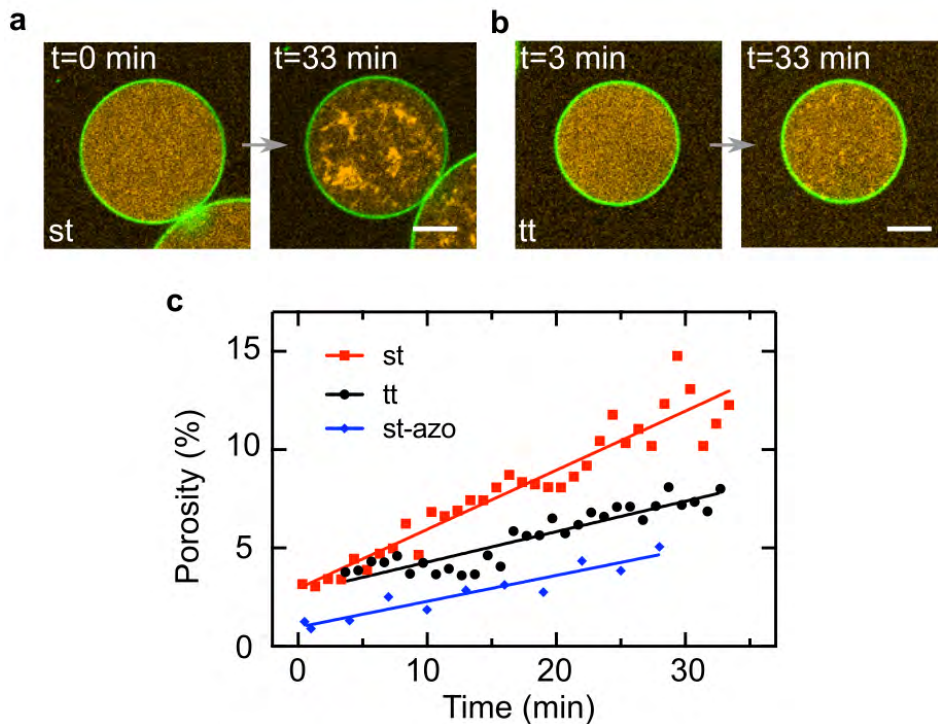


Figure 6: DNA filament assembly inside GUVs over time for st, tt and st-azo DNA filaments. **a** st DNA filaments (orange,  $\lambda_{ex} = 561$  nm) assemble within 30 min inside GUVs (green,  $\lambda_{ex} = 488$  nm) after the GUV formation process. Scale bar: 10  $\mu\text{m}$ . Note that they are in a disassembled state prior to the GUV release from the water-in-oil droplets due to the presence of Krytox. **b** tt DNA filaments (orange,  $\lambda_{ex} = 561$  nm) do not fully assemble within 30 min inside GUVs (green,  $\lambda_{ex} = 488$  nm). Their assembly takes about 2-3 h. Scale bar: 10  $\mu\text{m}$ . **c** Porosity over time for the assembly processes of st (red), tt (black) and st-azo (blue) DNA filaments inside GUVs. The data was fitted with a linear fit revealing slopes of  $0.30 \pm 0.02$   $\% \text{ min}^{-1}$  (st),  $0.15 \pm 0.01$   $\% \text{ min}^{-1}$  (tt) and  $0.13 \pm 0.01$   $\% \text{ min}^{-1}$  (st-azo). This indicates an at least two-fold faster assembly for st DNA filaments compared to tt and st-azo DNA filaments due to the necessity of two tiles or azobenzene cis-trans isomerization for filament assembly.

Supporting Figure 7: tt DNA filament clustering due to the presence of  $\text{Mg}^{2+}$

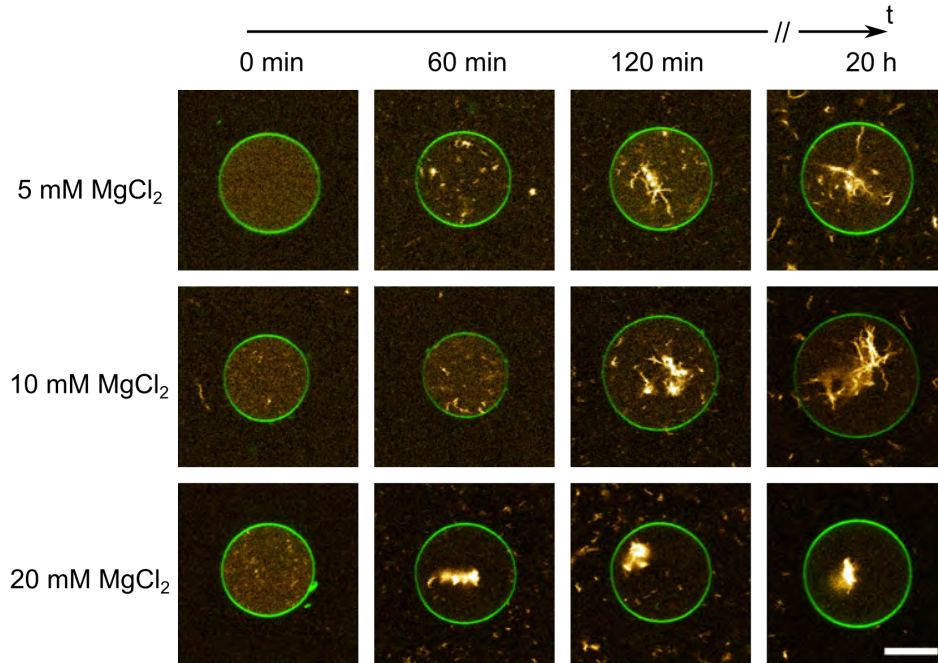


Figure 7: Confocal overlay images of 500 nM tt DNA filaments (orange, labelled with Cy3,  $\lambda_{ex} = 561$  nm) encapsulated into GUVs (green, 69% DOPC, 30% DOPG, 1% Atto488-DOPE,  $\lambda_{ex} = 488$  nm) in presence of 5 mM, 10 mM or 20 mM  $\text{MgCl}_2$  at different time points. tt DNA filaments have slower polymerization kinetics compared to st DNA filaments. DNA filaments cluster over time with increasing  $\text{Mg}^{2+}$  concentrations. At 20 mM  $\text{Mg}^{2+}$ , the filaments form a clump within the droplet lumen. Note that we used 10 mM  $\text{Mg}^{2+}$  for almost all experiments in the manuscript due to the enhanced GU formation compared to 5 mM  $\text{Mg}^{2+}$  (SUVs require  $\text{Mg}^{2+}$  to fuse to the droplet periphery <sup>[1]</sup>). Scale bar: 10  $\mu\text{m}$ .

**Supporting Figure 8: Schematic representation of the st overhang modified with azobenzene (st-azo)**

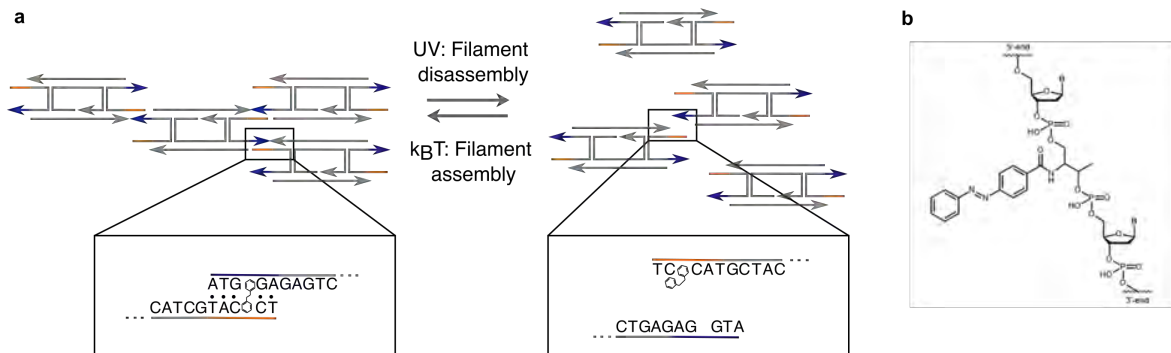


Figure 8: Schematic representation of the st overhang modified with azobenzene (st-azo) for reversible cytoskeleton assembly with UV light. **a** DNA filaments disassemble due to trans-cis isomerization induced via UV illumination and reassemble due to thermal cis-trans isomerization. **b** Chemical structure of the conjugation of azobenzene in between two bases at the DNA tile overhang.

**Supporting Figure 9: Azobenzene-modified DNA filaments disassemble within GUVs after UV illumination**

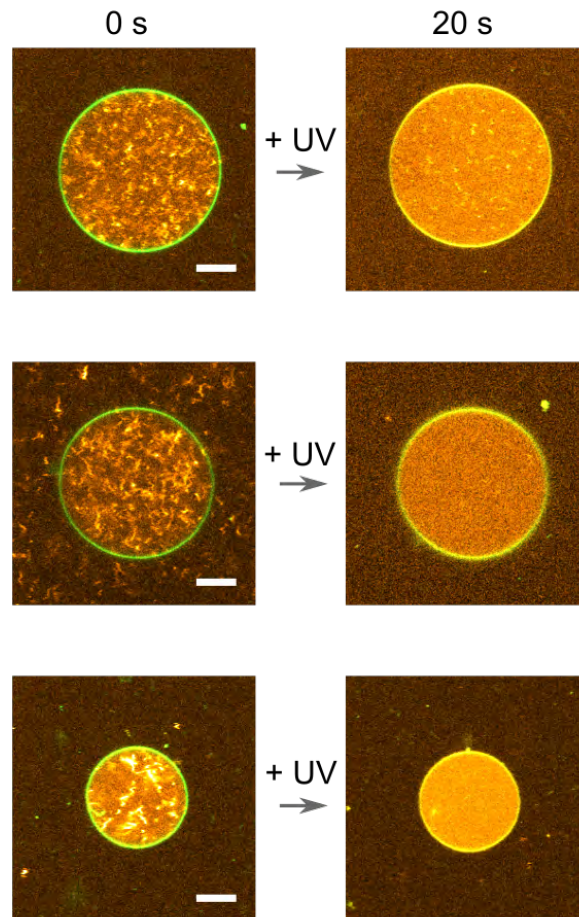


Figure 9: Azobenzene-modified DNA filaments (st-azo) disassemble within GUVs after 20 s of illumination with the UV laser of a confocal microscope. Confocal fluorescence images of GUVs (green,  $\lambda_{ex}$  =488 nm) containing 500 nM st-azo DNA filaments (orange,  $\lambda_{ex}$  =561 nm, for DNA sequences see Supporting Table 3). Confocal images are taken directly before (left column) and directly after the 20 s of UV illumination. Scale bar: 10  $\mu$ m.

## Supporting Figure 10: UV illumination does not affect unmodified DNA filaments inside GUVs

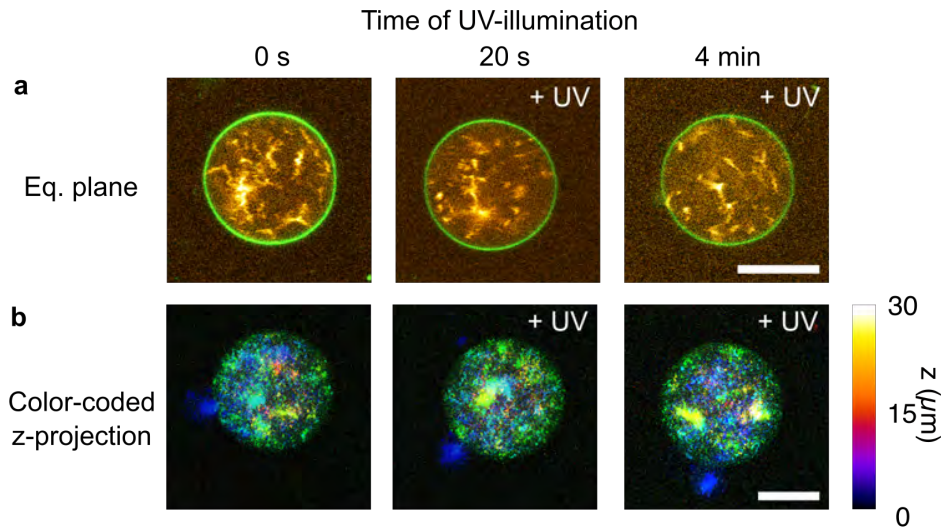


Figure 10: st filament disassembly upon UV-illumination is not observed in the absence of the azobenzene modification. Hence, UV illumination does not destroy st DNA filaments inside GUVs. Confocal images at different time points during UV-illumination show GUVs (green,  $\lambda_{ex} = 488$  nm) in the equatorial plane (**a**) or as color-coded z-projection (**b**). GUVs contain 500 nM unmodified st DNA filaments (orange,  $\lambda_{ex} = 561$  nm) during illumination with UV light for up to 4 min. Scale bar: 10  $\mu$ m. While some bleaching is observed, the filaments do not disassemble without the azobenzene modification.

Supporting Figure 11: Unmodified st DNA filaments do not disassemble during UV illumination.

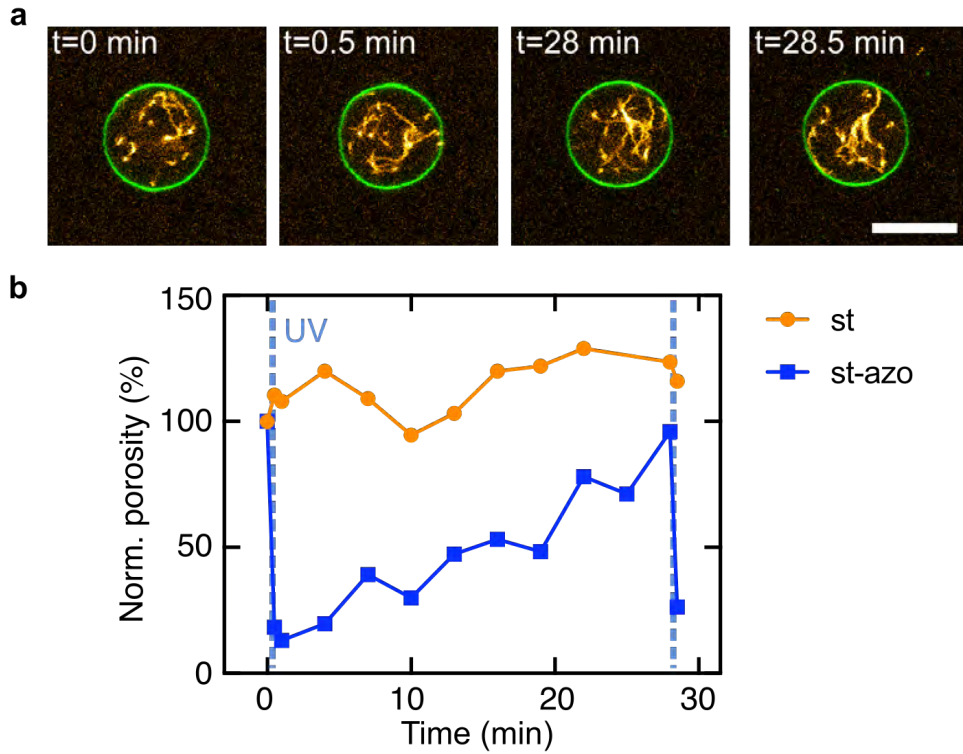


Figure 11: Unmodified st DNA filaments do not disassemble during UV illumination. **a** Confocal images of 500 nM st DNA filaments (orange, labelled with Cy3,  $\lambda_{ex} = 561$  nm) encapsulated within GUVs (green, 69% DOPC, 30% DOPG, 1% Atto488-DOPE,  $\lambda_{ex} = 488$  nm) before and after UV illumination. The GUV was illuminated with UV light for 20 s at 0 min and 28 min. Scale bar: 10  $\mu$ m. **b** Normalized porosity over time of st and st-azo DNA filaments within GUVs. We do not detect any significant decrease in the porosity, i.e. filament disassembly, of st DNA filaments over time.

## Supporting Figure 12: Analysis of the reversible assembly of azobenzene-modified DNA filaments within GUVs

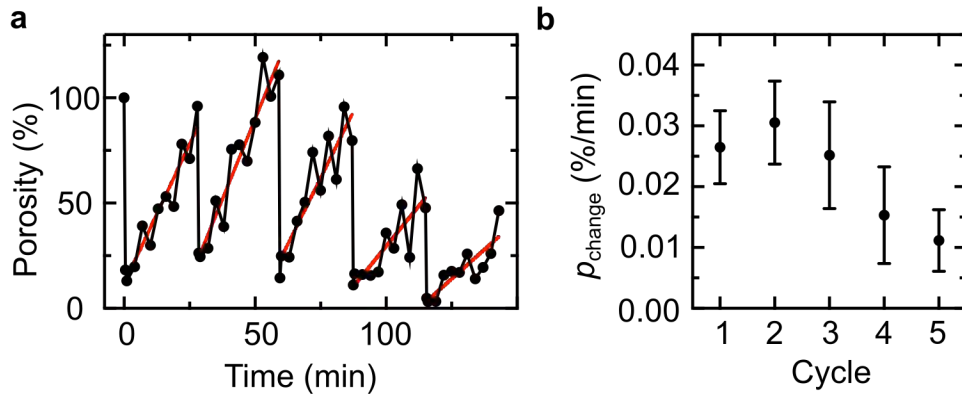


Figure 12: Analysis of the reversible assembly of azobenzene-modified DNA filaments (st-azo) within GUVs. **a** Porosity of DNA filament fluorescence, corresponding to the degree of filament polymerization, over time inside a GUV. Each reassembly process after UV illumination for 15 s was fitted (red lines) with a linear fit of the form  $y = p_{\text{change}}x + b$ . **b** Average slope of the linear fit  $p_{\text{change}}$  during each disassembly-reassembly cycle reveals the reversible assembly of DNA filaments with no fatigue for the first three cycles with an average porosity change of  $p_{\text{change}} = 0.027 \pm 0.003 \text{ \% min}^{-1}$ . The decrease of the porosity change in subsequent cycles can likely be attributed to a combination of photobleaching, UV damage and trapped states of the isomerization process.



**Supporting Figure 13: Azobenzene-modified DNA filaments assemble reversibly within GUVs**

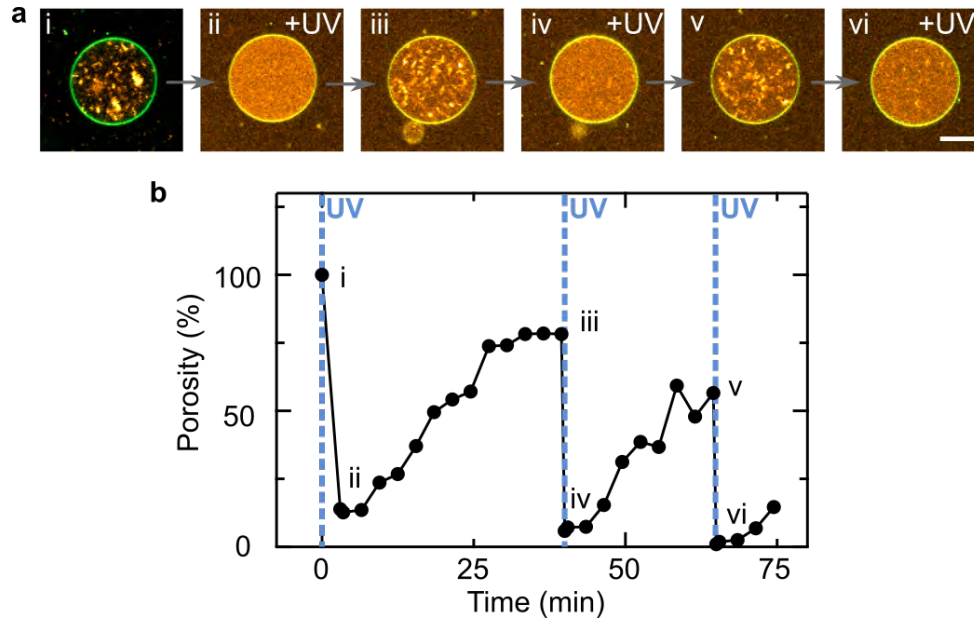


Figure 13: Azobenzene-modified (st-azo) DNA filaments assemble reversibly within GUVs. **a** Confocal fluorescence images of a GUV (green,  $\lambda_{ex} = 488$  nm) containing 500 nM st-azo DNA filaments (orange,  $\lambda_{ex} = 561$  nm, for DNA sequences see Supporting Table 3). DNA filament disassembly can be induced reversibly by UV illumination. Note that during the first illumination cycle the UV exposure was 3 min and 15 s for the others. **b** Porosity over time for the GUV shown in **a**. DNA filaments reassemble over the course of 30 min. Time points of UV illumination are indicated. Scale bar: 10  $\mu$ m.

**Supporting Figure 14: Dextran induces bundling of st DNA filaments in bulk and in GUVs**

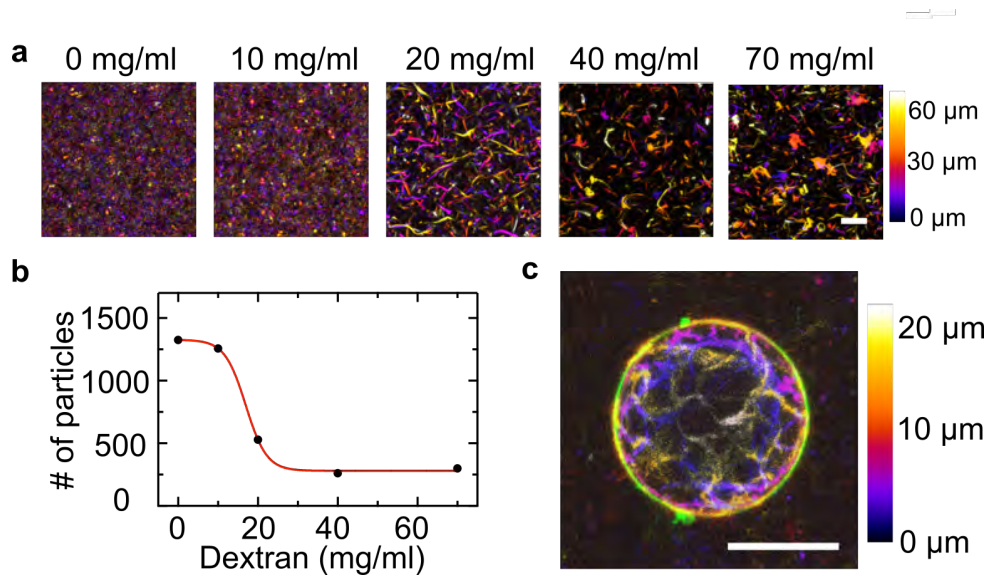


Figure 14: Dextran induces bundling of st DNA filaments in bulk and in GUVs. **a** Color-coded z-projections of st DNA filaments ( $\lambda_{ex}=561$  nm) with varied amounts of 35 kDa dextran as indicated. Scale bar: 50  $\mu$ m. **b** Number of detected filaments per image for varying dextran concentrations. The number of detected filaments corresponds to the degree of bundling as bundles are comprised of multiple st DNA filaments. **c** Overlay of the equatorial plane of a GUV (488 nm) and a color-coded z-projection of 500 nM st DNA filaments in presence of 20 mg/ml 35 kDa dextran. Scale bar: 10  $\mu$ m.

## Supporting Figure 15: Methylcellulose induces bundling of st DNA filaments in bulk

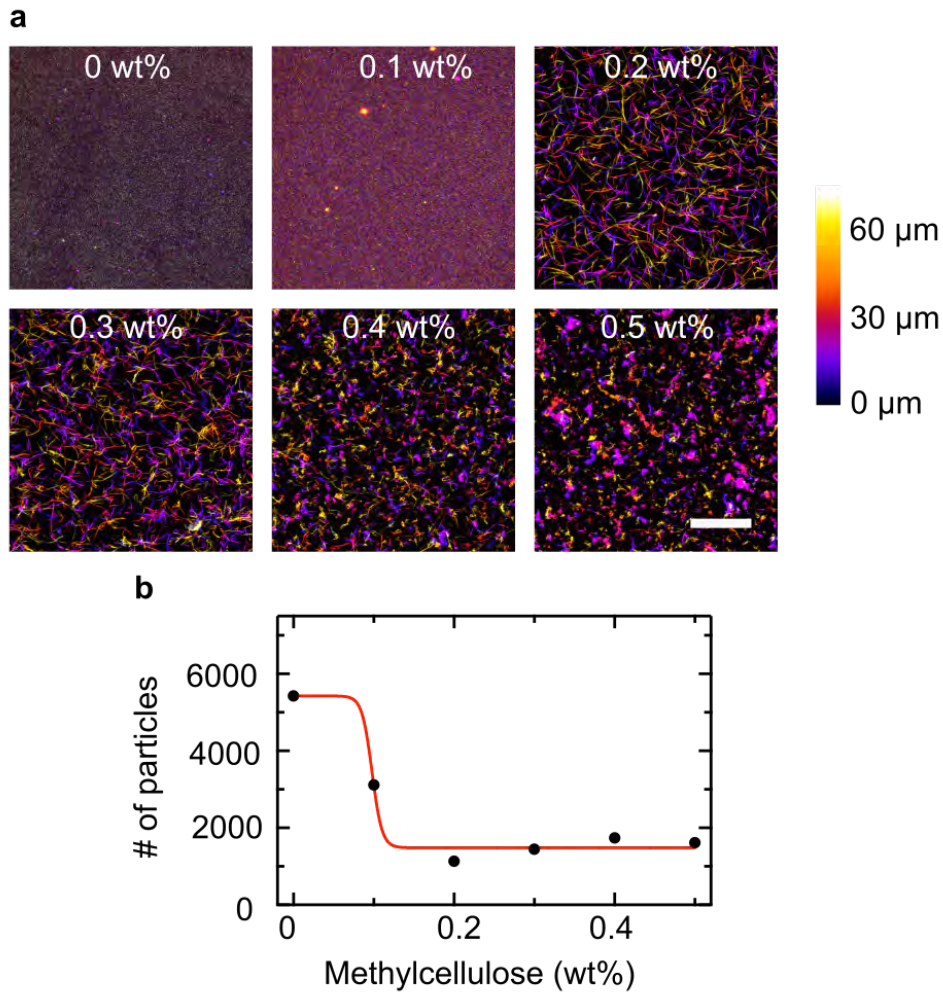


Figure 15: Methylcellulose (MC) induces bundling of st DNA filaments in bulk. **a** Colour-coded z-projections of st DNA filaments ( $\lambda_{ex}=561$  nm) with varied amounts of MC as indicated. Scale bar:  $50\ \mu\text{m}$ . **b** Number of detected particles per image for different MC concentrations. The number of detected particles corresponds to the degree of bundling as bundles are comprised of multiple st DNA filaments. The number of particles was analyzed from confocal images using the Analyze Particle function in ImageJ.

## Supporting Figure 16: Persistence length analysis

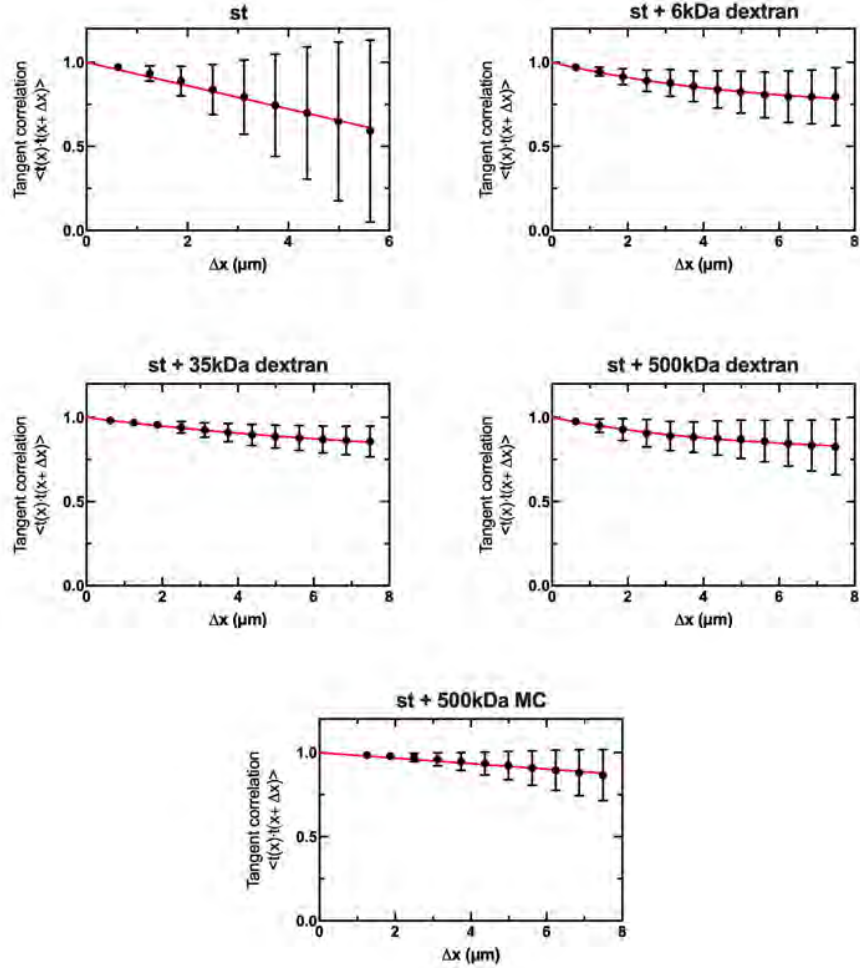


Figure 16: Persistence length analysis. Tangent correlation  $\langle \hat{t}(x) \cdot \hat{t}(x + \Delta x) \rangle$  over the distance  $\Delta x$  between the tangents from all considered filaments for the conditions st ( $n = 15$ ,  $l_p = 6.46 \pm 0.26 \mu\text{m}$ ), st + 6kDa dextran ( $n = 15$ ,  $l_p = 12.81 \pm 0.53 \mu\text{m}$ ), st + 35 kDa dextran ( $n = 11$ ,  $l_p = 21.73 \pm 0.59 \mu\text{m}$ ), st + 500 kDa dextran ( $n = 13$ ,  $l_p = 17.09 \pm 0.86 \mu\text{m}$ ) and st + 500 kDa methylcellulose ( $n = 13$ ,  $l_p = 26.75 \pm 0.80 \mu\text{m}$ ). The tangent correlation increases in presence of the molecular crowders.

**Supporting Figure 17: Cryo electron micrographs of st DNA bundles formed by addition of dextran**

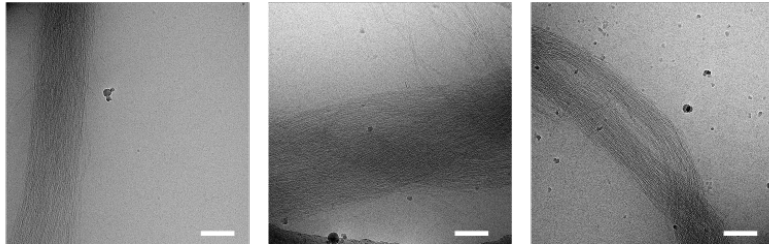


Figure 17: Cryo electron micrographs of st DNA bundles formed by addition of dextran to st DNA filaments. Scale bars: 200 nm.

**Supporting Figure 18: TEM images of st DNA bundles formed by addition of methylcellulose**

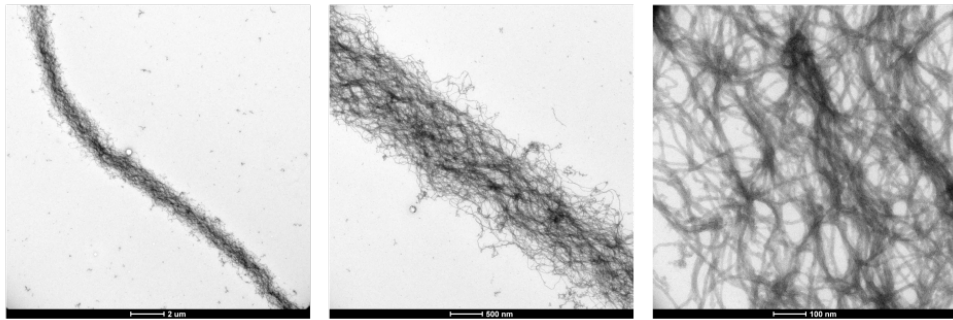


Figure 18: Transmission electron microscopy (TEM) images of DNA bundles formed by addition of methylcellulose (MC, 0.4wt%) to st DNA filaments. 500 nM DNA filaments form long and thick bundles because MC acts as a crowding agent. Scale bars (from left to right): 4 μm, 1 μm and 200 nm.

**Supporting Figure 19: st DNA bundles formed by addition of methylcellulose cannot be reconstituted into GUVs**

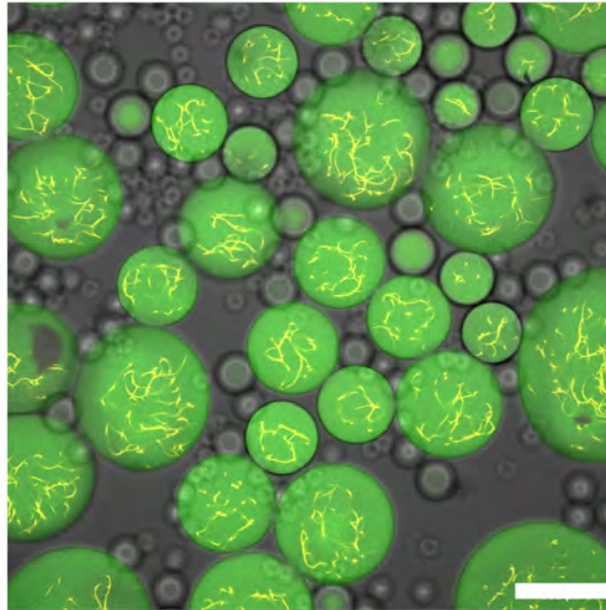


Figure 19: DNA bundles formed from st filaments by addition of methylcellulose (MC) cannot be reconstituted into GUVs using the droplet-stabilized GUV formation method.<sup>[2]</sup> Confocal image of st DNA bundles ( $\lambda_{ex} = 561$  nm inside water-in-oil droplets in presence of negatively charged fluorosurfactant Krytox and small unilamellar vesicles (SUVs,  $\lambda_{ex} = 488$  nm). Even after up to three days, SUVs do not fuse with the droplet periphery likely due to the high viscosity of the MC-containing solution. Therefore, GUVs containing MC cannot be formed with the droplet-stabilized method. We thus used dextran as an alternative crowding agent. Scale bar: 100  $\mu$ m.

**Supporting Figure 20: Confocal overlay of bundled st DNA filaments form ring-like structures inside GUVs**

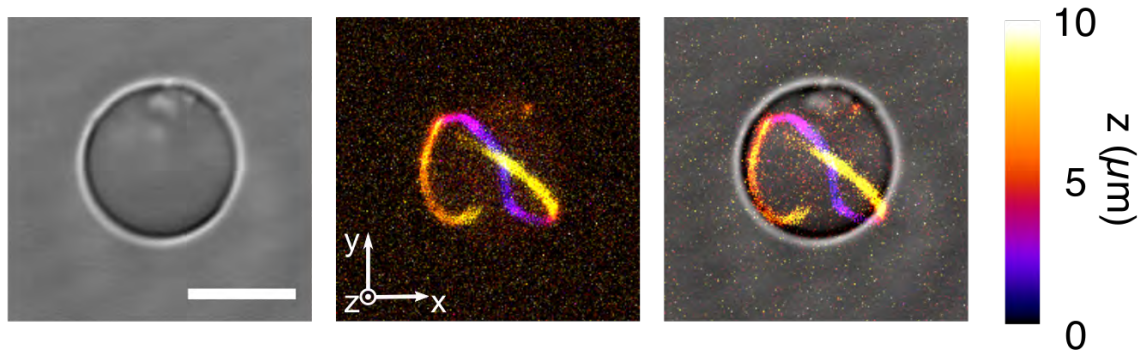


Figure 20: Color-coded confocal z-projection and corresponding brightfield image of 50 nM st filaments in presence of 20 mg/ml 35 kDa dextran inside a GUV. Scale bar: 5  $\mu\text{m}$ .



**Supporting Figure 21: Bundled st DNA filaments form ring-like structures inside GUVs**

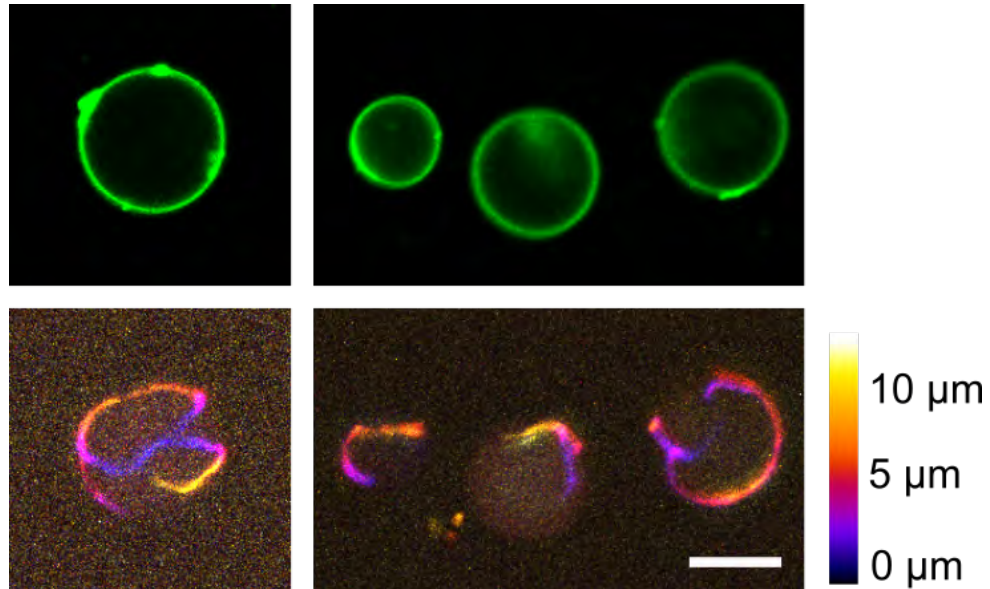


Figure 21: Bundled DNA filaments form ring-like structures inside GUVs. Exemplary confocal fluorescence images of GUVs (green, top row,  $\lambda_{ex}=488$  nm) containing 200 nM DNA filaments and 30 mg/ml dextran as a bundling agent. DNA bundles ( $\lambda_{ex}=561$  nm) are shown as colour-coded z-projections. After the formation of GUVs, the DNA filaments were re-annealed in the thermocycler. Scale bar: 10  $\mu$ m.

Supporting Figure 22: Disassembly of bundled *st*-azo DNA filaments inside GUVs

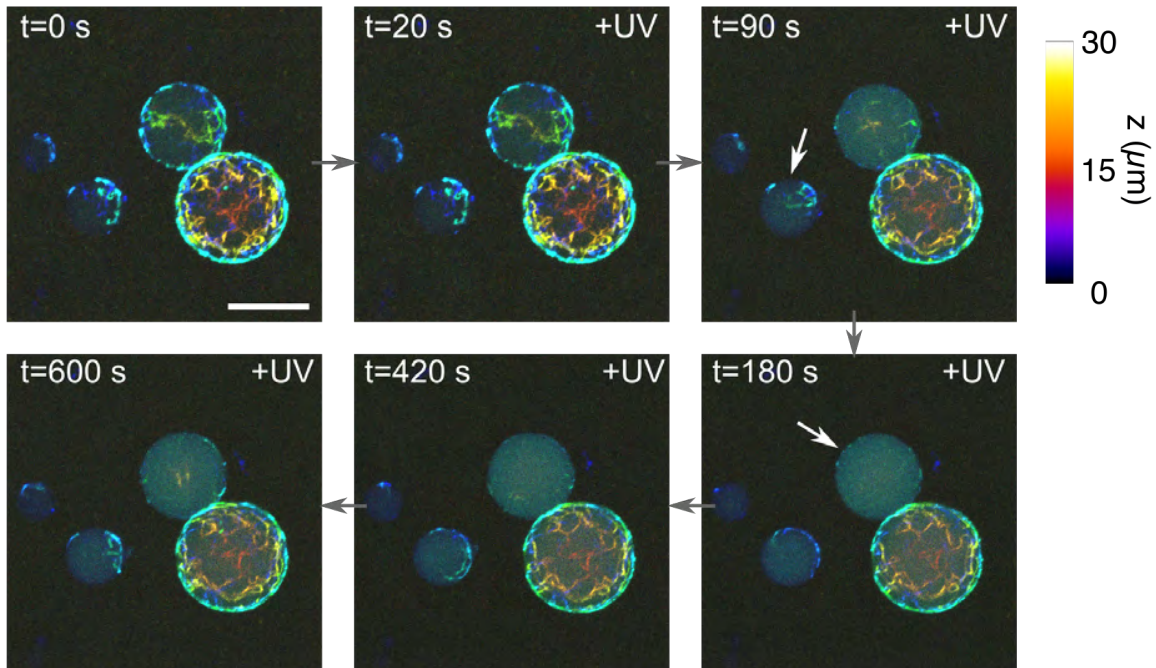


Figure 22: Color-coded z-projections of 500 nM *st*-azo DNA bundles (labelled with Cy3,  $\lambda_{ex} = 561$  nm) within GUVs during continuous UV illumination over time. DNA bundles also form for *st*-azo DNA filaments. Filament disassembly requires longer illumination times than in absence of the molecular crowder (180 s vs. 20 s). Filament disassembly of bundled filaments only worked in smaller GUVs (indicated by a white arrow). This is likely due to the fact that DNA bundles in smaller GUVs consist of less DNA filaments due to their limited availability. Scale bar: 20  $\mu\text{m}$ .

**Supporting Figure 23: GUV formation efficiency increases in presence of cholesterol-tagged DNA filaments**

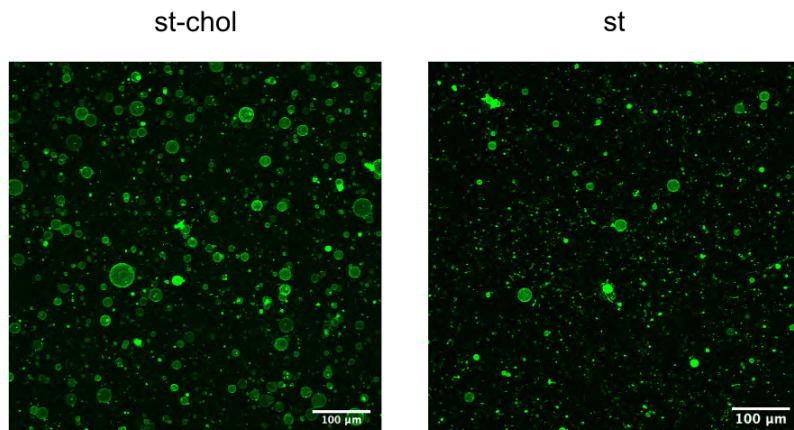


Figure 23: GUV formation efficiency increases in presence of membrane-bound st-chol DNA filaments. Confocal fluorescence z-projection of GUVs ( $\lambda_{ex}=488$  nm) containing  $1 \mu\text{M}$  st-chol or  $500 \text{ nM}$  st DNA filaments and  $1 \mu\text{M}$  of cholesterol-tagged DNA. Each individual tile of the DNA filaments contains a complementary overhang for the cholesterol-tagged DNA (for DNA sequences see Supporting Table 3). The release efficiency increases more than five-fold from  $\approx 1500$  GUVs/ $\mu\text{L}$  for st filaments to  $\approx 8000$  GUVs/ $\mu\text{L}$  for st-chol filaments. Scale bar:  $100 \mu\text{m}$ .

**Supporting Figure 24: DNA filaments are recruited to the inner membrane of GUVs in the presence of cholesterol-tagged DNA**

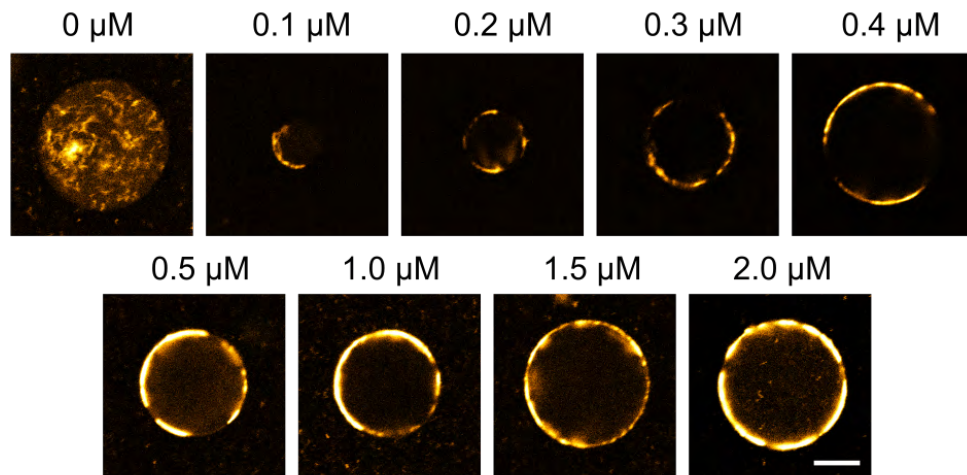


Figure 24: st DNA filaments are recruited to the inner membrane of GUVs in the presence of a cholesterol-tagged DNA which is complementary to a single-stranded overhang positioned on each individual st. Confocal fluorescence images of GUVs containing 500 nM st-chol DNA filaments (orange,  $\lambda_{ex} = 561$  nm) and varied amounts of cholesterol-tagged DNA. For DNA sequences see Supporting Table 3. Scale bar: 10  $\mu\text{m}$ .

**Supporting Figure 25: Membrane-bound DNA filaments suppress membrane fluctuations**

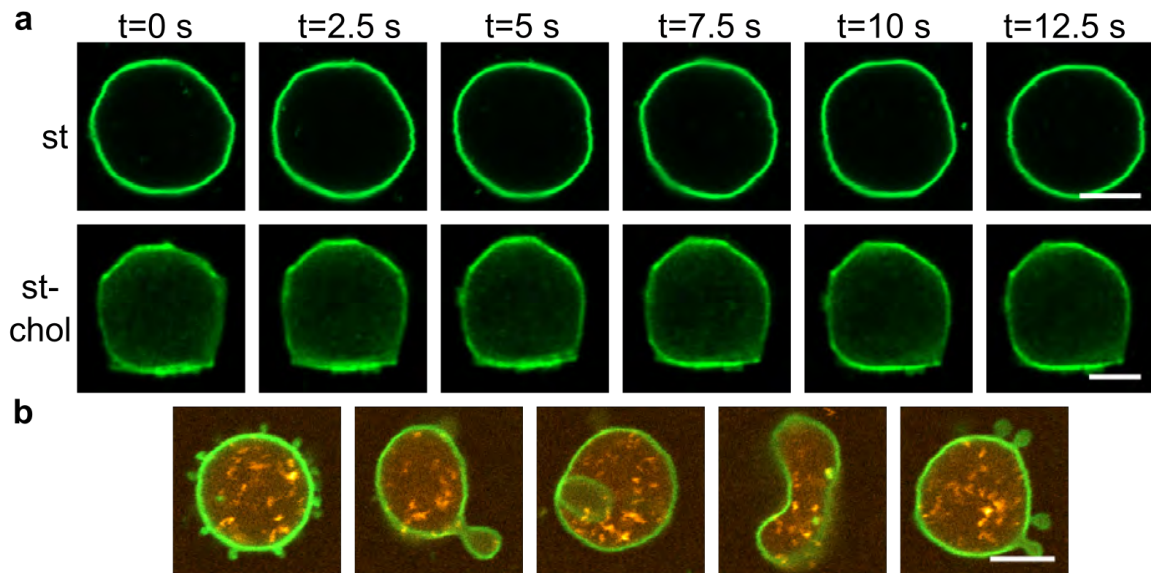


Figure 25: Membrane-bound DNA filaments suppress membrane fluctuations. **a** Confocal time series of deflated GUVs (green, 69% DOPC, 30% DOPG, 1% Atto488-DOPE,  $\lambda_{ex} = 488$  nm,  $c_{out}/c_{in} = 600$  mOsm/300 mOsm = 2) containing normal st or membrane-bound st-chol DNA filaments (orange, labelled with Cy3,  $\lambda_{ex} = 561$  nm) over time. Scale bar: 10  $\mu$ m and 5  $\mu$ m, respectively. See Videos 6 and 7 for the entire time series. **b** Deflated st DNA filament-containing GUVs fluctuate and undergo shape transformations. Such dynamics cannot be observed for membrane-bound st-chol DNA filaments. Scale bar: 10  $\mu$ m.

## Supporting Tables

### Supporting Table 1: DNA sequences for st DNA filaments

Table 1: DNA sequences from 5' to 3' for st DNA filaments, adapted from.<sup>[3]</sup>

Name	DNA sequence
S1	CTCAGTGGACAGCCGTTCTGGAGCGTTGGACGAAACT
S2	(Atto488-)TGGTATTGTCTGGTAGAGCACCCTGAGAGGTA
S3	CCAGAACGGCTGTGGCTAAACAGTAACCGAAGCA- CCAACGCTGGTAAGTCTCCTTCTTATCT(-Cy3/Atto633)
S4	CAGACAGTTTCGTGGTCATCGTACCT
S5	CGATGACCTGCTTCGGTACTGTTTAGCCTGCTCTAC

### Supporting Table 2: DNA sequences for two-tile DNA filaments

Table 2: DNA sequences from 5' to 3' for two-tile DNA filaments.

Name	DNA sequence
RE1	CGTATTGGACATTTCCGTAGACCGACTGGACATCTTC
RE2	TCTACGGAAATGTGGCAGAATCAATCATAAGACACCAGTCGG
RE3	CCTCACCTTCACACCAATACGAGGTA
RE4	CAGACGAAGATGTGGTAGTGGAATGC
RE5	CCACTACCTGTCTTATGATTGATTCTGCCTGTGAAGG
SE1	CTCAGTGGACAGCCGTTCTGGAGCGTTGGACGAAACT
SE2	GTCTGGTAGAGCACCCTGAGGCATT
S3	CCAGAACGGCTGTGGCTAAACAGTAACCGAAGCA- CCAACGCTGGTAAGTCTCCTTCTTATCT(-Cy3)
SE4	TGAGGAGTTTCGTGGTCATCGTACCT
SE5	CGATGACCTGCTTCGGTACTGTTTAGCCTGCTCTAC

### Supporting Table 3: DNA sequences for modified DNA filaments

Table 3: DNA sequences from 5' to 3' for modified DNA filaments. The symbol X represents the positioning of an azobenzene modification.

Name	DNA sequence
Invader	ACCAGACAATACCAATCCGC
S4-Azo	CAXGACAGTTTCGTGGTCATCGTACXCT
Chol-link	Chol-TTTAGATAAGAAGGAGACTTACC

## Supporting Movies

### **Supporting Movie 1: Dynamics of st DNA filaments inside GUVs**

Confocal fluorescence time series of 500 nM st DNA filaments (orange,  $\lambda_{ex}=561$  nm) within GUVs (green,  $\lambda_{ex}=488$  nm). DNA filaments are stably encapsulated and dynamic inside the GUV lumen. Scale bar: 10  $\mu\text{m}$ .

### **Supporting Movie 2: Bundling of st DNA filaments with polyethylene glycol as molecular crowder**

Confocal fluorescence time series of 500 nM st DNA filaments ( $\lambda_{ex}=561$  nm) in presence of 5 wt% polyethyleneglycol (8000 Da, PEG-8k). DNA filaments condense into bundles within minutes due to molecular crowding induced by PEG-8k. Scale bar: 50  $\mu\text{m}$ .

### **Supporting Movie 3: DNA cortex formation via bundling agents**

Confocal fluorescence z-stack of 500 nM st DNA filaments ( $\lambda_{ex}=561$  nm) in presence of 35 kDa dextran within a GUV. DNA filaments bundle and condense at the GUV periphery. Scale bar: 10  $\mu\text{m}$ .

### **Supporting Movie 4: st-chol DNA filaments diffuse on SLBs**

Confocal fluorescence time series of 5 nM st-chol DNA filaments ( $\lambda_{ex}=561$  nm) on a supported lipid bilayer (SLB,  $\lambda_{ex}=488$  nm). Filaments break and reform by diffusion on the lipid bilayer. Scale bar: 20  $\mu\text{m}$ .



### **Supporting Movie 5: DNA cortex formation induced by cholesterol-tagged DNA-mediated linking**

Confocal fluorescence z-stack of 500 nM st-chol DNA filaments ( $\lambda_{ex}=561$  nm) within a GUV. DNA filaments condense at the GUV periphery due to recruitment by the cholesterol-tagged DNA, which is complementary to a single-stranded DNA overhang on the filaments. Scale bar: 10  $\mu$ m.

### **Supporting Movie 6: GUVs are deformed by st-chol DNA filaments**

Confocal fluorescence time series of 1  $\mu$ M st-chol DNA filaments ( $\lambda_{ex}=561$  nm) within GUVs ( $\lambda_{ex}=488$  nm). DNA filaments deform the deflated GUV from within and suppress membrane fluctuations. Scale bar: 10  $\mu$ m.

### **Supporting Movie 7: Deflated GUV in presence of st DNA filaments**

Confocal fluorescence time series of 500 nM st DNA filaments ( $\lambda_{ex}=561$  nm) within GUVs ( $\lambda_{ex}=488$  nm). st DNA filaments do not deform deflated GUVs. Scale bar: 10  $\mu$ m.

## References

- (1) Haller, B.; Göpfrich, K.; Schröter, M.; Janiesch, J.-W.; Platzman, I.; Spatz, J. P. Charge-controlled microfluidic formation of lipid-based single- and multicompartiment systems. *Lab on a Chip* **2018**, *18*, 2665–2674.
- (2) Weiss, M. et al. Sequential bottom-up assembly of mechanically stabilized synthetic cells by microfluidics. *Nature Materials* **2017**, *17*, 89–96.
- (3) Rothmund, P. W. K.; Ekani-Nkodo, A.; Papadakis, N.; Kumar, A.; Fygenon, D. K.; Winfree, E. Design and Characterization of Programmable DNA Nanotubes. *Journal of the American Chemical Society* **2004**, *126*, 16344–16352.

## **A.8 Supporting Information for Publication 8: Division and regrowth of phase-separated giant unilamellar vesicles**

## Supporting Information

### **Division and Regrowth of Phase-Separated Giant Unilamellar Vesicles\*\***

*Yannik Dreher<sup>+</sup>, Kevin Jahnke<sup>+</sup>, Elizaveta Bobkova, Joachim P. Spatz, and Kerstin Göpfrich\**

ange\_202014174\_sm\_miscellaneous\_information.pdf

ange\_202014174\_sm\_VideoS1.mp4

ange\_202014174\_sm\_VideoS2.mp4

ange\_202014174\_sm\_VideoS3.mp4

ange\_202014174\_sm\_VideoS4.mp4

# Contents

<b>1</b>	<b>Materials and Methods</b>	<b>4</b>
1.1	GUV formation . . . . .	4
1.2	SUV formation . . . . .	5
1.3	Confocal fluorescence microscopy . . . . .	5
1.4	Theoretical predictions . . . . .	5
1.5	Determination of osmolality . . . . .	6
1.6	Enzymatic osmolarity change . . . . .	6
1.7	Light-mediated osmolarity change . . . . .	6
1.8	Absorbance measurements . . . . .	7
1.9	Calcium-mediated vesicle fusion . . . . .	7
1.10	DNA-mediated vesicle fusion . . . . .	7
<b>2</b>	<b>Supporting Tables</b>	<b>8</b>
2.1	Table S1: List of used lipids . . . . .	8
2.2	Phase separation of GUVs produced from different lipid mixtures . . . . .	9
2.2.1	Table S2: Influence of lipid type on phase separation . . . . .	9
2.2.2	Table S3: Influence of lipid charge on phase separation . . . . .	10
2.2.3	Table S4: Influence of the fluorescently-labeled lipid on phase separation . . . . .	11
2.3	Table S5: Electroformation protocol for phase-separated GUVs . . . . .	12
2.4	Table S6: Electroformation protocol for single-phased GUVs . . . . .	12
<b>3</b>	<b>Supporting Figures</b>	<b>13</b>
3.1	Figure S1: Area, volume and surface-to-volume ratio over time . . . . .	13
3.2	Figure S2: Overview confocal image and lipid tubulation . . . . .	14
3.3	Figure S3: GUV division upon water evaporation . . . . .	15
3.4	Figure S4: Phase separation of GUVs produced from different lipid mixtures . . . . .	16
3.5	Figure S5: Osmolarity mismatch after electroformation . . . . .	17
3.6	Figure S6: Necessity of $MgCl_2$ for attachment of cholesterol-tagged DNA . . . . .	18
3.7	Figure S7: Reduction of invertase activity in the presence of $MgCl_2$ . . . . .	19
3.8	Figure S8: Gentle shaking overcomes $MgCl_2$ -mediated electrostatic interaction between divided GUVs . . . . .	20
3.9	Figure S9: Microfluidic trapping approach . . . . .	21
3.10	Figure S10: Characterisation of CMNB-caged fluorescein via absorbance and osmolarity measurements . . . . .	23
3.11	Figure S11: Light-triggered division of phase-separated GUVs via uncaging of CMNB-caged fluorescein . . . . .	24
3.12	Figure S12: Illumination of CMNB-fluorescein with a 405 nm laser diode leads to uncaging of fluorescein . . . . .	26

3.13	Figure S13: 405 nm illumination in absence of CMNB-caged fluorescein does not lead to division of phase-separated GUVs . . . . .	27
3.14	Figure S14: Phase separation can be restored through Ca <sup>2+</sup> -mediated fusion of single-phased GUVs . . . . .	28
3.15	Figure S15: Phase separation can be restored through Ca <sup>2+</sup> -mediated fusion of SUVs to single-phased GUVs . . . . .	29
3.16	Figure S16: Tocopherol-tagged DNA is homogeneously distributed in the lo- and ld-phases of phase-separated GUVs . . . . .	30
3.17	Figure S17: DLS of lo SUVs . . . . .	31
3.18	Figure S18: DNA-mediated vesicle fusion leads to growth of lo-phase of initially single-phased GUVs . . . . .	32
3.19	Figure S19: DNA-functionalized lo SUVs do not fuse to plain ld GUV . . . . .	33
<b>4</b>	<b>Supporting Notes</b>	<b>34</b>
4.1	Note S1: Derivation of theoretical prediction . . . . .	34
4.2	Note S2: Considerations for osmolarity matching with CMNB-caged fluorescein . . . . .	35
4.3	Note S3: Osmolarity vs. osmolality . . . . .	36
<b>5</b>	<b>Supporting Videos</b>	<b>37</b>
5.1	Video S1: Conceptual model and confocal fluorescence time lapse of GUV division . . . . .	37
5.2	Video S2: Division of phase-separated GUV triggered by enzymatic decomposition . . . . .	37
5.3	Video S3: Light-triggered division of phase-separated GUVs by uncaging of CMNB-fluorescein . . . . .	38
5.4	Supporting Video S4: Calcium-mediated fusion of single-phase GUVs to restore phase-separation . . . . .	38
	<b>Supporting References</b>	<b>39</b>

# 1 Materials and Methods

## 1.1 GUV formation

18:1 Atto488-DOPE was purchased from ATTO-TEC GmbH. All other lipids were purchased from Avanti Polar Lipids, Inc., and stored in chloroform at  $-20\text{ }^{\circ}\text{C}$  (for a complete list of used lipids see Table S1). Giant unilamellar vesicles (GUVs) were produced via the electroformation method [1] using a VesiclePrepPro device (Nanon Technologies GmbH). Four types of GUVs were produced for the experiments shown in main. Phase-separated GUVs (Table S2, Mix 1) are composed of 27.125 % 18:1 DOPC, 24,75 % cholesterol, 37.125 % 16:0 DPPC, 10 % cardiolipin (CL), 1 % 18:1 LissRhod PE if not stated otherwise. Single-phase GUVs (Mix SP1) are composed of 70 % EggPC, 29 % EggPG, 1 % 18:1 Atto488-DOPE, whereas lo single-phase GUVs are composed of 49,5 % 18:1 DOPC, 49,5 % cholesterol, 1 % CF PE (lo Mix) and ld single-phase GUVs are composed of 4,75 % 18:1 DOPC, 74.25 % 16:0 DPPC, 20 % cardiolipin (CL), 1 % 18:1 LissRhod PE (ld Mix). Note that DPPC membranes containing 20 mol% CL were shown to exhibit a ld phase [2]. Furthermore, addition of  $< 10\text{ mol}\%$  of DOPC disrupts the order of DPPC membranes [3]. To test the phase separation behavior of GUVs, vesicles from twelve different additional lipid mixtures were prepared, for details see Tables S2-S4.  $40\text{ }\mu\text{l}$  of 1 mM lipid mix in  $\text{CHCl}_3$  were homogeneously spread on the conductive side of an indium tin oxide (ITO) coated glass coverslide (Viontek Systems Ltd) using a cover slide. The lipid-coated ITO slide was subsequently placed under vacuum for at least 30 min to achieve complete evaporation of the  $\text{CHCl}_3$ . A rubber ring with a diameter of 18 mm was placed on the lipid-coated ITO slide. The ring was filled with  $275\text{ }\mu\text{l}$  buffer solution, before creating a sealed chamber by placing a second ITO slide on top. The buffer solution used for the phase-separated GUVs contained 300 mM sucrose (Sigma-Aldrich Corp.) and 10 mM HEPES (Sigma-Aldrich Corp.). The solution for the lo and ld single-phase GUVs (lo Mix and ld Mix) contained 300 mM sucrose. Both solutions were preheated to  $65\text{ }^{\circ}\text{C}$ . For the single-phase GUVs (Mix SP1) a 500 mM sucrose solution at room temperature was used. The assembled electroformation chamber was placed into the VesiclePrepPro and connected to the electrodes. A programmable AC field was applied across the ITO slides. For the phase-separated GUVs, a custom-written multi-step program with defined temperature, voltage, AC-frequency and duration was used (see Table S5). For both single-phase GUVs the preinstalled *Standard* program was selected (see Table S6). GUVs were collected immediately after formation according to the protocol and stored at  $4\text{ }^{\circ}\text{C}$  for up to 2 days.

## 1.2 SUV formation

Small unilamellar vesicles (SUVs) composed of 49,5 % 18:1 DOPC, 49,5 % cholesterol, 1 % CF PE (lo Mix) were formed by mixing the lipids dissolved in  $\text{CHCl}_3$  in a glass vial and subsequent solvent evaporation under a stream of nitrogen gas. The glass vial was then placed under vacuum for at least 30 min to remove residual traces of solvent. A solution of 300 mM sucrose was preheated to 65 °C and added to the glass vial to resuspend the lipids at a concentration of 3 mM. After 10 min swelling at 65 °C the solution was vortexed at 1000 rpm for at least 5 min to trigger liposome formation. Homogenous SUVs were formed by extruding the liposome solution nine times through a polycarbonate filter with a pore size of 100 nm (Avanti Polar Lipids, Inc.). During this step the extruder was heated to 65 °C using a heating plate. The SUVs were stored at 4 °C for up to 5 days.

## 1.3 Confocal fluorescence microscopy

A confocal laser scanning microscope LSM 800 or LSM 880 (Carl Zeiss AG) was used for fluorescence imaging. The images were acquired using a 20x air (Objective Plan-Apochromat 20x/0.8 M27, Carl Zeiss AG) and a 40x water immersion objective (LD C-Apochromat 40x/1.1 W, Carl Zeiss AG). To visualize the phase separation of the SUVs, 6-FAM-labelled cholesterol-tagged DNA (Integrated DNA Technologies, Inc.; DNA sequence: 5' 6-Fam-CTATGTATTTTGCACAGTTT-Chol 3'; HPLC purified, DNA #1) was used which partitioned mainly into the lo phase [4]. LissRhod PE labelled the ld phase. 6-FAM and Atto488-DOPE were excited with a 488 nm diode laser (Carl Zeiss AG), LissRhod PE with a diode or Argon laser at 561 nm (Carl Zeiss AG). In order to release the fluorescein for the light-triggered division, CMNB-caged fluorescein was illuminated with a diode laser at 405 nm. Images were analyzed with ImageJ (contrast and brightness adjustments and TrackMate) and Matlab.

## 1.4 Theoretical predictions

All calculations were carried out with MathWorks Matlab (9.5.0.944444 R2018b) and Jupyter (v. 4.4.0) as described in the main text. The derivation of the equations is shown in Supplementary Note S1.



## 1.5 Determination of osmolality

The osmolality of all solutions was measured with the Osmomat 030 (Gonotec GmbH). Before use, the osmometer was calibrated with calibration solutions of 0, 300 and 900 mOsm/kg (Gonotec GmbH). Each measurement was carried out with a sample volume of 50  $\mu\text{l}$ . Note that for the quantities that are calculated here, the osmolality is a good approximation for the osmolarity (see Note S3). The measurement error of the osmometer itself (in terms of reproducibility) is below 0.5%.

## 1.6 Enzymatic osmolarity change

Invertase from bakers's yeast (*S. cerevisiae*) grade VII,  $\geq 300$  units/mg was purchased from Sigma-Aldrich Corp. Nominally, one unit of the enzyme hydrolyzes 1  $\mu\text{mol}$  of sucrose per minute to produce fructose and glucose at pH 4.5 at 55  $^{\circ}\text{C}$ . The GUV solution obtained from electroformation was mixed with a solution containing 1  $\text{mg ml}^{-1}$  invertase such that the final concentration of invertase was 44.4  $\text{mg l}^{-1}$  and in a second experiment 22.2  $\text{mg l}^{-1}$ . Immediately after mixing, a part of the solution was used for division experiments with phase-separated GUVs in a sealed observation chamber. The other part was used for osmolality measurements over time. The experiments were carried out at room temperature.

## 1.7 Light-mediated osmolarity change

CMNB-caged fluorescein (Fluorescein bis-(5-Carboxymethoxy-2-Nitrobenzyl)-Ether, dipotassiumsalt) was purchased from Sigma-Aldrich Corp., dissolved in 100 mM Tris buffer at pH 8.0 at a final concentration of 50 mM and stored at  $-20^{\circ}\text{C}$  until use. Phase-separated GUVs were produced in 13 mM sucrose and mixed with an osmolarity-matched solution of CMNB-caged fluorescein leading to a final concentration of 1.73 mM CMNB-caged fluorescein. Note that the concentration of the sucrose solution was reduced to ensure a sufficiently large osmolarity change despite the limited concentration of the caged fluorescein (see Note S2). Each phase-separated GUV was imaged with confocal fluorescence microscopy for at least 100 s before illumination with 405 nm laser light (70% laser intensity) leading to the uncaging of CMNB-caged fluorescein and hence a local increase in osmolarity.

## 1.8 Absorbance measurements

The absorbance of CMNB-caged fluorescein was measured with a plate reader (TECAN microplate reader SPARK®) in the range from 300-700 nm using a 96-well plate. The settle time was set to 50 ms. In order to induce uncaging of CMNB-fluorescein, the solution was transferred into a PCR-tube, diluted with MQ and put under a UV-lamp (Hamamatsu LIGHTNINGCURE Spot light source LC8, 100 % power). Subsequently, the solution was pipetted into the well-plate again and measured for a second time.

## 1.9 Calcium-mediated vesicle fusion

Ld-phase GUVs (20 % CL, 74.25 % DPPC, 4.75 % DOPC, 1 % LissRhod PE) and lo-phase SUVs or GUVs (49.5 % DOPC, 49.5 % cholesterol, 1 % CF PE) at lipid concentrations of  $\sim 0.3$  mM were mixed in a 1:1 ratio. Note that the lipid mix used for lo GUVs was shown to exhibit a homogeneous lo phase [5, 6]. The ld composition [3, 2] was chosen in order to obtain the initial phase-separated lipid mixture after fusion. A second type of GUVs, which we refer to as ld GUVs [3, 2], was formed, such that we obtain the initial phase-separated lipid mixture after fusion. After addition of isoosmolar  $\text{CaCl}_2$  at a final concentration of 20 mM, the vesicle-containing solution was observed with a confocal fluorescence microscope in a sealed observation chamber. After  $> 10$  min the first phase-separated GUVs containing both fluorescent dyes could be observed.

## 1.10 DNA-mediated vesicle fusion

In order to obtain DNA-mediated vesicle fusion we designed two complementary DNA sequences, adapted from [7], that arrange in a zipper like manner upon duplex formation, thereby bringing the membranes of two distinct vesicles in close proximity. Lo-phase SUVs (50 % DOPC, 50 % cholesterol) were incubated with 1  $\mu\text{M}$  cholesterol-tagged DNA (Biomers; DNA sequence: 5' TGGACATCAGAAAGGCACGACGA-Chol 3'; HPLC purified, DNA #2) and 10 mM  $\text{MgCl}_2$  for 20 min to minimize the amount of unbound DNA. On the other hand, ld-GUVs (20 % CL, 74.25 % DPPC, 4.75 % DOPC, 1 % LissRhod PE) were incubated with 1  $\mu\text{M}$  tocopherol-tagged DNA (from Biomers; DNA sequence: 5'-Toc TCCGTCGTGCCTTATTTCTGATGTCCA 3'; HPLC purified, DNA #3), which inserts into lo- and ld-lipid phases (see Figure S15). After incubation, lo-SUVs and ld-GUVs were mixed and observed with a confocal fluorescence microscope. To prove the successful regrowth of phase-separated GUVs, cholesterol-tagged 6-FAM DNA (Integrated DNA Technologies, Inc.; DNA sequence: 5' 6-Fam-CTATGTATTTTGCACAGTTT-Chol 3'; HPLC purified, DNA #1) was added to visualize the lo-phase as described previously.

## 2 Supporting Tables

### 2.1 Table S1: List of used lipids

Lipid	Abbreviation	Company
18:1 1,2-dioleoyl-sn-glycero-3-phosphocholine	DOPC	Avanti Polar Lipids, inc.
16:0 1,2-dipalmitoyl-sn-glycero-3-phosphocholine	DPPC	Avanti Polar Lipids, inc.
18:1 1,2-dioleoyl-3-trimethylammonium-propane	DOTAP	Avanti Polar Lipids, inc.
18:1 1,2-dioleoyl-sn-glycero-3-phospho-(1'-rac-glycerol)	DOPG	Avanti Polar Lipids, inc.
18:1 1,2-dioleoyl-sn-glycero-3-phosphoethanolamine	DOPE	Avanti Polar Lipids, inc.
cholesterol (ovine)	Chol	Avanti Polar Lipids, inc.
18:0 N-stearoyl-D-erythro-sphingosylphosphorylcholine	SM	Avanti Polar Lipids, inc.
Cardiolipin (Heart, Bovine)	CL	Avanti Polar Lipids, inc.
L- $\alpha$ -phosphatidylcholine	EggPC	Avanti Polar Lipids, inc.
L- $\alpha$ -phosphatidylglycerol	EggPG	Avanti Polar Lipids, inc.
18:1 1,2-dioleoyl-sn-glycero-3-phosphoethanolamine-N-(Cyanine 5)	Cy5 PE	Avanti Polar Lipids, inc.
18:1 1,2-dipalmitoyl-sn-glycero-3-phosphoethanolamine-N-(lissamine rhodamine B sulfonyl)	LissRhod PE	Avanti Polar Lipids, inc.
18:1 1,2-dioleoyl-sn-glycero-3-phosphoethanolamine-N-(carboxyfluorescein)	CF PE	Avanti Polar Lipids, inc.
16:1 1-palmitoyl-2-6-[(7-nitro-2-1,3-benzoxadiazol-4-yl)amino]hexanoyl-sn-glycero-3-phosphocholine	NBD PC	Avanti Polar Lipids, inc.
18:1 1,2-dioleoyl-sn-glycero-3-phosphoethanolamine-N-(7-nitro-2-1,3-benzoxadiazol-4-yl)	NBD PE	Avanti Polar Lipids, inc.
18:1 Atto488-labelled 1,2-Dioleoyl-sn-glycero-3-phosphoethanolamin	Atto488-DOPE	ATTO-TEC GmbH

#### Supporting Table S1

List of all lipids used in this study and their abbreviations.

## 2.2 Phase separation of GUVs produced from different lipid mixtures

### 2.2.1 Table S2: Influence of lipid type on phase separation

Mix No.	Lipid mixture	Phase separation
1	27.1% DOPC, 24.8% chol, 37.1% DPPC, 10% CL + 1% LissRhod PE	yes
2	37.1% DOPC, 24.8% chol, 37.1% DPPC + 1% LissRhod PE	yes
3	33 % DOPC + 33 % SM + 33 % chol + 1 % NBD PC	yes

#### Supporting Table S2

Overview of the influence of lipid type on phase separation behaviour of GUVs. All GUVs were prepared using a 300 mM sucrose solution and the electroformation method with the protocol presented in Supporting Table S5. For all mixes we obtained phase-separated GUVs with distinct hemispheres. For confocal fluorescence images of the GUVs see Figure S2.

### 2.2.2 Table S3: Influence of lipid charge on phase separation

Mix No.	Lipid type [mol % / lipid charge]	Additions	Phase separation
2	DOPC [37.1%/no]	-	yes
1	DOPC [27.1%/no]	-	yes
	CL [10%/-]		
4	DOTAP [27.1%/+]	-	yes
	CL [10%/-]		
5	DOTAP [27.1 %/+]	unlabeled DOPE instead of LissRhod PE, Chol-Atto390-DNA 10mM MgCl <sub>2</sub>	yes
	CL [10%/-]		
6	DOPG [27.1%/-]	-	yes
	CL [10%/-]		

#### Supporting Table S3

Overview of the influence of lipid-charge on phase separation of GUVs. All presented lipid mixtures contain 24.8% cholesterol, 37.1% DPPC and 1% LissRhod PE, supplemented with other lipids as listed in the table. The presented charges apply for physiological conditions. All GUVs were prepared using a 300mM sucrose solution and the electroformation method with the protocol presented in Supporting Table S5. Electroformation of Lipid Mix 6 did not yield GUVs and GUVs from this mix were, therefore, prepared via gentle hydration for two hours at 65 °C [8]. Phase-separated GUVs with two distinct hemispheres were obtained using neutral as well as positively or negatively charged lipids. For confocal fluorescence images of the GUVs see Figure S2.

**2.2.3 Table S4: Influence of the fluorescently-labeled lipid on phase separation**

Mix No.	Fluorophore	Additions	Phase separation
1	1 % LissRhod PE	-	yes
7	1 % LissRhod PE	Chol-6-FAM-DNA + 10mM MgCl <sub>2</sub>	yes
8	1 % Cy5-PE	-	yes
9	0.5 % Atto488-DOPE + 0.5 % LissRhod PE	-	yes
10	1 % NBD PE	-	no
11	0.5 % NBD PE + 0.5 % Cy5 PE	-	yes
12	1 % DOPE (no fluorophore)	Chol-6-FAM-DNA + 10mM MgCl <sub>2</sub>	no
13	0.5 % LissRhod PE + 1 % CF PE	-	yes

**Supporting Table S4**

Overview of the influence of the fluorophore on phase separation of GUVs. All listed lipid mixtures contained 27.1 % DOPC, 24.8 % cholesterol, 37.1 % DPPC, 10 % cardiolipin and 1 % of the labeled lipid as specified in the table. In all cases, the fluorophore was covalently linked to the lipid head group. All GUVs were prepared using a 300 mM sucrose solution and the electroformation method with the protocol presented in Supporting Table S5. It is important to note that the choice of fluorophore alone can influence the phase-separation behaviour of the GUVs, see Mix 10 and 12 (no phase-separation). For confocal fluorescence images of the GUVs see Figure S2.

### 2.3 Table S5: Electroformation protocol for phase-separated GUVs

Step	Time [s]	Ampl [V]	Freq [Hz]	Temp [°C]
Initiate	300	1	10	70
Main	2100	1	10	70
Detach1	2160	1	3	70
Detach2	3000	1	3	70
Detach3	3060	1	1	70
Detach4	3420	1	1	70
Detach5	3480	1	0.5	70
Detach6	3840	1	0.5	70
Detach7	3960	1	0	70

#### Supporting Table S5

Electroformation protocol for the formation of phase-separated GUVs using the Vesicle Prep Pro (Nanion Technologies GmbH). Custom-written multi-step program for formation of phase-separated GUVs, adapted from a previously published protocol [4]. Note that it is crucial to keep the temperature above the phase-transition temperature throughout the electroformation. Parameters are changed linearly over time from one step to the next.

### 2.4 Table S6: Electroformation protocol for single-phased GUVs

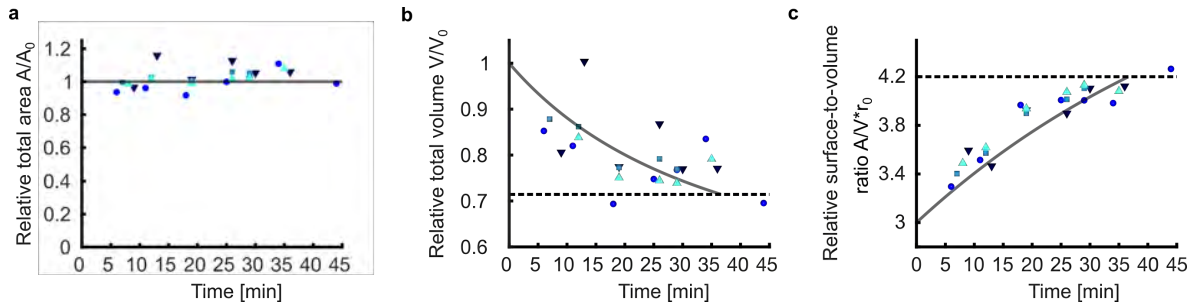
Step	Time [s]	Ampl [V]	Freq [Hz]	Temp [°C]
Initiate	180	3	5	37
Main	7380	3	5	37
Detach	7680	0	5	37

#### Supporting Table S6

Electroformation protocol for single-phase GUV formation using the Vesicle Prep Pro (Nanion Technologies GmbH). The programme was preinstalled as the standard protocol for GUV formation. Parameters are changed linearly over time from one step to the next.

### 3 Supporting Figures

#### 3.1 Figure S1: Area, volume and surface-to-volume ratio over time

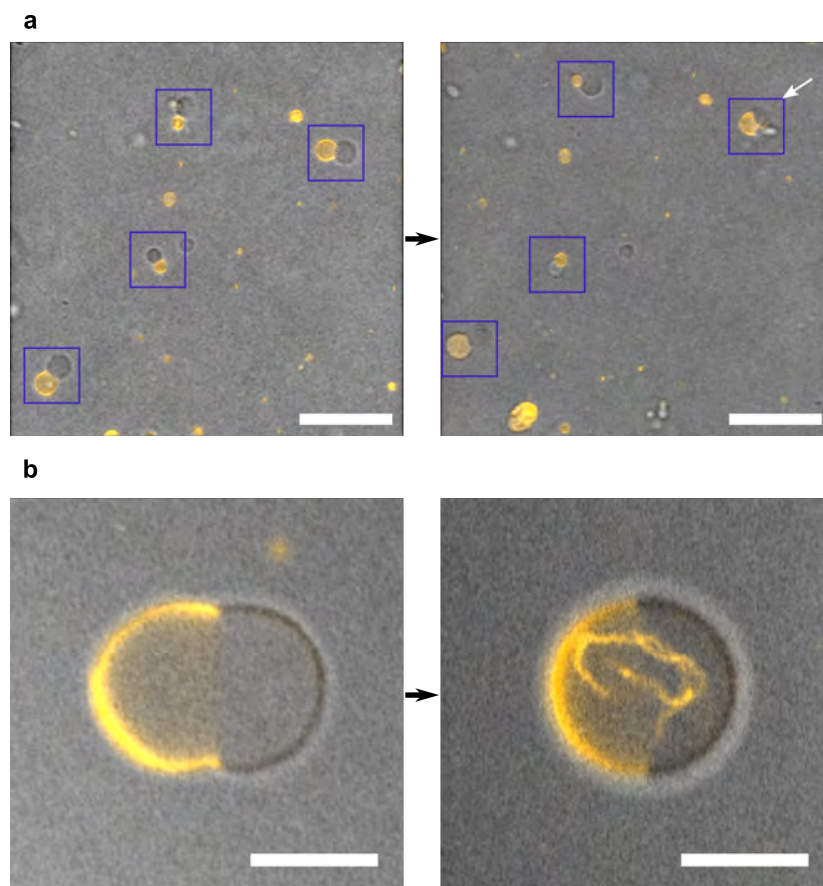


#### Supporting Figure S1

Relative area, volume and surface-to-volume ratio of phase-separated vesicles over time. The data was extracted from the same time series as the plot in Figure 3f of the main text. **a**, **b**, **c** triangles, circles and squares represent different vesicles with  $l = 0.5$  in the presence of invertase, solid grey line shows the expected curve as calculated from osmolarity measurements. Dashed black line shows the critical volume ratio **b** or surface-to-volume ratio **c** at which full division should occur. As assumed in our model, the surface area remains constant over time, while the surface-to-volume ratio increases.



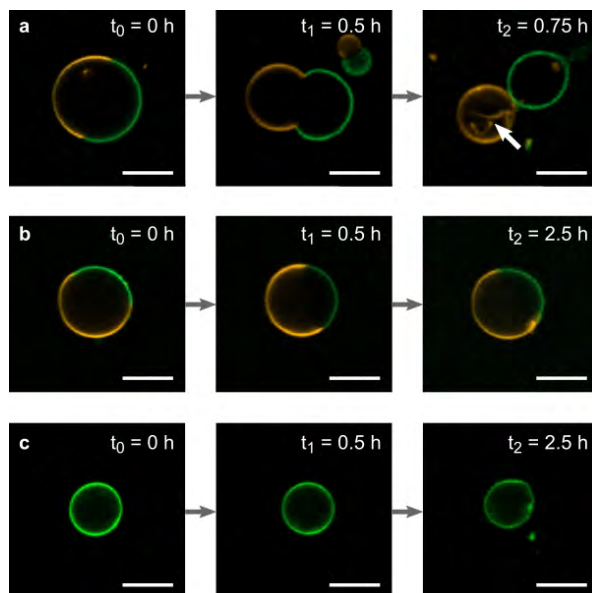
### 3.2 Figure S2: Overview confocal image and lipid tubulation



#### Supporting Figure S2

Reproducibility of the division process. **a** Overlays of confocal (ld phase labeled with LissRhod PE,  $\lambda_{\text{ex}} = 561 \text{ nm}$ ) and bright field images of multiple vesicles undergoing division due to a continuous increase of the outer osmolarity due to invertase activity. The white arrow highlights a vesicle that restores its spherical shape after the formation of lipid tubes – potentially due to interactions with the glass surface or too fast local osmolarity change. Scale bars:  $25 \mu\text{m}$  **b** Zoom image of a vesicle which shows tubulation. The GUV deforms initially (left image). As the osmotic pressure increases over time, lipid tubulation is observed and the spherical shape is restored (right image). This effect inhibits successful division of the GUVs. This occurred mainly when the osmolarity was too high, if it changed too quickly or if the GUV was in contact with surfaces. Scale bars:  $10 \mu\text{m}$ .

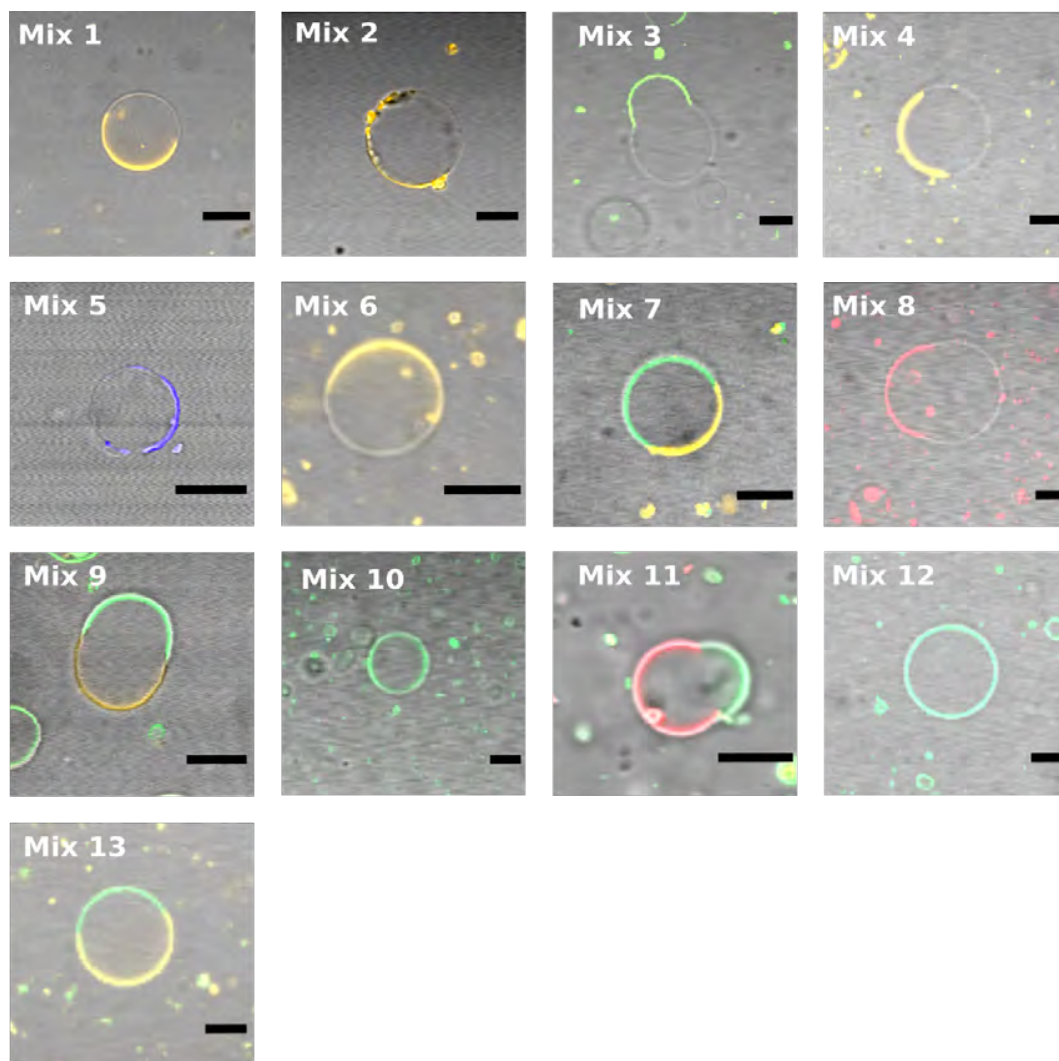
### 3.3 Figure S3: GUV division upon water evaporation



#### Supporting Figure S3

**a** Time series of confocal fluorescence images depicting the division process of a phase-separated GUV upon water evaporation. The white arrow highlights the formation of lipid tubes after the division is completed. **b** Control experiment with a phase-separated GUV in a sealed observation chamber preventing water evaporation. **c** Control experiment with a single-phase GUV in an unsealed observation chamber allowing for water evaporation. LissRhod PE labeled the ld phase (orange,  $\lambda_{\text{ex}} = 561$  nm) and 6-FAM-labeled cholesterol-tagged DNA partitioned in the lo phase (green,  $\lambda_{\text{ex}} = 488$  nm). Single-phase GUVs were labeled with Atto488-DOPE (green,  $\lambda_{\text{ex}} = 488$  nm). Scale bars: 10  $\mu\text{m}$

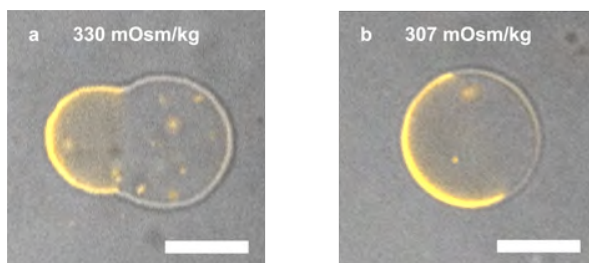
### 3.4 Figure S4: Phase separation of GUVs produced from different lipid mixtures



#### Supporting Figure S4

Representative overlays of confocal fluorescence and brightfield images of GUVs produced from different lipid mixtures as indicated in Tables S2-S4. Cy5 PE was excited with  $\lambda_{ex} = 633$  nm; NBD PE, NBD PC, CF PE, Atto488-DOPE and Chol-6-FAM-DNA were excited with  $\lambda_{ex} = 488$  nm; LissRhod PE was excited with  $\lambda_{ex} = 561$  nm; Chol-Atto390-DNA was excited with  $\lambda_{ex} = 405$  nm. Scale bars: 10  $\mu$ m.

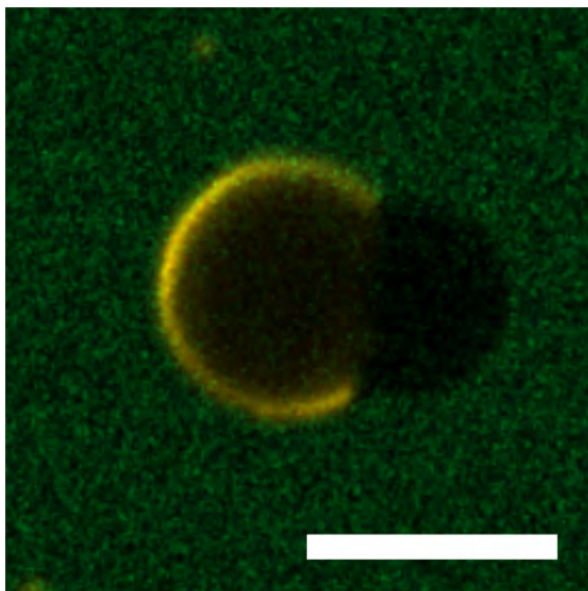
### 3.5 Figure S5: Osmolarity mismatch after electroformation



#### Supporting Figure S5

Overlays of confocal fluorescence (1d phase labeled with LissRhod PE,  $\lambda_{ex} = 561$  nm) and bright field images of GUVs in buffers of different osmolality. **(a)** Directly after electroformation, the GUVs exhibit a non-spherical shape even though the measured osmolality of the vesicle-containing solution does not increase enough for such a significant shape change ( $325 \text{ mOsm kg}^{-1}$  before electroformation,  $330 \text{ mOsm kg}^{-1}$ ). **(b)** If the buffer solution is diluted to  $307 \text{ mOsm kg}^{-1}$ , the GUV returns to its spherical shape. This may be due to the fact that the vesicles still grow after forming a sealed compartment, leading to a reduced sucrose concentration inside the vesicle. We thus diluted the outer aqueous phase until the GUVs were spherical to achieve our desired initial conditions. Scale bars:  $10 \mu\text{m}$ .

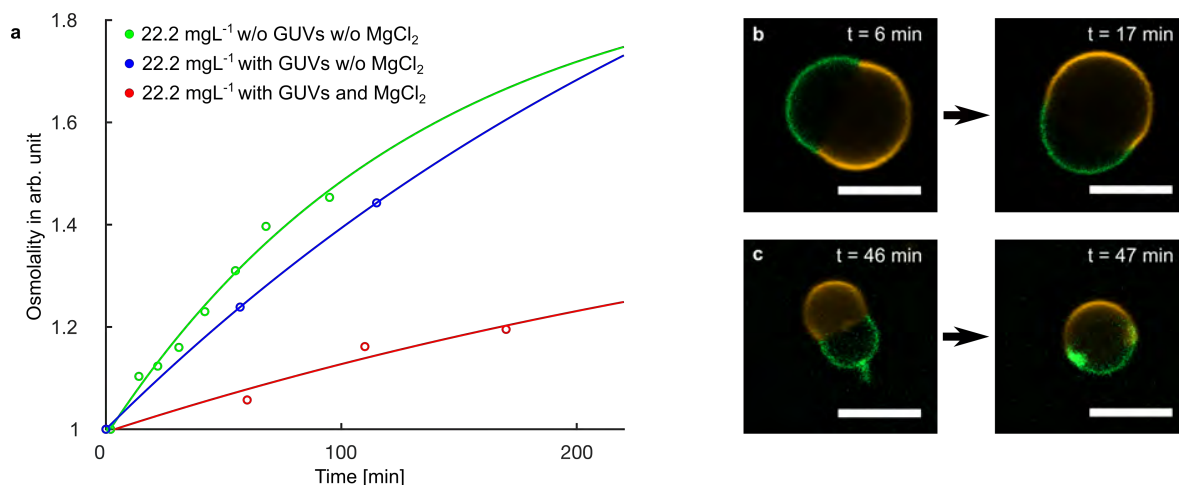
### 3.6 Figure S6: Necessity of $\text{MgCl}_2$ for attachment of cholesterol-tagged DNA



#### Supporting Figure S6

Confocal fluorescence microscope image of a GUV (ld phase labeled with LissRhod PE  $\lambda_{ex} = 561$  nm, orange) in a solution of 300 mM sucrose, 10 mM HEPES and 1  $\mu\text{M}$  6-FAM-labeled cholesterol-tagged DNA ( $\lambda_{ex} = 488$  nm, green). Due to lack of  $\text{MgCl}_2$ , the cholesterol-tagged DNA does not attach to the GUV membrane and is homogeneously distributed in the outer aqueous phase instead. For this reason, 10 mM  $\text{MgCl}_2$  was added to the outer aqueous phase for Figures 1 and 3 (main text), resulting in the attachment of the cholesterol-tagged DNA to the lo phase. Since  $\text{MgCl}_2$  inhibited the activity of invertase (see Figure S5), it was not possible to label the lo phase in Figure 4 (main text). Scale bar: 10  $\mu\text{m}$

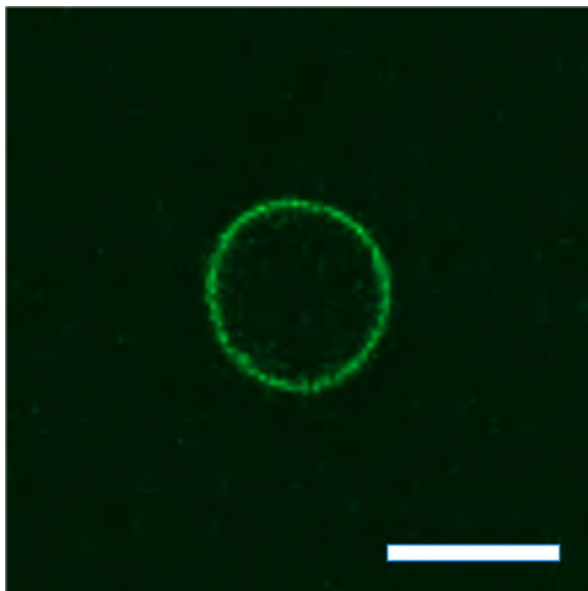
### 3.7 Figure S7: Reduction of invertase activity in the presence of $\text{MgCl}_2$



#### Supporting Figure S7

Effect of  $\text{MgCl}_2$  on invertase activity in the presence of GUVs. **a** Normalized osmolality measurements over time of a buffer containing 300 mM sucrose, 10 mM HEPES and  $22.2 \text{ mg l}^{-1}$  in the absence of GUVs and  $\text{MgCl}_2$  (green); with GUVs but without  $\text{MgCl}_2$  (blue) and with 10 mM  $\text{MgCl}_2$  and GUVs (red). Solid lines are limited growth fits. We hypothesize that the reduction of invertase activity in the presence of  $\text{MgCl}_2$  and GUVs could be caused by a charge-mediated adhesion of the invertase to the GUVs. **b**, **c** Confocal fluorescence microscopy images of GUVs in the presence of invertase and  $\text{MgCl}_2$ . The ld phase is labeled by LissRhod PE (orange,  $\lambda_{ex} = 561 \text{ nm}$ ) and the lo phase is visualized by Chol-6-FAM-DNA (green,  $\lambda_{ex} = 488 \text{ nm}$ ). The time after mixing with invertase is indicated. Under these conditions, almost all GUVs did not divide and returned to a spherical shape instead. These observations again point towards an interaction between the invertase and the surface of the GUVs, leading to the reduction of invertase activity. We hence performed the invertase experiments in the absence of  $\text{MgCl}_2$ .

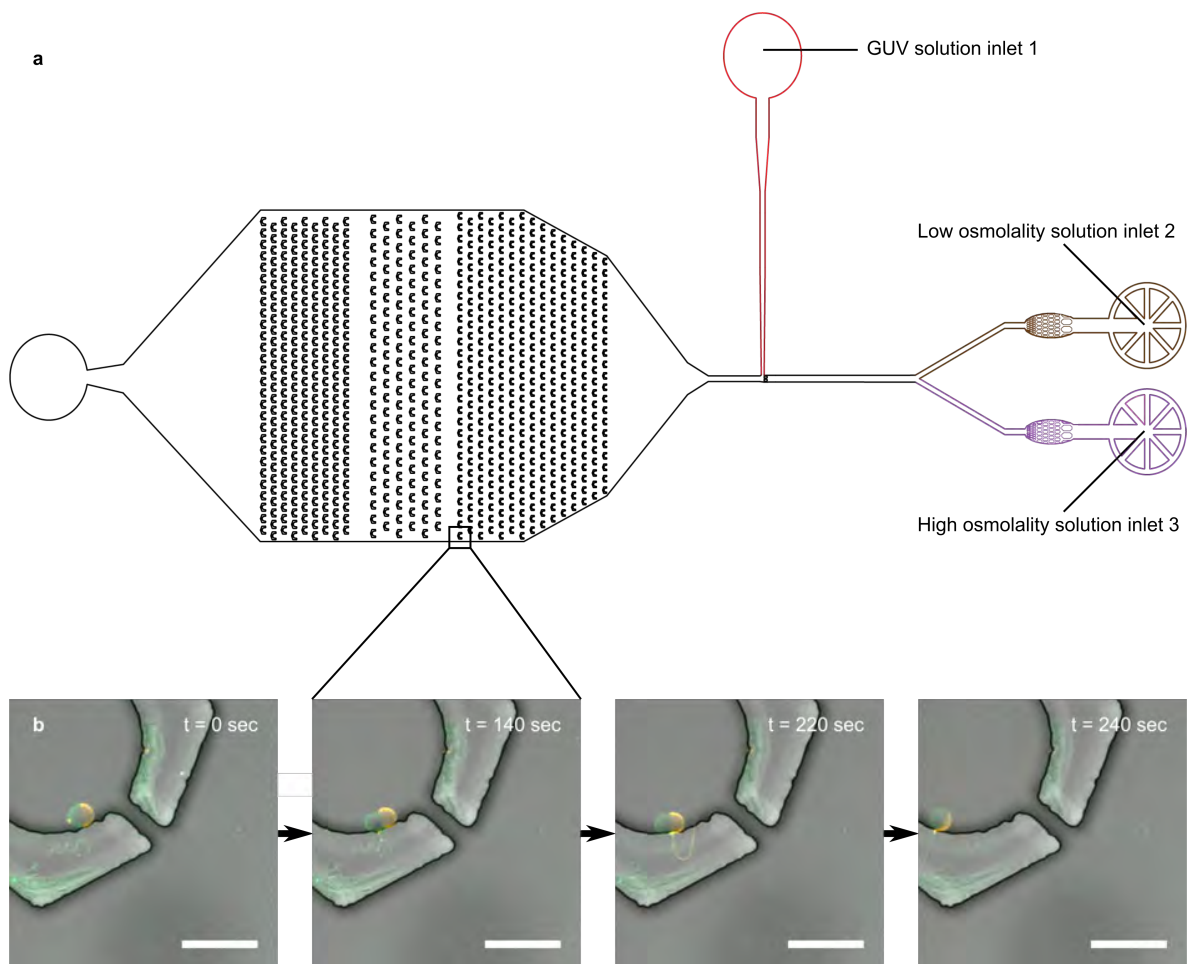
### 3.8 Figure S8: Gentle shaking overcomes MgCl<sub>2</sub>-mediated electrostatic interaction between divided GUVs



#### Supporting Figure S8

Confocal fluorescence microscope image of a GUV consisting only of the lo phase (green, 6-FAM labeled cholesterol-tagged DNA partitioned into the lo phase,  $\lambda_{ex} = 488$  nm) after mixing with a higher concentrated sucrose solution leading to an osmolarity ratio of  $C/C_0 = 1.44$ . At this ratio theoretically all GUVs should be fully divided, yet often adhere to one another if Mg<sup>2+</sup> is present in the buffer (see Figure 1, main text). Observation of the mixture after gentle shaking, however, yields a high amount of both types of single-phased GUVs. A possible explanation is that Mg<sup>2+</sup>-mediated electrostatic interactions between divided GUVs could be overcome mechanically due to the mixing process. Scale bar: 10  $\mu$ m.

### 3.9 Figure S9: Microfluidic trapping approach



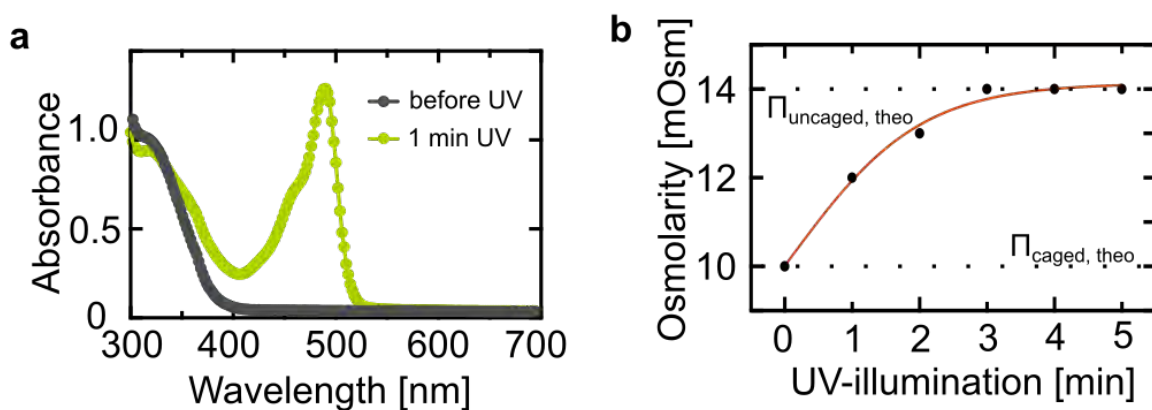
**Supporting Figure S9**  
(Continued on the following page.)



### Supporting Figure S9

Microfluidic approach for trapping and observation of GUV division. **a** Sketch of the microfluidic trapping device used for trapping of phase-separated GUVs. First, a solution containing GUVs was flushed into the device via Inlet 1. Subsequently, a low osmolality solution ( $280 \text{ mOsm kg}^{-1}$ , same osmolality as within the GUVs) was flushed into the device at a constant flow rate of  $1 \mu\text{l}/\text{min}$  via Inlet 2. In order to gradually increase the effective osmolality around the GUVs, a second high osmolality solution ( $600 \text{ mOsm kg}^{-1}$ ) was flushed in via Inlet 2, starting at a flow rate of  $0 \mu\text{l}/\text{min}$  which was gradually increased to  $2 \mu\text{l}/\text{min}$  over 40 min. **b** Time series of overlays of confocal fluorescence (ld phase labeled with LissRhod PE and lo phase labeled with 6-FAM-labeled cholesterol-tagged DNA,  $\lambda_{ex} = 561 \text{ nm}$  and  $\lambda_{ex} = 488 \text{ nm}$ , respectively) and bright field images of a phase-separated GUV in a trapping device. The interaction of the GUVs with the coverslide and the PDMS microstructures can lead to effects that inhibit the division process. The deformation process can be altered through contact of the GUV with solid interfaces and lead to lipid tubulation rather than splitting as visible in the confocal fluorescence images. Scale bars:  $30 \mu\text{m}$ .

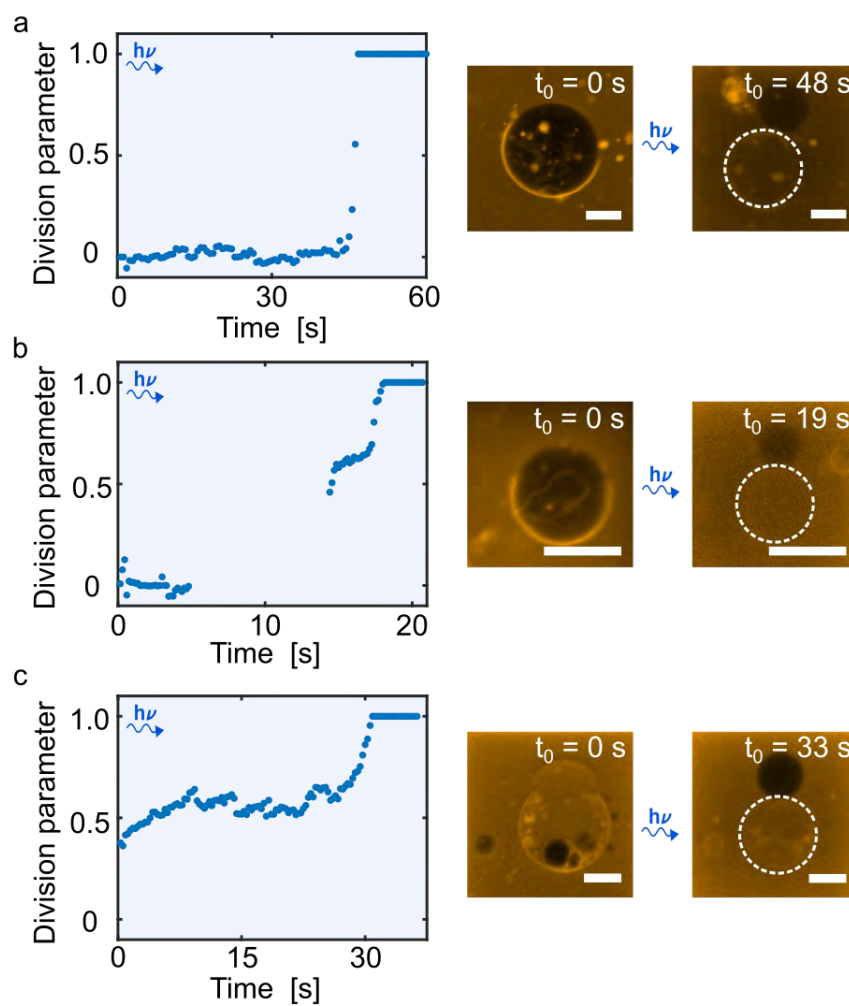
### 3.10 Figure S10: Characterisation of CMNB-caged fluorescein via absorbance and osmolarity measurements



#### Supporting Figure S10

Characterisation of CMNB-caged fluorescein via absorbance and osmolarity measurements. **a** Absorbance measurements of CMNB-caged fluorescein before and after illumination with a UV-lamp. 2 mM CMNB-caged fluorescein was dissolved in 100 mM Tris and its absorbance was measured from 300-700 nm with a plate reader before (dark green) and after 1 min of UV illumination (light green). The appearance of an absorbance maximum at  $\approx 488$  nm after UV-illumination proves successful uncaging of fluorescein. **b** Osmolarity measurements of CMNB-caged fluorescein (final concentration: 2 mM, diluted in MQ) dependent on the UV-illumination time. The maximal theoretical osmolarity of 14 mM – indicating an uncaging efficiency of 100% (every caged fluorescein splits into 3 parts, see Note S1) – is reached after 3 min. Note that these measurements were performed with a UV-lamp. They cannot directly be correlated with the uncaging dynamics that we obtain with confocal fluorescence microscopy, where we used a 405 nm laser diode for uncaging (see Figure 5, main text and Figure S10).

### 3.11 Figure S11: Light-triggered division of phase-separated GUVs via uncaging of CMNB-caged fluorescein

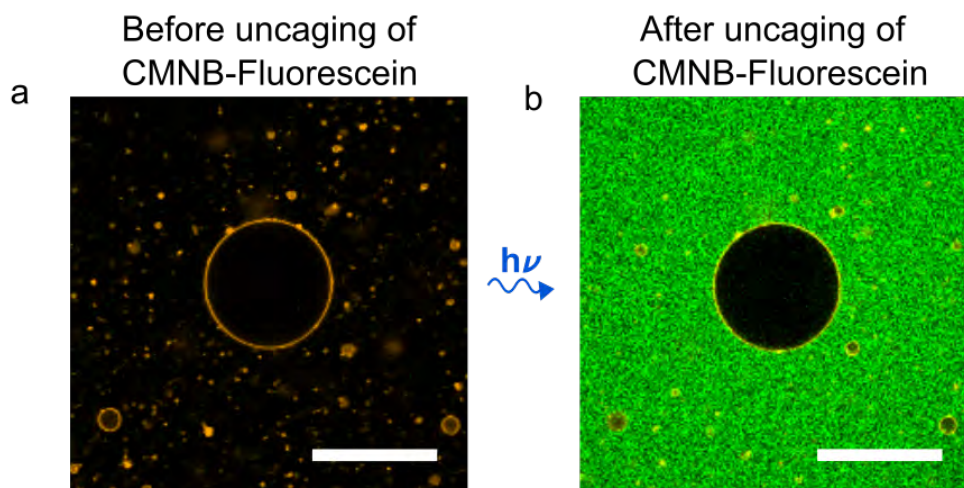


Supporting Figure S11  
(Continued on the following page.)

### Supporting Figure S11

Light-triggered division of phase-separated GUVs achieved by a local osmolarity increase due to release of CMNB-caged fluorescein. Division parameter as a function of time and corresponding representative confocal fluorescence images of dividing phase-separated GUVs (labelled with LissRhod PE,  $\lambda_{ex} = 561$  nm). All exemplary traces (**a-c**) show that phase-separated GUVs divide within seconds after uncaging of CMNB-caged fluorescein with a 405 nm laser diode. The background fluorescence is caused by bleed-through from the 405 nm excitation. Note that for **b** the shape transformations during the time frames from 5-15 could not be evaluated. The timescales of the light-triggered division process vary from 10 s to 40 s until complete division occurs. This can be explained by two main factors: (i) the differences in the lipid ratio  $l$  and (ii) by different uncaging efficiencies depending on the z-position of the GUVs. GUVs with a lipid ratio  $l < 0.5$  undergo division at a lower osmolarity ratio and thus at earlier time points during uncaging of CMNB-fluorescein. In addition to this, the absorption and uncaging efficiency depends on the axial position of the GUV within the observation chamber. The further away the GUV is from the bottom cover-slide, the more photons are absorbed by the underlying solution. On top of that, slightly different amounts of BSA on the bottom cover-slide can lead to a less efficient uncaging of CMNB-fluorescein due to absorption of light and therefore a longer timescale until division occurs. We need BSA in order to prevent fusion of the GUVs with the cover slide and imperfections in the coating process cannot be excluded. Scale bars: 10  $\mu$ m.

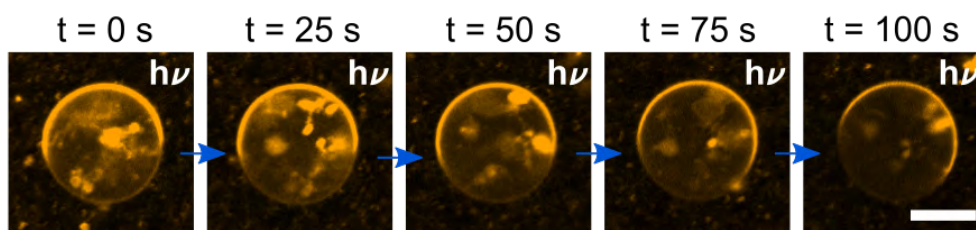
**3.12 Figure S12: Illumination of CMNB-fluorescein with a 405 nm laser diode leads to uncaging of fluorescein**



**Supporting Figure S12**

Illumination of CMNB-caged fluorescein with a 405 nm laser diode leads to uncaging of fluorescein. Confocal fluorescence images of single-phase GUVs (orange,  $\lambda_{ex} = 561$  nm) immersed in CMNB-caged fluorescein ( $\lambda_{ex} = 488$  nm) before (a) and after (b) illumination with a 405 nm diode laser. GUVs (99% DOPC, 1% 18:1 Liss Rhod PE) were mixed with an iso-osmolar solution of CMNB-caged fluorescein (final concentration 2 mM) and illuminated with 405 nm for 1 s. This results in uncaging of fluorescein and hence green fluorescence surrounding the GUV. This also indicates the impermeability of the caged as well as the uncaged compound across the lipid bilayer. Scale bars: 50  $\mu$ m.

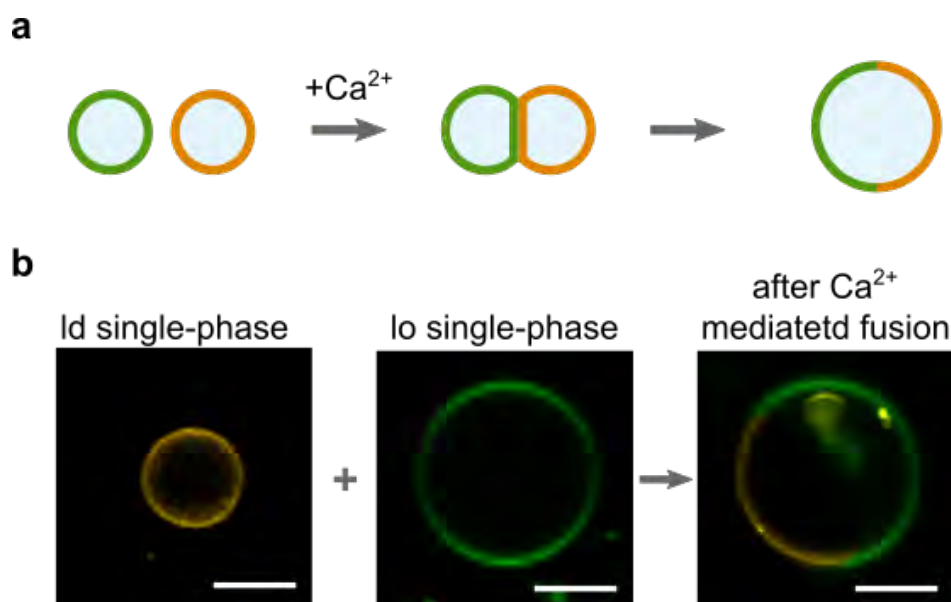
**3.13 Figure S13: 405 nm illumination in absence of CMNB-caged fluorescein does not lead to division of phase-separated GUVs**



**Supporting Figure S13**

405 nm illumination in absence of CMNB-caged fluorescein does not lead to division of phase-separated GUVs. Representative confocal fluorescence images of a phase-separated GUV (Table S2, Mix 1,  $\lambda_{ex} = 561$  nm) during illumination with a 405 nm laser diode. The GUV maintains its spherical shape throughout the recorded time frame of 100 s. This proves the need of CMNB-caged fluorescein to locally increase the osmolarity upon 405 nm illumination and hence trigger vesicle division. Scale bar: 10  $\mu$ m.

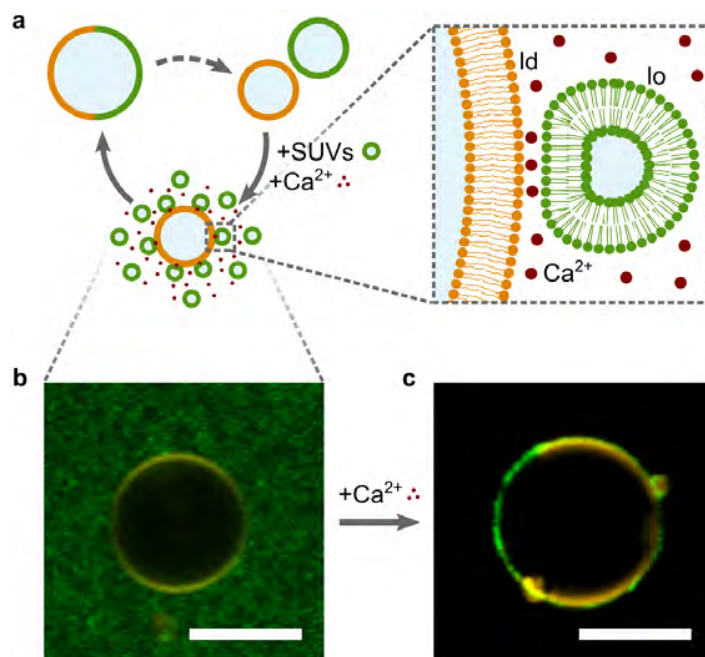
### 3.14 Figure S14: Phase separation can be restored through $\text{Ca}^{2+}$ -mediated fusion of single-phased GUVs



#### Supporting Figure S14

$\text{Ca}^{2+}$ -mediated fusion of a single-phased lo GUV and a single-phased ld GUV. **a** Schematic illustration of formation of phase-separated GUVs via  $\text{Ca}^{2+}$ -mediated fusion of single-phased GUVs of opposite phases. **b** Confocal fluorescence microscopy images of a single-phased ld (20% CL, 74.25% DPPC and 4.75% DOPC, 1% Liss Rhod PE  $\lambda_{ex}$  =561 nm, left) and a single-phased lo (49.5% chol, 49.5% DOPC, 1% CF PE,  $\lambda_{ex}$  =488 nm, middle) GUV in 300 mM sucrose. The image on the right hand side shows a phase-separated GUV after mixing the lo GUVs with the ld GUVs in the presence of 20 mM  $\text{CaCl}_2$ . The presence of both fluorescent dyes in the same vesicle and the phase separation can only be explained by fusion of a lo GUV with a ld GUV. A fusion event leads to an overall lipid mixture that exhibits phase separation and contains both fluorescent dyes. Note that the lipid mixture after fusion represents the mixture used for the division experiments in the main. Scale bar: 10  $\mu\text{m}$ .

### 3.15 Figure S15: Phase separation can be restored through $\text{Ca}^{2+}$ -mediated fusion of SUVs to single-phased GUVs

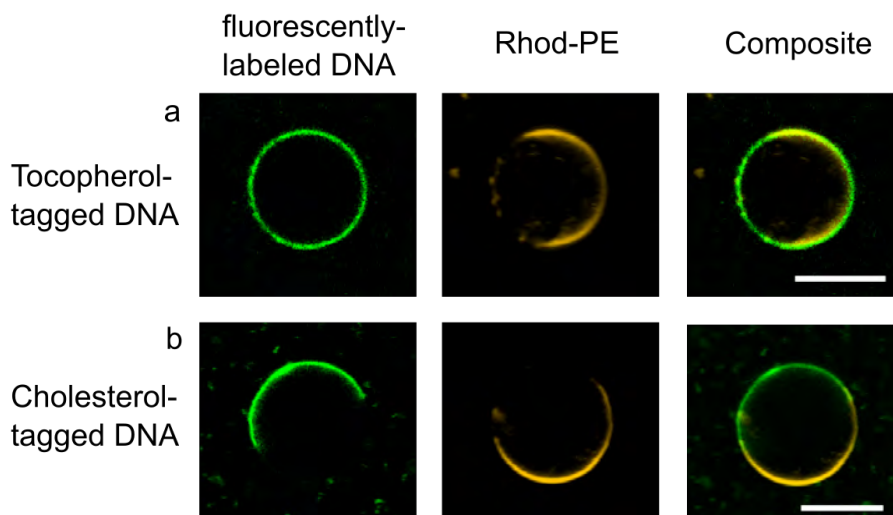


#### Supporting Figure S15

Phase separation can be restored through  $\text{Ca}^{2+}$ -mediated fusion of SUVs to single-phased GUVs. **a** Schematic illustration of a sustainable vesicle growth and division cycle mediated by calcium ions. **b**, **c** Representative confocal fluorescence images of fluorescently-labeled ld-phase GUVs (orange,  $\lambda_{ex} = 561$  nm) in a feeding bath of lo-phase SUVs (green,  $\lambda_{ex} = 488$  nm) prior (**b**) and after (**c**) addition of 20 mM  $\text{CaCl}_2$ . SUV fusion restores the phase separation of the GUV.



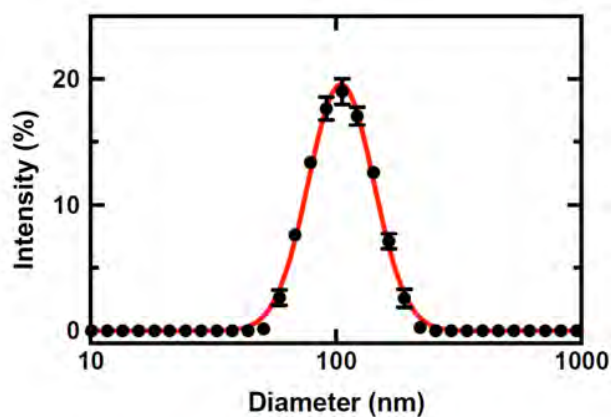
### 3.16 Figure S16: Tocopherol-tagged DNA is homogeneously distributed in the lo- and ld-phases of phase-separated GUVs



#### Supporting Figure S16

Tocopherol-tagged DNA is homogeneously distributed in the lo- and ld-phases of phase-separated GUVs. Confocal fluorescence images of GUVs (Lipid Mix 1) upon addition of fluorescently-labeled DNA ( $\lambda_{ex} = 405$  nm) with (a) a tocopherol and (b) a cholesterol modification (left images). The ld phase is labelled with 18:1 Liss Rhod PE ( $\lambda_{ex} = 561$  nm, middle images). Composite images are shown on the right. Whereas cholesterol-tagged DNA is preferentially localized in the lo-phase of phase-separated GUVs, tocopherol-tagged DNA is homogeneously distributed within both lo- and ld-phases. For the DNA fusion experiments (Figure 6, main text) we can thus use cholesterol-tagged DNA to selectively label the lo-phase and a complementary tocopherol-tagged DNA for the ld phase. Here,  $1 \mu\text{M}$  fluorescently-labeled (Atto390) DNA,  $10 \text{ mM}$   $\text{MgCl}_2$  and  $1\times$  PBS matching the osmolarity of the sucrose solution used for electroformation were added to a solution of phase-separated vesicles. Scale bar:  $10 \mu\text{m}$ .

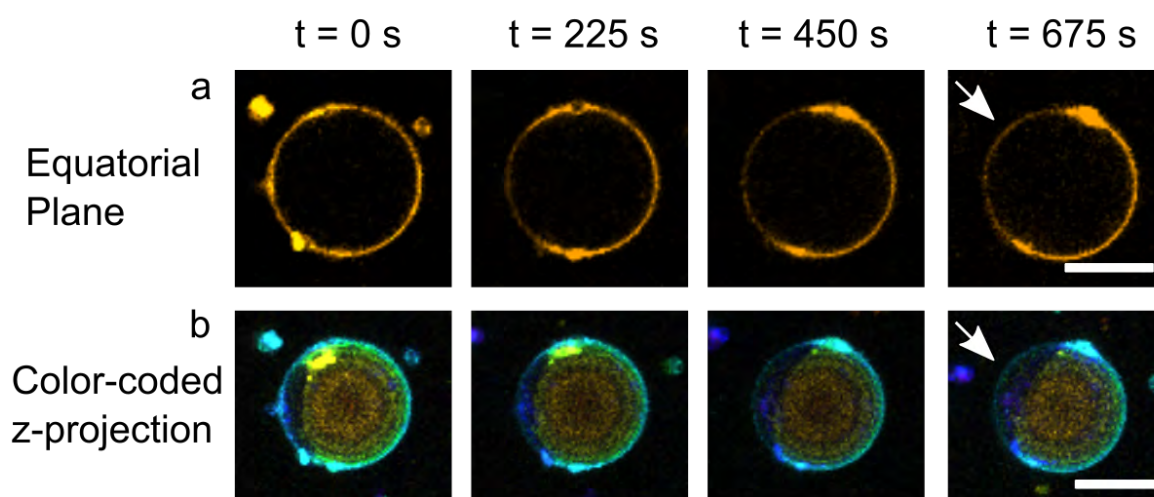
### 3.17 Figure S17: DLS of lo SUVs



#### Supporting Figure S17

Intensity distribution of the diameters of lo SUVs used for the regrowth of phase-separated GUVs, determined by dynamic light scattering (DLS). 3 mM SUVs (49.5 % DOPC, 49.5 % cholesterol, 1 % CF PE) were produced using the extrusion method with a 100 nm membrane filter in a 300 mM sucrose solution. The measurements were performed using a solution of 1 mL of 100  $\mu$ M SUVs. The average and standard deviation values were determined from 10 individual runs. The distribution was fitted with a log-normal Gaussian distribution (red line), revealing a mean diameter of  $115.1 \pm 1.4$  nm. This slightly larger measured hydrodynamic diameter is typical for SUVs extruded with a 100 nm membrane.

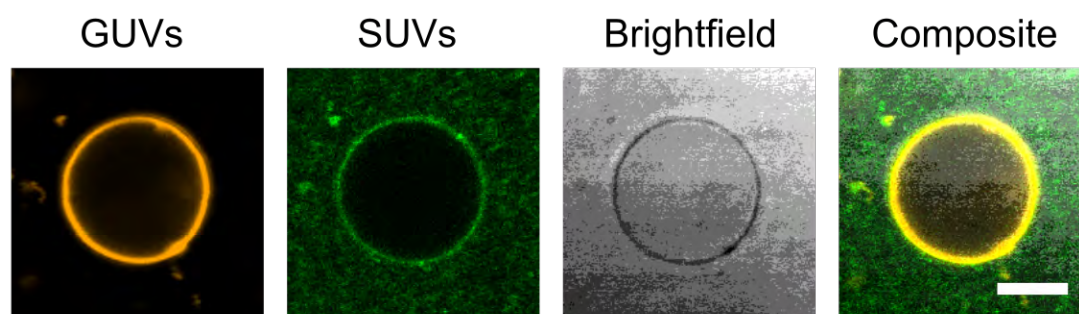
### 3.18 Figure S18: DNA-mediated vesicle fusion leads to growth of lo-phase of initially single-phased GUVs



#### Supporting Figure S18

DNA-mediated vesicle fusion leads to growth of lo-phase of initially single-phased ld GUVs. Confocal fluorescence time series of the equatorial plane (a) as well as color-coded z-projection (b) of a growing fluorescently-labeled GUV (18:1 Liss Rhod PE,  $\lambda_{ex} = 561$  nm) in presence of SUVs. Lo-phase SUVs (50% cholesterol, 50% DOPC) and ld-GUVs (20% CL, 74.25% DPPC, 4.75% DOPC, 1% Liss Rhod PE) were incubated with complementary cholesterol-tagged and tocopherol-tagged DNA, respectively. After incubation, lo-SUVs and ld-GUVs were mixed in presence of 10 mM  $MgCl_2$  and imaged over time. Duplex formation brings SUVs and GUVs in close proximity, eventually leading to vesicle fusion. This can be seen in form of the growing lo-phase of the GUV. Scale bar: 20  $\mu m$ .

### 3.19 Figure S19: DNA-functionalized lo SUVs do not fuse to plain ld GUV



#### Supporting Figure S19

DNA-functionalized lo SUVs do not fuse to bare ld GUV. Confocal fluorescence images of a fluorescently-labeled single-phase GUV (18:1 Liss Rhod PE,  $\lambda_{ex} = 561$  nm) in presence of SUVs incubated with cholesterol-tagged fusion DNA as well as cholesterol-tagged 6-FAM DNA (for labelling purposes,  $\lambda_{ex} = 488$  nm, see Methods). Lo-phase SUVs (50 % cholesterol, 50 % DOPC) were incubated with 1  $\mu$ M DNA #1 and #2 in presence of 5 mM  $MgCl_2$  for 20 minutes and afterwards mixed with ld-GUVs (20 % CL, 74.25 % DPPC and 4.75 % DOPC, 1 % Liss Rhod PE). Note that the tocopherol-tagged fusion DNA #3 was omitted. In this control experiment, no vesicle fusion leading to the formation of phase-separated GUVs could be detected. However, the presence of magnesium ions leads to the attachment of SUVs to the GUVs as visible in the representative confocal fluorescence image. It is conceivable that the single-stranded DNA acts as a spacer which prevents fusion. Scale bar: 10  $\mu$ m.

## 4 Supporting Notes

### 4.1 Note S1: Derivation of theoretical prediction

If we look at the initially spherical vesicle with an initial radius of  $r_0$  and a lipid ratio  $l$  the initial volume and areas are given by

$$V_0 = \frac{4}{3} \cdot \pi \cdot r_0^3 \quad (1)$$

$$A_{tot} = 4 \cdot \pi \cdot r_0^2 \quad (2)$$

$$A_{ld} = l \cdot A_{tot} \quad (3)$$

$$A_{lo} = (1 - l) \cdot A_{tot}. \quad (4)$$

The lipid phases can be represented as sphere segments with radius  $r_0$  and a height of

$$h_{ld} = A_{ld}/(2 \cdot \pi \cdot r_0) = 2 \cdot l \cdot r_0 \quad (5)$$

$$h_{lo} = A_{lo}/(2 \cdot \pi \cdot r_0) = 2 \cdot (1 - l) \cdot r_0 \quad (6)$$

and a base area of

$$s_0 = \sqrt{\frac{A_{ld}}{\pi} - h_{ld}^2} = 2 \cdot r_0 \cdot \sqrt{l - l^2}. \quad (7)$$

If the outer osmolarity is increased from  $C_0$  to  $C$  the vesicle will deflate and its volume reduce to

$$V = V_0 \cdot \frac{C_0}{C}. \quad (8)$$

We assume that the vesicle will deform in a way that the line tension, i.e. the circumference of the base of the spherical caps, gets minimized. This leads again to two spherical caps for each phase with the same reduced radius of the base of the spherical cap  $s$ . We can now define a division parameter  $d$  that quantifies the progress of the division process as

$$d = 1 - s/s_0. \quad (9)$$

The volume of each cap is then given by

$$V_i = \frac{\pi}{3} \left( r_i \pm \sqrt{r_i^2 - s^2} \right) \left( s^2 + r_i \left( r_i \pm \sqrt{r_i^2 - s^2} \right) \right) \quad (10)$$

with  $i = ld, lo$  and  $r_i$  the respective radius of the sphere segments. The area of the new sphere segments stay the same as before and are given by

$$A_i = 2 \cdot \pi \cdot r_i \cdot \left( r_i \pm \sqrt{r_i^2 - s^2} \right) \quad (11)$$

Inserting Eq. (11) into Eq. (10) leads to

$$V_i = \frac{\pi}{3} \frac{A_i}{2\pi r_i} \left( s^2 + \frac{A_i}{2\pi} \right) \quad (12)$$

The radii  $r_i$  of the spherical caps are given by

$$r_i = \frac{A_i}{2\pi h_{i,2}} \quad (13)$$

with

$$h_{i,2} = \sqrt{\frac{A_i}{\pi} - s^2} \quad (14)$$

the respective new height of the sphere segments. Inserting Eqs. (7), (9), (13) and (14) into Eq. (12) leads to

$$V_i = \frac{\pi}{3} \sqrt{\frac{A_i}{\pi} - 4r_0^2(l-l^2)(1-d)^2} \left( 4r_0^2(l-l^2)(1-d)^2 + \frac{A_i}{2\pi} \right) \quad (15)$$

By replacing  $A_i$  with Eq. (3) and Eq. (4) respectively and using Eq. (1) we obtain

$$V_{id} = V_0 \sqrt{l - (1-d)^2 \cdot (l-l^2)} \cdot (2 \cdot (1-d)^2(l-l^2) + l) \equiv V_0 \cdot T_1 \quad (16)$$

$$V_{io} = V_0 \sqrt{((1-l) - (1-d)^2 \cdot (l-l^2))} \cdot (2 \cdot (1-d)^2(l-l^2) + (1-l)) \equiv V_0 \cdot T_2. \quad (17)$$

Using Eq. (8) leads to the the direct dependence of the osmolarity ratio  $C/C_0$  and the division parameter  $d$

$$\frac{C}{C_0} = \frac{V_0}{V} = \frac{V_0}{V_{id} + V_{io}} = \frac{1}{T_1 + T_2}. \quad (18)$$

For symmetric vesicles with  $l = 0.5$  Eq. (18) becomes

$$C/C_0 = \frac{2}{\sqrt{2 - (1-d)^2((1-d)^2 + 1)}}. \quad (19)$$

## 4.2 Note S2: Considerations for osmolarity matching with CMNB-caged fluorescein

CMNB-caged fluorescein was dissolved in 100 mM Tris buffer to a final concentration of 50 mM. Since CMNB-caged fluorescein is twice negatively charged, the solution furthermore contains 100 mM potassium ions. This yields a total numerical osmolarity

of 250 mOsm. For the osmolarity measurements (Supporting Figure S9b), the caged fluorescein-containing solution was diluted in MQ to a final concentration of 2 mM CMNB-caged fluorescein leading to an overall osmolarity of 10 mOsm ( $\Pi_{caged,theo}$ ). Thus, an uncaging efficiency of 100% leads to a rise of the osmolarity from 10 mOsm to 14 mOsm ( $\Pi_{uncaged,theo}$ ) since each uncaged fluorescein molecule is accompanied by two CMNB molecules.

For the light-mediated division experiments, GUVs were electroformed in a solution of 13 mM sucrose and mixed with an isoosmolar solution of CMNB-caged fluorescein in a ratio of 1:2. Therefore, the final CMNB-caged fluorescein concentration is 1.73 mM, which, in a closed system, would yield a maximum osmolarity ratio of 1.27 assuming an uncaging efficiency of 100% (as obtained in the osmolarity measurements in Figure S9a). However, local concentration inhomogeneities, pipetting errors and different diffusion speeds of the uncaged molecules can lead to even higher local osmolarity changes. Since the lipid ratio for the vesicle presented in Figure 5 is  $l = 0.63$ , it should divide at an osmolarity ratio of 1.37 according to our model. This is hence in good agreement with the expected change in osmolarity due to the uncaging of CMNB-fluorescein.

### 4.3 Note S3: Osmolarity vs. osmolality

It is important to note that the measurements produced by the Osmomat 030 (Genotec GmbH) indicate the osmolality  $b$  of the sample solution. However, according to van't Hoff's law the osmotic pressure depends on the total particle concentration in the solution (osmolarity)  $C$ :  $\Pi = CRT$ , where  $C$  is the osmolarity of the solution,  $R$  the ideal gas constant and  $T$  the temperature. The osmolarity depends linearly on the osmolality  $C = (\rho_S - c_a) \cdot b$  where  $\rho_S$  is the density of the solution and  $c_a$  is the anhydrous solute concentration. The prefactor  $(\rho_S - c_a)$  is dependent on the solute. It can be neglected in most cases since  $(\rho_S - c_a) \approx 1 \text{ kg l}^{-1}$  [9]. However, for high concentrations of sugars as have been used here, the prefactor can deviate from  $1 \text{ kg l}^{-1}$ . Since we look at the osmotic pressure ratio  $C/C_0$ , the effect cancels out nevertheless. It can only play a role when using different solutions for the inner and outer phase like in Figure 3 (main text). However, even then, the deviation of the osmotic pressure ratio is negligible: For the solutions that were used here,  $(\rho_S - c_a)$  did not deviate more than 15% from  $1 \text{ kg l}^{-1}$ . Hence, the deviation of the osmotic pressure ratio  $C/C_0$  is below 1%. Furthermore, Moser and Frazer suggested that the osmotic pressure is better described by  $\Pi = \frac{n}{V'}RT = \rho_w b RT$ , for higher concentrations of glucose or sugar with  $V'$  the volume of pure water in the solution,  $\rho_w$  is the density of pure water and  $b$  is the osmolality of the solution [10]. Therefore, we used the osmolality instead of the osmolarity for the calculations.

## 5 Supporting Videos

### 5.1 Video S1: Conceptual model and confocal fluorescence time lapse of GUV division

Video S1 shows the theoretical prediction as well as experimental observations of the division process. It first visualizes the deformation and division process for increasing osmolarity ratios based on the predictions of the theoretical model. It then shows two independent time series of confocal fluorescence images of the division process of a phase-separated GUV (27.125 % DOPC, 24,75 % cholesterol, 37.125 % DPPC, 10 % CL, 1 % LissRhod PE) in an unsealed observation chamber which allows for water evaporation. The ld phase is labeled with LissRhod PE ( $\lambda_{ex} = 561$  nm) and 6-FAM-labeled cholesterol-tagged DNA ( $\lambda_{ex} = 488$  nm) partitioned into the lo phase. The time series were taken by manually tracking free-floating GUVs using the x-y-z piezo stage of the confocal microscope. The videos were generated by tracking the position of the GUV within the confocal image using the TrackMate plugin (ImageJ). Images were then truncated accordingly and the brightness- and contrast-adjusted fluorescence channels were overlaid. Note that within the confocal time series, other free-floating GUVs appear in the field of view, which show similar deformation stages as the GUV that was tracked.

### 5.2 Video S2: Division of phase-separated GUV triggered by enzymatic decomposition

Video S2 shows an overlay of confocal fluorescence and brightfield time series depicting the division process of a phase-separated GUV, whereby the osmolarity increase is achieved by the enzymatic decomposition of sucrose. Note that the phase-separated GUV is composed of a distinctly different lipid mixture (33 % SM, 33 % cholesterol and 33 % DOPC labeled with 1 % NBD PC  $\lambda_{ex} = 488$  nm, see Table S4, Mix No. 3). The fact that we still observe full division including neck fission indicates that our division mechanism is robust with respect to lipid type. GUVs were prepared via the electroformation method in 300 mM sucrose. After mixing with invertase, resulting in a final concentration of 44 mg l<sup>-1</sup> invertase the GUVs were observed in a sealed observation chamber under a confocal fluorescence microscope. NBD PC labeled the ld phase. The video was generated by tracking the position of the GUV within the confocal image using the TrackMate plugin (ImageJ). Images were then truncated accordingly and the brightness- and contrast-adjusted fluorescent and brightfield channel were overlaid. Scale bar: 10  $\mu$ m.



### 5.3 Video S3: Light-triggered division of phase-separated GUVs by uncaging of CMNB-fluorescein

Video S3 shows a confocal fluorescence time series of a phase-separated GUV (Supporting Table S4, Mix 1) before and during illumination with a 405 nm laser diode. The time series before 405 nm illumination depicts brightfield and fluorescence composite images of a phase-separated GUV ( $\lambda_{ex} = 561$  nm) for two minutes. The GUV does not show any deformation of its spherical shape. During 405 nm illumination, the GUV deforms at the phase-boundary leading to vesicle division within seven seconds due to uncaging of CMNB-fluorescein and hence a local osmolarity increase (see also Figure 5e in the main text for the calculation of the division parameter). After division, another composite confocal fluorescence image shows the divided vesicles post 405 nm illumination. Light-triggered release of caged fluorescein offers full spatiotemporal control of the division process of the selected vesicle.

### 5.4 Supporting Video S4: Calcium-mediated fusion of single-phase GUVs to restore phase-separation

Composite confocal fluorescence time series of single-phase GUVs (labeled with either Atto488-DOPE  $\lambda_{ex} = 488$  nm or Liss Rhod-PE  $\lambda_{ex} = 561$  nm) in an observation chamber to which 10 mM  $\text{CaCl}_2$  were added. Calcium-ions lead to an attachment and clustering of GUVs eventually resulting in vesicle fusion within minutes. This shows the possibility to regrow phase-separated GUVs.

## References

- [1] Angelova, M. I. & Dimitrov, D. S. Liposome electroformation. *Faraday Discussions of the Chemical Society* **81**, 303 (1986).
- [2] Phan, M. D. & Shin, K. Effects of cardiolipin on membrane morphology: a langmuir monolayer study. *Biophysical journal* **108**, 1977–1986 (2015). URL <https://pubmed.ncbi.nlm.nih.gov/25902437>.
- [3] Mills, T. T., Huang, J., Feigenson, G. W. & Nagle, J. F. Effects of cholesterol and unsaturated dopc lipid on chain packing of saturated gel-phase dppc bilayers. *General physiology and biophysics* **28**, 126–139 (2009). URL <https://pubmed.ncbi.nlm.nih.gov/19592709>.
- [4] Beales, P. A., Nam, J. & Vanderlick, T. K. Specific adhesion between dna-functionalized “janus” vesicles: size-limited clusters. *Soft Matter* **7**, 1747–1755 (2011).

- [5] Suga, K. & Umakoshi, H. Detection of nanosized ordered domains in dopc/dppc and dopc/ch binary lipid mixture systems of large unilamellar vesicles using a tempo quenching method. *Langmuir* **29**, 4830–4838 (2013). URL <https://doi.org/10.1021/la304768f>.
- [6] Kahya, N., Scherfeld, D., Bacia, K., Poolman, B. & Schwille, P. Probing lipid mobility of raft-exhibiting model membranes by fluorescence correlation spectroscopy. *Journal of Biological Chemistry* **278**, 28109–28115 (2003). URL <http://www.jbc.org/content/278/30/28109.abstract>. <http://www.jbc.org/content/278/30/28109.full.pdf+html>.
- [7] Chan, Y.-H. M., van Lengerich, B. & Boxer, S. G. Effects of linker sequences on vesicle fusion mediated by lipid-anchored dna oligonucleotides. *Proceedings of the National Academy of Sciences* **106**, 979–984 (2009).
- [8] Rodriguez, N., Pincet, F. & Cribier, S. Giant vesicles formed by gentle hydration and electroformation: A comparison by fluorescence microscopy. *Colloids and Surfaces B: Biointerfaces* **42**, 125 – 130 (2005). URL <http://www.sciencedirect.com/science/article/pii/S0927776505000603>.
- [9] Šklubalová, Z. & Zatloukal, Z. Conversion between osmolality and osmolarity of infusion solutions. *Scientia Pharmaceutica* **77**, 817–826 (2009).
- [10] Morse, H. N. & Frazer, J. C. W. The osmotic pressure and freezing-points of solutions of cane-sugar. *American Chemical Journal (Baltimore)* **34**, 1–99 (1905).

# Appendix B

## List of Publications

Publications (\* equal contribution, † corresponding author)

17. Walther T, **Jahnke K**, Abele T, Göpfrich K; ‘Printing DNA-based photore-sists in synthetic cells’, *submitted to Adv. Funct. Mat.*
16. **Jahnke K**, Maurer S.J., Weber C, Hernandez-Bücher J.E., Schönit A, D’Este E, Cavalcanti-Adam E.A., Göpfrich K; ‘Acto-myosin-assisted pulling of lipid nanotubes from lipid vesicles and cells’, *Nano Lett.* (2022), <https://doi.org/10.1021/acs.nanolett.1c04254>
15. **Jahnke K**, Huth V, Mersdorf U, Liu N, Göpfrich K; ‘Bottom-up assembly of synthetic cells with a DNA cytoskeletons’, *under review in ACS Nano*
14. Zhan P\*, **Jahnke K**\*†, Liu N†, Göpfrich K†; ‘DNA-based functional cytoskele-tons for synthetic cells’, *accepted in Nat. Chem.*
13. Staufer O, De Lora J, Bailoni E, Bazrafshan A, Benk A.S., **Jahnke K**, Manzer Z.A., Otrin L, Perez T.D., Sharon J, Steinkühler J, Adamala K.P., Jacobson B, Dogterom M, Göpfrich K, Stefanovic D, Atlas S.R., Grunze M, Lakin M.R., Shreve A.P., Spatz J.P., Lopez G.P.; ‘Science Forum: Building a community to engineer synthetic cells and organelles from the bottom-up’, *Elife* (2021), <https://doi.org/10.7554/eLife.73556>
12. Schönit A, Lo Giudice C, Hahnen N, Ollech D, **Jahnke K**, Göpfrich K, Cavalcanti-Adam EA; ‘Tuning epithelial cell-cell adhesion with functional DNA-E-cadherin hybrid linkers’, *Nano Lett.* (2021), <https://doi.org/10.1021/acs.nanolett.1c03780>
11. Lussier F, Schröter M, Diercks N, **Jahnke K**, Weber C, Frey C, Platzman I, Spatz J.P.; ‘pH-Triggered Assembly of Endomembrane Multicompartment in Synthetic Cells’, *ACS Syn. Bio.* (2021), <https://doi.org/10.1021/acssynbio.1c00472>
10. Abele T, Messer T, **Jahnke K**, Hippler M, Bastmeyer M, Wegener M, Göpfrich K; ‘Two-photon 3D laser printing inside synthetic cells’, *Adv. Mat.*, 202106709 (2021), <https://doi.org/10.1002/adma.202106709>

9. Dreher Y\*, **Jahnke K**\*<sup>†</sup>, Schröter M, Göpfrich K; ‘Light-Triggered Cargo Loading and Division of DNA-Containing Giant Unilamellar Vesicles’, *Nano Lett.* **21**, 5952-5957 (2021), <https://doi.org/10.1021/acs.nanolett.1c00822>
8. **Jahnke K**, Ritzmann N, Fichtler J, Nitschke A, Dreher Y, Abele T, Hoffhausen G, Platzman I, Schröder R, Spatz J.P., Müller D, Göpfrich K; ‘Proton-gradients from light-harvesting *E. coli* control DNA assemblies for synthetic cells’, *Nat. Comm.* **12**, 3967 (2021), <https://doi.org/10.1038/s41467-021-24103-x>
7. **Jahnke K**, Grubmüller H, Igaev M, Göpfrich K; ‘Choice of fluorophore affects dynamic DNA nanostructures’, *Nucleic Acids Res.* **49**, 4186-4195 (2021), <https://doi.org/10.1093/nar/gkab201>
6. Dreher Y\*, **Jahnke K**\*, Bobkova E, Spatz J.P., Göpfrich K; ‘Division and regrowth of phase-separated giant unilamellar vesicles’, *Angew. Chem. Int. Ed.* **133**, 10756-10764 (2020), <https://doi.org/10.1002/anie.202014174>
5. Haller B\*, **Jahnke K**\*, Weiss M, Göpfrich K, Platzman I, Spatz J.P.; ‘Autonomous Directional Motion of Cell-Sized Droplets’, *Adv. Int. Syst.* **3**, 2000190 (2020), <https://doi.org/10.1002/aisy.202000190>
4. Antona S, Abele T, **Jahnke K**, Dreher Y, Göpfrich K, Platzman I, Spatz J.P.; ‘Droplet-Based Combinatorial Assay for Cell Cytotoxicity and Cytokine Release Evaluation’, *Adv. Funct. Mat.* **30**, 2003479 (2020), <https://doi.org/10.1002/adfm.202003479>
3. **Jahnke K**, Weiss M, Weber C, Platzman I, Göpfrich K, Spatz J.P.; ‘Engineering Light-Responsive Contractile Actomyosin Networks with DNA Nanotechnology’, *Adv. Biosyst.* **4**, 2000102 (2020), <https://doi.org/10.1002/adbi.202000102>
2. Schaich M, Al Nahas K, Cama J, **Jahnke K**, Deshpande S, Dekker C, Keyser U.F.; ‘An integrated microfluidic platform for quantifying drug permeation across biomimetic vesicle membranes’, *Mol. Pharmaceutics* **16**, 2494-2501 (2019), <https://doi.org/10.1021/acs.molpharmaceut.9b00086>
1. **Jahnke K**, Weiss M, Antona S, Janiesch J-W, Platzman I, Göpfrich K, Spatz J.P.; ‘Programmable functionalization of surfactant-stabilized droplets via DNA-tags’, *Adv. Funct. Mat.* **29**, 1808647 (2019), <https://doi.org/10.1002/adfm.201808647>

# Appendix C

## Permissions

The following chapter comprises the permissions from publications that were not published under a Creative Commons Attribution 4.0 International License (CC BY) from which individual figures were adapted for the Introduction.

This is a License Agreement between Kevin Jahnke ("User") and Copyright Clearance Center, Inc. ("CCC") on behalf of the Rightsholder identified in the order details below. The license consists of the order details, the CCC Terms and Conditions below, and any Rightsholder Terms and Conditions which are included below.

All payments must be made in full to CCC in accordance with the CCC Terms and Conditions below.

Order Date	05-Feb-2022	Type of Use	Republish in a thesis/dissertation
Order License ID	1185788-1	Publisher	Nature Research
ISSN	1476-4679	Portion	Image/photo/illustration

## LICENSED CONTENT

Publication Title	Nature cell biology	Publication Type	e-Journal
Article Title	A unified vision of the building blocks of life.	Start Page	1015
		End Page	1015
Date	01/01/1999	Issue	9
Language	English	Volume	10
Country	United Kingdom of Great Britain and Northern Ireland	URL	<a href="http://www.nature.com/nature">http://www.nature.com/nature</a>
Rightsholder	Springer Nature BV		

## REQUEST DETAILS

Portion Type	Image/photo/illustration	Distribution	Worldwide
Number of images / photos / illustrations	1	Translation	Original language of publication
Format (select all that apply)	Print, Electronic	Copies for the disabled?	No
Who will republish the content?	Academic institution	Minor editing privileges?	No
Duration of Use	Life of current edition	Incidental promotional use?	No
Lifetime Unit Quantity	Up to 499	Currency	EUR
Rights Requested	Main product		

## NEW WORK DETAILS

Title	Rational engineering of cytoskeletons for synthetic cells	Institution name	Heidelberg University
Instructor name	Kerstin Göpfrich	Expected presentation date	2022-03-29

## ADDITIONAL DETAILS

The requesting person / organization to appear on the license	Kevin Jahnke
---	--------------

## REUSE CONTENT DETAILS

---

Title, description or numeric reference of the portion(s)	Figure 1	Title of the article/chapter the portion is from	A unified vision of the building blocks of life.
Editor of portion(s)	Marth, Jamey D.	Author of portion(s)	Marth, Jamey D.
Volume of serial or monograph	10	Publication date of portion	2008-09-01
Page or page range of portion	1015-1015		

## RIGHTSHOLDER TERMS AND CONDITIONS

If you are placing a request on behalf of/for a corporate organization, please use RightsLink. For further information visit <http://www.nature.com/reprints/permission-requests.html> and <https://www.springer.com/gp/rights-permissions/obtaining-permissions/882>. If the content you are requesting to reuse is under a CC-BY 4.0 licence (or previous version), you do not need to seek permission from Springer Nature for this reuse as long as you provide appropriate credit to the original publication. <https://creativecommons.org/licenses/by/4.0/>

## CCC Terms and Conditions

1. Description of Service; Defined Terms. This Republication License enables the User to obtain licenses for republication of one or more copyrighted works as described in detail on the relevant Order Confirmation (the "Work(s)"). Copyright Clearance Center, Inc. ("CCC") grants licenses through the Service on behalf of the rightsholder identified on the Order Confirmation (the "Rightsholder"). "Republication", as used herein, generally means the inclusion of a Work, in whole or in part, in a new work or works, also as described on the Order Confirmation. "User", as used herein, means the person or entity making such republication.
2. The terms set forth in the relevant Order Confirmation, and any terms set by the Rightsholder with respect to a particular Work, govern the terms of use of Works in connection with the Service. By using the Service, the person transacting for a republication license on behalf of the User represents and warrants that he/she/it (a) has been duly authorized by the User to accept, and hereby does accept, all such terms and conditions on behalf of User, and (b) shall inform User of all such terms and conditions. In the event such person is a "freelancer" or other third party independent of User and CCC, such party shall be deemed jointly a "User" for purposes of these terms and conditions. In any event, User shall be deemed to have accepted and agreed to all such terms and conditions if User republishes the Work in any fashion.
3. Scope of License; Limitations and Obligations.
  - 3.1. All Works and all rights therein, including copyright rights, remain the sole and exclusive property of the Rightsholder. The license created by the exchange of an Order Confirmation (and/or any invoice) and payment by User of the full amount set forth on that document includes only those rights expressly set forth in the Order Confirmation and in these terms and conditions, and conveys no other rights in the Work(s) to User. All rights not expressly granted are hereby reserved.
  - 3.2. General Payment Terms: You may pay by credit card or through an account with us payable at the end of the month. If you and we agree that you may establish a standing account with CCC, then the following terms apply: Remit Payment to: Copyright Clearance Center, 29118 Network Place, Chicago, IL 60673-1291. Payments Due: Invoices are payable upon their delivery to you (or upon our notice to you that they are available to you for downloading). After 30 days, outstanding amounts will be subject to a service charge of 1-1/2% per month or, if less, the maximum rate allowed by applicable law. Unless otherwise specifically set forth in the Order Confirmation or in a separate written agreement signed by CCC, invoices are due and payable on "net 30" terms. While User may exercise the rights licensed immediately upon issuance of the Order Confirmation, the license is automatically revoked and is null and void, as if it had never been issued, if complete payment for the license is not received on a timely basis either from User directly or

through a payment agent, such as a credit card company.

- 3.3. Unless otherwise provided in the Order Confirmation, any grant of rights to User (i) is "one-time" (including the editions and product family specified in the license), (ii) is non-exclusive and non-transferable and (iii) is subject to any and all limitations and restrictions (such as, but not limited to, limitations on duration of use or circulation) included in the Order Confirmation or invoice and/or in these terms and conditions. Upon completion of the licensed use, User shall either secure a new permission for further use of the Work(s) or immediately cease any new use of the Work(s) and shall render inaccessible (such as by deleting or by removing or severing links or other locators) any further copies of the Work (except for copies printed on paper in accordance with this license and still in User's stock at the end of such period).
  - 3.4. In the event that the material for which a republication license is sought includes third party materials (such as photographs, illustrations, graphs, inserts and similar materials) which are identified in such material as having been used by permission, User is responsible for identifying, and seeking separate licenses (under this Service or otherwise) for, any of such third party materials; without a separate license, such third party materials may not be used.
  - 3.5. Use of proper copyright notice for a Work is required as a condition of any license granted under the Service. Unless otherwise provided in the Order Confirmation, a proper copyright notice will read substantially as follows: "Republished with permission of [Rightsholder's name], from [Work's title, author, volume, edition number and year of copyright]; permission conveyed through Copyright Clearance Center, Inc. " Such notice must be provided in a reasonably legible font size and must be placed either immediately adjacent to the Work as used (for example, as part of a by-line or footnote but not as a separate electronic link) or in the place where substantially all other credits or notices for the new work containing the republished Work are located. Failure to include the required notice results in loss to the Rightsholder and CCC, and the User shall be liable to pay liquidated damages for each such failure equal to twice the use fee specified in the Order Confirmation, in addition to the use fee itself and any other fees and charges specified.
  - 3.6. User may only make alterations to the Work if and as expressly set forth in the Order Confirmation. No Work may be used in any way that is defamatory, violates the rights of third parties (including such third parties' rights of copyright, privacy, publicity, or other tangible or intangible property), or is otherwise illegal, sexually explicit or obscene. In addition, User may not conjoin a Work with any other material that may result in damage to the reputation of the Rightsholder. User agrees to inform CCC if it becomes aware of any infringement of any rights in a Work and to cooperate with any reasonable request of CCC or the Rightsholder in connection therewith.
4. Indemnity. User hereby indemnifies and agrees to defend the Rightsholder and CCC, and their respective employees and directors, against all claims, liability, damages, costs and expenses, including legal fees and expenses, arising out of any use of a Work beyond the scope of the rights granted herein, or any use of a Work which has been altered in any unauthorized way by User, including claims of defamation or infringement of rights of copyright, publicity, privacy or other tangible or intangible property.
  5. Limitation of Liability. UNDER NO CIRCUMSTANCES WILL CCC OR THE RIGHTSHOLDER BE LIABLE FOR ANY DIRECT, INDIRECT, CONSEQUENTIAL OR INCIDENTAL DAMAGES (INCLUDING WITHOUT LIMITATION DAMAGES FOR LOSS OF BUSINESS PROFITS OR INFORMATION, OR FOR BUSINESS INTERRUPTION) ARISING OUT OF THE USE OR INABILITY TO USE A WORK, EVEN IF ONE OF THEM HAS BEEN ADVISED OF THE POSSIBILITY OF SUCH DAMAGES. In any event, the total liability of the Rightsholder and CCC (including their respective employees and directors) shall not exceed the total amount actually paid by User for this license. User assumes full liability for the actions and omissions of its principals, employees, agents, affiliates, successors and assigns.
  6. Limited Warranties. THE WORK(S) AND RIGHT(S) ARE PROVIDED "AS IS". CCC HAS THE RIGHT TO GRANT TO USER THE RIGHTS GRANTED IN THE ORDER CONFIRMATION DOCUMENT. CCC AND THE RIGHTSHOLDER DISCLAIM ALL OTHER WARRANTIES RELATING TO THE WORK(S) AND RIGHT(S), EITHER EXPRESS OR IMPLIED, INCLUDING WITHOUT LIMITATION IMPLIED WARRANTIES OF MERCHANTABILITY OR FITNESS FOR A PARTICULAR PURPOSE.



ADDITIONAL RIGHTS MAY BE REQUIRED TO USE ILLUSTRATIONS, GRAPHS, PHOTOGRAPHS, ABSTRACTS, INSERTS OR OTHER PORTIONS OF THE WORK (AS OPPOSED TO THE ENTIRE WORK) IN A MANNER CONTEMPLATED BY USER; USER UNDERSTANDS AND AGREES THAT NEITHER CCC NOR THE RIGHTSHOLDER MAY HAVE SUCH ADDITIONAL RIGHTS TO GRANT.

7. Effect of Breach. Any failure by User to pay any amount when due, or any use by User of a Work beyond the scope of the license set forth in the Order Confirmation and/or these terms and conditions, shall be a material breach of the license created by the Order Confirmation and these terms and conditions. Any breach not cured within 30 days of written notice thereof shall result in immediate termination of such license without further notice. Any unauthorized (but licensable) use of a Work that is terminated immediately upon notice thereof may be liquidated by payment of the Rightsholder's ordinary license price therefor; any unauthorized (and unlicensable) use that is not terminated immediately for any reason (including, for example, because materials containing the Work cannot reasonably be recalled) will be subject to all remedies available at law or in equity, but in no event to a payment of less than three times the Rightsholder's ordinary license price for the most closely analogous licensable use plus Rightsholder's and/or CCC's costs and expenses incurred in collecting such payment.
8. Miscellaneous.
  - 8.1. User acknowledges that CCC may, from time to time, make changes or additions to the Service or to these terms and conditions, and CCC reserves the right to send notice to the User by electronic mail or otherwise for the purposes of notifying User of such changes or additions; provided that any such changes or additions shall not apply to permissions already secured and paid for.
  - 8.2. Use of User-related information collected through the Service is governed by CCC's privacy policy, available online here:<https://marketplace.copyright.com/rs-ui-web/mp/privacy-policy>
  - 8.3. The licensing transaction described in the Order Confirmation is personal to User. Therefore, User may not assign or transfer to any other person (whether a natural person or an organization of any kind) the license created by the Order Confirmation and these terms and conditions or any rights granted hereunder; provided, however, that User may assign such license in its entirety on written notice to CCC in the event of a transfer of all or substantially all of User's rights in the new material which includes the Work(s) licensed under this Service.
  - 8.4. No amendment or waiver of any terms is binding unless set forth in writing and signed by the parties. The Rightsholder and CCC hereby object to any terms contained in any writing prepared by the User or its principals, employees, agents or affiliates and purporting to govern or otherwise relate to the licensing transaction described in the Order Confirmation, which terms are in any way inconsistent with any terms set forth in the Order Confirmation and/or in these terms and conditions or CCC's standard operating procedures, whether such writing is prepared prior to, simultaneously with or subsequent to the Order Confirmation, and whether such writing appears on a copy of the Order Confirmation or in a separate instrument.
  - 8.5. The licensing transaction described in the Order Confirmation document shall be governed by and construed under the law of the State of New York, USA, without regard to the principles thereof of conflicts of law. Any case, controversy, suit, action, or proceeding arising out of, in connection with, or related to such licensing transaction shall be brought, at CCC's sole discretion, in any federal or state court located in the County of New York, State of New York, USA, or in any federal or state court whose geographical jurisdiction covers the location of the Rightsholder set forth in the Order Confirmation. The parties expressly submit to the personal jurisdiction and venue of each such federal or state court. If you have any comments or questions about the Service or Copyright Clearance Center, please contact us at 978-750-8400 or send an e-mail to [support@copyright.com](mailto:support@copyright.com).

This is a License Agreement between Kevin Jahnke ("User") and Copyright Clearance Center, Inc. ("CCC") on behalf of the Rightsholder identified in the order details below. The license consists of the order details, the CCC Terms and Conditions below, and any Rightsholder Terms and Conditions which are included below.

All payments must be made in full to CCC in accordance with the CCC Terms and Conditions below.

<b>Order Date</b>	28-Jan-2022	<b>Type of Use</b>	Republish in a thesis/dissertation
<b>Order License ID</b>	1183370-1	<b>Publisher Portion</b>	ANGEWANDTE CHEMIE Chart/graph/table/figure
<b>ISSN</b>	1521-3757		

## LICENSED CONTENT

<b>Publication Title</b>	Angewandte Chemie. Ausgabe A, Wissenschaftlicher Teil	<b>Rightsholder</b>	John Wiley & Sons - Books
<b>Article Title</b>	Amphipathic DNA Origami Nanoparticles to Scaffold and Deform Lipid Membrane Vesicles	<b>Publication Type</b>	e-Journal
<b>Author/Editor</b>	Gesellschaft Deutscher Chemiker.	<b>Start Page</b>	6601
<b>Date</b>	01/01/1949	<b>End Page</b>	6605
<b>Language</b>	German	<b>Issue</b>	22
<b>Country</b>	Germany	<b>Volume</b>	127

## REQUEST DETAILS

<b>Portion Type</b>	Chart/graph/table/figure	<b>Distribution</b>	Worldwide
<b>Number of charts / graphs / tables / figures requested</b>	1	<b>Translation</b>	Original language of publication
<b>Format (select all that apply)</b>	Print, Electronic	<b>Copies for the disabled?</b>	No
<b>Who will republish the content?</b>	Academic institution	<b>Minor editing privileges?</b>	No
<b>Duration of Use</b>	Life of current edition	<b>Incidental promotional use?</b>	No
<b>Lifetime Unit Quantity</b>	Up to 499	<b>Currency</b>	EUR
<b>Rights Requested</b>	Main product		

## NEW WORK DETAILS

<b>Title</b>	Rational engineering of cytoskeletons for synthetic cells	<b>Institution name</b>	Heidelberg University
<b>Instructor name</b>	Kerstin Göpfrich	<b>Expected presentation date</b>	2022-03-29

## ADDITIONAL DETAILS

The requesting person / organization to appear on the license Kevin Jahnke

## REUSE CONTENT DETAILS

<b>Title, description or numeric reference of the portion(s)</b>	Figure 1A	<b>Title of the article/chapter the portion is from</b>	Amphipathic DNA Origami Nanoparticles to Scaffold and Deform Lipid Membrane Vesicles
<b>Editor of portion(s)</b>	Dr.Czogalla, Aleksander; Kauert, Dominik J.; Dr.Franquelim, Henri G.; Dr.Uzunova, Veselina; Dr.Zhang, Yixin; Prof.Seidel, Ralf; Prof.Schwille, Petra	<b>Author of portion(s)</b>	Dr.Czogalla, Aleksander; Kauert, Dominik J.; Dr.Franquelim, Henri G.; Dr.Uzunova, Veselina; Dr.Zhang, Yixin; Prof.Seidel, Ralf; Prof.Schwille, Petra
<b>Volume of serial or monograph</b>	127	<b>Publication date of portion</b>	2015-05-26
<b>Page or page range of portion</b>	6601-6605		

## RIGHTSHOLDER TERMS AND CONDITIONS

No right, license or interest to any trademark, trade name, service mark or other branding ("Marks") of WILEY or its licensors is granted hereunder, and you agree that you shall not assert any such right, license or interest with respect thereto. You may not alter, remove or suppress in any manner any copyright, trademark or other notices displayed by the Wiley material. This Agreement will be void if the Type of Use, Format, Circulation, or Requestor Type was misrepresented during the licensing process. In no instance may the total amount of Wiley Materials used in any Main Product, Compilation or Collective work comprise more than 5% (if figures/tables) or 15% (if full articles/chapters) of the (entirety of the) Main Product, Compilation or Collective Work. Some titles may be available under an Open Access license. It is the Licensors' responsibility to identify the type of Open Access license on which the requested material was published, and comply fully with the terms of that license for the type of use specified Further details can be found on Wiley Online Library <http://olabout.wiley.com/WileyCDA/Section/id-410895.html>.

## CCC Terms and Conditions

1. Description of Service; Defined Terms. This Republication License enables the User to obtain licenses for republication of one or more copyrighted works as described in detail on the relevant Order Confirmation (the "Work(s)"). Copyright Clearance Center, Inc. ("CCC") grants licenses through the Service on behalf of the rightsholder identified on the Order Confirmation (the "Rightsholder"). "Republication", as used herein, generally means the inclusion of a Work, in whole or in part, in a new work or works, also as described on the Order Confirmation. "User", as used herein, means the person or entity making such republication.
2. The terms set forth in the relevant Order Confirmation, and any terms set by the Rightsholder with respect to a particular Work, govern the terms of use of Works in connection with the Service. By using the Service, the person transacting for a republication license on behalf of the User represents and warrants that he/she/it (a) has been duly authorized by the User to accept, and hereby does accept, all such terms and conditions on behalf of User, and (b) shall inform User of all such terms and conditions. In the event such person is a "freelancer" or other third party independent of User and CCC, such party shall be deemed jointly a "User" for purposes of these terms and conditions. In any event, User shall be deemed to have accepted and agreed to all such terms and conditions if User republishes the Work in any fashion.
3. Scope of License; Limitations and Obligations.

3.1. All Works and all rights therein, including copyright rights, remain the sole and exclusive property of the

Rightsholder. The license created by the exchange of an Order Confirmation (and/or any invoice) and payment by User of the full amount set forth on that document includes only those rights expressly set forth in the Order Confirmation and in these terms and conditions, and conveys no other rights in the Work(s) to User. All rights not expressly granted are hereby reserved.

- 3.2. General Payment Terms: You may pay by credit card or through an account with us payable at the end of the month. If you and we agree that you may establish a standing account with CCC, then the following terms apply: Remit Payment to: Copyright Clearance Center, 29118 Network Place, Chicago, IL 60673-1291. Payments Due: Invoices are payable upon their delivery to you (or upon our notice to you that they are available to you for downloading). After 30 days, outstanding amounts will be subject to a service charge of 1-1/2% per month or, if less, the maximum rate allowed by applicable law. Unless otherwise specifically set forth in the Order Confirmation or in a separate written agreement signed by CCC, invoices are due and payable on "net 30" terms. While User may exercise the rights licensed immediately upon issuance of the Order Confirmation, the license is automatically revoked and is null and void, as if it had never been issued, if complete payment for the license is not received on a timely basis either from User directly or through a payment agent, such as a credit card company.
  - 3.3. Unless otherwise provided in the Order Confirmation, any grant of rights to User (i) is "one-time" (including the editions and product family specified in the license), (ii) is non-exclusive and non-transferable and (iii) is subject to any and all limitations and restrictions (such as, but not limited to, limitations on duration of use or circulation) included in the Order Confirmation or invoice and/or in these terms and conditions. Upon completion of the licensed use, User shall either secure a new permission for further use of the Work(s) or immediately cease any new use of the Work(s) and shall render inaccessible (such as by deleting or by removing or severing links or other locators) any further copies of the Work (except for copies printed on paper in accordance with this license and still in User's stock at the end of such period).
  - 3.4. In the event that the material for which a republication license is sought includes third party materials (such as photographs, illustrations, graphs, inserts and similar materials) which are identified in such material as having been used by permission, User is responsible for identifying, and seeking separate licenses (under this Service or otherwise) for, any of such third party materials; without a separate license, such third party materials may not be used.
  - 3.5. Use of proper copyright notice for a Work is required as a condition of any license granted under the Service. Unless otherwise provided in the Order Confirmation, a proper copyright notice will read substantially as follows: "Republished with permission of [Rightsholder's name], from [Work's title, author, volume, edition number and year of copyright]; permission conveyed through Copyright Clearance Center, Inc. " Such notice must be provided in a reasonably legible font size and must be placed either immediately adjacent to the Work as used (for example, as part of a by-line or footnote but not as a separate electronic link) or in the place where substantially all other credits or notices for the new work containing the republished Work are located. Failure to include the required notice results in loss to the Rightsholder and CCC, and the User shall be liable to pay liquidated damages for each such failure equal to twice the use fee specified in the Order Confirmation, in addition to the use fee itself and any other fees and charges specified.
  - 3.6. User may only make alterations to the Work if and as expressly set forth in the Order Confirmation. No Work may be used in any way that is defamatory, violates the rights of third parties (including such third parties' rights of copyright, privacy, publicity, or other tangible or intangible property), or is otherwise illegal, sexually explicit or obscene. In addition, User may not conjoin a Work with any other material that may result in damage to the reputation of the Rightsholder. User agrees to inform CCC if it becomes aware of any infringement of any rights in a Work and to cooperate with any reasonable request of CCC or the Rightsholder in connection therewith.
4. Indemnity. User hereby indemnifies and agrees to defend the Rightsholder and CCC, and their respective employees and directors, against all claims, liability, damages, costs and expenses, including legal fees and expenses, arising out of any use of a Work beyond the scope of the rights granted herein, or any use of a Work

which has been altered in any unauthorized way by User, including claims of defamation or infringement of rights of copyright, publicity, privacy or other tangible or intangible property.

5. **Limitation of Liability.** UNDER NO CIRCUMSTANCES WILL CCC OR THE RIGHTSHOLDER BE LIABLE FOR ANY DIRECT, INDIRECT, CONSEQUENTIAL OR INCIDENTAL DAMAGES (INCLUDING WITHOUT LIMITATION DAMAGES FOR LOSS OF BUSINESS PROFITS OR INFORMATION, OR FOR BUSINESS INTERRUPTION) ARISING OUT OF THE USE OR INABILITY TO USE A WORK, EVEN IF ONE OF THEM HAS BEEN ADVISED OF THE POSSIBILITY OF SUCH DAMAGES. In any event, the total liability of the Rightsholder and CCC (including their respective employees and directors) shall not exceed the total amount actually paid by User for this license. User assumes full liability for the actions and omissions of its principals, employees, agents, affiliates, successors and assigns.
6. **Limited Warranties.** THE WORK(S) AND RIGHT(S) ARE PROVIDED "AS IS". CCC HAS THE RIGHT TO GRANT TO USER THE RIGHTS GRANTED IN THE ORDER CONFIRMATION DOCUMENT. CCC AND THE RIGHTSHOLDER DISCLAIM ALL OTHER WARRANTIES RELATING TO THE WORK(S) AND RIGHT(S), EITHER EXPRESS OR IMPLIED, INCLUDING WITHOUT LIMITATION IMPLIED WARRANTIES OF MERCHANTABILITY OR FITNESS FOR A PARTICULAR PURPOSE. ADDITIONAL RIGHTS MAY BE REQUIRED TO USE ILLUSTRATIONS, GRAPHS, PHOTOGRAPHS, ABSTRACTS, INSERTS OR OTHER PORTIONS OF THE WORK (AS OPPOSED TO THE ENTIRE WORK) IN A MANNER CONTEMPLATED BY USER; USER UNDERSTANDS AND AGREES THAT NEITHER CCC NOR THE RIGHTSHOLDER MAY HAVE SUCH ADDITIONAL RIGHTS TO GRANT.
7. **Effect of Breach.** Any failure by User to pay any amount when due, or any use by User of a Work beyond the scope of the license set forth in the Order Confirmation and/or these terms and conditions, shall be a material breach of the license created by the Order Confirmation and these terms and conditions. Any breach not cured within 30 days of written notice thereof shall result in immediate termination of such license without further notice. Any unauthorized (but licensable) use of a Work that is terminated immediately upon notice thereof may be liquidated by payment of the Rightsholder's ordinary license price therefor; any unauthorized (and unlicensable) use that is not terminated immediately for any reason (including, for example, because materials containing the Work cannot reasonably be recalled) will be subject to all remedies available at law or in equity, but in no event to a payment of less than three times the Rightsholder's ordinary license price for the most closely analogous licensable use plus Rightsholder's and/or CCC's costs and expenses incurred in collecting such payment.
8. **Miscellaneous.**
  - 8.1. User acknowledges that CCC may, from time to time, make changes or additions to the Service or to these terms and conditions, and CCC reserves the right to send notice to the User by electronic mail or otherwise for the purposes of notifying User of such changes or additions; provided that any such changes or additions shall not apply to permissions already secured and paid for.
  - 8.2. Use of User-related information collected through the Service is governed by CCC's privacy policy, available online here:<https://marketplace.copyright.com/rs-ui-web/mp/privacy-policy>
  - 8.3. The licensing transaction described in the Order Confirmation is personal to User. Therefore, User may not assign or transfer to any other person (whether a natural person or an organization of any kind) the license created by the Order Confirmation and these terms and conditions or any rights granted hereunder; provided, however, that User may assign such license in its entirety on written notice to CCC in the event of a transfer of all or substantially all of User's rights in the new material which includes the Work(s) licensed under this Service.
  - 8.4. No amendment or waiver of any terms is binding unless set forth in writing and signed by the parties. The Rightsholder and CCC hereby object to any terms contained in any writing prepared by the User or its principals, employees, agents or affiliates and purporting to govern or otherwise relate to the licensing transaction described in the Order Confirmation, which terms are in any way inconsistent with any terms set forth in the Order Confirmation and/or in these terms and conditions or CCC's standard operating procedures, whether such writing is prepared prior to, simultaneously with or subsequent to the Order Confirmation, and whether such writing appears on a copy of the Order Confirmation or in a separate instrument.

8.5. The licensing transaction described in the Order Confirmation document shall be governed by and construed under the law of the State of New York, USA, without regard to the principles thereof of conflicts of law. Any case, controversy, suit, action, or proceeding arising out of, in connection with, or related to such licensing transaction shall be brought, at CCC's sole discretion, in any federal or state court located in the County of New York, State of New York, USA, or in any federal or state court whose geographical jurisdiction covers the location of the Rightsholder set forth in the Order Confirmation. The parties expressly submit to the personal jurisdiction and venue of each such federal or state court. If you have any comments or questions about the Service or Copyright Clearance Center, please contact us at 978-750-8400 or send an e-mail to [support@copyright.com](mailto:support@copyright.com).

v 1.1

# SPRINGER NATURE LICENSE TERMS AND CONDITIONS

Jan 29, 2022

This Agreement between Kevin Jahnke ("You") and Springer Nature ("Springer Nature") consists of your license details and the terms and conditions provided by Springer Nature and Copyright Clearance Center.

License Number	5238280027567
License date	Jan 29, 2022
Licensed Content Publisher	Springer Nature
Licensed Content Publication	Nature Biotechnology
Licensed Content Title	Photosynthetic artificial organelles sustain and control ATP-dependent reactions in a protocellular system
Licensed Content Author	Keel Yong Lee et al
Licensed Content Date	May 28, 2018
Type of Use	Thesis/Dissertation
Requestor type	non-commercial (non-profit)
Format	print and electronic
Portion	figures/tables/illustrations
Number of figures/tables/illustrations	1
High-res required	no
Will you be translating?	no
Circulation/distribution	1 - 29
Author of this Springer Nature content	no
Title	Rational engineering of cytoskeletons for synthetic cells
Institution name	Heidelberg University
Expected presentation date	Mar 2022
Order reference number	1
Portions	Figure 4h, i and j
Requestor Location	Kevin Jahnke Jahnstraße 29  Heidelberg, other Germany Attn: Kevin Jahnke
Total	<b>0.00 EUR</b>
Terms and Conditions	

## Springer Nature Customer Service Centre GmbH Terms and Conditions

This agreement sets out the terms and conditions of the licence (the **Licence**) between you and **Springer Nature Customer**

**Service Centre GmbH (the Licensor).** By clicking 'accept' and completing the transaction for the material (**Licensed Material**), you also confirm your acceptance of these terms and conditions.

## 1. Grant of License

1. 1. The Licensor grants you a personal, non-exclusive, non-transferable, world-wide licence to reproduce the Licensed Material for the purpose specified in your order only. Licences are granted for the specific use requested in the order and for no other use, subject to the conditions below.
1. 2. The Licensor warrants that it has, to the best of its knowledge, the rights to license reuse of the Licensed Material. However, you should ensure that the material you are requesting is original to the Licensor and does not carry the copyright of another entity (as credited in the published version).
1. 3. If the credit line on any part of the material you have requested indicates that it was reprinted or adapted with permission from another source, then you should also seek permission from that source to reuse the material.

## 2. Scope of Licence

2. 1. You may only use the Licensed Content in the manner and to the extent permitted by these Ts&Cs and any applicable laws.
2. 2. A separate licence may be required for any additional use of the Licensed Material, e.g. where a licence has been purchased for print only use, separate permission must be obtained for electronic re-use. Similarly, a licence is only valid in the language selected and does not apply for editions in other languages unless additional translation rights have been granted separately in the licence. Any content owned by third parties are expressly excluded from the licence.
2. 3. Similarly, rights for additional components such as custom editions and derivatives require additional permission and may be subject to an additional fee. Please apply to [Journalpermissions@springernature.com/bookpermissions@springernature.com](mailto:Journalpermissions@springernature.com/bookpermissions@springernature.com) for these rights.
2. 4. Where permission has been granted **free of charge** for material in print, permission may also be granted for any electronic version of that work, provided that the material is incidental to your work as a whole and that the electronic version is essentially equivalent to, or substitutes for, the print version.
2. 5. An alternative scope of licence may apply to signatories of the [STM Permissions Guidelines](#), as amended from time to time.

## 3. Duration of Licence

3. 1. A licence for is valid from the date of purchase ('Licence Date') at the end of the relevant period in the below table:

Scope of Licence	Duration of Licence
Post on a website	12 months
Presentations	12 months
Books and journals	Lifetime of the edition in the language purchased

## 4. Acknowledgement

4. 1. The Licensor's permission must be acknowledged next to the Licenced Material in print. In electronic form, this acknowledgement must be visible at the same time as the figures/tables/illustrations or abstract, and must be hyperlinked to the journal/book's homepage. Our required acknowledgement format is in the Appendix below.



## 5. Restrictions on use

5. 1. Use of the Licensed Material may be permitted for incidental promotional use and minor editing privileges e.g. minor adaptations of single figures, changes of format, colour and/or style where the adaptation is credited as set out in Appendix 1 below. Any other changes including but not limited to, cropping, adapting, omitting material that affect the meaning, intention or moral rights of the author are strictly prohibited.
5. 2. You must not use any Licensed Material as part of any design or trademark.
5. 3. Licensed Material may be used in Open Access Publications (OAP) before publication by Springer Nature, but any Licensed Material must be removed from OAP sites prior to final publication.

## 6. Ownership of Rights

6. 1. Licensed Material remains the property of either Licensor or the relevant third party and any rights not explicitly granted herein are expressly reserved.

## 7. Warranty

IN NO EVENT SHALL LICENSOR BE LIABLE TO YOU OR ANY OTHER PARTY OR ANY OTHER PERSON OR FOR ANY SPECIAL, CONSEQUENTIAL, INCIDENTAL OR INDIRECT DAMAGES, HOWEVER CAUSED, ARISING OUT OF OR IN CONNECTION WITH THE DOWNLOADING, VIEWING OR USE OF THE MATERIALS REGARDLESS OF THE FORM OF ACTION, WHETHER FOR BREACH OF CONTRACT, BREACH OF WARRANTY, TORT, NEGLIGENCE, INFRINGEMENT OR OTHERWISE (INCLUDING, WITHOUT LIMITATION, DAMAGES BASED ON LOSS OF PROFITS, DATA, FILES, USE, BUSINESS OPPORTUNITY OR CLAIMS OF THIRD PARTIES), AND WHETHER OR NOT THE PARTY HAS BEEN ADVISED OF THE POSSIBILITY OF SUCH DAMAGES. THIS LIMITATION SHALL APPLY NOTWITHSTANDING ANY FAILURE OF ESSENTIAL PURPOSE OF ANY LIMITED REMEDY PROVIDED HEREIN.

## 8. Limitations

8. 1. **BOOKS ONLY:** Where 'reuse in a dissertation/thesis' has been selected the following terms apply: Print rights of the final author's accepted manuscript (for clarity, NOT the published version) for up to 100 copies, electronic rights for use only on a personal website or institutional repository as defined by the Sherpa guideline ([www.sherpa.ac.uk/romeo/](http://www.sherpa.ac.uk/romeo/)).
8. 2. For content reuse requests that qualify for permission under the [STM Permissions Guidelines](#), which may be updated from time to time, the STM Permissions Guidelines supersede the terms and conditions contained in this licence.

## 9. Termination and Cancellation

9. 1. Licences will expire after the period shown in Clause 3 (above).
9. 2. Licensee reserves the right to terminate the Licence in the event that payment is not received in full or if there has been a breach of this agreement by you.

### Appendix 1 — Acknowledgements:

#### **For Journal Content:**

Reprinted by permission from [the Licensor]: [Journal Publisher (e.g. Nature/Springer/Palgrave)] [JOURNAL NAME] [REFERENCE CITATION (Article name, Author(s) Name), [COPYRIGHT] (year of publication)]

**For Advance Online Publication papers:**

Reprinted by permission from [the Licensor]: [Journal Publisher (e.g. Nature/Springer/Palgrave)] [JOURNAL NAME] [REFERENCE CITATION (Article name, Author(s) Name), [COPYRIGHT] (year of publication), advance online publication, day month year (doi: 10.1038/sj.[JOURNAL ACRONYM].)]

**For Adaptations/Translations:**

Adapted/Translated by permission from [the Licensor]: [Journal Publisher (e.g. Nature/Springer/Palgrave)] [JOURNAL NAME] [REFERENCE CITATION (Article name, Author(s) Name), [COPYRIGHT] (year of publication)]

**Note: For any republication from the British Journal of Cancer, the following credit line style applies:**

Reprinted/adapted/translated by permission from [the Licensor]: on behalf of Cancer Research UK: : [Journal Publisher (e.g. Nature/Springer/Palgrave)] [JOURNAL NAME] [REFERENCE CITATION (Article name, Author(s) Name), [COPYRIGHT] (year of publication)]

**For Advance Online Publication papers:**

Reprinted by permission from The [the Licensor]: on behalf of Cancer Research UK: [Journal Publisher (e.g. Nature/Springer/Palgrave)] [JOURNAL NAME] [REFERENCE CITATION (Article name, Author(s) Name), [COPYRIGHT] (year of publication), advance online publication, day month year (doi: 10.1038/sj.[JOURNAL ACRONYM].)]

**For Book content:**

Reprinted/adapted by permission from [the Licensor]: [Book Publisher (e.g. Palgrave Macmillan, Springer etc)] [Book Title] by [Book author(s)] [COPYRIGHT] (year of publication)

**Other Conditions:**

Version 1.3

Questions? [customer-care@copyright.com](mailto:customer-care@copyright.com) or +1-855-239-3415 (toll free in the US) or +1-978-646-2777.

This is a License Agreement between Kevin Jahnke ("User") and Copyright Clearance Center, Inc. ("CCC") on behalf of the Rightsholder identified in the order details below. The license consists of the order details, the CCC Terms and Conditions below, and any Rightsholder Terms and Conditions which are included below.

All payments must be made in full to CCC in accordance with the CCC Terms and Conditions below.

<b>Order Date</b>	05-Feb-2022	<b>Type of Use</b>	Republish in a thesis/dissertation
<b>Order License ID</b>	1185789-1	<b>Publisher</b>	AMERICAN ASSOCIATION FOR THE ADVANCEMENT OF SCIENCE
<b>ISSN</b>	1095-9203	<b>Portion</b>	Chart/graph/table/figure

## LICENSED CONTENT

<b>Publication Title</b>	Science	<b>Publication Type</b>	e-Journal
<b>Article Title</b>	Light-powered CO <sub>2</sub> fixation in a chloroplast mimic with natural and synthetic parts.	<b>Start Page</b>	649
		<b>End Page</b>	654
		<b>Issue</b>	6491
<b>Author/Editor</b>	American Association for the Advancement of Science.	<b>Volume</b>	368
		<b>URL</b>	<a href="http://www.sciencemag.org/archive">http://www.sciencemag.org/archive</a>
<b>Date</b>	01/01/1880		
<b>Language</b>	English		
<b>Country</b>	United States of America		
<b>Rightsholder</b>	American Association for the Advancement of Science		

## REQUEST DETAILS

<b>Portion Type</b>	Chart/graph/table/figure	<b>Distribution</b>	Worldwide
<b>Number of charts / graphs / tables / figures requested</b>	1	<b>Translation</b>	Original language of publication
<b>Format (select all that apply)</b>	Print, Electronic	<b>Copies for the disabled?</b>	No
<b>Who will republish the content?</b>	Academic institution	<b>Minor editing privileges?</b>	No
<b>Duration of Use</b>	Life of current edition	<b>Incidental promotional use?</b>	No
<b>Lifetime Unit Quantity</b>	Up to 499	<b>Currency</b>	EUR
<b>Rights Requested</b>	Main product		

## NEW WORK DETAILS

<b>Title</b>	Rational engineering of cytoskeletons for synthetic cells	<b>Institution name</b>	Heidelberg University
--------------	---	-------------------------	-----------------------

Instructor name	Kerstin Göpfrich	Expected presentation date	2022-03-29
-----------------	------------------	----------------------------	------------

## ADDITIONAL DETAILS

---

Order reference number	N/A	The requesting person / organization to appear on the license	Kevin Jahnke
------------------------	-----	---	--------------

## REUSE CONTENT DETAILS

---

Title, description or numeric reference of the portion(s)	Figure 4	Title of the article/chapter the portion is from	Light-powered CO <sub>2</sub> fixation in a chloroplast mimic with natural and synthetic parts.
Editor of portion(s)	Miller, Tarryn E.; Beneyton, Thomas; Schwander, Thomas; Diehl, Christoph; Girault, Mathias; McLean, Richard; Chotel, Tanguy; Claus, Peter; Cortina, Niña Socorro; Baret, Jean-Christophe; Erb, Tobias J.	Author of portion(s)	Miller, Tarryn E.; Beneyton, Thomas; Schwander, Thomas; Diehl, Christoph; Girault, Mathias; McLean, Richard; Chotel, Tanguy; Claus, Peter; Cortina, Niña Socorro; Baret, Jean-Christophe; Erb, Tobias J.
Volume of serial or monograph	368	Issue, if republishing an article from a serial	6491
Page or page range of portion	649-654	Publication date of portion	2020-05-08

## RIGHTSHOLDER TERMS AND CONDITIONS

If the AAAS material covered by this permission was published in Science during the years 1974 - 1994, you must also obtain permission from the author, who may grant or withhold permission, and who may or may not charge a fee if permission is granted. See original article for author's address. This condition does not apply to news articles. Whenever possible, we ask that electronic uses of the AAAS material permitted herein include a hyperlink to the original work on AAAS's website (hyperlink may be embedded in the reference citation). AAAS material reproduced in your work identified herein must not account for more than 30% of the total contents of that work. AAAS must publish the full paper prior to use of any text. AAAS material must not imply any endorsement by the American Association for the Advancement of Science. AAAS makes no representations or warranties as to the accuracy of any information contained in the AAAS material covered by this permission, including any warranties of merchantability or fitness for a particular purpose.

## CCC Terms and Conditions

1. Description of Service; Defined Terms. This Republication License enables the User to obtain licenses for republication of one or more copyrighted works as described in detail on the relevant Order Confirmation (the "Work(s)"). Copyright Clearance Center, Inc. ("CCC") grants licenses through the Service on behalf of the rightsholder identified on the Order Confirmation (the "Rightsholder"). "Republication", as used herein, generally means the inclusion of a Work, in whole or in part, in a new work or works, also as described on the Order Confirmation. "User", as used herein, means the person or entity making such republication.
2. The terms set forth in the relevant Order Confirmation, and any terms set by the Rightsholder with respect to a particular Work, govern the terms of use of Works in connection with the Service. By using the Service, the person transacting for a republication license on behalf of the User represents and warrants that he/she/it (a) has been duly authorized by the User to accept, and hereby does accept, all such terms and conditions on behalf of User, and (b) shall inform User of all such terms and conditions. In the event such person is a "freelancer" or other third

party independent of User and CCC, such party shall be deemed jointly a "User" for purposes of these terms and conditions. In any event, User shall be deemed to have accepted and agreed to all such terms and conditions if User republishes the Work in any fashion.

### 3. Scope of License; Limitations and Obligations.

- 3.1. All Works and all rights therein, including copyright rights, remain the sole and exclusive property of the Rightsholder. The license created by the exchange of an Order Confirmation (and/or any invoice) and payment by User of the full amount set forth on that document includes only those rights expressly set forth in the Order Confirmation and in these terms and conditions, and conveys no other rights in the Work(s) to User. All rights not expressly granted are hereby reserved.
- 3.2. General Payment Terms: You may pay by credit card or through an account with us payable at the end of the month. If you and we agree that you may establish a standing account with CCC, then the following terms apply: Remit Payment to: Copyright Clearance Center, 29118 Network Place, Chicago, IL 60673-1291. Payments Due: Invoices are payable upon their delivery to you (or upon our notice to you that they are available to you for downloading). After 30 days, outstanding amounts will be subject to a service charge of 1-1/2% per month or, if less, the maximum rate allowed by applicable law. Unless otherwise specifically set forth in the Order Confirmation or in a separate written agreement signed by CCC, invoices are due and payable on "net 30" terms. While User may exercise the rights licensed immediately upon issuance of the Order Confirmation, the license is automatically revoked and is null and void, as if it had never been issued, if complete payment for the license is not received on a timely basis either from User directly or through a payment agent, such as a credit card company.
- 3.3. Unless otherwise provided in the Order Confirmation, any grant of rights to User (i) is "one-time" (including the editions and product family specified in the license), (ii) is non-exclusive and non-transferable and (iii) is subject to any and all limitations and restrictions (such as, but not limited to, limitations on duration of use or circulation) included in the Order Confirmation or invoice and/or in these terms and conditions. Upon completion of the licensed use, User shall either secure a new permission for further use of the Work(s) or immediately cease any new use of the Work(s) and shall render inaccessible (such as by deleting or by removing or severing links or other locators) any further copies of the Work (except for copies printed on paper in accordance with this license and still in User's stock at the end of such period).
- 3.4. In the event that the material for which a republication license is sought includes third party materials (such as photographs, illustrations, graphs, inserts and similar materials) which are identified in such material as having been used by permission, User is responsible for identifying, and seeking separate licenses (under this Service or otherwise) for, any of such third party materials; without a separate license, such third party materials may not be used.
- 3.5. Use of proper copyright notice for a Work is required as a condition of any license granted under the Service. Unless otherwise provided in the Order Confirmation, a proper copyright notice will read substantially as follows: "Republished with permission of [Rightsholder's name], from [Work's title, author, volume, edition number and year of copyright]; permission conveyed through Copyright Clearance Center, Inc. " Such notice must be provided in a reasonably legible font size and must be placed either immediately adjacent to the Work as used (for example, as part of a by-line or footnote but not as a separate electronic link) or in the place where substantially all other credits or notices for the new work containing the republished Work are located. Failure to include the required notice results in loss to the Rightsholder and CCC, and the User shall be liable to pay liquidated damages for each such failure equal to twice the use fee specified in the Order Confirmation, in addition to the use fee itself and any other fees and charges specified.
- 3.6. User may only make alterations to the Work if and as expressly set forth in the Order Confirmation. No Work may be used in any way that is defamatory, violates the rights of third parties (including such third parties' rights of copyright, privacy, publicity, or other tangible or intangible property), or is otherwise illegal, sexually explicit or obscene. In addition, User may not conjoin a Work with any other material that may result in damage to the reputation of the Rightsholder. User agrees to inform CCC if it becomes aware

of any infringement of any rights in a Work and to cooperate with any reasonable request of CCC or the Rightsholder in connection therewith.

4. Indemnity. User hereby indemnifies and agrees to defend the Rightsholder and CCC, and their respective employees and directors, against all claims, liability, damages, costs and expenses, including legal fees and expenses, arising out of any use of a Work beyond the scope of the rights granted herein, or any use of a Work which has been altered in any unauthorized way by User, including claims of defamation or infringement of rights of copyright, publicity, privacy or other tangible or intangible property.
5. Limitation of Liability. UNDER NO CIRCUMSTANCES WILL CCC OR THE RIGHTSHOLDER BE LIABLE FOR ANY DIRECT, INDIRECT, CONSEQUENTIAL OR INCIDENTAL DAMAGES (INCLUDING WITHOUT LIMITATION DAMAGES FOR LOSS OF BUSINESS PROFITS OR INFORMATION, OR FOR BUSINESS INTERRUPTION) ARISING OUT OF THE USE OR INABILITY TO USE A WORK, EVEN IF ONE OF THEM HAS BEEN ADVISED OF THE POSSIBILITY OF SUCH DAMAGES. In any event, the total liability of the Rightsholder and CCC (including their respective employees and directors) shall not exceed the total amount actually paid by User for this license. User assumes full liability for the actions and omissions of its principals, employees, agents, affiliates, successors and assigns.
6. Limited Warranties. THE WORK(S) AND RIGHT(S) ARE PROVIDED "AS IS". CCC HAS THE RIGHT TO GRANT TO USER THE RIGHTS GRANTED IN THE ORDER CONFIRMATION DOCUMENT. CCC AND THE RIGHTSHOLDER DISCLAIM ALL OTHER WARRANTIES RELATING TO THE WORK(S) AND RIGHT(S), EITHER EXPRESS OR IMPLIED, INCLUDING WITHOUT LIMITATION IMPLIED WARRANTIES OF MERCHANTABILITY OR FITNESS FOR A PARTICULAR PURPOSE. ADDITIONAL RIGHTS MAY BE REQUIRED TO USE ILLUSTRATIONS, GRAPHS, PHOTOGRAPHS, ABSTRACTS, INSERTS OR OTHER PORTIONS OF THE WORK (AS OPPOSED TO THE ENTIRE WORK) IN A MANNER CONTEMPLATED BY USER; USER UNDERSTANDS AND AGREES THAT NEITHER CCC NOR THE RIGHTSHOLDER MAY HAVE SUCH ADDITIONAL RIGHTS TO GRANT.
7. Effect of Breach. Any failure by User to pay any amount when due, or any use by User of a Work beyond the scope of the license set forth in the Order Confirmation and/or these terms and conditions, shall be a material breach of the license created by the Order Confirmation and these terms and conditions. Any breach not cured within 30 days of written notice thereof shall result in immediate termination of such license without further notice. Any unauthorized (but licensable) use of a Work that is terminated immediately upon notice thereof may be liquidated by payment of the Rightsholder's ordinary license price therefor; any unauthorized (and unlicensable) use that is not terminated immediately for any reason (including, for example, because materials containing the Work cannot reasonably be recalled) will be subject to all remedies available at law or in equity, but in no event to a payment of less than three times the Rightsholder's ordinary license price for the most closely analogous licensable use plus Rightsholder's and/or CCC's costs and expenses incurred in collecting such payment.
8. Miscellaneous.
  - 8.1. User acknowledges that CCC may, from time to time, make changes or additions to the Service or to these terms and conditions, and CCC reserves the right to send notice to the User by electronic mail or otherwise for the purposes of notifying User of such changes or additions; provided that any such changes or additions shall not apply to permissions already secured and paid for.
  - 8.2. Use of User-related information collected through the Service is governed by CCC's privacy policy, available online here:<https://marketplace.copyright.com/rs-ui-web/mp/privacy-policy>
  - 8.3. The licensing transaction described in the Order Confirmation is personal to User. Therefore, User may not assign or transfer to any other person (whether a natural person or an organization of any kind) the license created by the Order Confirmation and these terms and conditions or any rights granted hereunder; provided, however, that User may assign such license in its entirety on written notice to CCC in the event of a transfer of all or substantially all of User's rights in the new material which includes the Work(s) licensed under this Service.

- 8.4. No amendment or waiver of any terms is binding unless set forth in writing and signed by the parties. The Rightsholder and CCC hereby object to any terms contained in any writing prepared by the User or its principals, employees, agents or affiliates and purporting to govern or otherwise relate to the licensing transaction described in the Order Confirmation, which terms are in any way inconsistent with any terms set forth in the Order Confirmation and/or in these terms and conditions or CCC's standard operating procedures, whether such writing is prepared prior to, simultaneously with or subsequent to the Order Confirmation, and whether such writing appears on a copy of the Order Confirmation or in a separate instrument.
- 8.5. The licensing transaction described in the Order Confirmation document shall be governed by and construed under the law of the State of New York, USA, without regard to the principles thereof of conflicts of law. Any case, controversy, suit, action, or proceeding arising out of, in connection with, or related to such licensing transaction shall be brought, at CCC's sole discretion, in any federal or state court located in the County of New York, State of New York, USA, or in any federal or state court whose geographical jurisdiction covers the location of the Rightsholder set forth in the Order Confirmation. The parties expressly submit to the personal jurisdiction and venue of each such federal or state court. If you have any comments or questions about the Service or Copyright Clearance Center, please contact us at 978-750-8400 or send an e-mail to [support@copyright.com](mailto:support@copyright.com).

v 1.1





# Bibliography

1. Koshland, D. E. The Seven Pillars of Life. *Science* **295**, 2215–2216 (Mar. 2002).
2. Benner, S. A. Defining Life. *Astrobiology* **10**, 1021–1030 (Dec. 2010).
3. Schrodinger, E. & Penrose, R. *What is Life?* (Cambridge University Press, 2009).
4. Dawkins, R. & Davis, N. *The Selfish Gene* (Macat Library, July 2017).
5. Forterre, P. To be or not to be alive: How recent discoveries challenge the traditional definitions of viruses and life. *Studies in History and Philosophy of Science Part C: Studies in History and Philosophy of Biological and Biomedical Sciences* **59**, 100–108 (Oct. 2016).
6. Alberts, B. *et al.* *Molecular Biology of the Cell* (eds Wilson, J. & Hunt, T.) (W.W. Norton & Company, Aug. 2017).
7. Miller, T. E. *et al.* Light-powered CO<sub>2</sub> fixation in a chloroplast mimic with natural and synthetic parts. *Science* **368**, 649–654 (May 2020).
8. Sharon, N. & Lis, H. Lectins as Cell Recognition Molecules. *Science* **246**, 227–234 (Oct. 1989).
9. Cowin, P. & Burke, B. Cytoskeleton—membrane interactions. *Current Opinion in Cell Biology* **8**, 56–65 (Feb. 1996).
10. Mitchison, T. & Cramer, L. Actin-Based Cell Motility and Cell Locomotion. *Cell* **84**, 371–379 (Feb. 1996).
11. Rothmund, P. W. K. Folding DNA to create nanoscale shapes and patterns. *Nature* **440**, 297–302 (Mar. 2006).
12. Seeman, N. C. Nucleic acid junctions and lattices. *Journal of Theoretical Biology* **99**, 237–247 (Nov. 1982).
13. Seeman, N. C. & Sleiman, H. F. DNA nanotechnology. *Nature Reviews Materials* **3** (Nov. 2017).
14. Göpfrich, K., Platzman, I. & Spatz, J. P. Mastering Complexity: Towards Bottom-up Construction of Multifunctional Eukaryotic Synthetic Cells. *Trends in Biotechnology* **36**, 938–951 (Sept. 2018).
15. Marth, J. D. A unified vision of the building blocks of life. *Nature Cell Biology* **10**, 1015–1015 (Sept. 2008).

16. Rideau, E., Dimova, R., Schwille, P., Wurm, F. R. & Landfester, K. Liposomes and polymersomes: a comparative review towards cell mimicking. *Chemical Society Reviews* **47**, 8572–8610 (2018).
17. Nishimura, K. *et al.* Cell-Free Protein Synthesis inside Giant Unilamellar Vesicles Analyzed by Flow Cytometry. *Langmuir* **28**, 8426–8432 (May 2012).
18. Berhanu, S., Ueda, T. & Kuruma, Y. Artificial photosynthetic cell producing energy for protein synthesis. *Nature Communications* **10** (Mar. 2019).
19. Deshpande, S. *et al.* Spatiotemporal control of coacervate formation within liposomes. *Nature Communications* **10** (Apr. 2019).
20. Deng, N.-N. & Huck, W. T. S. Microfluidic Formation of Monodisperse Coacervate Organelles in Liposomes. *Angewandte Chemie International Edition* **56**, 9736–9740 (Aug. 2017).
21. Buddingh', B. C., Elzinga, J. & van Hest, J. C. M. Intercellular communication between artificial cells by allosteric amplification of a molecular signal. *Nature Communications* **11** (Apr. 2020).
22. Dupin, A. & Simmel, F. C. Signalling and differentiation in emulsion-based multi-compartmentalized in vitro gene circuits. *Nature Chemistry* **11**, 32–39 (Nov. 2018).
23. Lee, K. Y. *et al.* Photosynthetic artificial organelles sustain and control ATP-dependent reactions in a protocellular system. *Nature Biotechnology* **36**, 530–535 (May 2018).
24. Litschel, T. *et al.* Reconstitution of contractile actomyosin rings in vesicles. *Nature Communications* **12** (Apr. 2021).
25. Weiss, M. *et al.* Sequential bottom-up assembly of mechanically stabilized synthetic cells by microfluidics. *Nature Materials* **17**, 89–96 (Oct. 2017).
26. Otrin, L. *et al.* Toward Artificial Mitochondrion: Mimicking Oxidative Phosphorylation in Polymer and Hybrid Membranes. *Nano Letters* **17**, 6816–6821 (Oct. 2017).
27. Ohmann, A. *et al.* A synthetic enzyme built from DNA flips 107 lipids per second in biological membranes. *Nature Communications* **9** (June 2018).
28. Kurokawa, C. *et al.* DNA cytoskeleton for stabilizing artificial cells. *Proceedings of the National Academy of Sciences* **114**, 7228–7233 (June 2017).
29. Langecker, M. *et al.* Synthetic Lipid Membrane Channels Formed by Designed DNA Nanostructures. *Science* **338**, 932–936 (Nov. 2012).
30. Göpfrich, K. *et al.* Large-Conductance Transmembrane Porin Made from DNA Origami. *ACS Nano* **10**, 8207–8214 (Aug. 2016).
31. Parolini, L., Kotar, J., Michele, L. D. & Mognetti, B. M. Controlling Self-Assembly Kinetics of DNA-Functionalized Liposomes Using Toehold Exchange Mechanism. *ACS Nano* **10**, 2392–2398 (Feb. 2016).
32. Schwille, P. *et al.* MaxSynBio: Avenues Towards Creating Cells from the Bottom Up. *Angewandte Chemie International Edition* **57**, 13382–13392 (Sept. 2018).

33. Ho, B., Baryshnikova, A. & Brown, G. W. Unification of Protein Abundance Datasets Yields a Quantitative *Saccharomyces cerevisiae* Proteome. *Cell Systems* **6**, 192–205.e3 (Feb. 2018).
34. Marshall, W. F. *et al.* What determines cell size? *BMC Biology* **10** (Dec. 2012).
35. Cadart, C., Venkova, L., Recho, P., Lagomarsino, M. C. & Piel, M. The physics of cell-size regulation across timescales. *Nature Physics* **15**, 993–1004 (Aug. 2019).
36. Baret, J.-C. Surfactants in droplet-based microfluidics. *Lab Chip* **12**, 422–433 (2012).
37. Seemann, R., Fleury, J.-B. & Maass, C. C. Self-propelled droplets. *The European Physical Journal Special Topics* **225**, 2227–2240 (Nov. 2016).
38. Santiago, I. & Simmel, F. C. Self-Propulsion Strategies for Artificial Cell-Like Compartments. *Nanomaterials* **9**, 1680 (Nov. 2019).
39. Balasubramaniam, R. & Subramanian, R. S. Thermocapillary Migration of a Drop: An Exact Solution with Newtonian Interfacial Rheology and Stretching/Shrinkage of Interfacial Area Elements for Small Marangoni Numbers. *Annals of the New York Academy of Sciences* **1027**, 303–310 (Nov. 2004).
40. Balasubramaniam, R. & Subramanian, R. S. The migration of a drop in a uniform temperature gradient at large Marangoni numbers. *Physics of Fluids* **12**, 733–743 (Apr. 2000).
41. Gong, M. M. & Sinton, D. Turning the Page: Advancing Paper-Based Microfluidics for Broad Diagnostic Application. *Chemical Reviews* **117**, 8447–8480 (June 2017).
42. Zilionis, R. *et al.* Single-cell barcoding and sequencing using droplet microfluidics. *Nature Protocols* **12**, 44–73 (Dec. 2016).
43. Macosko, E. Z. *et al.* Highly Parallel Genome-wide Expression Profiling of Individual Cells Using Nanoliter Droplets. *Cell* **161**, 1202–1214 (May 2015).
44. deMello, A. J. Control and detection of chemical reactions in microfluidic systems. *Nature* **442**, 394–402 (July 2006).
45. Galdi, G. P. in *Fundamental Directions in Mathematical Fluid Mechanics* 1–70 (Birkhäuser Basel, 2000).
46. Rawicz, W., Olbrich, K., McIntosh, T., Needham, D. & Evans, E. Effect of Chain Length and Unsaturation on Elasticity of Lipid Bilayers. *Biophysical Journal* **79**, 328–339 (July 2000).
47. Lewis, B. A. & Engelman, D. M. Lipid bilayer thickness varies linearly with acyl chain length in fluid phosphatidylcholine vesicles. *Journal of Molecular Biology* **166**, 211–217 (May 1983).
48. Attwood, S., Choi, Y. & Leonenko, Z. Preparation of DOPC and DPPC Supported Planar Lipid Bilayers for Atomic Force Microscopy and Atomic Force Spectroscopy. *International Journal of Molecular Sciences* **14**, 3514–3539 (Feb. 2013).

49. Phillips, R., Kondev, J., Theriot, J., Garcia, H. G. & Orme, N. *Physical Biology of the Cell* (Garland Science, Oct. 2012).
50. Helfrich, W. Elastic Properties of Lipid Bilayers: Theory and Possible Experiments. *Zeitschrift für Naturforschung C* **28**, 693–703 (Dec. 1973).
51. Lipowsky, R. The conformation of membranes. *Nature* **349**, 475–481 (Feb. 1991).
52. Schwarz, U. *Theoretical Biophysics* Lecture Notes. 2021.
53. Seifert, U., Berndl, K. & Lipowsky, R. Shape transformations of vesicles: Phase diagram for spontaneous-curvature and bilayer-coupling models. *Physical Review A* **44**, 1182–1202 (July 1991).
54. Angelova, M. I. & Dimitrov, D. S. Liposome electroformation. *Faraday Discussions of the Chemical Society* **81**, 303 (1986).
55. Deshpande, S., Caspi, Y., Meijering, A. E. C. & Dekker, C. Octanol-assisted liposome assembly on chip. *Nature Communications* **7** (Jan. 2016).
56. Reeves, J. P. & Dowben, R. M. Formation and properties of thin-walled phospholipid vesicles. *Journal of Cellular Physiology* **73**, 49–60 (Feb. 1969).
57. Abkarian, M., Loiseau, E. & Massiera, G. Continuous droplet interface crossing encapsulation (cDICE) for high throughput monodisperse vesicle design. *Soft Matter* **7**, 4610 (2011).
58. Göpfrich, K. *et al.* One-Pot Assembly of Complex Giant Unilamellar Vesicle-Based Synthetic Cells. *ACS Synthetic Biology* **8**, 937–947 (May 2019).
59. Milo, R. & Phillips, R. *Cell Biology by the Numbers* (Garland Science, Dec. 2015).
60. Rothmund, P. W. K. *et al.* Design and Characterization of Programmable DNA Nanotubes. *Journal of the American Chemical Society* **126**, 16344–16352 (Nov. 2004).
61. Shen, Y. *et al.* Effects of Vimentin Intermediate Filaments on the Structure and Dynamics of In Vitro Multicomponent Interpenetrating Cytoskeletal Networks. *Physical Review Letters* **127** (Sept. 2021).
62. Ledbetter, M. C. & Porter, K. R. A "MICROTUBULE" IN PLANT CELL FINE STRUCTURE. *Journal of Cell Biology* **19**, 239–250 (Oct. 1963).
63. Holmes, K. C., Popp, D., Gebhard, W. & Kabsch, W. Atomic model of the actin filament. *Nature* **347**, 44–49 (Sept. 1990).
64. Pampaloni, F. *et al.* Thermal fluctuations of grafted microtubules provide evidence of a length-dependent persistence length. *Proceedings of the National Academy of Sciences* **103**, 10248–10253 (June 2006).
65. Gittes, F., Mickey, B., Nettleton, J. & Howard, J. Flexural rigidity of microtubules and actin filaments measured from thermal fluctuations in shape. *Journal of Cell Biology* **120**, 923–934 (Feb. 1993).

66. Molloy, J. E., Burns, J. E., Kendrick-Jones, J., Tregear, R. T. & White, D. C. S. Movement and force produced by a single myosin head. *Nature* **378**, 209–212 (Nov. 1995).
67. Tsai, F.-C., Stuhmann, B. & Koenderink, G. H. Encapsulation of Active Cytoskeletal Protein Networks in Cell-Sized Liposomes. *Langmuir* **27**, 10061–10071 (July 2011).
68. Bashirzadeh, Y., Wubshet, N. H. & Liu, A. P. Confinement Geometry Tunes Fascin-Actin Bundle Structures and Consequently the Shape of a Lipid Bilayer Vesicle. *Frontiers in Molecular Biosciences* **7** (Nov. 2020).
69. Juniper, M. P. N., Weiss, M., Platzman, I., Spatz, J. P. & Surrey, T. Spherical network contraction forms microtubule asters in confinement. *Soft Matter* **14**, 901–909 (2018).
70. Gavriljuk, K. *et al.* A self-organized synthetic morphogenic liposome responds with shape changes to local light cues. *Nature Communications* **12** (Mar. 2021).
71. Huang, P.-S., Boyken, S. E. & Baker, D. The coming of age of de novo protein design. *Nature* **537**, 320–327 (Sept. 2016).
72. Packer, M. S. & Liu, D. R. Methods for the directed evolution of proteins. *Nature Reviews Genetics* **16**, 379–394 (June 2015).
73. Milo, R., Jorgensen, P., Moran, U., Weber, G. & Springer, M. BioNumbers—the database of key numbers in molecular and cell biology. *Nucleic Acids Research* **38**, D750–D753 (Oct. 2009).
74. Caruthers, M. *et al.* in *Methods in Enzymology* 287–313 (Elsevier, 1987).
75. Meng, W. *et al.* An autonomous molecular assembler for programmable chemical synthesis. *Nature Chemistry* **8**, 542–548 (Apr. 2016).
76. Baumann, K. N. *et al.* Coating and Stabilization of Liposomes by Clathrin-Inspired DNA Self-Assembly. *ACS Nano* **14**, 2316–2323 (Jan. 2020).
77. Franquelim, H. G., Dietz, H. & Schwille, P. Reversible membrane deformations by straight DNA origami filaments. *Soft Matter* **17**, 276–287 (2021).
78. Franquelim, H. G., Khmelinskaia, A., Sobczak, J.-P., Dietz, H. & Schwille, P. Membrane sculpting by curved DNA origami scaffolds. *Nature Communications* **9** (Feb. 2018).
79. Czogalla, A. *et al.* Amphipathic DNA Origami Nanoparticles to Scaffold and Deform Lipid Membrane Vesicles. *Angewandte Chemie International Edition* **54**, 6501–6505 (Apr. 2015).
80. Jahnke, K. *et al.* Proton gradients from light-harvesting *E. coli* control DNA assemblies for synthetic cells. *Nature Communications* **12** (June 2021).
81. Green, L. N., Amodio, A., Subramanian, H. K. K., Ricci, F. & Franco, E. pH-Driven Reversible Self-Assembly of Micron-Scale DNA Scaffolds. *Nano Letters* **17**, 7283–7288 (Nov. 2017).

82. Fu, T. J. & Seeman, N. C. DNA double-crossover molecules. *Biochemistry* **32**, 3211–3220 (Apr. 1993).
83. Sa-Ardyen, P., Vologodskii, A. V. & Seeman, N. C. The Flexibility of DNA Double Crossover Molecules. *Biophysical Journal* **84**, 3829–3837 (June 2003).
84. Agarwal, S., Klocke, M. A., Pungchai, P. E. & Franco, E. Dynamic self-assembly of compartmentalized DNA nanotubes. *Nature Communications* **12** (June 2021).
85. Mohammed, A. M. & Schulman, R. Directing Self-Assembly of DNA Nanotubes Using Programmable Seeds. *Nano Letters* **13**, 4006–4013 (Aug. 2013).
86. Mohammed, A. M., Šulc, P., Zenk, J. & Schulman, R. Self-assembling DNA nanotubes to connect molecular landmarks. *Nature Nanotechnology* **12**, 312–316 (Dec. 2016).
87. Jorgenson, T. D., Mohammed, A. M., Agrawal, D. K. & Schulman, R. Self-Assembly of Hierarchical DNA Nanotube Architectures with Well-Defined Geometries. *ACS Nano* **11**, 1927–1936 (Jan. 2017).
88. Agrawal, D. K. *et al.* Terminating DNA Tile Assembly with Nanostructured Caps. *ACS Nano* **11**, 9770–9779 (Sept. 2017).
89. Jahnke, K. *et al.* Actomyosin-Assisted Pulling of Lipid Nanotubes from Lipid Vesicles and Cells. *Nano Letters* (Jan. 2022).
90. Haller, B. *et al.* Autonomous Directional Motion of Actin-Containing Cell-Sized Droplets. *Advanced Intelligent Systems* **3**, 2000190 (Nov. 2020).
91. Jahnke, K. *et al.* Engineering Light-Responsive Contractile Actomyosin Networks with DNA Nanotechnology. *Advanced Biosystems* **4**, 2000102 (July 2020).
92. Jahnke, K., Grubmüller, H., Igaev, M. & Göpfrich, K. Choice of fluorophore affects dynamic DNA nanostructures. *Nucleic Acids Research* **49**, 4186–4195 (Mar. 2021).
93. Dreher, Y., Jahnke, K., Bobkova, E., Spatz, J. P. & Göpfrich, K. Division and Regrowth of Phase-Separated Giant Unilamellar Vesicles. *Angewandte Chemie* **133**, 10756–10764 (Mar. 2021).
94. Folkman, J. & Moscona, A. Role of cell shape in growth control. *Nature* **273**, 345–349 (June 1978).
95. McBeath, R., Pirone, D. M., Nelson, C. M., Bhadriraju, K. & Chen, C. S. Cell Shape, Cytoskeletal Tension, and RhoA Regulate Stem Cell Lineage Commitment. *Developmental Cell* **6**, 483–495 (Apr. 2004).
96. Chen, C. S., Alonso, J. L., Ostuni, E., Whitesides, G. M. & Ingber, D. E. Cell shape provides global control of focal adhesion assembly. *Biochemical and Biophysical Research Communications* **307**, 355–361 (July 2003).
97. Kron, S. J. & Spudich, J. A. Fluorescent actin filaments move on myosin fixed to a glass surface. *Proceedings of the National Academy of Sciences* **83**, 6272–6276 (Sept. 1986).

98. Krawczyk, W. S. A pattern of epidermal cell migration during wound healing. *Journal of Cell Biology* **49**, 247–263 (May 1971).
99. Yamazaki, D., Kurisu, S. & Takenawa, T. Regulation of cancer cell motility through actin reorganization. *Cancer Science* **96**, 379–386 (July 2005).
100. Scopes, R. K. *Protein Purification* (Springer New York, 1994).
101. Rigaud, J.-L. & Lévy, D. in *Methods in Enzymology* 65–86 (Elsevier, 2003).
102. Yehl, K. *et al.* High-speed DNA-based rolling motors powered by RNase H. *Nature Nanotechnology* **11**, 184–190 (Jan. 2015).
103. Bazrafshan, A. *et al.* Tunable DNA Origami Motors Translocate Ballistically Over Micrometer Distances at nm/s Speeds. *Angewandte Chemie International Edition* **59**, 9514–9521 (Apr. 2020).
104. Shin, J.-S. & Pierce, N. A. A Synthetic DNA Walker for Molecular Transport. *Journal of the American Chemical Society* **126**, 10834–10835 (Aug. 2004).
105. Yin, P., Yan, H., Daniell, X. G., Turberfield, A. J. & Reif, J. H. A Unidirectional DNA Walker That Moves Autonomously along a Track. *Angewandte Chemie International Edition* **43**, 4906–4911 (Sept. 2004).
106. Olivi, L. *et al.* Towards a synthetic cell cycle. *Nature Communications* **12** (July 2021).
107. Pollard, T. D. Actin and Actin-Binding Proteins. *Cold Spring Harbor Perspectives in Biology* **8**, a018226 (Mar. 2016).
108. Roux, A. *et al.* A minimal system allowing tubulation with molecular motors pulling on giant liposomes. *Proceedings of the National Academy of Sciences* **99**, 5394–5399 (Apr. 2002).
109. Leduc, C. *et al.* Cooperative extraction of membrane nanotubes by molecular motors. *Proceedings of the National Academy of Sciences* **101**, 17096–17101 (Nov. 2004).
110. Koster, G., VanDuijn, M., Hofs, B. & Dogterom, M. Membrane tube formation from giant vesicles by dynamic association of motor proteins. *Proceedings of the National Academy of Sciences* **100**, 15583–15588 (Dec. 2003).
111. Vilfan, A. Ensemble velocity of non-processive molecular motors with multiple chemical states. *Interface Focus* **4**, 20140032 (Dec. 2014).
112. Sitarska, E. & Diz-Muñoz, A. Pay attention to membrane tension: Mechanobiology of the cell surface. *Current Opinion in Cell Biology* **66**, 11–18 (Oct. 2020).
113. Zhang, S. *et al.* Engineering motile aqueous phase-separated droplets via liposome stabilisation. *Nature Communications* **12** (Mar. 2021).
114. Ghosh, S. *et al.* Motility of Enzyme-Powered Vesicles. *Nano Letters* **19**, 6019–6026 (Aug. 2019).
115. Bartelt, S. M., Steinkühler, J., Dimova, R. & Wegner, S. V. Light-Guided Motility of a Minimal Synthetic Cell. *Nano Letters* **18**, 7268–7274 (Oct. 2018).

116. Andexer, J. N. & Richter, M. Emerging Enzymes for ATP Regeneration in Biocatalytic Processes. *ChemBioChem* **16**, 380–386 (Jan. 2015).
117. Kleineberg, C. *et al.* Light-Driven ATP Regeneration in Diblock/Grafted Hybrid Vesicles. *ChemBioChem* **21**, 2149–2160 (Apr. 2020).
118. Litschel, T. & Schwille, P. Protein Reconstitution Inside Giant Unilamellar Vesicles. *Annual Review of Biophysics* **50**, 525–548 (May 2021).
119. Walter, J. M., Greenfield, D., Bustamante, C. & Liphardt, J. Light-powering *Escherichia coli* with proteorhodopsin. *Proceedings of the National Academy of Sciences* **104**, 2408–2412 (Feb. 2007).
120. Shevchenko, V. *et al.* Inward H<sup>+</sup> pump xenorhodopsin: Mechanism and alternative optogenetic approach. *Science Advances* **3** (Sept. 2017).
121. Green, L. N. *et al.* Autonomous dynamic control of DNA nanostructure self-assembly. *Nature Chemistry* **11**, 510–520 (Apr. 2019).
122. Gerling, T., Wagenbauer, K. F., Neuner, A. M. & Dietz, H. Dynamic DNA devices and assemblies formed by shape-complementary, non-base pairing 3D components. *Science* **347**, 1446–1452 (Mar. 2015).
123. Bertosin, E. *et al.* A nanoscale reciprocating rotary mechanism with coordinated mobility control. *Nature Communications* **12** (Dec. 2021).
124. Cha, T.-G. *et al.* A synthetic DNA motor that transports nanoparticles along carbon nanotubes. *Nature Nanotechnology* **9**, 39–43 (Dec. 2013).
125. Bandara, H. M. D. & Burdette, S. C. Photoisomerization in different classes of azobenzene. *Chem. Soc. Rev.* **41**, 1809–1825 (2012).
126. Beharry, A. A. & Woolley, G. A. Azobenzene photoswitches for biomolecules. *Chemical Society Reviews* **40**, 4422 (2011).
127. Cáceres, R., Abou-Ghali, M. & Plastino, J. Reconstituting the actin cytoskeleton at or near surfaces in vitro. *Biochimica et Biophysica Acta (BBA) - Molecular Cell Research* **1853**, 3006–3014 (Nov. 2015).
128. Yao, G. *et al.* Meta-DNA structures. *Nature Chemistry* **12**, 1067–1075 (Sept. 2020).
129. Mangione, M. C. & Gould, K. L. Molecular form and function of the cytokinetic ring. *Journal of Cell Science* **132** (June 2019).
130. Urban, M. J. *et al.* Gold nanocrystal-mediated sliding of doublet DNA origami filaments. *Nature Communications* **9** (Apr. 2018).
131. Zhan, P., Both, S., Weiss, T. & Liu, N. DNA-Assembled Multilayer Sliding Nanosystems. *Nano Letters* **19**, 6385–6390 (Aug. 2019).
132. Steinkühler, J. *et al.* Controlled division of cell-sized vesicles by low densities of membrane-bound proteins. *Nature Communications* **11** (Feb. 2020).
133. Dong, R. *et al.* DNA origami patterning of synthetic T cell receptors reveals spatial control of the sensitivity and kinetics of signal activation. *Proceedings of the National Academy of Sciences* **118**, e2109057118 (Sept. 2021).



134. Jia, S. *et al.* Growth and site-specific organization of micron-scale biomolecular devices on living mammalian cells. *Nature Communications* **12** (Sept. 2021).
135. Schoenit, A. *et al.* Tuning Epithelial Cell–Cell Adhesion and Collective Dynamics with Functional DNA-E-Cadherin Hybrid Linkers. *Nano Letters* **22**, 302–310 (Dec. 2021).
136. Geary, C., Grossi, G., McRae, E. K. S., Rothmund, P. W. K. & Andersen, E. S. RNA origami design tools enable cotranscriptional folding of kilobase-sized nanoscaffolds. *Nature Chemistry* **13**, 549–558 (May 2021).
137. Jumper, J. *et al.* Highly accurate protein structure prediction with AlphaFold. *Nature* **596**, 583–589 (July 2021).
138. Zadeh, J. N. *et al.* NUPACK: Analysis and design of nucleic acid systems. *Journal of Computational Chemistry* **32**, 170–173 (Nov. 2010).

## Acknowledgements

First and foremost I want to thank my supervisor Kerstin Göpfrich for all the exciting and successful years that we have been working together. Her positive attitude, dedication and passion for her work have made me the scientist I am today. I am and will always be extremely grateful for calling her my mentor and admire her scientific curiosity. Thank you for allowing me to work alongside you for all those years and for jump-starting my academic career.

I also want to thank my committee members Prof. Michael Hausmann, Prof. Norbert Frank and Prof. Tilman Plehn for evaluating my work and taking their time for my scientific progress. I am especially content to have Prof. Michael Hausmann in my committee, whose lectures and group drove me towards the field of experimental biophysics.

Next, I want to thank all collaborators that I have had the pleasure to work with in the past. Among others these include Dr. Noah Ritzmann, Prof. Daniel Müller, Dr. Maxim Igaev, Prof. Helmut Grubmüller, Dr. Pengfei Zhan, Prof. Na Liu, Dr. Elisa D'Este, Ulrike Mersdorf, PD Dr. Ada Cavalcanti-Adam, Dr. Ilia Platzman and Prof. Joachim Spatz. I want to especially highlight the constant input and support by Ilia and Joachim, which has always helped me to grow scientifically and personally.

Another essential part of my work was the supervision of and collaboration with great students. I am very happy to have worked with so many gifted and talented researchers over the years and am grateful for their contribution to this work. In particular these include Anna Nitschke, Julius Fichtler, Tobias Abele, Mai Tran, Stefan Maurer, Vanessa Huth, Marlene Scheffold, Tobias Walther and Maja Illig - thank you all very much! In this regard, I also want to express my gratitude for the whole Biophysical Engineering Group and the Cellular Biophysics Department. They always made it fun to go to work and I am happy to have found these great colleagues and friends. I also want to thank Dr. Barbara Haller, Dr. Christoph Frey, Dr. Marian Weiss, Martin Schröter, Yannik Dreher, Dr. Oskar Staufer, Jochen Hernandez-Bücher and Cornelia Weber for their continuous support and investment that shaped my time and the environment at the MPI.

Finally, on a more personal note, I want to thank my friends and family for their constant motivation and for keeping up the good mood - also in difficult times. The weekly hikes with Thomas, Johannes, Lukas and Jakob were a great compensation for any working day and their opinions, comments and remarks were always helpful and insightful. I would not want to miss them!

I also want to thank my mom and dad for always believing in me and enabling me to pursue my dreams without ever holding me back. Your support allowed me to follow my academic path and I know that I can always count on you.

Lastly, I want to express my gratitude for Silvia. You have been with me since the start and witnessed all the good and bad, exhausting and exciting as well as sad and cheerful moments of my PhD. Still, you have always been there for me, had an open ear for me and supported me in any way you could. I thank you from the bottom of my heart for being this loving and caring person.